

**Exploring hearing loss and plastic adjustments
in the dorsal cochlear nucleus**

Thesis submitted for the degree of
Doctor of Philosophy
at the University of Leicester

Nadia Pilati

Department of Cell Physiology and Pharmacology
University of Leicester

August 2009

Exploring hearing loss and plastic adjustments in the dorsal cochlear nucleus

Nadia Pilati

Acoustic over exposure (AOE) triggers hearing loss and tinnitus but cellular mechanisms underlying those auditory defects are still poorly understood. This thesis explores the changes of excitability produced by AOE in identified cells of the rat dorsal cochlear nucleus (DCN) within the auditory brainstem. A development of a method combining Golgi silver impregnation with Nissl staining allowed study of the morphology and the distribution of the main DCN neuronal subtypes within slices containing the DCN. Whole cell patch clamp recordings allowed characterisation of the distinctive electrophysiological properties of the main DCN neuronal subtypes. *In vitro* stimulations of auditory or multisensory synaptic inputs showed fundamental differences in terms of the principal neurones firing pattern and the role of inhibitory synaptic transmission on firing pattern.

Wistar rats were exposed to loud (110 dB SPL) single tones (15 kHz) for a period of 4 hours (protocol of AOE). Non invasive auditory brainstem response recordings were performed after 3 to 4 days and showed a significant increase of the rat's hearing threshold for frequencies above 8 kHz. Whole cell recordings performed at a similar time (3 to 4 days) after AOE, showed that AOE led to a change of the passive and the active properties of DCN interneurons and principal cells. AOE also decreased the general excitability of the cellular network and affected differently excitatory and inhibitory synaptic transmission onto principal neurones depending on whether multisensory or auditory synaptic inputs were stimulated. Computational modelling allowed simulation of the effects of AOE on principal cell firing patterns and elaboration of a general theory whereby AOE triggers shifts of hearing thresholds concomitant with plastic adjustments in the DCN network.

In conclusion, an elevation of the hearing threshold accompanied by significant excitability changes within the central auditory system could represent fundamental steps towards the development of tinnitus.

ACKNOWLEDGMENTS

I would first like to thank my supervisor Dr. Martine Hamann for her encouragement and for all the knowledge and motivation that she gave me during these three years at the University of Leicester. In particular, I would like to thank her for her enormous support during the writing up period. Secondly, I would like to thank my industrial supervisor Dr. Charles Large for his excellent support and for all the stimulating discussions.

My thanks also go to the head of the Department, Dr. Blair Grubb, for his encouragement and advice.

Part of the work of this thesis was possible thanks to Dr. Mike Mulheram who provided the equipment for the *in vivo* studies. I would also like to thank Dr. Mike Mulheram for his help and advice throughout these three years.

Many thanks go to Dr. Revers Donga for being very supportive and for helping me to put things into perspective.

I would like to express my gratitude to Dr. Margaret Barnes Davies and Professor James Kaltenbach for examining this thesis.

Thanks to Dr. Matias Ison for his help with the modelling study and to Matt Barker for his help in the lab.

I acknowledge GlaxoSmithKline and Medisearch for funding this project. A special thanks also goes to the Biomedical Unit of the University of Leicester for the assistance that they provided during my *in vivo* experiments.

Thanks to all my friends in the Department, particularly to Ria, Alistair and Marianne that make me feel like I was home here in England and Emanuele for being a great housemate. Thank to Nicoletta and David for all their support, even if they were far away I felt like they were here.

Finally I want to thank my parents for always believing in me and giving me the strength to overcome all the difficulties. Thanks to my boyfriend for his enormous patience and all the love that he has given me.

TABLE OF CONTENT

CHAPTER 1

The auditory system: The importance of studying plastic changes

1.1. Transmission of the acoustic information	2
1.1.1. Synaptic transmission along the peripheral auditory pathway	2
1.1.2. Synaptic transmission along the central auditory pathway	6
1.2. Sound localization in the horizontal plane	11
1.2.1. Role of the medial nucleus of trapezoid body	11
1.2.2. Role of the lateral superior olive	12
1.2.3. Role of the medial superior olive	12
1.3.1. The DCN, a “cerebellum like” auditory circuit	16
1.3.2. Integration of acoustic signals within the dorsal cochlear nucleus	21
1.3.2. Integration of multisensory signals within the dorsal cochlear nucleus	24
1.3.2.1. Role of trigeminal projections	24
1.3.2.2. Role of dorsal column nuclei projections	26
1.3.2.3. Role of pontine nuclei projections	27
1.3.2.4. Role of vestibular projections	28
1.3.2.5. Role of raphe nuclei projections	28
1.4. Peripheral and central damage in the auditory system	29
1.5. Synaptic plasticity in the dorsal cochlear nucleus	33

CHAPTER 2

Material and Methods

2.1. Morphological studies	36
2.1.1. Study of the DCN cytoarchitecture	36
2.1.1.1. Fixation and cresyl violet staining	36
2.1.1.2. Analysis of the cell density and labelled cell body areas	37
2.1.2. Morphological studies	37
2.1.2.1. Principles of the Golgi method	37
2.1.2.2. Fixation and Golgi staining	39
2.1.2.3. Specific and non-specific staining	40
2.1.3. Study of the DCN cytoarchitecture and cellular morphology	41

2.1.4. Tri-dimensional reconstruction of the cochlear nucleus	41
2.1.5. Image acquisition and processing	42
2.2. Patch clamp recordings on slices	43
2.2.1. Preparation of slices	43
2.2.1.1. Dissection	43
2.2.1.2. Slicing	43
2.2.2. Cell identification	44
2.2.3. Electrophysiological setup	46
2.2.4. Differential interface contrast and fluorescence microscopy	47
2.2.5. Perfusion of solutions	47
2.2.6. Electrodes	48
2.2.6.1. Recording electrode	48
2.2.6.2. Stimulating electrode	48
2.2.7. Whole cell recordings using the patch clamp technique	48
2.2.7.1. The current clamp method	50
2.2.7.2. The voltage clamp method	51
2.2.7.3. Intracellular solutions	52
2.2.7.4. The liquid junction potential	53
2.2.8. Data acquisition and analysis	54
2.2.8.1. The membrane resistance	54
2.2.8.2. The membrane capacitance	55
2.2.8.3. The equilibrium potential	56
2.2.8.4. The resting potential	57
2.2.8.5. Properties of the action potential	57
2.2.8.6. Synaptic transmission	59
2.2.9. Statistics	61
2.2.11. Modelling studies	63
2.3. Auditory brainstem response recordings and acoustic over-exposure	65
2.3.1. Use of anesthetics	65
2.3.1.1. Isoflurane	65
2.3.1.2. Hypnorm® and Hypnovel®	65
2.3.1.3. Ketamine and xylazine	67

2.3.2. Auditory brainstem response recording	67
2.3.2.1. The auditory brainstem response	67
2.3.2.2. The recording setup	68
2.3.2.3. The auditory brainstem response recording procedure	69
2.3.2.4. Analysis	69
2.3.2.5. Calibration of the acoustic driver	69
2.3.3. Acoustic over-exposure	70

CHAPTER 3

The dorsal coclear nucleus: Cytoarchitecture and cellular morphology

Introduction	99
3.1. The model of Lister Hooded rat	99
3.2. DCN cytoarchitecture and cell types	101
Results	102
3.3. Cytoarchitecture and cell types in the DCN	102
3.3.1. DCN localization and cytoarchitecture	102
3.3.2. DCN cell labelling	104
3.3.3. Combined cytoarchitecture and cell type labelling	106
3.3.4. Characterization of cell types and distribution within the cell layers	110
3.4. Granule cell domains and reconstruction of the DCN	112
3.4.1. Granule cell domains in the DCN	112
3.4.2. Three-dimensional reconstruction of the dorsal cochlear nucleus	113
Discussion	114
3.5. A combined Golgi and Nissl study of the DCN	114
3.5.1. Cell labelling using the rapid the Golgi method	114
3.5.2. Cytoarchitecture labeling using cresyl violet staining	115
3.5.3. Estimation of the cell soma surface area	116
3.5.4. Laminar distribution of cell types	117

CHAPTER 4

Electrophysiological properties of dorsal cochlear nucleus neurones

Introduction	130
---------------------	------------

4.1. Role of intrinsic cellular excitability in a network	130
Results	133
4.2. Electrophysiological properties of identified cells of the dorsal cochlear nucleus	133
4.2.1. Passive properties	133
4.2.2. Properties of the action potentials	135
4.2.3. Firing frequency at different membrane potentials	136
4.2.4. Firing frequency in relation to step currents	142
Discussion	147
4.3. Electrophysiological properties of DCN neurons	147
4.3.1. Passive properties of DCN neurons	147
4.3.2. Modulation of firing activities of DCN neurones	149
4.3.3. Could DCN cellular excitability be affected by acoustic over-exposure?	151
4.3.4. Specific roles for the different cell types in the DCN network?	152

CHAPTER 5

Effect of acoustic over-exposure on auditory brainstem responses

Introduction	188
5.1. The effects of acoustic over-exposure on the auditory system	188
Results	190
5.2. Effect of acoustic over-exposure on the auditory brainstem responses	190
5.2.1. Auditory brainstem responses in Lister Hooded rats	190
5.2.2. Auditory brainstem responses in Wistar rats	192
5.2.3. Effect of acoustic over-exposure on the ABR threshold	192
5.3. Effect of acoustic over-exposure on the auditory brainstem response recordings	195
5.3.1. Difference in the ABR thresholds between different rat strains	195
5.3.2. ABR threshold in Wistar rats	197
5.3.3. Effects of acoustic over-exposure on ABR thresholds	197
5.3.4. ABR threshold shifts and tinnitus	199

CHAPTER 6

Effect of acoustic over-exposure on cellular excitability and synaptic transmission

Introduction	210
6.1. Acoustic over-exposure and homeostatic plasticity	210
Results	215
6.2. Effects of acoustic over-exposure	215
on dorsal cochlear nucleus intrinsic cellular excitability	215
6.2.1. Effect of acoustic over-exposure on granule cell excitability	216
6.2.1.1. Effects on granule cell passive properties	216
6.2.1.2. Absence of effect on granule cell action potentials	216
6.2.1.3. Absence of effect on granule cell firing at steady membrane potentials	218
6.2.1.4. Effects on granule cell firing with step potentials	219
6.2.2. Effects of acoustic over-exposure on fusiform cell excitability	223
6.2.2.1. Effects on fusiform cell passive properties	223
6.2.2.2. Acoustic over-exposure generates bursts in fusiform cells	223
6.2.2.3. Acoustic over-exposure decreases the firing frequency of fusiform cells while performing step currents	233
6.3. Effects of acoustic over-exposure on synaptic transmission in the dorsal cochlear nucleus	237
6.3.1. Stimulation of multisensory and auditory inputs	237
6.3.1.1. Post-synaptic responses evoked by stimulating multisensory inputs	238
6.3.1.2. Post-synaptic responses evoked by stimulating auditory inputs	242
6.3.1.3. Post-synaptic currents recorded in voltage clamp	249
6.3.2. Effect on multisensory and auditory synaptic transmission	251
6.3.2.1. Effects on multisensory synaptic transmission	251
6.3.2.2. Effect on auditory synaptic transmission	255
6.4. Effects on fusiform cell firing frequency and reliability	261
6.4.1. Fusiform cell responses to train stimulations	261
6.4.1.1. Responses to train stimulations of the multisensory inputs	261
6.4.1.2. Responses to train stimulations of the auditory inputs	265

6.4.2. Effects of acoustic over-exposure on responses to stimuli trains	267
6.4.2.1. Effect on the responses evoked by multisensory input stimuli	267
6.4.2.2. Effects on the responses evoked by auditory input stimuli	270
6.4.3. An Integrate and fire model to simulate the experimental data	273
Discussion	279
6.5. DCN cellular excitability in Lister Hooded and Wistar rats	279
6.6. Effects of acoustic over-exposure	280
on dorsal cochlear nucleus intrinsic cellular excitability	280
6.6.1. Acoustic over-exposure changed granule cell passive properties	281
6.6.2. Exploring the possibility of two pore potassium channel modulation	283
6.6.3. Granule cell high membrane resistance underlies their firing gain	287
6.6.4. Granule cell firing gain: effects on fusiform cell excitability?	290
6.6.5. Acoustic over exposure triggers bursts in fusiform cells	291
6.7. Effects of acoustic over-exposure on synaptic transmission	296
6.7.1. Excitatory synaptic transmission onto fusiform cells	296
6.7.2. Characteristics of the evoked action potentials	298
6.7.3. Inhibitory synaptic transmission onto fusiform cells	300
6.7.4. Inhibition ensures spike timing precision	303
6.7.5. Synaptic integration and modulation of fusiform cell firing rate	306
6.7.6. Functional role of the DCN in the auditory system	309
6.7.7. Importance of the excitatory and inhibitory synaptic transmission	311
6.7.8. Effects of acoustic over-exposure on the excitatory transmission	311
6.7.9. Effects of acoustic over-exposure on the inhibitory transmission	315
6.7.10. Effect of acoustic over-exposure on spike timing in fusiform cells	317
6.7.11. Effects of acoustic over-exposure on the synaptic integration	319
6.7.12. Homeostatic plasticity in the DCN neuronal network	322
6.7.13. Conclusions: Homeostatic plasticity, a role in tinnitus?	325
Appendix I: Abbreviations	382
Appendix II: Source of chemicals	384
Appendix III: A Rapid Method Combining Golgi and Nissl Staining to Study Neuronal Morphology and Cytoarchitecture	385
References	398

CHAPTER 1

The auditory system:

**The importance of studying
plastic changes**

The aim of this PhD was to investigate the effect of acoustic over-exposure on the cellular excitability of dorsal cochlear nucleus neurones. The dorsal cochlear nucleus is an auditory structure that lies in the brainstem and receives acoustic information directly from the cochlea and multiple inputs from various other sources. In this chapter I will first described the process of sound transduction and then mention hearing disorders affecting peripheral or central auditory structures. I will finally describe the dorsal cochlear nucleus, its synaptic circuitry and its role in the integration of auditory and non-auditory information.

1.1. Transmission of the acoustic information

1.1.1. Synaptic transmission along the peripheral auditory pathway

Sound enters the auditory canal in the outer ear as a mechanical energy, producing a vibration of the tympanic membrane. This mechanical wave is subsequently carried along

the three ossicles (malleus, incus and stapes) (middle ear) into the fluid-filled cochlea (inner ear) where it is converted into action potentials (figure 1.1). The electrical transduction of the sound waves takes place within the organ of Corti of the cochlea that contains inner and outer hair cells

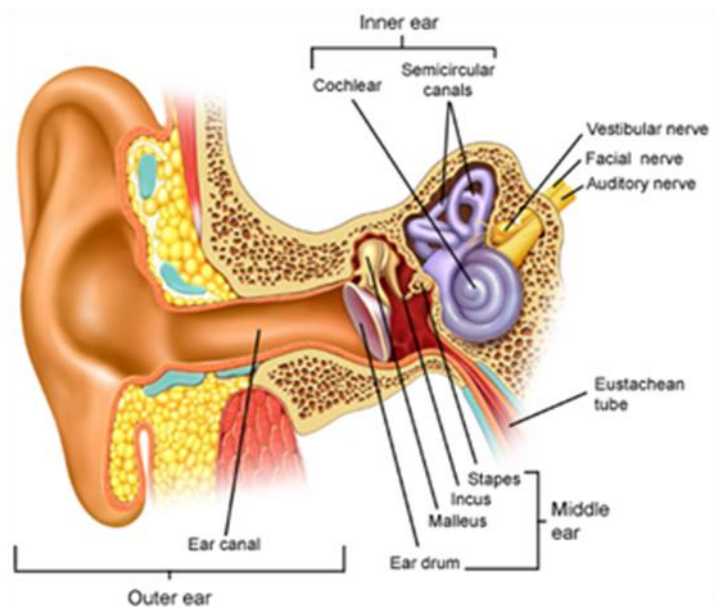


Figure 1.1 Anatomy of the human ear. Section of the human ear showing the outer ear, the middle ear and the inner ear. From: <http://www.virtualmedicalcentre.com/>

lying on a thin basilar membrane and covered by the tectorial membrane. The inner hair cells form a single row of cells that covers the full length of the cochlea. These cells are innervated by the myelinated spiral ganglion cells also called type I primary auditory neurons, which represent more than 90% of the total population of the spiral ganglion cells (Berglund and Ryugo, 1987; Brown, 1987; Echteler, 1992). The type I primary auditory neurons projections terminate in the cochlear nucleus within the central auditory system. The inner hair cells therefore dominate the acoustic inputs to the auditory nerve and this explains their principal role in the transduction of the acoustic signals into neuronal signals. The neurotransmitter released by the sensory inner hair-cells is glutamate (Puel, 1995) and RT-PCR and immunocytochemical studies reported the presence of different glutamate receptors in type I primary auditory neurons: NMDA receptors (NR1 and NR2A-D subunits), AMPA receptors (GluR2-4 subunits) and kainate receptors (GluR5, GluR6, KA1 and KA2 subunits) (Safieddine and Eybalin, 1992; Kuriyama et al., 1993; Niedzielski and Wenthold, 1995; Puel, 1995; Matsubara et al., 1996).

The outer hair cells are organized in three rows that run parallel to the inner cells. Outer hair cells are contacted postsynaptically by unmyelinated spiral ganglion cells also called type II primary auditory neurons that represent only a small percentage of the total primary auditory neuron population (Berglund and Ryugo, 1987; Brown, 1987; Echteler, 1992). The outer hair cells are mainly involved in amplifying the sound within the cochlea which is then transduced by the inner hair cells. Electrical stimulation of individual outer hair cells dissociated from the cochlea reported that those cells respond with an elongation when hyperpolarized and a shortening when depolarized (Brownell

et al., 1985; Ashmore, 1987, Gale and Ashmore, 1997). This ability is due to the motor protein prestin, a membrane protein permeable to the anions chloride and bicarbonate that belong to a family of anion transporters (SLC26) (Dallos et al., 1991, Kalinec et al., 1992; Zheng et al., 2000). Prestin is highly expressed in the outer hair cell (Zheng et al., 2000; 2002). When a positive stimulus deflects the hair bundle, the outer hair cell is depolarized and chloride ions dissociate from prestin, leading to conformational changes that reduce its cell surface area and cause its shortening. A negative stimulus will provoke cell hyperpolarization that promotes the binding of intracellular chloride ions to prestin and causes cell elongation (Oliver et al., 2001). Prestin is essential for the electromotility of the outer hair cells and for the cochlear amplifier. Studies on mutant mice that express a small level of prestin have shown a loss of outer hair cells electromotility and a reduction in the cochlear sensitivity, without any effect on the mechano-electrical transduction in outer hair cells (Liberman et al., 2002).

Both inner and outer hair cells are characterized by mechanosensing organelles called stereocilia, themselves organized into a hair bundle (hexagonal array of about 50-100 stereocilia projecting perpendicularly from the apical cellular surface, Hudspeth, 1989; 2005). Because the stereocilia's length varies across the surface of the cells, a hair bundle appears as a sloping structure with its length increasing from the left to the right edge (Hudspeth, 1989; 2005). A few molecular filaments called tip links connect the tip of one stereocilium to the side of the longest adjacent stereocilium (Tsuprun and Santi, 2002; Hudspeth, 2005). Mechanosensitive channels preferentially permeable to calcium (Ohmori, 1985) have a wide-diameter pore (Farris et al., 2004) and are present at one or both tip link ends. A small percentage of these channels are

open in resting conditions. Sound entering the cochlea moves the basilar membrane that will excite the hair cells by deflecting their hair bundles. Stimulus force that deflects the hair bundle towards its tall edge represents a positive stimulus that increases the tension in the tip link and provokes the opening of the mechanosensitive channels, allowing cation influx into the stereocilium cytoplasm and subsequent cellular depolarization (figure 1.2 below).

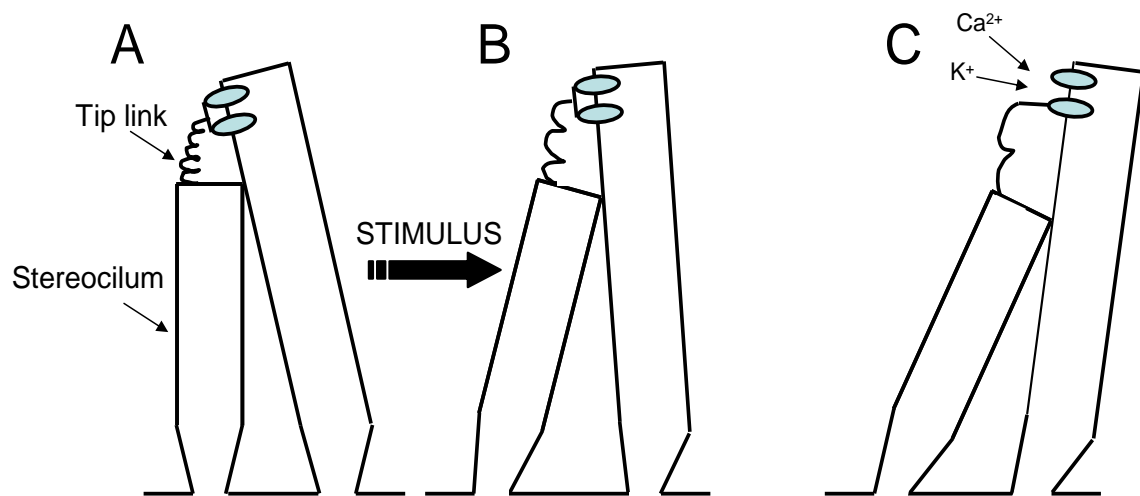


Figure 1.2. The mechano-electrical transduction. Schematic representation of the hair cell's stereocilium connected by tip links. **(A)** Under resting condition, most of the channels are closed. The elastic strand, (tip link) connects the tip of one stereocilium to the side of the longest adjacent stereocilium. The mechansensitive ion channel lies in the stereocilium and is gated by the tip link. **(B)** A stimulus force (positive stimulus) deflects the bundle towards its tall edge increasing the tension at the tip link. **(C)** The tension at the tip link promotes the channel opening and the consecutive influx of cations.

Movements of the hair bundle in the opposite direction (towards its short edge) reduce the tension of the tip links and close the channels that are opened at rest, resulting in a hyperpolarization of the cells. The depolarization, produced by the opening of the mechanosensitive channels, induces the opening of voltage-gated calcium channels (Tucker and Fettiplace, 1995) and subsequent exocytosis of glutamate that binds to its receptors (Kataoka and Ohmori, 1994) on the spiral ganglion cells.

The hair cells within the cochlea are tonotopically organized. There is a specific relationship between the position of the hair cells along the cochlea and the frequency at which they are most sensitive. Hair cells localized at the base of the cochlea are most sensitive to high frequency sound waves while hair cells localized at the apex of the cochlea are most sensitive to low frequency sound waves. Each auditory nerve fibre innervating the hair cell is in this way responsive to a particular sound frequency (characteristic frequency) and different set of fibres will therefore travel different auditory signals within the brain, preserving this frequency sensitivity within all the auditory structures of the auditory pathway. Hearing loss induced by mechanical lesion to the cochlea or by prolonged exposure to loud noise, or tinnitus, has been shown to lead to modifications in the tonotopic map within the primary auditory cortex (Willott et al., 1993; Muhlneckel et al., 1998; Eggermont and Komiya, 2000).

1.1.2. Synaptic transmission along the central auditory pathway

Acoustic signals coming from one (monaural) or both (binaural) ears leave the cochlea through spiral ganglion axons (composing the auditory nerve) to get further processed within the cochlear nucleus subdivided in two parts: the dorsal cochlear nucleus (DCN) and the ventral cochlear nucleus (VCN) (Osen, 1970). The VCN and the DCN are tonotopically organized with neurones located medially preferentially sensitive to high frequency sound waves and neurones located laterally preferentially sensitive to low frequency sound waves (Rose et al., 1960).

The ascending central auditory pathway is summarized in figure 1.3. The DCN sends contralateral projections to the inferior colliculus (IC) and to the medial geniculate nucleus (MNG). Different cells in the VCN send several

projections to: the contralateral IC, the bilateral medial superior olive (MSO), the contralateral medial nucleus of the trapezoid body (MNTB), the ipsilateral superior olivary nucleus (LSO) and to the nuclei of the lateral lemniscus (LL). The LL is a tract of axons in the brainstem that carries auditory inputs from the cochlear nucleus and from various brainstem nuclei (LSO, MNTB, ventral, intermediate and dorsal nuclei of the LL) and terminates to the IC (Adams, 1979a). The nuclei of the LL situated within the fibres of the LL are composed of the ventral, intermediate and dorsal nucleus of the LL. The ventral nucleus of the LL receives its main input from the octopus cells of the contralateral VCN (Adams, 1997a; Schofield and Cant, 1997) and sends inhibitory projections to the IC (Kelly et al. 1998; Zhao and Wu, 2001; Oertel and Wickesberg, 2002). The intermediate nucleus of the LL is innervated by the contralateral VCN and by the ipsilateral MNTB and projects to the IC (Kelly et al., 1998). The dorsal nucleus of the LL receives binaural projections from the MSO and the LSO (Elverland, 1978; Shneiderman et al., 1988) and provides contralateral projections to the opposite dorsal nucleus of the LL (Adams, 1979a) and bilateral inhibitory projections to the IC (Shneiderman and Oliver, 1989; Chen et al., 1999).

The inferior colliculus is a midbrain structure that integrates monaural and binaural auditory signals and is composed of three nuclei: the central nucleus, the dorsal nucleus and the external nucleus. The central nucleus of the IC integrates direct monaural projections from the DCN (Adams and Warr 1976; Oliver 1984) and indirect binaural projections from the MSO, the LSO and the dorsal nucleus of the LL (Stotler, 1953; Elverland, 1978; Adams, 1979; Kelly et al. 1998).

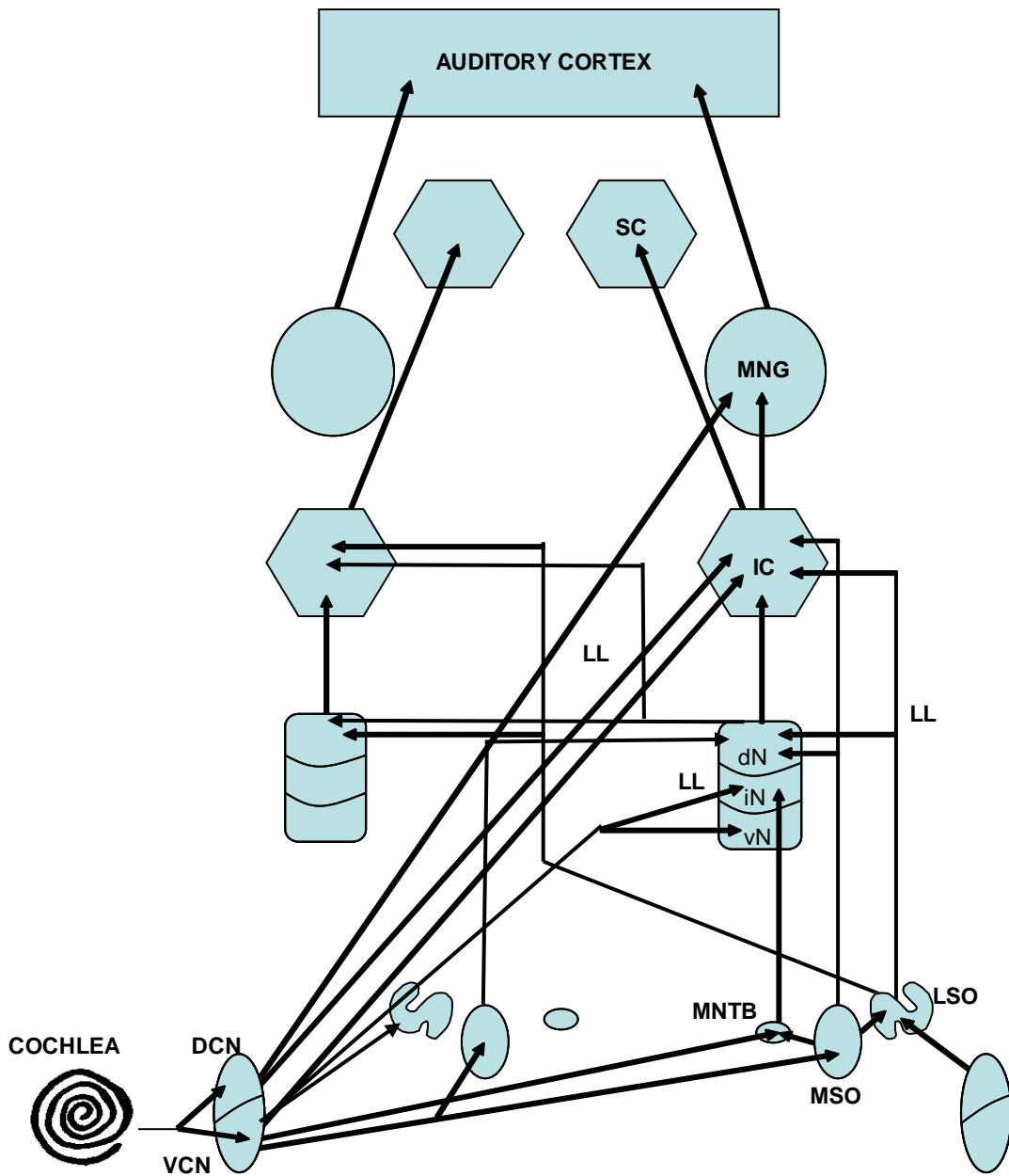


Figure 1.3. The ascending auditory pathway. Abbreviations: (DCN) dorsal cochlear nucleus, (VCN) ventral cochlear nucleus, (MSO) medial superior olive, (MNTB) medial nucleus of the trapezoid body, (LSO) lateral nucleus of the superior olivary complex, (LL) lateral lemniscus (LL), (dN) dorsal nucleus of the lateral lemniscus, (iN) intermediate nucleus of the lateral lemniscus, (vN) ventral nucleus of the lateral lemniscus, (IC) inferior colliculus, (MNG) medial geniculate nucleus, also called auditory thalamus, (SC) superior colliculus.

From the IC, a small portion of fibres reaches the superior colliculus while a large number of projections terminate in the medial geniculate nucleus (Kudo and Niimi 1980; Oliver and Hall 1978).

The superior colliculus is a laminated structure: the superficial layers receive visual sensory inputs while the deep layers receive inputs from both somatosensory and auditory sources (May, 2005). The neurones in the deep layers are organized to form topographical representation of the azimuthal dimension of auditory space (Palmer and King, 1982). Cells in the rostral regions are sensitive to sound stimuli originating from the front of the animal while cells in the caudal regions are more sensitive to sound stimuli originating from the rear.

The medial geniculate nucleus is part of the thalamus and lies in the midbrain. The nucleus is organized into a dorsal, ventral and medial part receiving projections from the IC (Andersen et al., 1980; Kudo and Niimi, 1980) and sending projections to the primary auditory cortex (Oliver and Hall, 1978; Willard and Ryugo, 1983). The ventral region of this nucleus is the only part that is tonotopically organized (Redies and Brandner, 1991).

The primary auditory cortex lies in the Sylvian fissure of the temporal lobe. Neurons in the auditory cortex are tonotopically organized: they are organized into two zones separated in alternating bands that extend perpendicular to the axis of the tonotopic map: the EE sensitive zones contain neurons that are excited by stimulation of either ear and the EI sensitive zones with neurones that are excited by unilateral inputs but inhibited by inputs from the opposite ear. The primary auditory cortex is surrounded by several areas

that are involved in the elaboration of particular types of auditory information and are essential for a more complex interpretation of sound.

Parallel to the ascending auditory pathway, there is a descending auditory pathway sending feedback projections from the central auditory system to the cochlea. The cochlea receives two types of inputs: *i*) inputs from the medial nuclei of the superior olivary complex (the medial olivocochlear pathway) that modulate the activity of the outer hair cells (Wiederhold, 1986; Warr et al., 1986; Puel, 1995). *ii*) inputs from the lateral nuclei of the superior olivary complex (the lateral olivocochlear pathway) that modulate the activity of the type I auditory nerve fibres innervating the inner hair cells (Warr et al., 1986; Puel, 1995). The medial olivocochlear projections have suppressive effects on cochlear sensitivity: activation of these fibres lead to a release of acetylcholine that binds to the $\alpha 9/ \alpha 10$ nicotinic receptor on the outer hair cells (Elgoyhen et al., 2001) leading to calcium entry and the activation of potassium channels (Housley and Ashmore, 1991) and to a reduction of the cochlear amplification via the outer hair cells. The lateral olivocochlear pathway releases acetylcholine (Felix and Ehrenberger, 1992), GABA (Arnold et al., 1998), opioid agonists (Sahley et al., 1991) and calcitonin gene related peptide (Bailey and Sewell, 2000) but the exact role of those transmitters is still unclear. It has been suggested that the release of the opioid dynorphin may be involved in the generation of tinnitus (Sahley et al., 1999). Dynorphin release is enhanced during episodes of physical or psychological stress and these episodes often result in the production or perception of tinnitus (Goldstein and Shulman, 1996; Nodar, 1996; Dobie and Sullivan, 1998). A possible mechanism is linked to dynorphin binding to NMDA receptors located on the type I auditory fibres,

potentiating the excitatory properties of glutamate (released by the inner hair cells) and leading to an altered neuronal excitability in the auditory nerve responsible for the generation of tinnitus.

1.2. Sound localization in the horizontal plane

The superior olivary complex comprises the MNTB, the MSO and the LSO and is involved in sound localization in the horizontal plane from its ability to process differences in sound timing and intensity between the two ears.

1.2.1. Role of the medial nucleus of trapezoid body

The medial nucleus of the trapezoid body (MNTB) sends glycinergic inhibitory projections to the ipsilateral LSO and MSO (Spangler et al., 1985; Adams and Mugnaini, 1990). The projections to the LSO provide information concerning the inter-aural level differences (ILD) (Boudreau and Tsuchitani, 1973; Tollin, 2003) while the inputs to the MSO neurons are involved in the analysis of the inter-aural time difference (ITD) (Brand et al., 2002; McAlpine and Grothe, 2003) (see below). MNTB neurones receive giant excitatory glutamatergic synapses from the contralateral globular bushy cells of the antero VCN, called the calyx of Held (Held, 1893; Lenn and Reese, 1966; Forsythe and Barnes-Davies, 1993). These giant synapses contain hundreds of active zones and thus a single presynaptic action potential releases hundreds of vesicular quanta generating a large EPSC principally mediated by the activation of AMPA receptors. Rapid depolarizations of MNTB neurons are responsible for a quick and accurate integration of the auditory signals which allows MNTB neurones to operate adequately during high-frequency signal transmission and preserve the timing of auditory signals (von Gersdorff and Borst, 2002; Schneggenburger and Forsythe, 2006).

1.2.2. Role of the lateral superior olive

Lateral superior olive (LSO) principal neurons detect inter-aural intensity differences or differences in the intensity of sound arriving at the two ears (Boudreau and Tsuchitani, 1973; Tollin, 2003). This characteristic is important for the localization of high-frequency sounds in the horizontal plane. These neurones are excited directly from spherical bushy cells of the ipsilateral aVCN and inhibited indirectly from the contralateral aVCN via MNTB neurones (Glendenning et al., 1985; Thompson and Thompson, 1987; 1991; Smith et al., 1993). In this way, LSO principal neurons integrate ipsilateral excitatory and contralateral inhibitory inputs and their response will depend on the strength and on the inter-pulse interval of the two inputs that are themselves related to the intensity of the sound stimulus (Boudreau and Tsuchitani, 1970; Sanes and Rubel, 1988; Sanes, 1990; Wu and Kelly, 1992). Inter-aural intensity differences processed by the LSO neurones are more accurate for high-frequency sounds (Tsuchitani, 1997) because the head absorbs short-wavelength sound better than long-wavelength sound. Additionally at high frequencies differences in inter-aural intensity result from reflection head shadow effects.

The principal output of the LSO reaches bilaterally the dorsal nucleus of the lateral lemniscus (Elverland, 1978) and the central nucleus of the inferior colliculus (Stotler, 1953; Adams, 1979a).

1.2.3. Role of the medial superior olive

The inter-aural time difference (ITD) is a primary cue for localizing low-frequency sounds in the horizontal plane (Goldberg and Brown, 1969) and is encoded by the MSO. A classical model for the detection of inter-aural timing differences has been outlined by Jeffress in 1948 and is summarized in figure

1.4. This neural mechanism has been described in avian nucleus laminaris neurons (Joseph and Hyson, 1993; Reyes et al., 1996) and in mammalian medial superior olive (MSO) neurons (Goldberg and Brown, 1969; Yin and Chan, 1990; Spitzer and Semple, 1995; Brand et al., 2002). However recent studies suggest that an ITD mechanism different from the Jeffress model might occur in mammals (McAlpine et al., 2001; McAlpine and Grothe, 2003).

According to this new theory the neural sensitivity to ITD is determined by the glycinergic inhibition of MNTB neurones onto MSO neurones rather than by a systematic arrangement of delay lines (figure 1.5.). It has indeed been shown that in the absence of these inhibitory inputs the axonal conduction delay is zero, in mammals (Brand et al., 2002).

The lateral position of the sound source is therefore determined by the activity of just two populations of cells, one on each side of the brainstem that is broadly tuned for ITD, and not by an array of cells sharply tuned to ITD. The inter-aural time difference information is sent from the MSO to the ipsilateral dorsal nucleus of the lateral lemniscus (Elverland, 1978) and to the central nucleus of the inferior colliculus (Stotler, 1953; Elverland, 1978) where they are integrated with other types of acoustic information.

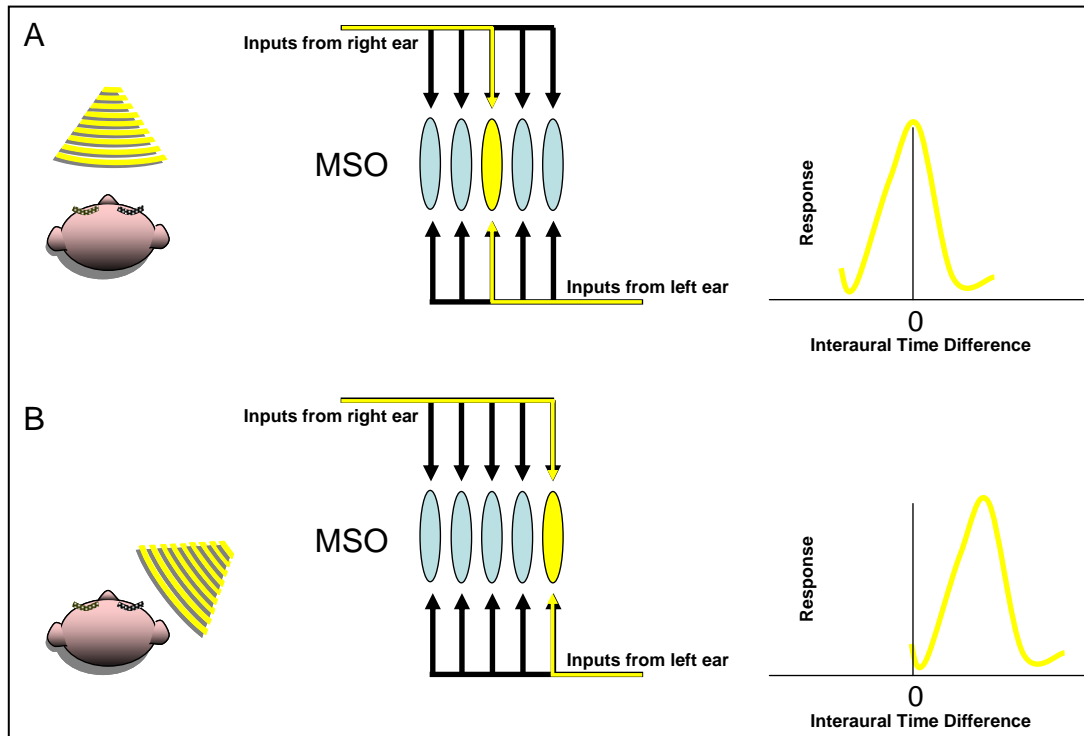


Figure 1.4. The coincidence detection model of Jeffress (1948). MSO neurones are bipolar neurones that receive excitatory inputs from both ipsilateral and contralateral aVCN onto their opposite dendrites, with the ipsilateral afferents terminating on the lateral dendrites and the contralateral afferents terminating on the medial dendrites (Stotler, 1953). A,B Centre: Five MSO cells are shown; each cells receives excitatory inputs from both left and right ear onto its opposite dendrites. The length of the innervating axons vary along the length of the nucleus, the longer axons will give longer latency responses. **(A)** (A,Left) Sound originates from a source in the midplane and will reach the two ears at the same time and ITD is equals to zero (A, centre). The labelled cell is the only cell that receives simultaneously inputs from the left and the right ear and therefore fires an action potential (right graph). This cell will only fire an action potential when the ITD is zero. Note that the axons innervating the cells have the same length. **(B)** (B, Left) Sound originates from a source near the right ear. (B, Centre) The labelled cell that receives the longest delay line response from the right ear and the shortest delay line response from the left ear is the only cell that receives an input from the right and the left ear simultaneously. The labelled cell fires an action potential (right graph), that is related to a certain ITD that is determined by the lateral position of the sound source. MSO neurones are in this way organized into a spatial array of cells, each tuned to different ITD. MSO neurones are more sensitive to low frequency sounds, because they analyze sound phase differences from both ears and when the sound frequency is high the wavelength becomes shorter and therefore the comparison becomes more difficult.

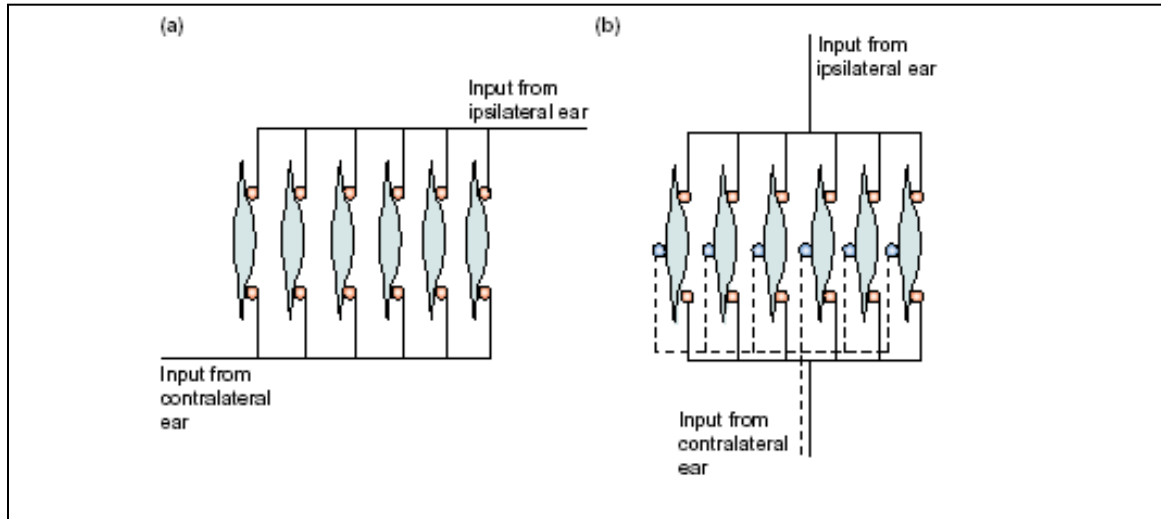


Figure 1.5. The potential model for ITD-sensitive neurons in mammals from McAlpine and Grothe (2003). **A.** In the absence of inhibitory inputs, axonal conduction delays are distributed around zero ITD, the axons innervating the MSO neurones have indeed the same length. **B.** Addition of glycinergic input from the contralateral ear (dotted lines) shifts the peaks of ITD functions towards longer ITDs.

1.3. Role of the DCN in sound localization and beyond

1.3.1. The DCN, a “cerebellum like” auditory circuit

The dorsal cochlear nucleus (DCN) has been reported to be a “cerebellum like” structure (Oertel and Young, 2004). Both structures are organized in cell layers with a similar cellular circuit (Oertel and Young, 2004). In rodents and cats, the DCN is organized in three cell layers, the molecular layer, the fusiform layer and the deep layer (figure 1.7, Osen, 1969; Browner and Baruch, 1982; Webster and Trune, 1982; Hackney et al., 1990; Alibardi, 2006):

The molecular layer is the superficial layer containing mainly the parallel fibres (the unmyelinated axons of the granule cells) that contact fusiform cell apical dendrites, cartwheel cell dendrites and stellate cell dendrites (Mugnaini et al., 1980a; Mugnaini, 1985). Like cerebellar stellate cells sending inhibitory projections onto Purkinje cells dendrites, stellate cells within the DCN send inhibitory projections onto fusiform and cartwheel cells (Osen et al., 1990). Cartwheel cells are considered to be the functional analogous of cerebellar Purkinje cells (Wouterlood and Mugnaini, 1984) as both cell types receive excitatory inputs from parallel fibres in the molecular layer (Weedman et al., 1996; Oertel and Young, 2004) and both cell types send inhibitory projections to the fusiform cells (for cartwheel cells) and the cerebellar nuclei (for Purkinje cells). Cartwheel cells and Purkinje cells contain the same calcium binding proteins like calbindin (Frisina et al., 1994; Caicedo et al., 1996) or cerebellin (Mugnaini and Morgan, 1987) and are similarly affected by genetic mutations (Lurcher or Stagger mutations) (Berrebi and Mugnaini, 1988). Both Purkinje cells and cartwheel cells can fire complex action potentials also called “bursts” which consist of brief clusters of high-frequency action potentials superimposed

on an underlying slow depolarization (Zhang and Oertel, 1993c; Manis et al., 1994; Oertel and Young, 2004; Kim and Trussel, 2007). Nevertheless, some differences exist as Purkinje cells are GABAergic neurones (Ito, 1984) while cartwheel cells are glycinergic neurones (Golding and Oertel, 1997). Cartwheel cells send also inhibitory projections onto other cartwheel cell and giant cell dendrites (Berrebi and Mugnaini, 1991; Golding and Oertel, 1997; Oertel and Young, 2004) whereas Purkinje cells have not been shown projecting onto other Purkinje cells or other cell types within the cerebellum. In addition, Purkinje cells are excited by climbing fibres and by the parallel fibres and send their projections to nuclei located outside the cerebellar cortex whereas cartwheel cells are only excited by the parallel fibres and terminate locally (projecting onto other DCN cells). Finally, Purkinje cells in the cerebellum form a layer of aligned cell bodies whereas cartwheel cells seem to be spreading at the interface between the molecular layer and the fusiform cell layer (Mugnaini, 1985).

The fusiform layer is occupied by fusiform cells and small clusters of granule cell domains (Osen, 1969; Mugnaini et al., 1980b; Browner and Baruch, 1982; Webster and Trune, 1982; Hackney et al., 1990; Alibardi, 2006). Fusiform cells are large bipolar, fusiform-shape neurons that send their apical dendrites into the molecular layer and their basal dendrites into the deep layer (Osen, 1969; Brawer et al., 1974). Based on a strict anatomical location, fusiform cells are the equivalent of the Purkinje cells as both cell types form the intermediate cell layer in the DCN and in the cerebellum respectively. Fusiform cells integrate auditory information (from the auditory nerve, Cohen et al., 1972; Fekete et al., 1984; Zhang and Oertel, 1994) and non-auditory information (from parallel fibres, Kane, 1974; Mugnaini et al., 1980b; Lorente de No, 1981; Hackney et al.,

1990). Fusiform cells represent the major output of the DCN, sending synaptic projections to the inferior colliculus (Adams and Warr, 1976; Oliver, 1984) and to the auditory thalamus also called MNG (Anderson et al., 2006).

The fusiform cell layer also contains granule cells that are the most numerous cells in the cochlear nucleus covering the whole external surface of the nucleus as well as expanding into its ventral and dorsal region (Mugnaini et al., 1980b). Granule cells are also the most numerous cells in the cerebellum, mainly located in the granule cell layer below the Purkinje cell layer (Hawkes and Mascher, 1995; Voogd et al., 1996). Granule cells in the DCN do not form a distinct layer like in the cerebellum; they are organized in small domains within the DCN and also within the VCN (Mugnaini et al., 1980b). Granule cells cover the lateral side of the VCN and also mark the medial border of the VCN and DCN. Granule cells are scattered along the cochlear nerve root with a sub-peduncular corner of granule cells also located ventral to the cerebellar peduncles at the dorsal edge of the VCN. A lamina of granule cells (so called granule cell lamina) also extends from the lateral (external) side towards the medial part of the cochlear nucleus thereby separating the VCN from the DCN. Granule cells are located at the dorsal side of the DCN and are scattered throughout the DCN fusiform and deep layer. The distribution of the granule cell domain in Lister Hooded rats has been investigated in chapter 3. As in the cerebellum, the granule cell domain is composed of granule cells, unipolar brush cells and Golgi cells (Mugnaini et al., 1980a, b; 1997). Together, these cells take part in the constitution of the glomerulus wrapped in glial processes (cerebellar glomerulus (Kane, 1974; Mugnaini et al., 1980a; Weedman et al., 1996). Figure 1.6 shows the glomerulus organization within the DCN

ovoidal cell body with 2-3 dendrites) (Mugnaini et al., 1980a; b; 1997,) and originate from the same embryonic tissue, the rhombic lip (Funfschilling and Reichardt, 2002). Moreover they are the only cells found to express the high affinity alpha 6 subunit of GABA-A receptors (Gutierrez et al., 1996).

The deep layer contains giant cells, tuberculoventral cells and granule cell domains (Zhang and Oertel 1993a, b; Mugnaini et al., 1997; Oertel and Young, 2004). Giant cells receive auditory signals from the auditory nerve (Cohen et al., 1972; Fekete et al., 1984) and send their axon to the inferior colliculus (Adams and Warr, 1976; Oliver, 1984) and to the contralateral cochlear nucleus (Cant and Gaston, 1982). Tuberculoventral cells receive information from the auditory nerve and the ventral cochlear nucleus (Oertel and Young, 2004; Rhode, 1999) and project inhibitory inputs to fusiform and giant cells (Oertel and Young, 2004; Zhang and Oertel, 1993).

In summary, the DCN and the cerebellum exhibit a similar composition of cells and a similar cellular architecture both organized into cell layers (the cytoarchitecture and the cell types are summarized in figure 1.7 below).

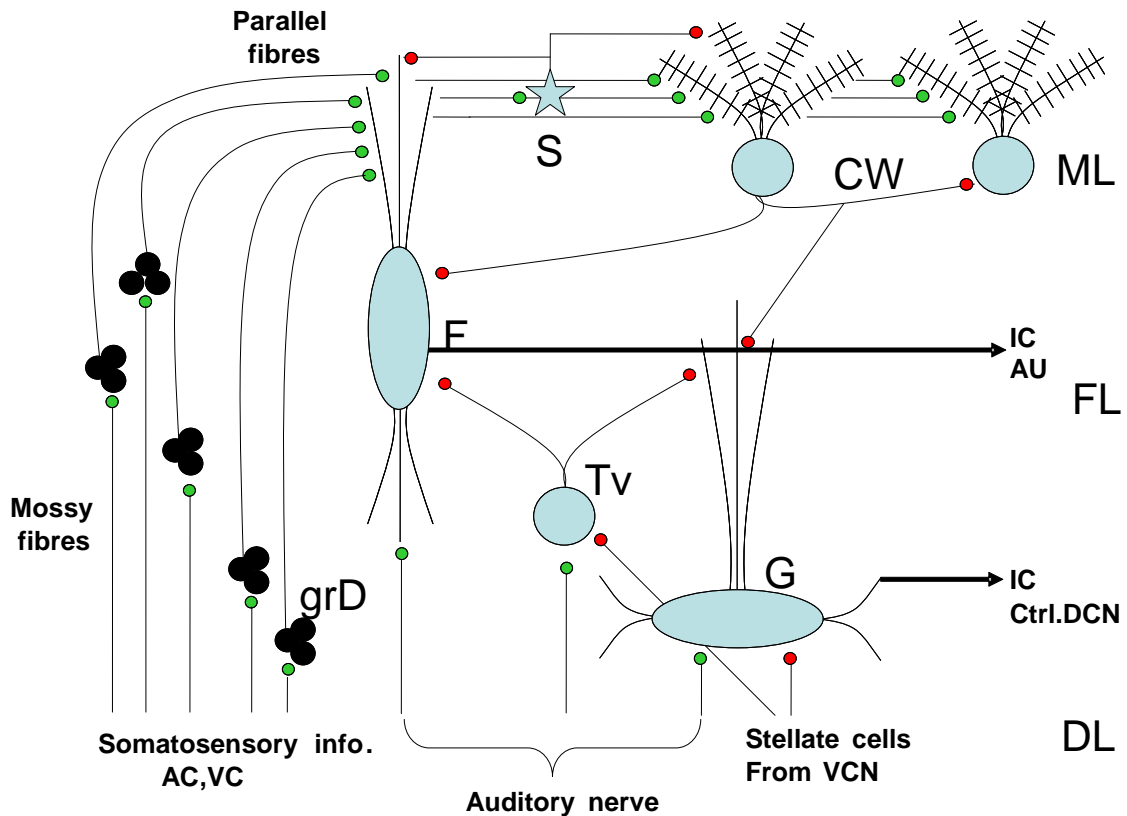


Figure 1.7. The cytoarchitecture of the DCN. Granule cells domains (grD) lie in small clusters in the deep layer (DL) and in the fusiform layer (FL). They are innervated from mossy fibers (somatosensory information) and from other structures of the brain: vestibular complex (VC); auditory cortex (AC). The axons of the granule cells form the parallel fibers in the molecular layer (ML) that excite stellate cell (S) and cartwheel cell (CW). S send inhibitory projection to fusiform cells (F) and to CW. CW inhibit other CW, F and giant cell (G). The two outputs of the DCN are F and G that project to the inferior colliculus (IC) and the auditory thalamus (AU) also called MNG and to the IC and the contralateral dorsal cochlear nucleus (ctrl. DCN) respectively. F and G cells are excited from the auditory nerve and inhibited from tuberculoventral (TV) cell. TV lie in the DL and receive inputs from the auditory nerve and from S of the ventral cochlear nucleus (VCN). S of VCN also inhibit G. Excitatory projections are in green and inhibitory in red. Figure adapted from Oertel and Young, 2004.

1.3.2. Integration of acoustic signals within the dorsal cochlear nucleus

The majority of the auditory nerve fibres (type I) terminate onto fusiform cells and giant cells (Cohen et al., 1972; Fekete et al., 1984; Zhang and Oertel, 1994). Auditory fibres that encode low frequency sounds innervate cells of the ventrolateral regions of the DCN while auditory fibres that encode high frequency sounds innervate cells of the dorsolateral regions of the DCN (Rose et al., 1960). In this way, fusiform and giant cells are arranged in sharply tuned

and tonotopically organized areas. Several *in vivo* electrophysiological studies have investigated the responses of both fusiform and giant neurones to acoustic stimulations (Evans and Nelson, 1973; Young and Brownell, 1976; Davis et al., 1996b). Both cells display variety of complex responses to pure-tone and noise stimuli (Evans and Nelson, 1973; Young and Brownell, 1976; Davis et al., 1996b). Evans and Nelson (1973) characterized five groups of neurones in the whole cochlear nucleus into (type I-V) according to their degree to which inhibition was elicited by single tones. Whereas the response type I involved no inhibition, the response type V was predominantly inhibitory. The intermediate types II, III and IV exhibited more complex responses depending on the frequency and the intensity of the tone (Evans and Nelson, 1973). Subsequent studies where intracellular single-unit recording were coupled to horseradish peroxidase and neurobiotin-marking techniques allowed establishing the relationships between the cell physiology and the cell morphology in the DCN (Ding and Voigt, 1997; Ding et al., 1999; Hancock and Voigt 2002).

The response type of a same cell was found to be different between different species (Ding and Voigt, 1997; Ding et al., 1999; Hancock and Voigt, 2002). In cats for example, fusiform and giant cells exhibited type IV responses (the response is mainly inhibitory over a wide band of frequencies with one or more excitatory frequency bands, Young, 1980). In gerbils, the majority of fusiform cells is associated with the type III response (the response is excitatory to best frequency tones with inhibition to one or more adjacent frequency sidebands, Ding et al., 1999) and giant cells are associated with the type IV responses (Ding et al., 1999). These studies were carried in un-anaesthetized animals as the response type was influenced by the presence of the

anaesthetics (Evans and Nelson, 1973; Ding and Voigt, 1997; Ding et al., 1999; Hancock and Voigt, 2002).

In the DCN, granule cells also receive auditory projections. Granule cells receive descending auditory signals from the auditory cortex (Weedman and Ryugo, 1996) as well as ascending auditory signals from the unmyelinated type II auditory nerve fibres (Brown et al., 1988; Brown and Ledwith, 1990; Berglund and Brown, 1994; Berglund et al., 1996; Benson and Brown, 2004). Compared to giant and fusiform cells, little is known about the response properties to sound of granule cells. The main reason is that their small size makes it difficult to record their activity with microelectrodes. The sensitivity of granule cells to sound was studied by Yang et al., (2005) who measured the expression of c-Fos (a nuclear regulatory protein that is related with the neuronal activity) in response to acoustic stimuli. The pattern of expression of c-Fos showed a tonotopical organization of the granule cell domains and suggested that these cells are characterized by a low threshold of activation and an activity that gets saturated at high sound intensity.

The DCN is thought to be involved in sound localization within the vertical plane by detecting specific spectral cues of sound spectra. When projections from the DCN to the higher auditory centres were interrupted, cats showed an impaired ability in their orientation of the head towards the sound source in the vertical plane (Sutherland et al., 1998; May, 2000). Spectral notches are the important spectral cues for the sound localization in the vertical plane (Rice et al., 1992) and both fusiform and giant cells are capable of detecting peak and notches in the sound spectrum. In fact the two cells are excited by broadband sounds and get inhibited by narrowband stimuli and by notch noise (Young and

Davis, 2002) Tuberculoventral cells are responsible for the inhibition onto fusiform and giant cells in presence of narrowband stimuli (Voigt and Young, 1990) while D-stellate cells in the VCN inhibit fusiform and giant cells in presence of spectral notches (Nelken and Young, 1994).

1.3.2. Integration of multisensory signals within the dorsal cochlear nucleus

The dorsal cochlear nucleus also integrates information from several non auditory structures: the spinal trigeminal nucleus, the dorsal column nuclei, the pontine nuclei, the vestibular complex and the raphe nucleus. The majority of these projections constitute the mossy fibre inputs to the granule cell domains while minor projections terminate within the fusiform and the deep layer. The integration of the multisensory inputs to DCN has been shown to have relevant implications in hearing and in tinnitus.

1.3.2.1. Role of trigeminal projections

Sensory information from various regions of the head and the face is conveyed from the trigeminal ganglion to the trigeminal nuclear complex via the trigeminal nerve (Shore et al., 2000, Zhou and Shore, 2004). The trigeminal nuclear complex is divided into three nuclei: the main, the spinal and the mesencephalic nucleus. The spinal trigeminal nucleus is further subdivided into three subdivisions all involved in the mediation of pain (Usunoff et al., 1997; Zhou and Shore, 2004) as well as being responsive to non-noxious stimuli such as vibrissae deflection, gentle pressure, tactile stimuli, and jaw movement (Jacquin et al., 1986; 1988; 1993; Zhou and Shore, 2004). Both the trigeminal ganglion and the spinal trigeminal nucleus project onto the cochlear nucleus. Trigeminal ganglion cells primarily innervate the VCN and the granule cell lamina (Shore et al., 2003) whereas projections from the spinal trigeminal nucleus terminate onto

the fusiform and the deep layer of the DCN and onto the granule cell lamina (Zhou and Shore, 2004; Haenggeli et al., 2005). Electrical stimulation of the trigeminal system evokes both excitatory and inhibitory responses in DCN neurones (Zhou and Shore, 2004; Shore, 2005). Concomitant stimulation of the auditory and the trigeminal nerves can elicit bimodal suppression and/or enhancement in the DCN (Shore, 2005). Bimodal suppression occurs when the bimodal response (elicited by acoustic and trigeminal stimulation) is less than the larger unimodal response (elicited for example by acoustic stimulation alone). By contrast, bimodal enhancement occurs when the bimodal responses exceed the sum of the individual unimodal responses. The large majority of DCN cells exhibited a depression of the responses to sound when the trigeminal system was concomitantly activated with the auditory system. It has been suggested this inhibition could serve suppressing internally generated sounds produced by chewing, respiration and also self vocalization (Shore, 2005; Shore and Zhou, 2006). By contrast, the bimodal enhancement that occurred in a minority of the cases might be important in improving signal-to-noise ratios when attention is directed to a particular location (Kanold and Young, 2001a; Shore and Zhou, 2006). The trigeminal projections to the cochlear nucleus are associated with the vesicular glutamate transporters VGLUT2 by contrast to auditory nerve projections that are associated with VGLUT1 (Zhou et al., 2007). A recent study showed that cochlear deafferentation is accompanied by a significant reduction in VGLUT1 and an increase in VGLUT2 suggesting a compensatory response from the somatosensory system to deafening (Zeng et al., 2009). Moreover the enhanced glutamatergic inputs from the trigeminal system could lead to an

increase in the spontaneous activity of DCN neurons that occur after hearing loss and this could be correlated with tinnitus (Zeng et al., 2009).

1.3.2.2. Role of dorsal column nuclei projections

Information relative to tactile sensation and proprioception coming from the head, the limbs and the trunk is transferred to the dorsal column nuclei in the medulla. Dorsal column nuclei comprise the cuneate and the gracile nuclei. The gracile nucleus receives fibres from the sacral, lumbar and lower thoracic segments while the cuneate nucleus receives information from the upper thoracic and the cervical segments (from the head and the external ear or pinna). Both nuclei project to the auditory thalamus (also called MNG) via the medial lemniscus. Anatomical projections from the cuneate nucleus to the fusiform layer of the DCN and to the granule cell lamina have been described in rats and in cats (Itoh et al., 1987; Weinberg and Rustioni, 1987; Wright and Ryugo, 1996; Wolff and Kunzle, 1997). Both electrical stimulation of the dorsal column nuclei and manual manipulation of the pinna in cat can induce a strong inhibition and a weak excitation of DCN principal cells (Young et al., 1995; Davies et al 1996a; Kanold and Young, 2001a). This led to the suggestion that inputs from the dorsal column nuclei might be used to coordinate the pinna movements towards the sound source in order to optimize the auditory perception (Kanold and Young, 2001a, b). Moreover the somatosensory inputs that come from the head could be involved in the perception of craniocervical tinnitus, in which movements of muscles and joints in the head and in the neck often result in the modulation of the perception of tinnitus perception (Levine, 1999).

1.3.2.3. Role of pontine nuclei projections

The pontine nuclei lie in the ventral part of the brainstem and are relay structures of the sensory motor pathway: the cerebro-ponto-cerebellar pathway linking the cerebral cortex to the cerebellum (Brodal and Bjaalie, 1992; Schmahmann and Pandya, 1997; Schwarz and Their, 1999). The cerebral cortex sends inputs to the pontine nuclei which project to the cerebellum via mossy fibres (Ramon y Cajal, 1909; Palay and Chan-Palay, 1974, Brodal and Bjaalie 1992). The cortico-pontine inputs arise from various regions within the cerebral cortex: the sensory motor cortex, the visual cortex (Hollander et al., 1979; Wiesendanger and Wiesendanger 1982a, b; Legg et al. 1989), the motor cortex (Allen and Tsukahara. 1974) and the auditory cortex (Wiesendanger and Wiesendanger, 1982a; Azizi et al., 1985; Knowlton et al., 1993; Kimura et al., 2004). The cerebellar cortex processes this information and sends it back to the cerebral cortex (via the thalamus and other structures) (Brodal and Bjaalie, 1992; Schmahmann and Pandya, 1997; Schwarz and Their, 1999). This multisensory integration within the cerebro-ponto-cerebellar pathway is important in the sensory guidance of the movements (Stein and Glickstein, 1992).

The pontine nuclei also project to the granule cell lamina of the cochlear nucleus (Ohlrogge et al., 2001). *In vitro* electrical stimulation of pontine nuclei elicited a mixture of polysynaptic excitatory and inhibitory responses in DCN fusiform cells suggesting pontine projections terminating onto DCN granule cells that ultimately modulate fusiform cell activity (via direct or indirect excitatory and inhibitory inputs, Babalian, 2005). The role of the pontine projections to the DCN remains to be determined.

1.3.2.4. Role of vestibular projections

The movements of the body such as posture, balance and coordination of head and eye movements are controlled by the vestibular system. The vestibular system is located within the cochlea and carries vestibular signals along the vestibular nerve that constitutes one of the two branches of the vestibulo-cochlear nerve (the cochlear or auditory nerve representing the other branch). The efferent fibres from the vestibular system connect to *i)* the flocculonodular lobe of the cerebellum where they control the balance; *ii)* the spinal cord where they are involved in the control of the body posture and balance; *iii)* the nuclei of the abducens, trochlear and oculomotor nerves where they are involved in the coordination of the head and eye movements. Studies in guinea pig, rabbit and gerbil reported vestibular synaptic projections to the DCN (Burian and Gstoettner, 1988; Kevetter and Perachio, 1989; Bukowska, 2002). The role of vestibular projections to the DCN is still unclear and could be linked to the head position and/or movement. Electrophysiological studies showed that vestibular afferents can be stimulated by acoustic stimulations (Cazals et al., 1983; McCue and Guinam, 1994; 1997) thereby suggesting a role for the vestibular complex in the hearing process. Additionally vestibular schwannoma is often associated with tinnitus (Baguley et al., 2006).

1.3.2.5. Role of raphe nuclei projections

Raphe nucleus neurones lie in the brainstem. Neurons in the rostral end of the raphe nucleus mainly projects to the forebrain where they are involved in neural mechanisms of sleep, affective and sexual behaviour, food intake and thermoregulation. Neurons in the dorsal, medial and caudal part of the nucleus project to other parts of the brainstem and the spinal cord where they regulate

the tone in the motor system and pain perception. Serotonin positive terminals originating in the medial and dorsal raphe nucleus have been found within the three layers of the DCN (especially in the molecular layer) (Klepper and Herbert, 1991; Thompson et al., 1994a, 1995; Thompson and Thompson, 2001). Studies on sound-induced serotonin release suggest that serotonergic inputs to the DCN might have a role in modulating the auditory processing (Cransac et al., 1998). Moreover it has been suggested that an inefficient serotonergic neuromodulation of central auditory pathways could be responsible for the development of tinnitus and hyperacusis (Thompson et al., 1994b; Marriage and Barnes, 1995).

1.4. Peripheral and central damage in the auditory system

Several types of hearing disorders usually arise after peripheral injuries in the middle or the inner ear. The most common form of hearing disorder is the sensorineural hearing loss, due to the damage of the inner ear following noise exposure or drug intake. Dendritic damage can be observed in primary auditory dendrites (spiral ganglion cells) after acoustic trauma (Spoendlin, 1976; Robertson, 1983; Puel et al., 1995) probably linked to glutamate excitotoxicity via non-NMDA receptors such as AMPA or kainate receptors (Puel et al., 1995). An exposure to loud (130 dB SPL) single tone for 15 minutes is sufficient to produce hair cell degeneration in guinea pig (Saunders et al., 1985). The mechanisms involved in hair cell damage are various and involve changes in the mechanical properties of the sensory hair bundle at the apical pole of the hair cells (Saunders et al., 1986), an increased calcium entry within the cytoplasm of outer hair cells (Fridberger et al., 1998) and an increased permeability of the endolymph-perilymph barrier to potassium and sodium ions

(Konist et al., 1982; Johnstone et al., 1989). Both damage to the hair cells and the spiral ganglion contribute to elevate the hearing thresholds (Dallos and Harris, 1978; Salvi et al., 1983). Other factors responsible for damaging the cochlea can lead to hearing loss. Aspirin (acetylsalicylic acid) can induce hearing loss by altering the electromotility of the outer hair cells (Shehata et al., 1991; Russell and Schauf, 1995) by acting on prestin (Oliver et al., 2001). Aminoglycosides are antibiotics used against bacterial infections. When used in large amounts, aminoglycosides provoke stereociliary damage and subsequent hair-cell degeneration (Wersäll et al., 1973). Those large polycationic molecules can block mechanosensitive channels in the outer hair cells (Ohmori, 1985; Kroese et al., 1989; Kimitsuki and Ohmori, 1993) and can also enter the hair cells through these channels (Marcotti et al., 2005). Hearing loss may also have a genetic basis. Clues to the molecular basis of the defects came from studies on the human Usher type I syndrome which is a frequent cause of deaf blindness in humans and is associated with defects in the expression of three proteins: myosin VIIa, harmonin and cadherin 23 (Weil et al., 1995; Bitner-Glindzicz et al., 2000; Bolz et al., 2001; Bork et al., 2001). All three proteins are essential for the hair cell's bundle constitution. Similar conclusions have been reached when using mouse mutants defective for these proteins as the mutant animals were deaf and their cochlear sensory cells displayed hair bundle disorganization (Mburu et al., 1997; Alagramam et al., 2001).

Another common hearing defect is represented by tinnitus linked to the perception of phantom sounds. Tinnitus is often accompanied by hearing loss and can also manifest itself as a hypersensitivity to various drugs. Considering the effects of aspirin and aminoglycosides on the auditory peripheral system,

tinnitus was initially considered as an auditory defect arising from cochlear damage. Studies showing that tinnitus was linked to alterations in the cochlear outer hair cells support this hypothesis (Stypulkowski, 1990; Mitchell and Creedon, 1995; Kaltenbach et al., 2002). However, there is no consensus on the nature of the mechanisms underlying tinnitus and there is increasing evidence that tinnitus can be associated with disturbances in the spontaneous neural activity of the central nervous system. The first finding supporting this hypothesis is represented by the fact that tinnitus persists in patients with acoustic neuroma after sectioning the auditory nerve (House and Brackmann, 1981, Matthies and Samii, 1997). Further studies with magnetic source imaging reported a marked shift of the cortical representation of the tinnitus frequency into an area adjacent to the expected tonotopic localization in subjects with tinnitus suggesting that tinnitus is related to plastic alterations within the auditory cortex (Mühlickel et al., 1998). Partial cochlear lesions on animals gave results similar to those obtained in patients with tinnitus. Studies in cats showed that the tonotopic map in the auditory cortex is altered after acoustic over-exposure (Eggermont and Komiya, 2000). Additionally, neurons in the affected region also showed increased spontaneous activity and increased neural synchrony (Eggermont and Komiya, 2000; Seki and Eggermont, 2003). Altogether these findings point to a potential link between a reorganization of the cortical tonotopic map, changes in neuronal activity and tinnitus. These changes do not occur in isolation and they are likely to be the results of a modification in the balance of excitation and inhibition at multiple levels of the auditory pathway. Acoustic over-exposure results in an increased activity of the inferior colliculus neurones (Szczepaniak and Moller, 1996; Basta and Ernest,

2004; Bauer et al., 2008) likely to be linked with decreased GABA-mediated inhibition (Szczepaniak and Moller, 1995). The DCN represents another central auditory structure that becomes hyperactive after acoustic damage (Zhang and Kaltenbach, 1998, Kaltenbach and Afman, 2000; Chang et. al. 2002). One week after acoustic over-exposure, glutamate release was increased within the DCN indicating that the excitatory synaptic transmission is increased after acoustic over-exposure (Muly et al., 2004). The same acoustic over-exposure conditions that increase the excitability of DCN neurones has also been shown to cause animals to experience tinnitus (Heffner and Harrington 2002, Brozosky et al., 2002) and this strongly correlated the DCN activity with the perception of tinnitus.

The causes of tinnitus might not only be linked to the central auditory system *per se* but might be due to an imbalance of multisensory input integration. Together with cochlear damage, another cause of tinnitus is represented by an abnormal activity in the somatosensory system (Levine et al., 2003; Cacace, 2003) resulting from head and neck injuries and various mandibular and dental problems (Rubinstein, 1993; Chan and Reade, 1994; Levine, 1999). The DCN is an important integration site for the auditory and somatosensory information (Shore and Zhou, 2006) where influences of the trigeminal nerve activity has been described (see section 1.3.2.1. above). Imbalances between the auditory and somatosensory inputs can be linked to imbalances between excitatory and inhibitory synaptic transmission ultimately leading to tinnitus.

1.5. Synaptic plasticity in the dorsal cochlear nucleus

Synaptic plasticity is another feature that the DCN shares with the cerebellum. Concomitant excitation of parallel and climbing fibres leads to long term depression (LTD) in Purkinje cells (Linden and Connor, 1991; Shigemoto et al., 1994; Nakamura et al., 1999; Ito, 2001). This form of plasticity in the cerebellum is essential to achieve some aspects of sensorimotor coordination like adaptation in ocular movements, production of eye blink reflex, adaptation in posture and locomotion, adaptation in hand/arm movement, motor coordination (Conquet et al., 1994; Ito, 2001). In the DCN, both LTD and long term potentiation (LTP) can be induced at the synapses between parallel fibres and cartwheel and fusiform cells (Fujino and Oertel, 2003). By contrast stimulation of the auditory nerve fibre inputs to fusiform cells fails to exhibit synaptic plasticity (Fujino and Oertel, 2003). How the DCN might use this synaptic plasticity which appears to be exclusively related to the multisensory inputs is still unknown. However based on the similarities between the DCN and the cerebellum several hypotheses have been drawn. In the cerebellum the information carried by the parallel fibres are used to achieve some features of the sensorimotor coordination with a mechanism that involves the prediction of sensory events (Nixon, 2003). By adjusting the strength of the parallel fibres on their target, the cerebellum can therefore select the appropriate signals from the multiple inputs carried by the parallel fibres. In the same way, the DCN could select the appropriate signals from the numerous multisensory signals transported by the parallel fibres (Oertel and Young, 2004). In the electrosensory lateral-line lobe (a cerebellum like nucleus) of the electric fish, the information regarding motor commands and proprioceptive signals that are carried by parallel fibres onto apical dendrites of principal cells, are used to predict and cancel the

self-generated electric field (Bell et al., 1997). The strength of the synapse between parallel fibres and their target is decreased in response to self generated field, so that only the electrical signals that come from external source generate a response in the principal cells (Bell et al., 1997). A similar mechanism has been proposed for the DCN that may use the inputs from the spinal trigeminal nucleus to predict self-generated noise (like chewing or respiration) and cancel them (Shore, 2005) and the inputs from the pinna to predict and suppress signals generated in the stimulus spectrum by the movements of the pinna (Kanold and Young, 2001a). Therefore plasticity in the DCN is likely to depend on the integration of various synaptic inputs. Several studies suggest a strong correlation between tinnitus (further described in section 1.4 below) and changes in excitability within the DCN (Kaltenbach and Godfrey, 2008), suggesting that plastic changes within the DCN are likely to occur as an experience-dependent plasticity (tinnitus being a representation of the memory of sound subsequent to plastic readjustments). Recent studies in the barrel cortex of mice showed that continued experience can result in an increasing potentiation of synaptic strength over time (Clem et al., 2008). A similar mechanism might be engaged by DCN. Enhancing synaptic efficacies within this structure could stabilize synapses over wider cortical territories and lead to the perception of sounds that are physically absent

Increasing evidences support the idea that tinnitus reflects plastic readjustments within the auditory system. I specifically investigated in this thesis which changes occur in the DCN shortly after acoustic over-exposure. This allowed exploring further the hypothesis that shortly after acoustic over-exposure, early changes within the DCN could ultimately be responsible for the perception of tinnitus.

CHAPTER 2

Material and Methods

2.1. Morphological studies

Morphological studies were used to investigate the cytoarchitecture and the three-dimensional structure of the DCN as well as the morphology of the principal DCN cell types. All the morphological studies were carried out on 18 days old Lister Hooded rats. Animals were killed by decapitation in accordance with the UK Animals (Scientific Procedures) Act 1986.

2.1.1. Study of the DCN cytoarchitecture

The cytoarchitectural organization of the DCN was studied using the Nissl staining technique. One of the most commonly used dyes for the Nissl staining is cresyl violet. This dye binds the acid components of the neuronal cytoplasm, including RNA-rich ribosomes, as well as the cell nuclei and nucleoli.

2.1.1.1. Fixation and cresyl violet staining

After decapitation, the brain was removed from the head cavity by cutting the nerves and the blood vessels and transferred into a fixative solution for at least two days at 21°C. The fixative solution consisted of 5% paraformaldehyde dissolved in a phosphate buffer solution (pH=7.4). For the source of chemical see Appendix II.

After fixation, the brainstem and the cerebellum were separated from the whole brain (as described in 2.2.1.1), mounted on a slicing platform and sliced in distilled water (the slicing procedure is detailed in section 2.2.1.2). Coronal (50 to 70 μm thick) slices containing the DCN were collected whilst viewing through a binocular microscope with a Leica Vibroslicer VT1000S (figure 2.2). Slices were then transferred onto a polysine slide and left to dry for 1 day at room temperature (21-23°C). Slices were then stained for 4 min. with 0.1% cresyl

violet (dissolved in distilled water and filtered) and maintained under agitation. The slides were then immediately transferred into pure ethanol for 2 min. and into xylene for another 2 min. before being mounted in DPX and covered with a coverslip.

2.1.1.2. Analysis of the cell density and labelled cell body areas

The analysis was performed on 3 to 4 slices per animal. Fifty micron slices were analysed between 150 and 650 μm after the DCN started to appear. Cell density per layer was measured on cresyl violet stained cells by drawing 3 squares per layer (89 x 55 μm) and by manually counting the cell numbers within those squares. The cell soma surface area per layer was measured in 2 out of those 3 squares per layer. Only cell soma surface areas $\geq 39 \mu\text{m}^2$ were taken into consideration corresponding to cells with diameter $> 7 \mu\text{m}$ (Soma surface area = $\pi r^2 = \mu\text{m}^2$). Cell surface areas were measured using the area calculator software of Image-J (ver. 1.36). The cell soma area was delimited with Image-J freehand selection tools before calculating the surface.

2.1.2. Morphological studies

2.1.2.1. Principles of the Golgi method

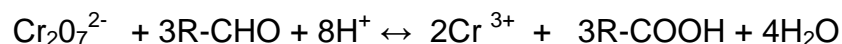
The morphology of the different DCN cell types was assessed with the Golgi technique. The Golgi staining is a histological technique that allows visualization of the soma and processes of the neurones. The method impregnates only some cells, thus allowing a description of their morphology and their site of projection. Nevertheless, the selectivity of the impregnation is uncontrolled: regions of intense staining can be interspersed with regions of no staining or with regions of a-specific staining that impairs the visualization of the cells. The Golgi impregnation is based on two reactions: the chromation reaction and the

impregnation reaction (detailed below). The chromation reaction consists in having the tissue in a fixative solution of potassium dichromate ($K_2Cr_2O_7$) while the impregnation step is based on the immersion of the sample in a silver nitrate ($AgNO_3$) solution. During the impregnation step, red to black crystals of silver dichromate ($Ag_2Cr_2O_7$) or silver chromate (Ag_2CrO_4) form deposits within the cells allowing their visualization. The reaction is not fully understood yet, although it is currently established that potassium dichromate and silver nitrate react together to give the final product silver dichromate or silver chromate (Morest and Morest, 1966; Ramon y Cajal and De Castro, 1933). Angulo et al. (1996) gave an exhaustive explanation of the chromation reaction.

In the first step of the chromation, the hexavalent chromium (Cr^{6+}) of the compound ($K_2Cr_2O_7$) reduces to trivalent chromium (Cr^{3+}):



Aldehydes (R-CHO) are usually present in the fixative medium, or added to the chromating solution because their presence improves the reaction. Indeed aldehydes are reducers, which enhance the oxidation potential of $Cr_2O_7^{2-}$ as follow:



Furthermore $Cr_2O_7^{2-}$ is a stronger oxidant in acidic medium, so the reaction usually starts in an acidic medium.

The second step of the chromation reaction is linked to the high affinity of Cr^{3+} for terminal carboxyl groups (Gustavson, 1956) and therefore Cr^{3+} cross-links the intracellular proteins of some neurones. In the third step of the chromation reaction, the positively charged Cr^{3+} -protein complexes form electrostatic bindings with $Cr_2O_7^{2-}$. Indeed not all the Cr^{6+} of the $Cr_2O_7^{2-}$ is

converted to Cr^{3+} (Gustavson, 1956). Some $\text{Cr}_2\text{O}_7^{2-}$ anions linked to the Cr^{3+} -protein complexes are in this way present within the neurones.

During the impregnation reaction, the tissue is exposed to AgNO_3 . $\text{Cr}_2\text{O}_7^{2-}$ anions (in cells or within the tissue) react with the AgNO_3 to generate the black precipitates of $\text{Ag}_2\text{Cr}_2\text{O}_7$ or Ag_2CrO_4 . The precipitates inside the neurons are responsible for the morphological visualization of the cells. The $\text{Cr}_2\text{O}_7^{2-}$ ions that did not link with the positively charged protein complex are responsible for the aspecific staining and form crystals within the tissue. From the reaction described above it can be deduced that a good balance between the two ions Cr^{3+} and $\text{Cr}_2\text{O}_7^{2-}$ in the first chromation step is essential. This first step is governed by the pH (as there is a consumption of protons) and by aldehydes (that are reagents in the reaction). In order to optimize the Golgi staining, I tried different pH and different aldehydes (paraformaldehyde, glutaraldehyde and chloral hydrate) in the chromation medium (detailed below).

2.1.2.2. Fixation and Golgi staining

After decapitation the whole brains were transferred into different fixative solutions comprising 5% paraformaldehyde dissolved in phosphate buffer solutions (PBS) composed of a mixture of Na_2HPO_4 and NaH_2PO_4 i.e. *i)* 9 mM Na_2HPO_4 – 90 mM NaH_2PO_4 ; *ii)* 80 mM Na_2HPO_4 – 20 mM NaH_2PO_4 ; *iii)* 86 mM Na_2HPO_4 – 13 mM NaH_2PO_4 giving a pH of 5.8, 7.4 and 7.6 respectively (pH was measured in the absence of paraformaldehyde). After at least two days, the brains were transferred to a freshly prepared chromation solution containing: 3% potassium dichromate in water or 3% potassium dichromate and 5% paraformaldehyde dissolved in water or PBS pH 5.8, 7.4 and 7.6 (using the same concentrations of Na_2HPO_4 and NaH_2PO_4 as during the fixation). I also

used 3% potassium dichromate, 5% paraformaldehyde and 2% glutaraldehyde dissolved in PBS pH 7.6 and 3% potassium dichromate, 4% paraformaldehyde and 2% chloral hydrate dissolved in PBS pH 7.6. The chromation solution was changed after 24 hours and the pH was measured with pH strips every 12 hours. After 48 hours, the brains were washed several times in 2% silver nitrate (diluted in water) and then immersed into the silver nitrate solution for another 48 hours. The containers with the brains remained covered with foil to avoid light exposure. The temperature was maintained at 21°C. Following this procedure fifty micron slices containing the DCN and the cerebellum were collected (as described in section 2.1.1.1.) and left to dry 1 day at room temperature 21-23°C, on a polysine slide. Slices were finally mounted in DPX and covered with a coverslip.

2.1.2.3. Specific and non-specific staining

In order to establish the best Golgi labelling conditions, I quantified the number of specifically labelled cells as well as the areas covered with a-specific staining. The analysis was performed on 3 to 4 slices per animal (3 to 4 animals per condition). Fifty microns slices were analyzed between 150 and 650 μm after the DCN started to appear. The number of labelled cells and the area covered with the a-specific staining were estimated within the whole area of the DCN (defined as black to orange precipitates within the DCN). Cell surface areas were measured as detailed in section 2.1.1.2. In some cases, the soma area of Golgi labelled cells was compared to the soma area of lucifer yellow labelled cells and the lucifer yellow staining is detailed in section 2.2.2.

2.1.3. Study of the DCN cytoarchitecture and cellular morphology

I developed a method combining cresyl violet with Golgi staining to study the DCN cytoarchitecture together with the cellular morphology. Brains were previously labelled with the Golgi method (section 2.1.2.2.) before performing 50 µm slices (as described in section 2.1.1.1.) and left to dry overnight on polysine slides. Slices were then stained for 4 min. with 0.1% cresyl violet (dissolved in distilled water) and maintained under agitation. The slides were then immediately transferred into pure ethanol for 2 min. and into xylene for another 2 min. before being mounted in DPX and covered with a coverslip.

2.1.4. Tri-dimensional reconstruction of the cochlear nucleus

A tri-dimensional reconstruction of the whole cochlear nucleus was obtained from staining thin (20 µm) slices with cresyl violet. After decapitation, the brainstem and cerebellum were separated from the whole brain (as described in section 2.2.1.1), transferred in Tissue-tek (Polyvinyl alcohol <11%, carbowax <5%, nonreactive ingredients >85%) and fast frozen in dry ice (in hexane). Tissue was then left for at least one day at -21°C. The frozen brainstem was cut into 20 µm thick sections using a freezing microtome. Coronal slices were collected and transferred onto polysine slides. Slides containing the cochlear nucleus slices were then transferred into a solution containing 5% paraformaldehyde dissolved into phosphate buffer (PBS, pH 7.4) for 15 min. and maintained under agitation. The slides were washed in 0.1% PBS (pH7.4) and put for another 15 min. in 5% paraformaldehyde. Slides were then stained for 4 - 5 min. with 0.1% cresyl violet (dissolved in distilled water) and maintained under agitation. The slides were then immediately transferred into pure ethanol for 2

min. and into xylene for another 2 min. before being mounted in DPX and covered with a coverslip.

2.1.5. Image acquisition and processing

All the images used for this study were acquired with a Nikon DXM1200F digital camera on a Nikon Eclipse TE2000-U inverted microscope. For pictures representing Golgi labelled cell types, a focal series of 2-4 microphotographs (z-stack) has been taken at different focal lengths and then put into a single focused image with the Image-J 1.36/ extended depth of field software.

To allow the reconstruction of the cochlear nucleus, 50 consecutive images were perfectly overlapped on a monitor and acquired with Reconstruct software (ImageJ). Areas were outlined with a freehand selection tool (ImageJ detailed in 2.1.1.2) to select the DCN, the VCN, the auditory nerve and granule cells domains.

In order to reproduce the DCN circuitry (shown in figure 3.9), drawings of Golgi impregnated cells were obtained with the Adobe Photoshop software. The area of the identified cell was retained and then extracted and the contrast between the image and the background was maximized in order to obtain a black cell in a nearly white background.

2.2. Patch clamp recordings on slices

2.2.1. Preparation of slices

2.2.1.1. Dissection

Lister Hooded and Wistar rats aged P14 to P20 were humanely killed by decapitation in accordance with Home Office regulations. Dissection of the brainstem were performed in ice cold low-sodium medium contained in mM: KCl 2.5, NaH₂PO₄ 1.2, D-Glucose 10, ascorbic acid 0.5, sucrose 250, NaHCO₃ 26, CaCl₂ 0.1, MgCl₂ 4 bubbled with 95% O₂ and 5% CO₂, pH 7.4. The low sodium concentration of the solution prevents cell swelling and lysis while the ice minimizes oxygen consumption (Aghajanian and Rasmussen, 1989). After the decapitation, the brain was removed from the head and placed with its ventral surface up (figure 2.1A). The meninges were removed from the brainstem with forceps. An incision was finally made at 45 degrees to separate the brainstem and the cerebellum from the rest of the brain (figure 2.1C-D).

2.2.1.2. Slicing

The brainstem and the cerebellum (figure 2.2A) were glued to a platform (figure 2.2B) with the spinal cord facing up to allow cutting coronal slices. The platform was introduced in a slicing chamber (figure 2.2C) of a vibroslicer (Leica VT 1000) and filled with the ice cold low-sodium medium described above. Slices were cut using a stainless steel blade (Campden instruments, UK) at a thickness between 160 and 200 μm . Once cut, each slice was transferred into a bubbling chamber (figure 2.3) with oxygenated artificial cerebrospinal fluid solution containing in mM: NaCl 125, KCl 2.5, NaH₂PO₄ 1.2, D-glucose 10, ascorbic acid 0.5, Na pyruvate 2, myo-inositol 3, NaHCO₃ 26, CaCl₂ 2 and

MgCl₂ 1 bubbled with 95% O₂ and 5% CO₂ pH 7.4. The bubbling chamber containing the DCN slices was left in a water bath at 37°C for the first hour before being left at room temperature for the rest of the day. Slices used for recording were transferred to the recording chamber of a Zeiss Axioskop upright microscope (sections 2.2.3 and 2.2.4) and the perfusion medium was the same as the oxygenated artificial cerebrospinal fluid described above.

2.2.2. Cell identification

Recordings were performed in the DCN (figure 2.4A) and cells were first identified according to their location within the nucleus (figure 2.4B) and to their soma shape and size. I developed a method that allowed characterizing simultaneously the morphology of individual neurons and the cytoarchitecture of a brain structure (Pilati et al., 2007). I used this method to study the morphological characteristics of the different DCN cell types are described in the first section of the results. Briefly, granule cells are the most numerous cells located within the deep layer and are the smallest cells with a diameter between 7 and 10 µm. Cartwheel cells, located between the molecular layer and the fusiform layer are characterized by a round cell body with a diameter between 20-25 µm. Fusiform cells are located in the fusiform layer and have a characteristic fusiform shape with a diameter between 20 and 25 µm in the narrowest part of the cell and 30 µm in the widest part. Giant cells are located within the deep layer and are characterized by their round shape and diameter larger than 30 µm. When studying the effects of acoustic over-exposure, I only selected cells that lied in the high frequency region of the DCN (Yajima and Hayashi, 1989) as I expect high frequencies regions to be affected by 15 kHz single tone exposure. This region is shown in figure 2.4B. I showed that DCN

cells filled with lucifer yellow have a similar cell soma surface area and a similar morphology than cells labelled with the Golgi method (Pilati et al., 2007). Cells were filled with lucifer yellow (0.1%) while proceeding to their whole cell recording. Once the whole cell recording was terminated, the morphology of the cell was confirmed with fluorescence microscopy (described in figure 2.5). The pipette was then removed from the cell by applying positive pressure to allow the observation of the cell on the confocal microscope and the slice was fixed into a solution of 4% paraformaldehyde dissolved in phosphate buffer (pH= 7.4) for a couple of hours. The slice comprising the lucifer yellow filled cell was then washed in phosphate buffer to remove the excess of paraformaldehyde and transferred on a slide. The excess fluid around the slice was removed with some filter paper. Agarose (1% in extracellular medium described in the section 2.2.1.2 above) was put on the slice which was then covered immediately with a cover slip. The edges of the cover slip were sealed with nail polish to prevent agarose dehydration. Slides were kept in the fridge until their observation with the confocal microscope (principles detailed in figure 2.6). Cells were also identified from their electrophysiological passive properties and this is detailed in section 2.2.9. In chapter 6 (paragraph 6.3) when the synaptic inputs to fusiform cells were studied, cells were not filled with lucifer yellow as fusiform cell could be clearly recognized based on the soma shape (fusiform) and location within the nucleus (fusiform layer).

Cells that were not firing overshooting action potentials were not accepted for the analysis.

2.2.3. Electrophysiological setup

The electrophysiological setup (figure 2.7) consists of a patch clamp amplifier Multiclamp 700A (Axon instruments, USA) connected to an analogical to digital converter (Digidata 1322A). The CV-7A headstage contains a current to voltage (I-V) converter used in voltage clamp mode and a voltage follower used in current clamp mode (described in section 2.2.7.1). A recording electrode filled with the intracellular medium described in section 2.2.6.1 is introduced in an appropriate holder (figure 2.8) containing a silver chloride wire linking the electrode to the headstage. A silver chloride earth electrode links the bath (figure 2.9) to the headstage. The headstage is connected to a motorized micromanipulator (Newport, Burleigh, Patch Clamp Driver PC5-250 figure 2.9) allowing precise positioning of the electrode under microscopic control. Slices were transferred to a perfusion chamber placed on the stage of an upright microscope (Zeiss, Axioskop) and cells were visualized with differential interface contrast optics (described in section 2.2.4). A 4x objective was used to localize the DCN whereas a 40X water immersion objective (Olympus) allowed identifying the cells. A charge coupled device (CCD) camera (Hamamatsu, C 3077) was fitted to the microscope and connected to a monitor (Hitachi) allowing high-resolution images under a variety of light conditions. The microscope was mounted on a home made X-Y translation table (Workshop Leicester University) allowing positioning of the objective around the environmental chamber that was fixed on a wide-based stage. The microscope and the manipulators were supported by an anti-vibration table (Went Worth Laboratories, LTD) and surrounded by a home made Faraday cage (Workshop Leicester University).

2.2.4. Differential interface contrast and fluorescence microscopy

Visualization of neurones on the Zeiss Axioskop microscope was achieved using differential interface contrast (DIC) optics to introduce contrast into non-adsorbent objects. Light is first polarised and then passed through Wollaston prisms which split light into two quasi-parallel beams. The light then passes through the specimens so that some beams will pass through the object and others to the edge of it. Beams that pass through the object will be slightly refracted with respect to those that do not. Both of the beams then pass through another Wollaston prism which recombines them. Finally the light passes through a polarising filter. Beams that have been refracted by an object will appear a different shade to those that have not, due to constructive or destructive interference on recombination of the beams, giving a perception of contrast. Fluorescence microscopy was used to check the identity of the cells that were filled with lucifer yellow (0.1mg/ml included in the intracellular medium). Fluorescence microscopy (described in figure 2.5) was achieved with the use of Xenon lamp with an excitation of 488 nm and by placing an emission filter (555 nm) in the filter unit.

2.2.5. Perfusion of solutions

Slices were held down with a hand-made harp (figure 2.10) and perfused at a rate of 1 ml/min using a peristaltic pump (Gilson, Miniplus 3, figure 2.11) with solutions first passing through 5 ml syringes (Figure 2.11B) to avoid bubbles reaching the perfusion chamber and to create a break in the solution lines thus preventing these acting as arials for noise. The solutions reached then the experimental chamber. Drugs were bath applied through separate perfusion lines. Lines were primed to speed up the application (the time for solution

exchange was approximately 2 minutes) and recordings were performed at room temperature.

2.2.6. Electrodes

2.2.6.1. Recording electrode

Glass electrodes were pulled from thick walled borosilicate (GC150F 7.5, Harvard apparatus, UK) using a two-stage puller (PB-10, Narishige, Tokyo, Japan detailed in figure 2.12). The resistance of the pipette R_p can be estimated by the equation: $R_p = R_e \cdot L/d$ where R_e is the medium resistance or resistivity, L is the length of the pipette tip and d the diameter of the pipette tip. All of these factors can interfere in the measurement of the currents by increasing or decreasing the pipette resistance. Final pipette resistance was between 3 and 5 M Ω when recording from fusiform, cartwheel and giant cells and 10-12 M Ω when recording from granule cells.

2.2.6.2. Stimulating electrode

Parallel fibres or auditory nerve fibres in the DCN were stimulated using a concentric bipolar electrode (FHC Inc, Bowdoinham, ME (USA), figure 2.13). The stimulating electrode was lowered into the bath and advanced towards the zone to be stimulated using a micromanipulator (Burleigh Newport). The stimulating electrode was connected to a constant voltage isolated stimulator (Digitimer LTD) and fibres were stimulated with 100 μ sec pulses of 5 to 60 V with frequencies between 0.3Hz and 100 Hz.

2.2.7. Whole cell recordings using the patch clamp technique

The patch clamp technique allows single channel or whole cell currents to be recorded with the advantage of controlling the intracellular medium. A glass

micropipette with an open tip diameter ($\sim 1\text{-}2\ \mu\text{m}$) is filled with a solution that is usually matching the ionic composition cytoplasm. A silver chloride wire is in contact with this solution and conducts electrical currents to the patch clamp amplifier. A high resistance seal between the pipette and the cell membrane (giga-ohm) is formed by pressing the pipette against the membrane (figure 2.14A) and by applying a light suction through a suction tube connected to the pipette holder (figure 2.8). The high resistance of this seal makes it possible to record currents with high resolution and low noise. Once the giga-ohm seal is established (figure 2.14B left), the positive pressure previously applied to the pipette is released. The whole cell configuration was then achieved by applying further suction to trigger the rupture of the membrane patch (figure 2.14B right). In the whole cell configuration, the membrane is ruptured and the tip of the pipette is sufficiently wide (around $1\ \mu\text{m}$ diameter) to allow the washout of the cytoplasm with a time constant described in section 2.2.8). After this time, the intracellular fluid can be considered equal to that of the intracellular medium contained in the pipette.

Different compensation steps were performed before and immediately after breaking into whole cell recording. When the recording pipette was first inserted in the bath, the difference in potential that was generated between the electrode and the Ag/AgCl earth electrode of the bath solution (liquid junction potential explained further in section 2.2.7.4) was corrected by the amplifier that zeroed the current (performed in voltage clamp mode). The cell resting potential (assessed as the potential value at 0 current in current clamp mode) was measured in the few sec. following the whole cell configuration (this is further described in section 2.2.9.4). The cell was then held at $-70\ \text{mV}$ (in voltage-

clamp mode) and a 10 mV step applied to enable the membrane capacitance to be measured and compensated using P-Clamp 9.2 (further described in section 2.2.9.2). Subsequent compensation steps were specific to the current clamp (section 2.2.7.1 below) or to the voltage clamp recording (section 2.2.7.2).

2.2.7.1. The current clamp method

The current clamp method (or current clamp recording mode) allowed recording the membrane potential by injecting current into a cell through the recording electrode. Unlike the voltage clamp mode where the membrane potential is held at a voltage determined by the experimenter, in the current clamp mode, the membrane potential is free to vary and the amplifier records spontaneous voltage variations or voltage deflections evoked by stimulations. The current clamp circuit is described in figure 2.15. The current clamp recording mode was used to record post synaptic potentials or action potentials and study the firing pattern or the firing frequency of a cell. This mode allowed measuring the resting potential immediately after rupturing the patch membrane (before dialysis of the cell). Cells were also held at different potentials via positive or negative current injections. Similarly to the voltage clamp recording mode, the current flow through the electrode produces a voltage drop across the electrode that depends on the product of the current and of the resistance of the electrode and this voltage drop will add to the recorded potential. In current clamp mode, the bridge balance control is used to balance out this voltage drop so that only the membrane potential is recorded. A differential amplifier is used to subtract a scaled fraction (the scaling factor is the pipette resistance) of the current from the voltage recorded in order to give the true membrane potential. The

capacitance of the pipette is also corrected with the pipette capacitance neutralization function.

2.2.7.2. The voltage clamp method

The voltage clamp method (or voltage clamp recording mode) allowed recording of ionic currents across the cell membrane at a fixed voltage and was used to record post synaptic currents in response to stimulations. In voltage clamp mode, the electrode is held at a certain command potential while measuring currents flowing down the electrode. This is achieved by a current-voltage converter that produces a voltage output that is proportional to the current input (see figure 2.16).

In the voltage clamp recording mode, a series resistance mainly due to the resistance of the electrode hinders the measurement of the real membrane potential and affects the fidelity of the whole-cell voltage clamp measurements. When currents flow across the membrane, the series resistance causes an error between the true cell potential and the measured potential, this is known as the series resistance error. For example if a 1 nA current is flowing and the series resistance is 10 M Ω , there will be a voltage error of 10 M Ω x 1 nA = 10 mV. Furthermore, following a step change of the command potential (V_C), the actual cell membrane potential (V_m) will respond with an exponential time course ($V_m = V_C(1 - e^{-t/\tau_s})$) with a time constant by $\tau_s = R_s \cdot C_m$ where C_m is the cell membrane capacitance and R_s the series resistance. Thus a series resistance of 20 M Ω of a 100 pF cell will result in a membrane charging time constant of 2 ms. This means that it will take over 10 ms to settle the membrane potential to within the 1% of the final value. Lastly, the series resistance in conjunction with the membrane capacitance form a one-pole RC filter with a

corner frequency given by $f = \frac{1}{2\pi \cdot R_s \cdot C_m}$ for the measurement of membrane currents. This filter will distort currents regardless of their amplitude. The MutliClamp 700A amplifier (and linked software) use a double approach for the correction of the above errors associated with R_s . This involves the capacitance compensation and the series resistance compensation. The series resistance compensation involves the use of prediction and correction compensation procedures. The prediction procedure adds a transient signal to the command potential to speed up the rate at which the true membrane potential will change in response to a step voltage command therefore overcoming the error linked to the time constant described before. The correction procedure compensates for the voltage drop and the filtering effect by adding a proportional voltage signal to the command voltage through the series resistance compensation system of the amplifier. Typical series resistance was 10-20 M Ω and was compensated by 60 to 70%. When these two factors are correctly adjusted, the electrode capacitive transients and the cell charge and discharge following a voltage step become invisible to the user.

2.2.7.3. Intracellular solutions

The electrodes were filled with different intracellular solutions depending on the recording mode. For current-clamp experiments two types of intracellular solutions were used. A first solution contained (mM): Kgluconate 97.5; KCl 32.5; EGTA 5.4; HEPES 10; MgCl₂ 1; NaCl 2 and adjusted to pH of 7.1-7.3 with KOH. This solution was used to achieve a chloride equilibrium potential of -35 mV (further explained in section 2.2.9.3). A second solution contained (mM): Kgluconate 130; EGTA 5.4; HEPES 10; MgCl₂ 1; NaCl 2 and adjusted to pH of 7.1-7.3 with KOH. This solution was used to achieve a chloride equilibrium

potential of -90 mV and allowed differentiating between IPSPs and EPSPs when studying synaptic transmission onto fusiform cells (further explained in the results section). A third solution was used while performing voltage clamp recordings and studying IPSCs and EPSCs and contained (mM): Cs gluconate 130; EGTA 5.4 HEPES 10; MgCl₂ 1; NaCl 2; QX314 2 and adjusted to pH of 7.1-7.3 with CsOH. This solution was also used to achieve a chloride equilibrium potential of -90 mV. The use of caesium instead of potassium allowed reducing the leak currents underlined by potassium fluxes. QX314 (2 μM) was used to block sodium channels and prevent unwanted unclamped action potentials. The intracellular medium was filtered using a 0.2 μm filter (Milipore, UK). Lucifer yellow (0.1 %) was sometimes added to the intracellular medium to allow morphological recognition of the cells.

2.2.7.4. The liquid junction potential

As previously mentioned, a stable electrode potential is essential for accurate whole cell recordings. Here an Ag/AgCl wire provides the electrical connection between the headstage of the patch-clamp amplifier and the pipette solution. At the junction between the Ag/AgCl wire and the pipette solution, the reaction is $\text{Ag} + \text{Cl}^- \leftrightarrow \text{AgCl} + \text{e}^-$. When the pipette solution has a low Cl⁻ concentration, the interface becomes non-reversible (polarized), and the electrode potential is vulnerable to drift with time (Purves, 1981; Snyder et al., 1999). This electrode potential drift can significantly confound measurements of cell membrane potentials or currents and bias the command voltages during voltage-clamp experiments. The magnitude of the junction potential depends on the ions present in the pipette and bath solutions, together with the relative ion concentration, the ionic valence and mobility and was between +11 mV and

+15 mV at 25°C. All voltage clamp or current clamp recordings were compensated for the liquid junction potentials using a generalized version of the Henderson equation (Barry and Lynch, 1991; Barry, 1994) incorporated in JPCalc software (integrated in Clampex 9.2.).

2.2.8. Data acquisition and analysis

Data (current and voltage clamp recordings) were acquired using Clampex 9.2 at a sampling rate of 20 kHz and filtered at 6 kHz using a 8-pole Bessel filter built within the software and analyzed using Clampfit 9.2 (PClamp 9.2, Axon, Molecular Devices). Final graphic representations were performed using Sigmaplot 2000 and Powerpoint 2007.

2.2.8.1. The membrane resistance

The membrane resistance (or its reciprocal the membrane conductance, G_m) describes the ion permeation through the cell membrane (through its channels). Ohm's law $V = I \cdot R_m$ relates the membrane potential (V) and the current (I) flowing through this resistance (R_m). The sum of all the ionic conductances in the cell therefore defines the cell membrane conductance. An ionic conductance can vary with the voltage across the membrane (voltage-dependent), with time (time-dependent) or remain constant (voltage and time independent). Because of this complexity of ionic currents the membrane resistance can be classified as linear or non linear (convention used by Jack et al., 1975). The membrane resistance is linear when there is a linear relation between the current that flows through the cell and the membrane potential. In this case, the current responsible for this linear conductance is called leak current (Hodgkin and Huxley, 1952) and defined as $I_L = G_m (V_m - E_L)$ where V_m is the membrane voltage, G_L is the leak conductance and E_L is the equilibrium

potential for the leak current. The leak current is classically considered to be mediated by potassium or chloride ions, but it could as well involve other ions like calcium or sodium. An example of membrane resistance calculation is shown in figure 2.17 in which positive and negative current injections (of 250 pA each) were performed from a hyperpolarized membrane potential of -70 mV (at this potential, I assume usual voltage-gated channels to be closed). The membrane voltage deflection (V_m) following each step current (I_m) was measured at steady-state and the membrane resistance (R_m) was calculated according to Ohm's law ($V_m = I_m \cdot R_m$). As the relationship between the membrane voltage and the step current is linear, I consider the membrane resistance (R_m) as being the leak resistance and in my thesis R_m was considered as exclusively depending on the leak currents and was calculated in voltage clamp and current clamp mode (values from 30 to 2500 M Ω , detailed in the results section). By contrast, non linear conductances contribute to the generation of action potentials where both sodium and potassium conductances are voltage dependent and vary with time (non linear voltage gated conductances were not investigated here).

2.2.8.2. The membrane capacitance

A capacitance is generated when two parallel conductors are separated by an insulator. Since the distance between the conductors is constant for bilayers, most membranes have a capacitance of 1 μ F.cm⁻². Consequently the capacitance can be used as a measure of the cell size. In my experimental conditions, the capacitance was obtained by direct reading of the Multiclamp Commander or by fitting a mono-exponential decay of the voltage subsequent to a current step. I calculated cell capacitances of 9 to 183 pF corresponding to

cell diameters of 17 to 76 μm respectively (further detailed in the results section). A rapid change in the voltage will trigger both ionic and capacitive currents and the current flowing through the membrane (I_m) is the product of ionic (I_i) and capacitive currents. $I_m = I_i + C \frac{dV}{dt}$ where I_i is the current flowing through the channels, C is the capacitance in Farads (mainly the cellular capacitance), V is the voltage and t is the time. Consequently, capacitance compensation must be applied when recording ionic currents to cancel the capacitive current ($C_m = \tau / R_m$) where τ is the time constant value and R_m is the membrane resistance.

2.2.8.3. The equilibrium potential

Electrochemical gradients between the intracellular and the extracellular solutions are maintained by a permeability barrier. The potential at which the electrochemical gradient is in equilibrium can be calculated using the Nernst equation:

$$E_{\text{ion}} = \frac{RT}{zF} \ln \frac{[\text{Ion}]_{\text{out}}}{[\text{Ion}]_{\text{in}}}$$

where R is the gas constant, T is the temperature in Kelvin, z is the valence of the ion and F is the Faraday constant. In my experimental conditions a potassium equilibrium potential (E_{K^+}) of -102 mV was obtained with $[K^+]_{\text{in}} = 130$ mM and $[K^+]_{\text{out}} = 2.5$ mM; the sodium equilibrium potential (E_{Na^+}) of +111 mV was obtained with $[Na^+]_{\text{in}} = 2$ mM and $[Na^+]_{\text{out}} = 154$ mM; the chloride equilibrium potential (E_{Cl^-}) of -35 mV was obtained with $[Cl^-]_{\text{in}} = 34.5$ mM and $[Cl^-]_{\text{out}} = 133.4$ mM and the chloride equilibrium potential (E_{Cl^-}) of -90 mV was obtained with $[Cl^-]_{\text{in}} = 4$ mM and $[Cl^-]_{\text{out}} = 133.4$ mM. Setting the E_{Cl^-} at -90 mV allowed separating excitatory and inhibitory inputs into depolarizing and

hyperpolarizing events respectively when cells were held between -60 and -70 mV.

2.2.8.4. The resting potential

The resting potential E_m is determined by the potential value at which net the ionic fluxes across the cell are zero:

$$E_m = \frac{RT}{F} \ln \left(\frac{P_{Na^+}[Na^+]_o + P_{K^+}[K^+]_o + P_{Cl^-}[Cl^-]_i}{P_{Na^+}[Na^+]_i + P_{K^+}[K^+]_i + P_{Cl^-}[Cl^-]_o} \right)$$

where R, T, and F have their usual meaning, P is the permeability of the given ion, $[ion]_i$ and $[ion]_o$ are the internal and the external ionic concentrations respectively. Note that whereas the sum of the conductances will be zero, each individual ion will be carrying a net current. In my experimental conditions the resting potential was determined in current clamp mode, at the start of the whole cell recording when the dialysis of the intracellular solution from the pipette to the cell is minimal (see also section 2.2.8). Resting potentials were usually between -45 mV and -57 mV (values compensated for the junction potential, section 2.2.7.4).

2.2.8.5. Properties of the action potential

Action potentials were first continuously recorded at different membrane potentials. Continuous recordings were performed at threshold (i.e. at the minimal depolarizing membrane potential eliciting low frequency action potentials.) The amplitude of the action potential, the 10-90 % rise time, the 90-10% decay time and the presence or absence of an undershoot were measured at their activation threshold to limit the interference with subsequent spikes. Continuous recordings were also performed at a supra threshold level in order to analyze the frequency of the firing in function of the membrane potential. For

each membrane potential the distribution of the inter-spike intervals was analyzed (calculated as the time from the peak of one action potential to the peak of the subsequent action potential). The coefficient of variation of the inter-spike interval distribution (defined as the ratio of the standard deviation to the mean) was also calculated. This provided a measuring index of the dispersion of the probability distribution and allowed assessing the regularity of the firing. Some cells displayed irregular trains of action potentials that were defined as bursts. In this latter case, an inter-spike interval was considered as an inter-burst interval if it was larger than the two preceding inter-spike intervals by a factor of at least 2 (as defined in Womack and Khodakhah, 2004).

Current voltage protocols allowed estimating the action potential frequency in function of the step currents. Increasing step currents were injected in the cell until they failed to overshoot. This firing rate curve was first fitted with a linear regression ($y = ax + b$) where x is the current (in pA), y is the frequency (Hz), a is the slope, b is the intercept on the y axis. The fitting was performed for all values but excluded minimal and maximal frequency values (Higgs et al. 2006) (see results section). The firing rate was also fitted with a sigmoidal function ($y = a / (1 + \exp^{-(x-x_0) / b})$) where x is the current (in pA), x_0 is the point of inflection of the curve, y is the frequency, a is the maximal frequency and b is the slope. Sigmoidal fitting allowed using all values in the distribution for which I reported the slope, the maximal firing frequency and the point of inflection (in some cases). The slope in both linear regression and sigmoidal fitting provided a measurement of the gain of a neuronal response to current injections (Chance et al., 2002; Higgs et al., 2006). Step current protocols of 1 second also allowed analyzing the inter-spike intervals (as

explained above) and the latency to the first action potential was also analyzed as it could give indications about differences in the passive properties or the channels activation/inactivation properties underlying the action potential.

2.2.8.6. Synaptic transmission

Auditory nerve fibres in the deep layer or parallel fibres in the molecular layer were stimulated with a concentric bipolar electrode (section 2.2.6.2, figure 2.13) in order to elicit synaptic potentials or action potentials in fusiform cells. The stimulation rate was 0.3Hz to avoid run down of the synaptic response that could result from vesicular depletion (Neher and Sakaba, 2008). The mixed EPSP threshold was defined as the minimal stimulus strength (voltage) necessary to elicit a depolarization in fusiform cells. The stimulus strength was then increased by 5V and 10 V in order to recruit additional inputs to the cell (synaptic spatial summation detailed in figure 2.18). Ten to twenty traces were averaged together and the EPSP/IPSP areas and peaks were calculated on the averaged trace. The action potential threshold was defined as the minimal stimulus strength (voltage stimulus) necessary to elicit an action potential in fusiform cells. In order to study the action potential amplitude, the 10-90% rise time, the 90-10% decay time and the spike latency, the stimulus strength was increased by a few (2-5V) volts above the action potential threshold voltage to ensure firing consecutive to each pulse. The spike latency was measured from the onset of the recording ($t=0$) to the peak of the postsynaptic action potential. These latencies therefore included 18 ms from the start of recording to the time of the stimulus. For each stimulus, spike temporal jitter was calculated as the standard deviation of the spike latency over at least 20 trials.

The auditory nerve or the parallel fibres were also stimulated with trains of 20 pulses for 2-3 trials with inter-trial intervals of 5-10 seconds. The stimulus rates within the trains were 10, 20, 50 and 100 Hz. Increasing the frequency of stimulus allowed studying the effect of synaptic temporal summation (detailed in figure 2.18) in fusiform cells. When stimulating with repetitive stimulations, the action potential threshold was defined as the minimal voltage to elicit few (1-7) action potentials in fusiform cells. The firing frequency was measured for each stimulating train at different voltages (i.e. threshold voltage and threshold voltage plus 5V and 10 V). The firing was considered reliable when a single action potential was triggered by one stimulation pulse. A reliable firing pattern is therefore represented as an accurate correspondence between the stimulation rate and the measured firing frequency. By contrast, a firing rate is considered as unreliable when a stimulus is followed by either zero or more than one action potential leading to either failures or aberrant firing respectively. Figure 2.19A shows three examples of firing following a train stimulus of 10 Hz. The firing is either reliable (top trace showing a 10 Hz firing) or unreliable (middle and bottom traces showing a firing with failures and a firing with aberrant action potentials respectively). This can be schematized as in figure 2.19 B which represents an input-output relationship of the spike frequency. The blue dot and the straight line represent a reliable firing pattern with a 1 to 1 relationship between the stimulation and the firing frequency. Values below and above the line refer both to an unreliable firing with either failures or aberrant action potentials respectively. The study of the evoked firing rate of fusiform cells allowed establishing whether the multisensory and auditory input stimulations evoked a reliable firing in fusiform cells and how this can be

modulated. The reliability shift was calculated as (mean firing – stimulating frequency) / stimulating frequency.

2.2.9. Statistics

Data are expressed as mean \pm s.e.m unless otherwise stated. Differences in means between two samples were calculated using either paired or unpaired Student's t-tests (Excel) depending on data originating from independent or dependent groups respectively. The Student's T test assumes the populations are normally distributed with a null hypothesis (Ho) claiming the absence of significant differences between the two data groups. The alternative hypothesis (H1) predicts a significant difference between the two groups. Data are considered different upon rejection of the null hypothesis with a P-value of at least 0.05.

A Chi-square test (X^2 test, GraphPad Software, QuickCalcs) was used to test differences between the expected frequencies (f_e) and the observed frequencies (f_o). The Chi-square test is calculated as $((f_o - f_e)^2 / f_e)$ and returns P values with one degree of freedom (two samples tested) indicating a significant difference between the observed and the expected frequencies when ≤ 0.05 .

One-way anova tests (Prism V3, GraphPad Software, San Diego, CA, USA) were used to test for differences among three or more normally distributed groups. Anova tests partition the variability due to group means (due to treatment) and the variability within the groups (also called the residual variation). Variability within groups is quantified as the sum of the squares of the differences between each group and its group mean. This is the residual sum of squares. Variation among groups (due to treatment) is quantified as the sum of the squares of the differences between the group means and the total mean

(the mean of all values in all groups). This becomes the treatment sum of squares. Each sum of squares is associated with a certain number of degrees of freedom and the mean square is computed by dividing the sum of the squares by the degrees of freedom. The F ratio is the ratio of two mean square values. The Anova test is based on the assumption that the populations have all the same variance. If the null hypothesis is true, F will have a value close to 1. P values will determine the chance that randomly selected groups would lead to this large value of F ratio. When an effect is statistically significant in the anova test, a Tukey post hoc test was performed to assess which groups are different from which other groups. Anova tests (F tests) were also used to test the differences between two standard deviations obtained for the inter-spike distribution and post hoc tests were omitted.

In all tests described before, the P-value providing the significance of test and used to reject the null hypothesis is a function of three factors: the observed effect, the size of the sample(s), the criterion required for significance. A power analysis (DSS Research) has been used to test the likelihood that the study would have been significant and is based on the same factors as described before: the larger the effect size used in the power analysis, the larger the sample size, and/or the more liberal the criterion required for significance, the higher the expectation that the study will yield a statistically significant effect. The power for a P value of 0.05 is $P(Z > 0.95)$ where Z is $(\mu_1 - \mu_2) / S.D_2$, μ_1 and μ_2 are the two independent populations means and S.D₂ is the standard deviation of the population test.

2.2.11. Modelling studies

A *Leaky Integrate and Fire* model (MATLAB) was used to simulate the firing of fusiform cells evoked while stimulating the multisensory and auditory fibres. This model assumes that action potentials are simple spikes occurring when the membrane potential reaches a voltage threshold V_{th} . After firing, the membrane potential is reset to a $V_{reset} < V_{th}$ until next threshold crossing occurs. The model also incorporates an absolute refractory period, where the membrane potential has reached the threshold and the dynamics are interrupted, allowing the integration to restart after this time. V_{reset} and V_{th} were set up at 0 and 20 mV respectively and the refractory period was fixed at 2.5 ms.

The model comprises three passive property parameters (R_m , the membrane resistance, C_m , the membrane capacitance and τ_m , the membrane time constant resulting from $C_m \cdot R_m$) with values similar to the experimental values detailed as follow: Granule cells ($R_m = 1900 \text{ M}\Omega$, $C_m = 10 \text{ pF}$ giving a τ_m of 19 ms); cartwheel and tuberculoventral cells ($R_m = 100 \text{ M}\Omega$, $C_m = 100 \text{ pF}$ giving a τ_m of 10 ms); fusiform cells ($R_m = 50 \text{ M}\Omega$ and $C_m = 200 \text{ pF}$ giving a τ_m of 10 ms). Auditory nerve fibres were given the following theoretical values ($R_m = 1000 \text{ M}\Omega$ and $C_m = 10 \text{ pF}$ giving a τ_m of 10 ms). All these parameters were fixed during the simulations except R_m of granule cells that was decreased to 1100 M Ω after acoustic over-exposure (see table 6.36 in results).

Two theoretical networks (multisensory and auditory) were built based on anatomical studies and the circuitries are shown in figures 2.20 and 2.21. Fusiform cell apical dendrites are likely to receive a large amount of parallel fibres (from granule cells) similar to those described in the cerebellum (Mugnaini et al. 1980b) and therefore the number of parallel fibres terminating

onto a single fusiform cell was set to 5000 (table 6.36). By contrast, fusiform cell basal dendrites receive a very small number (about 10 fibres with 10 terminals each) of auditory fibres (Ryugo and May,1993) which was set to 100 (table 6.36). Only two types of inhibitory neurons were considered, cartwheel and tuberculoventral cells projecting onto the apical and basal dendrites of fusiform cells respectively. The number of inhibitory neurones was set to 20 in both multisensory and auditory circuitry. Experimental data suggested that inhibition carried by the auditory inputs is stronger than the inhibition carried by the multisensory system and therefore it is reasonable to assume that there will be a lower ratio between the excitation and the inhibition in the auditory system (100/20) compared to multisensory system (5000/20). Both auditory and multisensory circuitry models were activated by an external stimulus (shown in figures 6.20 and 6.21) and consisting of 20 pulses delivered at a rate of 20 Hz giving a total duration of 1000 ms. Spatial fibre recruitment was simulated by varying the inactivation probability (from 0 to 0.49), so that probability of zero corresponds to the totality of cells being recruited. The pharmacological action of strychnine and gabazine on the inhibitory synaptic transmission was simulated by applying a factor 0 on the strength of the inhibitory synapses. For simplicity purpose, the model will refer to granule cells as the cell bodies of the parallel fibres.

2.3. Auditory brainstem response recordings and acoustic over-exposure

Experiments were carried out on Lister Hooded and Wistar rats mainly aged between 14-21 days, in accordance with Home Office Regulations as described in the Animals Act (Scientific Procedures 1986).

2.3.1. Use of anesthetics

Auditory brainstem recordings (ABR) and acoustic over-exposure were carried out on anaesthetized rats. The measurement of the ABR requires the animal to stay still with a good muscle relaxation and loss of reflex activity to obtain reproducible recordings. In order to comply with this, three different types of anesthetics have been initially tested in Lister Hooded rats. In all cases, loss of the pedal reflex was used to determine sufficient sedation.

2.3.1.1. Isoflurane

Isoflurane is a volatile anesthetic and was used as a safe method of anaesthesia for small animals offering a rapid onset and a good post-surgical recovery. The mechanism of action of isoflurane is still unclear but very recent studies suggest that it suppresses excitatory synaptic transmission by inhibiting the neurotransmitter release (Herring et al., 2009). Isoflurane (1-3%) was mixed with oxygen at a rate of 1l/minute.

2.3.1.2. Hypnorm® and Hypnovel®

Hypnorm® (VetaPharma Ltd) is a combination of fentanyl and fluanisone and is commonly used with other anaesthetic agents in small mammals (in this case Hypnovel also called midazolam) essential to maintain normothermia.

Intraperitoneal injections of Hypnorm were combined to Hypnovel (Roche) as follow: fentanyl (0.15mg/kg), fluanisone (5mg/kg) and Hypnovel (2.5 mg/kg).

Fentanyl is a highly potent and efficient μ opioid agonist acting similarly to morphine but 20 to 100 times more potent than morphine in terms of analgesia (Green, 1975). Fentanyl takes effect very rapidly but its duration of action is relatively short. Fentanyl can cause profound central nervous system and respiratory depression as well as bradycardia.

Fluanisone potentiates the analgesia provided by fentanyl with the additional benefit of antagonizing any respiratory depression (Inoue et al, 1994). Fluanisone is a tranquilizer that belongs to the butyrophenone group, with putative antipsychotic activity and dopamine antagonist properties. The combined action of fentanyl and fluanisone ensures a long duration of the anesthesia as rats were usually anesthetized for 1hour – 90 minutes without any top up.

Hypnovel® (Midazolam) is a potent sedative analgesic agent and a major tranquilizer that induces a state of central nervous system depression bordering on general anesthesia (also called neuroleptanalgesia, Green, 1975). Midazolam is a benzodiazepine with a rapid onset and a short duration of action due to its rapid metabolism (Flecknell and Mitchell, 1984). Midazolam on its own does not induce anesthesia in rodents but it potentiates the effects of fentanyl (Pieri et al, 1981). I used a combination of fentanyl, fluanisone and midazolam as this combination produces neuroleptanalgesia with good skeletal muscle relaxation in many rodents and also in rats (Flecknell and Mitchell, 1984). Supplementary doses were administered if the animal showed signs of arousal during the ABR recordings.

2.3.1.3. Ketamine and xylazine

The combination of ketamine and xylazine is popular for the anaesthesia of many rodents (Arras et al., 2001; Kawahara et al., 2005). Ketamine is a NMDA receptor antagonist (Hirota and Lambert, 1996) and xylazine it is an agonist at the α_2 class of adrenergic receptor (Hsu, 1981) used is a powerful sedative and analgesic. As an NMDA receptor antagonist, ketamine is not recommended when studying synaptic plasticity and I limited its use to few experiments on Lister Hooded rats (detailed in chapter 5). Lister Hooded rats were then anesthetized with intraperitoneal injections of ketamine (100mg/kg) and xylazine (10mg/kg).

2.3.2. Auditory brainstem response recording

2.3.2.1. The auditory brainstem response

The auditory brainstem response (ABR) is composed of waves produced by a brief acoustic signal such as a single tone frequency (tone pip) or a click (broadband stimulus). The rat ABR is composed of four vertex-positive waves (waves I to IV) occurring within 6 ms of the stimulus onset (Church et al., 1984). Waves are generated by a series of post-synaptic potentials and action potentials ascending the lower portion of the auditory pathway. The neurogenerators of the rat's ABRs have not been determined. However, in the mouse they reflect the neural activity of the auditory nerve (wave I), the cochlear nucleus (wave II), the superior olivary complex (wave III), and the lateral lemniscus and/or the inferior colliculus (wave IV) (Parham et al., 2001). One example of an ABR recorded in a rat is shown in figure 2.22. The ABR has many clinical implications as it provides an estimation of the hearing sensitivity

and allows identifying neurological abnormalities along the auditory pathway (Starr and Achor, 1975).

2.3.2.2. The recording setup

The recording setup is detailed in figure 2.23. Rats were stimulated with short (5 ms) tone pips of the desired frequencies (8 to 30 kHz) generated by a Thurlby Thandar arbitrary waveform generator (TGA 1230, 300 MHz, Tucker Davis, US). The maximum amplitude of the signal generated was 20 Volts peak to peak which corresponds to an intensity of 94 dB SPL. Control of the generator was performed via the ADC output of a PC. The rate of stimulus was set at 10 Hz and the total stimuli number was set between 100 and 400 depending on the resolution of the signal. The stimulus onset triggered the capture and the averaging of the ABR response by the PC. The stimulus signal was fed into two manually controlled, programmable digital attenuators (Tucker Davis Technology, USA). The first attenuator was used to attenuate the signal in 10 dB SPL steps whereas the second attenuator was used to attenuate the signal in 3 dB SPL steps. This final signal was fed to a reverse driven battery-operated B&K microphone (B&K 4134) serving as the acoustic driver (figure 2.23). The final ABR response constituted an average of 100-400 individual traces recorded by intradermal electrodes (figure 2.24) with an input gain of 20 μ V/div connected to an amplifier (figure 2.23, Medelc Sapphire 2A). From the amplifier the analogue signal was then fed via the ADC input of the ADC sampler at a rate of 16 kHz and the ABR signal was displayed on the PC (figure 2.23).

2.3.2.3. The auditory brainstem response recording procedure

Animals were anaesthetized and placed on a heating pad to maintain the body temperature at around 38°C. The ABR was recorded by three subdermal needles electrodes placed as follow: the positive electrode was placed on the top of the skull between the ears, the negative electrode was placed in front of the left ear and the third electrode, the earth, was placed on the rump (figure 2.24). Stimulations were performed in an open field (figure 2.25) conditions in which the acoustic driver was placed in a holder and positioned with the use of a manipulator on top of the left ear of the rat. I estimated that in this condition the acoustic driver was placed at a distance of 0.5 cm from the ear.

2.3.2.4. Analysis

To assess the hearing threshold, the initial stimulus delivered by the acoustic driver was set to 94 dB SPL and then reduced by 10 or 3 dB SPL step until the ABR wave I and II could no longer be defined. The amplitude and the latency of wave I obtained at maximal stimulus intensity of 94 dB SPL were also measured in certain cases. Details of the ABR analysis is described in the figure 2.26.

ABR were recorded before and 3 to 4 days after exposing the animals for the first time to a loud (110 dB SPL) single tones (14.8 kHz) (as described below). In the text I will refer to these animals or to these conditions as “over-exposed”. Controls (also referred as “unexposed”) were performed on similarly anaesthetized rats that stayed unexposed to the loud tone.

2.3.2.5. Calibration of the acoustic driver

A B&K 4134 microphone was used to measure the intensity of the sound emitted by the acoustic driver. The distance between the microphone and the acoustic driver was set to 0.5 cm in order to reproduce the same distance existing between

the rat's ear and the acoustic driver while recording the ABR. The output from the B&K 4134 microphone was fed into a digital oscilloscope (PicoScope ADC200 sys V6.2) and the intensity in dB Volt was further converted in dB SPL using the software sound level calibrator (CAL73). The values are detailed in the table below:

Acoustic driver signal		Intensity measured at 0.5 cm	
kHz	dB	dB Volt	dB SPL
8	94	-35	83
8	84	-46	72
8	74	-58	60
24	94	-32	86
24	74	-58	60
24	64	-62	56

2.3.3. Acoustic over-exposure

Acoustic over-exposure was performed in a home made sound insulated box (Figure 2.27) containing a loudspeaker (Prosound WF09K, freq range 4-40 kHz) delivering a single tone (14.8 kHz) at 110 dB SPL for 2-3 hours per session. Acoustic over-exposure was repeated two to three times with at least one day interval between the sessions. Wistar rats aged P14 and P19 were anesthetized with fentanyl (0.15mg/kg), fluanisone (5mg/kg) and Hypnovel (2.5 mg/kg) and placed on a heating pad in the box maintained at 23-24°C. Animals were usually anesthetised for the first hour (up to 90 minutes) and stayed sedated for the whole acoustic over-exposure procedure. Sometimes, the sedation in animals terminated before the end of the exposure and additional top up of anaesthetic was sometimes given to the rat if the rat showed signs of distress.

Dissection of the brainstem

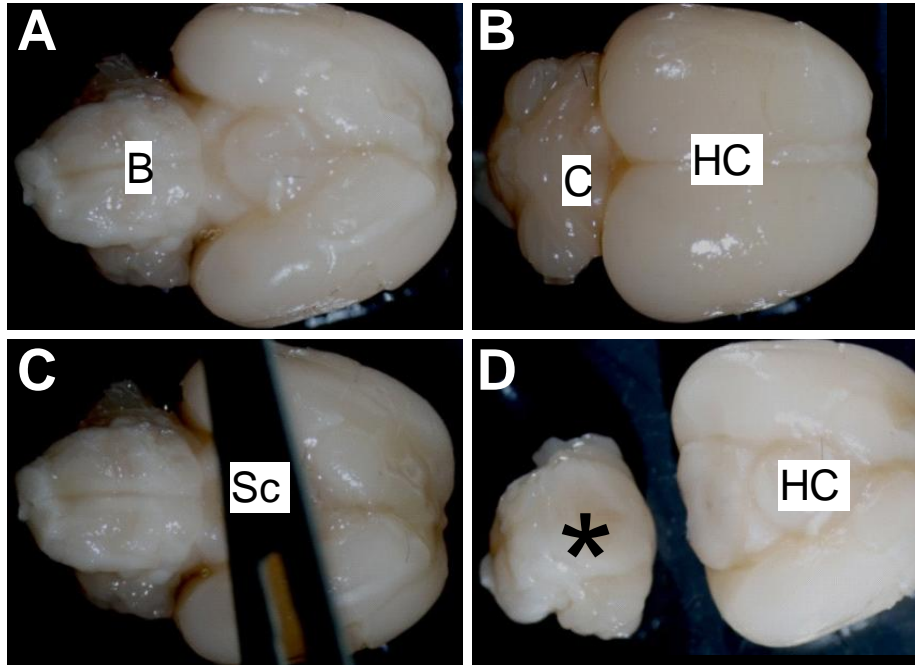


Figure 2.1: Dissection of the brainstem. A-D. Brain from a 17 days old Wistar rat. **(A)** shows the ventral surface of a whole brain with labelling B pointing to the brainstem. **(B)** shows the dorsal surface of the whole brain with labelling C showing the cerebellum and labelling HC showing the cerebral hemispheres. **(C)** shows the ventral view a whole brain with the scalpel blade (Sc) before separation of the brainstem. **(D)** shows the brainstem and cerebellum (*) separated from the cerebral hemispheres. Abbreviations: (B) brainstem, (C) cerebellum, (HC) cerebral hemispheres, (Sc) scalpel blade, (*) brainstem and cerebellum.

The slicing procedure

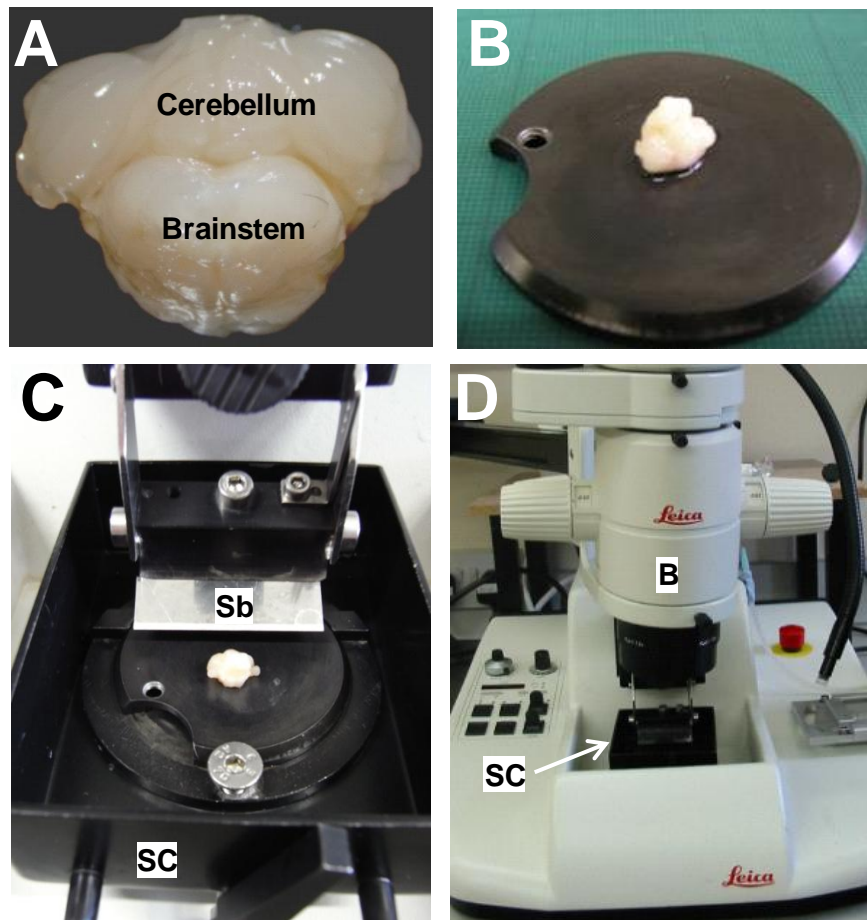


Figure 2.2: Slicing procedure. (A). View from the top of the brainstem and the cerebellum (originating from a 17 days old Wistar rat). (B) shows the brainstem and cerebellum viewed from the side and glued on the slicing platform. (C) shows the platform with the glued brainstem and the cerebellum in the slicing chamber (SC). The stainless steel blade (Sb) used to cut the slices is also shown. (D) shows the vibroslicer, the binocular (B) and the slicing chamber. Abbreviations: (B) binocular, (Sb) stainless steel blade, (SC) slicing chamber.

Maintenance of slices

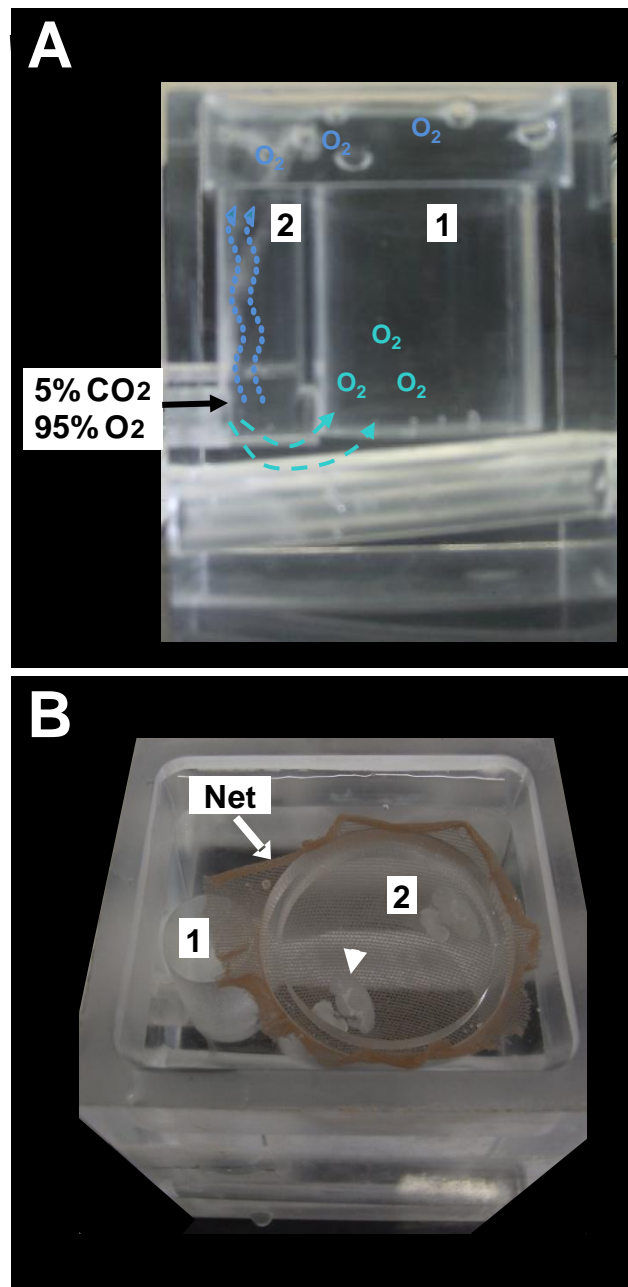


Figure 2.3 Slices are maintained in a home made bubbling chamber. (A) shows the chamber containing the medium in section 2.1.2 and bubbled with a mixture of 5% CO₂ and 95% O₂ through a tube connected to the gas cylinder. The presence of 5% CO₂ is important in maintaining the pH at around 7.4. Separation of chambers 1 and 2 allows the tissue to stay undisturbed from bubbles and the gas mixture gets evenly distributed throughout to chamber 2 containing the tissue. **(B)** Bubbling chamber viewed from top containing brainstem slices (shown with the arrowhead). The slices are lying on a net indicated by the arrow. Chamber 1 and chamber 2 are also shown.

Cytoarchitecture of the DCN

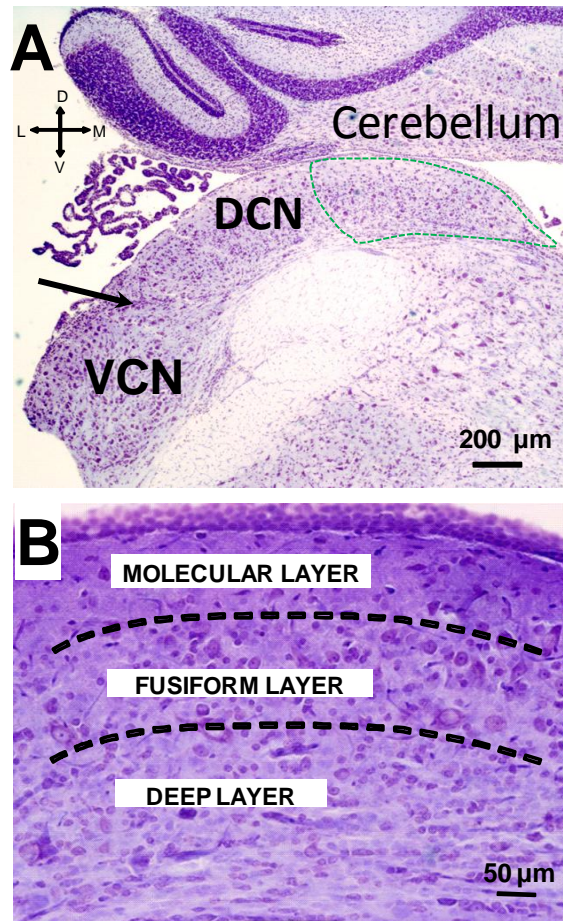


Figure 2.4: DCN slice stained with cresyl violet. (A) shows the location of the DCN separated from the VCN by a densely packed area of granule cells (arrow). The green dashed line indicates the area of high frequency encoding where cells are recorded from. **(B)** Shows the three layers of the DCN. Abbreviations: (DCN) dorsal cochlear nucleus, (VCN) ventral cochlear nucleus. (D) dorsal, (L) lateral, (M) medial, (V) ventral.

The fluorescence microscope

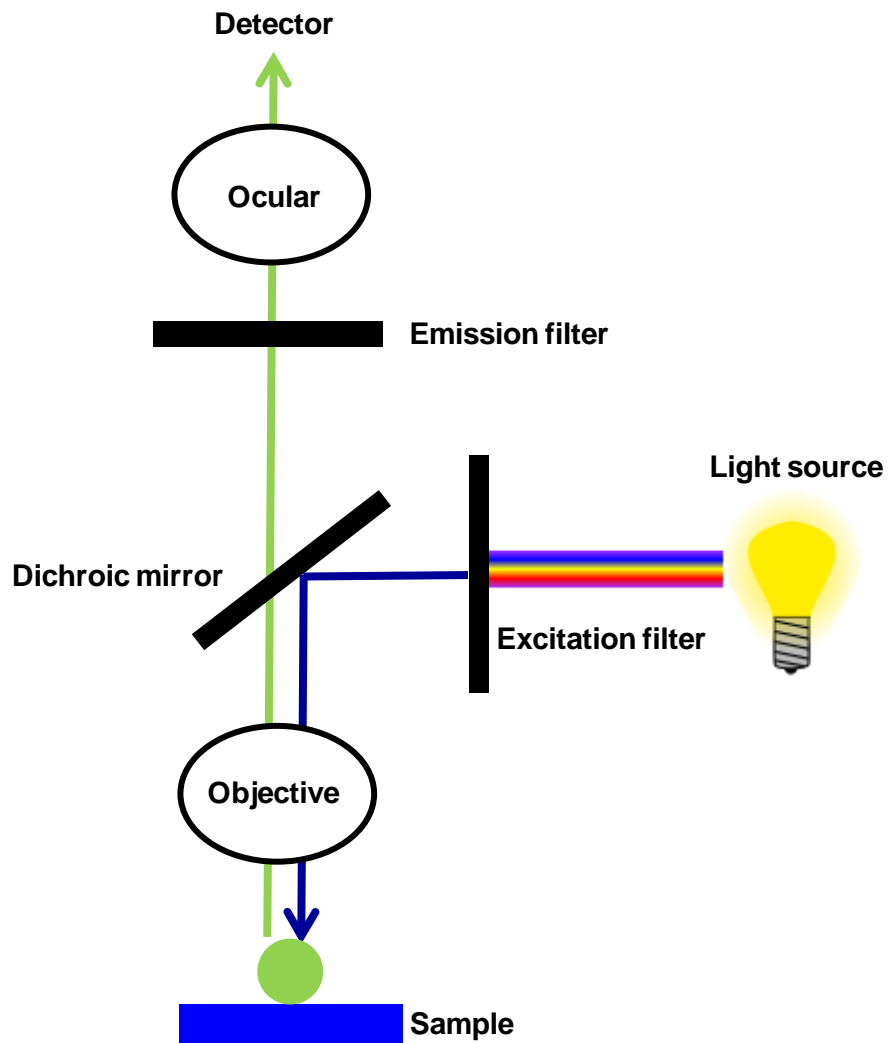


Figure 2.5: The fluorescent microscope. Ultraviolet light is used on the Zeiss Axiovert microscope to excite the fluorophore (lucifer yellow) introduced in the cell during the whole cell recording using a Xenon lamp. The excitation filter wavelength is between 450nm and 490nm whereas the emission filter wavelength is between 520nm and 560nm. For the fluorescent microscope to operate properly, the excitation light must be focused on the sample because the fluorophore will only be excited when the optics is focused on the sample. Moreover, in order to visualise the fluorescence from the fluorophore; the emitted light must be collected. The dichroic mirror reflects the wavelength passed by the excitation filter but not the emitted light.

The confocal microscope

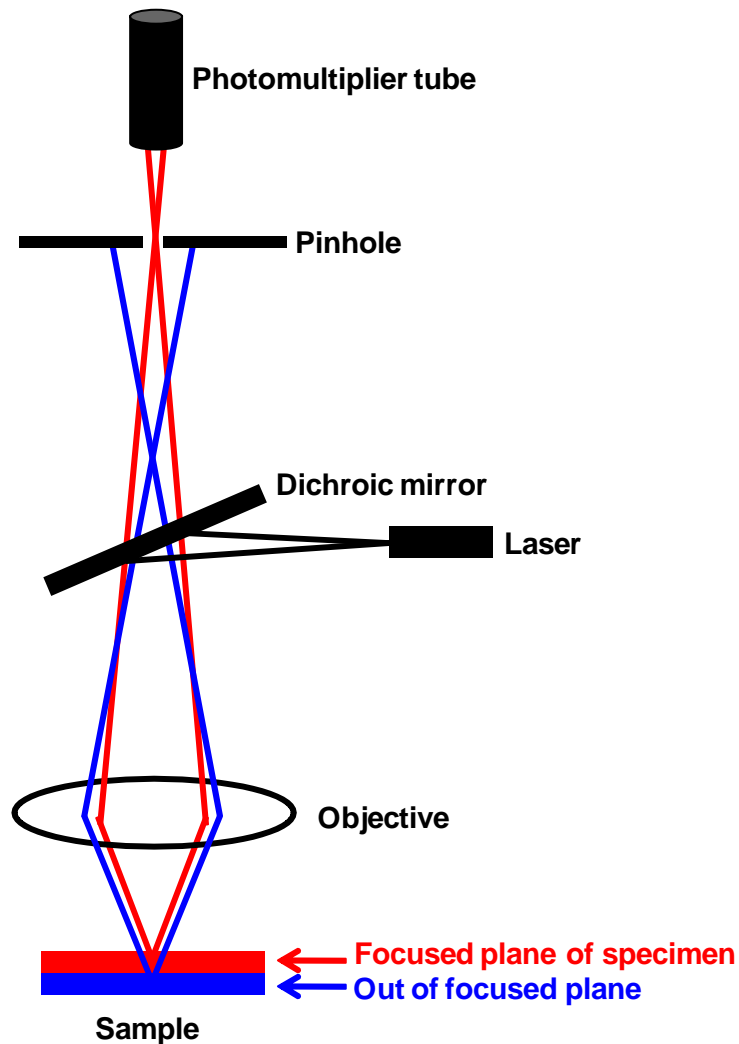


Figure 2.6 Confocal microscopy. Confocal microscopy was used subsequently to the patch clamp recording to allow cellular identification. The confocal microscope (Olympus IX70) uses laser light emitted from a single spot and focused on a pinhole before being detected by a photomultiplier tube. Focused light (red) reaches the photomultiplier tube whereas out of focus light (blue) is blocked by the confocal aperture (pinhole). The three-dimensional image is produced with the software Fluo View (Olympus software) by compiling several optical sections along the z-axes.

Patch clamp recording equipment

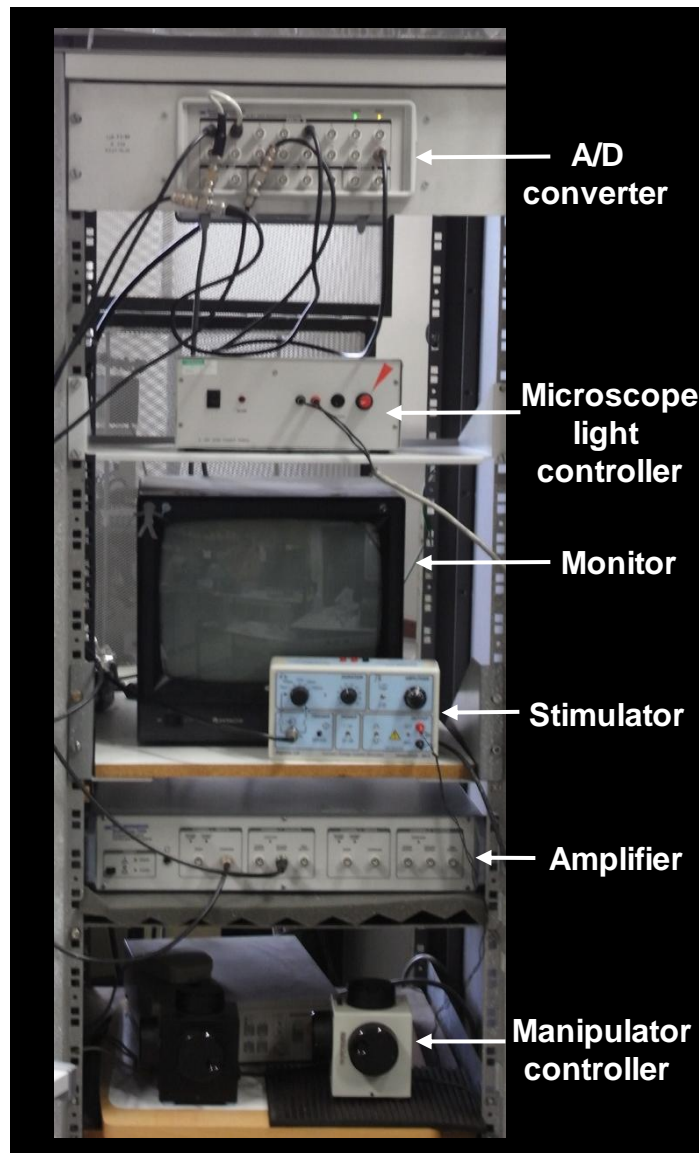


Figure 2.7 Patch clamp recording equipment. The electrophysiological setup consists of a patch clamp amplifier MultiClamp 700A connected to an analogical to digital (A/D) converter Digidata 1322A. Cells were visualized on a monitor connected to a CCD camera Hamamatsu. The motorized micromanipulator controller (Burleigh) and the voltage stimulator (Digitimer LTD) are also shown.

The electrode holder

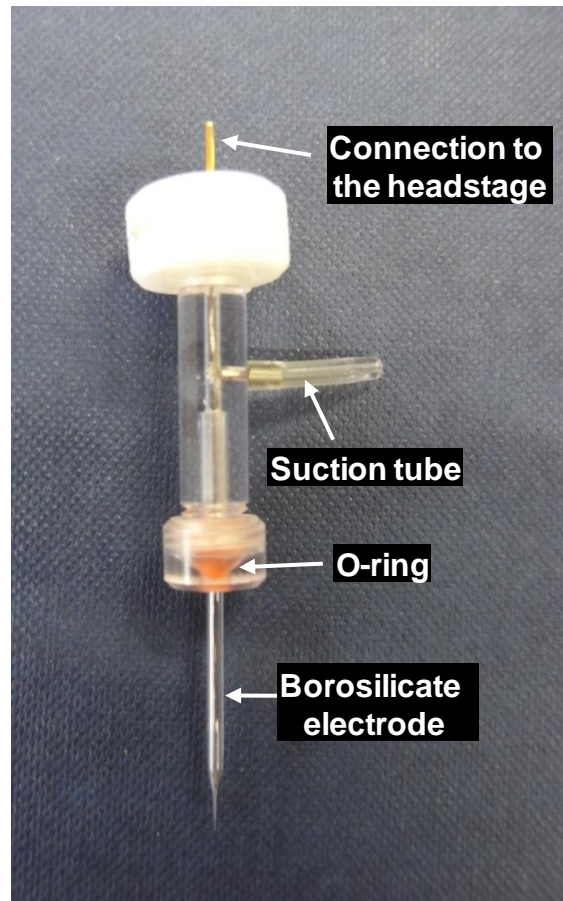


Figure 2.8: Electrode holder. The polycarbonate electrode holder contains a filament of Ag/AgCl linking the electrode to the headstage. Positive pressure in the pipette is applied through the suction tube. O-rings ensure the air pressure is maintained within the holder.

Patch clamp equipment close to the microscope

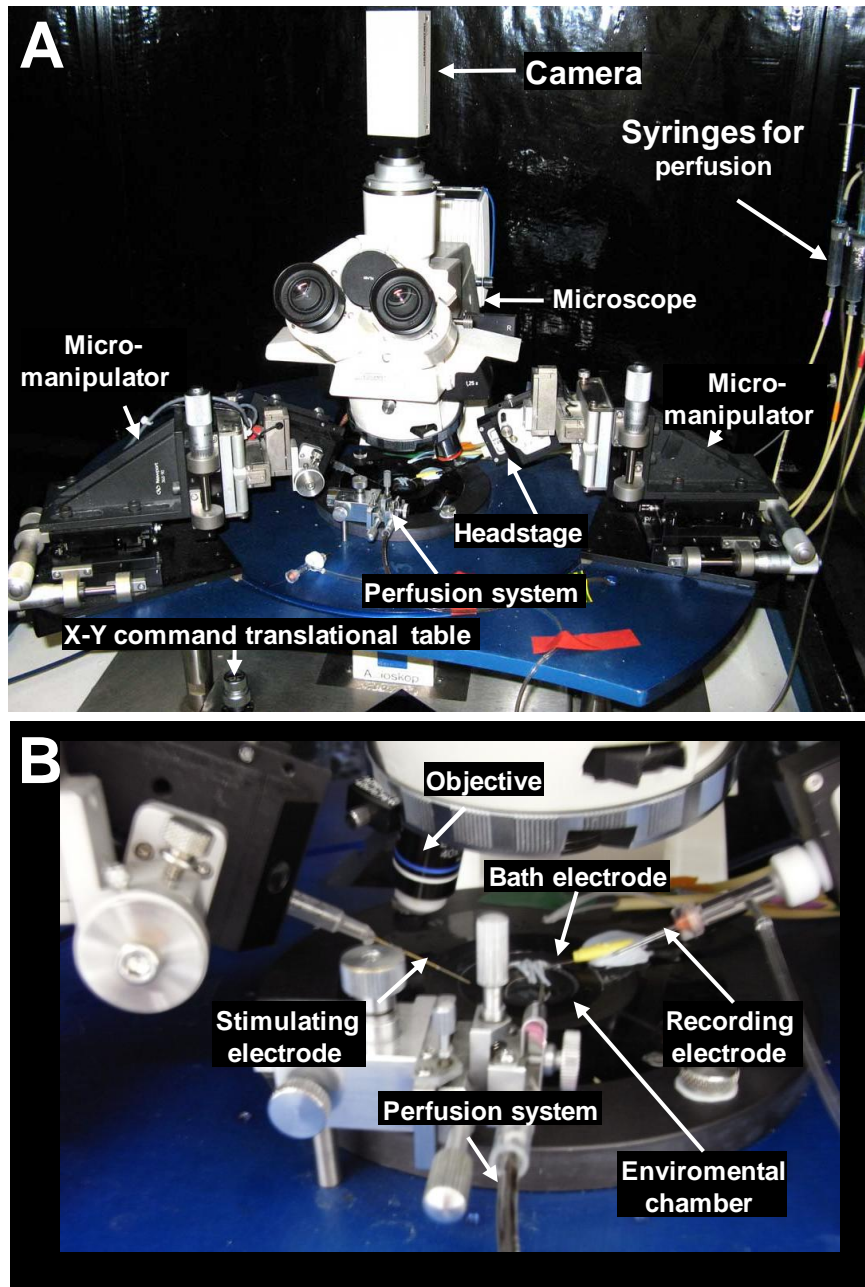


Figure 2.9: Recording equipment close to the microscope. (A). Shows the upright microscope (Zeiss, Axioscop) with a charge coupled device camera (Hamamatsu) and two micromanipulators (Burleigh) attached to the platform. A headstage is attached to one manipulator contains a current to voltage converter used in voltage clamp mode and a voltage follower used in current clamp mode. Slices are transferred to a perfusion chamber placed on the stage the microscope and the bath medium is continuously changed through perfusion lines linked to a peristaltic pump (shown in figure 2.11). **(B)** shows the environmental chamber with the recording, the stimulating and the bath electrodes.

Harp design



Figure 2.10: Harp to maintain slices in the perfusion chamber. The harp was hand made and composed of a platinum wire, previously flattened with a vice. Single nylon filaments were extracted from tights and glued to the border of the platinum wire with Super-Glue.

The perfusion system

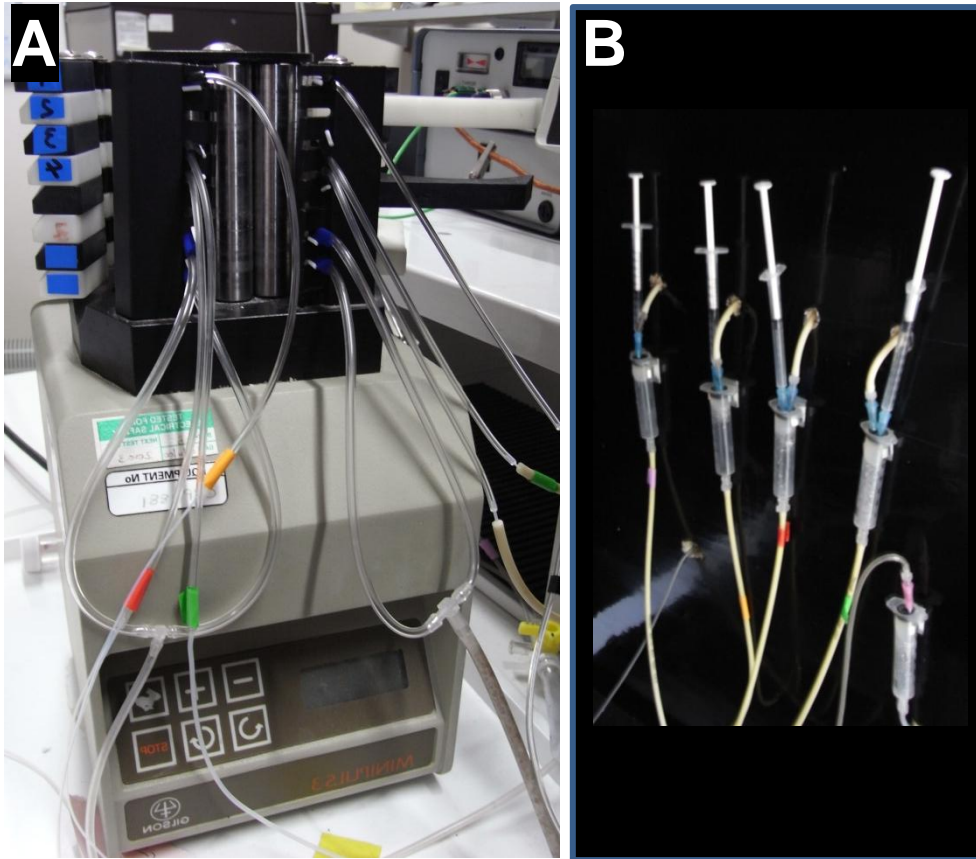


Figure 2.11: The perfusion system. (A) shows the peristaltic pump with four separate perfusion lines flowing into the chamber and two perfusion lines flowing out of the chamber (this ensures a solution turn over within the bath of about 1 minute). (B) Solutions were first transferred into 5 ml syringes to avoid bubbles and then into the experimental chamber.

The electrode puller

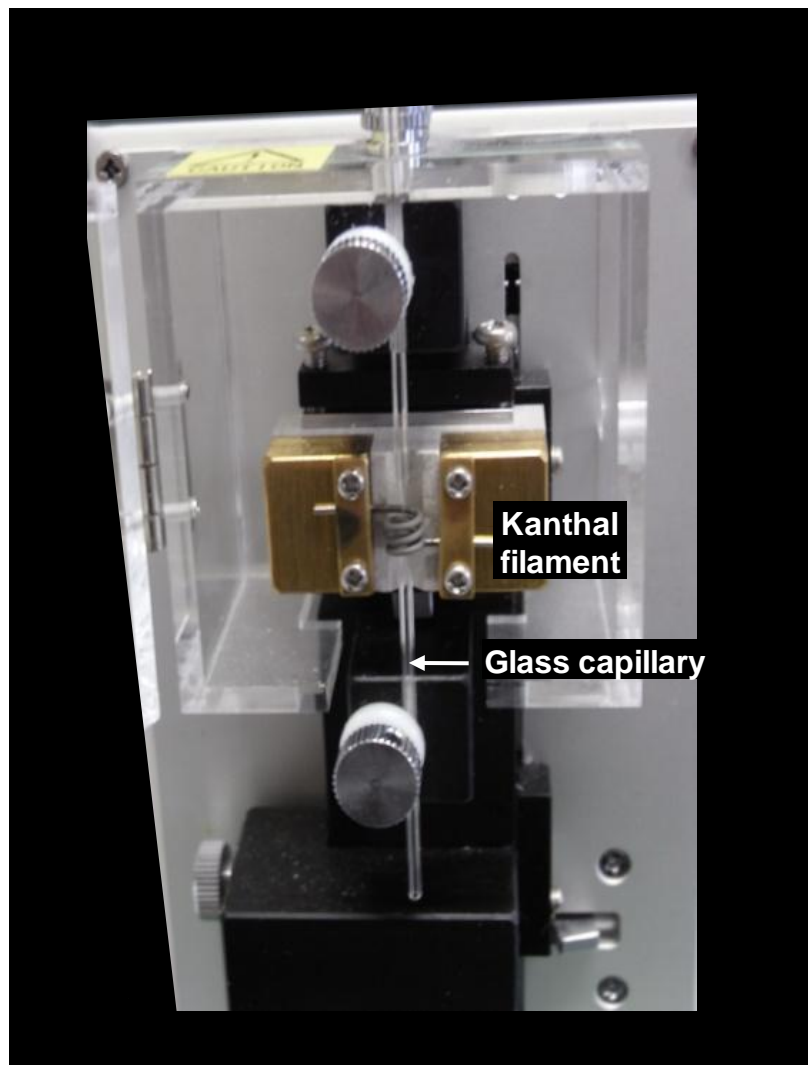


Figure 2.12: Electrode puller. The puller pulls the borosilicate glass capillary vertically, using the force of its own weight. Electrodes are pulled through a solenoid filament made of Kanthal which is an alloy of mainly iron, chromium (20–30 %) and aluminium (4–7.5 %). The process involves two stages in which the solenoid filament is heated with specific heating temperature. The first heating stage ensures an appropriate pipette length whereas the second heating stage ensures the appropriate pipette diameter.

The stimulation electrode

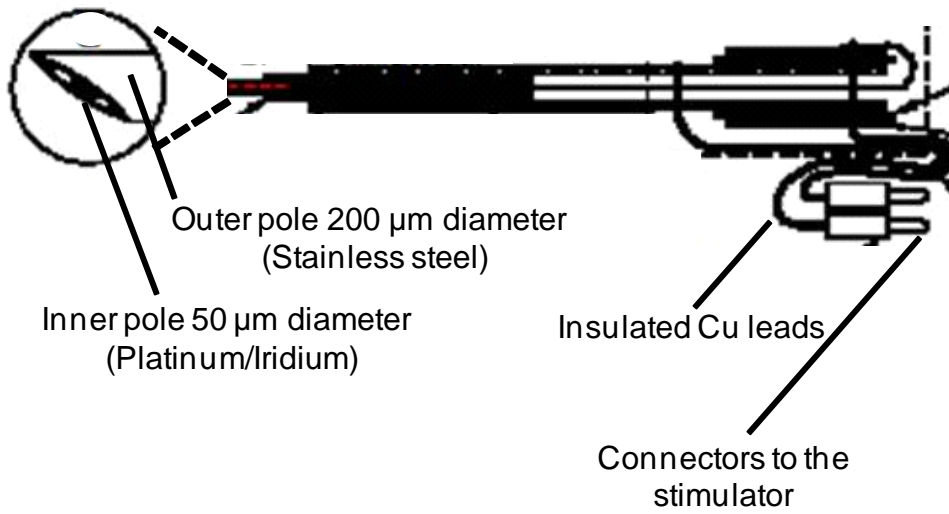


Figure 2.13: Stimulating bipolar concentric electrode. The stimulating electrode (FHC Inc) had an outer pole of 200 μm diameter and a inner pole of 50 μm diameter connected to a voltage stimulator trough two insulated copper leads.

The method of patch clamp recording

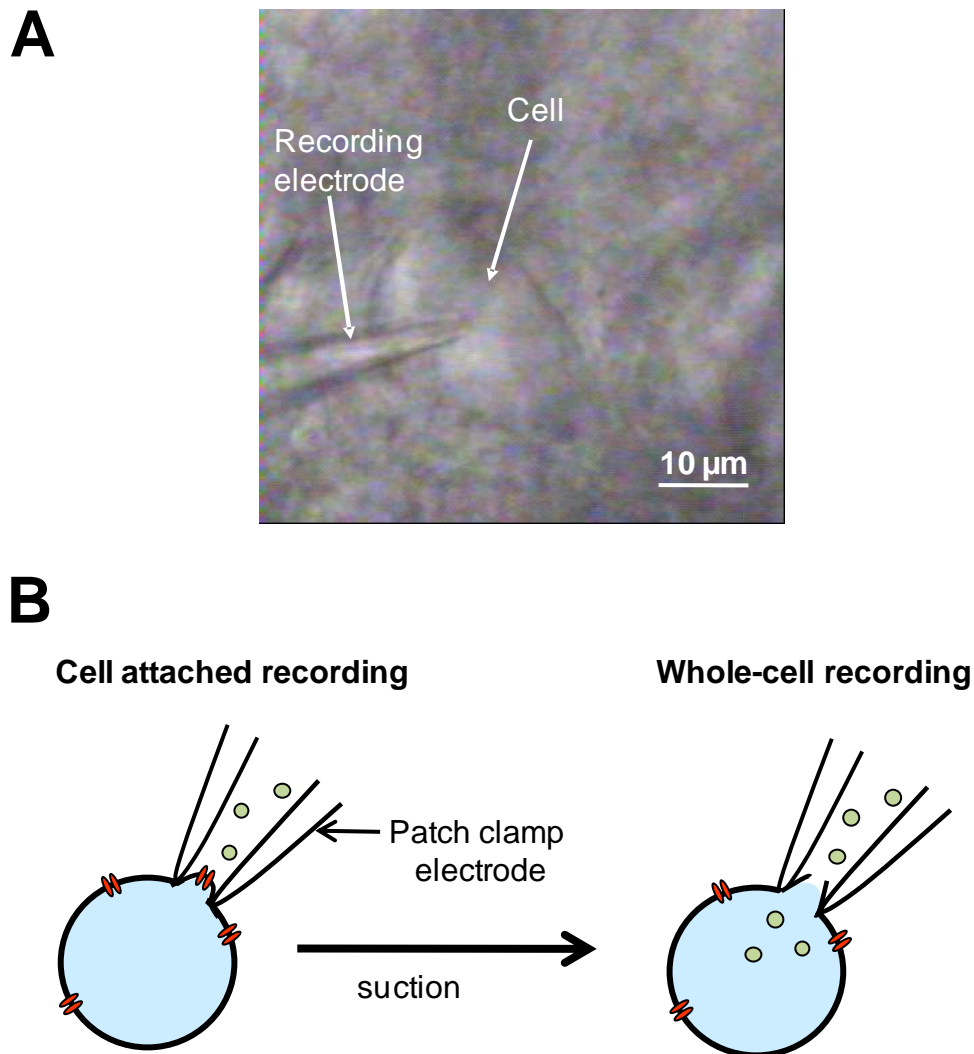


Figure 2.14: Patch clamp recording. (A). Recording electrode on top of a DCN fusiform cell. **(B).** Left: schematic diagram of the cell attached configuration obtained by release of the positive pressure previously applied to the pipette. Isolated channels can be recorded in this configuration. Right: whole cell recording obtained by applying a suction to the pipette that will trigger the rupture of the membrane patch and the dialysis of the cell.

The current clamp circuit

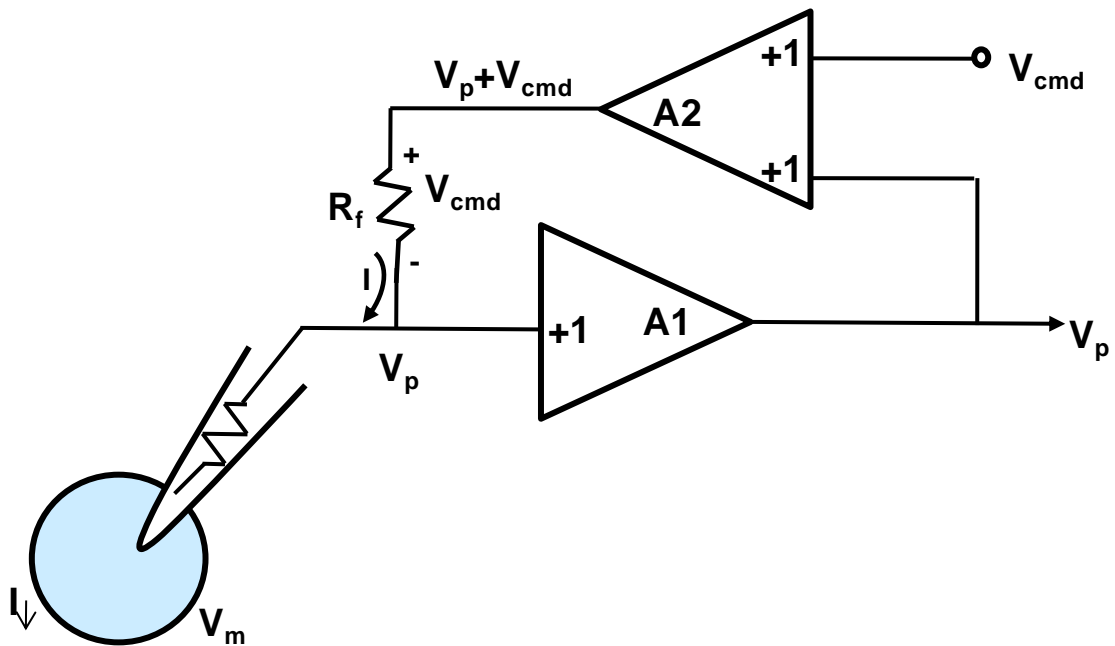


Figure 2.15. Circuit of the current clamp mode. In the current clamp mode of the MultiClamp 700A amplifier, the headstage is a voltage follower circuit comprised of an infinite input resistance unity gain op-amp (A1). The output of V1 is the pipette voltage, A2 is a summing amplifier (summing V_p to V_{cmd} , the command potential) used for injecting current into the cell. The voltage across the headstage resistor R_f is equal to V_{cmd} regardless of V_p . Thus the current through R_f is given exactly by $I = V_{cmd} / R_f$.

The voltage clamp circuit

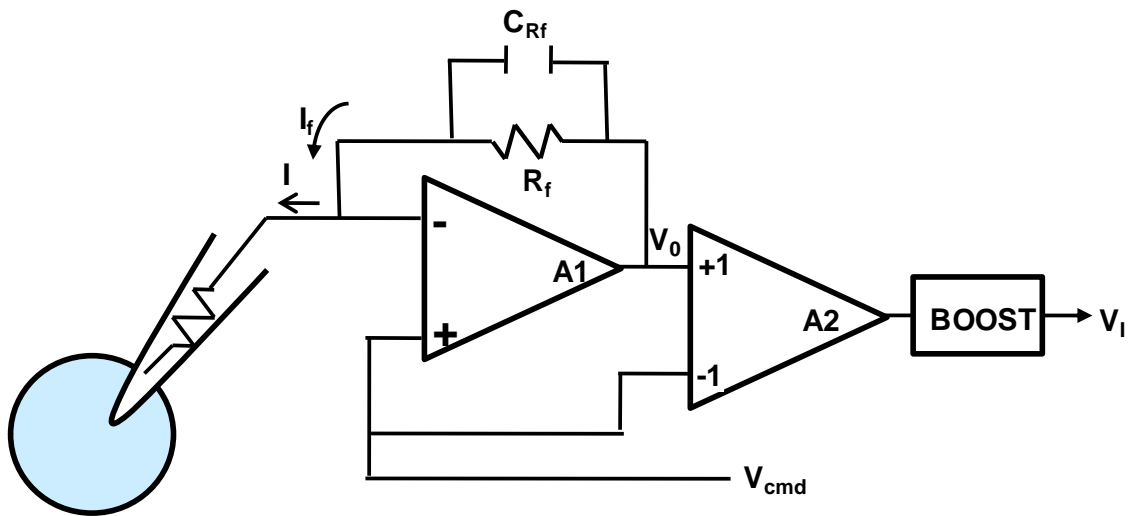


Figure 2.16. Voltage clamp circuit. An operational amplifier A1 is configured as a current to voltage converter producing a voltage output that is proportional to the current input. The op amp has an infinite resistance with no current flowing into the “-” input of the op amp. Therefore the current flowing out of the electrode is equal to the current flowing through the feedback resistance (R_f). As an op-amp, the two voltage inputs are equal and therefore, the voltage at the “+” input and the voltage at the “-” input is V_{cmd} (or V_p). The voltage across R_f is $V_p - V_o = I_f \cdot R_f$. The electrode current is given by $I_e = I_f = (V_p - V_o) / R_f$. As R_f is very large, the circuit can measure very small currents (in the pA range). The differential amplifier A2 subtracts V_{cmd} (the voltage command) from the output of A1 to generate a voltage that is proportional to the voltage across R_f (the feedback resistance) and hence the feedback current I_f . The boost circuit increases the high-frequency gain to compensate for the narrow bandwidth of the feedback resistor.

Measurement of the membrane resistance

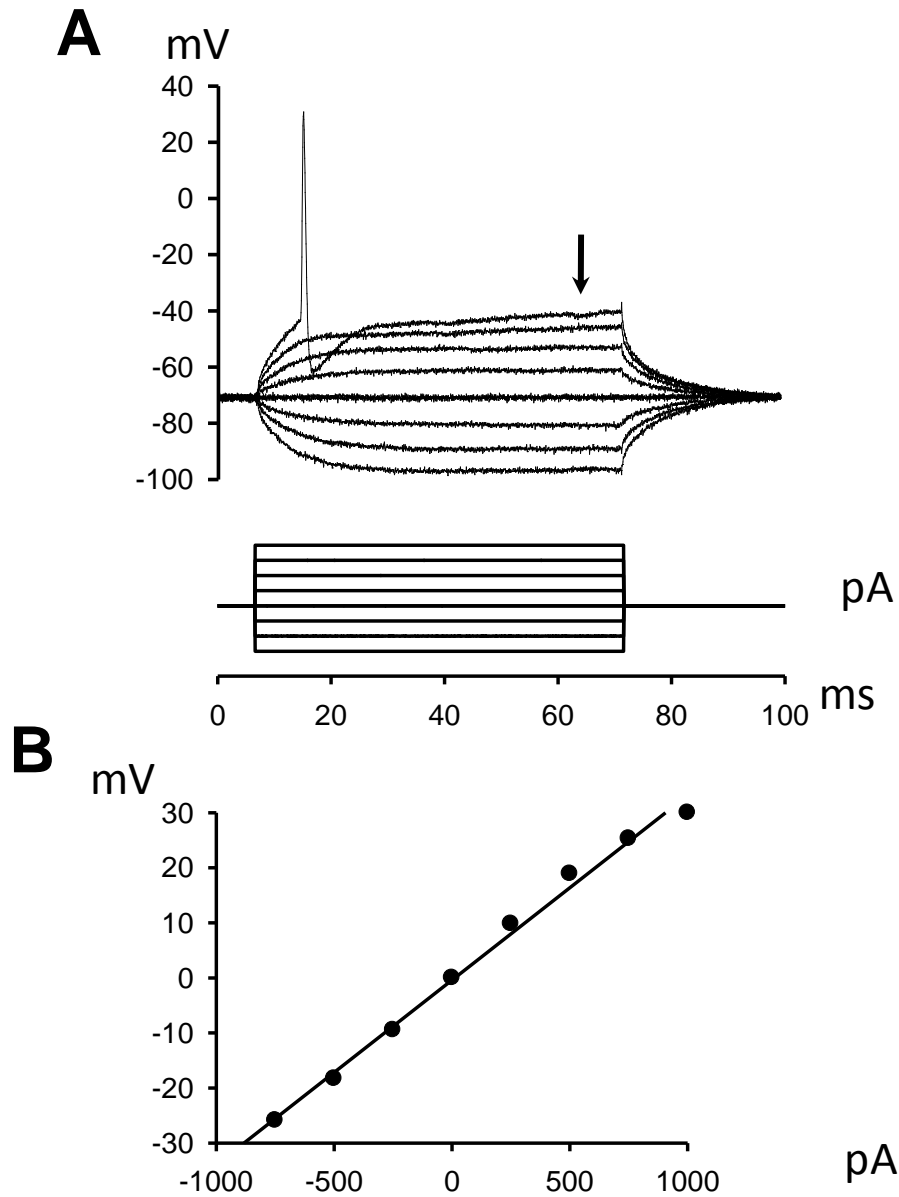


Figure 2.17 : Measurement of the membrane resistance. (A) Example of step currents generating voltage deflections in a fusiform cell. The cell was held at -70 mV while applying 250 pA hyperpolarizing and depolarizing step currents. **(B)** The injected step current and the membrane voltage deflection are plotted at the point of the arrow. The membrane resistance is calculated as the slope of this linear fit and is 30 M Ω for this cell.

Temporal and spatial summation

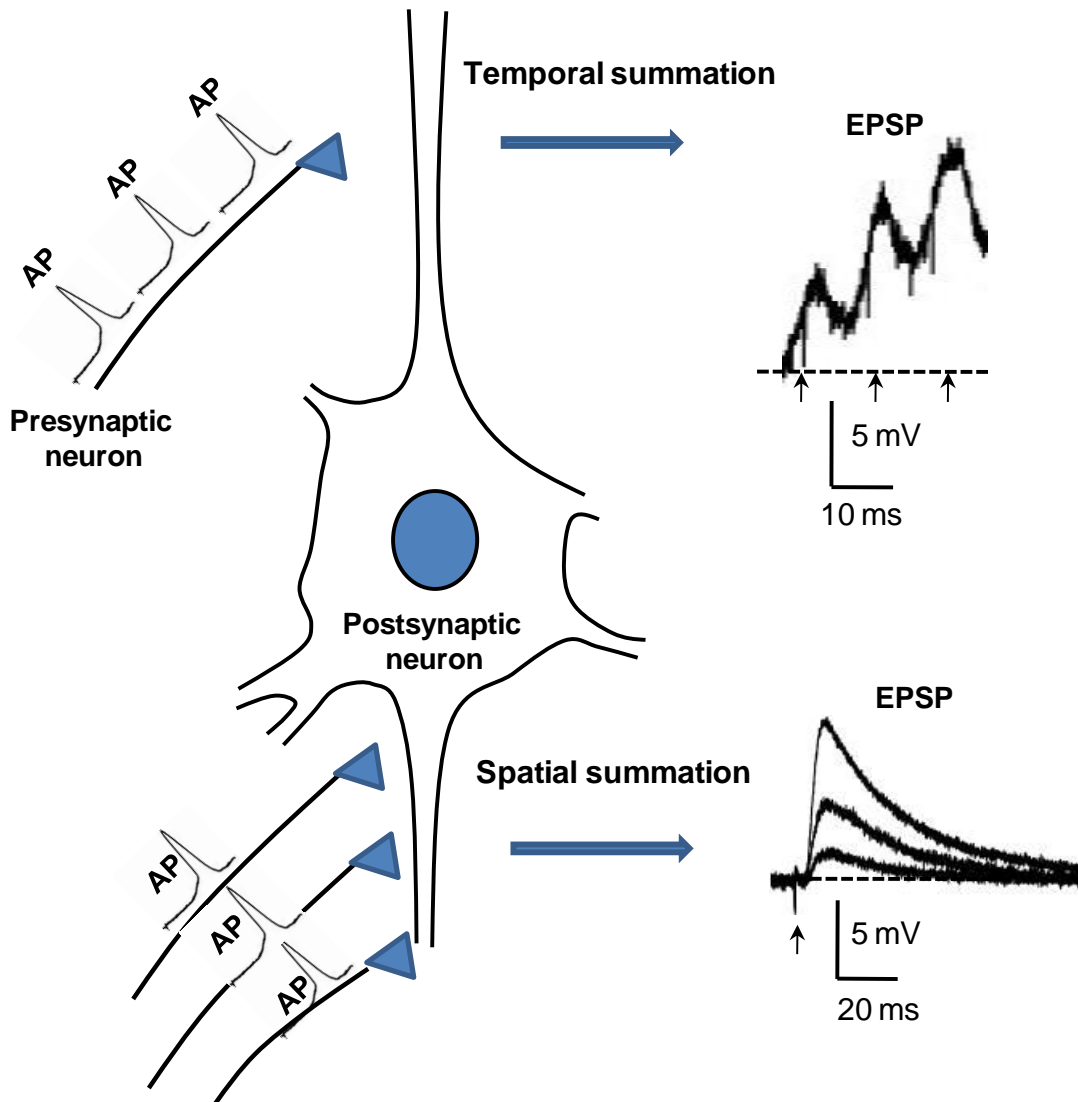


Figure 2.18: Spatial and temporal summation. Dendrites and soma integrate excitatory and inhibitory inputs to determine when the neuron should discharge action potentials (AP). The passive membranes of the neurone are critical for determining how well a neuron can integrate synaptic inputs. The length constant which is the distance at which 37% of V_{\max} has decreased from the synapse allows EPSPs to spread and summate with other EPSPs. This integrative property is called spatial summation. To integrate a sequence of incoming inputs the post synaptic neuron must have a long time constant so that the first EPSP persists long enough to summate with a subsequent EPSP (temporal summation). The traces at the right are obtained from DCN fusiform cells. The example shown in the trace on top shows the temporal summation at 10 Hz. The time constant is the product of the membrane resistance and the membrane capacitance and was 15 ± 4 ms in 6 fusiform cells.

Examples of firing pattern

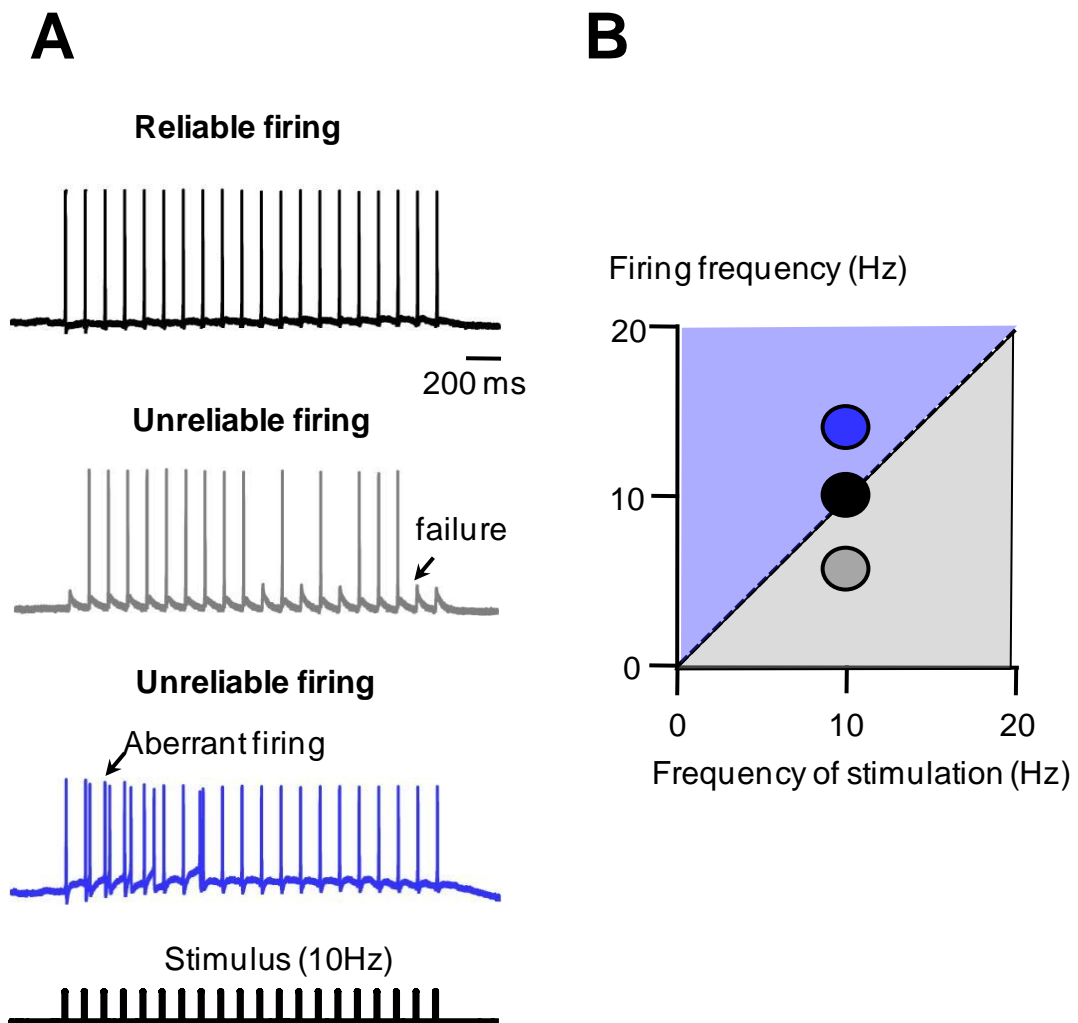


Figure 2.19 Examples of cell firing in response to a 10 Hz stimulation. Firing frequency is either reliable (10 Hz, top) or unreliable with either failures (7 Hz, arrows middle trace) or aberrant firing (14 Hz, arrows bottom trace). **B.** The firing frequency of the three traces in A is plotted in relation to the frequency of stimulation (represented as colour coded dots). The dotted line representing the reliable firing pattern for frequencies ranging from 0 to 20 Hz separates two areas of unreliable firing pattern (similarly colour coded with the traces).

Circuitry used for modelling the connections of the multisensory inputs to the fusiform cell

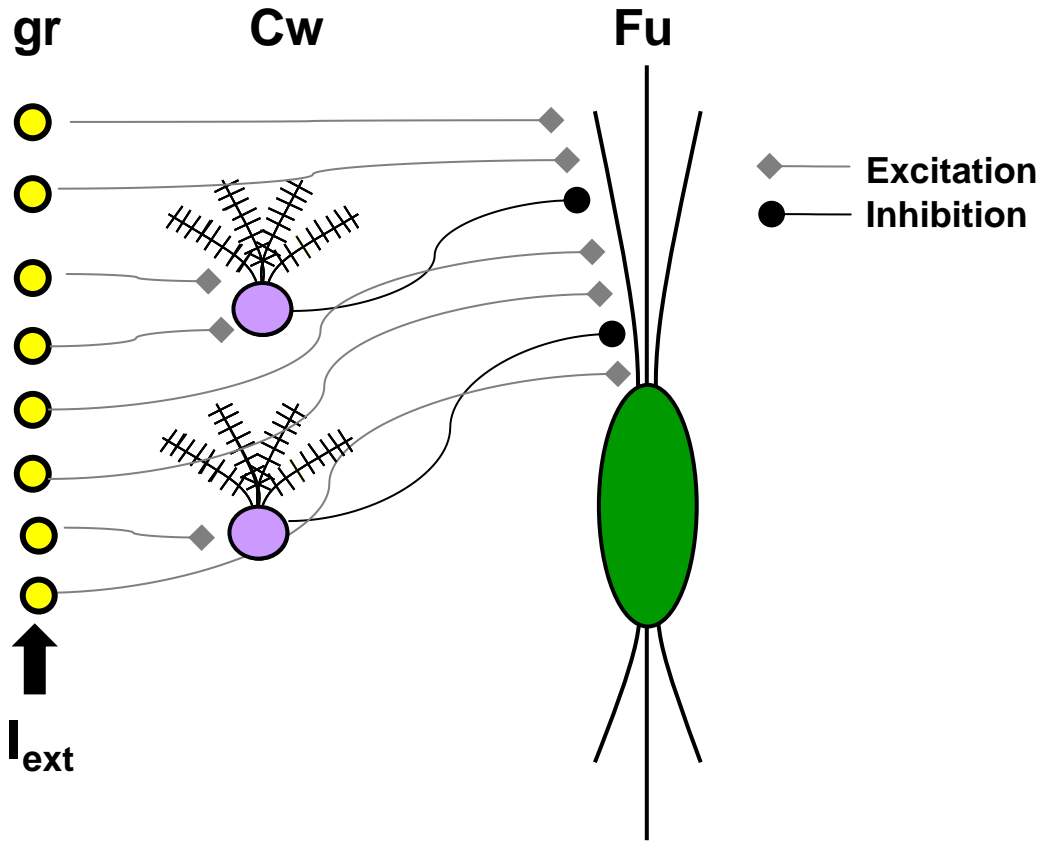


Figure 2.20: Schematic representation of the circuitry used for modelling the connections from multisensory inputs to the fusiform cell. The modelled fusiform cell (Fu) receives excitatory inputs (grey diamonds) from parallel fibres, the axons of granule cells (gr). Granule cells also stimulate inhibitory neurones cartwheel cells (Cw) inhibit fusiform cells (black circle). Granule cells are stimulated by an external current (I_{ext}) to reproduce the stimulation on the parallel fibres onto the fusiform cell.

Circuitry used for modelling the connections of the auditory inputs to the fusiform cell

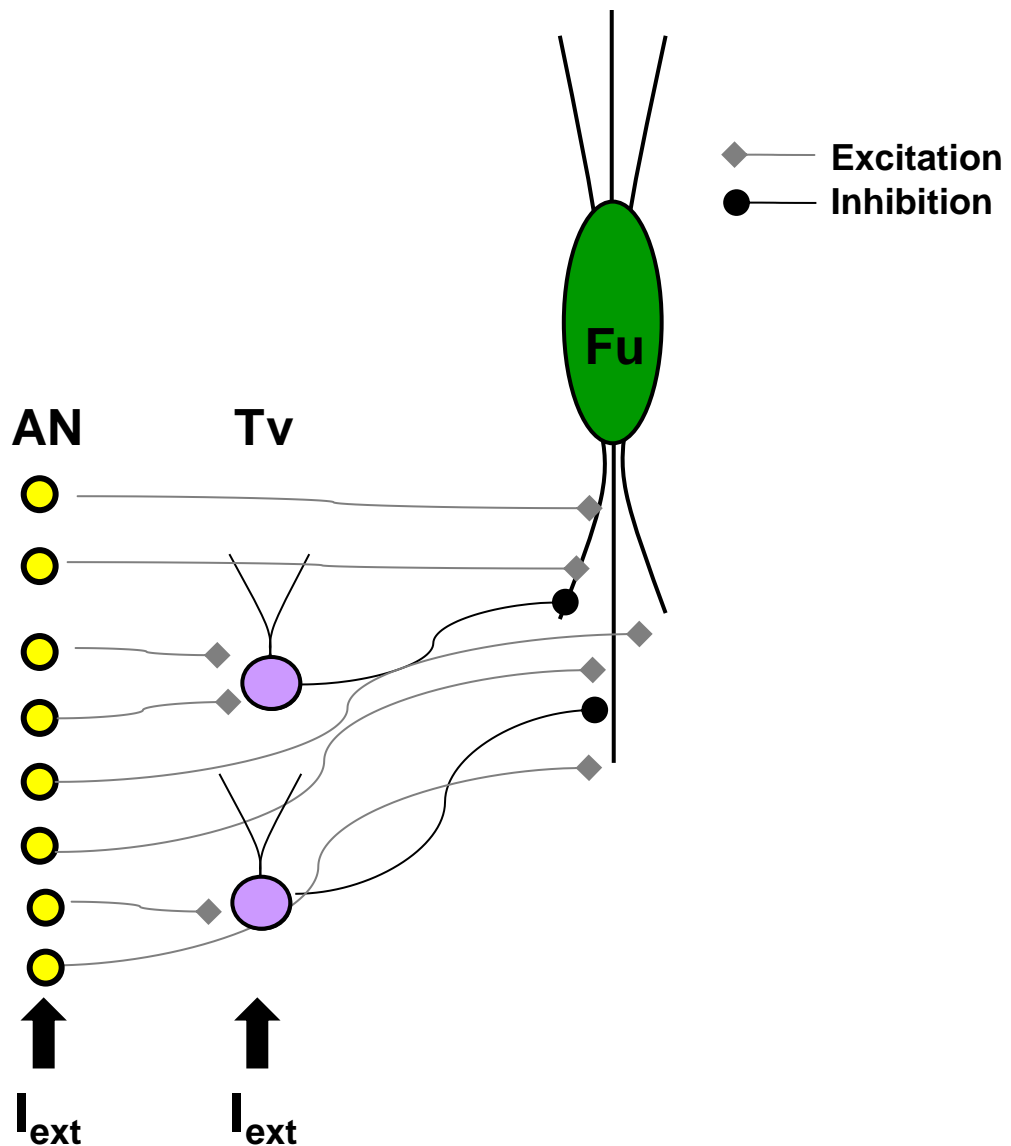


Figure 2.21: Schematic representation of the circuitry used for modelling the connections from auditory inputs to the fusiform cell. The modelled fusiform cell (Fu) receives excitatory inputs (grey diamonds) from auditory nerve fibres (AN). Auditory nerve fibres also stimulate tuberculoventral cells (Tv) that inhibit fusiform cells. Note that Tv are stimulated in parallel to AN as I observed monosynaptic IPSCs onto fusiform cells while stimulating the auditory fibres (see results 6.3.1.3).

Example of an auditory brainstem response

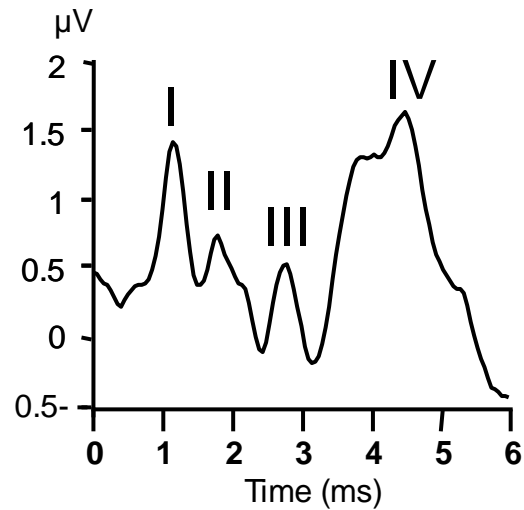


Figure 2.22: Example of an auditory brainstem response (ABR) recorded in a Wistar rat. The ABR was elicited by a single tone of 30 kHz with an intensity of 94dB SPL. The wave I is generated by the auditory nerve, the wave II represents the activity of the cochlear nucleus, the wave III represents the activity of the superior olivary complex and the wave IV represents the activity of the lateral lemniscus and the inferior colliculus.

Auditory brainstem recording setup

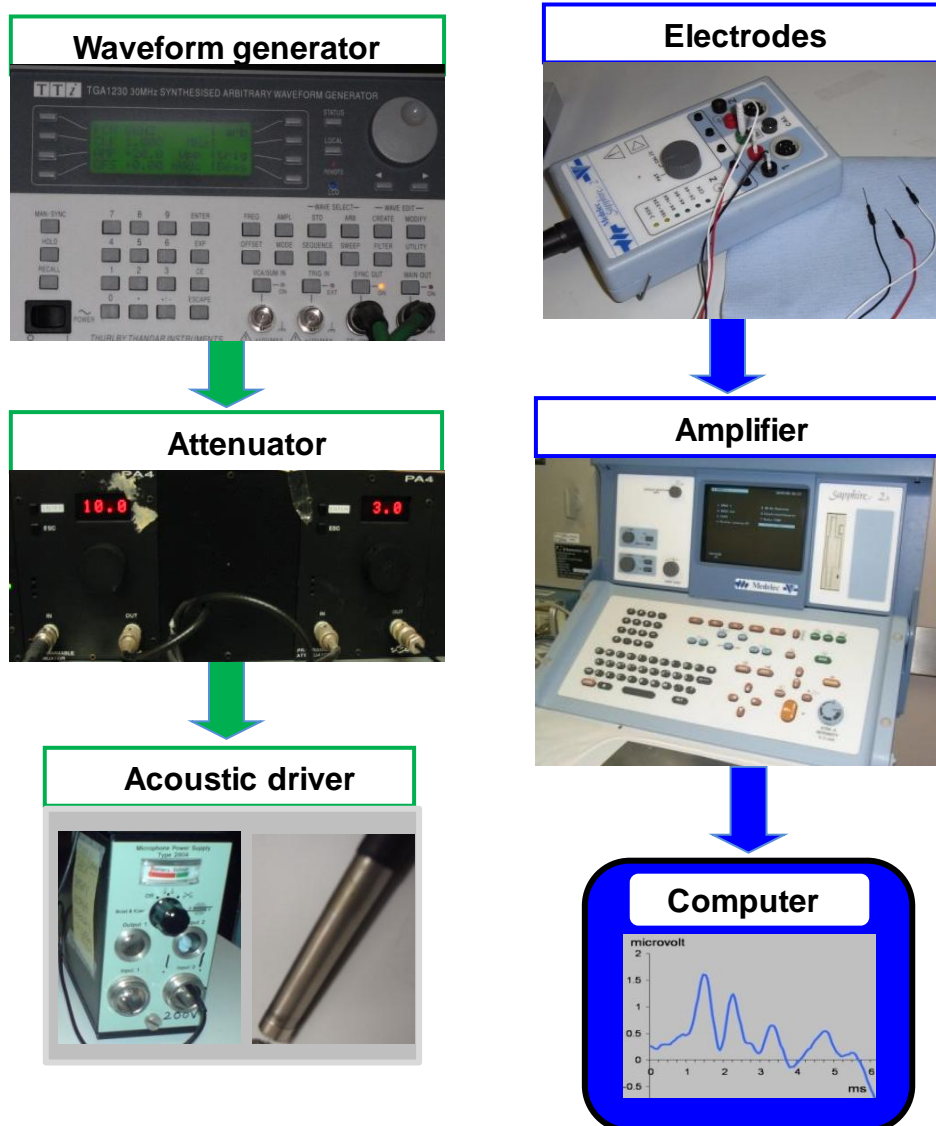


Figure 2.23: Auditory brainstem recording (ABR) setup. The ABR setup comprises elements for delivering the acoustic signal (green boxes and green arrows) and elements for recording the ABR (blue boxes and blue arrows). The setup consists of a waveform generator delivering single tones tips with frequencies between 8-30 kHz and an intensity of 94dB SPL. The signal is attenuated by an attenuator and transferred to an acoustic driver. The ABR was recorded using three sub-dermal electrodes connected to an amplifier. The electrical signal was sent from the amplifier to a computer where the ABR was recorded.

Placement of the recording electrodes

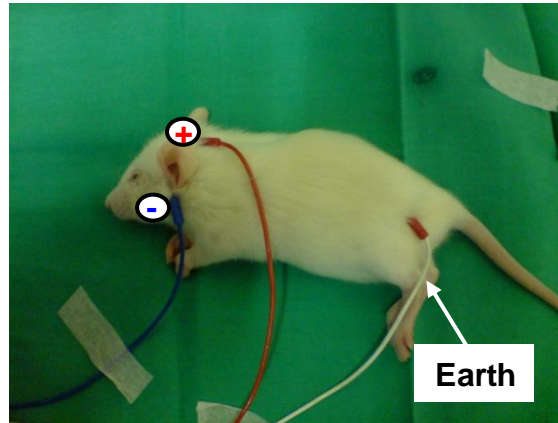


Figure 2.24: Placement of the recording electrodes used to record an auditory brainstem response (ABR). The photograph represents an anesthetised Wistar rats with the ABR being recorded through sub-dermal needles electrode. The positive electrode is placed on the top of the skull between the ears (red cable), the negative electrode is placed in front of the left ear (blue cable). The earth electrode is placed on the rump (white cable).

Placement of the acoustic driver

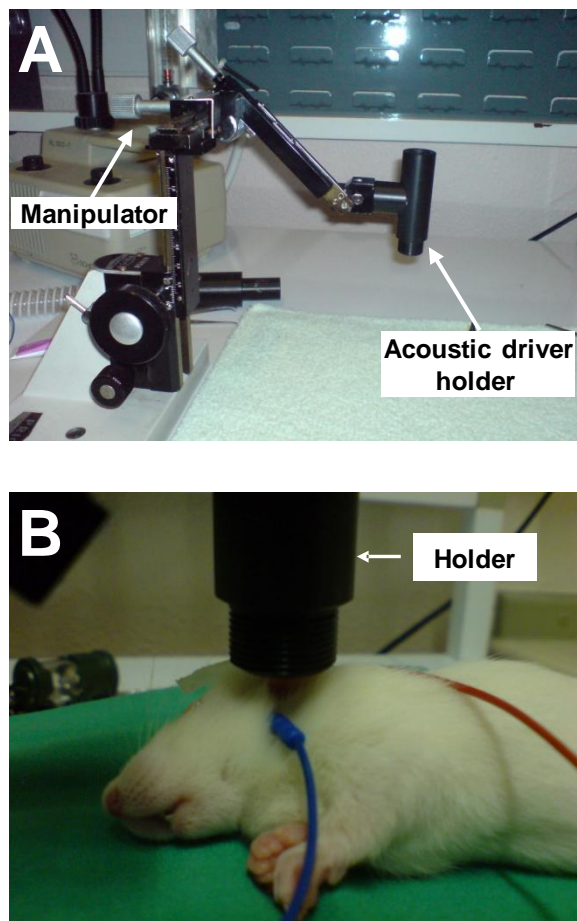


Figure 2.25: Placement of the acoustic driver used for delivering single tones. (A) The holder is connected to a manipulator allowing the positioning of the driver close to the rat's ear. **(B)** The photograph represents an anesthetised Wistar rats with sub-dermal electrodes recording the auditory brainstem response. The holder containing the acoustic driver (not represented) is placed at a distance of 0.5 cm from the left ear (open field).

Analysis of an auditory brainstem response

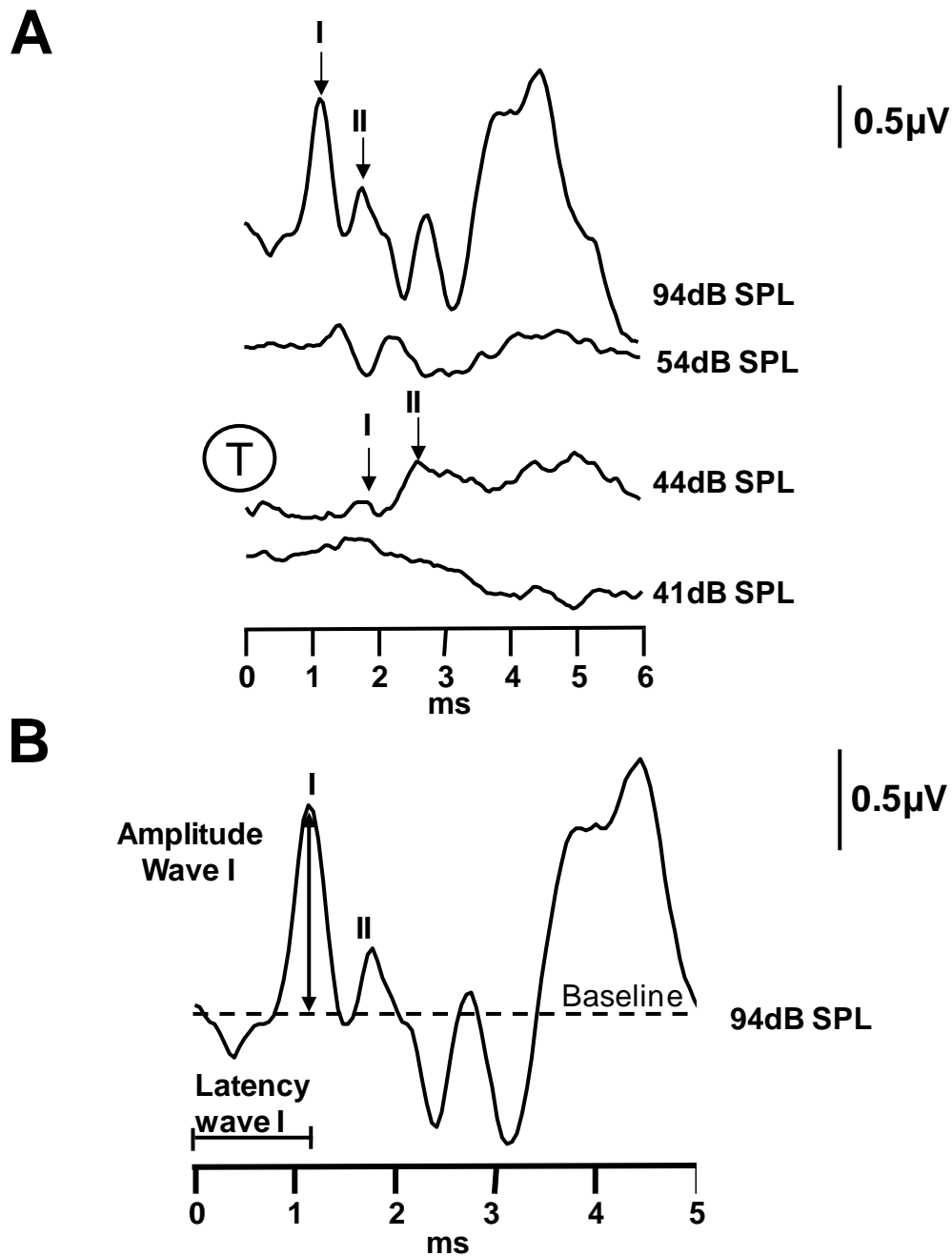


Figure 2.26: Analysis of auditory brainstem responses (ABR) recorded in a 16 day old Wistar rat. (A) ABR evoked by single tone of 24 kHz delivered at different intensities (dB SPL). The threshold, shown as a circled T, is defined as the lowest intensity at which wave I and II are detectable. The black arrows indicate wave I and II. Note that the wave latencies become longer as intensities decrease. **(B)** Same trace as in (A) top) recorded after delivering a single tone of 24 kHz and 94 dB SPL. The latency to the peak of wave I is determined relative to the onset of the stimulus. The amplitude of wave I is determined relative to the baseline (dashed line).

Equipment used for performing acoustic over-exposure

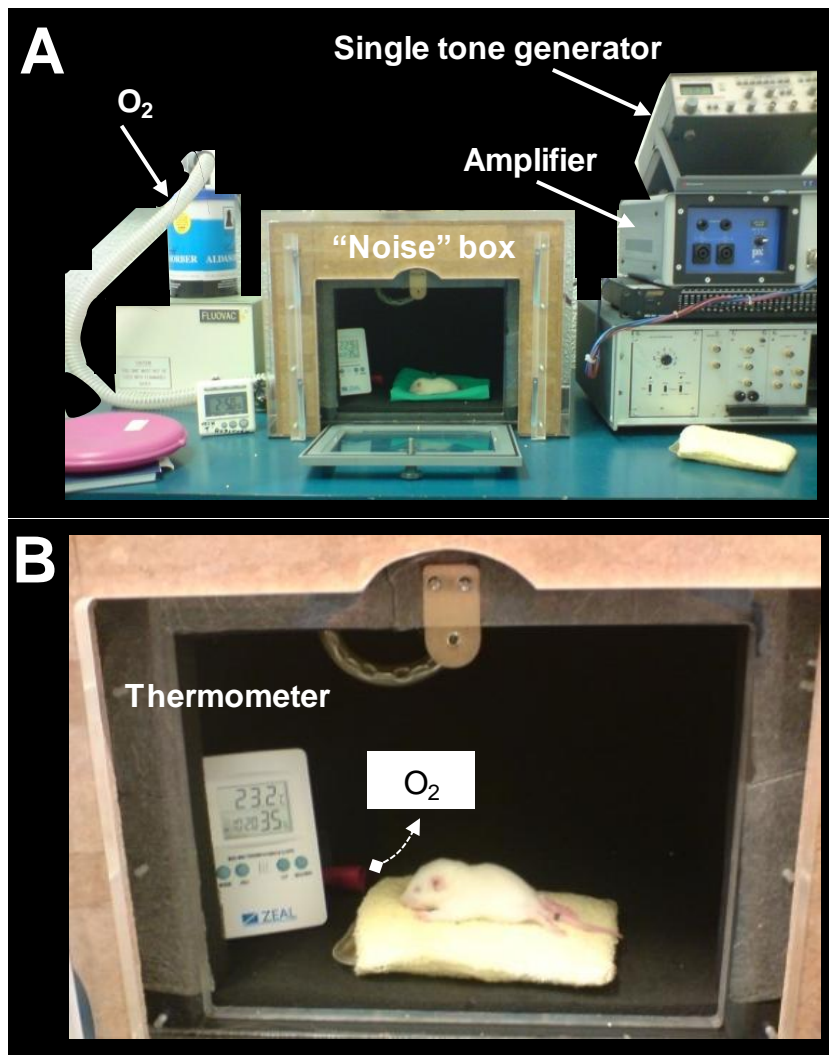


Figure 2.27: Equipment used for performing acoustic over-exposure. (A) Acoustic over-exposure of single tones (94 dB SPL, 14.8 kHz, 2-3 hours per session) was performed in an insulated box containing a loudspeaker (not visible). The single tone is generated by a tone generator that is connected to an amplifier. The amplified single tone is then sent to the loudspeaker. (B) Photograph of a sedated Wistar rat lying on a heating pad during the acoustic over-exposure. The nose of the animal is close to an inlet (in red) diffusing oxygen within the box. The thermometer is used to assess that the temperature within the box does not exceed 24°C.

CHAPTER 3

The dorsal coclear nucleus:

Cytoarchitecture

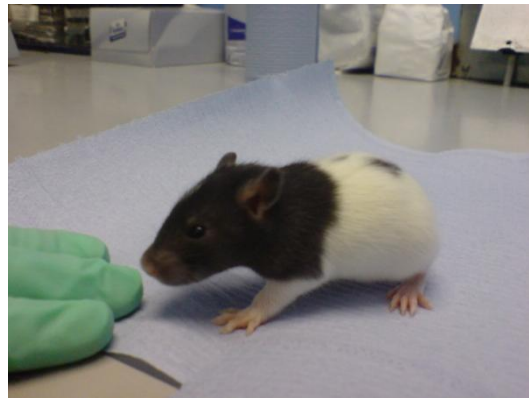
and cellular morphology

INTRODUCTION

3.1. The model of Lister Hooded rat

The aim of my PhD project was to investigate the effect of acoustic over-exposure on the synaptic activity of the rat DCN. The most commonly used laboratory rats are mutants of the Gray Norway rat (*Rattus norvegicus*) selective bred over hundreds of years. Whereas Sprague-Dawley and Wistar rats are the prevailing laboratory rats, they are also

albino rats and can be distressed by bright light. Pigmented, black-eyed rats are less common (picture at right). My initial studies were conducted in Lister Hooded (LH) rats as *i*) they have got a far better vision compared to that of



albino rats *ii*) many studies related to synaptic activity in auditory brainstem structures have been conducted on LH rats at the University of Leicester and this strain was easily accessible.

The cytoarchitecture of the DCN has been described in a number of species. The most complete studies were conducted in cat (Osen et al., 1969; Lorente de No' 1933, 1981; Brawer, 1974) followed by other exhaustive studies in mice (Browner and Baruch, 1982; Webster and Trune, 1982; Oertel and Wu, 1989) and in guinea pig (Hackney et al., 1990). There are few descriptions of the morphological organization of the DCN in rats and studies were performed in the Wistar and in the Sprague Dawley strains (Mugnaini, 1980a, 1980b; Alibardi, 2006) which are both suffering from visual deficits.

Studies so far failed to address the morphological organization of the DCN within LH rats and although it is reasonable to assume that albino animals should not suffer from auditory deficits, previous reports have found that the sensitivity to inter-aural time differences of tones and noise was somewhat diminished in Creel albino cats as compared to normally pigmented cats. Cell bodies in the medial superior olive of the albino cats were also less elongated than in normal cats (Yin et al., 1990). The DCN integrates auditory and multisensory inputs and DCN cellular subtypes could display morphological differences depending on whether rats are albino or pigmented.

This chapter will describe the morphological organization of the DCN of the LH rat and will address how cells are organized within the nucleus, with particular attention being given to the granule cell domain as granule cells are the major site for the multisensory integration that occurs within the DCN. The second part of the study aims to describe the morphology of the different cell types and their distribution within the DCN.

3.2. DCN cytoarchitecture and cell types

Although the Golgi Silver-impregnation method is a powerful tool for studying neuronal morphology, its usefulness for quantitative analysis of labeled neurones is limited by its capricious nature. In contrast, the Nissl staining approach allows visualization of all somata in appropriately prepared tissue sections. Its major drawback is that it provides poor labeling of neuronal processes. Thus, to establish the morphological profiles of neurones within a nucleus or a laminar structure, a combined approach using the Golgi Silver impregnation technique and the Nissl staining method is desirable. It is possible to counterstain cells previously treated with the Golgi-silver impregnation technique with the Nissl stain (Werner and Brauer, 1984; Werner et al., 1986, 1989). A drawback with this approach is that the Golgi-stained neurones must be de-impregnated before Nissl counterstaining. Many neurones then lose their morphological characteristics before they take up the Nissl stain. Recently, Friedland et al. (2006) described staining for cresyl violet around neurones labeled with the Golgi method that was rather faint and suggested that pH changes during the Golgi staining might reduce the affinity for the cresyl violet. In this study, I report the successful combination of Golgi – cresyl violet staining method that allowed us to simultaneously characterize the morphology of individual neurones together with the cytoarchitecture of the dorsal cochlear nucleus (DCN) in the LH rat. I started by characterizing the cell layers within the dorsal cochlear nucleus using cresyl violet staining. I then developed protocols for staining individual cells with the Golgi silver-impregnation method. Finally, I combined the two staining methods without the need for deimpregnating the Golgi silver stain.

RESULTS

3.3. Cytoarchitecture and cell types in the DCN

3.3.1. DCN localization and cytoarchitecture

The DCN has been defined as the cerebellar circuit of the auditory system (Oertel and Young, 2004) and shares not only common morphological features but also functional aspects with the cerebellum (Mugnaini et. al. 1980a; Wouterlood and Mugnaini, 1984; Fujino and Oertel, 2003; Oertel and Young, 2004). The cerebellum is a widely studied structure, with a well defined cytoarchitecture and functional role. Ramon y Cajal first described the cerebellum in 1888 (Ramon y Cajal, 1888) and since then, many studies provided additional information regarding synaptic connections in the cerebellum (Chan-Palay and Palay, 1972; Berthie and Axelrad, 1994; Shinoda et al., 2000). I carried out a preliminary study on the cytoarchitectural organization of the cerebellum in LH rats and subsequently characterized the cytoarchitecture of the DCN using a Nissl staining (cresyl violet staining) technique that allows visualizing neuronal somata and cell layers.

When observed in a coronal plane, the cochlear nucleus lies as a separate lobe on the lateral side of the brainstem and ventral to the cerebellum (figure 3.1). The DCN is separated from the VCN by a thin shell of small highly packed cells, identified as the granule cells that form the granule lamina (Mugnaini et al. 1980a; 1980b).

The cytoarchitecture of the cerebellum was characterized using the Nissl stain. The cerebellar cortex is reported to contain three distinctive cell layers identified with the cresyl violet staining: the molecular layer located peripherally,

the Purkinje cell layer located centrally and the granule cell layer that lies in the deepest region. An example of cerebellar coronal slice in figure 3.2 is showing the cerebellar cytoarchitecture. The external layer that contains few labeled small cells (as expected for a layer containing mainly parallel fibers and small stellate cells) is the molecular layer. The inner medial layer contains bigger cells (Purkinje cells) that are mainly aligned and forming the Purkinje cell layer. Finally, the deeper layer contains a high concentration of small cells, the granule cells and is therefore the granule cell layer.

The cytoarchitecture of the DCN was characterized using the Nissl stain, cresyl violet on coronal sections. I identified the DCN as a 1 to 1.2 mm thick brain structure occurring at the level of the superior olivary complex of the auditory brainstem, presenting as a lobulated laminar structure on the dorso-lateral aspect of the tissue block. Figure 3.3A shows the cochlear nuclear complex formed by the dorsal and the ventral cochlear nuclei. The insert in figure 3.3.A shows in greater detail the intervening structure between the DCN and the ventral cochlear nucleus taken to be the granule cell domain (Doucet and Ryugo, 1997; Mugnaini et al. 1980a, 1980b; Ryugo et al., 2003).

In order to characterize the DCN cytoarchitecture, I tested whether the DCN is made from a homogeneous cell population and whether it can be subdivided into layers. To answer this question, I established a matrix of 9 squares distributed as 3 rows, namely dorsal, intermediate and inner layer. From these I quantified the cellular density and cell soma surface areas as illustrated in figure 3.3B (showing the DCN at higher power with one square per row). Figure 3.3C shows a summary plot of soma surface area as a function of cell density calculated from the squares located within the dorsal, the

intermediate and the inner layer. It is clear from this picture that the DCN can be sub-divided into three layers from the external to the inner part. The external layer was characterized by the lowest cell density of 1.6 ± 0.7 cells/1000 μm^2 (n=9) compared to the cell density of 4.5 ± 1.0 cells/1000 μm^2 in the medial layer ($P= 1.5 \times 10^{-05}$, paired T test, n=9) and to the cell density of 7.2 ± 1.0 cells/1000 μm^2 in the inner layer ($P= 7.6 \times 10^{-10}$, paired T test, n=9). Cellular densities were also different between the intermediate and the inner layer ($P= 5 \times 10^{-05}$, paired T test, n=9). Cells in the intermediate layer were characterized by a larger soma surface area when compared to cells within the molecular layer ($112.2 \pm 18.0 \mu\text{m}^2$, and $50.9 \pm 6.0 \mu\text{m}^2$, respectively, $P= 3.5 \times 10^{-05}$, paired T test, n=9) and by a larger soma surface area when compared to cells within the inner layer ($57.8 \pm 10.8 \mu\text{m}^2$, $P= 7.5 \times 10^{-05}$, paired T test, n=9). This observation is in line with previous reports from various species commonly used in neuro-anatomy (Osen et al., 1969; Brawer et al., 1974; Mugnaini 1980a; 1980b; Browner and Baruch, 1982; Hackney et al., 1990). Three distinct cell layers can therefore be identified within the DCN of the Lister Hooded rat and I will refer to the external layer as the molecular layer (ML in figure 3.3B), to the intermediate layer as the fusiform cell layer (FL in figure 3.3B) and to the inner layer as the deep layer (DL in figure 3.3B).

3.3.2. DCN cell labelling

I used the rapid variant of the Golgi-silver impregnation method to label neurones of the DCN over 4 days. This labeling method can be divided into two steps. Firstly, target cells are impregnated with both trivalent and hexavalent chromium ions during a 2 days chromation step. This process requires the presence of aldehydes and is known to be influenced by time, temperature and

pH (Colonnier, 1964; Kopsch, 1896). The chromation step was then followed by a 2 days precipitation step in which, the chromium ions react with heavy metal ions, silver in this case, to give a chromogenic reaction product that serves as the visual marker of the labeled cells. I optimized the protocols by experimenting with various aldehyde donors during the chromation step, namely paraformaldehyde, glutaraldehyde or chloral hydrate and also using phosphate buffer to give us a pH range of 5.8 to 7.6. In another set, the chromation step was carried out in the absence of buffer with or without paraformaldehyde (5%). The quality of the Golgi staining was assessed by determining whether the staining was confined to neurons alone (neuronal staining: figure 3.4C and D) or to neurons as well as non-specific staining, figure 3.4A and B). The stained neurons displayed clearly visible cell bodies, dendrites and initial segments of their axons (see for example figure 3.4C and D) whilst non specific labeling had an undefined patchy presentation instead of a neuronal shape. Figure 3.4E shows a histogram plot illustrating the effects on neuronal and non-neuronal staining by varying the labeling conditions. It shows the average number of neurons labeled per given DCN slice (open, white bars) as well as the average surface area of the tissue in which labeling was taken to be non-neuronal (black bars; i.e. non specific labeling shown in figure 3.4A and B). Ideal conditions that favored the labeling of a large number of neurons were those in which paraformaldehyde alone and paraformaldehyde and chloral hydrate were used as aldehyde donors and the pH of the buffer set at pH 7.6. Table 3.1 below summarizes the p values obtained for the different staining conditions regarding the number of labeled cells and the extent of non neuronal staining, in relation to the best labeling condition, pH 7.6 and 5% paraformaldehyde. Labeling of

neurons was poor in the presence of paraformaldehyde and glutaraldehyde with pH set at 7.6, suggesting that glutaraldehyde provides for unfavorable staining conditions. Finally, more acidic pH conditions (figure 3.4E and table 3.1) reduced the numbers of labeled neurons whilst not having a similarly severe effect on non-specific labeling. From figure 3.4E, it can be concluded that the chromating solution dissolved in a phosphate solution at pH 7.6 and in 5% paraformaldehyde produced the best labeling conditions i.e. the higher number of labeled cells combined to the lowest area not specifically stained.

PBS (pH 7.6) and 5% PF versus condition below	Number of labelled cells	Percentage of aspecific staining
H ₂ O, 5%PF	P< 0.0001	P=0.18
H ₂ O	P< 0.0001	P=0.09
PBS (pH 5.8), 5%PF	P< 0.0001	P=0.29
PBS (pH 7.4), 5%PF	P< 0.0001	P<0.05
PBS (pH 7.6), 5%PF, 2%GT	P< 0.0001	P<0.01
PBS (pH 7.6), 4%PF, 2%CH	P= 0.74	P<0.05

Table 3.1. One factor ANOVA- Tukey's tests comparing the labelling obtained in various chromating solutions. P values refer to comparing the chromating condition in PBS pH 7.6, 5% paraformaldehyde versus the other conditions in the table. Abbreviations: chloral hydrate (CH), glutaraldehyde (GT), paraformaldehyde (PF), phosphate buffer solution (PBS). P values are reported for the number of labelled cells per DCN slice and the not specifically stained relative to the total DCN area.

3.3.3. Combined cytoarchitecture and cell type labelling

In order to attribute neurons previously labeled with the Golgi stain to their defined layers within the DCN, slices of Golgi labeled tissue containing the DCN were counterstained with cresyl violet. In addition to acting as a control stain of

the neuronal tissue, cresyl violet allowed us to study the silver-impregnated neurons in the context of the previously described layering within the DCN. Figure 3.5 shows the morphologies of five silver-impregnated neurons before (panels A and C) and after (panels B and D) the tissue was counterstained with cresyl violet. In previous reports using cresyl violet solely, tissue slices were first hydrated with distilled water then stained with cresyl violet and finally dehydrated by processing them through progressively graded solutions of ethanol, namely 50% to 70% and 100% ethanol (Gittins and Harrison, 2004; Friedland et al., 2006). In my experience, I found that this commonly used approach produced cracking within Golgi labeled tissue, which led me to modify the protocol such that sections were transferred directly to the cresyl violet solution without hydrating and then from the cresyl violet solution directly to 100% ethanol for 2 minutes. Figure 3.5B and D are photomicrographs of two DCN slices labeled with cresyl violet and Golgi staining. The cresyl violet stain shows higher density of labeling suggestive of cell layering whilst Golgi stained cells showed typical neuronal morphologies. Cresyl violet stain did not interfere with the quality of images of Golgi stained neurons although cresyl violet stained tissues appeared less crisp after Golgi staining. Figure 3.6 illustrates cells within slices labeled with cresyl violet alone (figure 3.6A) and within slices after Golgi silver impregnation staining (figure 3.6B). In both cases, cells with round or ovoid cell bodies can be identified and cells also display discernible cellular inclusions and in particular the nuclei and their nucleoli. In order to be confident that the Golgi staining procedures did not interfere fundamentally with the native cytoarchitecture of the DCN, I quantified the cell density and the soma surface area and used cresyl violet staining of tissue sections stained with

the Golgi silver-impregnation method. Demarcations between cell layers are shown by the dashed lines in figures 3.5B and D. A statistical analysis of the cell density and cell soma surface area was performed in a similar fashion as that applied for figure 3.3C. Fig. 3.6C shows a summary plot of soma surface area as a function of cell density calculated within the dorsal, the intermediate and the inner layer, for cresyl violet alone (black circles, same as figure 3.3C) or for cresyl violet after Golgi staining (white circles). Figure 3.6C shows that cells of the DCN were still organized in layers even after Golgi staining. The molecular layer is characterized by a lower cell density of 1.7 ± 0.6 cells/1000 μm^2 (n =8) compared to the cell density of 3.8 ± 1.4 cells/1000 μm^2 (n = 8) within the fusiform layer ($P= 3 \times 10^{-3}$, paired T test) and to the cell density of 6.7 ± 0.7 cells/1000 μm^2 (n=8) within the deep layer ($P= 2.8 \times 10^{-8}$, paired T test). As described previously, cellular densities were also different between the fusiform layer and the deep layer ($P= 4 \times 10^{-4}$, paired T test). Cells in the fusiform layer were also characterized by a larger soma surface area ($95.1 \pm 23.2 \mu\text{m}^2$, n=8) compared to cells within the molecular layer and the deep layer ($54.7 \pm 9.0 \mu\text{m}^2$, $P=2 \times 10^{-3}$ paired T test and $59.5 \pm 6.3 \mu\text{m}^2$, $P=1 \times 10^{-3}$ paired T test, n= 8, respectively). Moreover, I found no difference between the cell density and the cell soma surface area within each layer, with or without previous Golgi labeling (figure 3.6C), showing that layer characteristics stayed unchanged despite the Golgi labeling. Although the cytoarchitecture stayed unchanged while using the combined Golgi-cresyl violet staining, we noticed that some cells labeled with the Golgi method have a larger cell soma surface area compared to the average cell soma surface area in cresyl violet staining condition. For example, giant cells are the largest cells within the DCN (figure 3.5B and C) and are

characterized by a soma surface area of $426 \pm 181 \mu\text{m}^2$ ($n=16$) while stained with the Golgi method. This value exceeds by 2.5 times the highest values of the cell soma area measured in cresyl violet staining condition ($172 \pm 63 \mu\text{m}^2$, $P=1 \times 10^{-5}$, $n=16$). The cell soma surface area was calculated for cells stained with cresyl violet only (open circles) and for Golgi labeled cells (black triangles) and their distribution plotted as a cumulative amplitude plot for each layer as illustrated in figures 3.7A, B and C. These cumulative distributions appear to be different for the fusiform cell layer (figure 3.7B) and the deep layer (figure 3.7C) whilst no major difference was observed for the molecular layer. This therefore suggests that Golgi labeled cells are larger than cresyl violet stained cells within the fusiform and the deep layers. This difference in cell soma surface area revealed with the two staining methods can be represented as the area difference between the two curves. I further tested whether there was any correlation between this difference area and the cell density reported for the different layers. Figure 3.7D shows a correlation ($r^2=0.83$) between the cell surface soma area and the cell density indicating that larger cells within a dense layer are more likely to be underestimated when quantified with the cresyl violet staining method. I filled cartwheel, fusiform and giant cells, with lucifer yellow in order to compare their cell soma surface area with those obtained with the Golgi method and found similar values of soma surface areas when those cells were filled with lucifer yellow or when labeled with the Golgi method $288 \pm 64 \mu\text{m}^2$ (4 cells) and ($274 \pm 40 \mu\text{m}^2$, 6 cells) respectively for cartwheel cells ($P=0.67$, unpaired T test), $436 \pm 100 \mu\text{m}^2$ (6 cells) and $518 \pm 63 \mu\text{m}^2$ (5 cells) respectively for fusiform cells ($P=0.15$, unpaired T test), $529 \pm 209 \mu\text{m}^2$ (3 cells) and $684 \pm$

203 μm^2 (6 cells) respectively for giant cells ($P=0.32$, unpaired T test) (see attached publication).

3.3.4. Characterization of cell types and distribution within the cell layers

The combined Golgi-cresyl violet staining method allowed me not only to describe the morphology of silver-impregnated neurons, but it also made it possible to attribute their location within the three layers of the DCN with a high degree of certainty. Figure 3.8 gives an overview of morphological cell types observed in this study whilst figure 3.9 shows the cell types within their respective layers within the DCN. Within the molecular layer, small cells (likely to be granule cells) (Mugnaini et. al. 1980b) are characterized by an ovoid cell body of approximately $8.8 \pm 2.2 \mu\text{m}$ diameter ($n=3$) and two to three primary dendrites (figures 3.8H and 3.9). Cartwheel cells of approximately $20 \mu\text{m}$ diameter ($n=2$) have a thick primary dendrite that gives rise to arborisations in the form of a tree that extends into the molecular layer (figure 3.8B) and are found at the boundary between the molecular layer and the fusiform cell layer (figure 3.9). Within the fusiform cell layer, fusiform cells are characterized by an elongated cell body of $30.2 \pm 5.7 \mu\text{m}$ diameter ($n=4$) across their major axis and a diameter of $16.9 \pm 1.9 \mu\text{m}$ ($n=4$) across their minor axis. Fusiform cells are also characterized by basal dendrites directed towards the deep layer and apical dendrites directed towards the molecular layer (figure 3.9). Usually, the apical dendrite divides into several branches (figures 3.5B, 3.8A and 3.9). The shape of the soma was often fusiform although we labeled a few cells with a pyramidal shape that could be classified as fusiform cells (figures 3.8C and 3.9). Unipolar brush cells characterized by a cell body of about $9.2 \pm 1.7 \mu\text{m}$ diameter ($n=4$) and a single thick dendritic tree with a typical brush shape were also

found in the fusiform cell layer as well as granule cells (diameter= 12.1 ± 1.3 μm , n=3) (figures 3.8E and 3.9). A variety of cells were present in the deep layer. Giant cells with a cell body exceeding 30 μm diameter (diameter of 37.9 ± 6.5 μm , n=4) are characterized by multiple thick dendrites projecting along the deep layer and towards the fusiform cell layer. (figures 3.5D, 3.8D, 3.9). Multipolar medium sized cells with a diameter of around 25 μm displayed many dendrites protruding at widely spaced angles from the soma (figures 3.8C, 3.9). Tuberculoventral cells are characterized by an elongated or ovoid cell body of around 13.5 ± 0.4 μm diameter (n= 3) across their widest section and an apical dendrite oriented towards the fusiform cell layer (figures 3.8F, 3.9). Granule cells were also found in the deep layer (diameter of 10.5 ± 1.7 μm , n=3) (figures 3.8G, 3.9) as well as cells with a morphology similar to fusiform cells (minor axis diameter of 18 ± 3.8 μm , major axis diameter of 26.5 ± 1.8 μm , n= 4) (figures 3.8A,3.9).

3.4. Granule cell domains and reconstruction of the DCN

3.4.1. Granule cell domains in the DCN

Granule cells are present in both the DCN and the cerebellum (see introduction in chapter 1). In the cochlear nucleus, granule cells are organized in several domains that cover the external surface of the nucleus and also expand into its ventral and dorsal region (Mugnani et. al.1980b). The granule cell domains are important sites for the integration of somatosensory signals within the DCN (Itoh et al., 1987; Wright and Ryugo, 1996; Ohlrogge et al., 2001). Granule cell's axons form the parallel fibres of the molecular layer that modulate the activity of the fusiform and cartwheel cells. It is therefore important to study where granule cells are localized within the nucleus.

Serial coronal thin sections (20 μm) were stained with cresyl violet. In Nissl stained sections of the DCN, granule cells were differentiated from the other cells by their diameter of 7-13 μm . The granule domains appeared as darker structures within the DCN as containing densely packed small cells. Figure 3.10 represents some examples of the identified granule cell domains: the lamina that separates the VCN from the DCN (figure 3.10B), the subpeduncular corner of granule cells, located at the dorsal edge of the VCN (figure 3.10B), the strial corner located in the dorsomedial pole of the DCN (figure 3.10D), one of the small granule domains that is distributed within the fusiform and deep layer of the DCN (figure 3.10D). I also identified a superficial layer of granule cells that mainly covers the whole superficial layer of the VCN and the DCN as well as a medial sheet of granule cells that marks the medial border of the DCN.

3.4.2. Three-dimensional reconstruction of the dorsal cochlear nucleus

Thin serial coronal sections (20 μm) of the cochlear nucleus have been stacked together in order to obtain a three-dimensional visualization of the nucleus (figure 3.11 and 3.12). The granule cells domains have been delimited so that it was possible to determine how they expand within the nucleus. The descending branch of the auditory nerve that is known to terminate in the posterior part of the VCN and in the dorsal cochlear nucleus was labelled as well. The granule cell lamina separating the DCN from the VCN was present in all the sections within the whole volume of the cochlear nucleus, whereas the subpenducular corner, the strial corner and the medial sheet were only present within a limited number of sections occupying therefore a small volume of the cochlear nucleus. In the superficial layer granule cells were aligned and were present in almost all the sections. The small domains of granule cells distributed within the deep and the fusiform layer were not labeled for the 3-D reconstruction as they were widely distributed all over the two layers. From this 3-D reconstruction, we can conclude that the whole cochlear nucleus is mainly covered by a thin external shell of granule cells that also expands within several regions of the VCN and DCN

DISCUSSION

3.5. A combined Golgi and Nissl study of the DCN

The aim of this first part was to study the morphology of neurones of the DCN in the Lister-hooded rat using the Golgi-silver impregnation technique. I also used the Nissl stain alongside the Golgi-Silver-staining method to place labeled neurones within the well known lamina structure of the DCN, and I was able to counter-stain our tissue sections without the need to de-impregnate the silver-stain as has been the case in most published literature on this subject (Pasternak and Woolsey, 1975; Werner and Brauer, 1984; Werner et. al., 1986; 1989). I had to overcome two major obstacles that attend the Golgi Silver-impregnation technique, firstly on its own and secondly, in combination with cresyl violet.

3.5.1. Cell labelling using the rapid the Golgi method

The Golgi silver-impregnation method is unreliable as potassium dichromate and silver nitrate can react unselectively, forming bulk crystals at the specimen surface (Pasternak and Woolsey, 1975). Many procedures are based on the modified Golgi-Kopsch method (1896) adding formaldehyde or on the Golgi-Colonnier method (1964) adding glutaraldehyde to the potassium dichromate solution. Those methods have been shown to improve the quality and the reaction time of the Golgi staining. Other modifications like using microwaves (Marani et al., 1987; Zhang et al., 2003); altering the composition of the chromation solution and its pH (Van der Loos, 1956; Morest and Morest, 1966; Adams, 1979; Grandin et al., 1988; Angulo et al., 1994, 1996) or using a vacuum (Friedland et al. 2006) improved the labeling of neurones compared to

non specific staining. I compared the quality of the Golgi staining by altering the aldehydes (paraformaldehyde, glutaraldehyde or chloral hydrate) as well as the pH of the phosphate buffer used in the chromating solution. I showed that dissolving potassium dichromate into a phosphate buffered medium at a weak basic pH (pH 7.6) with 5% paraformaldehyde favoured the labeling of neurones over non-specific labeling within the tissue. The non specific staining is likely to be due to the uncontrolled chemical reaction between potassium dichromate, which acts as the primary impregnation compound and the chromogen, silver nitrate, which is governed by the ratio of Cr^{3+} and $\text{Cr}_2\text{O}_7^{2-}$ ions. This ratio is dependent on the concentration of protons and the presence of aldehydes (Angulo et al., 1996). Chromium (III) cross links the carboxyl terminal of intracellular proteins and binds to $\text{Cr}_2\text{O}_7^{2-}$ (Angulo et al., 1996). Nevertheless, Cr^{3+} does not react with the silver nitrate by contrast to $\text{Cr}_2\text{O}_7^{2-}$ which produces the black silver chromate thereby defining the morphological profile of neurones. The low quality staining obtained at more acidic pH could be related to an excess of Cr^{3+} relative to $\text{Cr}_2\text{O}_7^{2-}$. Good labeling conditions are therefore dependent on an adequate ratio of Cr^{3+} and $\text{Cr}_2\text{O}_7^{2-}$ (Angulo et al., 1996).

3.5.2. Cytoarchitecture labeling using cresyl violet staining

The DCN is reported to contain three distinctive cell layers in many species including cat (Osen et. al. 1969; Brawer 1974), mouse (Browner and Baruch, 1982; Webster and Trune, 1982; Oertel and Wu, 1989), guinea pig (Hackney et al., 1990), Wistar rat (Alibardi, 2006) and the Sprague Dawley rat (Mugnaini et al., 1980a, 1980b) but it appears that the DCN has not been studied in the Lister Hooded rat. My detailed analysis of the cell density and the cell soma surface area within the DCN of the LH rat revealed three distinct layers similar

to the previous studies mentioned above. The peripheral (molecular) layer is characterized by a low density of cells in Nissl staining and the presence of granule cells when labeled with the Golgi silver method. The low density of cell labeling with the Nissl stain is probably due to the fact that the molecular layer contains mainly parallel fibers and processes of fusiform cells and cartwheel cells. In contrast to the molecular layer, the fusiform and the deep layers had higher densities of cells and can therefore be clearly distinguished from the molecular layer on the basis of the Nissl stain. Another difference was that cells within the fusiform cell layer had larger soma surface areas in Nissl stain compared to cells of the molecular and deep layers. These two characteristics (cell density and soma surface areas) allowed characterizing three layers of the DCN. My results further showed that the laminar organization of the DCN appears to be unaffected by the Golgi staining histological procedures. Consequently, the combined Nissl-Golgi staining method can be used to characterize different cell types and assign them to specific DCN layers.

3.5.3. Estimation of the cell soma surface area

My study also revealed that Golgi labeled cells had larger cell somas compared to their equivalents labeled with Nissl stain. Nissl stain tends to be directed primarily at Nissl substance of the cytoplasm and not at the boundaries of the cell as defined by the cell membrane. This might therefore explain why the general cell outline is underestimated by Nissl stain, hence the discrepancies in cell sizes between the Nissl and Golgi staining. My study showed that bigger cells within a dense layer are more likely to be underestimated when quantified with the cresyl violet staining method. This could be explained by Golgi precipitates bursting out of the cell body making the cell body appearing larger

but this is unlikely to be the case as cells filled with lucifer yellow had similar soma surface areas to those measured in Golgi stained cells (see publication). It is likely that cresyl violet staining tends to underestimate the cell soma surface area due to the Nissl stain being directed primarily at Nissl substance of the cytoplasm and not at the boundaries of the cell (cell membrane). This might therefore explain why the general cell outline is underestimated by Nissl stain, hence the discrepancies in cell sizes between the Nissl and Golgi staining. Given the abbreviated Nissl staining procedure used in this study, it is possible that cell bodies are not that well stained. As I measured the size of the cell body using a standard cresyl violet staining method that used progressive dehydration, I found that the cell body size is similar between the two cresyl violet methods and therefore cannot relate the underestimation of the cell body size to the dehydration procedure. Interestingly, Geisler et al., (2002) reported an increased staining intensity of the cell bodies when cresyl violet at a pH of 4.5 to 5 was used in combination with luxol fast blue and it is possible that the pH of the cresyl violet solution affects the estimation of the cell body size.

3.5.4. Laminar distribution of cell types

From the observations made in this study, the predominant DCN cell types have been characterized and mapped within the three cell layers. Granule cells are the only cell type found in all three cell layers. This is in accordance with previous studies showing that granule cells are organized in small domains throughout the layers (Mugnaini et al., 1980b). In the granule cell domains, unipolar brush cells were also labeled in accordance with previous studies (Mugnaini et al., 1997). Cartwheel cells are localized between the molecular and the fusiform cell layer whereas fusiform cells are localized in the fusiform

cell layer (Mugnaini, 1985; Hackney et al., 1990; Maruyama and Ohmori, 2006). The deep layer comprises multiple cell types characterized in other species and including multipolar cells (Hackney et al., 1990), giant cells (Hackney et al., 1990; Zhang and Oertel, 1993a) and tuberculoventral cells (Hackney et al., 1990, Zhang and Oertel, 1993b, Alibardi, 2006). I found that fusiform cells are not only localized within the fusiform cell layer but also in the deep layer and therefore in the LH rat, fusiform cells are differently distributed compared to the guinea pig, cat or Wistar rat (Brawer et al., 1974; Hackney et al., 1990, Osen, 1969; Maruyama and Ohmori, 2006). I can now conclude that the Lister Hooded rat has a laminated DCN structure similar to that seen in other species. The cellular composition observed here is similar to that of other species, and this validates the method combining the Golgi silver impregnation technique with Nissl staining, without the need for de-impregnation as an intervening step. Electrophysiological studies were performed on cellular subtypes identified by their position within the slices and also by their morphology. In the following studies, cells were filled with lucifer yellow (chapter 4, figure 4.1) and their morphology compared to the cells stained with the Golgi method.

The location of the dorsal cochlear nucleus and the cytoarchitecture of the cerebellum

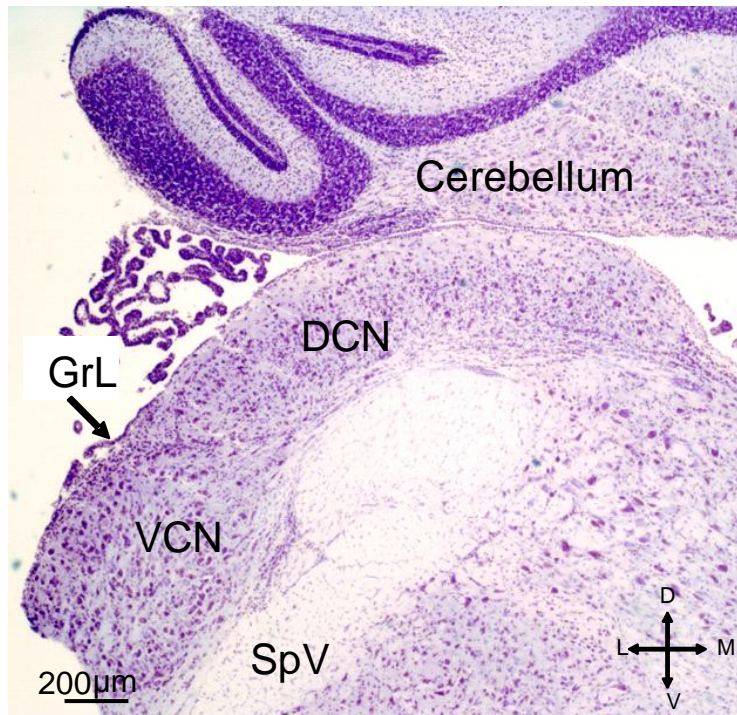


Figure 3.1: The cochlear nucleus lies in the brainstem. Photomicrograph of cochlear nucleus coronal slices (20 μm thick) labelled with cresyl violet. The cochlear nucleus, lies at the lateral side of the brainstem, ventral to the cerebellum. The nucleus consists of two regions: the dorsal cochlear nucleus (DCN) and the ventral cochlear nucleus (VCN, separated by the granule cell lamina (GrL).The spinal tract of the trigeminal nerve (spV) is shown.

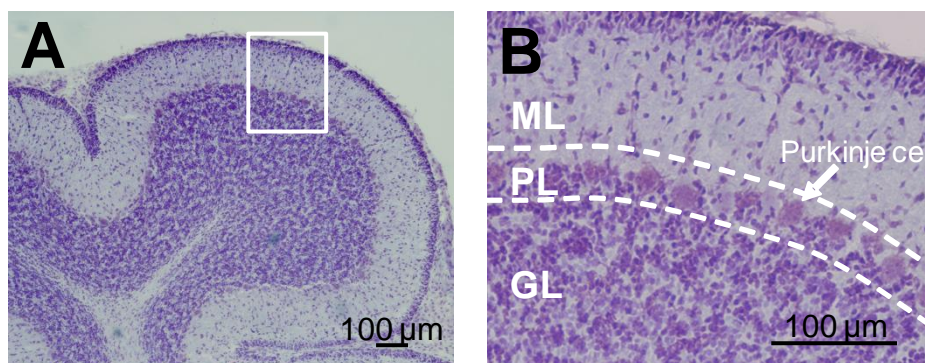


Figure 3.2: The cerebellum is organized in three layers. (A) Photomicrograph of one lobe of a rat cerebellar slice (20 μm thick) stained with cresyl violet. **(B)** Bigger magnification of the square in A. The dashed lines delimitate the three layers: ML, molecular layer with small number of cells labelled; PL, Purkinje cell layer with big oval, aligned cell bodies, the Purkinje cells; GL, granule cell layer, with high density of small cells (mainly the granule cells). The arrow is pointing to a Purkinje cell body.

Cytoarchitecture of the dorsal cochlear nucleus

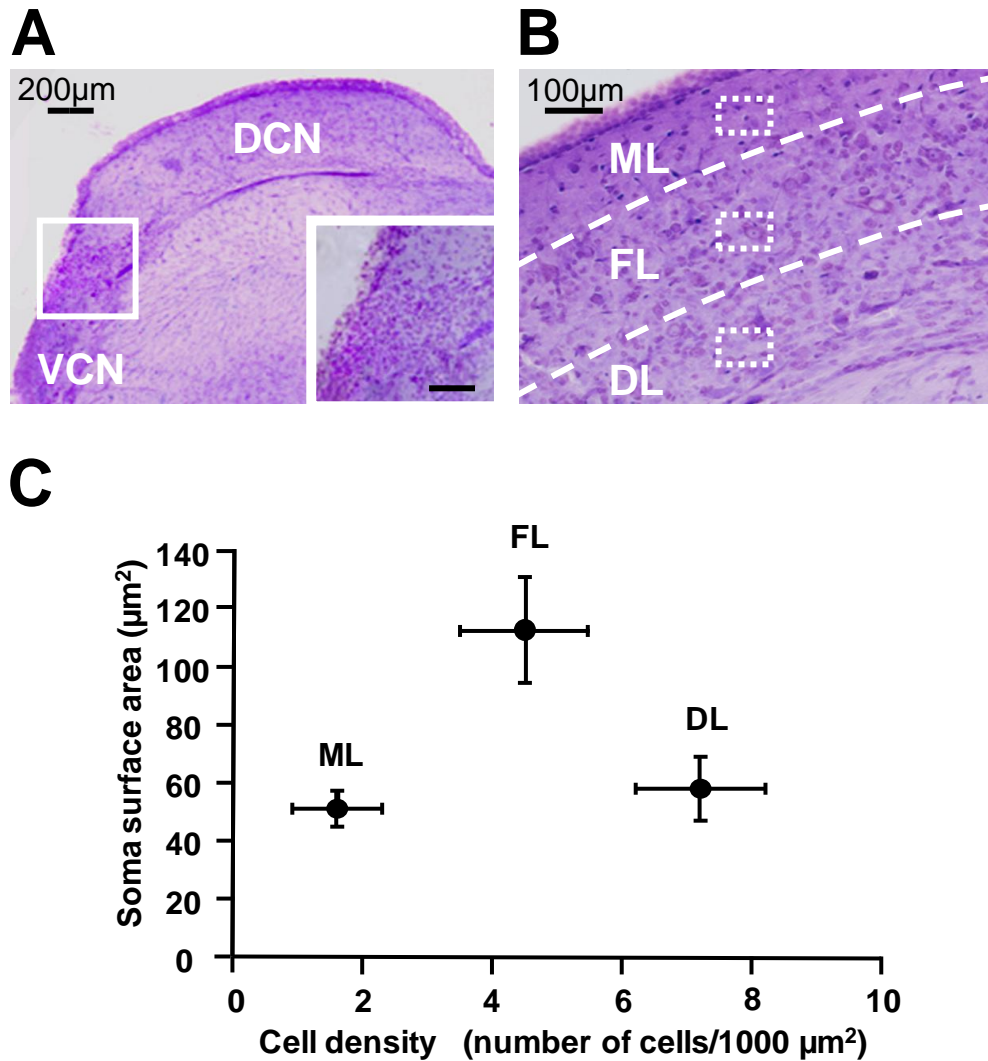


Figure 3.3: DCN cytoarchitecture. (A-B) Photomicrographs of the dorsal cochlear nucleus stained with cresyl violet. In **(A)** the granule cell lamina separates the DCN from the ventral cochlear nucleus and is magnified in the insert (scale bar for the insert A is 100 μm). **(B)** shows the lamination within the DCN with dashed lines defining boundaries between the molecular layer, the fusiform layer and the deep layer. For each layer, areas within the squares are analyzed (as in C). **(C)** Summary plot representing the cell soma surface area and the cell density for the molecular layer, the fusiform layer and the deep layer after cresyl violet staining. ML: molecular layer; FL: fusiform cell layer; DL: deep layer

Golgi staining in different chromating solutions

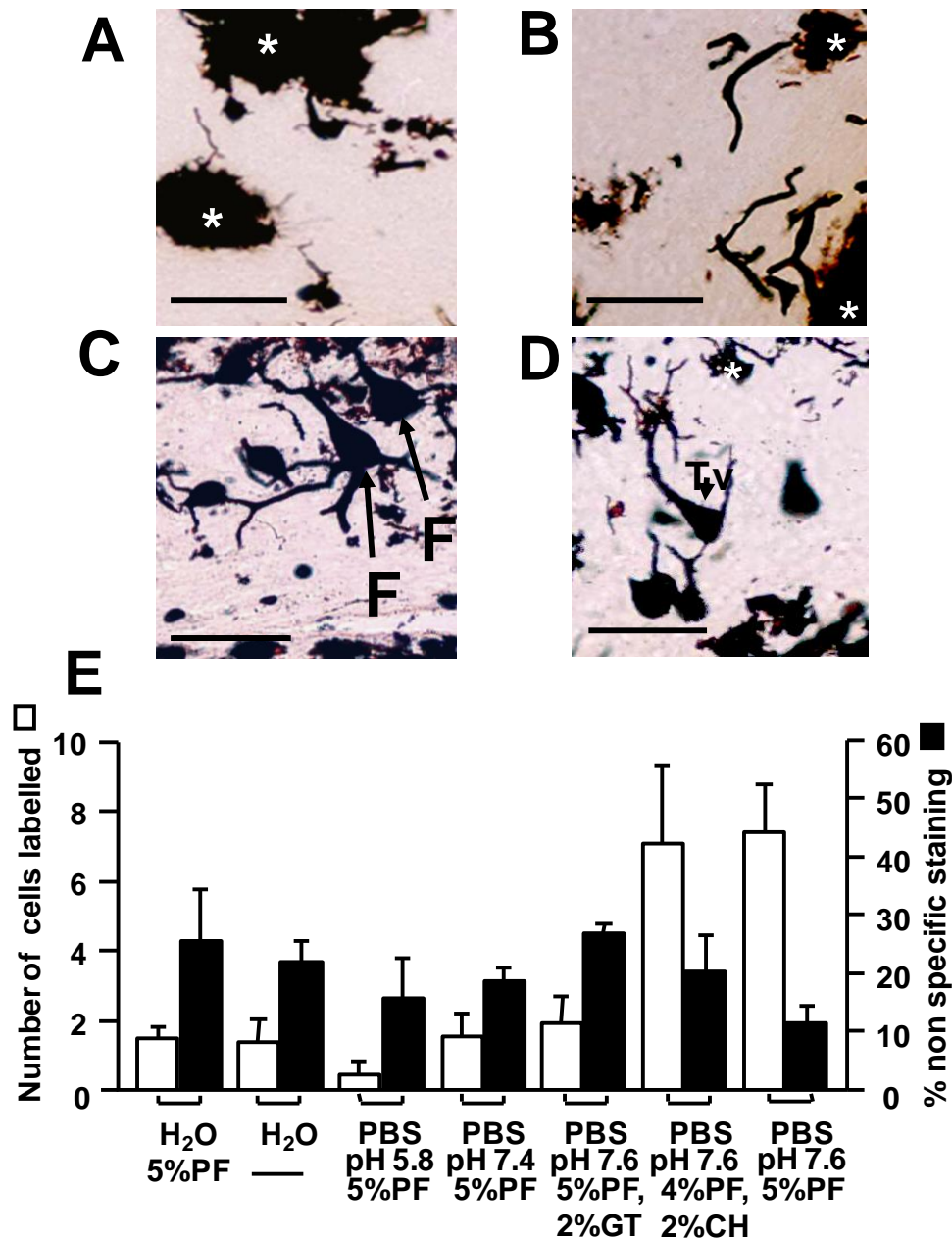


Figure 3.4: Golgi staining of DCN neurones is dependent on the chromating solution. (A-D) show photomicrographs of a DCN slice after the tissue was incubated in (A) Potassium dichromate dissolved in H₂O and 5% paraformaldehyde (PF) (B) Potassium dichromate dissolved in phosphate buffer solution (PBS) pH 5.8 and 5% PF (C) Potassium dichromate solution dissolved in PBS pH 7.6 and 4% PF plus 2% chloral hydrate (CH) and (D) Potassium dichromate dissolved in PBS pH 7.6 and 5% PF. Examples of non specific staining are shown in (A) and (B) (asterisks). (C) and (D) show neurone-specific labeling highlighted by arrows whilst the asterisk shows a non specific labeling. F labels a fusiform cell whereas TV labels a tuberculo ventral cell. Scale bars A-D = 50 μ M. (E) Summary histograms representing the number of labeled cells per DCN slice (white) (mean \pm S.D; n=3-4) and the percentage of area not specifically stained relative to the total DCN area (black) (mean \pm S.D. values; n=3-4).

Golgi and cresyl violet counterstaining of the dorsal cochlear nucleus

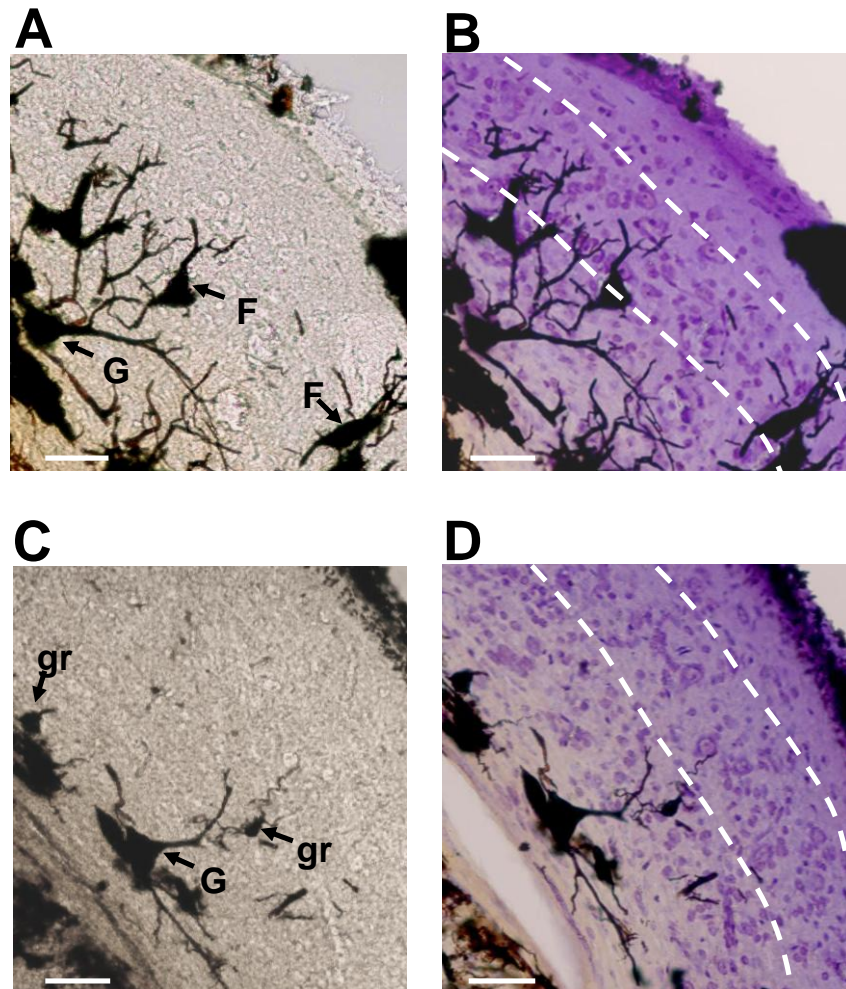


Figure 3.5: Combined labeling of DCN neurones and DCN cytoarchitecture. Photomicrographs showing DCN neurones stained with the Golgi method (**A, C**) and the same neurones after counterstaining the slices with cresyl violet (**B, D**). The chromating solution contained potassium dichromate dissolved in PBS pH 7.6 and 5% paraformaldehyde. In (**B**) and (**D**), the dashed lines define the boundaries between the molecular layer, the fusiform cell layer and the deep layer. Labeled neurones are fusiform cells (**F**) projecting their apical dendrite within the molecular layer; giant cells (**G**) with large soma and thick dendrites within the deep layer; granule cells (**gr**) with their small cell body and two to four dendrites. Two fusiform cells are within the fusiform cell layer and at the boundary between the fusiform cell layer and deep layer. Scale bars A-D = 50 μ M.

Golgi and cresyl violet counterstaining and dorsal cochlear nucleus cytoarchitecture

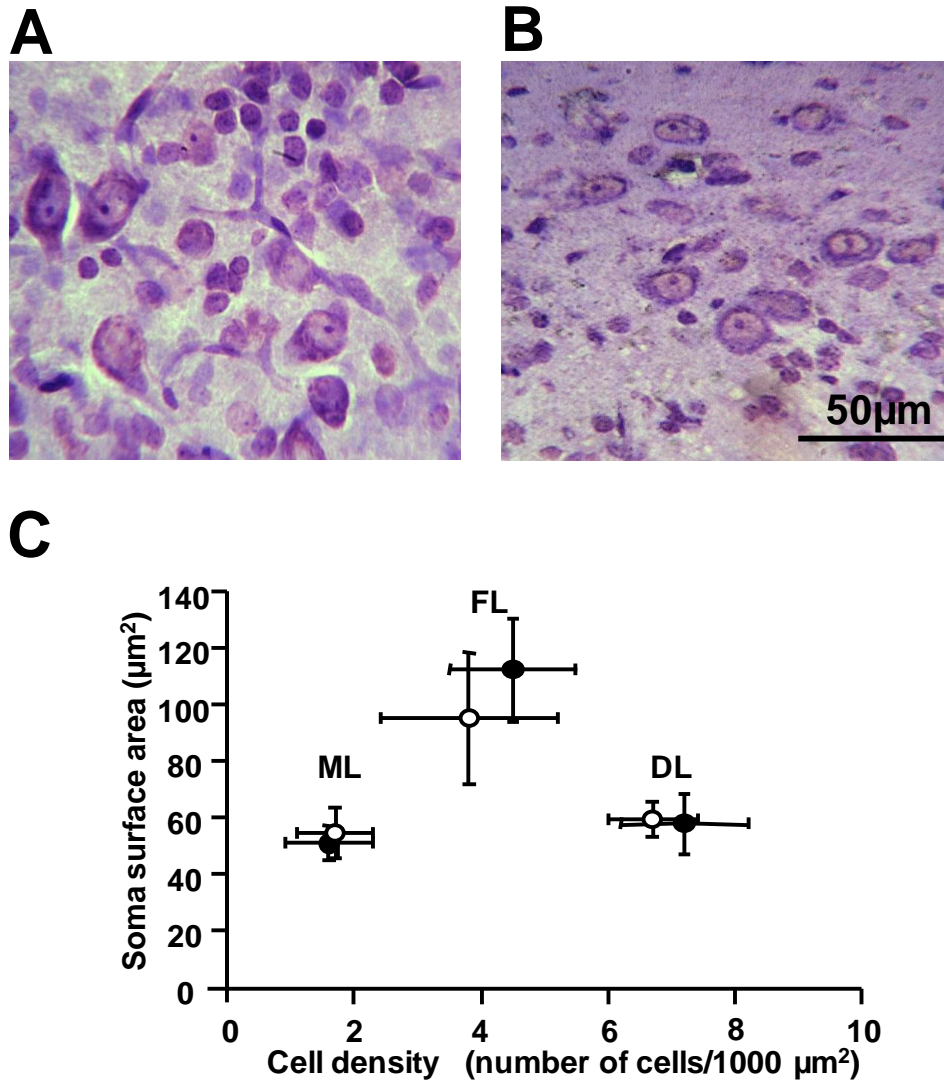


Figure 3.6.: Comparative analysis of the DCN architecture. (A) Example of cresyl violet staining within the fusiform cell layer. (B) Example of cresyl violet staining within the fusiform cell layer post Golgi staining. (C) Summary plot representing the cell soma surface area and the cell density (mean \pm S.D) for the molecular layer (ML), the fusiform cell layer (FL) and the deep layer (DL) in the two staining conditions illustrated in A and B. Black circles represent the same values as in figure 3.3C (cresyl violet only) whereas white circles represent values obtained with cresyl violet staining post Golgi staining.

Golgi and cresyl violet counterstaining of the dorsal cochlear nucleus

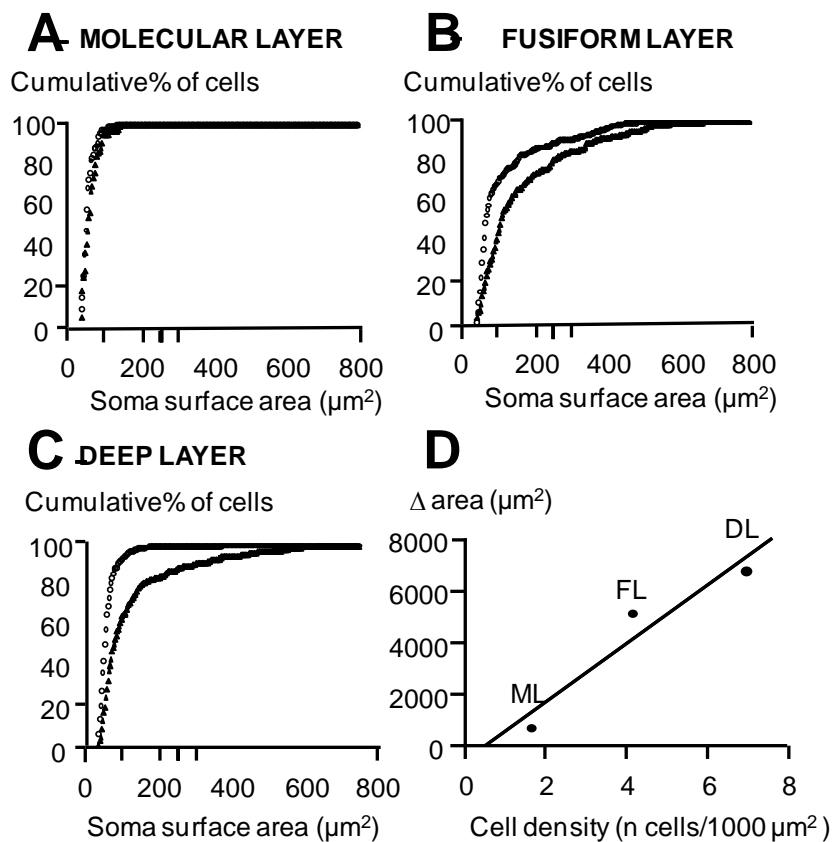


Figure 3.7 Comparative analysis of the cell soma surface area. For each layer, a cumulative frequency plot represents the cumulative % of cells in function of the soma surface area of cells labeled with cresyl violet (white circle) and with the Golgi method (black triangle). **(A)** In the molecular layer, 50% of cells have a soma surface area equal or less than $53 \mu\text{m}^2$ and $60 \mu\text{m}^2$ when labeled with cresyl violet (67 cells analyzed) and with the Golgi method (76 cells analyzed). Maximal values (representing the total number of cells) are similar for both staining conditions (reaching around $100 \mu\text{m}^2$). **(B)** In the fusiform cell layer, 50% of cells have a soma surface area equal or less than $64 \mu\text{m}^2$ and $107 \mu\text{m}^2$ when labeled with cresyl violet (284 cells analyzed) and with the Golgi method (291 cells analyzed) respectively. Cell soma surface areas do not exceed $490 \mu\text{m}^2$ when staining with cresyl violet whereas cell soma surface areas of Golgi stained cells reach $674 \mu\text{m}^2$. **(C)** In the deep layer, 50% of cells have a soma surface area equal or less than $58 \mu\text{m}^2$ and $81 \mu\text{m}^2$ when labeled with cresyl violet (488 cells analyzed) and with the Golgi method (377 cells analyzed) respectively. Cell soma surface area does not exceed $398 \mu\text{m}^2$ when staining with cresyl violet whereas cell soma surface area of Golgi stained cells reach values of $883 \mu\text{m}^2$. **(D)** Insert: The area between the two curves represented as white circles and black triangles was calculated for the three layers and plotted against the cell density values. The correlation factor obtained after linear regression (r^2) is 0.83. Molecular layer (ML), Fusiform layer (FL), Deep layer (DL).

Cell types of the dorsal cochlear nucleus

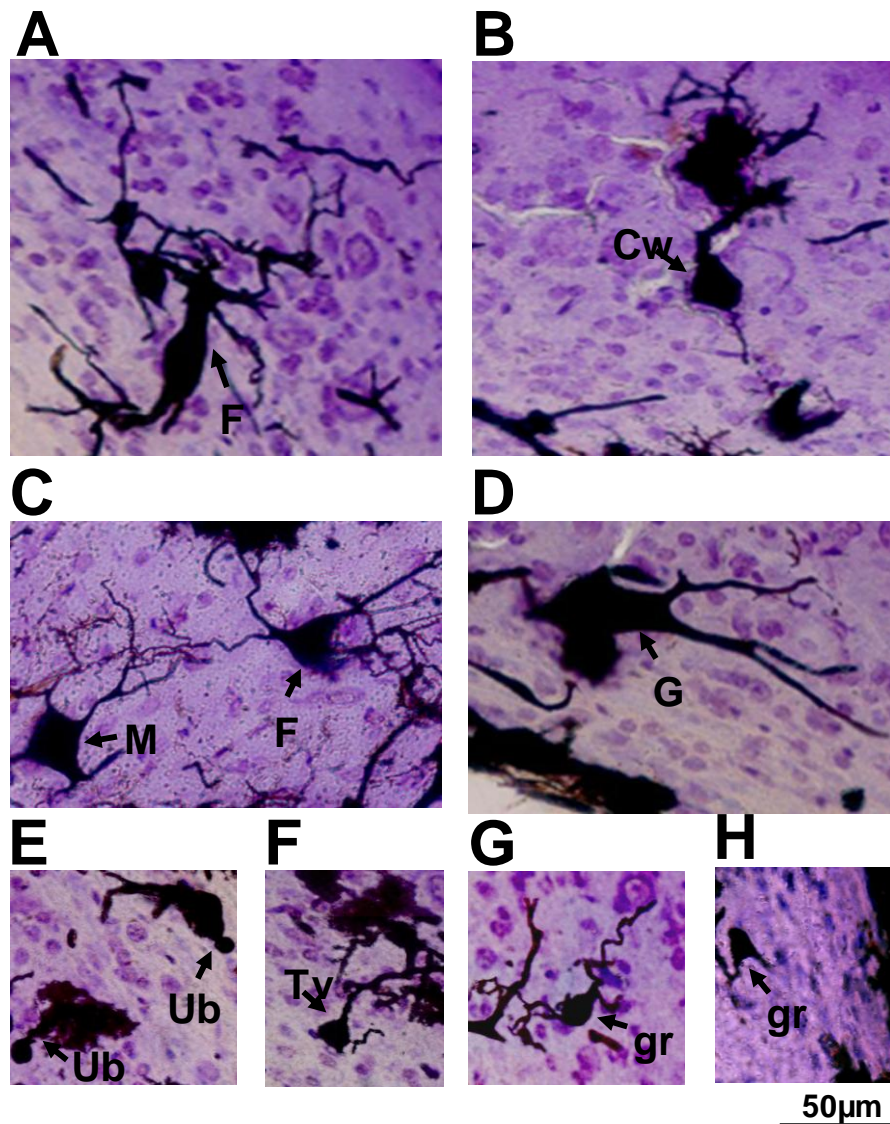


Figure 3.8: DCN cell types. Photomicrographs of DCN cell types obtained from slices labeled with the combined Golgi-cresyl violet method. **(A)** The arrow points to a fusiform cell (F) with its large elongate cell body. Its basal dendrites lie in the deep layer while the apical dendrites are oriented towards the molecular layer. **(B)** The arrow indicates a cartwheel cell (Cw) with a small oval cell body, an axon extending into the fusiform layer and a large spiny dendritic tree in the molecular layer. **(C)** A multipolar cell (M) in the deep layer characterised by its dendrites at widely spaced angles and a fusiform cell (F) with a pyramidal shape in the fusiform layer. **(D)** A giant cell (G) with its large soma exceeding 30 µm diameter and many thick dendrites is in the deep layer. **(E)** Two unipolar brush cells (Ub) with a single thick dendritic brush shape in a granule cell lamina within the deep layer. **(F)** A tuberculoventral cell (Tv) with its small soma in the deep layer and its apical dendrite projecting to the fusiform layer. **(G)** A granule cell in the deep layer (gr) with its two main dendrites ending in claw-like protuberances. **(H)** A granule cell (gr) in the molecular layer. Same scale A-H.

The circuitry of the dorsal cochlear nucleus

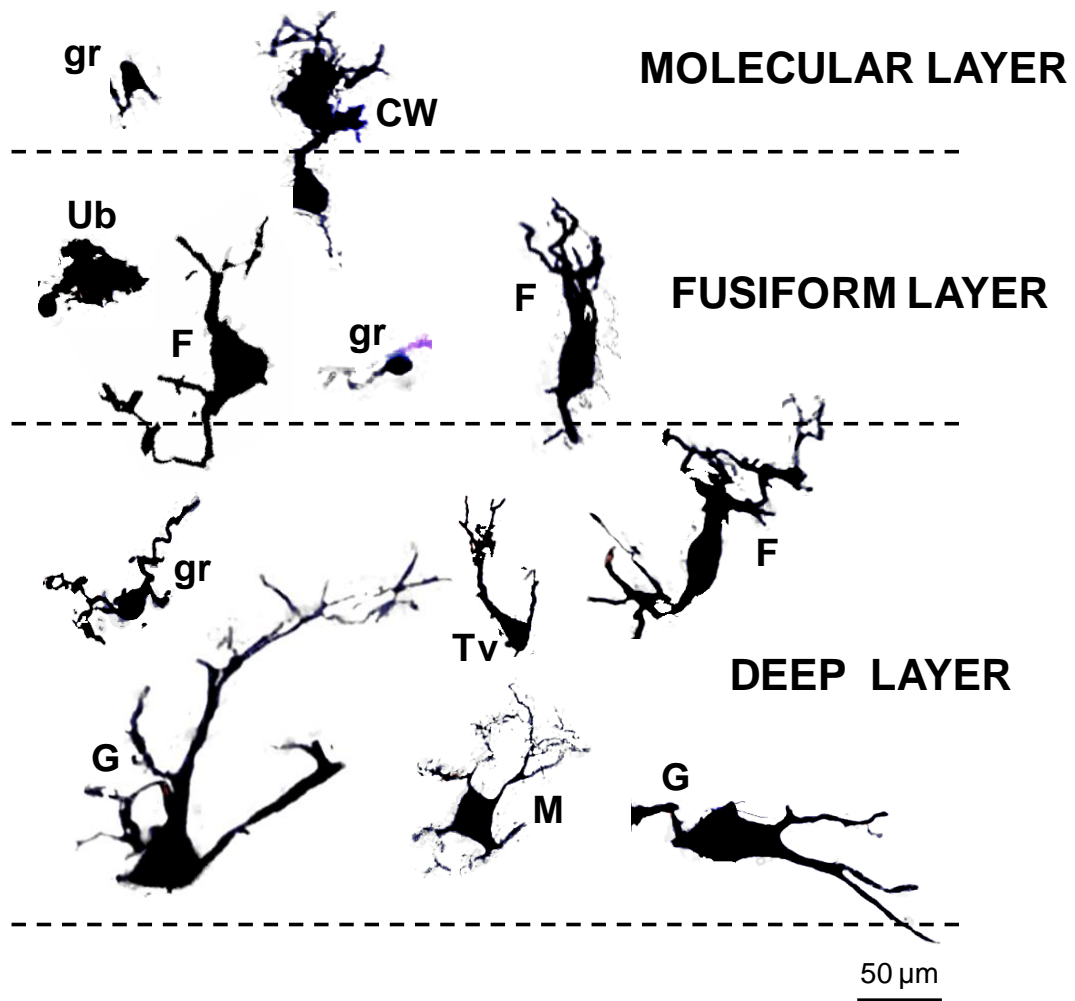


Figure 3.9: DCN cell types and localization within the layers. Schematic representation of the relative position of the cell types throughout the DCN layers. The molecular layer contains granule cells (gr) as well as cartwheel cell dendrites (Cw). The fusiform cell layer contains fusiform cells (F), unipolar brush cells (Ub), granule cells (gr) and cartwheel cell bodies. The deep layer comprises multipolar cells (M) giant cells (G), tuberculo-ventral cells (Tv), granule cells (gr) and fusiform cells (F).

The granule cell domain of the dorsal cochlear nucleus

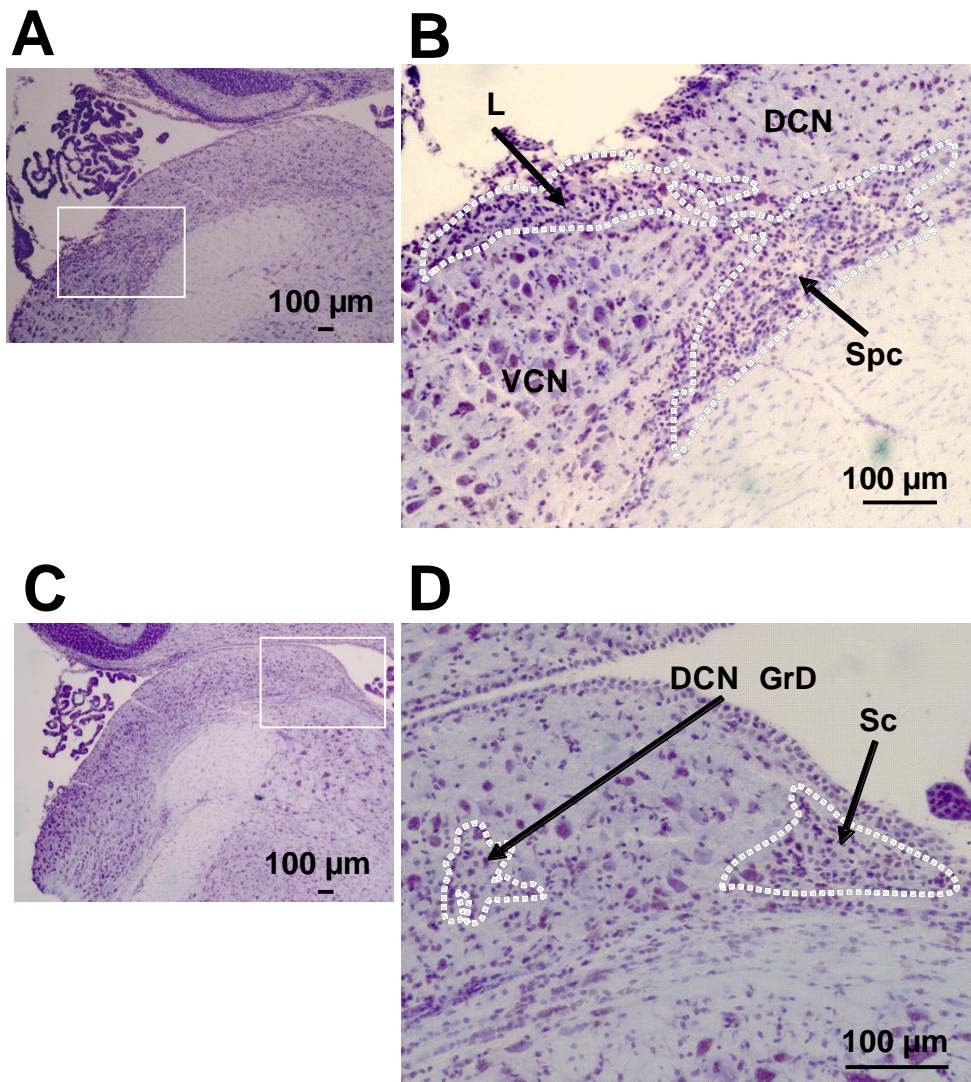


Figure 3.10. Identification of the granule cell domain within the dorsal cochlear nucleus. (A-D) Photomicrographs of DCN coronal slices (20 μ m thick) stained with cresyl violet. **(A, C)** The whole cochlear nucleus is shown. **(B)** Bigger magnification of the square in A. The granule cell lamina (L) that separates the DCN from the VCN is delimited by the dashed lines. The subpeduncular corner (Spc) is shown **(D)** bigger magnification of the square in (C). The strial corner (delimited by the dashed lines) lies on the dorso medial pole of the DCN. A small domain of granule cells within the fusiform layer is shown (DCN GrD).

Tri-dimensional reconstruction of the dorsal cochlear nucleus

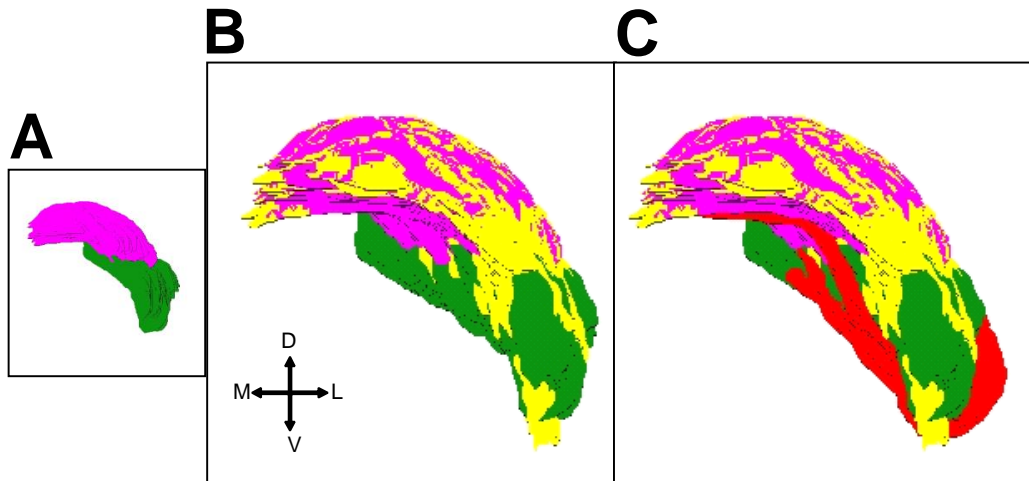


Figure 3.11. Three-dimensional reconstruction of the cochlear nucleus. (A) Coronal serial reconstruction of the cochlear nucleus. The DCN is in pink and the VCN is in green (B) Bigger magnification of the cochlear nucleus in A in which the granule domains are labelled in yellow (C) Same figure as in B with the descending branch of the auditory nerve labelled in red

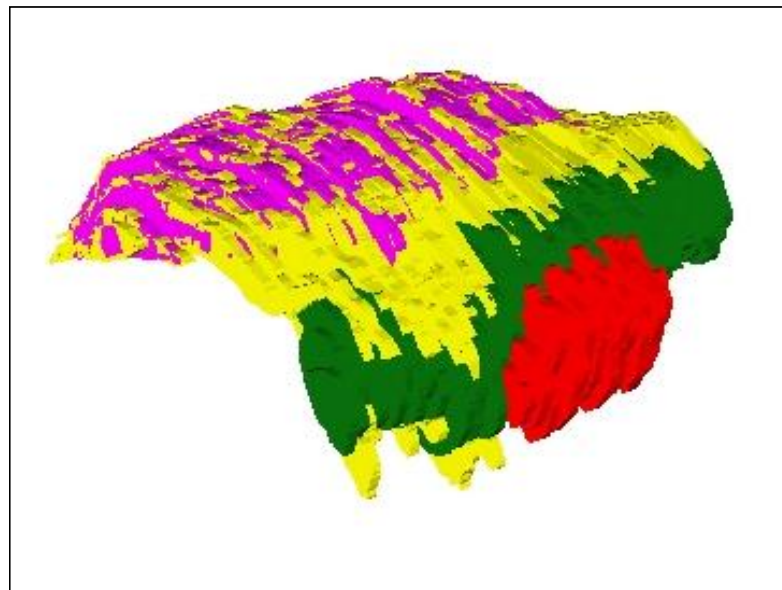


Figure 3.12. Three-dimensional reconstruction of the cochlear nucleus. The same reconstructed structure as in figure 4. is rotated 45° laterally. The DCN is in pink and the VCN is in green, the granule domains in yellow the descending branch of the auditory nerve is in red

CHAPTER 4

Electrophysiological properties of dorsal cochlear nucleus neurones

INTRODUCTION

4.1. Role of intrinsic cellular excitability in a network

Dynamics of neural networks arise through a complex interplay between excitatory and inhibitory synaptic inputs and the intrinsic electrical properties of individual neurons (Marder et al., 1996). Indeed, both intrinsic membrane properties and synaptic inputs are fundamental in determining the cellular excitability of a neuron (Hille, 1992). Intrinsic ionic conductances of a cell not only determine its characteristics like the membrane resistance, the resting potential, the action potential threshold, the amplitude and the duration of the action potentials but also many other events such as synaptic integration (Marder et al., 1996; Storm, 1988), the pattern and the rate of firing (Turrigiano et al., 1995) and synaptic plasticity (Hoffman et al., 1997; Magee and Johnston, 1997). Neurons can display a variety of activity patterns depending on the number and the type of voltage gated channels and the types of synaptic inputs. Some neurons for example are silent and fire action potentials only when they are excited by synaptic inputs whereas other neurons are spontaneously active (Marder et al., 1996). Early postnatal spiral ganglion neurons fire action potentials spontaneously independently of inputs from hair cells and this is related to the intrinsic membrane properties of spiral ganglion neurons (Lin and Chen, 2000). In the cerebellum, Purkinje neurons can also fire spontaneously and regularly in the absence of synaptic input but generate an irregular firing pattern in the presence of tonic synaptic inhibition (Häusser and Clark, 1997). In this latter case, the firing pattern is regulated by synaptic inputs. Some other neurons can display intrinsic oscillatory properties involving periodic bursts of

action potentials where the interplay of different types of voltage-gated channels can generate spontaneous rhythmic bursting activities (Hille, 1992). The bursting activity can also be regulated by synaptic inputs. In invertebrate preparations, neurons fire in bursts as a consequence of synaptic inputs from other neurons whereas in absence of these inputs they fire tonically (Turrigiano et al., 1995; Turrigiano, 1999).

A precise regulation of neural excitability is therefore essential for the stability of a neural circuit, where the output of a neuronal circuit depends critically on the interaction between the synaptic strength of the various inputs and the intrinsic properties of the pre- or post-synaptic neurones. Changes involving the synaptic efficacy and the intrinsic neuronal properties occurring independently or concurrently can modify the dynamics of the network.

The excitability of neurons can be affected by development or after injuries (Davis and Bezprozvanny, 2001). One example is represented by the effects of acoustic over-exposure at the level of the DCN. The spontaneous activity of DCN neurones is reduced shortly (2-3 days) after acoustic over-exposure (Kaltenbach et al., 1998) and then is largely increased for the following months (Kaltenbach and McCaslin 1996; Kaltenbach et al., 1998; 2000; Kaltenbach and Zhang, 1998). The aim of this chapter was to investigate the cellular excitability of identified DCN neurones in control condition to subsequently study whether intrinsic changes of excitability can occur after acoustic over-exposure (detailed in chapter 6). I used whole cell current clamp recording in Lister Hooded rat brainstem slice preparations. Although the physiology of DCN neurons has been classically described in many rodents, it had not been characterized in this rat strain. Passive properties like resting

potentials, membrane resistance and capacitance and active properties like action potential characteristics firing frequency were analyzed. These properties will give information on the involvement of different voltage gated ionic currents that could be modulated after acoustic over-exposure. I studied the electrophysiological properties of fusiform cells receiving auditory and non-auditory inputs and also studied the excitability properties of giant cells that only receive auditory inputs. I also characterized the electrophysiological properties of cartwheel cells, the interneurons inhibiting fusiform cells and characterized the electrophysiological properties of granule cells that transmit multisensory excitatory inputs onto fusiform and cartwheel cells. All cells were filled with lucifer yellow to confirm their morphology.

RESULTS

4.2. Electrophysiological properties of identified cells of the dorsal cochlear nucleus

I compared the passive and the active properties of four main cell types in the Lister Hooded DCN: fusiform cells, granule cells, cartwheel cells and giant cells. Cells were identified by their location in the slice as well as by their morphology assessed by lucifer yellow filling and confocal microscopy (examples of the major DCN cell types are shown in figure 4.1). Long term recordings of giant cells were difficult to obtain and only three giant cells were successfully recorded for a period exceeding ten minutes. This could be due to the fact that giant cells have extensive dendrites that could have been cut during the slicing procedure.

4.2.1. Passive properties

The analysis of the passive properties includes the resting potential, the capacitance and the membrane resistance as described in the methods (section 2.2.9.) and as detailed in the table 4.1 below. The resting potential was between -45 mV and -57 mV for the different cell types with cartwheel cells showing more depolarized resting potentials i.e. -45 ± 2 mV (n= 10) when compared to giant cells (-57 ± 3 mV, n= 6). Giant cells and fusiform cells were characterized by a larger capacitance (183 ± 56 pF, n= 6 and 166 ± 17 pF, n= 13 respectively) compared to cartwheel cells (90 ± 10 pF, n=10) and granule cells (8 ± 2 pF, n=11). It appears that, after morphological identification, fusiform cells and giant cells were also the largest cells (diameter of 26 ± 0.9 μ m, n=6 and 32 ± 0.6 μ m,

n= 3 for fusiform and giant cells respectively) compared to cartwheel cells and granule cells (mean diameter of $17 \pm 0.8 \mu\text{m}$ n=4 and $8 \pm 1.4 \mu\text{m}$ n=3 μm for cartwheel cells and granule cells respectively). Finally, granule cells were characterized by a higher membrane resistance ($1.4 \pm 0.1 \text{ G}\Omega$, n=11) by comparison to cartwheel cells ($128 \pm 23 \text{ M}\Omega$, n=8), fusiform cells ($70 \pm 18 \text{ M}\Omega$, n=10) and giant cells $142 \pm 56 \text{ M}\Omega$, n=6). Passive properties for the four cell types and the degrees of significance are summarized in the table 4.1 (below).

	Resting potential (mV)	Membrane Resistance (M Ω)	Capacitance (pF)
Fusiform cells (n=10-13)	-53 ± 2	70 ± 18	166 ± 17
Cartwheel cells (n=10-8)	-45 ± 2	128 ± 23	90 ± 10
Giant cells (n=6)	-57 ± 3	142 ± 56	183 ± 56
Granule cells (n=11)	-46 ± 3	1384 ± 102	8 ± 2
Fu versus Cw	N.S.	N.S.	N.S.
Fu versus Gi	N.S.	N.S.	N.S.
Fu versus gr	N.S.	P<0.01**	P<0.01**
Cw versus Gi	P<0.05*	N.S.	P<0.05*
Cw versus gr	N.S.	P<0.05*	P<0.05*
Gi versus gr	N.S.	P<0.01**	P<0.01**

Table 4.1: Analysis of DCN cell type passive properties. Mean \pm s.e.m values for the resting potential, the membrane resistance and the capacitance measured in fusiform (Fu), cartwheel (Cw), giant (Gi) and granule (gr) cells. P values are from anova-one way-Tukey test comparing resting potential, membrane resistance and capacitance between the different cell types (* = $P \leq 0.05$, ** = $P \leq 0.01$), N.S. = non significant with P values >0.05.

4.2.2. Properties of the action potentials

The analysis of the action potential properties includes the amplitude of the action potential, the 10-90% rise time, the 90-10% decay time and the presence or the absence of an undershoot (examples are shown in figure 4.2). Action potential properties have been characterized at threshold when the firing rate was minimal (summarized in table 4.2 below). The amplitude of the action potential was between 69 mV and 87 mV for all cell types and a difference in the action potential amplitude was only observed between fusiform cells (87 ± 3 mV, $n=9$) and granule cells and (69 ± 4 mV, $n=12$ mV, $P<0.01$, anova-one way). Granule cell action potentials display the slowest 10-90% rise time of 12 ± 2 ms ($n=12$) compared to fusiform cells (0.6 ± 0.1 ms, $n=9$, $P<0.01$, anova-one way), giant cells (0.4 ± 0.1 ms, $n=3$, $P<0.01$, anova-one way) and cartwheel cells (4 ± 1 ms, $n=8$, $P<0.01$, anova-one way) (see figures 4.2 and 4.3). Granule cell 10-90% rise time includes subthreshold depolarization which is not part of action potential and for this reason they exhibit the slowest rise time. In order to properly compare the rise times it may have been better to calculate the 20-80% rise time.

In figure 4.3, the 10-90% rise time of granule cell action potentials starts during the first 9-10 ms and is not represented on the graph. Cartwheel cell action potentials are characterized by the longest 90-10% decay time (i.e. 8 ± 1 ms, $n=8$) compared to fusiform cells (0.7 ± 0.03 ms, $n=9$, $P<0.01$, anova-one way), giant cells (0.8 ± 0.2 ms, $n=3$, $P<0.01$, anova-one way) and granule cells (2 ± 0.7 ms, $n=12$, $P<0.01$, anova-one way) and examples are shown in figure 4.4. The long decay time of cartwheel cells is likely to be result of calcium channels and small conductance calcium activated potassium channels (SK) and this is

further discussed in section 4.3.2. Fusiform and giant cells are also characterized by an action potential followed by an undershoot (figure 4.2 A and B) that may be linked to a delayed rectifier potassium current and/or a calcium-activated potassium current (Hirsch and Oertel, 1988). Altogether, different action potential properties suggest different the involvement of different voltage gated ionic currents that can be modulated after acoustic over- exposure

	Amplitude (mV)	10-90% rise time (ms)	90-10% decay time (ms)	Undershoot (cell number)
Fusiform cells (n=9)	87 ± 3	0.6 ± 0.1	0.7 ± 0.03	9
Cartwheel cells (n=8)	74 ± 2	4 ± 1	8 ± 1	0
Giant cells (n=3)	80 ± 9	0.4 ± 0.1	0.8 ± 0.2	3
Granule cells (n=12)	69 ± 4	12 ± 2	2 ± 0.7	0
Fu versus Cw	N.S.	N.S.	P<0.01**	
Fu versus Gi	N.S.	N.S.	N.S.	
Fu versus gr	P<0.01**	P<0.01**	N.S.	
Cw versus Gi	N.S.	N.S.	P<0.01**	
Cw versus gr	N.S.	P<0.01**	P<0.01**	
Gi versus gr	N.S.	P<0.01**	N.S.	

Table 4.2: Analysis of the action potential properties. Mean ± s.e.m values for the amplitude, the 10-90% rise time and the 90-10% decay time measured in fusiform (Fu), cartwheel (Cw), giant (Gi) and granule (gr) cells. P values are from anova-one way - Tukey tests comparing the amplitude, the 10-90% rise time and the 10-90% decay time between the different cell types. (** = P≤0.01), N.S. = non significant for P values >0.05

4.2.3. Firing frequency at different membrane potentials

Table 4.3 and table 4.4 summarize the analysis of the spike frequency and the regularity of the firing as cells are maintained at different steady state

membrane potentials (at threshold and when cells reached the maximal firing frequency) for 1 – 4 minutes for every different membrane potential.

As cells were maintained at their threshold potential, different variables were quantified such as the frequency, the membrane potential and the coefficient of variation of the interspike interval (ISI) (examples are shown in panel A of figures 4.5, 4.7., 4.9., 4.10., 4.12. and values with degrees of significance detailed in table 4.3 below). When maintained at firing threshold, the firing frequency (at around 1-2 Hz) and the coefficient of variation (between 1.5 and 2.5) were similar between all cell types. Nevertheless cartwheel cells started to fire at a less depolarized membrane potential (-72 ± 2 mV, $n= 8$) compared to fusiform cells (-64 ± 1 mV, $n= 7$, $P<0.05$, anova-one way), indicating that their threshold of activation is lower compared to fusiform cells.

As cells get more depolarized, the firing frequency increased until a maximal firing was reached and the firing pattern became more regular (lower values of the coefficient of variation of the ISI distribution). Examples for fusiform cells, cartwheel cells, giant cells and granule cells are given in panels B to D of figures 4.5., 4.7., 4.9., 4.10., 4.12 respectively. The maximal firing with the correspondent coefficient of variation and membrane potential was quantified for each cell type and values are reported in table 4.4 below. It is worth noticing that when cells were depolarized above their maximal limit, the firing frequency was either decreased or the action potentials stopped overshooting. Fusiform cells fired with the highest firing frequency (35 ± 5 Hz, $n=7$) amongst the other DCN cell types (maximal firing frequency between 12-17 Hz, see table 4.4). Nevertheless the coefficient of variation of the ISI distribution in fusiform cells was similar to the coefficient of variation of the other

cell types, indicating that despite fusiform cells firing at higher frequencies, the firing pattern became indistinctly homogeneous and regular for all cells as the membrane potential became more depolarized.

I previously reported that cartwheel cells started to fire at a less depolarized membrane potential compared to fusiform cells. Parallel to this, I also found that cartwheel cells reached their maximal firing frequency at membrane potentials more hyperpolarized (-63 ± 2 mV, $n= 8$) compared to fusiform cells (-55 ± 1 mV, $n= 7$, $P<0.05$, anova-one way).

	Frequency at threshold (Hz)	CV at threshold	MP at threshold (mV)
Fusiform cells (n=7)	0.9 ± 0.4	1.3 ± 0.1	-64 ± 1
Cartwheel cells (n=8)	0.8 ± 0.2	1.6 ± 0.3	-72 ± 2
Giant cells (n=3)	1.9 ± 0.9	2.6 ± 0.6	-66 ± 3
Granule cells (n=7)	1.2 ± 0.2	1.7 ± 0.3	-67 ± 2
Fu versus Cw	N.S	N.S.	$P<0.05^*$
Fu versus Gi	N.S.	N.S.	N.S.
Fu versus gr	N.S.	N.S.	N.S.
Cw versus Gi	N.S.	N.S.	N.S.
Cw versus gr	N.S.	N.S.	N.S.
Gi versus gr	N.S.	N.S.	N.S.

Table 4.3: Analysis of the action potential firing properties at threshold. Mean \pm s.e.m values for the firing frequency, the coefficient of variation (CV) and the membrane potential (MP) measured at threshold in different cell types. P values were obtained with anova one-way-Tukey test comparing for the firing frequency, the coefficient of variation and the membrane potential between the different cell types. (* = $P \leq 0.05$), N.S. = non significant for P values >0.05 . Abbreviations: fusiform (Fu), cartwheel (Cw), giant (Gi) and granule (gr) cells.

The minimal firing frequency (at threshold) and the maximal firing frequency were plotted in function of their respective membrane potential and respective coefficient of variation for each cell type (see panels A-B of figures 4.6., 4.8., 4.11., 4.13.) and the linear regression slopes were analyzed with values reported in table 4.5 below. Slopes of the firing frequency relative to the membrane potentials were similar between all cell types, despite fusiform cells firing with a maximal firing rate (i.e. about 35 Hz compared to about 15 Hz for the other cell types). By contrast, the slope of the firing frequency relative to the coefficient of variation was significantly steeper in fusiform cells (-33 ± 5 Hz, $n=7$) compared to the other cell types (see table 4.5) indicating that there is a strong dependency between the fusiform cell firing rate and their regularity of firing. Figure 4.14 summarizes the firing frequencies in relation to the membrane potential (A) and to the coefficient of variation (B) for the different cell types. Fusiform cell display clear higher maximal firing frequencies at potentials as depolarized as -45 mV (figure 4.14A). Fusiform cells also display the higher firing frequency rates in relation to the firing regularity (figure 4.14B).

	Frequency at Fmax (Hz)	CV at Fmax	MP at Fmax (mV)
Fusiform cells (n=7)	35 ± 5	0.3 ± 0.1	-55 ± 1
Cartwheel cells (n=8)	14 ± 1	0.5 ± 0.1	-63 ± 2
Giant cells (n=3)	17 ± 6	0.1 ± 0.001	-62 ± 1
Granule cells (n=8)	12 ± 1	0.8 ± 0.2	-59 ± 1
Fu versus Cw	P<0.01**	N.S.	P<0.01**
Fu versus Gi	P<0.05*	N.S.	N.S.
Fu versus gr	P<0.01**	N.S.	N.S.
Cw versus Gi	N.S.	N.S.	N.S.
Cw versus gr	N.S.	N.S.	N.S.
Gi versus gr	N.S.	N.S.	N.S.

Table 4.4: Analysis of the action potential firing properties at maximal frequency. Mean ± s.e.m values for the frequency, the coefficient of variation (CV) and the membrane potential (MP) all measured at maximal frequency (Fmax) in different cell types. The P values were obtained with anova one-way-Tukey test comparing frequency, the coefficient of variation and the membrane potential measured at maximal frequency between different cell types. (**= P≤0.01, * = P≤0.05), N.S. = non significant for P values >0.05. Abbreviations: fusiform (Fu), cartwheel (Cw), giant (Gi) and granule (gr) cells.

	Slope (a) Hz ⁻¹	Slope (a') Hz/mV
Fusiform cells (n=7)	-0.03 ± 0.003	3.4 ± 0.4
Cartwheel cells (n=8)	-0.09 ± 0.01	2.7 ± 1
Giant cells (n=3)	-0.17 ± 0.03	5.6 ± 3
Granule cells (n=7)	-0.05 ± 0.05	1.7 ± 0.8
Fu versus Cw	N.S.	N.S.
Fu versus Gi	N.S.	N.S.
Fu versus gr	N.S.	N.S.
Cw versus Gi	N.S.	N.S.
Cw versus gr	N.S.	N.S.
Gi versus gr	N.S.	N.S.

Table 4.5: Analysis of the action potential firing properties at maximal frequency. Mean ± s.e.m values for the slopes *a* and *a'* as represented in figures 4.5., 4.7., 4.9., 4.10., 4.12. *a'* represents the slope of the firing frequency in relation to the coefficient of variation; *a* represents the slope of the firing frequency in relation to the membrane potential. *P* values were obtained with anova one-way-Tukey test comparing slopes *a* and *a'* between different cell types N.S. = non significant for *P* values >0.05. Abbreviations: fusiform (*Fu*), cartwheel (*Cw*), giant (*Gi*) and granule (*gr*) cells.

When held at membrane potentials above the action potential threshold, some cartwheel cells exhibited trains of action potentials that were characterized as “bursts”. Examples of bursts are shown in figure 4.7 B (left) and figure 4.9B (left) and in this case the corresponding ISI distribution was bimodal with two Gaussian functions fitting the distribution (shown in figure 4.7 B, right and figure 4.9 B, right). For example, the ISI distribution in figure 4.9 B could be fitted with two Gaussian functions with peak values at 98 ms and 400 ms. When bursts were exclusively selected, the ISI distribution became

monomodal and could be fitted with one Gaussian distribution showing a single peak at 100 ms. From this, it can be concluded that bimodal distributions of the ISI distributions of cartwheel cells represent two types of firing: “simple” firing at 10 Hz versus “bursts” firing at 4 Hz (values estimated from figure 4.9). Half of the cartwheel cells (4 out of 8) exhibited spontaneous bursts firing at specific membrane potentials (between -70 and -65 mV). Cartwheel cells never showed any burst activity at threshold firing or when maintained at membrane potentials more depolarized than -65 mV. In those cases, the ISI distribution returned to a monomodal single peak distribution. This is represented in Figure 4.9D where a bimodal distribution gives place to a monomodal distribution at more depolarized levels.

4.2.4. Firing frequency in relation to step currents

After having established the properties of the firing rate in function of the membrane potential, the firing frequency was also analyzed in response to step currents from a single membrane potential of -80 mV (examples for the different cell types are given in figures 4.15., 4.20., 4.24., 4.28.). Step currents were used to mimic synaptic inputs onto the cells. I considered the fact that step current pulses only poorly mimic real synaptic inputs and other protocols would have been more suitable i.e. noisy current injections, current injections with specific rise times and decay time in dynamic clamp; Destexhe and Paré, 1999; Prescott and De Koninck, 2003). Table 4.6. summarizes the spike frequencies obtained after injections of step currents to different DCN cell types. Similarly to the previous observations, I found that fusiform cells reached the highest firing frequencies (119 ± 27 Hz, $n=5$) compared to other cell types that fired between 30-72 Hz (see table 4.6 for details). The firing rate-step current dependency

was first fitted with a linear regression function (one example is shown in figure 4.17A) and slopes and intercepts considered as measuring indexes (figure 4.17B). The slope of the frequency – current relation is considered as a measurement of the gain of the neuronal response (Chance et al., 2002; Higgs et al., 2006) and the summary in figure 4.32 clearly shows that the slope was significantly steeper in granule cells (1.4 ± 0.2 Hz/pA, $n= 7$) compared to fusiform cells (0.1 ± 0.02 Hz/pA, $n=5$, $P<0.01$ anova one way), cartwheel cells (0.3 ± 0.1 Hz /pA, $n=6$, $P<0.01$ anova one way) and giant cells (0.1 ± 0.05 Hz/pA, $n=3$, $P<0.01$ anova one way). Mean intercept values were not significantly different between the different cell types (figure 4.32B).

Linear regressions were not fitting accurately all data (see figure 4.17) and I also used sigmoidal functions to fit the firing rate-step current dependency. All fits are represented in figures 4.16., 4.21., 4.25. and figure 4.29 and mean values for the slope are reported in table 4.6. Slopes were significantly steeper in granule cells (2.2 ± 0.4 pA/Hz, $n=10$) compared to fusiform cells (0.06 ± 0.01 pA/Hz, $n=5$, $P<0.05$, anova-one way) but not compared to cartwheel cells (1.1 ± 0.7 pA/Hz, $n=5$, N.S. anova-one way) or to giant cells (0.1 ± 0.05 pA/Hz, $n=3$, N.S. one-way anova). In summary, linear fitting reported slope values for granule cells which were significantly higher than all the other cell types, but in the case of sigmoidal fitting values were only higher when compared to fusiform cells.

Previous studies showed that specific membrane currents can influence the latency to the first action potential in cochlear nucleus neurons (Manis, 1990; Rusznak et al., 1997). I therefore compared the latency to the first action potential (measured at the minimal step current to elicit action potential)

represented in figures 4.18., 4.22., 4.26. and figure 4.30. for each cell type. The latency to the first action potential was significantly higher in fusiform cells (141 ± 19 ms, $n=5$, figure 4.18) compared to cartwheel cells (38 ± 9 ms, $n=5$, $P<0.01$ anova one way), to giant cells (30 ± 13 ms, $n=3$, $P<0.01$ anova-one way) and to granule cells (72 ± 19 ms, $n=10$, $P<0.01$ anova-one way). Values are summarized in the table 4.6 below.

	Slope (Hz/pA)	Fmax (Hz)	Latency (ms)
Fusiform cells (n=5)	0.06 ± 0.01	119 ± 27	141 ± 19
Cartwheel cells (n=5)	1.1 ± 0.7	53 ± 11	38 ± 9
Giant cells (n=3)	0.1 ± 0.05	75 ± 9	30 ± 13
Granule cells (n=10)	2.2 ± 0.4	66 ± 7	72 ± 19
Fu versus Cw	N.S.	$P<0.05^*$	$P<0.01^{**}$
Fu versus Gi	N.S.	$P<0.01^{**}$	$P<0.01^{**}$
Fu versus gr	$P<0.05^*$	$P<0.05^*$	$P<0.01^{**}$
Cw versus Gi	N.S.	N.S.	N.S.
Cw versus gr	N.S.	N.S.	N.S.
Gi versus gr	N.S.	N.S.	N.S.

Table 4.6. Analysis of the action potential firing properties of fusiform cells when injecting step currents in different cell types. Mean \pm s.e.m values for the values of the slope of the sigmoidal curve, the maximal firing frequency (Fmax), and the latency to first action potential (measured at minimal step current that elicited the action potential). P values were obtained with anova one-way-Tukey test comparing slopes obtained by sigmoidal fits, maximal firing frequencies and the latencies to first action potential between the different cell types. (**= $P\leq 0.01$, *= $P\leq 0.05$), N.S. = non significant for P values >0.05 . Abbreviations: fusiform (Fu), cartwheel (Cw), giant (Gi) and granule (gr) cells.

Long action potential latencies within DCN fusiform cells have been linked to the activation of an A-type potassium current (Manis, 1990). This suggests that not only background synaptic conductances but also the intrinsic voltage dependent membrane conductances can contribute to the generation of the temporal discharge patterns of DCN cell types.

Ultimately I quantified the interspike interval at different times during the current step to investigate firing adaptation during the 1 sec firing (see figures 4.19., 4.23., 4.27., 4.31. and table 4.7.). Little adaptation was exhibited by fusiform cells and giant cells (i.e. the ISI measured at the beginning of the step was similar to the ISI along the step). This is in accordance with previous studies that suggest that the firing properties of fusiform cells are stable over time (Manis, 1990). By contrast, cartwheel and granule cells showed an adaptation that occurs during the first half second (i.e. the ISI measured at the beginning of the step was smaller than the ISI measured after 0.5 sec (see table 4.7 below).

In summary, passive and active properties allowed discriminating between different DCN cell types. Granule cells can be distinguished by their small capacitance (around 8 pF) and high membrane resistance (1.4 G Ω) and a slow action potential rise time (around 12 ms). When performing step current injections, granule cells reached their maximal firing frequency (around 60 Hz) with the highest rate (2 Hz/pA) and displayed adaptation. Cartwheel cells fired action potentials characterized by a long decay time (around 8 ms) and were the only cells within the nucleus that fired with bursts of action potentials. Fusiform cells reached the highest firing frequencies (110 Hz with step currents) with a firing pattern becoming regular at the quickest rate. Fusiform cells were

also characterized by the longest latency to the first action potential (around 140 ms). All those characteristics can potentially be modulated by acoustic over-exposure and therefore induce a change in the excitability of the DCN network.

	ISI at t=0 sec (ms)	ISI at t=0.5 sec (ms)	ISI at t=1 sec (ms)
Fusiform cells (n=4)	11.4 ± 2.6	17.3 ± 4.7	22.7 ± 7.3
Cartwheel cells (n=4)	14.7 ± 3.6	31.7 ± 3.2	27 ± 2.5
Giant cells (n=2)	11.9 ± 2.2	22.2 ± 2.7	22.3 ± 0.7
Granule cells (n=7)	27.7 ± 3.6	31.5 ± 4.5	30.3 ± 5.7
	ISI _{t0} vs ISI _{t0.5} (P values)	ISI _{t0.5} vs ISI _{t1} (P values)	
Fusiform cells	0.07	0.1	
Cartwheel cells	0.03*	0.4	
Giant cells	0.1	0.9	
Granule cells	0.02*	0.3	

Table 4.7. Analysis of the action potential firing properties of fusiform cells when injecting step currents in different cell types. Mean ± s.e.m. values the interspike interval (ISI) at time = 0 sec, at time = 0.5 sec and at time = 1 sec. P values were obtained with paired T test comparing the ISI at t = 0 sec (t_0) with the ISI at t = 0.5 sec ($t_{0.5}$) and the ISI a time 0.5 sec with the ISI at time = 1 sec (t_1) in each cell type. (* = $P \leq 0.05$).

DISCUSSION

4.3. Electrophysiological properties of DCN neurons

I showed in chapter 3 that specific cell types were spatially organized within the DCN of Lister Hooded rats. In this chapter, I investigated the basic electrophysiological properties of those cells originating from Lister Hooded rats; all those properties could potentially change after acoustic over-exposure.

4.3.1. Passive properties of DCN neurons

Passive properties such as resting potential, capacitance and membrane resistance allowed discriminating granule cells from all the other cell types. Cartwheel cells could be distinguished from giant cells based on their depolarized resting potentials and their smaller capacitance. By contrast, fusiform cells could not be distinguished from either giant cells or cartwheel cells based on their passive properties.

Passive properties reported were similar to previous studies performed in fusiform cells (Kanold and Manis, 1999; Street and Manis, 2007), in giant cells (Zhang and Oertel, 1993a) and in cartwheel cells (Zhang and Oertel, 1993c) with the exception of the resting potentials of cartwheel cells (-44 ± 5.5 mV (S.D.), $n=10$) that were more depolarized compared to -62 ± 8 mV (S.D), $n=8$, $P<0.05$), values reported by Zhang and Oertel (1993c). In this latter study, resting potentials were measured by intracellular recordings and it is possible that depolarized resting potentials measured here in whole cell recordings were due to intracellular dialysis. Nevertheless, this is unlikely to be the case as resting potentials were measured immediately after the rupture of the patch and the dialysis time of cartwheel cells was estimated to be around 8 min (section

2.2.8). Differences in the resting potentials could be due to less disruptive intracellular recordings or to a difference in species (mice versus rats).

Analysis of the passive properties allowed distinguishing granule cells from the other cell types. Indeed granule cells exhibited the highest membrane resistance (1.4 G Ω) and the smallest capacitance (8 pF) compared to the other cell types. Previous studies on DCN granule cells from Wistar rats (Balakrishnan and Trussell, 2008) also reported similar small capacitance for those cells but also reported membrane resistance that are significantly higher (2.3 ± 0.8 G Ω (S.D), n=22) compared to the study here (1.4 ± 0.4 G Ω (S.D), n=11, $P < 0.05$ unpaired T test). This is unlikely to be due to a difference in the rat strain as similar membrane resistances were observed between granule cells originating from Wistar rats (chapter 6) and granule cells originating from LH rats. Alternative explanations for this difference could be due to the temperature at which cells were recorded (recordings were performed at room temperature in the study here versus 34–36°C reported in Balakrishnan and Trussell (2008). Previous studies reported that closing of some TRP channels (TRPV3 and/or TRPV4) by lowering temperature may be partly responsible for the neuroprotective effect of hypothermia (Lipski et al., 2006). This is however unlikely to be the case here as a closure of channels at room temperature would have triggered an increase in the membrane resistance in LH rats.

All DCN cell types could be discriminated based on a conjunction of characteristics: location, morphology and passive properties. Granule cells could easily be distinguished based on their density, small size, low capacitance and high membrane resistance. Fusiform cells could be distinguished based on their characteristic fusiform shape and their location in the fusiform layer by

contrast to cartwheel cells characterized by a rounder cell body and a location closer to the molecular layer. Giant cells were exclusively located in the deeper layer and could not be confused with cartwheel cells or fusiform cells located closer or within the fusiform cell layer. Cells could also be characterized by their action potential characteristics and their firing properties (see below). Finally, cells were filled with lucifer yellow allowing establishing a clear morphology.

4.3.2. Modulation of firing activities of DCN neurones

All cell types studied were spontaneously firing in accordance with previous studies performed in the DCN (Zhang and Oertel, 1994; Waller and Godfrey, 1994; Golding and Oertel, 1997).

Both fusiform and giant cells fired action potentials that were followed by an undershoot that may be produced by a delayed rectifier and a calcium-activated potassium current (Hirsch and Oertel 1988a).

Regular and high firing rates were observed in DCN fusiform cells. Similar firing frequencies were also observed in previous studies (Manis, 1990; Zhang and Oertel, 1994). High firing rates are likely to be permitted by a high threshold activated potassium current (Kv3). Indeed, Kv3 potassium channels produce a current that specifically enables a repetitive firing at high frequencies (Rudy and McBain, 2001) and Kv3 potassium channel expression was reported in fusiform cells (Friedland et al., 2007; Rusznák et al., 2008).

Granule cells displayed a slow action potential 10-90% rise time due to slow subthreshold depolarization which could be linked to a persistent sodium current like described in cerebellar granule cells (D'Angelo et al., 1998). Granule cells also displayed a high firing gain that is explained by their high membrane resistance leading to their immediate firing in response to small

current injections (like previously observed in the cerebellar granule cells (D'Angelo et al., 1995; Brickley et al., 1996)).

Cartwheel cells are interneurons that have got similar properties to cerebellar Purkinje cells. The two cell types share a similar morphology and contain many of the same proteins (Oertel and Young, 2004). Both cell types also fire in bursts (cartwheel cells: Zhang and Oertel, 1993a; Kim and Trussell, 2007; Bender and Trussell, 2009; Purkinje cells: Thach, 1967; Ito, 1984; Ito, 2001; Swensen and Bean, 2003). Whereas bursts in cerebellar Purkinje cells are due to dendritic calcium spikes mediated by P/Q-type calcium channels (Womack and Khodakhah, 2004), bursts in cartwheel cells are due to the activation of T- and R-type voltage-gated calcium channels co-localized with sodium channels on the axon initial segment (Bender and Trussell, 2009). Whereas constant bursts are in general observed in Purkinje cells, bursts were bimodal in cartwheel cells and this could be due to a difference in their underlying activation properties or to a difference in the distribution of ionic channels responsible for those bursts. It is also possible that the axon initial segment got cut in cartwheel cells that then failed to display bursts (this was the case of half of the cartwheel cells). In cerebellar Purkinje cells, big conductance (BK) and small conductance (SK) calcium activated potassium channels contribute to the interspike and the interburst intervals (Womack and Khodakhah, 2004). In DCN cartwheel cells, SK channels and T/R-type calcium channels are responsible for the long decay time of the action potential (Kim and Trussell, 2007).

Altogether these data show that different intrinsic ionic conductances could be responsible for different active and passive properties within DCN cells

types. How these intrinsic properties participate to the specific firing excitability is discussed in the section 4.3.4.

4.3.3. Could DCN cellular excitability be affected by acoustic over-exposure?

Modulation of individual conductances can profoundly alter the electrical properties of neurons (Kaczmarek and Levitan, 1987). During learning and development the sensory systems can modulate the balance of ionic conductances. Persistent visual stimulation increases the intrinsic excitability of optic tectal neurons which is correlated with enhanced voltage-gated sodium currents (Aizenman et al., 2003). In the cochlea, immature inner hair cells fire spontaneous action potentials which are then suppressed with development via an expression of a fast potassium conductance (Kros et al., 1998). Changes in ionic conductances might also be triggered by acoustic over-exposure or hearing loss (for review see Kaltenbach, 2007). Cochlear ablation changed the action potential characteristics and passive properties of aVCN neurones (Francis and Manis, 2000) and altered the expression of two-pore domain potassium channels in the whole cochlear nucleus (Holt et al., 2006). Moreover studies on congenitally deaf mice showed altered expression of potassium channels (Leão et al., 2004) and sodium channels (Leão et al., 2006) accompanied by changes in the cellular excitability in the MNTB (Leão et al., 2004; 2006). Studies therefore suggest that acoustic over-exposure could affect the active and/or the passive properties of DCN neurones. An alteration of those properties could alter the dynamics of the DCN network and provide the phenotype of an acoustic trauma linked to acoustic over-exposure.

4.3.4. Specific roles for the different cell types in the DCN network?

Cell types within the DCN are characterized by their specific morphology as well as by their specific passive and active properties indicating a functional specificity within the network. Fusiform cells represent the major DCN output integrating auditory and multisensory information before passing it on to higher auditory centres. Fusiform cells are able to fire action potentials with the highest frequency (above 100 Hz in this study). Firing rate of fusiform cells becomes quickly regular suggesting a precise transmission of the signal. This hypothesis is also supported by previous studies showing that fusiform cells can respond to time-varying stimuli with reliable and precise trains of action potentials (Street and Manis, 2007). The activity of fusiform cells is regulated by granule cells that integrate auditory signals (Weedman and Ryugo, 1996) and multisensory signals (Weinberg and Rustioni, 1987; Itoh et al., 1987; Shore et al., 2000).

The high number of granule cells projecting onto fusiform cells via numerous parallel fibre inputs (Mugnaini et al., 1980b; Lorente de No, 1981) together with the high firing gain (about 2 Hz/pA) of granule cells suggest a major influence of granule cells in modulating the synaptic outcome of the network. Granule cell firing gain will indeed determine cartwheel and fusiform cell activity and therefore control the signal transmission from the DCN to higher auditory centres. Gain modulation is one of the primary mechanisms of the information processing involved in eye movements, spatial perception, attention, object recognition (Salinas and Thier, 2000). Previous works showed that the gain of neuronal response can be modulated by varying the level of background synaptic noise (Chance et al., 2002; Higgs et al., 2006). Gain modulation by background synaptic inputs to granule cells may arise from a

distal source (like the dorsal column nuclei, the vestibular periphery and/or auditory nuclei) or from a proximal source (from Golgi cells and/or unipolar brush cells within the granule cell domain). Changes in the level of the synaptic background could be the end product of an acoustic insult (i.e. increased activity of somatosensory inputs towards the auditory inputs) and the modification in the neuronal gain of granule cells could be one of the consequences of acoustic over-exposure. Changes in granule cell gain will not only reflect onto the excitability of fusiform cells but also onto the excitability of cartwheel cells. The monomodal or bimodal firing pattern in relation to the membrane potential suggests that cartwheel cells can enter into two different pattern of activity (continuous firing or bursting) and this may be regulated by the synaptic inputs they receive (parallel fibres).

When cerebellar Purkinje cells fire with bursts, more than half of the action potentials fail to propagate down the Purkinje cell axon (Khaliq and Raman, 2005; Monsivais et al., 2005) indicating that bursts are a limiting factor to the action potential propagation in Purkinje cells. This mechanism does not occur in cartwheel cells where bursts are reliably propagated to the axon terminals to elicit powerful and temporally precise postsynaptic responses onto fusiform cells (Roberts et al., 2008). Cartwheel cells could therefore operate in a transistor like mode firing switching from tonic to bursting firing to improve the transmission of the signal. It has been suggested that inhibitory inputs onto fusiform cells can enhance the precision of spike timing in fusiform cells (Street and Manis, 2007). Cartwheel cell with their bursting firing might therefore contribute to the precision of spike timing of fusiform cells.

Altogether this suggests that the output of the DCN circuit is accurately controlled by the activity of different cell types and depends critically on the interactions between synaptic strength and various intrinsic properties. The figure below is a schematic representation the specific role of fusiform cells, granule cells and cartwheel cells within the DCN.

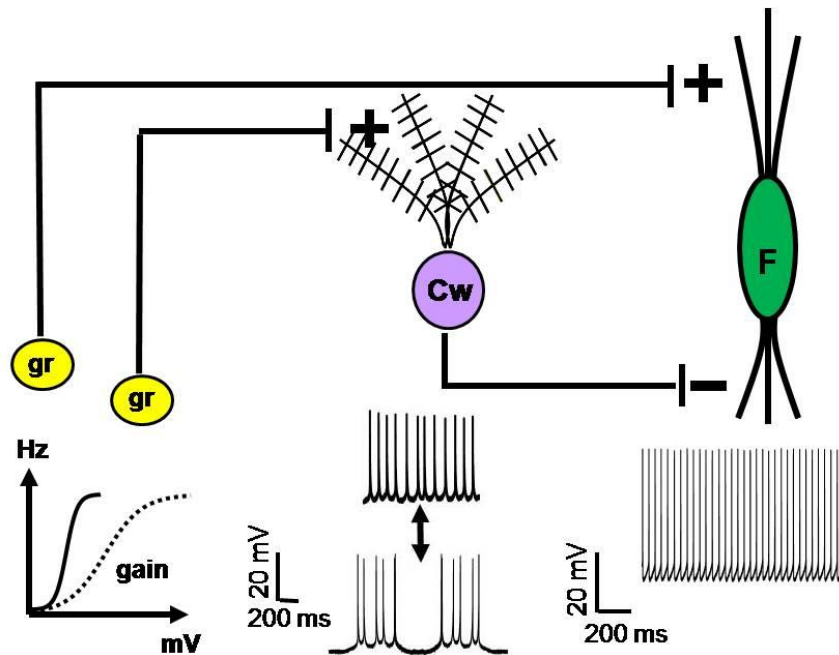


Figure 4.33: Schematic representation of dorsal cochlear nucleus cell firing activity. Fusiform cells can fire at high frequency (up to 120 Hz) and are responsible for a precise information transfer to higher auditory centres. Granule cells (gr) send excitatory projections to fusiform cells via their axons, the parallel fibres. Although not demonstrated, it is likely that multiple granule cells send their projections to a single fusiform cell. Granule cells are characterized by a high firing gain and it is therefore likely that a modulation of the gain will influence the fusiform cell firing rate and pattern. Cartwheel cells (Cw) are stimulated by granule cells and send inhibitory projections to fusiform cells. Cartwheel cell inhibition onto fusiform enhances spike timing (Street and Manis, 2007). Cartwheel cells can switch between a tonic or a bursting firing pattern according to their membrane potential and this could be due to differential granule cell activation (either via the number of granule cell activated or via a modulation of their firing gain). This switch of the pattern of inhibition will reflect onto fusiform cell firing activity. Granule cells are therefore responsible of modulating the frequency of transmission of the signal, directly via parallel fibres and as well of controlling the precision of the signal, indirectly via cartwheel cells.

Morphology of the principal dorsal cochlear nucleus cell types

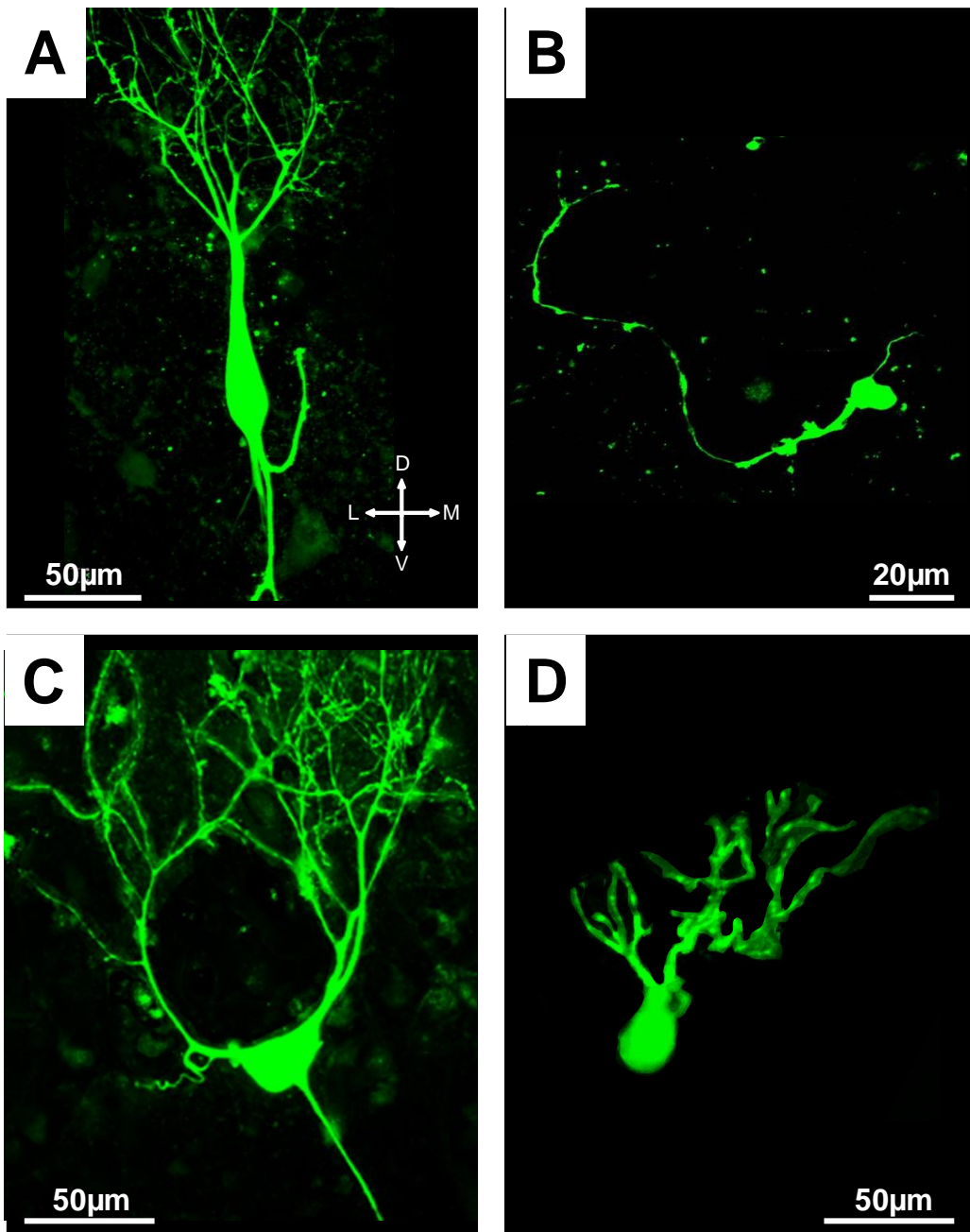


Figure 4.1: Photomicrographs of various DCN cells filled with the fluorescent dye lucifer yellow. (A) Fusiform cell lying in the fusiform layer with its large elongate cell body and its basal dendrites projected the deep layer while the apical dendrites are oriented towards the molecular layer. **(B)** A granule cell lying into the fusiform layer, its axon is directed towards the molecular layer. In the molecular layer granule cell axons constitute the parallel fibres. **(C)** Giant cell in the deep layer, the multiple dendrites are oriented towards the fusiform layer and the axon lies in the deep layer. **(D)** Cartwheel cell with its small oval cell body lying between the fusiform and the molecular layer and with a large spiny dendritic tree in the molecular layer.

Action potentials in dorsal cochlear nucleus cell types

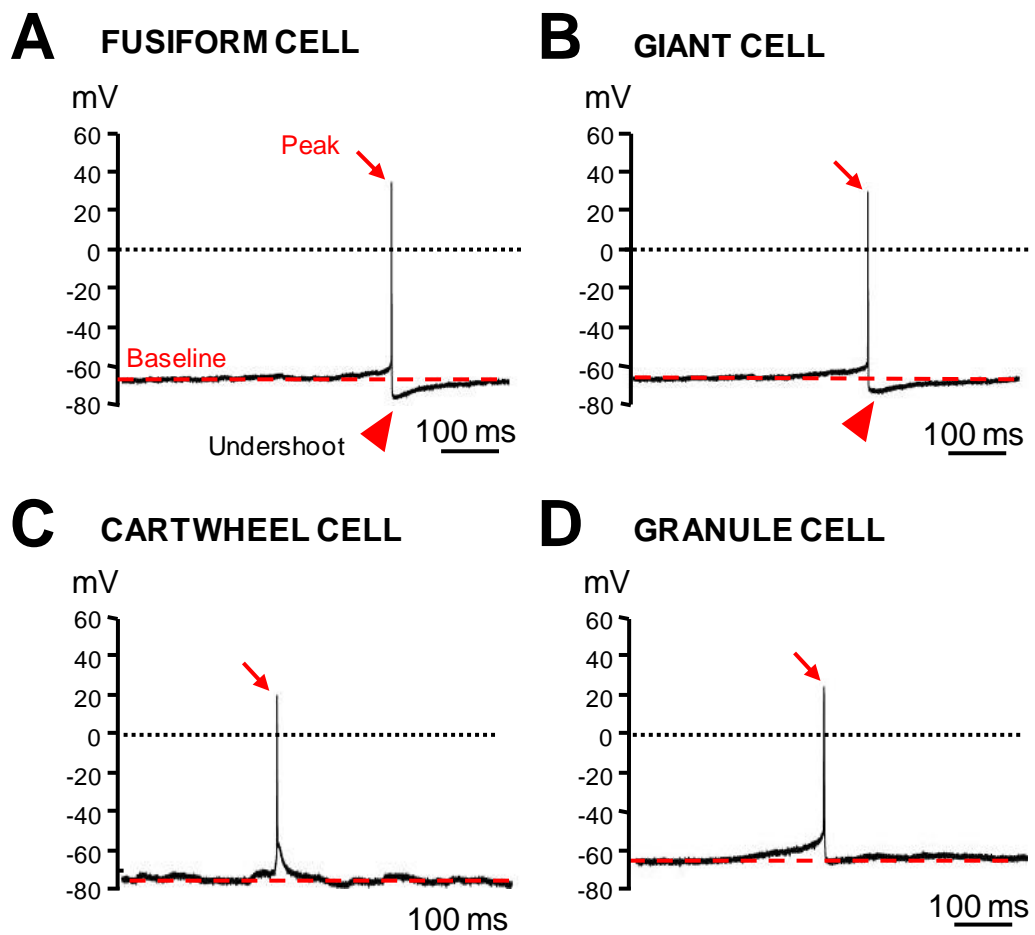


Figure 4.2: Action potentials recorded at threshold in different dorsal cochlear nucleus cell types. (A) Action potential of a fusiform cell (B) action potential of giant cell. (C) action potential of a cartwheel cell. (D) action potential of a granule cell. Note that (A) and (B) are characterized by an undershoot (arrowhead) by contrast to (C) and (D). Action potentials were recorded at their minimal firing frequency (threshold) at a holding potential between -75 and -60 mV. The dashed line represents the baseline and the dotted line represents the value of 0 mV. The arrow indicates the peak of the action potential.

Action potential rise time in dorsal cochlear nucleus cell types

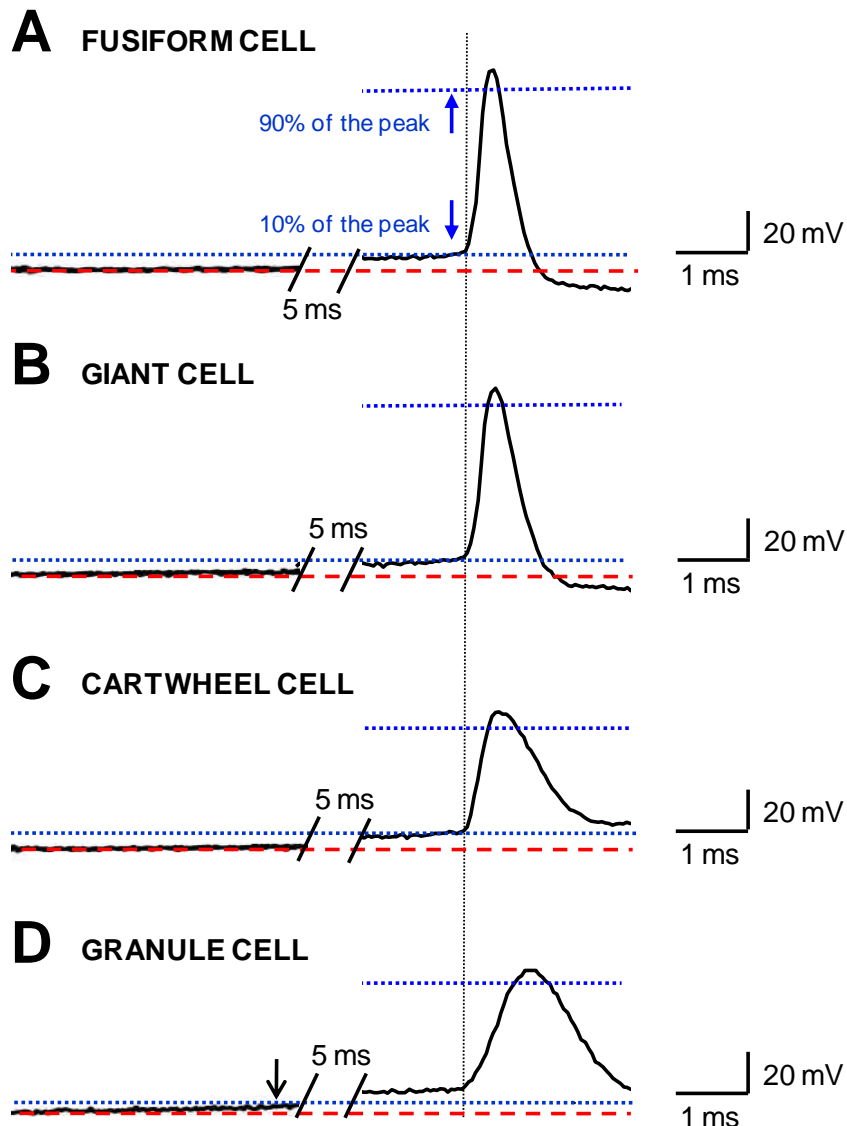


Figure 4.3: Action potential rise time in different dorsal cochlear nucleus cell types (A-D). Same action potentials as in figure 4.2. The 10-90% rise time (ms) is the time for the action potential to reach 90% of its maximal amplitude from a level of 10% above the baseline (red dashed line). The 10-90% rise time is estimated between the two dotted lines. The vertical dotted line represents the start of the action potential in a fusiform cell and all action potentials have been aligned to this line according to the fast kinetic of the rising time. The membrane potential at the level of the baseline is represented for each cell types. The time course of the membrane potential between the baseline and action potential has been cut for graphical reason. Note that the granule cell 10-90% rise time relative to the baseline is starting before the other cell types (arrow) explaining the 12 ms value obtained in table 4.2.

Action potential decay time in dorsal cochlear nucleus cell types

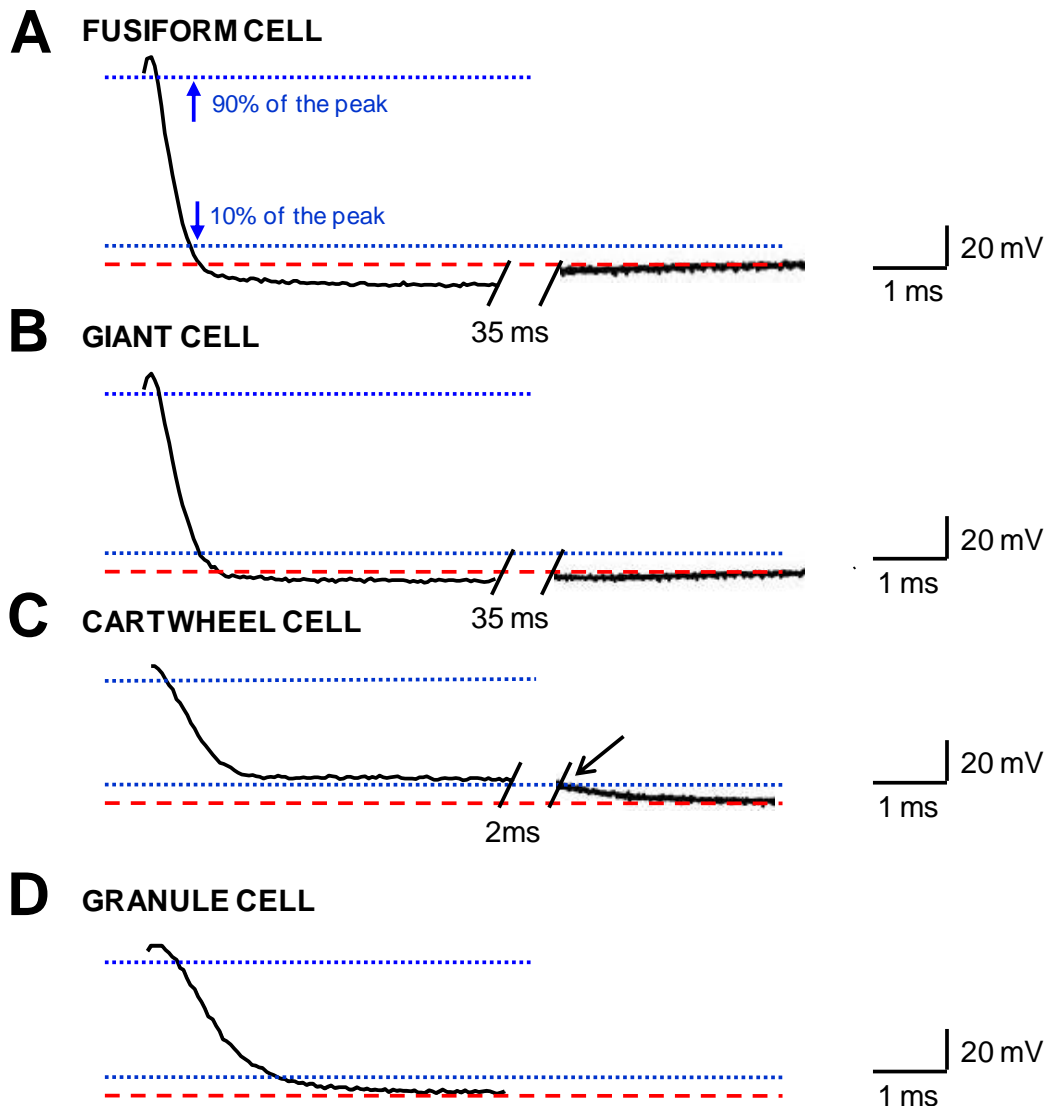


Figure 4.4: Action potential decay time in different cell types (A-D). Same action potentials as in figure 4.2. The 90-10% decay time (ms) is the time for the action potential decaying from the 90 % level of the maximal amplitude to a 10% level above the baseline (dashed line). The 90-10% decay time is estimated between the two dotted lines. The membrane potential at the level of the baseline is represented for each cell types. The time course of the membrane potential between the baseline and action potential has been cut for graphical reason. Note that the undershoot following the action potential in giant cells and in fusiform cells has not been taken into consideration in the baseline and is therefore not taken into account for the calculation of the decay time. Note that the cartwheel cell 90-10% decay time is measured to the arrow.

Example of a fusiform cell firing at different holding potentials

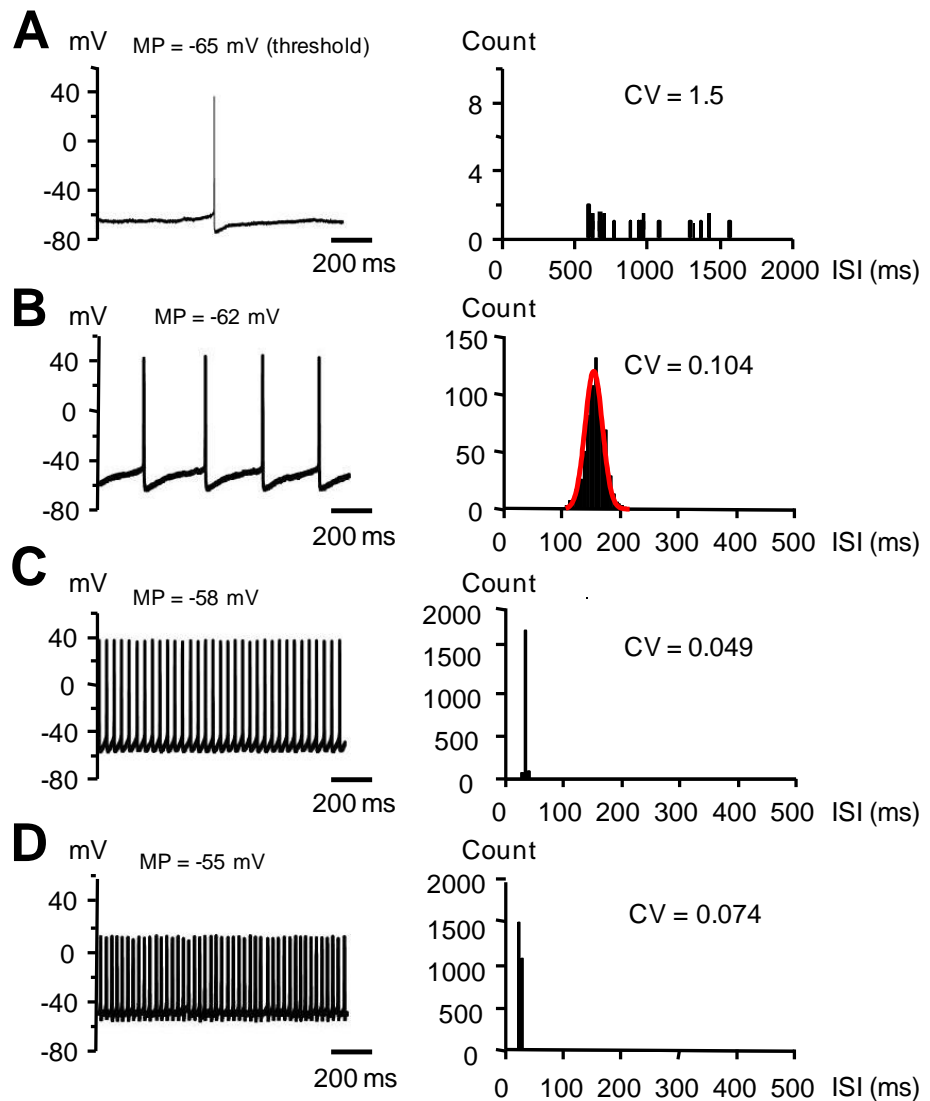


Figure 4.5: Firing properties of a DCN fusiform cell held at different holding potentials (A-D). Left, examples of the fusiform cell firing at different frequencies (in Hz) in function of the membrane potentials (MP in mV). Right, histograms showing the distribution of the interspike interval (ISI) for those membrane potentials. Above each histogram the coefficient of variation (CV) relative to the distribution is shown. **(A)** At threshold (MP = -65 mV) the cell is firing at 0.7 Hz. **(B)** At MP = -62 mV the cell is firing at 6 Hz. The ISI distribution (explained in section 2.2.9.5.) is fitted with a normal Gaussian function (shown in red, $y = [a1 \cdot \exp(-0.5((x-x1)/b1)^2)]$) that peaks at 155 ms. **(C)** Left, at MP = -58 mV the cell is firing at 31 Hz. **(D)** Left, at MP = -55 mV the cell is firing at 45 Hz. Note the smaller CV values for higher firing frequencies.

Analysis of the firing properties of a fusiform cell at different holding potentials

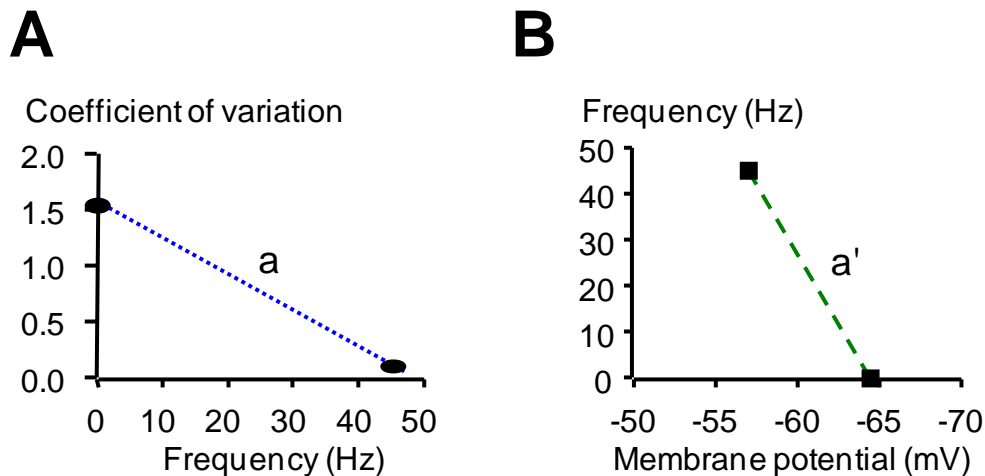


Figure 4.6: Firing frequency of a fusiform cell in relation to its holding potential and to the coefficient of variation of the interspike intervals. Same cell as in figure 4.5. **(A)** Graph representing the firing frequency (in Hz) in function of the coefficient of variation of the interspike intervals. **(B)** Graph representing the firing frequency (in Hz) in function of the membrane potential. The maximal and the minimal (threshold) firing frequency have been plotted. $a = -0.03 \text{ Hz}^{-1}$ and $a' = 6.0 \text{ Hz} \cdot \text{mV}^{-1}$ are slopes for the dotted and dashed lines in (A) and (B) respectively.

Example of a cartwheel cell firing at different holding potentials

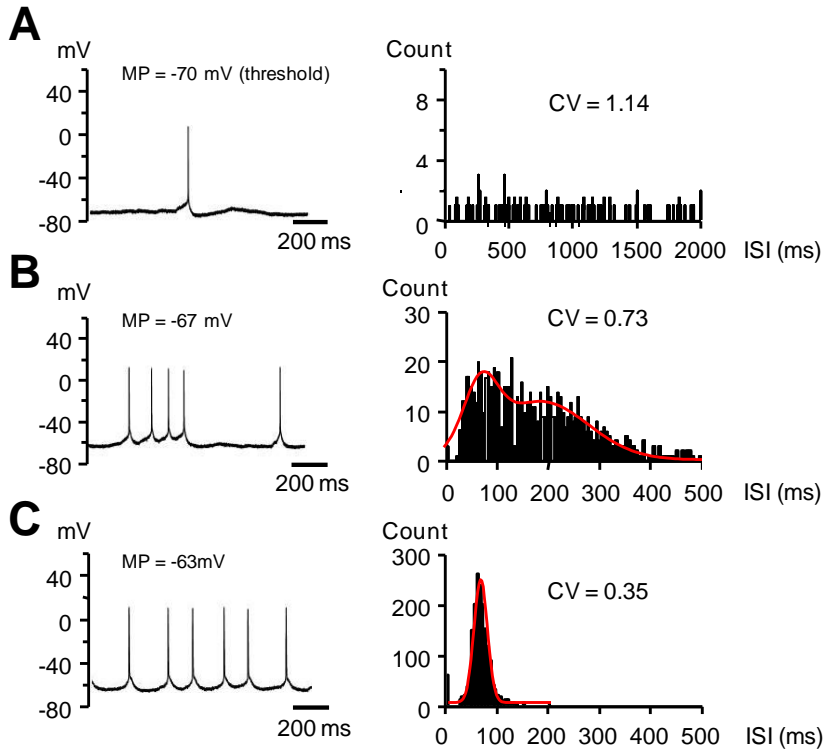


Figure 4.7: Firing properties of a DCN cartwheel cell held at different holding potentials (A-D). Left, Examples of the cartwheel cell firing at different frequencies (in Hz) in function of the membrane potentials (MP in mV). Right, Histograms showing the distribution of the interspike interval (ISI) for those membrane potentials. Above each histogram the coefficient of variation (CV) relative to the distribution is shown. **(A)** At threshold (MP = -70 mV) the cell is firing at 0.4 Hz. **(B)** At MP = -67 mV the cell is firing at 7.3 Hz. The distribution of all ISI is fitted with two normal Gaussian functions that peak at 83 ms and 200 ms respectively. $y = [a1 \cdot \exp(-0.5((x-x1)_d / b1)^2) + [a2 \cdot \exp(-0.5((x-x2)_d / b2)^2)]$. **(C)** At MP = -63 mV the cell is firing at 14.7 Hz. The distribution of all ISI is fitted with a normal Gaussian function $y = [a1 \cdot \exp(-0.5((x-x1)_d / b1)^2)]$ that peaks at 65 ms.

Analysis the firing properties of a cartwheel cell at different holding potentials

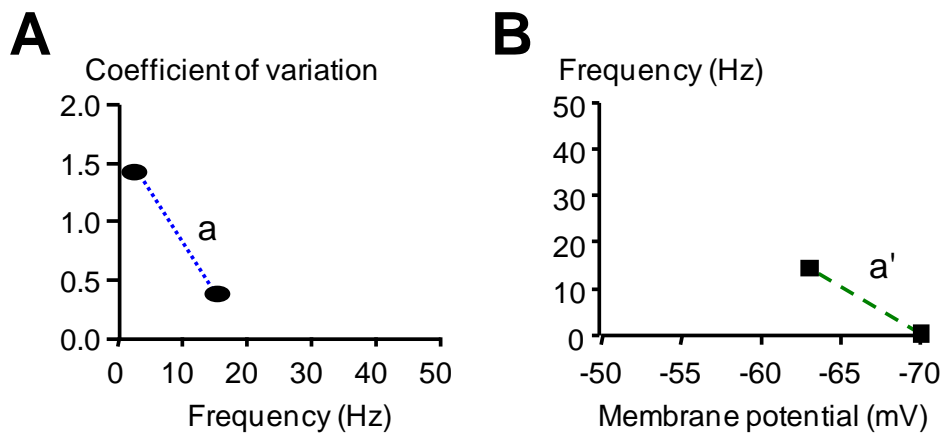


Figure 4.8: Firing frequency of a cartwheel cell in relation to its holding potential and to the coefficient of variation of the interspike intervals. Same cell as in figure 4.7. **(A)** Graph representing the firing frequency (in Hz) in function of the coefficient of variation of the interspike intervals. **(B)** Graph representing the firing frequency (in Hz) in function of the membrane potential. The maximal and the minimal (threshold) firing frequency have been plotted. $a = -0.07 \text{ Hz}^{-1}$ and $a' = 2.0 \text{ Hz.mV}^{-1}$ are slopes for the dotted and dashed lines in (A) and (B) respectively

Example of a cartwheel cell firing with bursts

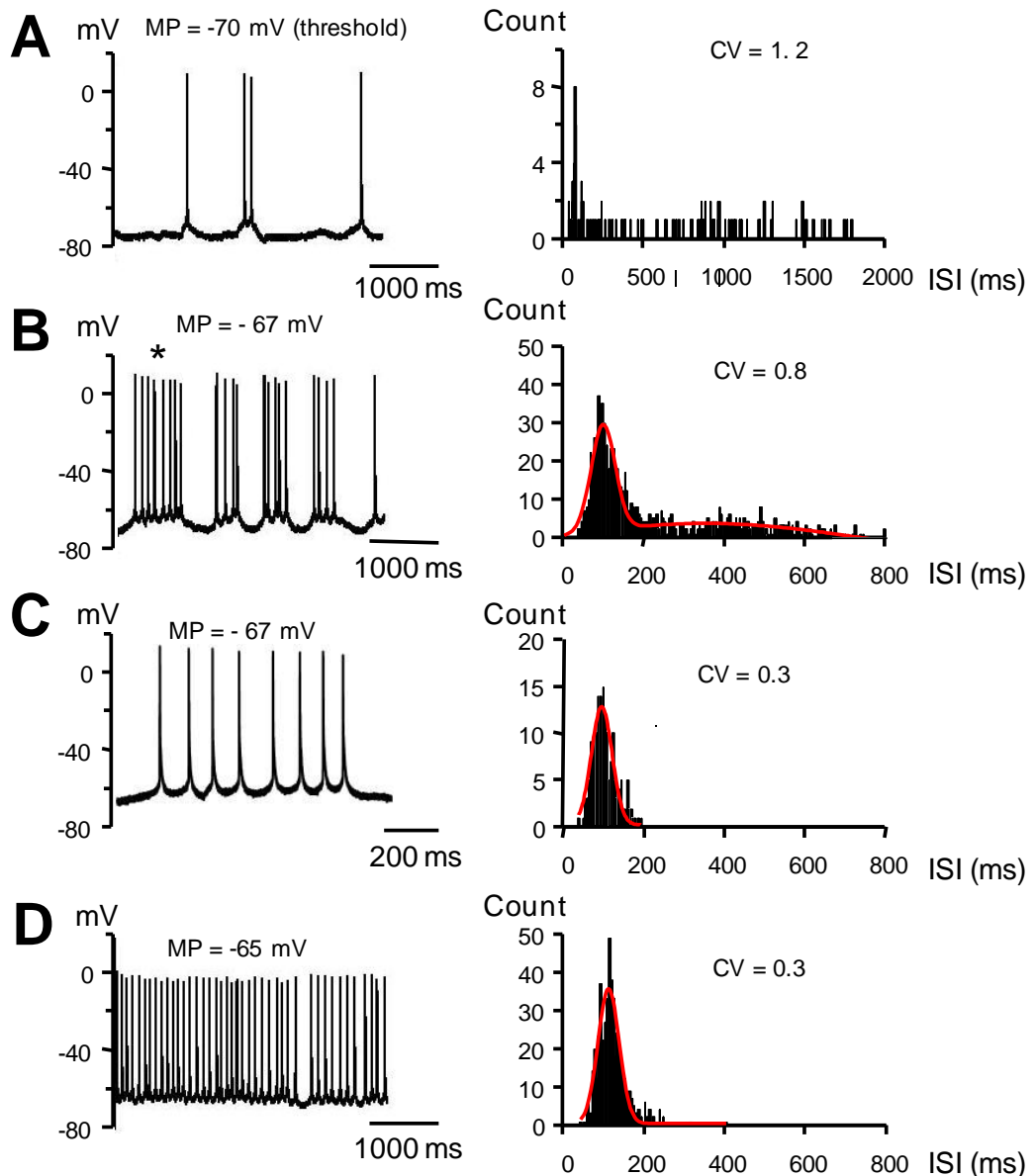


Figure 4.9: Firing properties of a cartwheel cell that displayed bursting activity at a holding potential of -67 mV. Left: Cartwheel cell firing at different frequencies (in Hz) in function of the membrane potentials (HP in mV). Right, Histograms showing the distribution of the interspike interval (ISI) for those membrane potentials. Above each histogram the coefficient of variation (CV) relative to the distribution is shown. **(A)** At threshold (MP = -70 mV) the cell is firing at 1.06 Hz. **(B)** At MP = -67 mV the cell is firing bursts of action potentials. The distribution of all ISI is fitted with two normal gaussian functions $y = [a1 \cdot \exp(-0.5((x-x1)/b1)^2) + [a2 \cdot \exp(-0.5((x-x2)/b2)^2)]$ that peak at 98 ms and 400 ms respectively. **(C)** Left, same trace as in (B) on a larger time scale showing one single burst (labelled with * in B). The firing frequency within this burst is 9.6 Hz and the histogram shows the distribution of the ISI within individual bursts that is fitted with one single gaussian function with an average peak of 100 ms. **(D)** At MP=-65 mV the cell is firing at 8.2 Hz and the distribution is fitted with one normal Gaussian function that peaks at 117 ms.

Example of a granule cell firing at different holding potentials

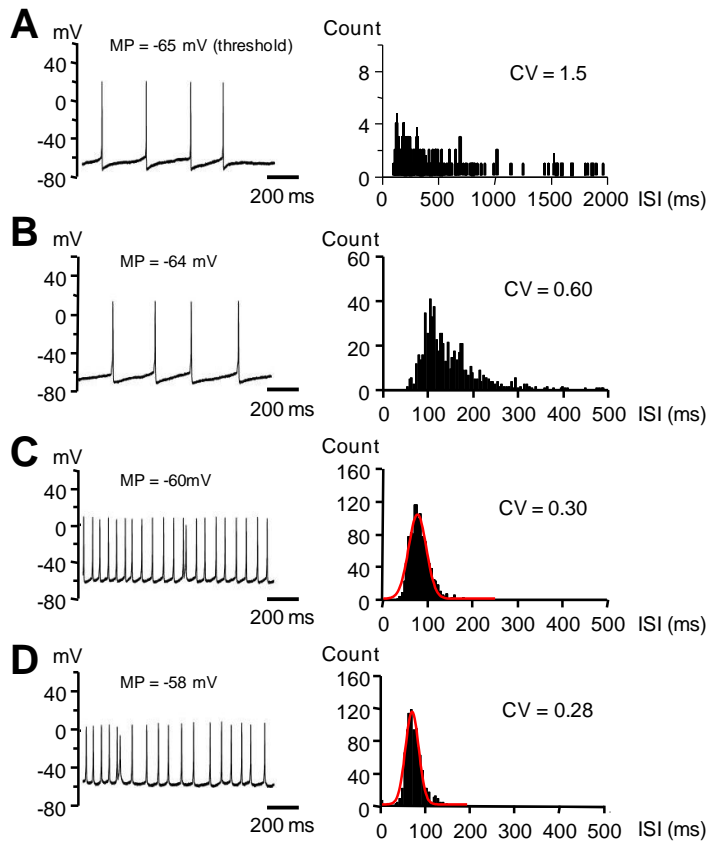


Figure 4.10: Firing properties of a DCN granule cell held at different holding potentials (A-D). Left, examples of the granule cell firing at different frequencies (in Hz) in function of the membrane potentials (MP in mV). Right, histograms showing the distribution of the interspike interval (ISI) for those membrane potentials. Above each histogram the coefficient of variation (CV) relative to the distribution is shown. **(A)** Left, at threshold (MP = -65 mV) the cell is firing at 1Hz. **(B)** Left, at MP = -64 mV the cell is firing at 6.4Hz. **(C)** Left, at MP = -60 mV the cell is firing at 12.1Hz. **(D)** left, at MP = -58 mV the cell is firing at 13.4 Hz. Note the smaller CV for higher firing frequencies. Normal Gaussian functions are fitting the distributions in (C) and (D) and the peak is at 79 ms and 70 ms respectively

Analysis of the firing properties of a granule cell at different holding potentials

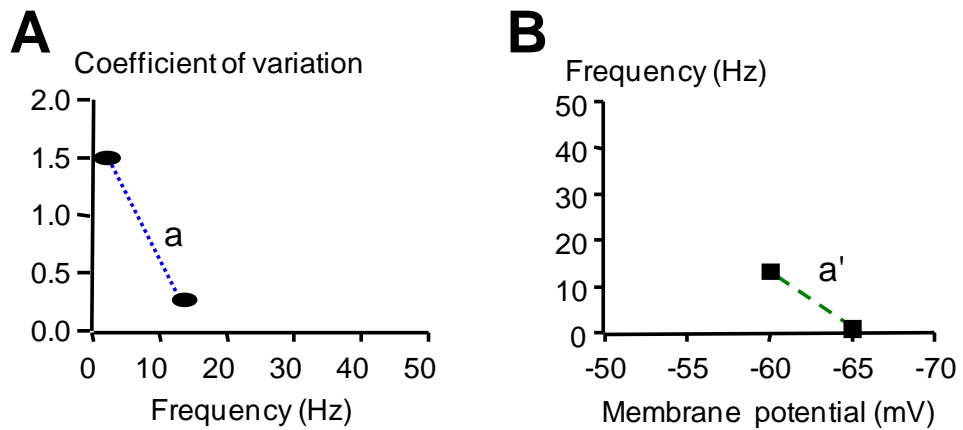


Figure 4.11: Firing frequency of a granule cell in relation to the holding potential and to the coefficient of variation of the interspike intervals. Same cell as in figure 4.10. **(A)** Graph representing the firing frequency (in Hz) in function of the coefficient of variation of the interspike intervals (CV). **(B)** Graph representing the firing frequency (in Hz) in function of the membrane potential. The maximal and the minimal (threshold) firing frequency have been plotted. $a = -0.14\text{Hz}^{-1}$ and $a'=2.5\text{Hz}\cdot\text{mV}^{-1}$ are slopes for the dotted and dashed lines in (A) and (B) respectively..

Example of a giant cell firing at different holding potentials

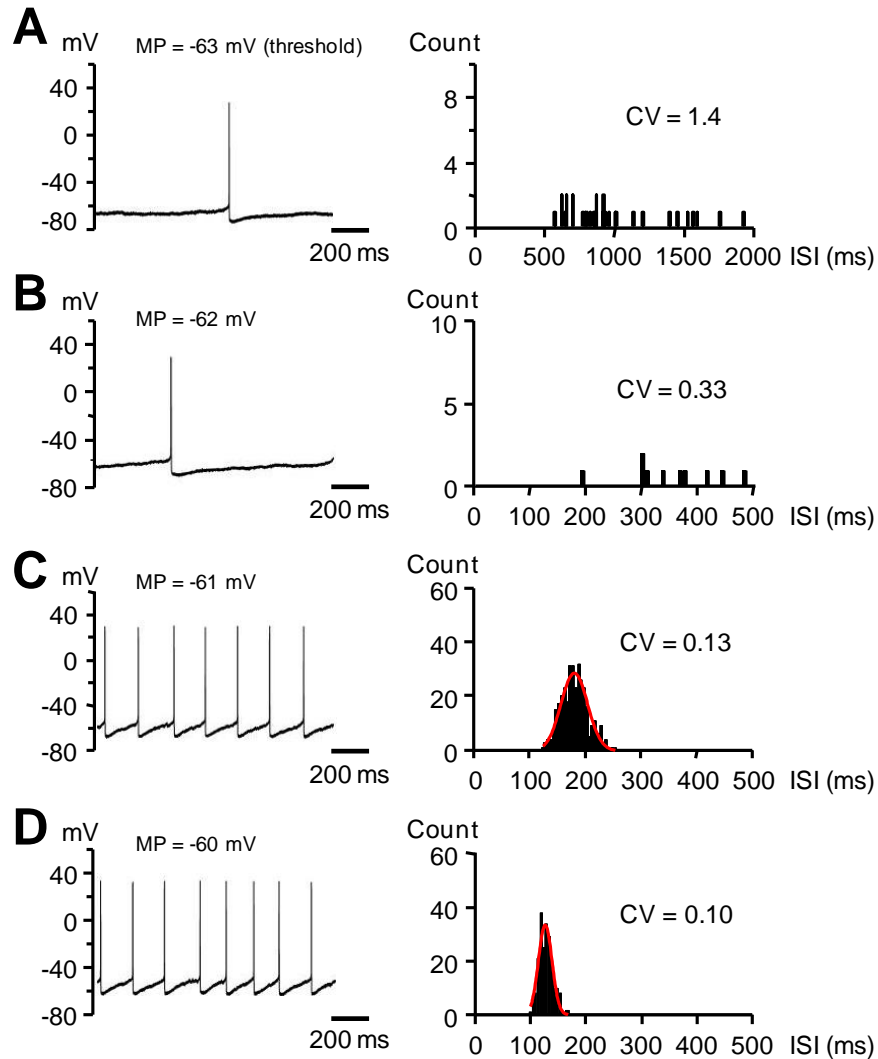


Figure 4.12: Firing properties of a DCN giant cell held at different holding potentials (A-D). Left, examples of the giant cell firing at different frequencies (in Hz) in function of the membrane potentials (MP in mV). Right, histograms showing the distribution of the interspike interval (ISI) for those membrane potentials. Above each histogram the coefficient of variation (CV) relative to the distribution is shown. **(A)** At threshold (MP = -63 mV) the cell is firing at 0.6 Hz. **(B)** At MP = -62 mV the cell is firing at 2.2 Hz. **(C)** At MP = -61 mV the cell is firing at 5.3 Hz. **(D)** At MP = -60 mV the cell is firing at 7.9 Hz. Note the smaller CV for higher firing frequencies. Normal functions are fitting the distributions in (C) and (D) and the peak is at 178 ms and 135 ms respectively.

Analysis of the firing properties of a giant cell at different holding potentials

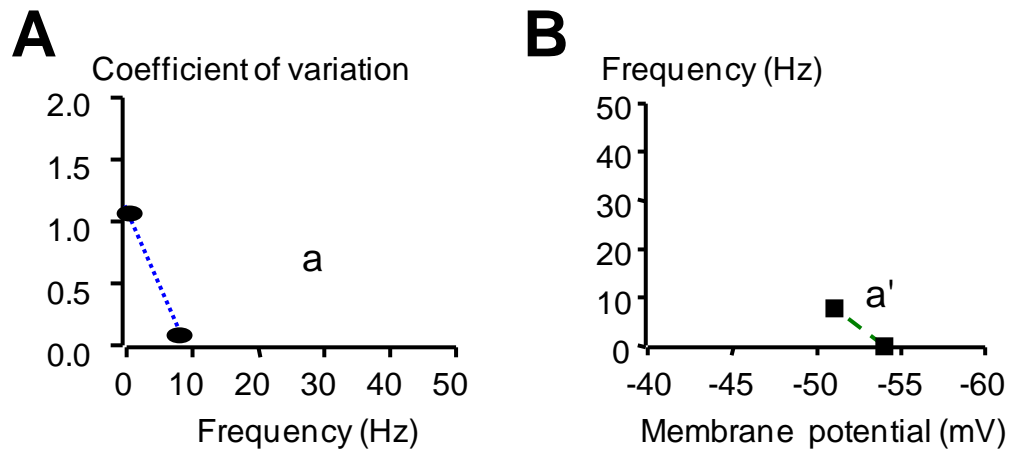


Figure 4.13: Firing frequency of a giant cell in relation to its holding potential and to the coefficient of variation of the interspike intervals. Same cell as in figure 4.12 **(A)** Graph representing the firing frequency (in Hz) in function of the coefficient of variation of the interspike intervals. **(B)** Graph representing the firing frequency (in Hz) in function of the membrane potential. The maximal and the minimal (threshold) firing frequency have been plotted. $a = -0.11 \text{ Hz}^{-1}$ and $a' = 2.6 \text{ Hz.mV}^{-1}$ are slopes for the dotted and dashed lines in (A) and (B) respectively.

Firing frequency in relation to the holding potential and the coefficient of variation

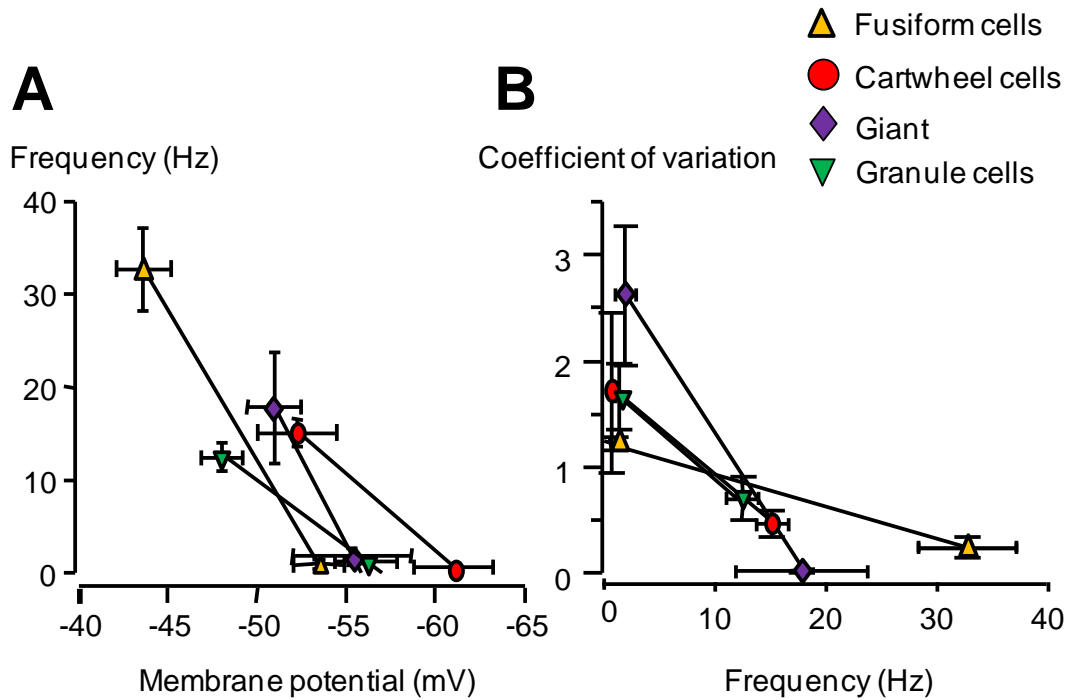


Figure 4.14: Firing frequency in relation to the membrane potential (A) and to the coefficient of variation (B) in different cell types. The maximal and the minimal (threshold) firing frequency at the correspondent membrane potentials and coefficient of variation have been plotted for each cell types. Values are mean \pm s.e.m for $n=7$ fusiform cells, $n=7$ cartwheel cells, $n=3$ giant cells and $n=7$ granule cells. In certain cases, error bars were masked by the symbol.

Frequency to step current relation in a fusiform cell

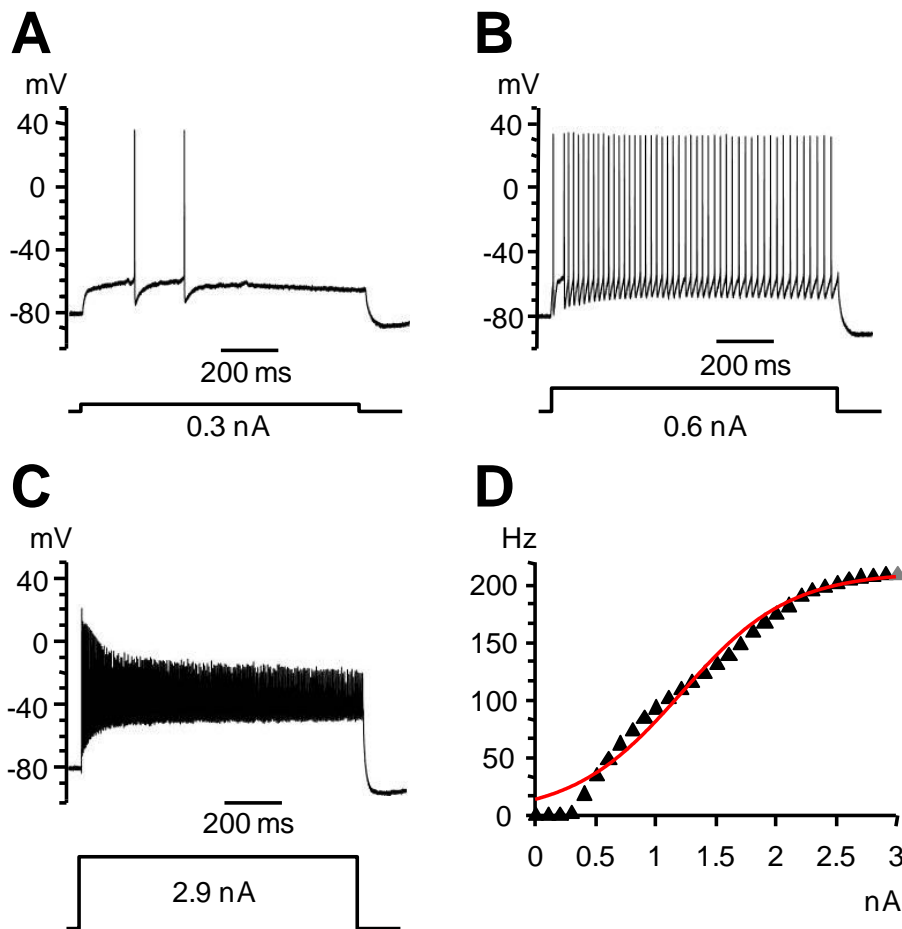


Figure 4.15: Action potential firing of a fusiform cell in response to 1 s step currents. (A) The injection of a 0.3 nA step current evokes 2 action potentials (this is the threshold in this cell). **(B)** The injection of a 0.6 nA step current evokes action potentials firing at 48Hz. **(C)** The injection of a 2.9 nA step current evokes action potentials firing at 209 Hz, which is the maximal firing frequency for this cell. **(D)** Frequency-current relationship for this cell. Data are fitted with a sigmoidal curve $y = [a / (1 + \exp^{-(x-x_0)/b})]$ (shown with the solid line). The rate b (slope) and the point of inflection x_0 are 0.02 pA/Hz and 1210 pA respectively. The grey symbol at the end of the curve fitting is not a real data but has been added to increase the quality of the fit at those maximal values. Data from a 16 days old Lister Hooded rat. The resting potential for this cell is -60 mV, the membrane resistance is 44 m Ω and the capacitance is 115 pF. Membrane potential is -80 mV.

Frequency to step current relation in fusiform cells: Sigmoidal fitting

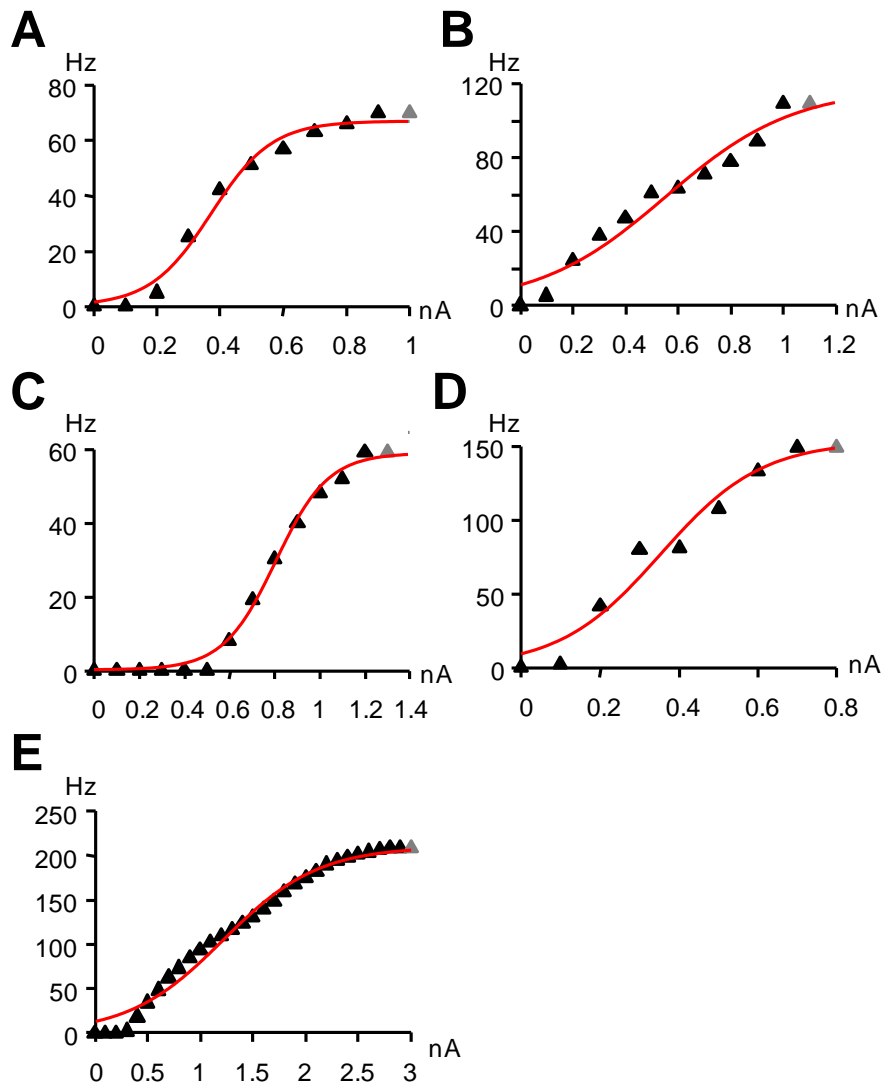


Figure 4.16: (A-E) Frequency to step current relation in all fusiform cells. Data are fitted with a sigmoidal curve $y = [a / (1 + \exp^{-(x-x_0)/b})]$ (shown with the solid line). The slope b is fitted for each cell and the mean values \pm s.e.m. are reported in table 4.6. The grey symbol at the end of the curve fitting is not a real data but has been added to increase the quality of the fit at those maximal values. (E) is the same cell as in Figure 4.15.

Frequency to step current relation in fusiform cells: Linear regression fitting

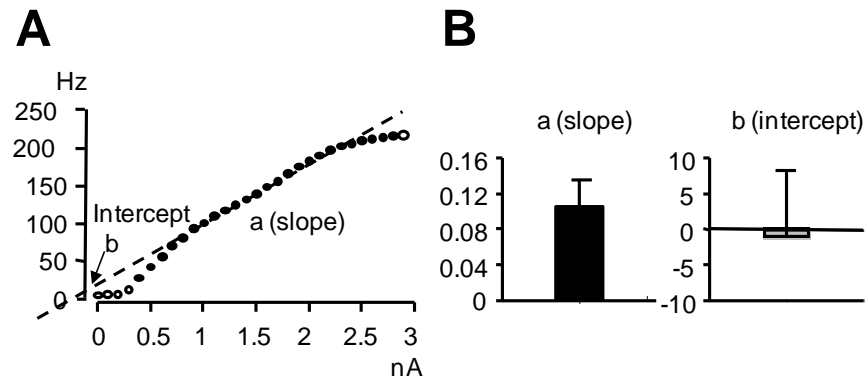


Figure 4.17: Frequency to current relation in a fusiform cell. **(A)** Frequency-current relationship in a fusiform cell. A Linear regression ($y = ax + b$) (dashed line) is obtained by fitting the values represented as filled points (corresponding to the first value above the threshold and the last value before the maximal firing rate). The slope (a) and the intercept (b) are 0.08 Hz/pA and 8.4 Hz respectively. **(B)** Histograms representing the mean values (\pm s.e.m.) for the slope (a) and the intercept (b) obtained from 5 fusiform cells.

Time to the first action potential following step currents in a fusiform cell

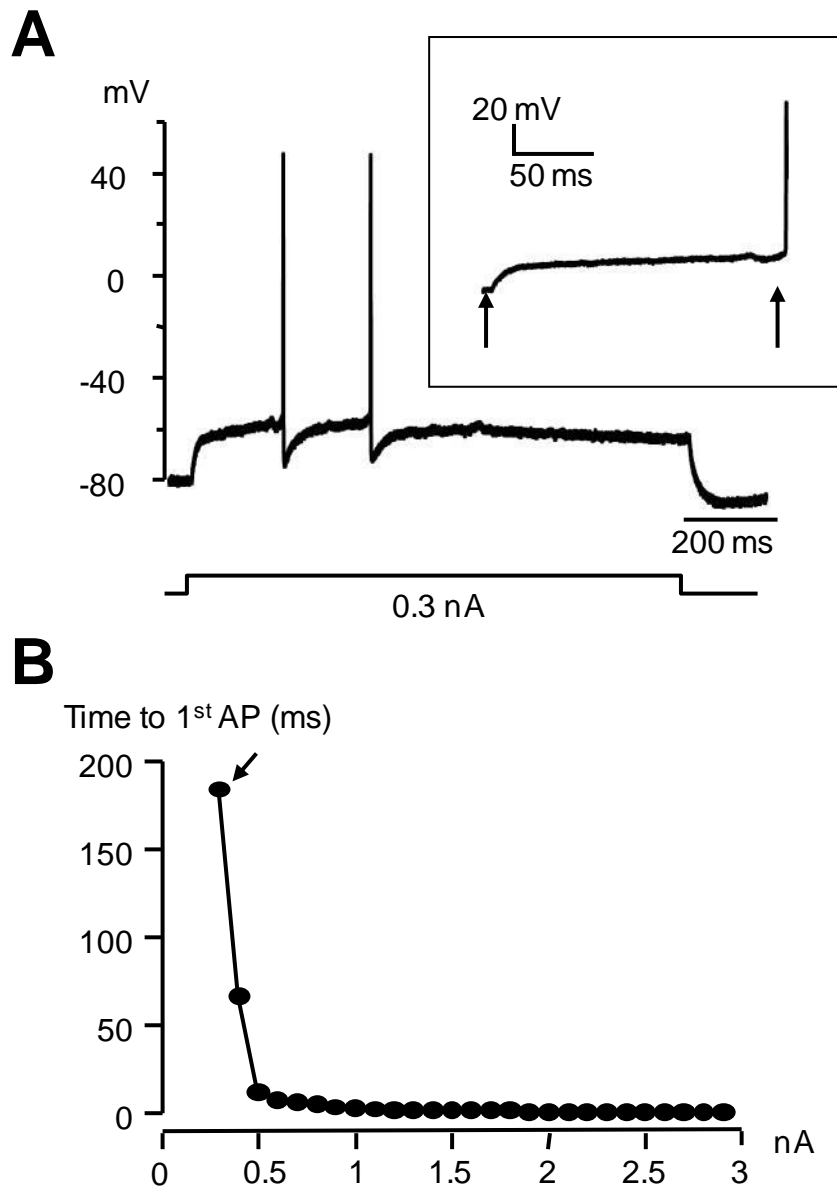


Figure 4.18: Time to the first action potential in a fusiform cell. (A) Same cell as in figure 4.15. The injection of a step current of 0.3 nA from a membrane potential of -80 mV evokes 2 action potentials (threshold). The insert shows the same trace on a larger time scale with two arrows indicating the time to the first action potential. **(B)** Relation between the time to the first action potential (AP) and the injected current. The arrow indicates the value at threshold.

Frequency to step current relation in a fusiform cell: Analysis of interspike intervals

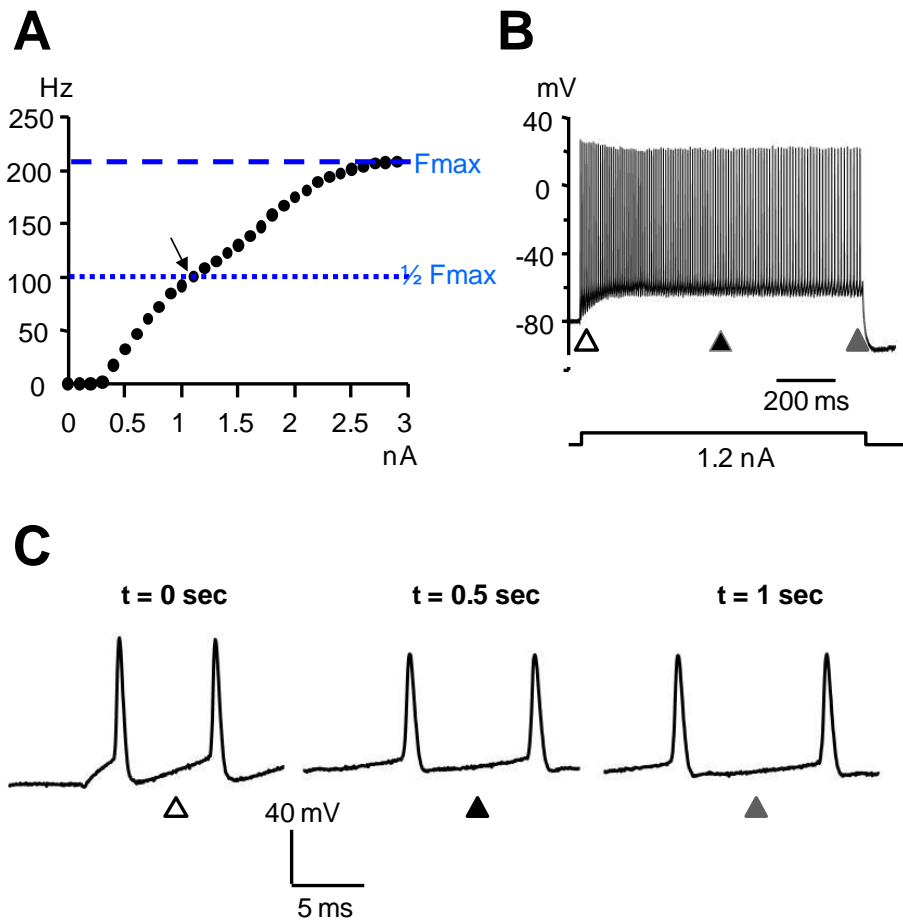


Figure 4.19: Action potential firing in a fusiform cell following step current injections (same cell as figure. 4.15.) (A) Frequency to current relationship. The maximal frequency (F_{max}) (209 Hz for this cell) and the half maximal frequency ($1/2 F_{max}$) are shown with the two dashed and dotted lines respectively. **(B)** Same cell as in (A) showing its firing at 109 Hz (i.e. obtained at 1.2 nA current step which is the first step above the estimated half maximal frequency for this cell). **(C)** Same trace as in (B) showing the prolongation of the interspike interval in function of the time within the step. Two action potentials with their interspike intervals are represented at a magnified time scale at time 0 sec (white triangle), 0.5 sec (black triangle) and 1sec (grey triangle). Triangles pointing to the interspike intervals are also represented in (B).

Frequency to step current relation in a cartwheel cell

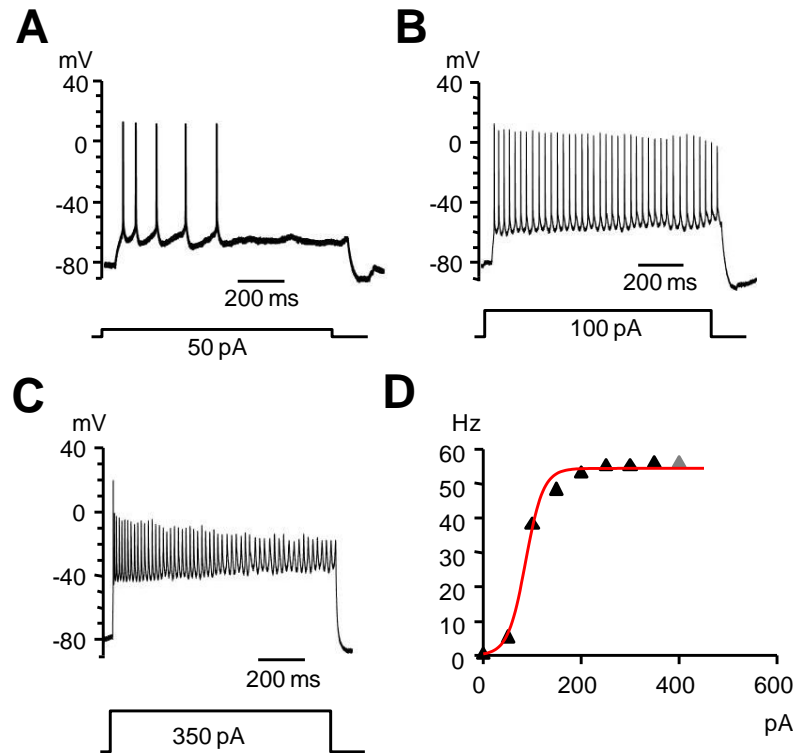


Figure 4.20: Action potential firing of a cartwheel cell in response to a 1 s step current. (A) The injection of a 50 pA step current evokes 5 action potentials (this is the threshold in this cell). **(B)** The injection of a 100 pA step current evokes action potentials firing at 38Hz. **(C)** The injection of a 350 pA step current evokes action potentials firing at 56 Hz, which is the maximal firing frequency for this cell. **(D)** Frequency-current relationship for this cell. Data are fitted with a sigmoidal curve $y = [a / (1 + \exp^{-(x-x_0)/b})]$ (shown with the solid line). The rate b (slope) and the point of inflection x_0 are 0.5 pA/Hz and 86.60 pA respectively. The grey symbol at the end of the curve fitting is not a real data but has been added to increase the quality of the fit at those maximal values. Data from a 16 days old Lister Hooded rat. The resting potential for this cell is -40 mV, the membrane resistance is 220 m Ω and the capacitance is 46 pF. Membrane potential is -80 mV.

Frequency to step current relation in cartwheel cells: Sigmoidal fitting

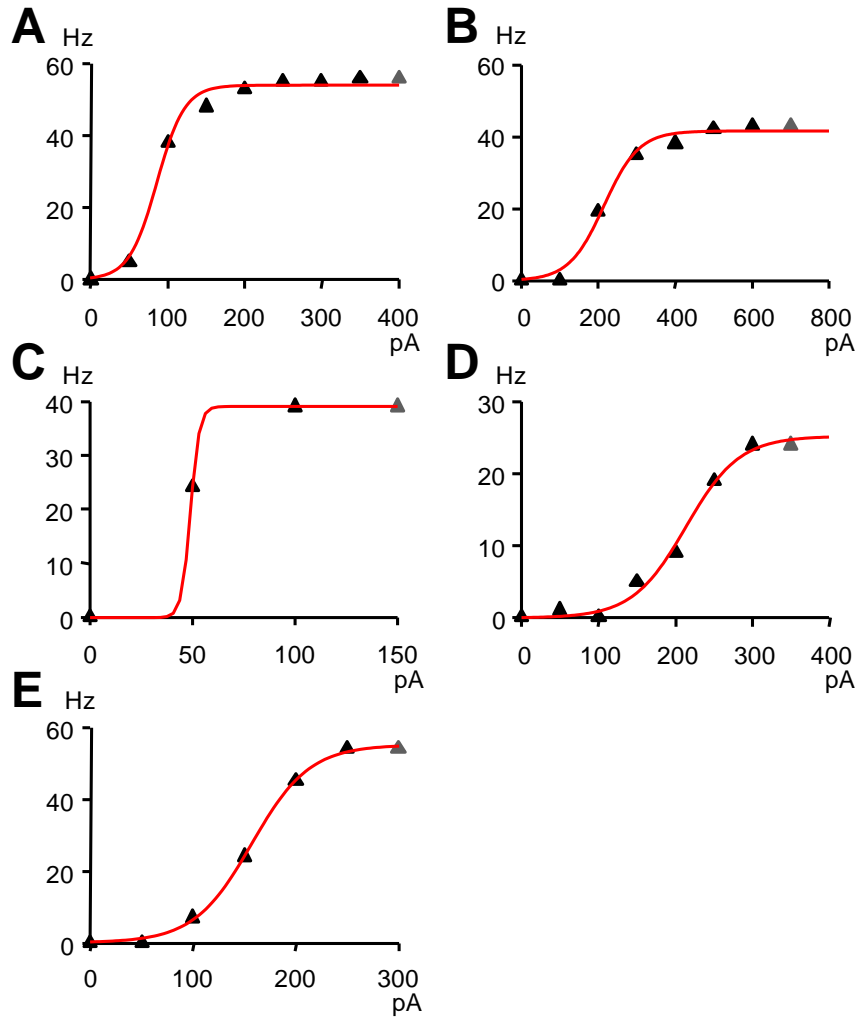


Figure 4.21: (A-E) Frequency to step current relation in all cartwheel cells. Data are fitted with a sigmoidal curve $y = [a / (1 + \exp^{-(x-x_0) / b})]$ (shown with the solid line). The slope b is fitted for each cell and the mean values \pm s.e.m. are reported in table 4.6. The grey symbol at the end of the curve fitting is not a real data but has been added to increase the quality of the fit at those maximal values. (A) is the same cell as in figure 4.20.

Time to the first action potential following step currents in a cartwheel cell

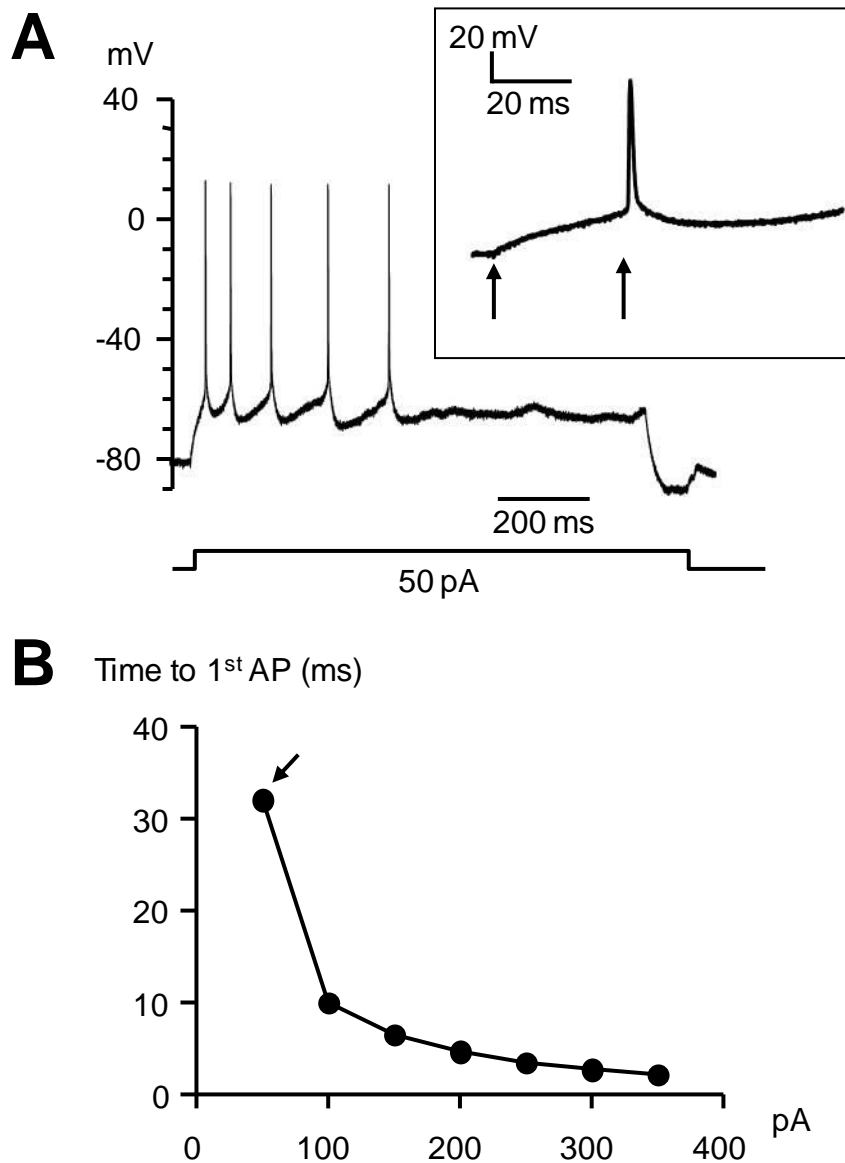


Figure 4.22: Time to the first action potential in a cartwheel cell. (A) Same cell as in figure 4.20. The injection of a 50 pA step current from a membrane potential of -80 mV evokes 5 action potentials (this is the threshold in this cell). In the insert, the same trace is shown on a larger time scale with two arrows indicating the start of the pulse and the start of the first action potential **(B)** Relation between the time to the first action potential (AP) and the injected current. The arrow indicates the value at threshold.

Frequency to step current relation in a cartwheel cell: Analysis of interspike intervals

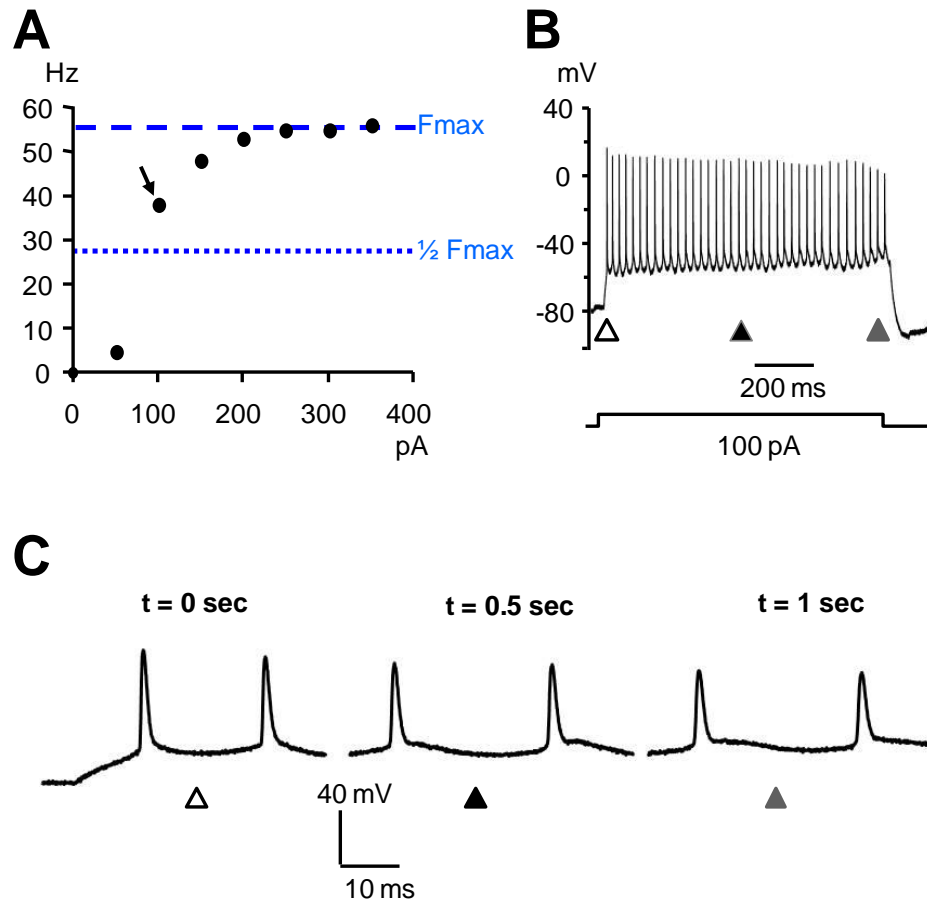


Figure 4.23: Action potential firing in a cartwheel cell following step current injection (same cell as figure 4.20) (A) Frequency to current relationship. The maximal frequency (F_{max}) (for this cell is 56 Hz) and the half maximal frequency ($1/2 F_{max}$) are shown with the dashed and dotted lines respectively. (B) Same cell as in (A) showing its firing at 38 Hz (i.e. obtained at 100 pA current step which is the first step above the estimated half maximal frequency for this cell). (C) Same trace as in (B) showing the prolongation of the interspike interval in function of the time within the step. Two action potentials with their interspike intervals are represented at a magnified time scale at time 0 sec (white triangle), 0.5 sec (black triangle) and 1sec (grey triangle). Triangles pointing to the interspike intervals are also represented in (B).

Frequency to step current relation in a granule cell

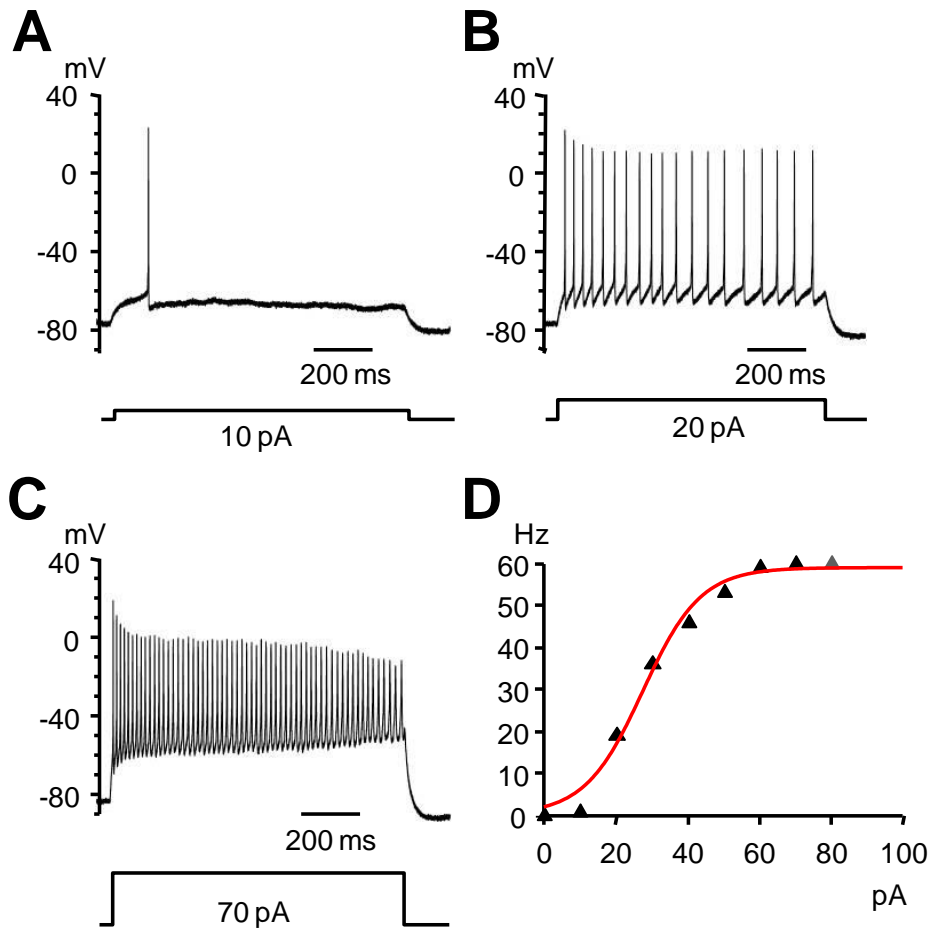


Figure 4.24: Action potential firing of a granule cell in response to 1 s step currents. (A) The injection of a 10 pA step current evokes 1 action potential (this is the threshold in this cell). **(B)** The injection of a 20 pA step current evokes action potentials firing at 19Hz. **(C)** The injection of a 70 pA step current evokes action potentials firing at 60 Hz, which is the maximal firing frequency for this cell. **(D)** Frequency-current relationship for this cell. Data are fitted with a sigmoidal curve $y = [a / (1 + \exp^{-(x-x_0)/b})]$ (shown with the solid line). The rate b (slope) and the point of inflection x_0 are 1.2 pA/Hz and 28 pA respectively. The grey symbol at the end of the curve fitting is not a real data but has been added to increase the quality of the fit at those maximal values. Data from a 18 days old Lister Hooded rat. The resting potential for this cell is -44 mV, the membrane resistance is 1.2 G Ω and the capacitance is 8 pF. Membrane potential is -80 mV.

Frequency to step current relation in granule cells: Sigmoidal fitting

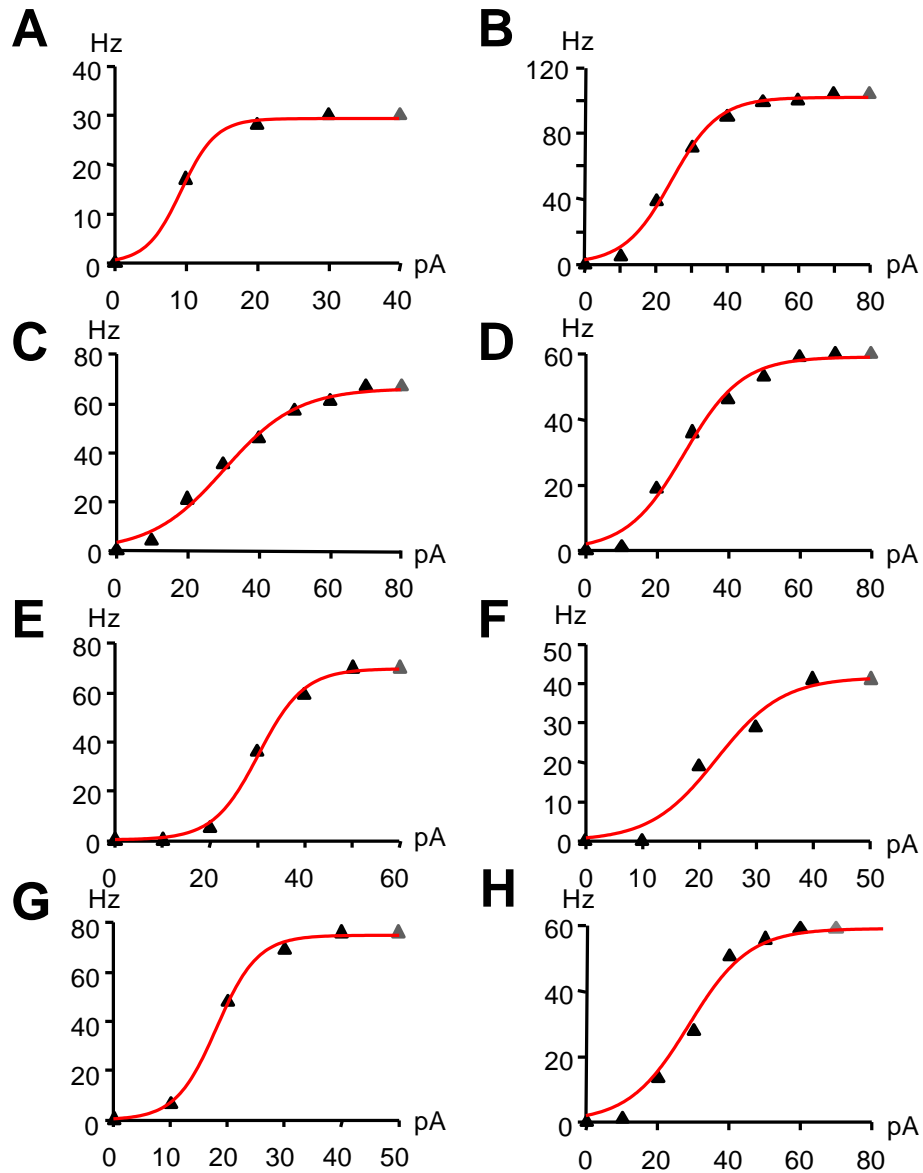


Figure 4.25: (A-H) Frequency to step current relation in all granule cells. The frequency-current curves are fitted by a sigmoidal function $y = [a / (1 + \exp^{-(x-x_0) / b})]$ (shown with the solid line). The slope b is fitted for each cell and the mean values \pm s.e.m. are reported in table 4.6. The grey symbol at the end of the curve fitting is not a real data but has been added to increase the quality of the fit at those maximal values. (D) is the same cell as in figure 4.24

Time to the first action potential following step currents in a granule cell

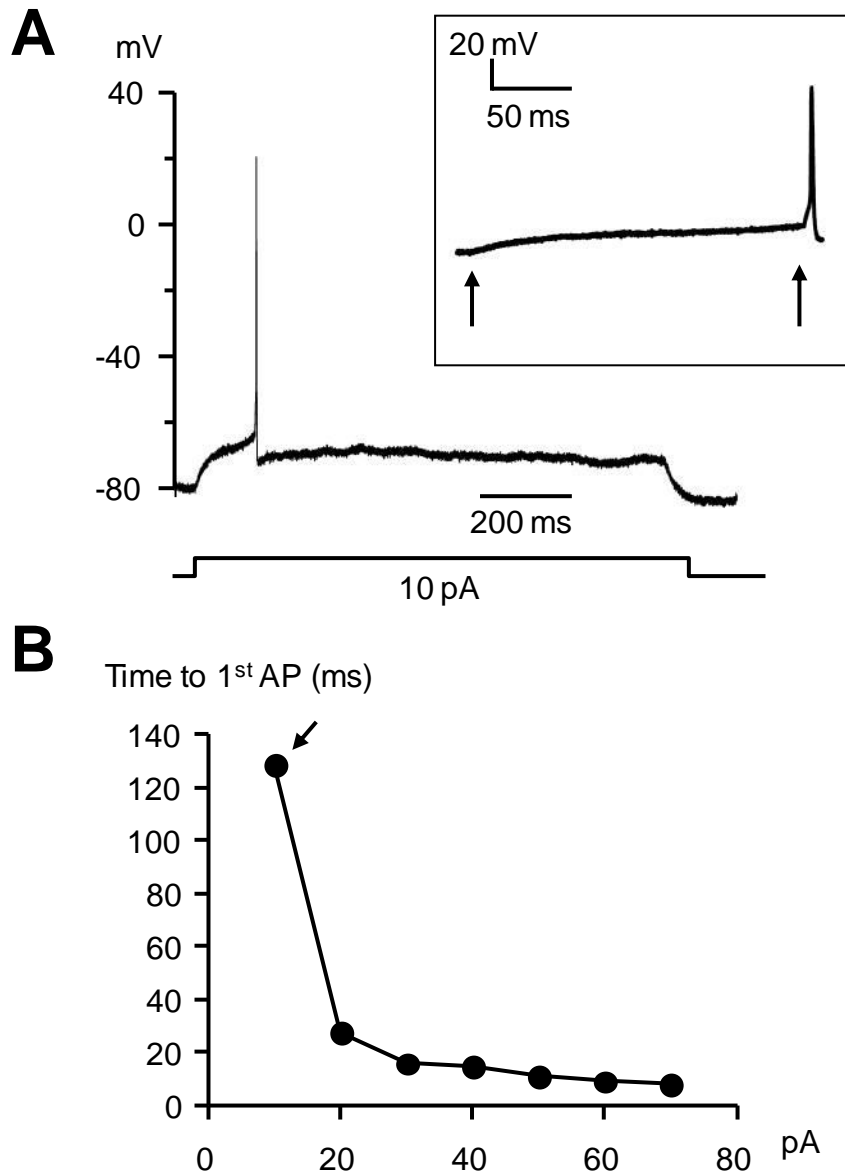


Figure 4.26: Time to the first action potential in a granule cell. (A) Same cell as in figure 4.24. The injection of a 10 pA step current from a membrane potential of -80 mV evokes 1 action potential (this is the threshold in this cell). The insert shows the same trace on a larger time scale with two arrows indicating the start of the pulse and the start of the first action potential. **(B)** Relation between the time to the first action potential (AP) and the injected current. The arrow indicates the value at threshold.

Frequency to step current relation in a granule cell: Analysis of interspike intervals

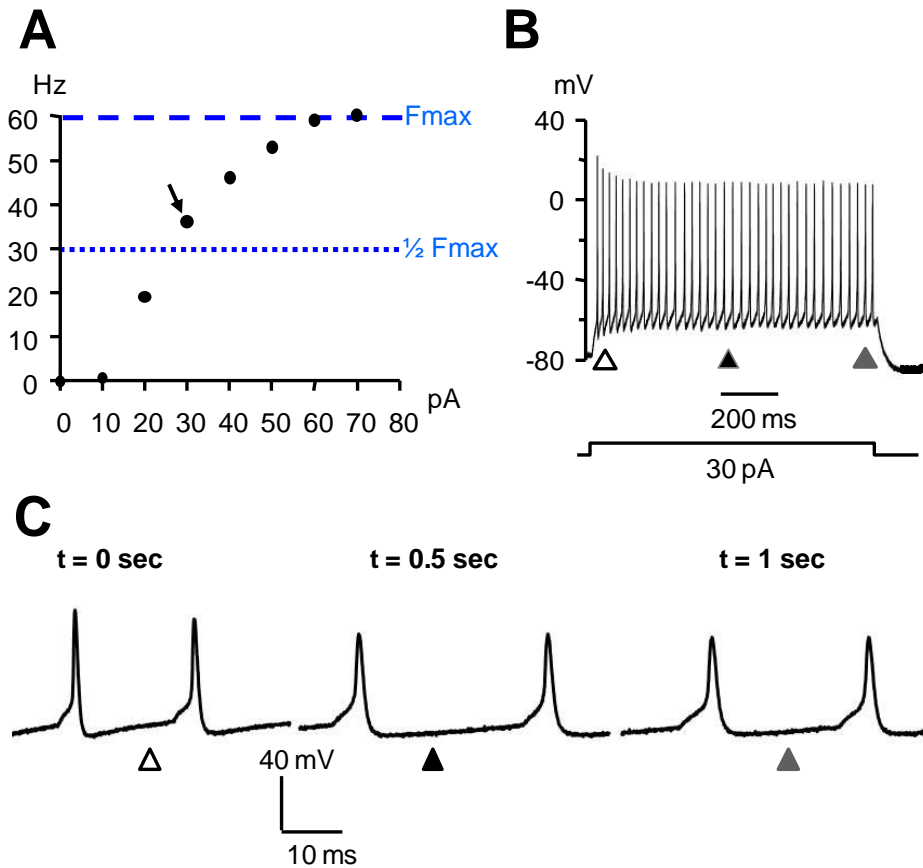


Figure 4.27: Action potential firing in a granule cell following step current injection (same cell as figure 4.24) (A) Frequency to current relationship. The maximal frequency (F_{max}) (for this cell is 60 Hz) and the half maximal frequency ($1/2 F_{max}$) are shown with the dashed and dotted lines respectively. (B) Same cell as in (A), showing its firing at 36 Hz (i.e. obtained at 30 pA current step which is the first step above the estimated half maximal frequency for this cell). (C) Same trace as in (B) showing the prolongation of the interspike interval in function of the time within the step. Two action potentials with their interspike intervals are represented at a magnified time scale at time 0 sec (white triangle), 0.5 sec (black triangle) and 1 sec (grey triangle). Triangles pointing to the interspike intervals are also represented in (B).

Frequency to step current relation in a giant cell

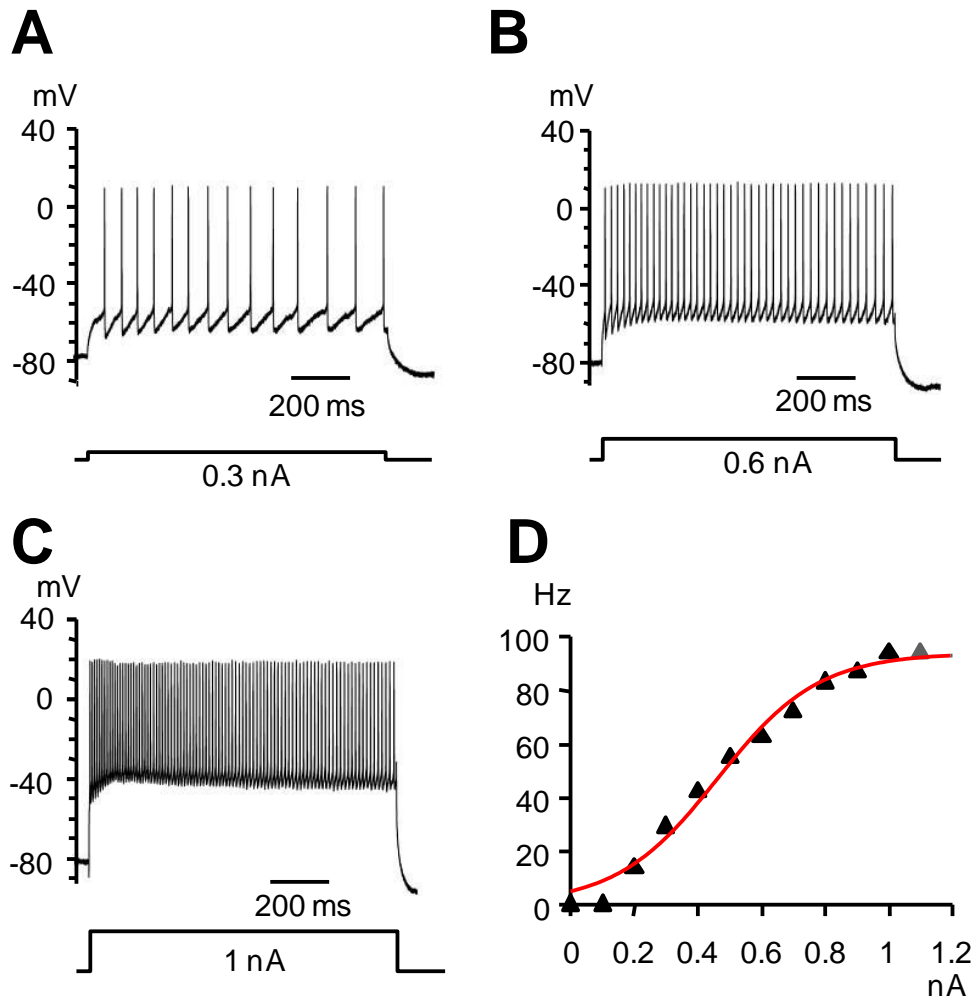


Figure 4.28: Action potential firing of a giant cell in response to 1 s step currents. (A) The injection of a 0.3 nA step current evokes 14 action potentials (this is the threshold in this cell). **(B)** The injection of a 0.6 nA step current evokes action potentials firing at 63Hz. **(C)** The injection of a 1 nA step current evokes action potentials firing at 94 Hz, which is the maximal firing frequency for this cell. **(D)** Frequency-current relationship for this cell. Data are fitted with a sigmoidal curve $y = [a / (1 + \exp^{-(x-x_0) / b})]$ (shown with the solid line). The rate b (slope) and the point of inflection x_0 are 0.06 pA/Hz and 454 pA respectively. The grey symbol at the end of the curve fitting is not a real data but has been added to increase the quality of the fit at those maximal values. Data from a 16 days old Lister Hooded rat. The resting potential for this cell is -57 mV, the membrane resistance is 90 m Ω and the capacitance is 166 pF. Membrane potential is -80 mV.

Frequency to current relation in giant cells: Sigmoidal fitting

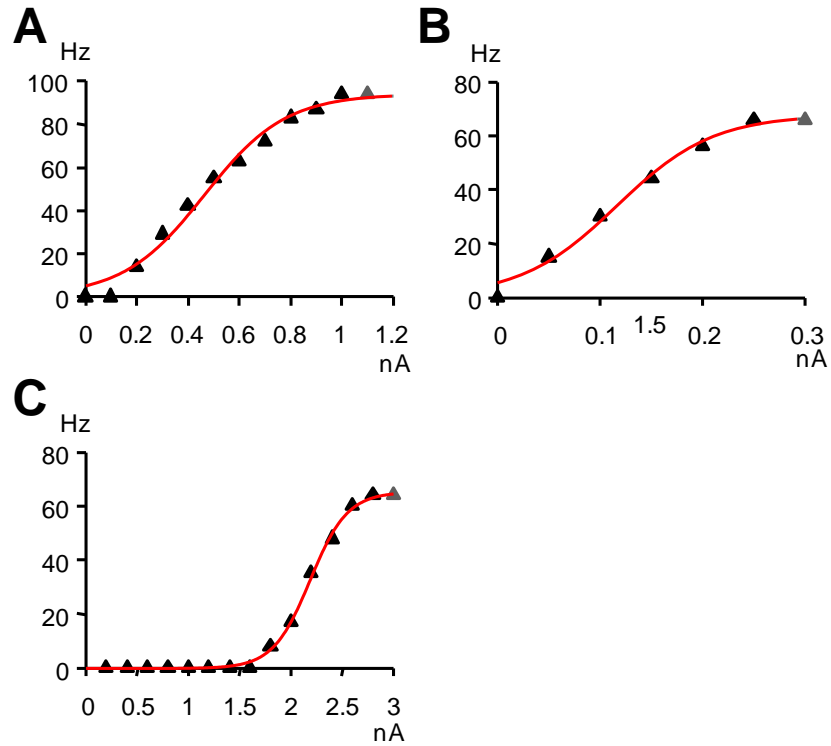


Figure 4.29: (A-C). Frequency to step current relation in all giant cells. The frequency-current curves are fitted by a sigmoidal function $y = [a / (1 + \exp^{-(x-x_0)/b})]$ (shown with the solid line). The slope b is fitted for each cell and the mean values \pm s.e.m. are reported in table 4.6. The grey symbol at the end of the curve fitting is not a real data but has been added to increase the quality of the fit at those maximal values. (A) is the same cell as in figure 4.28.

Time to the first action potential following step currents in a giant cell

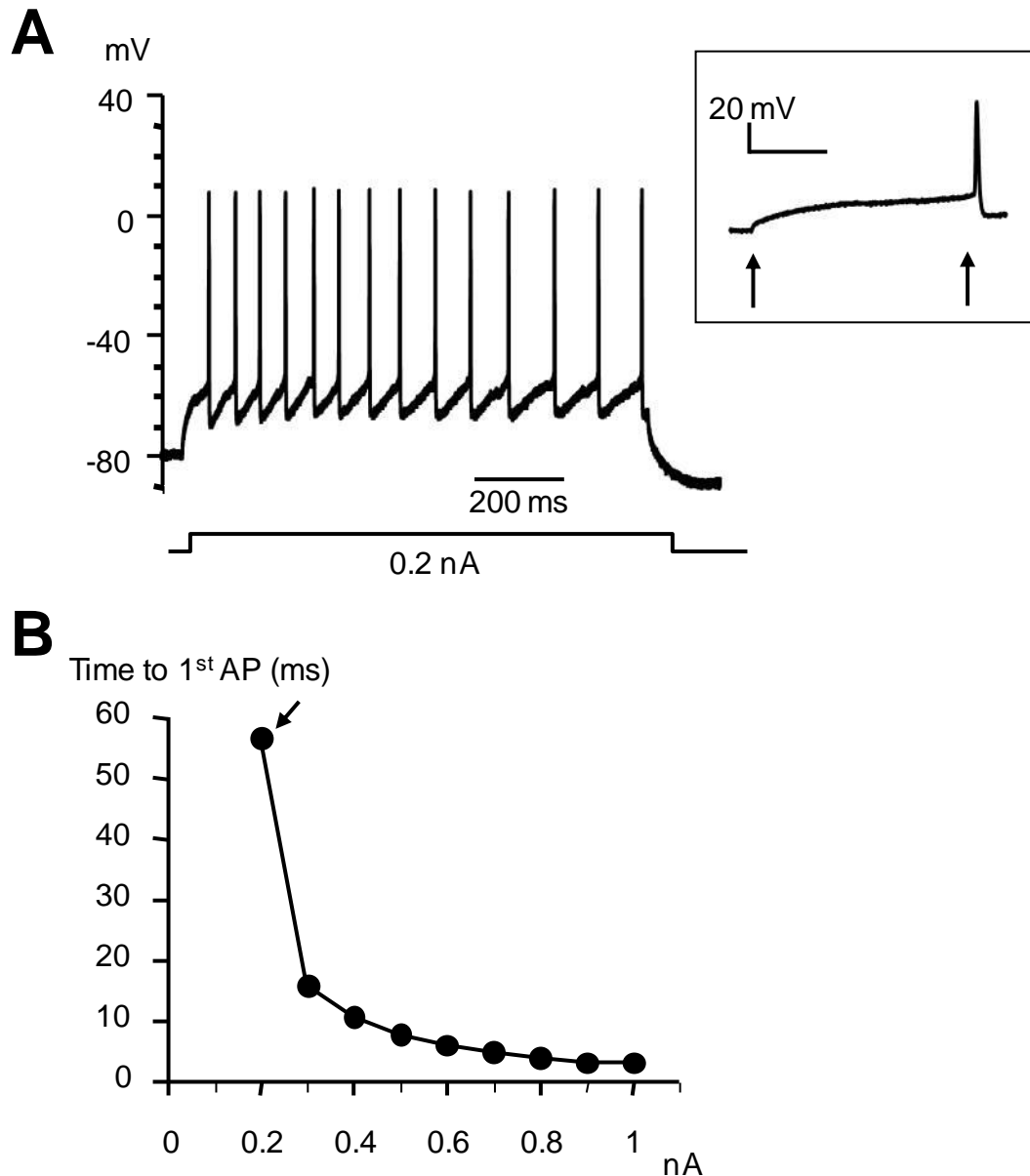


Figure 4.30: Time to the first action potential in a giant cell. (A) Same cell as in figure 4.28. The injection of a 0.2 nA step current from a membrane potential of -80 mV evokes 14 action potentials (this is the threshold in this cell). In the insert, the same trace is shown on a larger time scale with two arrows indicating the start of the pulse and the start of the first action potential. **(B)** Relation between the time to the first action potential (AP) and the injected current. The arrow indicates the value at threshold.

Frequency to step current relation in a giant cell: analysis of interspike intervals

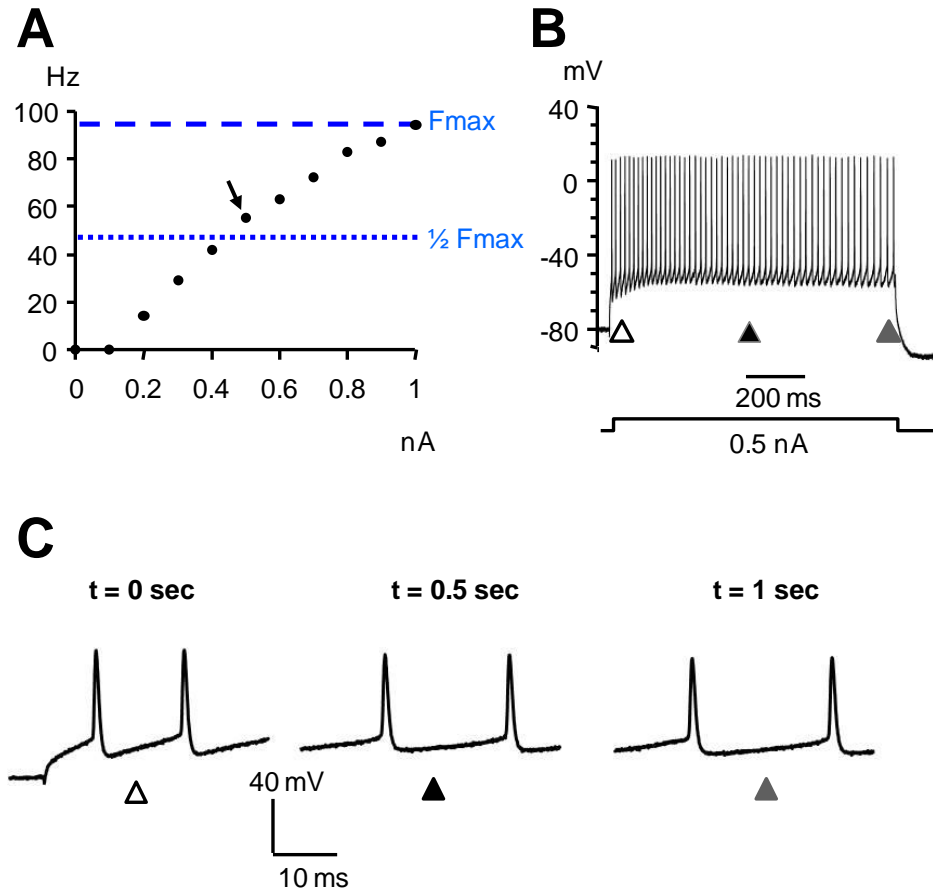


Figure 4.31: Action potential firing in a giant cell following step current injection (same cell as figure 4.28). (A) Frequency to current relationship. The maximal frequency (F_{max}) (for this cell is 94 Hz) and the half maximal frequency ($1/2 F_{max}$) are shown with the dashed and dotted lines respectively. (B) Same cell as in (A) showing its firing at 55 Hz (i.e. obtained at 0.5 nA current step which is the first step above the estimated half maximal frequency for this cell). (C) Same trace as in (B) showing the prolongation of the interspike interval in function of the time within the step. Two action potentials with their interspike intervals are represented at a magnified time scale at time 0 sec (white triangle), 0.5 sec (black triangle) and 1sec (grey triangle). Triangles pointing to the interspike intervals are also represented in (B).

Frequency-current relationship analysis using a linear regression function

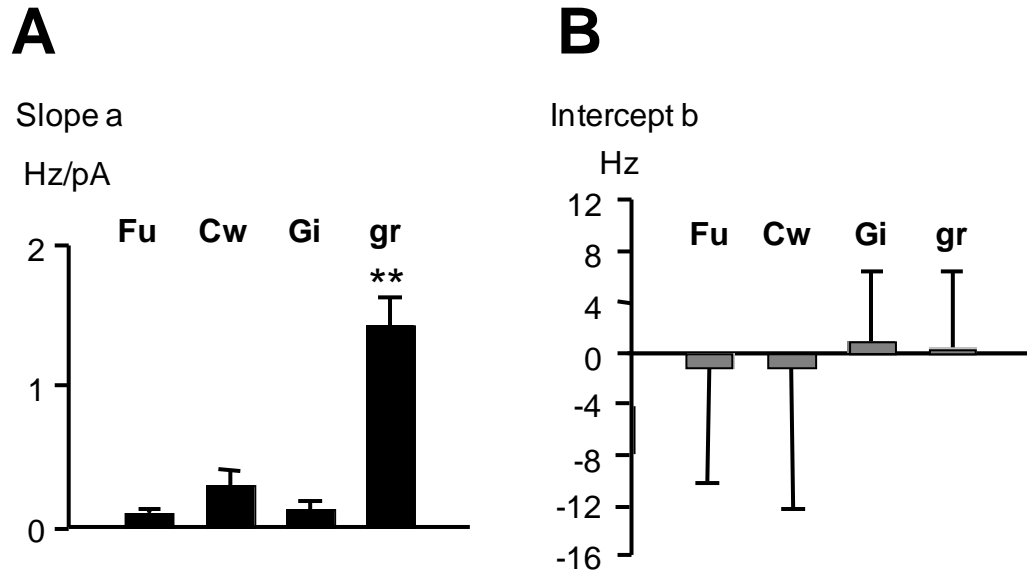


Figure 4.32: (A-B) Summary histograms representing the mean values (\pm s.e.m.) for the slope a (**A**) and the intercept b (**B**) of the frequency-current curves fitted with the linear regression function ($y = ax + b$). Data obtained from 5 fusiform cells (Fu), 6 cartwheel cells (Cw), 3 giant cells (Gi) and 7 granule cells (gr). ** stands for $P < 0.01$ using anova one way-Tukey test. Note that the slope value is significantly larger in granule cells compared to other cell types. By contrast the intercept is similar between all the cell types.

CHAPTER 5

Effect of acoustic over-exposure on auditory brainstem responses

INTRODUCTION

5.1. The effects of acoustic over-exposure on the auditory system

One of the most common noise-induced alterations in the auditory system is represented by changes in the hearing threshold. Short-term exposure to noise with relatively low sound intensities results in a temporary hearing loss with a limited threshold shift and recovery of hearing sensitivity after some time (Syka, 2002). By contrast exposure to high intensities (>100 dB SPL) of noise even for a short period (hours) produces damage in the cochlea with permanent shifts of the hearing thresholds (Syka, 2002). In humans, acoustic over-exposure is often associated with hearing loss, poor frequency selectivity and impaired speech discrimination (Wightman, 1982; Salvi and Ahroon 1983; Salvi et al., 2000). The functional integrity of brainstem nuclei along the ascending auditory pathway can be studied in humans and animals by the auditory brainstem response (ABR). This technique is useful in a wide array of studies and clinical applications. Indeed, auditory brainstem responses are usually used to assess hearing loss (in human: Markand, 1994; Mitchell et al., 2004, in animals: Church and Kaltenbach, 1993). Auditory brainstem responses are affected by language (Krishnan et al., 2005), musical experience (Musacchia et al., 2007; Wong et al., 2007) and attention (Galbraith et al., 1998). Auditory brainstem response recordings are also often used to detect language impairment in children (Cunningham et al., 2001; Russo et al., 2008).

Recent studies suggest that the brainstem is not only specialized in detecting and preserving temporal information but can as well undergo plastic

adjustments (Tzounopoulos and Kraus, 2009). This makes the ABR an even more powerful technique that allows studying learning and memory in the auditory brainstem.

Together with hearing loss, tinnitus can also be triggered by acoustic over-exposure in humans (Loeb and Smith, 1967). This hearing defect was originally believed to originate from the hyperactivity of the auditory nerve (Salvi et al, 2000). However several physiological studies reported no change or a reduction of spontaneous activity at the level of the auditory nerve following acoustic over-exposure (Kiang et al., 1970; Dallos and Harris, 1978). Moreover tinnitus persists in patients after transection of the auditory nerve (House and Brackmann, 1981) suggesting that tinnitus may originate in the central nervous system. Acoustic over-exposure also generates tinnitus in animal models (Kaltenbach and Afman, 2000; Brozoski et al., 2002) where it was correlated with hyperactivity at the level of many central auditory structures such as the DCN (Kaltenbach and Afman, 2000; Kaltenbach et al., 2004; Kaltenbach and Godfrey 2008), the inferior colliculus (Basta and Ernest 2004; Bauer et al., 2008) and the auditory cortex (Syka et al., 1994; Sun et al., 2008). Throughout the recent years, evidence has therefore accumulated that tinnitus is associated with disturbances in the spontaneous neural activity of the central nervous system and increasing evidence supports the theory that the DCN is participating to the aetiology of tinnitus (Kaltenbach and Afman 2000; Kaltenbach 2007). In this chapter I investigate the effects of acoustic over-exposure on the hearing thresholds of Wistar rats by measuring the ABR. This allowed correlating the ABR changes triggered by acoustic over-exposure with changes in the cellular excitability of identified DCN neurones (chapter 6).

RESULTS

5.2. Effect of acoustic over-exposure on the auditory brainstem responses

Auditory brainstem response (ABR) recordings were first performed in LH rats in order to provide substantial links between shifts in hearing thresholds and change in DCN cellular excitability. As described below, LH exhibited abnormal high ABR hearing thresholds. ABR recordings coupled with acoustic over-exposure were therefore subsequently performed in Wistar rats.

5.2.1. Auditory brainstem responses in Lister Hooded rats

Auditory brainstem responses (ABR) were measured in LH rats anaesthetised with a combination of Hypnorm® and Hypnovel® (section 2.3.1.2. in the methods). ABR were first recorded at P14-22 days. ABR waves start to appear between 12-14 postnatal days in rats and reach the adult thresholds at about 24-36 postnatal days (Iwasa and Potsic, 1982; Blatchley et al., 1987). Being aware of the fact that the hearing thresholds might not be fully developed, I first investigated the ABR in young rats (14-22 days old) as this would allow combining the ABR with *in vitro* patch clamp recordings in the DCN. Indeed, as rats get older than 22 days, patch clamp recordings within slices become increasingly difficult due to the amount of glial and myelination that impedes cell visualization and the formation of the seal.

Auditory brainstem response thresholds were in general exceeding 80 dB SPL in LH rats. This was true at postnatal day 14-22 as shown in figure 5.1A where a tone pip of 24 kHz started to trigger an ABR wave at threshold of 88 dB SPL. Another example in figure 5.1C shows ABRs where the threshold

could not be determined due to the absence of waves even at the maximal intensity 94 dB SPL. Absence of any ABR waves for 94 dB SPL counted for 55% of the cases (8 out of 20 LH rats aged 15-22 days old). This was also the case when LH rats were older and figure 5.1B provides an example where a tone pip of 24 kHz applied to a 50 day old LH rat generates an ABR with a threshold of 81 dB SPL. The summary plots in figure 5.4 show high ABR thresholds exceeding 80 dB SPL for each age group of LH rats: *i*) 14-22 days old (circles in figure 5.4A); *ii*) 26-33 days old (circles in figure 5.4B) and *iii*) 40-50 days old (circles in figure 5.4C). This shows that LH rat's high hearing thresholds were not linked to a slow development of the auditory system. Considering that about half of the LH population was not included in the final analysis due to thresholds exceeding 94 dB SPL, it is reasonable to assume that LH rats have got a hearing threshold of at least 80 dB SPL and this can be observed in at all age groups.

As previously mentioned, experiments were carried out on LH rats anaesthetized with a combination of Hypnorm® and Hypnovel® (section 2.3.1.2. in the methods). The anaesthetic used could be responsible for the high ABR thresholds by suppressing the activity of the auditory nucleus. ABR waves and middle latency responses (monitoring the activity of the auditory cortex) are affected by several general anaesthetics in humans (Nuwer 1986; Heneghan et al., 1987; Plourde and Villemure, 1996) as well as animals (Haberham et al. 2000, Santarelli et al., 2003). LH rats were therefore anesthetised with isoflurane or with ketamine and xylazine (for details see sections 2.3.1.1 and 2.3.1.3). Similar ABR threshold values exceeding 80 dB SPL were obtained while using ketamine and xylazine or isoflurane

(2 and 9 rats respectively, examples shown in figure 5.2). I additionally observed that isoflurane slightly increased the ABR hearing thresholds in a time dependent manner (i.e. after 20 min recording, the ABR thresholds were increased by 3dB SPL, $P < 0.001$, Paired T test, $n=4$).

5.2.2. Auditory brainstem responses in Wistar rats

Auditory brainstem responses (ABRs) were therefore measured in another rat strain, the Wistar rats. Like previously described for LH rats, Wistar rats were anaesthetised with a combination of Hypnorm® and Hypnovel® (section 2.3.1.2). Figure 5.3 represents two ABRs recorded from an 18 day old (A) and from a 40 day old Wistar rat (B) and both recordings show clear thresholds below 50 dB SPL. ABR thresholds were significantly lower in Wistar rats compared to LH rats and this can be observed for all frequencies varying between 8 kHz and 30 kHz and for all three age groups reported above (results summarized in figure 5.4). By contrast, wave I maximal amplitudes (figure 5.5) and latencies to wave I (figure 5.6) obtained at maximal stimulus intensity of 94 dB SPL were significantly different between Wistar rats and LH rats for specific age groups and frequencies. Altogether these results indicate that *i*) Wistar rats constitute a suitable model to study a potential effect of acoustic over-exposure on the ABR *ii*) a shift of the ABR threshold constitutes an adequate parameter for quantifying the extent of the effect of acoustic over-exposure (measured in the next section).

5.2.3. Effect of acoustic over-exposure on the ABR threshold

Auditory brainstem responses (ABRs) were measured in Wistar rats aged 14-22 days similarly anaesthetised with a combination of Hypnorm® and Hypnovel® and ABR thresholds were measured at day 0 and at day 4.

Whereas one group was exposed to loud (110 dB SPL) single tone (14.8 kHz) for a total of 4-9 hours (over-exposed conditions in the text) between day 0 and day 3, the other group was left unexposed to those loud tones. Figure 5.7A-B shows ABR recordings evoked in two littermate rats (14 days old) by a tone pip of 94dB SPL (24 kHz) at day 0. Both ABR displayed the characteristic waves (I to IV). At day 4, the same tone pip evoked a clear ABR in the “unexposed” rat (figure 5.7C) whereas a flat ABR trace was recorded in the “over-exposed” rat (figure 5.7D). ABR thresholds (8-30kHz) were unaffected by acoustic over-exposure after 4 days in about a third of the Wistar rats (8 out of 28 rats) and these animals were dismissed for subsequent *in vitro* recordings. Flat ABR traces after acoustic over-exposure were observed in 43% of the cases (12 out of 28) when applying a 30 kHz and a 24 kHz tone pip for. For the other 29% (8 out of 28) of the rats, ABR thresholds were 74 ± 4 dB SPL (n=8) for a 30 kHz tone pip and 77 ± 4 dB SPL (n=8) for a 24 kHz tone pip. A representative example is shown in figure 5.8 where the threshold was shifted from 64dB SPL (24 kHz) before the acoustic over-exposure (figure 5.8A) to 84 dB SPL (24 kHz) 4 days after the acoustic over-exposure (figure 5.8B). Auditory brainstem responses were always detectable after acoustic over-exposure when tested for a 16 kHz tone pip and were shifted from 61 ± 4 dB SPL to 75 ± 2 dB SPL (n=14) after acoustic over exposure (figure 5.9 B).

Considering that flat ABR traces were observed after acoustic over-exposure in a significant proportion of the Wistar rats (43% of the cases when applying a 30 kHz and a 24 kHz tone pip), ABR thresholds could not be determined with accuracy for those frequencies. For this reason I assigned a theoretical threshold value of 95 dB SPL to this group of rat and this allowed

quantifying the data. Proceeding with this method of quantification, figure 5.9 shows that the ABR thresholds were significantly increased after acoustic over-exposure for all the frequencies tested above 8 kHz whereas being unaffected at 8 kHz. In summary, exposing Wistar rats to loud (110 dB SPL) single tone (14.8 kHz) increased the ABR thresholds for frequencies equal and above 16 kHz.

DISCUSSION

5.3. Effect of acoustic over-exposure on the auditory brainstem response recordings

5.3.1. Difference in the ABR thresholds between different rat strains

The LH colony was initially chosen as an experimental model as they are pigmented rats by comparison to Wistar rats which are albino rats. In many species such as cats and human, albinism is associated with hearing impairments (Creel, 1980; Conlee et al., 1984). Albino rats have impaired vision and impaired sense of smell (Donatien and Jeffery, 2002; Heiduschka and Schraermeyer, 2008) but they appear to have normal hearing (Duan et al., 2006). The unexpected high hearing thresholds found in LH rats is unlikely to be due to the specific sensitivity to the anaesthesia, as different anaesthetics gave similar results, although it cannot be excluded that this strain is sensitive to all types of anaesthetics and in this case other types of measurements such as behavioural measurement of the hearing thresholds tests that does not require the use of anaesthesia could provide useful information (Kurata et al., 1997; Heffner et al., 2008).

The high hearing thresholds could be due to a defect in the myelin sheath surrounding of the auditory nerve as those defects will affect the conduction along nerves (Bostock et al., 1983). In accordance with this hypothesis, chinchillas with severe myelin damage display flat ABR recordings (El-Badry et al., 2007). If this is the case in the LH rats, other types of recordings could provide useful information like the cochlear micro-phonic

compound action potentials (CAP) which allows recording the activity generated by cochlear hair cells (Dallos, 1973; Patuzzi et al., 1989) independently of the transmission along the auditory nerve (measured by the ABR recordings). Micro-phonic compound action potentials were indeed present in chinchillas with auditory nerve myelinopathy although their thresholds and amplitudes were affected by severe damage (El-Badry et al., 2007).

A different physiological development between LH and Wistar rats is unlikely to be the reason for the difference in ABR threshold between the two strains as I showed that older LH rats (40-50 days) still exhibited high ABR thresholds. Physiological differences between LH and Wistar rats (like sensitivity to stress) could explain the results I obtained. Previous studies reported higher hearing thresholds in prenatally stressed Sprague Dawley rats (Kadner et al., 2006). Although Wistar and LH rats are bred in same environment, it is possible that the two strains react differently to stress. Indeed, Commissaris *et al.* (2000) showed that a single tone stimulus of 95-110 dB SPL (lasting up to 9 min) was specifically eliciting a running behaviour and convulsions in LH rats by comparison to Wistar rats. This could be indicative of LH rats being more susceptible to the presentation of stressful acoustic stimuli. Inter-strain differences in startle reflexes have also been reported (Neophytou et al., 2000; Weiss et al., 2002) and LH rats appear to be more reactive to low frequencies (below 10 kHz) pulses (Błaszczuk and Tajchert, 1997). In summary, differences exist between rat strains like the sensitivity to startle stimuli or to the external environment. Differences in hearing sensitivity could constitute another difference.

5.3.2. ABR threshold in Wistar rats

Wistar rats showed ABR thresholds around 50 dB SPL. These thresholds are between 10- 20 dB SPL higher than the ABR hearing thresholds reported in the same rat strain and age (Church et al., 2007) and also in other strains like Long-Evans (Brozoski et al., 2007) and Sprague-Dawley (Duan et al., 2006). Several factors could be responsible for this difference.

First, the single tone intensity emitted by the acoustic driver (see section 2.3.3.5.) is attenuated by 10 dB SPL for a distance of 0.5 cm (which corresponds to the distance between the rat's ear and the acoustic driver), indicating that the hearing thresholds were in fact 10 dB lower than the one reported. Second, the majority of the studies are performed in sound attenuated chambers allowing measuring lower ABR thresholds (Duan et al., 2006; Brozoski et al., 2007; Church et al., 2007) compared to the ABR thresholds that I measured in an un-insulated room. Considering the experimental conditions at which I performed the ABR recordings, it is reasonable to assume that the hearing thresholds exhibited by Wistar rats used here is physiological and comparable to previous studies.

5.3.3. Effects of acoustic over-exposure on ABR thresholds

The effect of acoustic insult was assessed by the shift of the hearing threshold in the ABR as reported in previous studies (Church and Kaltenbach, 1993; Brozoski et al., 2002, Heffner and Harrington, 2002). The shift of the ABR hearing threshold reported here affected frequencies that were above the 14.8 kHz "loud" tone. Similar results have also been reported by previous studies (Salvi et al., 1979; Brozoski et al., 2002) where the maximal effect occurred between half an octave and one octave above the frequency of the

acoustic insult (Salvi et al., 1979). This is due to the optimal vibration point of the cochlear basilar membrane leading to frequencies being maximally amplified at half an octave above their incoming rate (Puel et al., 1988). I reported that about 40% of the Wistar did not exhibit ABR waves when stimulated with 94dB SPL single tones, this effect specifically occurred at stimulating frequencies of 24 kHz and 30 kHz which are around half an octave and one octave respectively above the 14.8 kHz used during acoustic over-exposure. By contrast at 16 kHz this effect was never observed although an elevation of the hearing thresholds was reported.

I showed previously that about 30% of the rats tested failed to display any shift of the hearing threshold and this could be due to the quick recovery of their hearing threshold. This is however unlikely to be the case. Exposing adult (2 months old) rats to high sound intensities (>100 dB SPL) produced a shift in the hearing threshold that was followed by a partial or a complete recovery of the ABR thresholds usually occurring after months (Brozoski et al., 2002; Turner et al., 2006). Performing the same experiment on younger rats (less than 6 weeks old) produced permanent shifts of the hearing thresholds (Rybalko and Syka, 2001; Syka, 2002). Although I did not fully investigate this matter, I checked in one Wistar rat whether ABR thresholds were still shifted 9 days following acoustic over-exposure (performed at postnatal day 15). Similarly to previously described at 4 days after acoustic over-exposure, I observed no detectable ABR waves 9 days after acoustic over-exposure, at 30 kHz and 24 kHz and a 20 dB SPL elevation of the hearing threshold at 16 kHz. Although unproven at that stage, it is likely that shifts of the hearing thresholds reported above were permanent in young Wistar rats.

5.3.4. ABR threshold shifts and tinnitus

Previous studies correlating acoustic over-exposure and tinnitus showed that frequency-specific psychophysical shifts do not parallel the ABR threshold shifts caused by acoustic over-exposure. The tinnitus pitch is usually below the frequency of the insult whereas the ABR threshold shifts are maximally affected at the frequencies above the frequency used during the acoustic over-exposure (Brozoski et al., 2002, Turner et al., 2006). The same studies have shown a recovery of the hearing threshold shifts but this was not accompanied by a recovery from the perception of the tinnitus (Brozoski et al., 2002; Turner et al., 2006).

The perception of tinnitus has been correlated with hyperactivity of the DCN neurons which usually occurs below or at the same frequency of the acoustic insult (Kaltenbach et al., 1998; Zhang and Kaltenbach, 1998; Kaltenbach and Afman, 2000; Brozoski et al., 2002). Altogether these observations suggest that there is a poor correlation (in terms of frequency) between the ABR threshold shifts, the perception of tinnitus and the hyperactivity in the DCN. Nevertheless the ABR is a powerful tool to assess the effect of acoustic over-exposure and is often used in combination with behavioural and electrophysiological studies to quantify the extent of the hearing deficit.

In summary, although the ABR technique does not provide information about the tinnitus onset or the hyperactivity within the DCN, it provides with useful information on the shift of the hearing thresholds at the earliest stages following acoustic over-exposure. This allowed correlating those shifts with excitability changes within the DCN.

Auditory brainstem response recordings in Lister Hooded rats

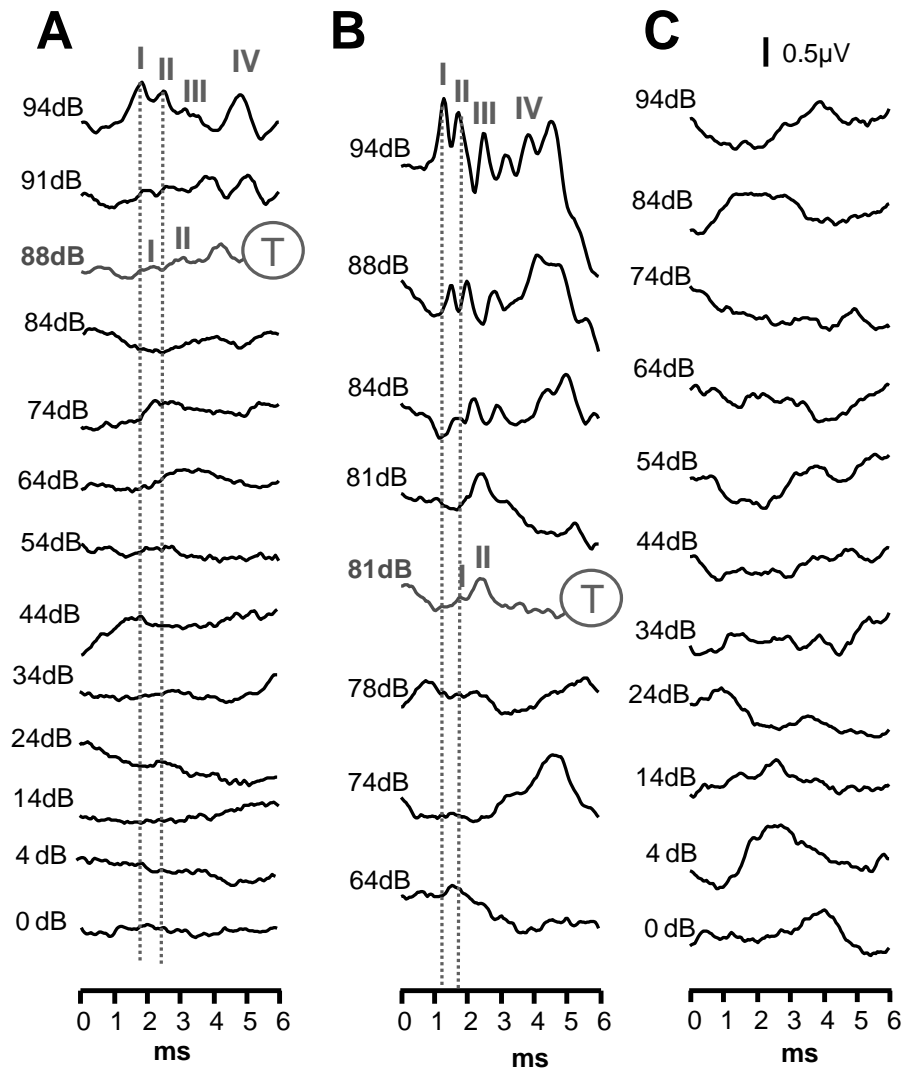


Figure 5.1: Auditory brainstem responses (ABR) evoked by an acoustic tone pip of 24kHz delivered at different intensities (dB SPL) and recorded in three Lister Hooded rats (A-C). The response threshold is shown as a circled T in (A) and (B) whereas in (C) no wave (or threshold) was observed. The pattern in (C) was present in 8 out of 20 Lister Hooded rats. The dotted lines in (A) and (B) are aligned on the peak of wave I and II at 94 dB SPL to show the shift of the latency to the peak as the intensity is decreasing. **(A)** ABR from a 18 days old rat whereas **(B)** is from 50 days old rats and **(C)** is from a 22 days old rat are. All rats were anaesthetised with fentanyl (0.15mg/kg), fluanisone(5mg/kg) and midazolam (2.5 mg/kg). Same scale bar for (A-C)

Auditory brainstem response recordings in Lister Hooded rats (using different anesthetics)

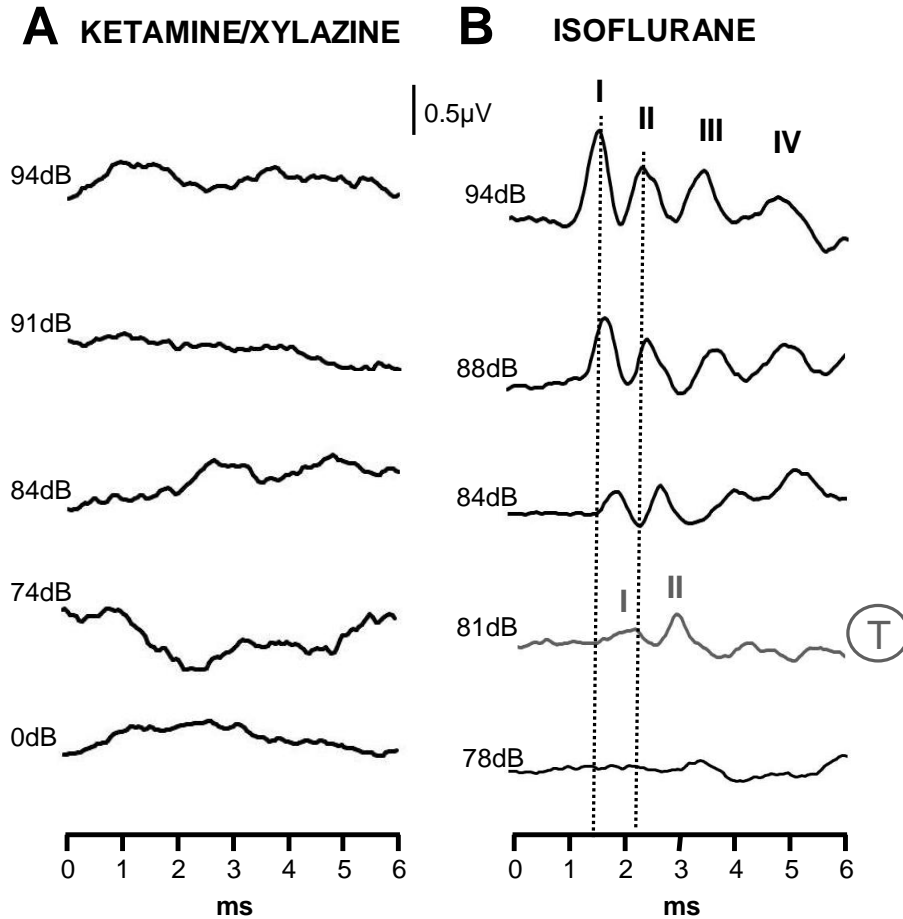


Figure 5.2: Auditory brainstem responses (ABR) evoked by an acoustic tone pip of 24kHz delivered at different intensities (dB SPL) and recorded in two Lister Hooded rats anaesthetized with ketamine (100mg/kg) and xylazine (10mg/kg) (A) or 2% isoflurane (B). The response threshold is shown as a circled T in (B) whereas in (A) no wave (or threshold) was observed. The dotted lines in (B) are aligned on the peak of wave I and II at 94 dB SPL to show the shift of the latency to the peak as the intensity is decreasing. (A) ABR from a 22 days old rat; (B) ABR from a 17 days old rat. Similar results as in (A) were obtained in 1 rat (ketamine and xylazine) and 5 rats (isoflurane) and similar results as in B were found in other 4 rats (isoflurane).

Auditory brainstem response recordings in Wistar rats

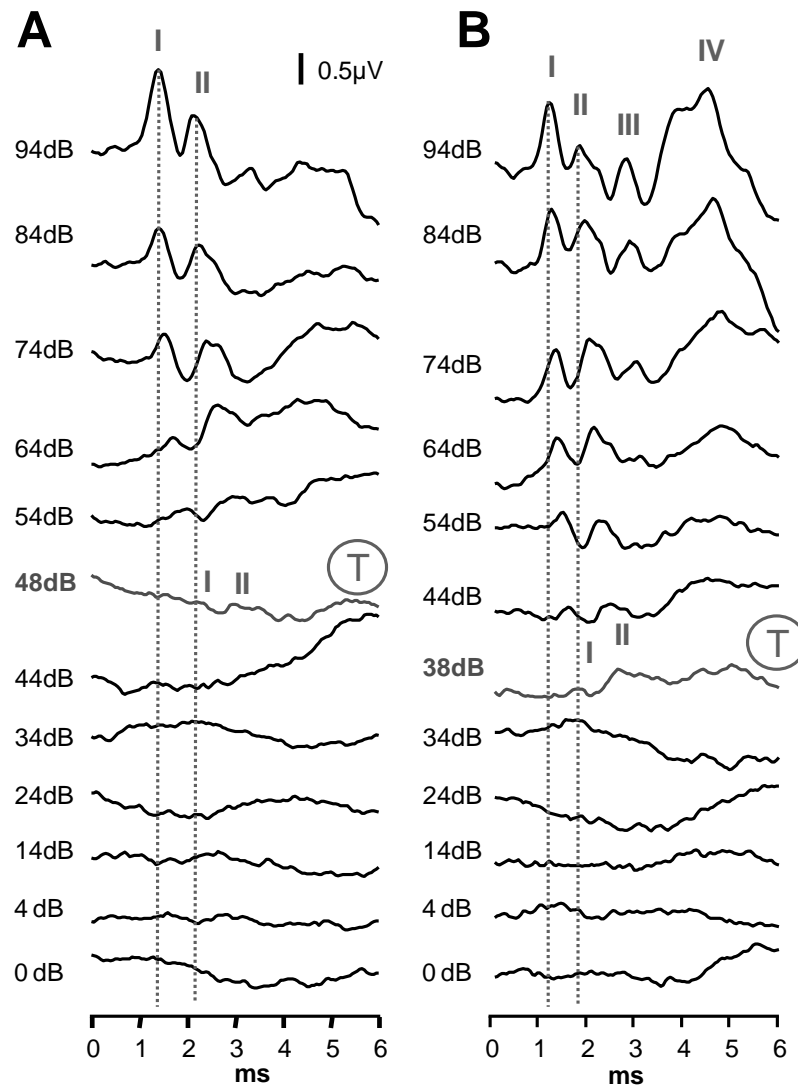


Figure 5.3: Auditory brainstem responses (ABR) evoked by an acoustic tone pip of 24kHz delivered at different intensities (dB SPL) and recorded in two Wistar rats (A-B). The response threshold is shown as a circled T and the dotted lines are aligned on the peak of wave I and II at 94 dB SPL to show the shift of the latency to the peak as the intensity is decreasing. **(A)** ABR from a 18 days old rat; **(B)** ABR from a 40 days old rat. Rats were anaesthetised with fentanyl (0.15mg/kg), fluanisone(5mg/kg) and midazolam (2.5 mg/kg). Same scale bar for (A-B)

Summary of ABR thresholds in Lister Hooded rats and in Wistar rats

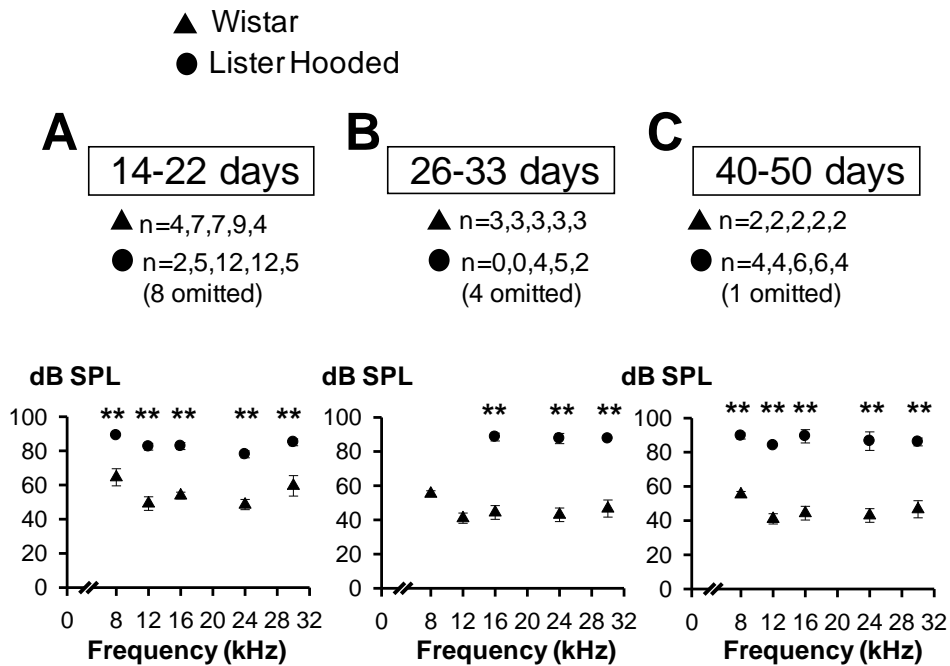


Figure 5.4: Summary plots representing the auditory brainstem response (ABR) thresholds (dB SPL) in function of the single tone pip frequencies (from 8 to 30 kHz) in Wistar rats (triangles) and in Lister Hooded rats (circles). The data have been grouped according to the age of the rats **(A):** 14-22 days old, **(B):** 26-33 days old, **(C):** 40-50 days old. Values are mean \pm s.e.m with numbers above the graph indicating a series of n numbers for each frequency ($n_{8\text{kHz}}, n_{12\text{kHz}}, n_{16\text{kHz}}, n_{24\text{kHz}}, n_{30\text{kHz}}$). Note that the summary plot only included ABR recordings that could be quantified and therefore excluded ABR recordings that showed no wave (like figure 5.1 panel C). The omitted n numbers are mentioned for information. Stars indicate $P \leq 0.01$ for the unpaired T test comparing ABR thresholds between Wistar and Lister Hooded rats at each frequency in the different groups. Rats were anaesthetised with fentanyl (0.15mg/kg), fluanisone(5mg/kg) and midazolam (2.5 mg/kg). Note that the ABR threshold is significantly higher in Lister Hooded rats compared to Wistar rat at all the frequencies and at all age.

Summary of the ABR wave I amplitude in Lister Hooded rats and in Wistar rats

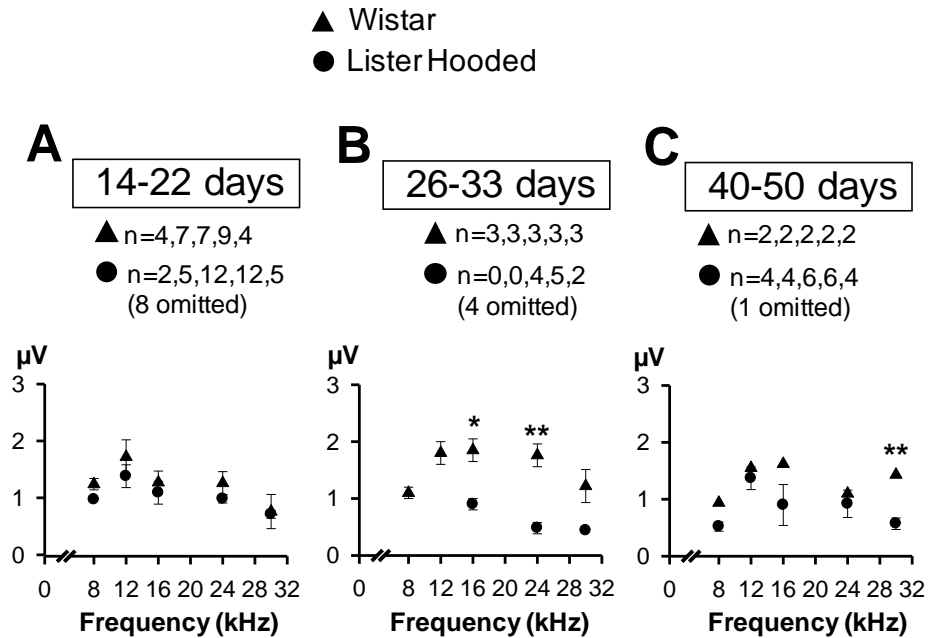


Figure 5.5: Summary plots representing the wave I amplitude of the auditory brainstem response (ABR) in function of the acoustic single tone pip frequencies (from 8 to 30 kHz) in Wistar rats (triangles) and in Lister Hooded rats (circles). ABR coming from the same set of data as for figure 5.4. with the same conditions applying. Data were grouped according to the age of the rats **(A):** 14-22 days old, **(B):** 26-33 days old, **(C):** 40-50 days old. Values are mean \pm s.e.m. with numbers above the graph indicating a series of n numbers for each frequency ($n_{8\text{kHz}}, n_{12\text{kHz}}, n_{16\text{kHz}}, n_{24\text{kHz}}, n_{30\text{kHz}}$). Note that the summary plot only included ABR recordings that could be quantified and therefore excluded ABR recordings that showed no wave (like figure 5.1 panel C). The omitted n numbers are mentioned for information. Stars indicate P values (* $P \leq 0.05$, ** $P \leq 0.01$) for the unpaired T test comparing ABR wave I amplitude between Wistar and Lister Hooded rats at each frequency in the different groups. Rats were anaesthetised with fentanyl (0.15mg/kg), fluanisone(5mg/kg) and midazolam (2.5 mg/kg). Note that the ABR wave I amplitude is significantly smaller in Lister Hooded rats compared to Wistar rat in (B) at 16 and 24 kHz and in (C) at 30 kHz.

Summary of the latency to wave I in Lister Hooded rats and in Wistar rats

▲ Wistar
● Lister Hooded

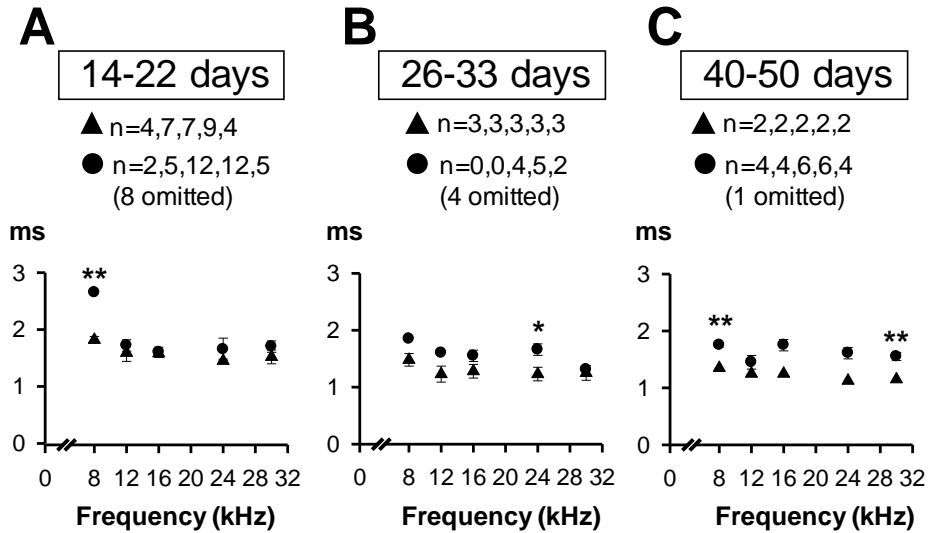


Figure 5.6: Summary plots representing the latency to the wave I of the auditory brainstem response (ABR) in function of the single tone pip frequencies (from 8 to 30 kHz) in Wistar rats (triangles) and in Lister Hooded rats (circles). ABR coming from the same set of data as for figure 5.4. and figure 5.5 with the same conditions applying. Data were grouped according to the age of the rats **(A):** 14-22 days old, **(B):** 26-33 days old, **(C):** 40-50 days old. Values are mean \pm s.d. with numbers above the graph indicating a series of n numbers for each frequency ($n_{8\text{kHz}}, n_{12\text{kHz}}, n_{16\text{kHz}}, n_{24\text{kHz}}, n_{30\text{kHz}}$). Note that the summary plot only included ABR recordings that could be quantified and therefore excluded ABR recordings that showed no wave (like figure 5.1 panel C). The omitted n numbers are mentioned for information. Stars indicate P values (* $P \leq 0.05$, ** $P \leq 0.01$) for the unpaired T test comparing ABR wave I latency between Wistar and Lister Hooded rats at each frequency in the different groups. Rats were anaesthetised with fentanyl (0.15mg/kg), fluanisone(5mg/kg) and midazolam (2.5 mg/kg). Note that the latency to wave I is significantly longer in Lister Hooded rats compared to Wistar rat in (A) at 8kHz and, in (B) at 24 kHz and in C at 8 and 30 kHz.

Effect of acoustic over-exposure on the auditory brainstem response

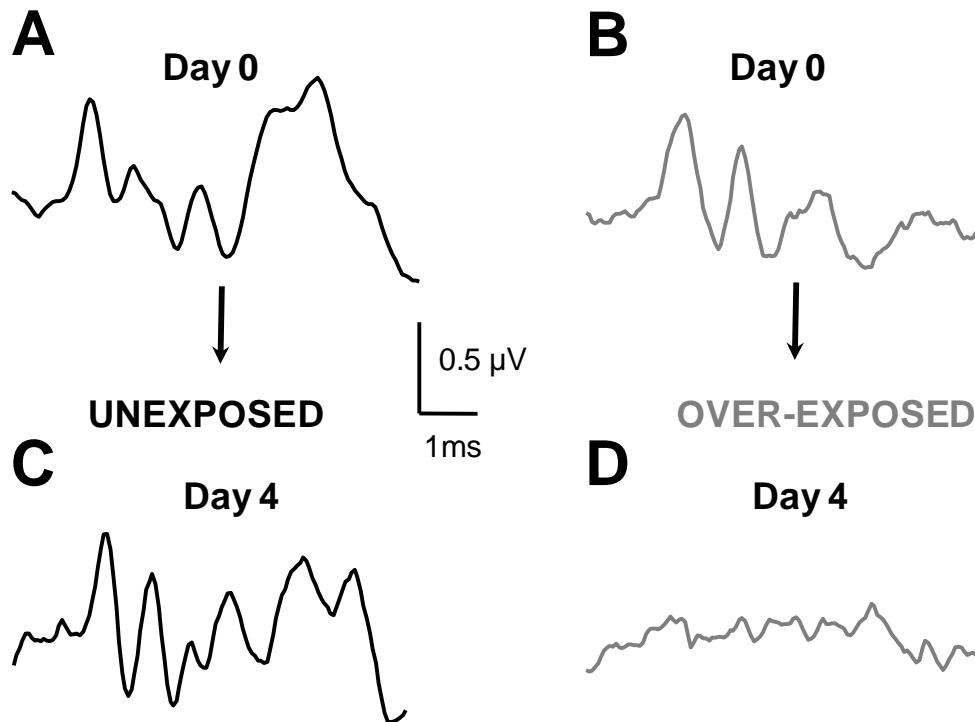


Figure 5.7: Effect of acoustic over-exposure on the auditory brainstem response (ABR) recorded following a 24 kHz tone pip at 94dB SPL. (A-B) Examples of ABR measured at day 0 in two littermate Wistar rats (14 days old). Rat in (B) was anaesthetised and exposed to loud (110dB SPL) single tone (14.8 kHz) for 2 hours at day 0 and at day 1 whereas rat in (A) was anaesthetised at day 0 and at day 1 (see methods). **(C-D)** ABR measured after 4 days. (C) same rat as in (A). (D) same rat as in (B). Rats were anaesthetised with fentanyl (0.15mg/kg), fluanisone(5mg/kg) and midazolam (2.5 mg/kg). Note the flat ABR 4 days after acoustic over-exposure.

Effect of acoustic over-exposure on the auditory brainstem response

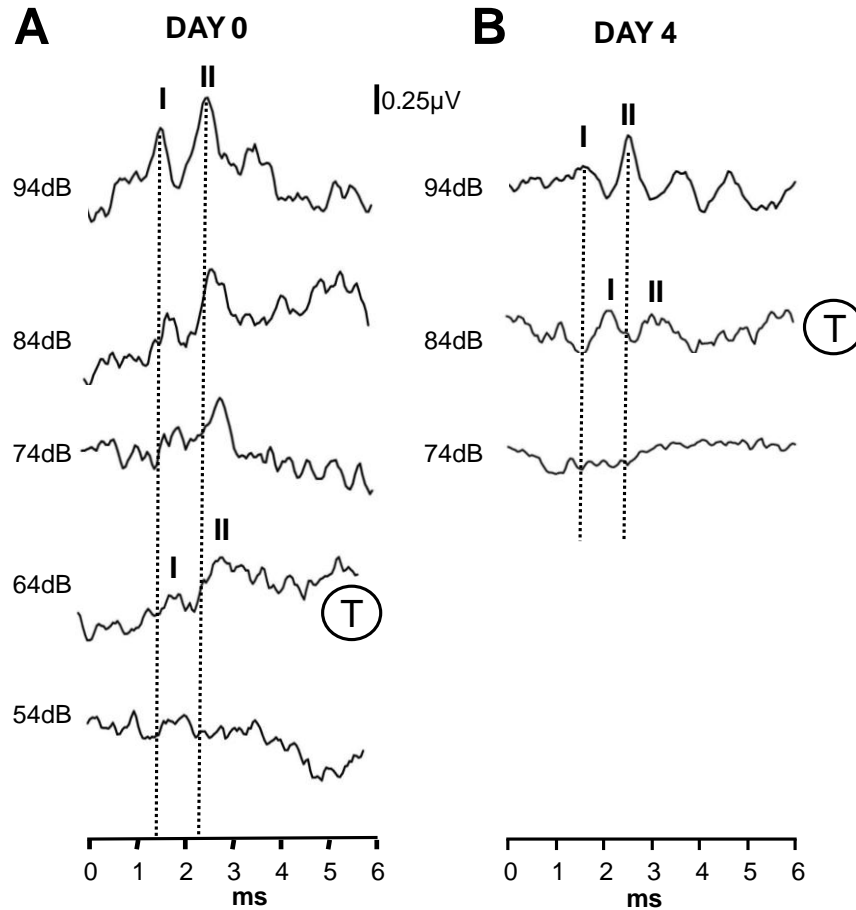


Figure 5.8: Auditory brainstem responses (ABR) evoked by a tone pip of 24kHz delivered at different intensities (dB SPL) recorded in a Wistar rat before (A) and after acoustic over-exposure (B). The response threshold is shown as a circled T and the dotted lines are aligned on the peak of wave I and II at 94 dB SPL to show the shift of the latency to the peak as the intensity is decreasing. The rat was 16 days old and was anaesthetised with fentanyl (0.15mg/kg), fluanisone(5mg/kg) and midazolam (2.5 mg/kg). Same scale bar for (A-B). Note that the ABR threshold is 20 dB higher at day 4 after acoustic over-exposure compared to day 0 before acoustic over-exposure.

Effect of acoustic over-exposure on the ABR hearing threshold of Wistar rats

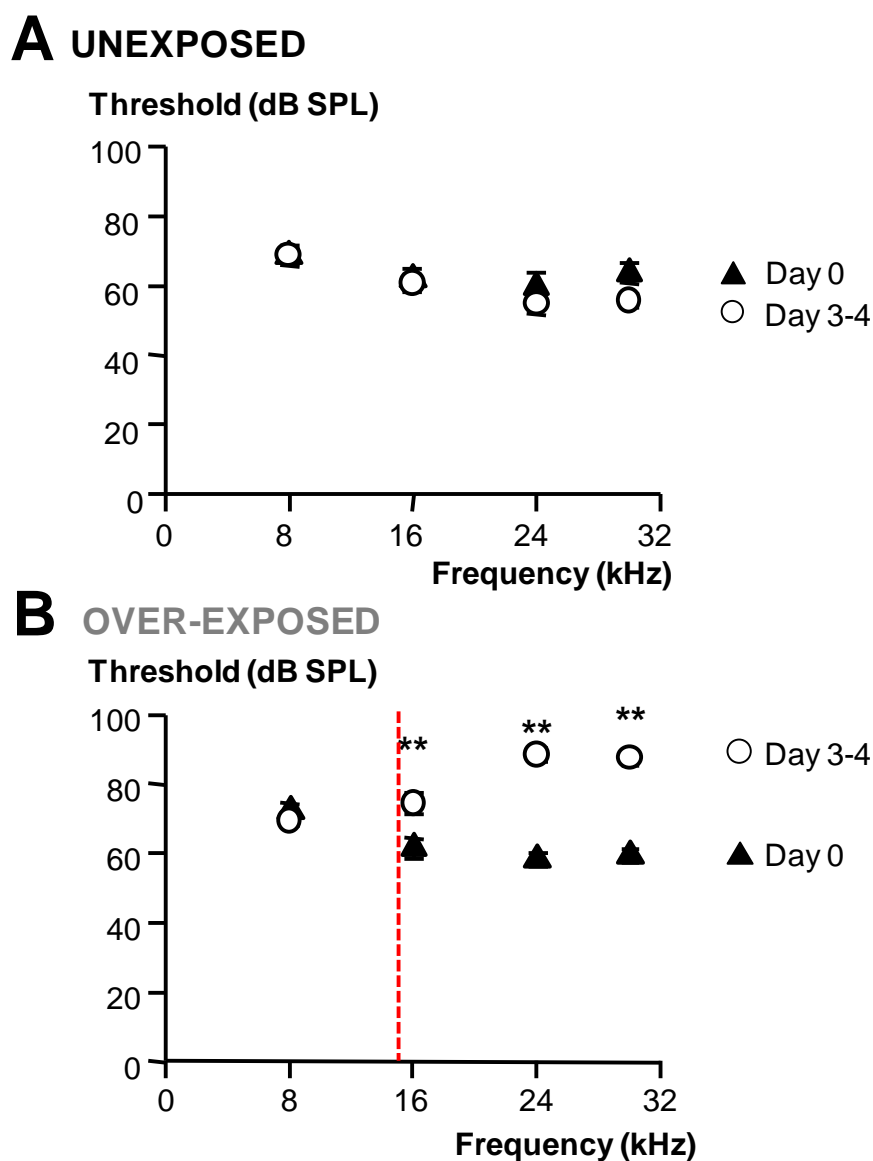


Figure 5.9: Summary plots of the effect of acoustic over-exposure on the auditory brainstem response (ABR) thresholds. Same experimental conditions as in figure 5.7 with ABR thresholds measured at day 0 and day 4 in Wistar rats unexposed (**A**) or exposed to loud (110 dB SPL) single tone (14.8 kHz) for a total of 4 hours (**B**). Values are mean \pm s.e.m. with $n=13$ for (A) and $n=20$ for (B). (** $P \leq 0.01$, paired T test between thresholds obtained at day 0 and threshold obtained at day 3-4). In 12 cases, ABR thresholds at 24 kHz and 30 kHz were exceeding 94 dB SPL and were therefore given an arbitrary value of 95 dB SPL. Rats were anaesthetised with fentanyl (0.15mg/kg), fluanisone (5mg/kg) and midazolam (2.5 mg/kg). Note the ABR threshold elevation for all frequencies exceeding 8 kHz. The dashed line represents the frequency of the loud single tone.

CHAPTER 6

Effect of acoustic over-exposure on cellular excitability and synaptic transmission

INTRODUCTION

6.1. Acoustic over-exposure and homeostatic plasticity

Primary damage to inner and outer hair cells contributes to elevate the auditory fibre thresholds after acoustic over-exposure (Dallos and Harris, 1978; Salvi et al., 1983). Cochlear damage also triggers functional changes within the central auditory pathway (Schmiedt et al., 1980; Salvi et al., 2000). Earliest processing stages occur at the level of the DCN where two to three days after the acoustic trauma, the spontaneous activity is reduced below control level (Kaltenbach et al., 1998) and this is followed by an increased spontaneous firing rate that lasts for months (Kaltenbach et al., 1996, 1998, 2000; Kaltenbach and Zhang, 1998). Behavioural studies showed that hyperactivity in the DCN is correlated with tinnitus-like perception (Brozoski et al., 2002; Heffner and Harrington, 2002; Kaltenbach and Godfrey, 2008). It is thought that the central auditory system compensates for the original decrease of cellular activity through homeostatic plasticity (Kaltenbach et al., 1998; Wang et al., 2002; Seki and Eggermont, 2003; Ma et al., 2006; Schaette and Kempster, 2006). The origin of this phenomenon is still unknown but it is suggested that it is triggered by plastic adjustments within the DCN (Kaltenbach, 2007; Kaltenbach and Godfrey, 2008). Homeostatic plasticity is triggered when the mean firing of neurons undergoes sustained changes and aims to stabilize the mean firing rate (Turrigiano, 1999). Following this line, the reduced activity of the auditory fibres would trigger the initial decreased excitability in the DCN and the DCN would compensate by increasing its excitability and strengthening its excitatory synapses (Schaette and Kempster, 2006).

DCN neurons may respond to changes in the auditory nerve activity by regulating their intrinsic excitability in order to promote stability in firing. The intrinsic cellular excitability of a neuron is regulated by passive properties (i.e. cell capacitance, membrane resistance and resting potential) that contribute to set the resting conditions of the cell and also by active properties (voltage-gated currents). The changes in the DCN excitability observed after acoustic over-exposure could therefore directly originate from changes of the intrinsic properties within the different cell types and/or result from changes of the properties linked to the synapse. In the following chapter, I will investigate the modifications that occur in the early stages of “deafness” (3-4 days after the acoustic over-exposure) assessed as a shift in the auditory brainstem response threshold. I will investigate potential changes of the intrinsic cellular excitability of identified DCN neurons and will also study potential changes occurring after stimulating synaptic inputs.

Changes of cellular excitability will be investigated within DCN granule and fusiform cells. The relevance in this investigation relies in the anatomical connections between the auditory nerve and the cellular subtypes in the DCN. Auditory nerve fibres originate mainly from inner hair cells and are responsible for sending excitatory projections onto the basal dendrites of the fusiform cells (Cohen et al., 1972; Fekete et al., 1984; Zhang and Oertel, 1994). Those fibres (myelinated, called type I) also stimulate tuberculoventral cells that send inhibitory inputs onto fusiform cell basal dendrites (Oertel and Wu, 1989; Smith and Rhode 1989; Oertel et al.; 1990 Oertel and Wickesberg, 1993). A minority of auditory nerve fibres originate from the outer hair cells and send excitatory inputs onto granule cells (Golding et al., 1993). Granule cells receive additional

inputs from neurons of higher auditory centres, such as the inferior colliculus (Caicedo and Herbert, 1993), the auditory cortex (Weedman and Ryugo, 1996), olivocochlear neurons (Brown et al., 1988) and also non-auditory projections from the trigeminal ganglion (Shore et al., 2000; Zhou and Shore, 2004), the dorsal column nuclei (Itoh et al., 1987) and the spinal trigeminal nuclei (Haenggeli et al., 2005), the cuneate nucleus (Weinberg and Rustioni 1987; Wright and Ryugo, 1996) as well as vestibular ganglions and nuclei (Burian and Gstoettner, 1988; Kevetter and Perachio, 1989; Bukowska, 2002). Thus, the granule cell domain represents an important element in the convergence of somatosensory and auditory signals. Perturbations at the level of the auditory nerve or the central auditory nuclei provoked by acoustic over-exposure could therefore alter granule excitability. Additionally changes in the auditory signal could trigger over-compensatory mechanisms at the level of the somatosensory inputs onto granule cells as this could also trigger changes within granule cell passive or active properties. Fusiform cells receive the multisensory information via granule cell axons (the parallel fibres) and are responsible of sending the processed information to the inferior colliculus and auditory thalamus (Adams, 1979a; Anderson et al., 2006). Changes at the level of the auditory nerve and/or granule cells could therefore modulate fusiform cell excitability and this would ultimately affect the signal that the DCN sends to higher auditory centres.

The cellular excitability can also be modulated through synaptic transmission. Numerous studies illustrated how damage to the cochlea results in alterations of the neurotransmission within the central auditory pathway. Such modifications have been observed in the auditory cortex and in the brainstem where the excitatory synaptic transmission was strengthened and the inhibitory

transmission was weakened after acoustic trauma (Vale and Sanes, 2002; Muly et al., 2004; Kotak et al., 2005). I therefore examined the inhibitory (GABAergic and/or glycinergic) and the excitatory (glutamatergic) synaptic transmission onto fusiform cells and determine whether they get modified in the early stages that follow acoustic over-exposure. Changes in synaptic transmission could also affect the fusiform cell firing pattern, firing frequency and reliability but also the spike timing as described below.

Spike timing is an important feature of the sensory system (Berry et al., 1997; Nowak et al., 1997; Buonomano, 2003). In the auditory system, many neurons are specialized to maintain the auditory timing information that comes from the cochlea. The temporal code can be maintained through a mechanism called phase locking occurring when the onset of an action potential is evoked reproducibly at a particular part of the cycle of the incoming sound source. Along the auditory pathway several structures are capable of phase locking like the inferior colliculus, the auditory thalamus, the ventral cochlear nucleus (Joris et al., 1994; Paolini et al., 2001; Liu et al., 2005; Wallace et al., 2007). In the ventral cochlear nucleus, the mechanisms through which bushy cells phase-lock to the auditory nerve fibre inputs involve the convergence and the coincident excitation from two or more auditory nerve fibres (Joris et al., 1994; Paolini et al., 2001). In the medial superior olive, principal neurons are sensitive to the differences in the time-of-arrival of sound at the two ears (inter-aural time difference) and inhibitory inputs are particularly important in ensuring the temporal fidelity of the action potentials (Grothe and Sanes, 1994). The DCN exhibits poor phase locking to high-frequency pure tones (Goldberg and Brownell, 1973; Rhode and Smith, 1986b). However recent evidence suggests

that spike timing can be an important aspect of information coding in the DCN where fusiform cells exhibit synchronization to the envelope frequency of the amplitude-modulated tones (Frisina et al., 1994; Joris and Smith, 1998; Neuert et al., 2005). Moreover, parallel fibre synapses onto fusiform cells exhibit spike-timing-dependent plasticity (Tzounopoulos et al., 2004). My thesis will investigate whether acoustic modulates spike timing of DCN fusiform cells as this could significantly affect the temporal integration of multisensory and/or auditory inputs.

RESULTS

6.2. Effects of acoustic over-exposure

on dorsal cochlear nucleus intrinsic cellular excitability

My preliminary experiments have shown that LH rats cannot be used as a model of investigation as their hearing threshold is well above normal values in control conditions. In the following sections, experiments were mainly performed in Wistar rats. Wistar rats used in this study were exposed to an intense (110 dB SPL) single tone (15 kHz) for a minimal amount of time of 4 hours. The auditory function was monitored by measuring the thresholds of the auditory brainstem responses (ABR). Using this technique, I have shown that the hearing thresholds were significantly increased by 20-40 dB SPL for frequencies above 15 kHz, 3-4 days after the acoustic over-exposure (see chapter 5). *In vitro* patch-clamp recordings were conducted at the stage where Wistar rats showed a shift in the ABR thresholds and all Wistar rats used for *in vitro* experiments have been checked for a shift of their hearing threshold, on the day of the patch clamp recording. Animals were between 16 and 21 days: at this stage, *in vitro* patch clamp recordings can be successfully obtained. After this stage, the success rate of the recordings decreased as the amount of connective tissue was hindering the quality of the seal. Littermate Wistar rats were usually investigated in parallel as one rat was exposed to the loud single tone (designated as over-exposed in the figures) whereas the other was unexposed to loud single tone but similarly anesthetized to its littermate. Sometimes patch clamp recordings were designed to do a double dissection the

same day and I used one “unexposed” rat and one “over-exposed” rat. Cells are identified based on their localization in the slice (cytoarchitecture), their shape and their size. Cells were also filled with lucifer yellow to subsequently check their morphology on the confocal microscope.

6.2.1. Effect of acoustic over-exposure on granule cell excitability

6.2.1.1. Effects on granule cell passive properties

Granule cell passive properties in the Lister Hooded and Wistar rats.

Analysis of passive properties on granule cells included the membrane resistance, the membrane capacitance and the resting potential (described in the methods sections 2.2.9.1, 2.2.9.2 and 2.2.9.4 respectively). The values for the LH rats are detailed in table 4.1 whereas the values for the Wistar rats are detailed in the table 6.1 below. Granule cells originating from unexposed Wistar rats displayed values of resting potential, membrane resistance and capacitance similar to the one recorded in LH rats (with P values comparing those characteristics in the two strains of 0.48, 0.08 and 0.18 respectively, unpaired T test).

Acoustic over-exposure and granule cell passive properties. Effects of acoustic over-exposure on Wistar rats are also detailed in the table 6.1 below. The table shows that acoustic over-exposure was leading to granule cell resting potentials being 14 mV more hyperpolarized and to the granule cell membrane resistance being decreased by about 60%. By contrast, the granule cell capacitance was unaffected by acoustic over-exposure.

6.2.1.2. Absence of effect on granule cell action potentials

Characteristics of the action potential. The analysis of the action potential included its amplitude, its 10-90% rise time and its 90-10% decay time and was

performed when granule cells started to fire (i.e. at their membrane potential threshold of -70 mV).

	Resting potential (mV)	Membrane Resistance (GΩ)	Capacitance (pF)
Unexposed (n=7)	-43 ± 4.3	1.9 ± 0.3	5.2 ± 0.8
Overexposed (n=10)	-57 ± 4.0	1.1 ± 0.2	9.0 ± 2.7
P, Unpaired T Test	0.02 *	0.04 *	0.2

Table 6.1: Analysis of granule cell passive properties. Mean ± s.e.m values for the resting potential, the membrane resistance and the capacitance measured in granule cells from unexposed and over-exposed Wistar rats. (* = P≤0.05)

Indeed, at those threshold potentials, granule cells fired at around 0.2Hz, allowing action potentials to be analyzed as single events. The values for the LH rats are detailed in table 4.2 whereas the values for the Wistar rats are detailed below in table 6.2. Granule cells originating from unexposed Wistar rats displayed action potentials with an amplitude, a rise time and a decay time similar to the one recorded in LH rats (with P values comparing those characteristics in the two strains of 0.96, 0.43 and 0.86 respectively, unpaired T test).

	Amplitude (mV)	10-90% rise time (ms)	90-10% decay time (ms)
Unexposed (n=5)	70 ± 4.3	15.7 ± 5.9	1.95 ± 0.15
Overexposed (n=6)	74 ± 2.6	10.3 ± 3.3	2.4 ± 0.5
P, Unpaired T Test	0.45	0.42	0.57

Table 6.2: Analysis of the action potential properties. Mean ± s.e.m values for the amplitude, the 10-90% rise time and the 90-10% decay time measured in granule cells from unexposed and over-exposed Wistar rats.

Acoustic over-exposure and granule cell action potentials. Figure 6.1 and table 6.2 show that neither the amplitude nor the 10-90% rise time or the 90-10% decay time of the granule cell action potential was affected by acoustic over-exposure in Wistar rats.

6.2.1.3. Absence of effect on granule cell firing at steady membrane potentials

Granule cell action potential firing in the Lister Hooded and Wistar rats.

Granule cell action potentials were studied at different steady state membrane potentials (at threshold and when cells reached the maximal firing frequency). Usually granule cells were maintained for 1 to 4 minutes at those two specific membrane potentials. Properties like firing frequencies (at threshold and maximal frequency), coefficient of variation (at threshold and at maximal frequency), membrane potentials (at threshold and at maximal frequency) were found to be similar between LH rats (table 4.3 and table 4.4) and unexposed Wistar rats (table 6.3 and table 6.4 below). P values (unpaired T test) comparing those characteristics in the two strains were 0.61, 0.33 and 0.50 respectively at threshold and 0.12, 0.59 and 0.30 respectively at maximal firing frequency.

Acoustic over-exposure and granule cell firing. Acoustic over-exposure did not affect the granule cell firing pattern (frequency and regularity) when cells were firing at threshold or at their maximal firing frequency. This is shown in figure 6.2 with values detailed in the tables 6.3. and 6.4 below. The following experiments will address whether acoustic over-exposure affects the firing of granule cells when constant current injections were replaced by step currents.

	Frequency at threshold (Hz)	CV at threshold	HP at threshold (mV)
Unexposed (n=7)	0.8 ± 0.3	1.9 ± 0.4	-71 ± 5.1
Overexposed (n=8)	0.9 ± 0.4	2.2 ± 0.5	-73 ± 2.9
P, Unpaired T Test	0.88	0.65	0.20

Table 6.3: Analysis of the action potential firing properties at threshold. Mean ± s.e.m values for the firing frequency, the coefficient of variation (CV) and the membrane potential (HP) measured at threshold in granule cells from unexposed and over-exposed Wistar rats.

	Frequency at Fmax (Hz)	CV at Fmax	HP at Fmax (mV)
Unexposed (n=7)	9.1 ± 1.5	0.7 ± 0.1	-63 ± 3.4
Overexposed (n=8)	14 ± 2.9	0.4 ± 0.1	-60 ± 1.7
P, Unpaired T Test	0.18	0.22	0.48

Table 6.4: Analysis of the action potential firing properties at maximal frequency. Mean ± s.e.m values for the frequency, the coefficient of variation (CV) and the membrane potential (HP) all measured at maximal frequency (Fmax) in granule cells from unexposed and over-exposed Wistar rats.

6.2.1.4. Effects on granule cell firing with step potentials

Effects on the firing gain. Figure 6.3 represents examples of granule cells firing in response to one second step currents of 10 pA and 30 pA, from a membrane potential of -80 mV in both unexposed and over-exposed conditions. It can be noticed that the firing frequency increased in response to increasing the step current amplitude (i.e. from 2 to 52 Hz in the unexposed condition and from 0 to 9 Hz for the over-exposed rats). This is also represented in the graphs in figure 6.3E and figure 6.3F summarizing the relationship between the injected current and the firing frequency for these two cells. Values were fitted with a

sigmoidal function (see methods section 2.2.9.5.) and show that the slope is less steep in the over-exposed compared to the unexposed conditions (i.e. 0.8 Hz/pA and 1.9Hz/pA respectively) whereas the maximal firing rate is similar for the two conditions (78 Hz and 70 Hz respectively). Granule cell maximal firing and slope measured in unexposed condition (Wistar rats) were similar to the granule cell maximal firing and slope measured in LH rats ($P=0.12$ and $P=0.56$ for maximal firing and slope respectively, unpaired T test, values are reported in table 4.6.)

Data analysis for the unexposed and over-exposed condition is summarized in the histograms in figure 6.4A and values are given in the table 6.5 below.

	Slope (Hz/pA)	Fmax (Hz)	Ithreshold (pA)	V threshold (mV)
Unexposed (n=10)	2.5 ± 0.4	47 ± 4	22 ± 4	33 ± 3
Overexposed (n=9)	1.4 ± 0.2	56 ± 9	22 ± 6	38 ± 2
P, Unpaired T Test	0.04*	0.4	1	0.1

Table 6.5: Analysis of the action potential firing properties of granule cells when injecting step currents in unexposed and over exposed conditions. Mean ± s.e.m values for the values of the slope (Hz/pA) reported in figure 6.4A (column 2), the maximal firing frequency (Fmax, column 3), the current at threshold (minimal current to elicit an action potential, column 4) and the voltage at threshold (minimal step voltage to elicit an action potential from a membrane potential of -80 mV, column 4). (* = $P \leq 0.05$)

Data were normalized relatively to the maximal frequency and to the current at threshold (see figure 6.4 B) providing the advantage of performing a sigmoidal fit on averaged normalized values (see table 6.6 below). Whereas the maximal values are unaffected between the unexposed and the over-exposed conditions (fit on normalized values), the slope of the sigmoidal curves is less steep in the

over-exposed (1.4 Hz/pA) compared to the unexposed conditions (5.4 Hz/pA, $P=0.0001$).

	Slope (Hz/pA)	Fmax (Hz)
Unexposed (n=10)	1.4 ± 0.4	0.9 ± 0.03
Overexposed (n=9)	5.4 ± 0.5	0.9 ± 0.04
P, Unpaired T test	0.0001**	1

Table 6.6: Analysis of the action potential mean firing slope (Hz/pA) of granule cells when injecting step currents. Mean ± s.e.m values correspond to figure 6.4B with a normalized maximal firing frequency (** = $P \leq 0.01$).

Granule cells fire with a high neuronal gain (represented by the slope of the sigmoidal curve) as expected in the case of a high membrane resistance triggering action potentials for minimal current values. It is therefore unsurprising that a decrease of the membrane resistance (see section 6.2.1.1) after acoustic over-exposure triggers less action potentials compared to the unexposed conditions. Possible reasons of this phenomenon are discussed in section 6.6.1. and 6.6.2.

Absence of effect on the firing accommodation. In the previous section, the firing frequency was determined as an average frequency for the whole duration of the step current. Therefore the analysis did not take into account the accommodation of the action potentials as observed in figure 6.5A and B, where the inter-spike interval increases at the end of the step current. Granule cells are accommodating in over-exposed and over-exposed conditions (figure 6.5 A and B) and this is shown by the larger inter-spike interval at the end compared to the inter-spike interval at the beginning of the pulse. Accommodation indexes were calculated as the ratio of two inter-spike intervals taken at the beginning

and at the end of the step current (see methods) with values of 1 reflecting a constant firing frequency (absence of accommodation). Accommodation indexes were calculated for threshold and supra-threshold depolarizations (three steps above the action potential threshold) and the mean values are reported in figure 6.5C for the over-exposed and the exposed conditions. No difference was observed between the accommodation indexes of granule cells originating from unexposed or over-exposed rats (also reported in the table 6.7 below).

		Current above threshold (pA)				
		0	10	20	30	40
A.I. Unexposed	Mean	0.77	0.73	0.8	0.62	0.69
	s.e.m.	0.05	0.07	0.04	0.15	0.15
	n	4	10	9	5	4
A.I. Over-exposed	Mean	0.64	0.59	0.58	0.56	0.60
	s.e.m.	0.25	0.15	0.14	0.1	0.1
	n	4	8	8	8	6
P, Unpaired T test		0.62	0.43	0.16	0.73	0.96

Table 6.7: Summary table showing the accommodation index (A.I.) calculated for different amplitude of currents. Same protocol as described in figure 6.5. Currents have been expressed relative to the threshold current value. Note that although granule cell action potential firing is accommodating in unexposed or over-exposed conditions, there is no difference between the two conditions.

In summary, analyzing the granule cell firing frequency in relationship to step currents allowed identifying a decrease in the neuronal gain after acoustic over-exposure and this decrease is unrelated to an action on the accommodation properties.

6.2.2. Effects of acoustic over-exposure on fusiform cell excitability

6.2.2.1. Effects on fusiform cell passive properties

Fusiform cell passive properties in the Lister Hooded and Wistar rats.

Similarly to granule cells, fusiform cells originating from unexposed Wistar rats displayed resting potential, membrane resistance and capacitance values similar to the one recorded in LH rats (Values for the LH rats and the Wistar rats are detailed in table 4.1 and table 6.8 respectively and P values comparing those characteristics in the two strains were 0.07, 0.12 and 0.34 for the resting potential, the membrane resistance and the capacitance respectively, unpaired T test).

Acoustic over-exposure and fusiform cell passive properties. Acoustic over-exposure on Wistar rats did not affect the passive properties of the fusiform cells as detailed in the table 6.8 below.

	Resting potential (mV)	Membrane resistance (M Ω)	Capacitance (pF)
Unexposed (n=6)	-47 \pm 4.3	120 \pm 40	151 \pm 36
Overexposed (n=11)	-52 \pm 4.0	100 \pm 18	145 \pm 16
P, Unpaired T Test	0.28	0.93	0.53

Table 6.8: Analysis of fusiform cell passive properties. Mean \pm s.e.m values for the resting potential, the membrane resistance and the capacitance measured in fusiform cells from unexposed and over-exposed Wistar rats.

6.2.2.2. Acoustic over-exposure generates bursts in fusiform cells

Fusiform cell action potentials in Lister Hooded rats and Wistar rats. The analysis of the amplitude, the 10-90% rise time and the 90-10% decay time of the action potential was performed in fusiform cells as previously described for granule cells, with fusiform cells maintained at their activation threshold

potential (i.e. between -70 mV and -60 mV). At those potentials, fusiform cells fired at around 0.2Hz, allowing action potentials to be analyzed as single events. Fusiform cells originating from Wistar rats display action potentials similar to the one recorded in LH rats (table 4.2 and table 6.9 respectively). In unexposed conditions, fusiform cells fired simple action potentials (figure 6.6 A and table 6.9 below) with similar amplitudes, rise times and decay times between the two strains ($P=0.6$, 0.2 and 0.3 respectively). Fusiform cells also fired with an undershoot in the repolarization phase as shown in figure 6.6. This undershoot is also observed for LH rats.

Acoustic over-exposure and fusiform cell action potentials. Results are summarized in table 6.9 below. When Wistar rats were over-exposed to loud single tones, action potentials characteristic were unchanged in two third of fusiform cells. I called this sub-population over-exposed type I. Indeed, over-exposed type I fusiform cells fired action potentials (shown in figure 6.6B) with an amplitude, a 10-90% rise time and a 90-10% decay time similar to action potentials recorded in unexposed conditions ($P>0.05$ for all three parameters, anova one way test). Over-exposed type I cells also displayed an undershoot following the action potential similar to the unexposed conditions. By contrast, after acoustic over-exposure one third of the fusiform cells (6 out of 18 cells) fired trains of action potentials or bursts (figure 6.6C) generally arising on top of a smaller (12 ± 1.2 mV, $n=5$) transient depolarization phase. In those cells, the undershoot following the action potential was absent. For simplification, those fusiform cells are called over-exposed type II cells and their action potential characteristics are described in the table 6.9 below. In general fusiform cells do not fire any action potentials when maintained at -70 mV and start to fire action

potentials at around -57 mV (average membrane potential threshold for the action potential). Such small depolarizing events from a membrane potential of -70 mV are leading to an atypical spike initiation in those cells. When I took into account the level of the potential reached by those small depolarizing events, it appeared that the actual threshold voltage for the action potential was left unchanged between the fusiform cells recorded in the unexposed conditions, the overexposed type I and type II fusiform cells (i.e $-65 \pm 1.7\text{mV}$ (n= 5 cells, 4 animals), $-60 \pm 1.5\text{ mV}$ (n= 5 cells, 4 animals) and $-60 \pm 0.5\text{mV}$ (n= 5 cell, 4 animals) respectively, $p>0.05$ anova one way).

	Amplitude (mV)	10-90% rise time (ms)	90-10% decay time (ms)	Under-shoot
Unexposed (n=5)	91 ± 7.7	1.3 ± 0.8	0.8 ± 0.1	5
Over-exposed type I (n=5)	86 ± 3.6	0.9 ± 0.3	0.7 ± 0.05	5
Over-exposed type II (n=5)	69 ± 2.5	0.6 ± 0.1	2.3 ± 0.1	0
Unexposed versus Over-exposed type I	N.S.	N.S.	N.S.	
Unexposed versus Over-exposed type II	$P<0.05^*$	N.S.	$P<0.001^{**}$	
Over-exposed type I vs Over-exposed type II	N.S.	N.S.	$P<0.001^{**}$	

Table 6.9: Analysis of the properties of the fusiform action potentials. Mean \pm s.e.m values for the amplitude, the 10%-90% rise time, the 90%-10% decay time measured in fusiform cells originating from unexposed or over exposed Wistar rats. The number of cells showing an undershoot in the repolarizing phase has been reported in the last column. P values were obtained with anova one-way tests comparing the three populations of cells. N.S.= non significant for P values >0.05 . Note that in the case of the over exposed type II cells, the action potential amplitude was measured relative to the dashed line shown in figure 6.6C.

Action potential characteristics like amplitude, 10-90% rise time and 90-10% decay time (table 6.9) were determined after setting the baseline artificially at the top of the small depolarizing phase (dashed line in figure 6.6C). In this condition, over-exposed type fusiform II cells fired action potentials characterized by significantly longer decay time compared to the unexposed and the over-exposed type I fusiform cells (table 6.9 and figure 6.7). As the baseline setting already excluded the depolarizing phase, the longer decay time observed for the over-exposed type II fusiform cells is likely to be related to intrinsic electrical excitability changes of those cells. I also observed that the action potential amplitude of the over-exposed type II population was significantly smaller compared to the action potential amplitude of the unexposed population (see table 6.9) whereas the 10-90% rise time was similar between the three populations (table 6.9). To check whether the depolarizing phase contributed to the decreased in the action potential amplitude in over-exposed type II fusiform cells, the analysis of the amplitude was also performed by taking into account the small depolarizing phase preceding the action potential. In this case the baseline was set at the start of the depolarizing phase (represented by the dotted line in figure 6.6C) and only the first action potential of the burst was analyzed. By taking into account the small depolarizing phase, the action potential amplitude for the over-exposed II population was $89 \text{ mV} \pm 2.8 \text{ mV}$ ($n= 5$) similar to the unexposed and to the over-exposed type I population ($P>0.05$ anova one way). This suggests that the depolarizing phase accounts for the decrease in the action potential amplitude reported in table 6.9. I next investigated whether the depolarizing phase was an EPSP (due to the activation of NMDA and AMPA glutamate receptors). As the equilibrium

potential for Cl^- was -35mV (therefore above the membrane potential at which I performed the recordings), I could also investigate whether it was an IPSP (due to the activation of glycine and/or GABA receptors). As the small depolarizing events arose spontaneously and below the threshold of the action potentials, I analyzed the rise time and the decay time of those events in isolation from the action potentials and found a 10-90%rise time and a 90-10%decay time of $38.5 \pm 8.5\text{ms}$ ($n=5$) and $72.6 \pm 17\text{ms}$ ($n=5$) respectively. I checked whether the small depolarizing phase was an EPSP or an IPSP by perfusing with NBQX ($10 \mu\text{M}$), D-AP5 ($50 \mu\text{M}$), strychnine ($10 \mu\text{M}$) and gabazine ($20 \mu\text{M}$) to block AMPA, NMDA, glycine and GABA_A receptors respectively and figure 6.8 shows that those blockers left the depolarizing phase unaffected.

Bursting activities could be correlated with a change in the passive properties of the cells affecting for example the time constant of the membrane and the passive propagation of the signals along proximal dendrites. This was not the case as fusiform cells of the over-exposed type II population showed similar passive properties to the unexposed and over-exposed type I population (see table 6.10 below).

	Resting potential (mV)	Membrane resistance (mΩ)	Capacitance (pF)
Unexposed (n=6)	-47 ± 2.5	120 ± 40	151 ± 36
Over-exposed type I (n=6)	-54 ± 3.9	89 ± 28	167 ± 26
Over-exposed type II (n=5)	-49 ± 1.4	113 ± 23	117 ± 10
Unexposed versus Over-exposed type I	N.S.	N.S.	N.S.
Unexposed versus Over-exposed type II	N.S.	N.S.	N.S.
Over-exposed type I vs Over-exposed type II	N.S.	N.S.	N.S.

Table 6.10: Analysis of fusiform cell passive properties. Mean ± s.e.m values for the resting potential, the membrane resistance and the capacitance measured in fusiform cells from unexposed, over-exposed type I over-exposed type II population. P values were obtained with anova one way tests comparing the parameters between the three populations of cells. N.S. = non significant for P values >0.05. Note that acoustic over-exposure left fusiform cell passive properties unaffected.

Fusiform cell action potential firing in the Lister Hooded and Wistar rats.

As for granule cells, the analysis of the firing consisted of the frequency and the regularity of action potentials measured at threshold and when cells reached their maximal firing frequency. Firing frequency, coefficient of variation and membrane potentials measured at the threshold of the action potentials were similar between LH rats (values detailed in table 4.3) and Wistar rats (values detailed in table 6.11) with P values for unpaired Student t tests of 0.06, 0.18 and 0.85 respectively. Firing frequency, coefficient of variation and membrane potentials measured at the maximal firing were also similar between the two strains with P values for unpaired Student tests of 0.11, 0.45 and 0.83 respectively (detailed in tables 4.5 for LH rats and in table 6.12 for Wistar rats).

Bursting type fusiform cells display an irregular pattern. Properties like membrane potentials, firing frequency and coefficient of variation were

measured at threshold firing, half maximal and maximal firing frequency. Those properties were compared between fusiform cells in the exposed and over-exposed conditions. Figure 6.9 shows three examples of fusiform cells firing when held at just above their activation threshold in the unexposed (A), the over-exposed type I (B) and the over-exposed type II population (C). The cells in A and B (unexposed and over-exposed type I respectively) share similar properties with simple action potentials starting to fire at low frequency (between 0.1 and 1 Hz) at a membrane potential of around -65 mV. At this threshold potential, the coefficient of variation of the inter-spike interval distribution of 3.9 (figure 6.9A) and 2.1 (figure 6.9B) for the unexposed and the overexposed type I population respectively indicates an irregular firing pattern as expected at threshold potentials. As the two cells in figure 6.10A and B (corresponding to the unexposed and the overexposed type I population) get more depolarized by about 5 mV, the spike frequency increases to about 15 Hz to reach a similar maximal frequency of about 35 Hz at a potential of -55 mV (shown in figure 6.11A and B). As cells are depolarized, the firing pattern becomes more regular with a coefficient of variation of the inter-spike interval distribution decreasing to 0.1 and 0.06 for the unexposed and the over-exposed type I population respectively (figure 6.10 left A and B). When both unexposed and over exposed type I cells reached their maximal firing frequency, the coefficient of variation decreases even further (i.e. to 0.05 and 0.03 respectively, figure 6.11A and B). Tables 6.11, 6.12 and 6.13 summarize the membranepotentials and the values of the coefficient of variation for three selected firing rates: at threshold (table 6.11), half maximal frequencies (table 6.12) and maximal frequencies (table 6.13). As described in the previous

section, fusiform cells from the over-exposed type II population fired bursts of action potentials when constantly held at their action potential threshold. The membrane potential at which the cells started to fire was more hyperpolarized in the overexposed type II cells (-73 ± 5 mV, $n=5$) compared to -65 ± 4 mV ($n=5$) and -61 ± 5 mV ($n=7$) ($P<0.05$, anova one way) for the unexposed and the over-exposed type I fusiform cells respectively. This is due to the presence of the depolarizing phase that artificially shifts the threshold for the action potential of the over exposed type II fusiform cells.

	Frequency at threshold (Hz)	CV at threshold	MP at threshold (mV)
Unexposed (n=5)	0.2 ± 0.1	1.7 ± 0.1	-65 ± 1.8
Over-exposed type I (n=7)	0.5 ± 0.1	1.9 ± 0.4	-61 ± 1.9
Over-exposed type II (n=5)	3.4 ± 1.9	4.4 ± 1.4	-74 ± 2.3
Unexposed versus Over-exposed type I	N.S.	N.S.	N.S.
Unexposed versus Over-exposed type II	N.S.	N.S.	$P<0.05^*$
Over-exposed type I versus Over-exposed type II	N.S.	N.S.	$P<0.01^{**}$

Table 6.11: Analysis of the action potential firing properties at threshold. Mean \pm s.e.m values for the firing frequency, the coefficient of variation (CV) and the membrane potential (HP) measured at threshold in fusiform cells from unexposed and over-exposed rats. *P* values were obtained with anova one-way tests. N.S. = non significant for *P* values >0.05 . Note the higher threshing potentials for the over-exposed type II fusiform cells.

	Frequency at ½ Fmax (Hz)	CV at ½ Fmax	MP at ½ Fmax (mV)
Unexposed (n=5)	9 ± 1.7	0.19 ± 0.04	-50 ± 2.2
Over-exposed type I (n=7)	11 ± 2	0.15 ± 0.04	-48 ± 1.6
Over-exposed type II (n=5)	5 ± 2.7	3.05 ± 1.90	-60 ± 1.4
Unexposed versus Over-exposed type I	N.S.	N.S.	N.S.
Unexposed versus over-exposed type II	N.S	P<0.01**	N.S.
Over-exposed type I vs over-exposed type II	N.S.	P<0.01**	N.S.

Table 6.12: Analysis of the action potential firing properties at half of the maximal firing frequency. Mean ± s.e.m values for the frequency, the coefficient of variation (CV) and the membrane potential (MP) measured at half maximal frequency (1/2 FMax) in fusiform cells from unexposed and over-exposed rats. P values were obtained with anova one-way tests. N.S. = non significant for P values >0.05. Note the higher coefficient of variations for the over-exposed type II fusiform cells.

	Frequency at Fmax (Hz)	CV at Fmax	MP at Fmax (mV)
Unexposed (n=5)	23 ± 4.7	0.19 ± 0.1	-44 ± 2.9
Over-exposed type I (n=7)	29 ± 2.5	0.05 ± 0.01	-43 ± 1.9
Over-exposed type II (n=5)	15 ± 2.1	1.8 ± 0.6	-53 ± 3.1
Unexposed versus Over-exposed type I	N.S.	N.S.	N.S.
Unexposed versus over-exposed type II	N.S	P<0.05*	N.S.
Over-exposed type I vs over-exposed type II	N.S.	P<0.01**	N.S.

Table 6.13: Analysis of the action potential firing properties at maximal frequency. Mean ± s.e.m values for the frequency, the coefficient of variation (CV) and the membrane potential (HP) measured at maximal frequency in fusiform cells from unexposed and over-exposed rats. P values were obtained with anova one-way tests. N.S. = non significant for P values >0.05. Note the higher coefficient of variations for the over-exposed type II fusiform cells.

At the threshold potential of around -70 mV, the firing pattern of the over-exposed type II cells can be described by the presence of bursts solely. As these cells get more depolarized by about 5 mV, the duration and the frequency of the bursts increased and when cells are depolarized even further, their firing frequency increases even further with a firing pattern consisting of a mixture of bursts and regular firing. This is shown in figures 6.9 C and 6.10 C where an overexposed type II cell fires at 1.6 Hz at its threshold and at 3.4 Hz at about 5 mV above its threshold. When the cell was held at an even more depolarized membrane potential it reaches its maximal firing rate of about 15 Hz (figure 6.11C). Note the presence of bursts and simple action potentials at this final depolarization level. Table 6.11, 6.12 and 6.13 show that despite the presence of bursts in the over-exposed type II fusiform cells, the mean values of firing frequency are all similar between the three cellular subtypes recorded. As over-exposed type II cells fire in bursts, their firing rate is nevertheless more variable compared to the unexposed and the over-exposed type I cells. The fusiform cell in figure 6.9C shows a coefficient of variation of 1.9 at threshold, 1.8 at half maximal frequency (figure 6.10 C), and of 0.4 at maximal frequency (figure 6.11C) and tables 6.11, 6.12 and 6.13 summarize the coefficient of variations for all cell types. Table 6.13 indicates that despite reaching a maximal frequency similar to the unexposed and the over exposed type I cell, the firing pattern of the over-exposed type II cells never reaches the same degree of regularity than the unexposed and the over exposed type I cells (shown by a coefficient of variation of 1.8 ± 1.4 (n=5), 0.2 ± 0.25 (n=5) and 0.05 ± 0.02 (n=6, $P < 0.05$ anova one way) respectively

Acoustic over-exposure therefore modulates the firing pattern of a sub-population of fusiform cells by switching from a highly regular to a more irregular bursting pattern. The firing pattern of the over-exposed type II cells is also different to the firing pattern of the unexposed and the over-exposed type I cells following the injections of 1 second step currents (described in the next section).

6.2.2.3. Acoustic over-exposure decreases the firing frequency of fusiform cells while performing step currents

Fusiform cell excitability following step current injections in Lister Hooded and Wistar rats. Step currents of increasing amplitudes were injected in fusiform cells from a membrane potential of -80 mV. Fusiform cells originating from Wistar rats generally fired with one or a few action potentials (figure 6.12 A left) at a threshold potential which was on average $-54 \pm 2\text{mV}$, ($n=9$) for a step current of $230 \pm 47\text{pA}$, ($n=9$). The firing frequency increased with the amplitude of the step current, reaching a maximal frequency of $83 \pm 11\text{Hz}$, ($n=5$). The maximal firing frequency was similar to the one observed in LH rats (summarized in table 4.6, $P=0.26$, unpaired T test). Similar firing rate slopes were also observed between fusiform cells originating from Wistar rats ($0.09 \pm 0.02 \text{ Hz/pA}$, $n=5$) and fusiform cells originating from LH rats ($0.06 \pm 0.01 \text{ Hz/pA}$, $n=5$, $P=0.11$, unpaired T test). I also analyzed the latency to the first action potential (elicited by the smallest step current triggering action potentials) and observed that in both LH rats (figure 4.18) and in Wistar rats (figure 6.12A), fusiform cells are characterized by a long lasting latency to the first action potential at threshold (i.e. $141 \pm 19\text{ms}$, $n=5$ and $180 \pm 43\text{ms}$, $n=5$ respectively, $P=0.4$, unpaired Student T test). This long latency has been suggested to be dependent on an A-type potassium current (Manis, 1990).

Effects of acoustic over-exposure on the response to step current injections. In the previous section I described the properties of fusiform cells following acoustic over-exposure and showed the presence of a small depolarization preceding the action potentials as well as the presence of bursts in a third of fusiform cells (over-exposed type II cells). When the same over-exposed type II cells were depolarized in response to step currents, they sometimes displayed clusters of action potentials (bursts) within the step potential (one example is shown in figure 6.13) but in the majority of the cases they fired simple action potentials for the whole duration of the step. Characteristics of the action potentials after acoustic over-exposure in Wistar rats are detailed in the table 6.14 below. Action potentials of the over-exposed type II fusiform cells were characterized by an absence of undershoot (shown in figure 6.12C) by contrast to fusiform cells from the unexposed and over-exposed type I population which action potentials were followed by an undershoot (figure 6.12A-B). After acoustic over-exposure, characteristics like the minimal step current necessary to elicit an action potential, the voltage threshold for the action potential and the latency to the first action potential were unchanged between the unexposed, the over-exposed type I and the over-exposed type II cells. Similar maximal firing frequencies were reached between the unexposed and the over-exposed type I fusiform cells ($83 \pm 11\text{Hz}$ ($n=5$) and $100 \pm 23\text{ Hz}$ ($n=5$) respectively, $P > 0.05$, anova one way) by contrast to over-exposed type II fusiform cells which fired with a lower maximal firing frequency $43 \pm 6\text{ Hz}$ ($n=5$, $P < 0.05$ anova one way). Examples of maximal firing for each cell sub-type are shown in figure 6.12 (middle panel) and the firing frequency

plotted in function of the step current for each cell subtype is shown in figure 6.12 right.

	Slope (Hz/pA)	Fmax (Hz)	I threshold (pA)	V threshold (mV)	Latency (ms)
Unexposed (n=5-9)	0.09 ± 0.02	83 ± 11	230 ± 47	-54 ± 2	180 ± 43
Over-exposed I (n=5-7)	0.06 ± 0.01	100 ± 23	264 ± 52	-51 ± 1	202 ± 25
Overexposed II (n=5)	0.56 ± 0.25	43 ± 6	83 ± 15	-53 ± 4	108 ± 29
Unexposed versus Over-exposed type I	N.S.	N.S.	N.S.	N.S.	N.S.
Unexposed versus Over-exposed type II	N.S.	P<0.05*	N.S.	N.S.	N.S.
Over-exposed type I vs Over-exposed type II	P<0.05*	P<0.05*	N.S.	N.S.	N.S.

Table 6.14 Analysis of the action potential firing properties of fusiform cells when injecting step currents in unexposed and over-exposed conditions. Mean ± s.e.m values for the values of the slope, the maximal firing frequency (Fmax), the minimal injected current to elicit an action potential (I threshold), the minimal voltage reached to elicit an action potential from a membrane potential of -80 mV (voltage at threshold and the latency to first action potential (measured at minimal step current that elicited the action potential). Values in brackets are the number of fusiform cells for each condition.

Similar firing rate slopes were observed between the unexposed (0.09 ± 0.02 Hz/pA, n=5) and the over-exposed type I fusiform cells (0.06 ± 0.01 Hz/pA, n=7, P>0.05 anova one way) whereas steeper slopes were observed in the over-exposed type II cells (0.56 ± 0.25 Hz/pA, n=5 p<0.05) suggesting that the over-exposed type II cells reach their maximal firing frequency for the smallest current injections. The over-exposed type II

population could therefore be differentiated from the unexposed and over-exposed type I population using a step current protocol.

In summary, acoustic over-exposure dramatically changed the DCN cellular excitability. This was seen first at the level of granule cells where both passive and active properties were modulated to lead to a reduced firing gain. Acoustic over-exposure also affected the active properties of a significant proportion of fusiform cells by introducing bursts and decreasing their maximal firing frequency (significant in the step current protocol). Fusiform cells receive direct projections from granule cells (via parallel fibres which represent the multisensory inputs to the DCN) and their firing activity is therefore modulated by the granule cell firing. Multisensory and auditory synaptic transmission onto fusiform cells will be analyzed in the next chapter.

6.3. Effects of acoustic over-exposure on synaptic transmission in the dorsal cochlear nucleus

6.3.1. Stimulation of multisensory and auditory inputs

Excitatory and inhibitory synaptic inputs originating from the auditory nerve were evoked by placing the stimulating electrode in the DCN deep layer whereas multisensory synaptic inputs were stimulated by placing the stimulating electrode in the molecular layer (figure 6.14). The influence of acoustic over-exposure onto the synaptic transmission originating from those two separate inputs is unstudied. Unstudied is also the role of inhibitory inputs within those two pathways. To understand the functional relevance of inhibitory synaptic inputs onto fusiform cells, the inhibitory inputs were abolished by strychnine (10 μ M) and gabazine (20 μ M) in order to block glycine and GABA_A receptors respectively. Fusiform cells were held between -60 mV and -70 mV and the equilibrium potential for chloride was set at -90 mV (see methods 2.2.7.3) to discriminate between depolarizing excitatory postsynaptic potentials (EPSPs) and hyperpolarizing inhibitory postsynaptic potentials (IPSPs). Post synaptic responses were evoked by low frequency stimulations (0.3 Hz) to avoid a possible run down of the synaptic responses due to vesicular depletion or other short term plastic modulation (Thomson 2000; Neher and Sakaba, 2008). Characteristics of the post-synaptic potentials such as peak and area were reported as well as the action potential peak, rise time, decay time and latency. This last parameter allowed determining the spike timing of fusiform cells. This is important as precise spike timing is crucial in the information encoding (Abeles et al., 1993; Berry et al., 1997; Nowak et al., 1997; Buonomano, 2003).

6.3.1.1. Post-synaptic responses evoked by stimulating multisensory inputs

Characteristics of the EPSP and the IPSP. When fusiform cells were held at -70 mV, stimulating the parallel fibres at low voltage (around 10 V) elicited a small EPSP in fusiform cells (threshold voltage for the EPSP, figure 6.15A second trace from top) that increased in amplitude while increasing the strength of the stimulus (to 15-20 V) (figure 6.15A third and last trace from the top) until an action potential was elicited (threshold of the action potential at around 25V) (figure 6.15B). The direction of the synaptic response makes it an EPSP but it is well understood that this response is a mixed EPSP representing a mixture of excitatory (depolarizing, EPSP) and inhibitory (hyperpolarizing, IPSP) synaptic inputs (Zhang and Oertel, 1994). The total synaptic inputs were first recorded in control medium (mixed EPSP) and subsequently strychnine and gabazine were applied to the bath, in order to record the EPSP in isolation. As predicted, the amplitude of the EPSP (in isolation) has increased while blocking the inhibitory inputs to the cell (figure 6.16B upper right panel). Subtracting the EPSP in isolation (recorded in strychnine and gabazine) from the mixed EPSP (recorded in control medium) allowed isolating the inhibitory postsynaptic potentials (IPSP, figure 6.16 lower right panel). Figure 6.16A also shows that threshold stimulating voltages (for the mixed EPSP) elicited preferentially EPSPs and that IPSPs were absent in 6 out of 8 fusiform cells for those threshold voltages. Increasing the stimulus voltage of 5V (to 15-20V, figure 6.16B) elicited an IPSP which was smaller compared to the EPSP. This is detailed in figure 6.17 and the table 6.15 below summarizes values obtained for the peak amplitude (mV) and the area (mV·ms) for the EPSPs (in isolation) and the IPSPs (in isolation) elicited at 5 V above the threshold voltage for the mixed EPSP.

	Peak (mV)	Area (mV.ms)
EPSPs	5.5 ± 0.6	216 ± 35
IPSPs	2.0 ± 0.4	83 ± 17
P, Paired T test	0.0002**	0.002**

Table 6.15: Characteristics of the EPSPs (in isolation) and the IPSPs (in isolation) recorded in fusiform cells following stimulation of the multisensory inputs. Inputs are stimulated at 5 V above the threshold voltage for the mixed EPSP and cells held at -70 mV. Mean ± s.e.m values of the peak amplitude (mV) and the area (mV*ms) are reported for 8 cells and P values comparing the characteristics are obtained using a paired Student's T test (** P ≤0.01). Note the larger EPSP peaks and areas compared to the IPSPs. Abbreviations: (EPSP) excitatory post synaptic potential, (IPSP) inhibitory post synaptic potential.

In summary, stimulation of the parallel fibres elicited EPSPs in fusiform cells that are predominant to the IPSPs in terms of amplitude and area. Excitatory inputs were also recruited prior to the inhibitory inputs and action potentials could be elicited upon increasing the stimulus voltage (see below)

Characteristics of the action potential. Fusiform cells fired simple action potentials (figure 6.18) in response to stimulating the parallel fibres with a peak, rise time and decay time summarized in the table 6.16 below. Half of the fusiform cells (5 out of 10 cells) fired with a small undershoot (hyperpolarization) following the action potential (figure 6.18A) whereas the other half displayed instead a clear depolarizing phase following the action potential (figure 6.18B). I did not investigate the nature of this depolarizing phase but hypotheses regarding its origin are discussed in section 6.7.2.

	Amplitude (mV)	10-90% rise time (ms)	90-10% decay time (ms)
Control	87 ± 4.8	1.1 ± 0.2	1.0 ± 0.09
Strychnine and gabazine	78 ± 4.6	0.9 ± 0.2	1.2 ± 0.2
P, Paired T Test	0.04*	0.26	0.34

Table 6.16: Characteristics of the action potential evoked by stimulation of the multisensory inputs in control medium and in presence of strychnine and gabazine. Stimulation was at 0.3 Hz while membrane the fusiform cell at -70 mV. Values represent the mean ± s.e.m for 6 cells and P values are obtained using a paired Student's T test (* P ≤ 0.05). Note that blocking the inhibitory synaptic transmission decreased the amplitude of the evoked action potential

When the inhibitory inputs were removed by the addition of strychnine and gabazine, action potentials were still characterized by their original over- and undershoot phase but the amplitude of the action potentials was decreased by about 10 mV. Their 10-90% rise time and the 90-10% decay time were left unaffected (table 6.16). Possible reasons for the effect on the amplitude are discussed in section 6.7.2. I next investigated the latency to the peak of the fusiform action potential in response to multisensory input stimulation. Twenty-five to forty action potentials were taken into account for each fusiform cell and measurements were repeated in presence of strychnine and gabazine (figure 6.19A). The time to the action potential peak showed little variation in control medium (accurate spike timing) by contrast to a larger variation of the time to the peak observed in presence of strychnine and gabazine as shown in the example in figure 6.19B where the standard deviation of the time to the peak doubled from 0.14 to 0.28 in presence of strychnine and gabazine ($P = 6 \times 10^{-6}$, F test). This pattern was present in 7 out of 10 cells and results are summarized in

the table 6.17 below. This result indicates that the inhibitory inputs carried by the multisensory system ensure the accurate spike timing in fusiform cells. A possible reason for this has been investigated in section 6.3.1.3 and is discussed in section 6.7.3.

	Time to the peak (ms)		
	Control	Strychnine and gabazine	FTEST
Cell 1	26.2 ± 0.30, n=25	26.7 ± 0.82, n=25	P=0.0002**
Cell 2	24.1 ± 0.17, n=30	26.6 ± 0.12, n=30	P=0.056
Cell 3	26.6 ± 0.18, n=30	26.4 ± 0.26, n=30	P=0.047*
Cell 4	22.9 ± 0.17, n=30	23.4 ± 0.26, n=30	P=0.039*
Cell 5	22.6 ± 0.04, n=37	22.3 ± 0.07, n=37	P=0.038*
Cell 6	24.6 ± 0.33, n=38	23.4 ± 0.21, n=38	P=0.011
Cell 7	23.1 ± 0.12, n=40	22.8 ± 0.21, n=40	P=0.0029**
Cell 8	24.3 ± 0.14, n=40	24.6 ± 0.28, n=40	P=0.00006**
Cell 9	27.4 ± 0.29, n=30	27.3 ± 0.56, n=30	P=0.0004**
Cell 10	23.0 ± 0.20, n=30	23.1 ± 0.12, n=30	P=0.006*

Table 6.17: Summary table representing the individual values of the time to the peak obtained for each fusiform cell after stimulating the multisensory inputs. Same experimental conditions than in figure 6.19 with 25-40 action potentials recorded for each cell (n). P values are obtained with the F test (* P ≤0.05), (P ≤0.01) comparing the S.D. value of the time to the peak in control condition with the S.D. value obtained in presence of strychnine and gabazine. Note that in 7 out the 10 cells, the S.D. is significantly larger in presence of strychnine and gabazine (stars) whereas cells 2, 6 and 10 were characterized by either a similar (cell 2) or a smaller S.D value (cells 6 and 10) between the two conditions. Cells 8, 9, 10 are from LH rats whereas all the other cells are from Wistar rats.**

6.3.1.2 .Post-synaptic responses evoked by stimulating auditory inputs

Characteristics of the EPSP and the IPSP. While stimulating the auditory fibres, fusiform cells were initially held at the same potential (-70 mV) as previously reported in section 6.3.1.1. The minimal stimulus voltage (threshold voltage) to induce a mixed EPSP was higher after stimulating auditory inputs than after stimulating multisensory inputs (i.e. 19 ± 3.5 V, $n=4$ and 12 ± 0.7 V $n=8$, respectively, $P = 0.02$, unpaired T test). Increasing the stimulus voltage while stimulating the auditory inputs (up to 40-50 V) also increased the EPSP amplitude without eliciting any action potential in 4 out of 5 fusiform cells (a typical example is represented in figure 6.20). The graph in figure 6.21 compares the mixed EPSP peak amplitude evoked by stimulating the multisensory inputs with the mixed peak EPSP amplitude evoked by stimulating the auditory inputs and shows clearly the difference in the voltage threshold of the mixed EPSP evoked by stimulating multisensory or auditory inputs to two distinct fusiform cells. Figure 6.21 also shows the difference in the maximal amplitude of the mixed EPSP evoked by stimulating multisensory or auditory inputs to the two cells (determined by the activation of the action potential in the case of the multisensory input stimulation and by the relationship reaching a plateau phase in the case of the auditory input stimulation). Those differences in the threshold stimulus voltages could be due to less excitatory fibre recruitment whereas differences in the maximal mixed EPSP peak amplitudes could be due to fibres reaching a saturation level after stimulating auditory inputs (for example at a stimulus voltage of 30 V for the cell represented in figures 6.20 and 6.21). Differences could also be due to the strength of the inhibitory inputs that counteracts the amplitude of the depolarizing synaptic potential as the EPSP shown in figure 6.20 represents a mixture of excitatory and inhibitory synaptic

potentials (mixed EPSP similar to the mixed EPSP previously described for multisensory input stimulation). To discriminate between those two hypotheses, the total synaptic inputs were first recorded in control medium (to record mixed EPSPs) and subsequently strychnine and gabazine were applied to the bath, in order to record the EPSP in isolation. As expected in the case of a strong recruitment of inhibitory inputs while recording mixed EPSPs, the amplitude of the EPSP (in isolation) has increased while blocking inhibitory inputs to the cell (figure 6.22A and B right). When applying minimal threshold voltages (for the mixed EPSPs), a clear IPSP could be evoked in all 4 fusiform cells after auditory input stimulation (figure 6.22A right) whereas the same conditions applied to multisensory inputs only elicited IPSPs in one third (2 out of 6) of the fusiform cells (figure 6.16A right). When inputs were stimulated at 5V exceeding the voltage threshold (i.e. 17 V and 25 V for the multisensory and the auditory inputs respectively), all fusiform cells displayed an IPSP (independently of the inputs). I therefore analyzed EPSPs in isolation and IPSPs in isolation at those “supra threshold” stimulus voltages (table 6.18 below).

	Peak (mV)	Area (mV*ms)
EPSPs	7.3 ± 2	417 ± 99
IPSPs	3.9 ± 0.9	269 ± 58
P, Paired T test	0.06	0.05 *

Table 6.18: Characteristics of the EPSPs (in isolation) and the IPSPs (in isolation) recorded in fusiform cells following stimulation of the auditory inputs. Inputs are stimulated at 5 V above the threshold voltage for the mixed EPSP and cells held at -70 mV. Mean ± s.e.m values of the peak amplitude (mV) and the area (mV*ms) are reported for 4 cells and P values comparing the characteristics are obtained using a paired Student’s T test (* P ≤ 0.05). Note the larger EPSP areas compared to the IPSP areas. Abbreviations: (EPSP) excitatory post synaptic potential, (IPSP) inhibitory post synaptic potential.

Tables 6.15 and 6.18 describe the properties of the EPSP and the IPSP when stimulating multisensory and auditory inputs respectively. The table 6.19 below allows a direct comparison of the EPSP and the IPSP evoked by stimulating the multisensory or auditory inputs.

	EPSP Peak (mV)	EPSP Area (mV*ms)	IPSP Peak (mV)	IPSP Area (mV*ms)
Multisensory (n=8)	5.5 ± 0.6	216 ± 35	2.0 ± 0.4	83 ± 17
Auditory (n=4)	7.3 ± 2	417 ± 99	3.9 ± 0.9	269 ± 58
P, Unpaired T test	0.31	0.03*	0.04*	0.003**

Table 6.19: Comparison of the EPSPs (in isolation) and the IPSPs (in isolation) recorded in fusiform cells following stimulation of the multisensory or auditory inputs. Inputs are stimulated at 5 V above the threshold voltage for the mixed EPSP and cells held at -70 mV. Mean ± s.e.m values of the peak amplitude (mV) and the area (mV*ms) are reported and P values comparing the characteristics are obtained using an unpaired Student's T test (* P ≤0.05, ** P≤0.01). Note larger EPSP areas as well as larger IPSP peaks and IPSP areas when stimulating the auditory inputs comparing to stimulating the multisensory inputs. Abbreviations: (EPSP) excitatory post synaptic potential, (IPSP) inhibitory post synaptic potential.

The EPSP amplitude was similar after stimulation auditory or the multisensory inputs whereas the EPSP area was larger when stimulating the auditory inputs compared to the EPSP evoked by stimulating the multisensory inputs. Both IPSP peaks and IPSP areas were larger when evoked by auditory input stimulation by comparison to multisensory input stimulation (shown in figure 6.23 and summarized in the table 6.19 above). This clearly indicates that the stronger inhibition elicited upon auditory input stimulation compared to multisensory input stimulation is responsible for the differences in the maximal mixed EPSPs. I hypothesized above that the difference in the mixed EPSP maximal amplitudes could have been due to a minimal recruitment of excitatory fibres that reach a saturation level after stimulating auditory inputs and therefore

lead to smaller EPSPs when compared to the EPSPs obtained after multisensory stimulation. The analysis of the isolated EPSP characteristics shows that this is not the case as the EPSPs evoked upon auditory stimulation were either similar (peak) or larger (area) when compared to the EPSPs evoked upon multisensory stimulation. Peak and the area ratios of the IPSP relative to the EPSP were also larger after stimulating the auditory inputs by comparison to stimulating the multisensory inputs (see table 6.20 below).

	(IPSP Peak) / (EPSP Peak)	(IPSP Area) / (EPSP Area)
Multisensory (n=8)	0.35 ± 0.05	0.38 ± 0.04
Auditory (n=4)	0.56 ± 0.04	0.64 ± 0.05
P, Unpaired T test	0.01**	0.04*

Table 6.20: Comparison of the ratios of the IPSPs (in isolation) relative to the EPSPs (in isolation) following stimulation of the multisensory or auditory inputs. Inputs are stimulated at 5 V above the threshold voltage for the mixed EPSP and cells held at -70 mV. Mean ± s.e.m are reported and P values comparing the characteristics are obtained using an unpaired Student's T test (* P ≤0.05, ** P≤0.01). Note the larger peak and area ratios when stimulating the auditory inputs comparing to stimulating the multisensory inputs. Abbreviations: (EPSP) excitatory post synaptic potential, (IPSP) inhibitory post synaptic potential.

Results therefore indicate that a strong inhibitory component rather than a weak excitatory component contributes to the overall small mixed EPSP observed after stimulating the auditory inputs and this inhibitory component is responsible for preventing fusiform cells from firing an action potential.

Characteristics of the action potential. Fusiform cells were held at a depolarized membrane potential (i.e. -60 mV instead of -70 mV) to elicit action potentials when stimulating auditory inputs. At this depolarized membrane potential, stimulus voltages of 45 ± 5 V (n= 4) induced simple action potentials

in 4 out of 5 cells (an example is given in figure 6.24B) that were followed by an undershoot, similarly to previously described for the action potentials triggered by multisensory input stimulation. Whereas the voltage required to elicit action potentials was higher compared to stimulus voltages used while stimulating multisensory inputs (i.e. 45 ± 5 V, $n=4$ and 25 ± 2 V, $n=6$, $P=0.002$, for auditory and multisensory stimulation respectively, unpaired T test), action potentials main characteristics were similar when stimulating multisensory or auditory inputs (detailed in tables 6.21 and 6.22 below). It is worth noting that action potentials characteristics were similar when evoked by auditory or multisensory input stimulation despite the difference in the membrane potential that could have generated variations. A depolarizing phase following the action potential was observed in fifty per cent of the cells after multisensory input stimulation (figure 6.18). This depolarizing phase was only present in twenty per cent (1 out of 5) cells after stimulation of the auditory inputs. This difference in the proportion of cells expressing the depolarizing phase is not significant as shown by the Chi-square test ($P=0.18$) and a higher number of action potentials is required to analyse the relevance of this apparent difference.

In the previous section, I described that blocking inhibitory inputs decreased the action potential amplitude. Repeating the same experiment (adding strychnine and gabazine while stimulating the auditory inputs) left the characteristics of the evoked action potentials unaffected (summarized in table 6.21 below). Also, all action potentials were still followed by an undershoot in presence of strychnine and gabazine (figures 6.25A right and 6.26A right).

	Amplitude (mV)	10-90% rise time (ms)	90-10% decay time (ms)
Control	86 ± 3.5	0.9 ± 0.5	0.8 ± 0.09
Strychnine and gabazine	80 ± 3.4	0.9 ± 0.4	0.8 ± 0.07
P, Paired T Test	0.16	0.90	0.31

Table 6.21: Characteristics of the action potential elicited by stimulation of the auditory inputs in control medium and in presence of strychnine and gabazine. Stimulation was at 0.3 Hz while fusiform cell membrane potential was -60 mV. Values represent the mean ± s.e.m for 4 cells and P values are obtained using a paired Student's T test. Note that blocking the inhibitory synaptic transmission does not affect the characteristics of the action potential.

Finally the action potentials evoked by stimulation of the multisensory or the auditory inputs displayed a similar amplitude, 10-90% rise time and 90-10% decay time (summarized in the table 6.22 below).

	Amplitude (mV)	10-90% rise time (ms)	90-10% decay time (ms)
Multisensory (n=6)	87 ± 4.8	1.1 ± 0.2	1.0 ± 0.09
Auditory (n=4)	86 ± 3.5	0.9 ± 0.5	0.8 ± 0.09
P, Unpaired T Test	0.80	0.70	0.15

Table 6.22: Comparison of the action potential characteristics following stimulation of the multisensory or auditory inputs in control medium. Stimulation was at 0.3 Hz while membrane potential of the fusiform cell was at -70 mV (multisensory stimulation) or at -60 mV (auditory stimulation). Mean ± s.e.m are reported and P values comparing the characteristics are obtained using an unpaired Student's T test. Note that the action potential characteristics were similar when stimulating the multisensory inputs comparing to stimulating the auditory inputs.

I next investigated the latency to the peak of the fusiform cell action potential in response to auditory input stimulation. Twenty-five to thirty action potentials were taken into account for each fusiform cell and measurements were repeated in presence of strychnine and gabazine (two typical examples

are shown in figures 6.25 and 6.26). While stimulating multisensory inputs (section 6.3.1.1), I observed that action potentials were strictly timed to the stimulus showing a small variation of the time to the action potential peaks in control medium (mean standard deviations of 0.2 ± 0.03 , $n=10$ cells). When stimulating auditory inputs I observed that this was not the case (figures 6.25 and 6.26) with the time to the action potential peaks displaying larger variations in the control condition (mean standard deviations of 5 ± 3 ms, $n= 6$ cells, $P= 0.05$, unpaired T test). When stimulating multi sensory inputs, I also showed that the accurate spike timing was due to the presence of inhibitory inputs. Repeating the same experiment (adding strychnine and gabazine while stimulating the auditory inputs) did not affect the S.D value in 50 % (3/6) of the cells (see the example in figure 6.25B showing S.D. values of 0.67 and 0.51 in control and in presence of strychnine-gabazine respectively, $P= 0.19$, F test). In the other half of the population (3/6), the S.D. became smaller in strychnine and in gabazine ($P <0.05$, F test, typical example given in figure 6.26). A detailed analysis of the cells is given in the table 6.23 below. In conclusion, when action potentials are evoked by auditory input stimulation in a normal control medium, they display a variable spike timing by contrast to the precise action potential timing observed when stimulating multisensory inputs. Furthermore, blocking inhibitory inputs either generates more or generates less variation of the action potential timing when stimulating multisensory or auditory inputs respectively. To investigate this phenomenon further, similar experiments were performed in voltage clamp and this is described in the next section.

	Time to the peak (ms)		
	Control	Strychnine and gabazine	F test
Cell 1	29.8 ± 1.11, n=10	26.9 ± 1.95, n=10	P=0.11
Cell 2	28.8 ± 1.91, n=30	24.5 ± 2.35, n=30	P=0.25
Cell 3	36.2 ± 20.2, n=30	18.9 ± 1.20, n=30	P=4·10 ^{-12**}
Cell 4	26.4 ± 1.37, n=30	23.2 ± 0.49, n=30	P=2·10 ^{-7**}
Cell 5	24.1 ± 0.67, n=26	23.6 ± 0.51, n=26	P=0.19
Cell 6	29.2 ± 4.66, n=15	24.87 ± 0.8, n=30	P=6·10 ^{-8**}

Table 6.23: Summary table representing the individual values of the time to the peak obtained for each fusiform cell after stimulating the auditory inputs, Same experimental conditions than in figure 6.25 with 10-30 action potentials recorded for each cell (n= 6 cells). P values are obtained with the F test (P≤0.01) comparing the S.D. value of the time to the peak in control condition with the S.D. value obtained in presence of 10 μM strychnine and 20 μM gabazine. Note that jittering action potentials were unaffected by gabazine and strychnine in cells 1, 2 and 5 whereas action potentials became more timed in presence of strychnine and gabazine in cells 3, 4 and 6. Cells 4, 5 and 6 are coming from LH rats and cells 1, 2, and 3 are coming from Wistar rats.**

6.3.1.3. Post-synaptic currents recorded in voltage clamp

The precision of the action potential timing depends on the membrane time constant and as well on fluctuations in both excitatory and inhibitory inputs (Häusser and Clark, 1997; Jaeger and Bower 1999; Azouz and Gray, 2000; Gauck and Jaeger, 2000; 2003). Several studies showed that inhibitory inputs are particularly important in ensuring the temporal fidelity of the action potentials (Häusser and Clark, 1997; Gauck and Jaeger, 2000; Pouille and Scanziani, 2000) and that the time window of their integration with the excitatory inputs is crucial to the temporal fidelity (Pouille and Scanziani, 2000). I checked whether fusiform cells might employ similar strategies and I analyzed the integration

window between the excitatory and the inhibitory component. In order to record the underlying synaptic events following multisensory or auditory stimulation without eliciting any action potential, experiments were performed in voltage clamp mode (see methods). Multisensory or auditory inputs were stimulated at 0.3 Hz and cells were voltage clamped at -60 mV. Excitatory and inhibitory postsynaptic currents (EPSCs and IPSCs respectively) were obtained as described above for the EPSPs and IPSPs (EPSCs were recorded in strychnine and gabazine and IPSCs were obtained by subtracting the trace recorded in strychnine and gabazine (EPSCs) from the trace recorded in control medium). As previously reported for the current clamp recordings, I observed that the stimulation of the auditory fibres elicited larger IPSCs compared to the IPSCs evoked by multisensory fibres stimulation (shown in figure 6.27). Additionally when stimulating the multisensory fibres, the onset of the IPSC was delayed by 6.8 ± 0.2 ms (n=3) with respect to the EPSC whereas both IPSC and EPSC were simultaneously triggered when stimulating the auditory fibres (i.e. no delay). A representative example is shown for two cells in figure 6.27 where the 7 ms delay between the IPSC and the EPSC elicited by the multisensory input stimulation contrasts with the absence of delay after auditory input stimulation. In conclusion, my results suggest that EPSCs evoked upon stimulation of the multisensory inputs are carried via a monosynaptic pathway directly from the parallel fibres to the fusiform cells whereas the late IPSCs could be mediated through a polysynaptic pathway where parallel fibres activate cartwheel cells that inhibit fusiform cells. Late IPSCs could constrict EPSCs in a specific time window and therefore enable the precise spike timing of fusiform cells. This could explain why this precision is lost when inhibitory inputs are blocked. By

contrast, stimulating the auditory nerve results in the concomitant activation of the EPSC and the IPSC suggesting that excitatory inputs coming from the auditory nerve are coincident to the inhibitory inputs located in the DCN deep (presumably tuberculoventral cells). By contrast to the multisensory system stimulation, spike timing seems to be less relevant when stimulating the auditory nerve. Instead, IPSCs synchronous to the EPSCs contribute to generating a powerful concomitant inhibition.

6.3.2. Effect of acoustic over-exposure on multisensory and auditory synaptic transmission

6.3.2.1. Effect of acoustic over-exposure on the post synaptic responses evoked by stimulation of the multisensory inputs

In section 6.2.1.1 I described how acoustic over-exposure modulated granule cell active and passive properties. In the following section, I will report how these changes could translate onto fusiform cell excitability and therefore analyze synaptic inputs and action potentials evoked by parallel fibre stimulation in acoustically over-exposed rats.

Characteristics of the EPSP and the IPSP. Acoustic over-exposure damages cochlear sensory hair cells (inner and outer hair cells) that in turn decrease the cellular excitability of the auditory nerve. Compensatory mechanisms could be generated at the level of the central auditory system as changes in the excitatory and/or inhibitory transmission would occur to restore the original level of activity of the peripheral auditory fibres. Considering that granule cells receive inputs from multiple sensory sources and also from auditory projections originating from the outer hair cells, I expect to see an effect of acoustic over-

exposure on the synaptic signals elicited while stimulating granule cell axons (parallel fibres).

Fusiform cells were recorded in similar conditions like previously described for the unexposed conditions. They were held at -70mV and their multisensory inputs were stimulated first at minimal voltage (threshold voltage) to induce a mixed EPSP then with increasing stimulating voltages. A striking difference compared to the unexposed conditions was linked to the threshold voltage that was higher ($16 \pm 1.8V$, $n=6$) when rats were previously exposed to a high intensity sound compared to the unexposed rats (i.e. $12 \pm 0.8V$, $n=8$, $P=0.042$, unpaired T test, see also figure 6.28). This could be due to a decrease of the recruitment of excitatory parallel fibres and/or to an increase of the recruitment of inhibitory inputs counteracting the depolarizing effects of the excitatory inputs. I next elicited a mixed EPSP and pharmacologically separated in isolated EPSPs and isolated IPSPs. I further observed that IPSPs were still absent in the majority (4/6) of the fusiform cells at threshold stimulating voltages and this indicates that, similarly to the unexposed condition, excitatory inputs were still recruited at lower voltages compared the inhibitory inputs after acoustic over-exposure. When supra-threshold voltages were applied (5 V above the threshold voltage), EPSPs were elicited in all 6 fusiform cells whereas the IPSPs were present in only 4 of the 6 cells. This is different from the unexposed condition where EPSPs and IPSPs were elicited in all fusiform cells. Altogether, these results indicate that after acoustic over-exposure, both EPSPs and IPSPs in isolation are recruited at a higher threshold voltage. This could be due to the degeneration of a proportion of inhibitory and excitatory fibres leading to higher voltages required to stimulate the remaining functional

excitatory and inhibitory fibres. Fibre degeneration is likely to translate into a decrease of the amplitude and the area of the isolated EPSP and IPSP. Nevertheless isolated EPSPs and isolated IPSPs had a similar amplitude and a similar area compared to the unexposed conditions (figures 6.29, 6.30 and table 6.24 below) and this could be explained by a general increase of the activation threshold of the inhibitory and the excitatory fibres linked to changes of the presynaptic passive membrane properties and unrelated to cell death. Indeed, in section 6.2.1.1, I have described that following acoustic over-exposure, granule cells have got more hyperpolarized resting potentials and this could be responsible to the higher activation threshold observed here (this will be discussed further in the discussion section).

	EPSP peak (mV)	EPSP area (mV*ms)	IPSP peak (mV)	IPSP area (mV*ms)
Unexposed (n=8)	5.5 ± 0.6	216 ± 35	2.0 ± 0.4	83 ± 17
Over-exposed (n=4-6)	3.7 ± 0.5	142 ± 21	1.0 ± 0.5	42 ± 18
P, Unpaired T test	0.22	0.11	0.33	0.13

Table 6.24: Comparison of the multisensory input evoked EPSP and IPSP between unexposed and over-exposed condition. Stimulation intensities were set at 5 V above the threshold voltage for the mixed EPSP. Mean ± s.e.m are reported and P values comparing the characteristics are obtained using an unpaired Student's T test. Note that the EPSPs and IPSP peaks and areas are unaffected after acoustic over-exposure.

Characteristics of the action potential. At supra-threshold voltages, fusiform cells fired simple action potentials with characteristics similar to the one described in section 6.3.1.1 for the unexposed conditions (summarized in table 6.16). Similar to the unexposed condition, half of the fusiform cells (3 out of 6 cells) fired with an undershoot following the action potential whereas the other half of the fusiform cells displayed a depolarizing phase following the action

potential (not shown). When the inhibitory inputs were pharmacologically blocked, the action potential amplitude was decreased from 90 ± 5.3 mV to 75 ± 4.1 mV ($n=5$, $P=0.03$) whereas the 10-90% rise time and the 90-10% decay time were left unaffected (see table 6.25). The same pattern was also observed in cells coming from unexposed rats and the possible reasons of this effect are discussed in section 6.7.2. Action potential evoked by multisensory stimulations were unaffected by acoustic over-exposure with P values (unpaired T test comparing values in table 6.16 and table 6.25) of 0.37, 0.12 and 0.79 for the amplitude, the 10-90% rise time and the 90-10% decay time respectively).

	Amplitude (mV)	10-90% rise time (ms)	90-10% decay time (ms)
Control	90 ± 5.3	1.8 ± 0.3	1.0 ± 0.15
Strychnine and gabazine	75 ± 4.6	1.1 ± 0.3	1.0 ± 0.1
P, Paired T Test	0.03*	0.08	0.96

Table 6.25: Analysis of the action potential amplitude, the 10-90% rise time and 90-10% decay time after acoustic over-exposure. Action potential was evoked by stimulating the multisensory inputs at 0.3 Hz while membrane the fusiform cell at -70 mV in over-exposed condition. Means \pm s.e.m for 4 cells are reported in control medium and in presence of 10 μ M strychnine and 20 μ M gabazine. P values were obtained using a paired Student's T test. (* $P \leq 0.05$) Note the decrease of the action potential amplitude in presence of strychnine and gabazine.

I next investigated the effect of acoustic over-exposure on the time to the action potential. Figure 6.31A shows a representative example of 30 superimposed traces of a fusiform cell firing in control medium and in strychnine and gabazine with the time to the action potential peak showing a large variation in control medium (S.D. of 3.7) that is significantly decreased to 0.28 ($P= 6.3 \cdot 10^{-17}$, F test) in presence of strychnine and gabazine. This pattern was present in 3 out of 5 cells and results are summarized in table 6.26. This is the opposite effect to

the effect described in the unexposed condition where the action potentials were precisely timed (small S.D.) in control medium and become less timed (S.D. increased) in strychnine and gabazine. In paragraph 6.3.1.3 I suggested that the precise spike timing observed upon multisensory input stimulation could be related to the delay that exists between the EPSP and the IPSP (or between the EPSC and the IPSC), variations in this delay could also be responsible for the effect on the time to the peak.

	Time to the peak (ms)		
	Control	Strychnine and gabazine	FTEST
Cell 1 (n=30)	36.1 ± 3.72	28.3 ± 0.28	P=6·10 ⁻¹⁷ **
Cell 2 (n=30)	26.6 ± 0.19	26.4 ± 0.21	P=0.5
Cell 3 (n=30)	26.9 ± 0.25	25.5 ± 0.17	P=0.05 *
Cell 4 (n=21)	26.5 ± 0.51	23.7 ± 0.32	P=0.05 *
Cell 5 (n=30)	23.6 ± 0.22	24.3 ± 0.68	P=3·10 ⁻⁸ **

Table 6.26 Summary table representing the time to the action potential peak obtained for each fusiform cell after acoustic over-exposure. Twenty to thirty action potentials were evoked by stimulating the multisensory inputs at 0.3 Hz while the fusiform cell membrane potential was -70 mV in control condition and in presence of 10 μ M strychnine and 20 μ M gabazine. P values (*P \leq 0.05, **P \leq 0.01) are obtained with the F test comparing the S.D. value of the time to the peak in control condition with the S.D. value obtained in presence of strychnine and gabazine. Note that in 3 out the 5 cells the S.D. is significantly smaller in presence of strychnine and gabazine (stars) whereas similar S.D. values were obtained in one cell (cell 2). Only cell 5 showed a larger S.D. after blocking the inhibitory inputs with strychnine and gabazine

6.3.2.2. Effect of acoustic over-exposure on the synaptic responses evoked by stimulation of auditory inputs

Effects on the EPSP and the IPSP. Fusiform cells were recorded in similar conditions like previously described for the unexposed conditions. They were held at -70 mV and the auditory inputs were stimulated first at minimal voltage

(threshold voltage) to induce a mixed EPSP then with increasing voltages above the threshold voltage. The minimal voltage (threshold voltage) to induce a mixed EPSP was 30 ± 7 V (n=6) similar to the 19 ± 3.5 V (n=4, P=0.2, unpaired T test) used in the unexposed condition and this constitutes a difference to the effect of acoustic over-exposure elevating the threshold voltages while stimulating multisensory inputs. As the amplitude of the stimulus increased (up to 50V) the amplitude of the mixed EPSP increased until a plateau was reached as previously found for the unexposed condition. After acoustic over-exposure, cells therefore never reached the threshold for the action potential at a membrane potential of -70 mV (figure 6.32).

The mixed EPSP was then pharmacologically separated to obtain EPSPs and IPSPs in isolation (figure 6.33). Similarly to the unexposed condition, IPSPs were evoked at threshold stimulus voltages concomitantly to the EPSPs after acoustic over-exposure. IPSPs represented also a significant proportion of the total synaptic inputs (see figure 6.33 and 6.34A). At threshold voltages, EPSP and IPSP peak and areas were similar between the unexposed and the over exposed-conditions. When increasing the stimulus voltage to 5V above threshold, the amplitude and the area of the IPSPs (see figure 6.34B) decreased by about two third after acoustic over-exposure compared to the values recorded in the unexposed conditions (details and P values found in table 6.27 below). EPSP peaks and areas also seem to be decreased after acoustic over-exposure (see figure 6.34B and table 6.27) but values failed to reach significance (P=0.1 and P=0.09, unpaired T test). A statistical power test (explained in the methods section) performed on the measurements of EPSP peaks and areas gave values of 41.3% and 43.9%, thereby assessing that the

lack of significance was due to the small number of data within the samples. Fifteen cells for each group would be required to get a 5% degree of significance (i.e. and get a power of 95%). To overcome the absence of significance, I measured the first EPSP elicited upon 10 Hz stimulations (delivered at 50 – 60V, section 6.4. below) and observed EPSP peaks of 10 ± 1 mV (n=5) significantly decreased to 5 ± 1 mV (n=5, P=0.02 unpaired T test) after acoustic over-exposure. While using data modelling (section 6.4.3.), I considered that EPSP peaks were decreased by half.

Altogether, acoustic over-exposure did not affect the ratio of the IPSP area relative to the EPSP area (0.64 ± 0.05 (n=4) and 0.33 ± 0.11 (n=5), P=0.07 (unpaired T test), in the unexposed condition and after acoustic over-exposure respectively) whereas it significantly decreased the ratio of the IPSP peak relative to the EPSP peak (from 0.56 ± 0.04 (n=4) to 0.43 ± 0.02 (n=5), P=0.03, unpaired T test).

	EPSP Peak (mV)	EPSP Area (mV*ms)	IPSP Peak (mV)	IPSP Area (mV*ms)
Unexposed (n=4)	7.3 ± 2	417 ± 99	3.9 ± 0.9	269 ± 58
Over-exposed (n=5)	3.6 ± 0.9	229 ± 53	1.5 ± 0.3	85 ± 43
P, Unpaired T test	0.11	0.09	0.03*	0.03*

Table 6.27: Comparison of the auditory input evoked EPSP and IPSP between unexposed and over-exposed condition. Stimulation intensity was set at 5 V above the threshold voltage for the mixed EPSP. Mean \pm s.e.m are reported and P values comparing the characteristics are obtained using an unpaired Student's T test (*P \leq 0.5). Note the decrease of the IPSP peaks and amplitudes after acoustic over-exposure.

Therefore, acoustic over-exposure affects both excitatory and inhibitory auditory synaptic transmission. Auditory fibres project onto tuberculoventral

cells projecting onto fusiform cells and the reduction of the IPSPs could reflect the diminished activity of auditory nerve fibres (see discussion).

Effects on the action potential. I next examined the effect of acoustic over-exposure using supra-threshold stimulation voltages whereby a larger amount of fibres are recruited in order to elicit an action potential in fusiform cells. Although the inhibitory component was found to be reduced after acoustic over-exposure, none of the recorded cells held at -70 mV (0 out of a total of 9 recorded) could reach the threshold for the action potential with stimuli of 40-50V. At more depolarized potentials (-60 mV) a third of the cells (3 out of 9) reached the threshold for the action potential whereas in the unexposed condition 80% of the cells (4 out of 5) fired an action potential when held at -60 mV.

	Amplitude (mV)	10-90% rise time (ms)	90-10% decay time (ms)
Control	77 ± 7.6	1.7 ± 0.8	0.8 ± 0.1
Strychnine and gabazine	77 ± 3.4	0.9 ± 0.3	0.8 ± 0.1
P, Paired T Test	0.99	0.21	0.25

Table 6.28: Analysis of the action potential amplitude, 10-90% rise time and 90-10 % decay time after acoustic over-exposure. Action potential was evoked by stimulating the auditory inputs at 0.3 Hz while the fusiform cell membrane potential was -60 mV in over-exposed condition. Mean ± s.e.m. for 3 cells are reported in control medium and in presence of 10 µM strychnine and 20 µM gabazine. P values were obtained using a paired Student's T test. Note that the action potential amplitude is not affected by the presence of strychnine and gabazine.

The absence of firing was also observed when the inhibitory inputs were removed by addition of strychnine and gabazine to the medium (not shown). These results suggest that acoustic over-exposure down-regulates the

excitatory synaptic transmission and this effect becomes more apparent when a larger percentage of fibres are recruited (see discussion). When action potentials could be elicited at more depolarized membrane potentials (i.e. in 3 cells), their characteristics were left unaffected by the removal of the inhibitory inputs (summarized in the table 6.28 above). The action potential characteristics were similar between the unexposed conditions (summarized in table 6.21) and the over-exposed conditions (table 6.28 above) with P values (unpaired T test) of 0.31, 0.37 and 0.82 for the amplitude, the 10-90% rise time and the 90-10% decay time respectively. The time to the action potential peak \pm S.D. of three fusiform cells was determined in control and in strychnine and gabazine with values reported in the table 6.29 below.

	Time to the peak (ms)		
	Control	Strychnine and gabazine	F TEST
Cell 1 (n=26)	66.1 \pm 44	120 \pm 95	P=0.0002**
Cell 2 (n=22)	97 \pm 58	24.1 \pm 1.38	P=3·10 ^{-36**}
Cell 3 (n=20)	25.0 \pm 2.6	21.1 \pm 0.21	P=8·10 ^{-12**}

Table 6.29: Summary table representing the time to the action potential peak obtained for each fusiform cell after acoustic over-exposure. Twenty to twenty six action potentials were evoked by stimulating the auditory inputs at 0.3 Hz while the fusiform cell membrane potential was -60 mV in control condition and in presence of 10 μ M strychnine and 20 μ M gabazine. P values (**P \leq 0.01) were obtained with the F test comparing the S.D. value of the time to the peak in control condition with the S.D. value obtained in presence of strychnine and gabazine. Note that in 2 out of the 3 cells the S.D. is significantly smaller in presence of strychnine and gabazine whereas one cell (cell 1) showed a larger S.D. after blocking the inhibitory inputs with strychnine and gabazine.

The example in figure 6.35 (also cell 2 in table 6.29 above) shows the large standard deviation in control medium being decreased in strychnine and gabazine. A similar effect was observed in another cell (cell 3 in table 6.29) whereas cell 1 (table 6.29) showed an increased standard deviation in strychnine and gabazine. This suggests that although the inhibitory component was diminished after acoustic over-exposure, it still contributes to the inaccurate action potential timing as 2 out of 3 cells fired more precisely when the inhibitory inputs were removed.

In conclusion I showed that the synaptic transmission is altered within the DCN, 3 to 4 days after acoustic over-exposure. I showed an increase in the activation threshold for the inhibitory and excitatory postsynaptic potentials carried by the multisensory pathway and a down regulation of both excitatory and inhibitory transmission elicited by stimulation of the auditory fibres. I also showed that the temporal precision observed while stimulating multisensory inputs is controlled by the delay between the evoked EPSP and the evoked IPSP and that the precise spike timing of the action potentials evoked upon multisensory input stimulation was also lost after acoustic over-exposure. Overall these results suggest that the strength of the excitatory and inhibitory synapses onto fusiform cells is scaled down and I next investigate how this is correlated with fusiform cell evoked firing frequency and pattern.

6.4. Effects of acoustic over-exposure

on the fusiform cell firing frequency and reliability

6.4.1. Fusiform cell responses to train stimulations

Action potentials were evoked in fusiform cells by stimulating the multisensory or the auditory synaptic inputs at 10 to 100 Hz in order to generate a temporal summation of the synaptic inputs. For each stimuli train, the stimulus voltage was increased to recruit input fibres (spatial summation). Fusiform cells were held between -60 mV and -70 mV and the evoked firing frequency was first measured in control medium and then in presence of 10 μ M strychnine and 20 μ M gabazine to study the effects of blocking glycine and GABA-A receptors respectively. I studied the effects on the fusiform cell firing frequency as well as on the fusiform cell firing reliability (as described in methods section).

6.4.1.1. Responses to train stimulations of the multisensory inputs

Parallel fibres were first stimulated at threshold voltage which is the minimal voltage to elicit a few action potentials. Threshold voltages were determined in control medium and values were left unchanged in presence of strychnine and gabazine. An example is shown in figure 6.36 A-D (left) where 10 to 100 Hz trains of stimuli are triggering a mixture of action potentials and failures. At threshold voltages, the firing pattern is on average unreliable for all the frequencies tested, with failures counting for fifty to ninety percent of the total number of pulses. The input - output relationship is represented in figure 6.37A as the mean \pm s.e.m. of the firing frequency plotted as a function of the frequency of stimulus (for further details see methods section 2.2.9.6.). The dotted line in the graph represents a reliable firing pattern characterized by a

single action potential in response to a single stimulus (corresponding to a one to one relationship between the input (stimulus) and the output (firing frequency)). At threshold voltages, some action potentials fail to be triggered upon repetitive stimulations and therefore average firing frequency values lie below the dotted line for each stimulation frequency. In addition, the graph shows that for threshold voltages, there is an increase of the proportion of failures (unreliability) with the stimulation frequency (this is discussed in section 6.7.5).

At suprathreshold voltages (5 and 10V above the threshold voltage), the proportion of failures strongly decreased for all stimulation frequencies and stimulations generally triggered either single or multiple action potentials depending on the stimulus voltage as detailed below. Ten to 50 Hz stimulations at 5 V above the threshold triggered a reliable firing pattern with a single action potential elicited in response to each single pulse (one example is shown in figure 6.36 A-C middle). At higher stimulating frequencies (100 Hz) a consistent number of failures was displayed in the majority of the cells (4/6 cells) (figure 6.36D middle). Figure 6.37A summarizes (amongst others) the average response to 5V suprathreshold voltages in 6 cells showing a reliable firing for 10 to 50 Hz (points superimposed on the dotted line) whereas firing frequencies corresponding the 100 Hz stimuli are well below the dotted line. When the amplitude of the stimulus was further increased to 10 V above the threshold, cells tended to fire multiple action potentials per single pulse (figure 6.36 B-C right). Although a reliable firing was still elicited at the lowest stimulation frequency (10Hz, figure 6.36A right) the firing pattern was predominantly aberrant at higher stimulation frequencies (20 and 50 Hz) (figure 6.36 B and C

right). This trend is shown in the summary graph in figure 6.37A where the firing frequency values elicited by 10 Hz stimulus are aligned on the dotted line by contrast to the firing frequency values elicited by 20 and 50 Hz stimuli that are above this line. Stimulating at 100 Hz elicited both action potentials and failures leading to a mean firing frequency below the dotted line (mean firing being unreliable). Collectively these results indicate that the firing reliability is dependent on the frequency of stimulation and on the stimulation voltage representing typical temporal and spatial summation of the synaptic inputs respectively. Fusiform cells are capable of firing reliably up to approximately 50 Hz and fire with failures at 100 Hz stimulation (discussed in section 6.7.5.). Fusiform cells also fire reliably in response to stimulating voltages up to 5 V above the threshold. Below or above this voltage value, their firing is unreliable with either failures or aberrant action potentials. The switch of the reliability pattern (in function of the stimulating voltage) for 10-100 Hz stimuli is represented in figure 6.37B, where the reliability shift is plotted as a function of the stimulating voltage. A value of 0 along the y axes means that the cell is firing in a reliable manner whereas negative and positive values represent the firing with failures and the aberrant firing respectively. In conclusion, cells fire unreliably with failures for low stimulating voltages (threshold voltages). An increase in the stimulus voltage (threshold plus 5 V) allows cells to follow reliably stimuli up to 50 Hz. At highest stimulus level (threshold voltage plus 10 V) cells fire reliably (at 10 Hz stimulus), aberrantly (at 20 and 50 Hz stimulus) or with failures (at 100 Hz stimulus).

	Threshold V			
	10Hz	20 Hz	50 Hz	100 Hz
Control	2 ± 1	9 ± 3	20 ± 7	23 ± 8
Strychnine and gabazine	6 ± 2	14 ± 3	34 ± 9	40 ± 13
P, Paired T test	0.03*	0.02*	0.01**	0.02*
	Threshold +5 V			
	10Hz	20 Hz	50 Hz	100 Hz
Control	10 ± 0.1	21 ± 0.7	53 ± 5	62 ± 11
Strychnine and gabazine	11 ± 0.8	28 ± 4	64 ± 9	73 ± 12
P, Paired T test	0.2	0.09	0.1	0.04*
	Threshold + 10 V			
	10Hz	20 Hz	50 Hz	100 Hz
Control	11 ± 0.7	30 ± 4	70 ± 8	84 ± 6
Strychnine and gabazine	15 ± 2	37 ± 5	78 ± 9	93 ± 11
P, Paired T test	0.08	0.1	0.09	0.12

Table 6.30: Effect of strychnine and gabazine on fusiform cell firing in response to multisensory input stimulation. Firing frequencies were measured for different stimulation voltages and frequencies up to 100 Hz. P values (* $P \leq 0.05$, ** $P \leq 0.01$) were obtained using a paired Student's T and data reported as mean \pm s.e.m. ($n=6$). Note that the firing frequency is significantly increased in the presence of strychnine and gabazine for all stimulation frequencies at threshold voltage.

Blocking inhibitory synaptic transmission while stimulating the multisensory inputs increased fusiform cell firing rates particularly when stimulations were performed with threshold voltages (see example in figures

6.36 and 6.38 comparing the firing in control medium and in presence of strychnine and gabazine respectively). This is also summarized in the figure 6.39 and in the table 6.30 above. Figure 6.40 shows that blocking inhibitory synaptic transmission also increased fusiform cell firing reliability when stimulations were performed with threshold voltages. This increase of firing excitability and reliability occurred for all stimulation frequencies.

6.4.1.2. Responses to train stimulations of the auditory inputs

In the section 6.3.1.2, I showed that a strong inhibitory component recruited after auditory fibre stimulation is responsible for preventing fusiform cells from firing when held at -70 mV. Fusiform cells were therefore held at more depolarized membrane potentials (-60 mV) to facilitate the triggering of action potentials when stimulating the auditory inputs. Stimulating the auditory inputs at different stimulation frequencies and voltages triggered action potentials in all fusiform cells held at -60 mV (figure 6.41) but fusiform cells firing pattern also displayed a proportion of failures that made the firing pattern unreliable. This was true for all stimulation frequencies and cells never fired reliably or with aberrant action potentials even when increasing the stimulation voltages (figure 6.41, summarized in figure 6.42A). This clearly contrasts with the increasing firing frequency observed while stimulating multisensory inputs at increasing stimulating voltages (shown in figure 6.36). Figure 6.42B shows that cells are always firing with a mixture of action potentials and failures when stimulating auditory inputs and the figure also shows that the pattern is generally unreliable with failures for all stimulating conditions. Blocking inhibitory synaptic transmission with strychnine and gabazine increased drastically the number of evoked action potentials as seen in figures 6.41 and 6.43 comparing the firing

property of the same cell in control medium and in presence of strychnine and gabazine respectively.

	Threshold V			
	10Hz	20 Hz	50 Hz	100 Hz
Control	0.9 ± 0.5	4 ± 1	9 ± 3	16 ± 7
Strychnine and gabazine	7 ± 2	17 ± 4	43 ± 9	62 ± 13
P, Paired T test	0.02*	0.01**	0.01**	0.007*
	Threshold +5V			
	10Hz	20 Hz	50 Hz	100 Hz
Control	3 ± 0.3	8 ± 1	22 ± 1	36 ± 5
Strychnine and gabazine	11 ± 1	27 ± 2	61 ± 3	89 ± 4
P, Paired T test	0.007**	0.005**	0.001**	0.003**
	Threshold +10 V			
	10Hz	20 Hz	50 Hz	100 Hz
Control	4 ± 1	9 ± 3	20 ± 4	28 ± 7
Strychnine and gabazine	11 ± 2	26 ± 6	58 ± 11	78 ± 14
P, Paired T test	0.009**	0.009**	0.006**	0.006**

Table 6.31: Effect of strychnine and gabazine on the fusiform cell firing in response to auditory input stimulation. Firing frequencies were measured for different stimulation voltages and frequencies up to 100 Hz. P values (* $P \leq 0.05$, ** $P \leq 0.01$) were obtained using a paired Student's T and data reported as mean \pm s.e.m. (n=6). Note that the firing frequency is increased by the presence of strychnine and gabazine for all stimulation frequencies and voltages.

Figure 6.41 shows that the cell is mainly firing with failures and figure 6.43 shows the same cell either firing reliably or with aberrant action potentials

in presence of strychnine and gabazine. Altogether, blocking inhibitory transmission while stimulating the auditory inputs shifted the firing frequency and the firing reliability towards the left and this is summarized in the graphs in figure 6.44 and figure 6.45 respectively. Details of the values and significance of the results are reported in the table 6.31 above and show that blocking inhibitory synaptic transmission increases the firing frequency for all stimulating frequencies and voltages. In summary, the presence of failures while stimulating auditory inputs is due to the strong inhibitory synaptic transmission onto those cells.

6.4.2. Effects of acoustic over-exposure on responses to stimuli trains

6.4.2.1. Effect on the responses evoked by multisensory input stimuli trains

Fusiform cell firing was evoked like previously described for the unexposed conditions. Cells were held at -70mV and the multisensory inputs were stimulated with train pulses delivered at 10 to 100 Hz at threshold voltages to elicit few action potentials and then with increasing voltages. Similarly to the unexposed conditions, fusiform cells were firing in a reliable manner within a specific stimulating voltage window (typically between 20V and 30V which corresponds to 5V above the threshold voltage). Below and above this voltage the firing pattern displayed failures and aberrant action potentials respectively (summarized in figure 6.46) and values of the firing frequencies were all similar to the unexposed conditions. Fusiform cell firing frequency evoked by pulse trains of multisensory inputs was therefore unaffected by acoustic over-exposure when recorded in control medium where both inhibitory and excitatory inputs are activated.

Section 6.4.1.1 described the properties in the unexposed conditions and particularly how blocking inhibitory synaptic transmission increased fusiform cell firing frequencies when stimulations were performed with threshold stimulating voltages. Interestingly, this was not observed after acoustic over-exposure and blocking inhibitory synaptic transmission did not alter fusiform cell firing frequencies (detailed in the table 6.32 below). As a consequence, after acoustic over-exposure, firing frequencies in presence of strychnine and gabazine were in certain cases significantly lower compared to the unexposed conditions where firing frequencies were measured in presence strychnine and gabazine. This was the case at low stimulation voltages (threshold and threshold + 5V) and low stimulation frequencies (10-20Hz) (represented in figure 6.47 and summarized in the table 6.33 below). Figure 6.48B shows that the firing reliability in presence of strychnine and gabazine was also affected at those specific stimulating voltages and stimulating frequencies.

In conclusion the absence of effect of strychnine and gabazine after acoustic over-exposure clearly suggests that acoustic over-exposure down regulates the inhibitory synaptic transmission originating from multisensory connections. Acoustic over-exposure does not affect the overall firing rate measured in control medium and this also suggests that acoustic over-exposure down regulates the excitatory synaptic transmission leading to an unaffected firing rate (further discussed in section 6.7.11).

	Threshold V			
	10Hz	20 Hz	50 Hz	100 Hz
Control	2 ± 0.7	4 ± 2	19 ± 7	19 ± 8
Strychnine and gabazine	1 ± 0.8	3 ± 1	21 ± 12	17 ± 7
P, Paired T test	0.5	0.5	0.7	0.5
	Threshold +5 V			
	10Hz	20 Hz	50 Hz	100 Hz
Control	8 ± 1	21 ± 3	53 ± 8	66 ± 13
Strychnine and gabazine	7 ± 2	21 ± 2	47 ± 11	56 ± 12
P, Paired T test	0.2	0.8	0.3	0.2
	Threshold +10 V			
	10Hz	20 Hz	50 Hz	100 Hz
Control	13 ± 2	34 ± 6	73 ± 9	89 ± 10
Strychnine and gabazine	13 ± 2	35 ± 6	71 ± 10	83 ± 11
P, Paired, T test	0.8	0.3	0.4	0.2

Table 6.32: Effect of strychnine and gabazine on the fusiform cell firing in response to multisensory input stimulation after acoustic over-exposure. Firing frequencies were measured for different stimulation voltages and frequencies up to 100 Hz. P values were obtained using a paired Student's T and data reported as mean ± s.e.m. (n=6). Note that the firing frequency stays unaffected after blocking inhibitory synaptic transmission.

	10 Hz	20 Hz	50 Hz	100 Hz
	Threshold voltage (strychnine and gabazine)			
Unexposed	6 ± 2	14 ± 3	34 ± 9	40 ± 13
Over-exposed	1 ± 0.8	3 ± 1	21 ± 12	17 ± 7
Unpaired T test	0.04*	0.007**	0.41	0.16
	threshold voltage + 5V (strychnine and gabazine)			
Unexposed	11 ± 0.8	28 ± 4	64 ± 9	73 ± 12
Over-exposed	1 ± 2	21 ± 2	47 ± 11	56 ± 12
Unpaired T test	0.05*	0.11	0.25	0.32
	threshold voltage + 10 V (strychnine and gabazine)			
Unexposed	15 ± 2	37 ± 5	78 ± 9	93 ± 11
Over-exposed	13 ± 2	35 ± 6	71 ± 10	83 ± 11
Unpaired T test	0.56	0.8	0.55	0.55

Table 6.33: Effect of acoustic over-exposure on fusiform cell firing frequencies evoked upon multisensory input stimulation, in strychnine and gabazine. Mean ± s.e.m. (n=6) of the firing frequency measured at different frequency of stimulation and different voltages in strychnine and gabazine. P values (*P≤0.05, **P≤0.01) were obtained using unpaired Student's T test to compare unexposed and over-exposed condition. Note that the firing frequency is reduced after acoustic over-exposure at low stimulating voltages and frequencies.

6.4.2.2. Effects on the responses evoked by auditory input stimuli trains

Fusiform cells were recorded like previously described: cells were held at -60 mV to elicit action potentials while 10-100 Hz train pulses of increasing stimulating voltages were applied at the level of the auditory fibres. Fusiform cells showed a similar trend to the one described in the unexposed condition: cells responded to the stimuli with few action potentials and a large number of

failures even when increasing the stimulating voltage to recruit additional fibres. Acoustic over-exposure left the overall firing rate unaffected at low stimulating voltages but decreased the firing frequencies for higher stimulating voltages and preferentially for 10 Hz and 20 Hz stimulation frequencies (summarized in figure 6.49 and in the table 6.34 below).

The question then arises whether this is a consequence of an increased inhibitory component after acoustic over-exposure however blocking the inhibitory synaptic transmission did not abolish the decrease of the firing frequency observed at 10 Hz and 20 Hz stimulations (shown in figure 6.50 and in the table 6.35 below). Figure 6.51 shows that acoustic over-exposure similarly decreased the firing reliability of fusiform cells preferentially for 10 Hz and 20 Hz stimulation frequencies and that the presence of strychnine or gabazine did not abolish this effect.

Acoustic over-exposure reduced the cellular excitability even when blocking inhibitory synaptic transmission suggesting a reduction of the excitatory synaptic transmission (discussed in section 6.7.11) although a concomitant reduction of the inhibitory synaptic transmission cannot be excluded as IPSPs were also reduced after acoustic over-exposure (section 6.7.11).

	10 Hz	20 Hz	50 Hz	100 Hz
	Threshold voltage (control)			
Unexposed	0.9 ± 0.5	4 ± 1	9 ± 3	16 ± 7
Over-exposed	0.4 ± 0.4	2 ± 1	8 ± 3	15 ± 4
P, Unpaired T test	0.42	0.22	0.72	0.87
	Threshold voltage + 5V (control)			
Unexposed	3 ± 0.3	8 ± 1	22 ± 1	36 ± 5
Over-exposed	0.7 ± 0.7	3 ± 2	12 ± 5	21 ± 8
P, Unpaired T test	0.02*	0.05*	0.09	0.17
	Threshold voltage + 10 V (control)			
Unexposed	4 ± 1	9 ± 3	20 ± 4	28 ± 7
Over-exposed	0.5 ± 0.5	2 ± 13	11 ± 3	19 ± 5
P, Unpaired T test	0.02*	0.03*	0.09	0.33

Table 6.34: Effect of acoustic over-exposure on fusiform cell firing frequencies evoked upon auditory input stimulation. Mean ± s.e.m. (n=6) of the firing frequency measured at different frequency of stimulation and different voltages in control medium. P values (*P≤0.05) were obtained using unpaired Student's T test to compare unexposed and over-exposed conditions. Note that the firing frequency is reduced after acoustic over-exposure at high stimulating voltages and low stimulation frequencies.

	10 Hz	20 Hz	50 Hz	100 Hz
Threshold voltage (strychnine and gabazine)				
Unexposed	7 ± 2	17 ± 4	43 ± 9	62 ± 13
Over-exposed	2 ± 1	8 ± 3	24 ± 7	38 ± 12
P, Unpaired T test	0.05*	0.08	0.13	0.20
Threshold voltage + 5V (strychnine and gabazine)				
Unexposed	11 ± 1	27 ± 2	61 ± 3	89 ± 4
Over-exposed	5 ± 2	11 ± 5	34 ± 11	51 ± 18
P, Unpaired T test	0.04*	0.02*	0.05*	0.08
Threshold voltage + 10V (strychnine and gabazine)				
Unexposed	11 ± 2	26 ± 6	58 ± 11	78 ± 14
Over-exposed	3 ± 2	10 ± 4	30 ± 10	46 ± 15
P, Unpaired T test	0.03*	0.05*	0.10	0.16

Table 6.35: Effect of acoustic over-exposure on fusiform cell firing frequencies evoked upon auditory input stimulation, in strychnine and gabazine. Mean ± s.e.m. (n=6) of the firing frequency measured at different frequency of stimulation and different voltages in strychnine and gabazine. P values (*P≤0.05) were obtained using unpaired Student's T test to compare unexposed and over-exposed condition. Note that the firing frequency is reduced after acoustic over-exposure at high stimulating voltages and low frequencies

6.4.3. Use of an *Integrate and fire* model to simulate the experimental data

The various effects of acoustic over-exposure on synaptic integration in fusiform cells were simulated using A *Leaky Integrate and Fire* model (explained in section 2.2.11.) implemented into MATLAB software by Dr. Matias Ison (Engineering Department, University of Leicester). Modelled data are represented in figures 6.52 and 6.53 and details of the values given in section 2.2.11.).

Multisensory fibre stimulations: Figure 6.52 shows the simulated effect of acoustic over-exposure on a modelled fusiform cell firing in response to 20 Hz stimulation pulses delivered at the level of granule cells (parallel fibres). The modelled data clearly show a switch of the firing reliability (from a pattern with failures to a reliable and an aberrant pattern) occurring with fibre recruitment and also after blocking the inhibitory transmission onto fusiform cells. Acoustic over-exposure decreased the firing frequency in modelled fusiform cells and similarly to the experimental data, this was observed only at threshold voltages (high inactivation probability of granule cells, see methods 2.2.11.) and in absence of inhibitory synaptic transmission (synaptic strength of inhibitory synapses equals 0 see methods 2.2.11.). The decreased membrane resistance (from 1.9 G Ω to 1.1 G Ω) observed experimentally in granule cells after acoustic over-exposure was computed into the model and was partially responsible for the decreased firing rate. I considered the degeneration of very small number of granule cells (0.03%) as my experimental data suggested that a largest proportion of parallel fibres were still functional after acoustic over-exposure. To match the down regulation of inhibitory synaptic transmission onto fusiform cells, the spontaneous activity and the synaptic strength of the cartwheel cell connections were decreased to 5% and 1% of the original values respectively (all the values used for the modelling are detailed in the table below 6.36).

Auditory nerve fibres stimulations: Figure 6.53 shows the simulated effect of acoustic over-exposure on a modelled fusiform cell firing with mainly failures in response to 20 Hz stimulation pulses delivered at the level of the auditory nerve fibres. This was also the case in the experimental conditions

where a strong inhibition prevented fusiform cells from firing reliably. Reliable and aberrant action potentials could be simulated by setting the synaptic strength of the inhibitory synapses to a null value, reproducing the experimental data where strychnine and gabazine massively increased the firing frequency of fusiform cells. Acoustic over-exposure reduced the firing rate in modelled fusiform cells and similarly to the experimental data, this was observed independently of the synaptic strength of the inhibitory synapses (to reproduce the absence or presence of strychnine and gabazine).

Parallel fibre stimulation (multisensory)								
	gr	Cw	gr-Cw	gr-Fu	Cw-Fu	gr	gr	Cw
	Cell number		Synaptic strength			(M Ω)	Spontaneous activity	
UN	5000	20	25	25	25	1900	0.027 (0.026)	0.2 (0.2)
AOE	4850	20	25	25	0.3	1100	0.027 (0.026)	0.01 (0.01)
Auditory fibre stimulations								
	AN	Tv	AN-Tv	AN-Fu	Tv-Fu	AN	AN	Tv
	Cell number		Synaptic strength			(M Ω)	Spontaneous activity	
UN	100	20	40	40	40	1000	0.024 (0.024)	0.3 (0.3)
AOE	53	20	5	38	4	1000	0.024 (0.024)	0.3 (0.3)

Table 6.36: Model parameters used to simulate the excitability changes in fusiform cells following acoustic-overexposure (AOE). The total number of cells computed in the unexposed (UN) and over-exposed (OE) is reported together with the synaptic strength, the membrane resistance (M Ω) and the spontaneous activity of the presynaptic neurone. Abbreviations: (AN) auditory nerve; (Cw) cartwheel cells, (Fu) fusiform cells, (gr) granule cells, (OAE) over-exposed, (Tv) tuberculo ventral cells, (UN) unexposed.

To match the down regulation by half of the EPSPs observed experimentally (section 6.3.2.2.), I considered the degeneration of half of the

auditory fibres. Additionally the strength of the excitatory synapses between the auditory nerve fibres and the tuberculoventral cells was decreased from 40 to 5 arbitrary units (a.u.) and the strength of the excitatory synapses between the auditory nerve fibres and the fusiform cells was reduced from 40 to 38 (a.u.). To match the down regulation of the IPSPs observed experimentally (section 6.3.2.1.), the strength of the inhibitory synapses between tuberculoventral and fusiform cells was reduced from 40 to 4 a.u. (all the values used for the modelling are detailed in the table 6.36 above).

In conclusion, data modelling supports the experimental data describing a down regulation of the excitatory together with the inhibitory synaptic transmission onto fusiform cells. There is also a general down regulation of the resulting overall excitability that might constitute fundamental mechanisms underlying homeostatic plasticity within the DCN (further discussed in section 6.7.11.).

In summary I have shown that acoustic over-exposure led to a change of the passive and active properties of granule or fusiform cells. The decrease of the granule cell membrane resistance along with their resting potentials becoming more hyperpolarized decreased the general granule cell firing gain, and this is likely to contribute to a decrease of the fusiform cellular excitability when stimulating the multisensory inputs. I have also shown that a proportion of fusiform cells intrinsically fired with bursts after acoustic over-exposure contributing to a decrease of the intrinsic firing reliability and to a decrease of the maximal firing frequency in cells firing with bursts.

Stimulation of auditory or multisensory inputs has shown fundamental differences in terms of the fusiform cell firing pattern and the role of inhibitory

synaptic transmission onto the firing pattern. Whereas action potentials were reliably triggered when stimulating multisensory inputs to the fusiform cells, this was not the case when stimulating the auditory inputs evoking a substantial proportion of failures in fusiform cells. I have shown that large IPSPs concomitant to the EPSPs were responsible for the large proportion of failures when stimulating the auditory inputs to the fusiform cells. Multisensory input stimulations evoked smaller IPSPs resulting in a weaker inhibition of fusiform cells. Although the inhibition was weakly efficient in this case, it ensured an accurate spike timing.

Acoustic over-exposure left fusiform cell action potential kinetics unaffected whether action potentials were evoked by multisensory or auditory inputs. Acoustic over-exposure affected synaptic transmission onto fusiform cells by increasing the activation thresholds of the EPSPs and the IPSPs evoked by multisensory input stimulations and decreased the size of both the EPSPs and IPSPs evoked by auditory input stimulations. This indicates that excitatory and inhibitory synaptic transmission originating from both multisensory and auditory connections got down regulated after acoustic over-exposure.

Acoustic over-exposure decreased the firing rate measured in control medium upon stimulation of the auditory inputs. This effect was apparent for higher stimulating voltages and preferentially for lower stimulation frequencies and was still observed after blocking inhibitory synaptic transmission. This suggests that acoustic over-exposure mainly affects the excitatory synaptic transmission mediated by the auditory nerve without excluding an effect on the inhibitory synaptic transmission (see above).

Acoustic over-exposure did not affect the firing rate measured in control medium upon stimulation of the multisensory inputs, suggesting an absence of effect on the firing rate. Nevertheless the firing rate measured while blocking inhibitory synaptic transmission was decreased after acoustic over-exposure. This was due to acoustic over-exposure leading to an overall down-regulation of the inhibitory synaptic transmission. The unaffected firing rate in control medium further indicates that the excitatory synaptic transmission got also down regulated by acoustic over-exposure.

In conclusion, acoustic over-exposure affects differently excitatory and inhibitory synaptic transmission depending on the type of synaptic inputs (multisensory or auditory). The discussion will be addressing the different hypotheses linked to those effects with the aim of providing a unified theory taking into consideration changes of granule and fusiform cell intrinsic properties and synaptic transmission onto fusiform cells. Fundamental questions will be addressed: is acoustic over-exposure affecting the viability of the auditory fibres therefore decreasing their excitability? What is the contribution of synaptic inhibition on this reduced firing? Is acoustic over-exposure decreasing the firing gain of granule cells therefore shifting the activation threshold of the EPSPs and the IPSPs evoked by multisensory input stimulations? Is inhibitory synaptic transmission preferentially affected when stimulating multisensory inputs? I will also discuss some data modelling (described in the section above) to explain how a differential recruitment of fibres alongside with a differential synaptic strength could explain the overall and specific effects of acoustic over-exposure.

DISCUSSION

6.5. Dorsal cochlear nucleus intrinsic cellular excitability in Lister Hooded and Wistar rats

My PhD project initially aimed to investigate the effects of acoustic over-exposure in a rat strain bred in house: the LH. I investigated the morphological (chapter 3) and the basic electrophysiological properties (chapter 4) of the different DCN cell types in this strain and subsequently showed that LH rats exhibited unusual high hearing thresholds (chapter 5) making the strain unsuitable to subsequently study the effects of acoustic over-exposure. Wistar rats showed acceptable hearing threshold and constituted a suitable model of investigation. Surprisingly, when comparing the “intrinsic” cellular excitability in fusiform and granule cells in those two strains, I found no differences in the basic firing properties like the firing frequency and the firing regularity. At this stage of the investigation, it is too early to conclude whether those firing characteristics are irrelevant to auditory encoding or whether LH high hearing threshold are related to an unusual sensitivity to the anaesthetics (affecting the hearing threshold). Both hypotheses are still potentially valid in explaining why such a drastic difference in the hearing threshold is failing to translate into different firing patterns within an auditory structure encoding for sound spectra. Furthermore similar excitability characteristics do not rule out differences in the auditory or the multisensory synaptic transmission onto fusiform cells. Subsequent studies involving acoustic over-exposure were only performed on Wistar rats in order to provide links between clear shifts of the hearing threshold and potential changes in the excitability or the synaptic transmission.

6.6. Effects of acoustic over-exposure

on dorsal cochlear nucleus intrinsic cellular excitability

Previous studies reported that the excitability of the DCN is decreased two to three days after acoustic over-exposure (Kaltenbach et. al., 1998) and this is followed by a hyperactivity of DCN neurons that is maintained for months (Kaltenbach, 1996, 1998, 2000). Changes that occur within the DCN may involve different mechanisms. The loss of auditory inputs from the cochlea could be due to fibre degeneration and trigger plastic adjustments resulting in changes the neurons membrane properties (i.e. change of passive or active properties activation/inactivation of ion channels). Changes could also be due to alterations at the synaptic level (like changes in the neurotransmitter release, postsynaptic receptors, number of synapses). I investigated changes within identified DCN cell types, three to four days after the acoustic over-exposure. Auditory nerve fibres terminate onto DCN granule and fusiform cells which receive projections from the outer hair cells and inner hair cells respectively. I therefore studied whether changes occurred in these two cell types. I investigated changes in the passive and active properties and also whether changes occurred at the level of the synaptic transmission onto fusiform cells.

The table below summarizes the major changes that I observed 3 -4 days after acoustic over-exposure in the dorsal cochlear nucleus and each single change is discussed in the following paragraphs.

Cell excitability					
Granule cells			Fusiform cells		
<i>R_m</i> (MΩ)	<i>R_p</i> (mV)	<i>Firing gain</i> (Hz/pA)	<i>Firing pattern</i>	<i>Regularity of firing</i> (CV)	<i>Firing gain</i>
↓	↓	↓	Bursts	↓	↓

Synaptic inputs to fusiform cells								
Multisensory inputs					Auditory inputs			
<i>EPSP</i>	<i>IPSP</i>	<i>Firing at T</i>	<i>Firing above T</i>	<i>Timing precision</i>	<i>EPSP</i>	<i>IPSP</i>	<i>Firing at T</i>	<i>Firing above T</i>
↓	↓	↓	=	↓	↓	↓	=	↓

Table 6.37: Summary of the principal changes triggered by acoustic over-exposure in the dorsal cochlear nucleus. Abbreviations: (↓) decreased; (=) unaffected, (*T*) threshold voltage. In the case of granule cell resting potentials ↓ refers to more hyperpolarized resting potentials.

6.6.1. Acoustic over-exposure changed granule cell passive properties

Acoustic over-exposure significantly decreased (by half) the membrane resistance of granule cells and also affected their resting potentials which became more hyperpolarized by 14 mV. The decreased membrane resistance and the more hyperpolarized resting potentials observed after acoustic over-exposure are unlikely to be artefacts for the following reasons.

The high membrane resistance of granule cells observed in unexposed conditions (1.9 GΩ) is in accordance with previous studies on DCN granule cells (2.3 GΩ, Balakrishnan and Trussell, 2007) and also on the cerebellar granule cells (2.3 GΩ, D'Angelo et al., 1995). Cerebellar and DCN granule cells share many features: they develop from a common population of neurons (Funfschilling and Reichardt, 2002; Oertel and Young 2004), express similar proteins, (i.e. the high affinity alpha 6 subunit of GABA_A receptors) (Gutierrez et al. 1996; Oertel and Young 2004). The fact that the granule cell membrane

resistance reported in this project is similar to the membrane resistance observed in previous studies suggests that its decrease to 1.1 G Ω observed after acoustic over-exposure is not an artefact

Granule cell resting potential was measured immediately after the rupture of the patch in order to minimize the effect of internal dialysis of the cell with the pipette contents and therefore measure resting potentials that are as close as possible to the physiological resting potentials. In order to measure the real resting potential in a cell, I could have performed intracellular recordings where the resistance of the electrode is very high so that there is no dialysis. Nevertheless so far as whole cell patch clamp recordings are concerned, resting potentials of about -43 mV obtained in DCN granule cells are in accordance with values obtained in cerebellar granule cells (-36 mV) for a similar age and similar recording condition (8-21 days, Rossi et al., 1998). The same study has also shown that the resting potentials of cerebellar granule cells became more hyperpolarized at around -57 mV after 21 days (Rossi et al., 1998). Hyperpolarized resting potentials measured in DCN granule cells after acoustic over-exposure were observed in age matched animals (16 to 21 days old) further suggesting that the effect of acoustic over-exposure on the granule cell resting potential is not an artefact.

Granule cells are associated with inhibitory interneurons, Golgi cells that lie in the granule cell domain (Mugnaini et al. 1980a). Identification of Golgi cells is difficult because they are small and interspersed among granule cells in small numbers. Although Golgi cells have a diameter that is slightly larger (20 μm , Irie et al., 2006) than granule cells (10 μm) we can not completely rule out the possibility that some of the recordings belonged to Golgi cells.

6.6.2. Exploring the possibility of two pore potassium channel modulation

Are leak channels responsible for the changes in the membrane resistance and in the resting potential observed after acoustic over-exposure? The membrane resistance was measured at steady state while cells were hyperpolarized from a membrane potential of -80 mV (see methods 2.2.9.1 and figure 2.17). The membrane resistance is modulated by a background conductance also called leak conductance that is either mediated by potassium or chloride ions (Häusser and Clark, 1997; Patel and Honore, 2001). Resting potentials are also dependent on leak conductances (Patel and Honore, 2001; Berntson and Walmsley, 2008) but also by voltage activated channels that govern the granule cell firing properties, as granule cells were spontaneously firing at their resting potentials (section 6.2.1).

Changes in membrane resistance and in resting potential observed after acoustic over-exposure could both be explained by the opening of leak potassium channels leading to an increase in the cell conductance (and therefore a decrease in the membrane resistance) and to the resting potential becoming more hyperpolarized (Millar et al., 2000; Talley et al., 2000). The modulation of voltage independent potassium channels could occur via the two pore potassium channels. Although it is still unknown whether specific part of the cochlear nucleus and whether specific cell types express specific two pore potassium channels, many of them are described in the cochlear nucleus like the acid sensitive potassium channels TASK (TASK-1, TASK-3 and TASK-5) (Karschin et al., 2001; Talley et al., 2001), the weakly inwardly rectifying TWIK (TWIK-1 and TWIK-2), the halothane-inhibited (THIK-1 and THIK-2) and the arachidonic and mechanosensitive TREK (TREK-1, TREK-2 and TRAAK)

(Talley et al., 2001; Holt et al., 2006). Mouse cerebellar granule cells express TASK-1, TASK-3, TREK-2 (Talley et al., 2001; Aller et al., 2005). Because of the common characteristics of the DCN and the cerebellar granule cells, the same channels could be present in DCN granule cells. A change in the expression of two pore potassium channels (TASK, TWICK, TRAAK and THIK) was found in the cochlear nucleus after cochlear ablation (Holt et al., 2006). Quantitative real-time PCR showed that the expression of both TASK (TASK-5, TASK-1 and TASK-3) and TRAAK channels was significantly decreased three days after cochlear ablation. A less prominent decrease was also observed for TWIK-1 and THIK-2 channels. The decrease of the expression of those channels generally persisted after 3 months although the expression of TRAAK and TASK-3 came back to normal values after 3 months (Holt et al., 2006). The decrease of the expression of two pore potassium channels reported in this study is in apparent contradiction with the results presented here. Nevertheless the expression on the two pore potassium channels was quantified within the whole cochlear nucleus (ventral and dorsal cochlear nucleus) and it cannot be excluded that two pore domain potassium channels expression was selectively decreased in granule cells. Additionally the type of insult used in Holt's study (cochlear ablation) is different from the one I used (acoustic over-exposure). Cochlear ablation immediately eliminates all the auditory inputs to the cochlear nucleus, leading to severe synaptic terminal and fibre degeneration whereas acoustic over-exposure triggers a gradual fibre degeneration that increases with time (Kim et. al. 1997). Several studies showed that acoustic over-exposure and cochlear ablation generate different effects on synaptic neurotransmission (Kaltenbach, 2007). For example the ablation of the cochlea decreases

D-aspartate release in the cochlear nucleus (Potashner et al., 1997; Wenthold and Gulley, 1997) whereas the opposite pattern (i.e. increase in the aspartate release) is observed after acoustic over-exposure (Muly et al., 2004). The same opposite effects could occur in the case of two pore potassium channels.

Altogether, it is possible that acoustic over-exposure increases the expression of two pore channels that might have a role in auditory nuclei dysfunctions. Previous studies have shown that TASK-1 and TREK-1 are inhibited by local anaesthetics (Lesage, 2003; Punke et al., 2003) at doses used to treat tinnitus (Zenner and Ernst, 1993; Simpson and Davies, 1999). Additionally TASK-1 is also inhibited by zinc (Lesage, 2003; Kanjhan et al., 2004) which has also been shown to be beneficial for the treatment of tinnitus (Arda et al., 2003; Ochi et al., 2003).

Could other channels be involved? Inward rectifiers are activated by hyperpolarization and could also be involved in setting the membrane potential and regulating the membrane resistance (Nichols and Lopatin, 1997). Although there is currently no information regarding their expression within the DCN granule cells, the inward rectifier K^+ (Kir) channel is expressed in cerebellar granule cells (Karschin et al., 1996; Mathie et al., 2003) where its Kir2 subtype is inhibited by the activation of $GABA_B$ receptors (Rossi et al., 2006). DCN granule cells receive strong glycinergic and GABAergic inhibitory inputs (Balakrishnan and Trussell, 2008) that could inhibit the Kir current in control condition and a reduction in the inputs to granule cells triggered by acoustic over-exposure could lead to an increased Kir current leading to a decrease in the membrane resistance and to a depolarized resting potential.

Similarly to an effect on the two pore potassium channel mediated current, the activation of a tonic chloride conductance would lead to a smaller membrane resistance and to more hyperpolarized resting potentials (Semyanov et al., 2004; Farrant and Nusser, 2005; Eisenman et al., 2006). Chloride currents in DCN granule cells are mediated by glycine and GABA release. These are large currents and well suited to abruptly overwhelm excitatory synaptic activity (Balakrishnan and Trussell, 2008). Inhibitory currents to granule cells are likely to be carried by neurons that are primarily activated by auditory inputs and they could play a role in shaping the response to somatosensory stimuli (Balakrishnan and Trussell, 2008). A reduction in the strength of these inhibitory inputs triggered by acoustic over-exposure could lead to significant changes in the chloride conductance. In cerebellar granule cells, there is a tonic inhibitory current that is mediated by low concentration of ambient GABA acting on GABA_A receptors containing $\alpha 6$ and high affinity σ subunits (Rossi and Hamann, 1998; Hamann et al., 2002). DCN granule cells contain the $\alpha 6$ but lack σ subunit (Campos et al., 2001) and is likely to be the reason why the tonic GABA current is absent in these cells (Balakrishnan and Trussell, 2008). Acoustic over-exposure could also trigger a change in the GABA subunits leading to the expression of the missing σ subunit and generate a tonic current responsible of the decreased membrane resistance and the more hyperpolarized resting potentials. Selective alterations in GABA_A receptor subtypes are often triggered by diseases, like epilepsy (Loup et al., 2000) or bipolar disorders (Dean et al., 2005) and also modulated during the development (Mathews et al., 1994).

I mentioned at the beginning of the paragraph that granule cells were spontaneously firing at their resting potentials and that their membrane resting

potentials may also be partly dependent on voltage activated channels. Therefore other factors, such as changes in potassium or sodium channel characteristics may also play a role in the hyperpolarized resting potentials. These changes could involve shift in the voltage dependence the ion conductance, or changes in total conductance due to reduced expression, reduced open probability, or changes in inactivation.

In summary, leak potassium channels (two pore or inward rectifier) are likely candidates to be modulated by acoustic over-exposure considering the effects on both the membrane resistance and the resting potential (which is in majority dependent on the potassium equilibrium potential (Hille, 1992). If we consider E_K , the equilibrium potential of a typical mammal neuron being -86 mV (Pritchard and Alloway, 1999) and $R_{p_{UN}}$ and $R_{p_{OAE}}$ the resting potentials of granule cells in unexposed conditions and after acoustic over-exposure respectively, this would result in driving forces ($E_K - R_{p_{UN}}$) and ($E_K - R_{p_{OAE}}$) of 43 mV and 29 mV in unexposed conditions and after acoustic over-exposure respectively. The 14 mV decrease of the driving force observed after acoustic over-exposure is consistent with a membrane potential shift resulting from a decrease in the membrane resistance (i.e. 20 pA flowing through membrane resistances of 1900 M Ω and 1100 M Ω would generate potentials of 38 mV and 22 mV respectively i.e. resulting in a potential difference of 16 mV comparable to the 14 mV driving force decrease reported above.

6.6.3. Granule cell high membrane resistance underlies their firing gain

The granule cell high firing gain is determined by the granule cell's intrinsic properties. I showed in chapter 4 that granule cells exhibit the highest firing gains (i.e. 2.1 Hz/pA) compared to fusiform cells (0.06 Hz/pA) or giant cells

(0.01 Hz/pA). Granule cell high firing gain is a direct consequence of their high membrane resistance and the injection of small step currents (10-20 pA) is sufficient to allow granule cells to fire. The high firing gain suggests that granule cells are capable of responding to a very small number of excitatory synaptic inputs.

Gain modulation is a widespread neuronal phenomenon that modifies the response amplitude. At the level of single neurons, the relationship between input amplitude and spike output will determine large-scale neuronal processing, such as sensory perception. Gain modulation has been shown in humans and other species in association with sensory, motor, and cognitive functions. Gaze direction signals regulate neuronal response gain in primary visual cortex (Weyand and Malpeli, 1993; Trotter and Celebrini, 1999) and modulate the gain of midbrain auditory responses (Winkowski and Knudsen, 2006). Under behavioural conditions, the sensory-driven network activity is continuously changing. Cardin et al. (2008) recently showed that visually evoked membrane potential fluctuations alone failed to significantly modulate the neuronal gain but did affect spike timing. In contrast, membrane potential fluctuations in combination with changes in the mean input resistance consistently resulted in gain modulation. The variation in network synaptic activity may act rapidly to enhance or diminish the sensitivity of neurons to inputs, providing an adaptive or a protective mechanism by which networks adjust to their sensory context.

Granule cell firing gain was significantly decreased after acoustic over-exposure compared to their firing gain measured in the unexposed condition. This is likely to be a direct consequence of the reduced membrane resistance

and previous studies showed that an increased input conductance associated with two-pore potassium channels reduces the neuronal excitability (Goldstein et al., 2001; Patel and Honore, 2001; Brickley et al., 2001).

Gain modulation is a primary mechanism by which neurones combine and process information (Salinas and Thier, 2000) and the decreased activity of granule cells could translate in a reduced excitability of fusiform cells but could also release fusiform cells from the some inhibitory effects of cartwheel cells (this is further discussed in section 6.7.11.). Granule cell maximal firing frequency is not affected by acoustic over-exposure suggesting that the maximal information transfer onto fusiform cells is preserved if granule cells get synchronously bombarded by many inputs.

The minimal current to elicit an action potential in granule cells was similar in unexposed conditions or after acoustic over-exposure. Considering a decrease of the firing gain, I would have expected a higher threshold current after acoustic over-exposure and this discrepancy is likely to be due to a limitation of the protocol used. Indeed, currents were injected with 10 pA steps that might have been too large considering a gain of 2.5 Hz/pA. I could have assessed the action potential threshold more precisely by injecting smaller steps of current (i.e. 2 or 4 pA). After acoustic over-exposure, I also expected a lower spontaneous action potential firing rate at threshold when granule cells were maintained at constant membrane potential. This could be due to changes in the synaptic inputs (cells were recorded in a control medium without blocking excitatory and/or inhibitory synaptic transmission) that could have masked the reduced excitability (i.e. reduced inhibition after acoustic over-exposure). Discrete and long lasting steps of membrane potentials (chosen at the action

potential threshold and at the maximal firing frequency) were used to measure the coefficient of variation and the firing gain and both parameters were left unaffected by acoustic over-exposure. Ramps where the membrane potentials are progressively and continuously changed could have constituted a best protocol to show a sustained effect on the firing gain. In summary, acoustic over-exposure decreased the granule cell firing gain while leaving the maximal firing frequencies unaffected suggesting that the physiological activity of granule cells is preserved when they are maximally activated.

6.6.4. Granule cell firing gain: effects on fusiform cell excitability?

Granule cells get their input from type II spiral ganglion cells which carry inputs from the cochlear outer hair cells. Exposure to high intensities of sound even for a short period can permanently damage the cochlea and trigger a shift in the hearing thresholds (Syka, 2002). In chapter 5 of my thesis, I showed that the auditory brainstem thresholds were significantly increased shortly after acoustic over-exposure. The primary reason for this threshold elevation could be the loss of outer and inner hair cells in the cochlea (Syka, 2002) shown to occur in guinea pigs after 2 hours of acoustic over-exposure (4kHz, 108 dB, Kim et al., 1997) or to a partial the degeneration of auditory nerve fibres (Kim et al., 1997; Syka, 2002). It is therefore likely that a small proportion of auditory inputs onto granule cells have degenerated after acoustic over-exposure. Previous studies suggested that auditory inputs activate inhibitory inputs to granule cells (Balakrishnan and Trussell, 2008). A degeneration of auditory fibres would therefore also decrease the inhibitory synaptic transmission to granule cells. Granule cells are the site of convergence of auditory and multisensory inputs

and a degeneration of auditory nerve fibres could shift the balance towards an excitatory drive originating from the multisensory inputs.

Nevertheless the degeneration of auditory nerve fibres might not be the primary cause of the decrease of excitability. During acoustic over-exposure the auditory nerve fibres are hyperactive due to the over-stimulation and this could be responsible for the changes observed in granule cells. Auditory nerve hyperactivity may produce oxidative stress in the cochlear nucleus. Superoxide formation alters the physiological neuronal properties (Hasan et al., 2007) and occurs immediately after acoustic insult (Samson et al., 2008). In neural cell cultures, the oxidative stress induces the hyperpolarization of the membrane by acting on an inwardly rectifying current (Dringer et al., 2003). In dentate granule cells, oxidative stress enhances the L-type Ca^{2+} channel current (Akaishi et al., 2004) and in hippocampal neurons, it increases the sodium current (Meng and Nie, 2004). The role of antioxidants in the management of hearing loss (Darrat et al., 2007) suggests cellular changes resulting from oxidative stress may occur at the level of the peripheral or central auditory system. One hypothesis is that oxidative stress might modulate the expression of two pore potassium channels in DCN granule cells. Changes observed in granule cells will affect fusiform cell evoked excitability and this is discussed in the section 6.7

6.6.5. Acoustic over exposure triggers bursts in fusiform cells

My studies showed that acoustic over-exposure affected the spontaneous firing rate in a third of fusiform cells (called over-exposed type fusiform II cells) characterized by bursts and an irregular firing pattern. Previous studies using extracellular recordings in DCN slices already reported a prevalent bursting activity following acoustic over-exposure (Chang et al., 2002) but this study did

not allow correlating the firing pattern with a specific cell type and the authors concluded that the prevalence of bursting activity could be linked to an increase in the proportion of spontaneous firing in cartwheel cells or to a change of the firing pattern at the level of fusiform cells. My data indicate that the increased bursting activity recorded by Chang *et al.* (2002) is partially or solely due to the bursting activity of fusiform cells. In the results described in this thesis, I showed that fusiform cell bursting activity was observed three to four days after acoustic over-exposure and this affected only third of the cells. By contrast Chang *et al.* (2002) performed extracellular recordings one to three weeks following the over-exposure and the bursting firing was predominant in all the recordings, suggesting that it did affect the cellular network and/or a majority of the cells. The DCN is tonotopically organized and the bursting activity could be specific to a sub-population of fusiform cells located in the region of the acoustic insult (15 kHz in my study and 10 kHz in Chang's study). Both studies were using high intensity, single tone frequencies and I recorded within the region of high frequency encoding (figure 2.4). It is therefore unlikely that the apparent smaller percentage of bursting fusiform cells reported here is due to a localized area of insult within the DCN. Furthermore, auditory brainstem response recordings show a shift of the hearing threshold for all frequencies above 8 kHz suggesting that the area of insult is not restricted to the 15 kHz sound encoding area. A likely explanation could be linked to the time at which the recordings were performed in the DCN. It is possible that the switch of the fusiform firing pattern is a process that starts shortly after the acoustic over-exposure within a small portion of cells and terminates weeks after the insult with a larger proportion of cell being affected.

Over-exposed type II fusiform cells also fired with bursts (action potential clusters) while injecting step currents cells although most of the times they would fire simple action potentials characterized by a typical absence of undershoot for the whole duration of the step. As the step duration lasted 1 s, it is possible that such a short pulse triggered a single burst that lasted the whole duration of the step.

What triggers this bursting activity? I have shown that the bursting activity was not triggered by glutamatergic and/or GABA/glycinergic inputs as specific blockers of those inputs left the bursting activity unaffected. It is possible that the bursting activity is due to other synaptic inputs like cholinergic inputs present at the level of the dorsal cochlear nucleus (Chen et al., 1998) or to the activation of other (glutamate or GABA) receptors. In the cerebellum, Purkinje neurons exhibit a spontaneous bursting activity which is not triggered by synaptic inputs (Womack and Khodakhah, 2002; 2004). T-type calcium, BK and SK potassium channels all contribute in regulating the bursting activity of cerebellar Purkinje cells but the P/Q-type calcium channels are required to sustain the spontaneous bursting and terminate bursts by generating a dendritic calcium spike (Womack and Khodakhah, 2002; 2004). A partial block of P/Q calcium channels can cause a switch from bursting to tonic firing (Womack and Khodakhah, 2004). Therefore the interplay between intrinsic dendritic and somatic conductances is essential in controlling the pattern of activity of cerebellar Purkinje cells. Previous studies showed that action potentials evoked a calcium influx into the apical and basal dendrites of DCN fusiform cells with sodium channel-mediated action potentials required to evoke the calcium influx into fusiform cell dendrites (Molitor and Manis, 2003). The distinct

electrophysiological responses exhibited by fusiform cells of the over-exposed type II population could result from differences in the pattern of dendritic calcium channel activation initiated by sodium-channel mediated action potential. In the DCN, cartwheel cells fire spontaneously with bursts (Kim and Trussell, 2007). Bursts and complex spikes in cartwheel cells are due the activation of T- and R-type voltage-gated calcium channels colocalized with sodium channels at the initial segment of the axon (Bender and Trussell, 2009). Fusiform cells could gain the ability of firing with bursts by similar mechanisms. We can exclude the possibility that bursting fusiform cells are in fact cartwheel cells as all bursting cells were localized in the fusiform cell layer. Additionally cells were filled with lucifer yellow and the morphology of fusiform cells was always confirmed.

It is possible that other voltage gated channels are involved in the bursting activity like voltage activated potassium channels. Fusiform cells express Kv3 potassium channels (Friedland et al., 2007; Rusznák et al., 2008). These channels produce currents that can specifically enable fast repolarization of action potentials without compromising spike initiation or spike height thus enabling repetitive firing at high frequencies (Rudy and McBain, 2001). Kv3 mediated potassium currents could be involved in the high regularity of fusiform cell firing observed in chapter 4 and a decrease in the Kv3 mediated current could lead to prolonged action potentials that would result in the bursting activity. Over-exposed type fusiform II cells fired action potentials characterized by significantly longer decay time compared to the “unexposed” and the over-exposed type I fusiform cells; this further supports the idea that Kv3 mediated potassium currents are down-regulated after acoustic over-exposure. Fusiform cell’s ability to fire at high frequencies was lost in the over-exposed type II cells

compared to the other two populations of cells, this could be due to a down regulation of Kv3 channels, and as consequence the loss of the ability of high frequency firing (determined with step current protocols).

Homeostatic plasticity stabilizes the properties of neuronal circuits by regulating neuronal excitability (Turrigiano, 1999). Fusiform cell switch of pattern could represent a form of homeostatic plasticity that is engaged to restore the stability of the network. Fusiform cell bursting activity could be a consequence of the decreased firing gain previously observed in granule cells (section 6.2.1.) or could be the consequence of the reduced auditory nerve activity previously reported after acoustic over-exposure (Dallos and Harris, 1978; Salvi et al., 1983).

6.7. Effects of acoustic over-exposure on the synaptic transmission onto fusiform cells

6.7.1. Excitatory synaptic transmission onto fusiform cells

Stimulating auditory or multisensory inputs elicited synaptic responses that were in general depolarizing for both types of inputs (and were therefore called mixed EPSPs). Differences in those mixed EPSPs could be observed whether stimulating auditory or multisensory inputs. First mixed EPSPs were elicited at a higher stimulation voltage while stimulating auditory fibres compared to stimulating multisensory inputs. Second, mixed EPSPs generated by auditory input stimulations stayed sub-threshold and were insufficient to allow the activation of action potentials in fusiform cells, even when increasing the stimulus voltage. This could be due to a limited recruitment of excitatory fibres when stimulating auditory fibres compared to the extensive fibre recruitment after stimulating the parallel fibres. Indeed, like cerebellar parallel fibres (Napper and Harvey, 1988; Harvey and Napper, 1991) hundred thousand DCN parallel fibres could form single en-passant synapses with fusiform cell apical dendrites (Mugnaini et al., 1980b; Wouterlood and Mugnaini, 1984; Oertel, 2004). By contrast, a smaller number of auditory fibres (around 12 with around 10 terminals each) contact 2 to 48 fusiform cells on their basal dendrites (Smith and Rhode, 1985; Ryugo and May, 1993). From an anatomical point of view, the limited number of auditory fibre synapses could therefore explain the smaller mixed EPSPs evoked by auditory input stimulation preventing fusiform cells from firing action potentials. Adding blockers of inhibitory synaptic transmission allowed determining the strength of the EPSPs in isolation and

unexpectedly resulted in isolated EPSPs of similar amplitudes and even wider areas when stimulating auditory inputs compared to stimulating parallel fibres. Moreover, an increase of the stimulus voltage while stimulating auditory inputs increased the amplitude of the isolated EPSPs, indicating spatial recruitment of the auditory nerve fibres.

Auditory nerve fibres arising from the cochlea project preferentially on basal dendrites in the DCN deep layer (Smith and Rhode, 1985) whereas multisensory inputs establish their synaptic connections via parallel fibres onto the apical dendrites in the DCN molecular layer (Wouterlood and Mugnaini, 1984). In addition, stimulating auditory inputs in the deep layer triggers late EPSCs in fusiform cells that have been interpreted as excitatory polysynaptic connections originating from ventral cochlear nucleus interneurons (Zhang and Oertel, 1994). It is therefore possible that the summation of distinct EPSPs arising from spatially separated inputs and which reach fusiform cell basal dendrites at different times contribute to the large isolated EPSP area when stimulating auditory inputs in the deep layer (Heck et al., 2003; Gullledge et al., 2005). Independently of the number of synaptic inputs, EPSP kinetics are also linked to presynaptic modulation of release (Neher and Sakaba, 2008) or post synaptic modulation via specific receptors. NMDA and AMPA receptors are present on both apical and basal dendrites of fusiform cells but the AMPA receptors subunit GluR4 is present only at the basal dendrite synapses (Rubio and Wenthold, 1997). However this difference is less likely to account for the large EPSP areas following stimulation of the auditory nerve as previous studies suggested that this GluR4 on fusiform cell basal dendrites is the subunit responsible for a fast deactivation and recovery of the glutamate mediated

EPSP (Gardner et al., 1999; Petralia et al., 2000) and this would be consistent with smaller rather than larger EPSP areas. The metabotropic receptors mGluR1 α mediating slow EPSPs in the cerebellum (Knöpfel and Grandes, 2002) are exclusively present at the basal dendrite synapses in the DCN (Petralia et al., 2000) but are unlikely to contribute to the large EPSP area observed while stimulating auditory inputs as EPSPs were abolished by NMDA and AMPA/kainate receptor antagonists. Finally, EPSP kinetic differences could be explained by a difference in glutamate spill over (DiGregorio et al., 2002), glutamate transporters (Takahashi et al., 1996; Otis et al., 1997; Marcaggi et al., 2003) and/or dendritic filtering (Williams and Stuart, 2003).

6.7.2. Characteristics of the action potentials elicited by auditory versus multisensory inputs

Action potentials displayed similar characteristics when evoked by stimulation of auditory or multisensory inputs. This is surprising considering that the action potential rise time, decay time or amplitude should differ as action potentials were evoked from either -60 mV or at -70 mV when stimulating the auditory or the multisensory inputs respectively. An explanation of this absence of differences is likely to be due to action potential thresholds being more depolarized (by about 6 mV) while stimulating the auditory inputs, further explained by a difference in the activation and inactivation properties of the sodium channels towards more depolarized potentials in the case of auditory stimulation compared to multisensory stimulation. The involvement of different sodium channels localized onto apical and basal dendrites could also be the responsible for the fact that the reduced action potential amplitude measured in

strychnine and gabazine is specifically linked to action potentials elicited upon multisensory input stimulations.

When stimulating multisensory inputs, half of the fusiform cells displayed a depolarizing phase following the action potential (for comparison, only one out of five fusiform cells displayed this phase after stimulation of the auditory inputs). Although a higher number of cells are required to proof the statistical significance of these results, the depolarizing phase could be due to several factors. First, it could be due to dendritic calcium transients as reported by Molitor and Manis (2003) who performed simultaneous fluorescence imaging and electrophysiological recordings to evoke calcium transients into fusiform cell apical and basal dendrites. Although calcium transients were triggered at a similar distance (hundred microns) from the nucleus, the fluorescence was greater in the apical dendrites relative to the basal dendrites (Molitor and Manis, 2003). Multisensory input stimulations activate apical dendrites and this could generate higher magnitude calcium transients (by contrast to auditory inputs activating basal dendrites). Second, the presence of the depolarizing phase could also be linked to more hyperpolarized resting or membrane potentials as reported for cerebellar granule cells (Magistretti et al., 2006). When stimulating auditory inputs, fusiform cells were held at depolarized potentials in order to elicit action potentials and this could explain why the depolarizing phase was observed only in few fusiform cells following auditory nerve stimulation, by contrast to multisensory input stimulation. Third, the depolarizing phase could represent the decay phase of a large excitatory postsynaptic input underlying an action potential. Spatial summation of the excitatory inputs is inherent to synaptic integration and large and long lasting EPSPs could reflect the

activation of multiple parallel fibres by contrast to a small proportion of auditory nerve fibres terminating onto fusiform cells (Ryugo and May, 1993; Oertel and Young, 2004). EPSP kinetics may also reflect asynchronous transmitter release (Neher and Sakaba, 2008), differences in transmitter uptake (Takahashi et al., 1995; Bergles et al., 1999) or the slowly activating-deactivating NMDA receptor (Forsythe and Westbrook 1988; Stern et al., 1992). Although the origin of the after-depolarizing phase remains to be studied, it might play a crucial role on the integration of temporally segregated excitatory inputs or modulate the synaptic efficacy of inhibitory inputs.

6.7.3. Inhibitory synaptic transmission onto fusiform cells

Stimulating auditory or multisensory inputs elicited IPSPs that were abolished by concomitant application of gabazine and strychnine and therefore limits conclusions on the involvement of specific (GABA_A versus glycine) receptors. However, anatomical and histochemical studies indicate a preferential activation of glycine receptor mediated IPSPs evoked either by multisensory or by auditory input stimulations. Glycinergic terminals in the DCN represent 92% of all inhibitory synaptic endings (Rubio, 2004). Fusiform cells receive glycinergic inhibitory inputs from tuberculoventral cells on their basal dendrites in the deep layer (Oertel and Young 2004) and from VCN D-stellate cells (Oertel and Young, 2004). Fusiform cells also receive glycinergic inputs on their apical dendrites in the molecular layer originating from cartwheel cells (Mugnaini, 1985; Golding and Oertel, 1997; Oertel and Young, 2004). Stellate cells in the molecular layer constitute the only GABAergic input onto fusiform cell apical dendrites (Casparly et al., 1987; Oertel and Young, 2004).

Auditory input stimulation triggered IPSPs with larger peak amplitudes and areas compared to IPSPs evoked by multisensory input stimulation, explaining why stimulating auditory nerve fibres hardly triggered any action potentials in fusiform cells. We can reasonably conclude that a strong inhibitory synaptic transmission from the auditory system specifically prevents action potentials in DCN fusiform cells. It is possible that a larger number of inhibitory interneurons projecting onto fusiform cell basal dendrites account for the larger IPSP amplitudes and areas evoked by stimulating auditory inputs. Different types of receptors or different subunit for the same receptors could influence the IPSP kinetics but this unlikely to be the case as the same glycine receptor isoforms are present on both basal and apical fusiform cell dendrites (Piechotta et al., 2001; Rubio, 2004). Presynaptic factors like the quantal size, the number of release sites or the probability of release can also contribute to the IPSP amplitude and area (Katz, 1969). For example, a tight coupling between Ca^{2+} source and Ca^{2+} sensor in tuberculoventral cells or D-stellate cells may lead to high probability of glycine release as it does in the GABAergic cells of the hippocampus (Kraushaar and Jonas, 2000; Bucurenciu et al., 2008). A likely contributing factor to the size of the IPSP is the size of the readily releasable pool (Wölfel and Schneggenburger, 2003). Indeed, synaptic vesicles are less densely packed in cartwheel cell synaptic endings by contrast to the high number of readily releasable vesicular pool in tuberculoventral cell terminals (Rubio, 2004). We can exclude the depletion of the readily releasable vesicular pool as causing the differences in the IPSP amplitudes as stimulations were performed at a low frequency (0.3Hz) and vesicular depletion is relevant for stimulations above 10 Hz (Neher and Sakaba, 2008).

When stimulating the multisensory inputs, fusiform cell responded first with an EPSP. IPSPs could be elicited only when increasing the stimulation voltage. This was not the case for auditory input stimulation where IPSPs were evoked together with the EPSPs immediately at threshold voltages. When performing voltage clamp recordings while stimulating the auditory nerve fibres, IPSCs and EPSCs were concomitantly elicited onto fusiform cells whereas IPSCs evoked by multisensory input stimulation were always following the EPSCs with a latency of around 8 ms. The longer latency of the IPSC compared to the EPSC reflects an indirect synaptic inhibition via interneurons. Indeed parallel fibres make synaptic contact with the inhibitory interneurons cartwheel and stellate cells (Wouterlood and Mugnaini 1984; Wouterlood et al., 1984) that inhibit fusiform cells via a feedforward inhibition (Berrebi and Mugnaini, 1991). A similar synaptic circuitry is activated when stimulating auditory inputs as auditory nerve fibres contact tuberculoventral cells and D-stellate cells in the ventral cochlear nucleus that inhibit fusiform cells via a feedforward inhibition. Nevertheless by contrast to what was expected when stimulating auditory nerve fibres, IPSCs and EPSCs were concomitantly elicited onto fusiform cells with a short latency relatively to the offset stimulus (about 5 ms). This suggests that by placing the stimulating electrode in the DCN deep layer in order to directly activate excitatory inputs from the auditory nerve fibres I might have also directly activated inhibitory inputs lying in the deep layer such as tuberculoventral cells. Similar results were reported in a previous study by Zhang and Oertel (1994) although poly-synaptic inhibition originating from auditory input stimulation could be observed for weaker stimuli. Poly-synaptic connections were not observed in my studies reported above and the reason could be linked

to the thickness of the slices (about 200 μm , versus 300-400 thick slices used in Zhang and Oertel, 1994). It is reasonable to assume that auditory nerve fibres might have been cut in thinner slices and therefore auditory nerve projections onto DCN tuberculoventral or VCN D-stellate cells might have been affected.

In summary stimulating auditory inputs evoked a strong inhibitory synaptic component preventing fusiform cells from firing. This inhibitory component was characterized by large IPSPs synchronous to the EPSPs. By contrast stimulating multisensory inputs evoked a smaller inhibitory synaptic component that decreased the firing rate of fusiform cells without preventing them from firing. In this case, inhibitory synapses were recruited at higher stimulating voltages and were also elicited with a longer latency compared to the evoked EPSPs. IPSCs recruited upon multisensory input stimulation were also evoked with a delay (of about 8 ms) compared to the EPSCs and the existence of this time window between excitation and inhibition might be essential for spike timing precision (as discussed below). Although it was not observed in my experimental conditions it can not be excluded that such a time window might also exist between the excitatory and inhibitory inputs carried by auditory pathway.

6.7.4. Inhibition ensures spike timing precision

Action potentials were evoked with a precise timing when stimulating multisensory inputs by contrast to spike jitter observed after auditory input stimulation. As fusiform cells were held at different membrane potentials (-60 mV and -70 mV in the case of auditory and multisensory stimulation respectively) we cannot eliminate the possibility of an influence of the membrane potential on the spike jitter. This possibility is however unlikely as

spike jitter was also observed when blocking the inhibitory synaptic transmission while stimulating multisensory inputs specifically indicating that the inhibitory transmission carried by the multisensory system ensures accurate spike timing in fusiform cells. The role of the inhibitory transmission on spike timing has never been directly demonstrated in the DCN but modelling studies have reported that simulated IPSPs superimposed on a noise stimulus can enhance the precision of spike timing in DCN fusiform cells (Street and Manis, 2007). The role of inhibitory transmission on spike timing has been documented in the cerebellum (Gauck and Jaeger, 2000) and in the medial superior olive (Grothe and Sanes, 1994) where it allows cells to fire only when multiple excitatory synaptic events are coincidentally integrated within the cells leading to more reliable spikes. Spike timing precision could be linked to the phenomenon described in the previous paragraph where IPSPs occur with a delay (about 8 ms) relatively to the EPSPs. This hypothesis is supported by a similar observation showing a disynaptic feed-forward inhibition onto hippocampal pyramidal cells following a monosynaptic excitation (Pouille and Scanziani, 2001). In their study, the authors suggest that the timing of feed-forward inhibition (about 2 ms) determines the time window in which EPSPs summate to reach the action potential threshold and therefore ensures precise coincidence detection in hippocampal pyramidal cells. Similar di-synaptic inhibitory input onto DCN fusiform cells is likely to be responsible for the precise spike timing observed in fusiform cells when stimulating multisensory inputs. While a larger time window between EPSPs and IPSPs (8 ms) was observed in the DCN compared to the time window reported in the hippocampus (2 ms), this is likely to be linked to the recruitment of different inhibitory interneurons. The role of

the time window is still very hypothetical and could find its explanation in a previous study where Tzounopoulos *et al.* (2004) showed that long term potentiation or long term depression in DCN fusiform cells depend on the timing of the depolarization triggered action potentials relatively to the EPSPs evoked from parallel fibre stimulation. Spike timing could therefore be an essential feature of plastic synapses. Interestingly, neither long term potentiation nor long term depression were observed at auditory synapses in the DCN (Tzounopoulos *et al.*, 2004) and this could be linked to the absence of precise action potential timing following auditory input stimulation observed in my studies.

When stimulating the auditory inputs to DCN fusiform cells, I also observed that the time to the action potential peak is on average 5 ms longer compared to the action potential delay measured after multisensory input stimulation. *In vitro* recordings combined to modelling studies in DCN fusiform cells showed that IPSPs preceding or concomitant with a depolarization can increase the spike latency and the mechanism involves changes in the cellular intrinsic conductances (Kanold and Manis, 2005). In particular the hyperpolarization from the IPSPs increases the availability of a transient potassium current that will then result in a prolongation of the time to the action potential peak (Kanold and Manis, 2005). It is therefore likely that the concomitant recruitment of inhibitory and excitatory inputs while stimulating the auditory inputs contributes to decrease the spike timing precision observed in fusiform cells.

The temporal precision of inhibition is critical for circuits involved in sound localization like in the medial superior olive nucleus (MSO) where the

timing of synaptic inhibition acts as a coincidence detector involved in the encoding of the inter-aural time difference of the arrival of sound between the ears (Grothe and Sanes, 1994). The underlying mechanism is supposed to rely on a coincidence of excitatory inputs from the two ears that are phase-locked to either the stimulus frequency or the stimulus envelope. Although anatomical studies seemed to be consistent with delay lines from contralateral excitatory inputs to the MSO (Smith et al., 1993; Beckius et al., 1999), functional studies show that the coincidence detection is the result of the temporal integration of both EPSPs and IPSPs (Grothe and Sanes, 1994) and that synaptic inhibition is tuning the MSO neurons to specific inter-aural time differences (Joris and Yin, 2007; Pecka et al., 2008). A similar mechanism could be present in the DCN, where fusiform cell firing is related to the time window between excitation and inhibition. Synaptic inhibition could enable fusiform cells to respond selectively to frequency spectra differences (firing specifically in response to broadband stimuli by contrast to narrowband stimuli (Oertel and Young, 2004).

Inhibition is a critical element of sensory coding in the DCN. The picture of a differential role of inhibition is emerging: inhibition ensures precise spike timing while multisensory inputs are activated and suppresses firing while auditory inputs are active. This differential effect of synaptic inhibition was also observed on fusiform cell firing frequency evoked upon repetitive stimulations.

6.7.5. Synaptic integration and modulation of fusiform cell firing rate

Synaptic integration onto fusiform cells was studied by delivering trains of stimuli varying from 10 to 100 Hz from multisensory inputs or from auditory inputs. Stimulating multisensory inputs up to 50 Hz triggered reliable action potentials in fusiform cells. Fusiform cells fired with failures above this

stimulation frequency (i.e. at 100 Hz). I have shown that fusiform cells can fire up to ~ 30 Hz when maintained at a steady depolarized level. *In vivo* studies reported that fusiform cells can fire up to 200 Hz in response to acoustic stimulation (Stabler et al., 1996; Hancock and Voigt, 2002) and can also fire with a spontaneous rate between 45 Hz and 177 Hz (Zhang and Kaltenbach, 1998). Potential high firing rates could be due to fusiform cell expressing Kv3 potassium channels (Friedland et al., 2007; Rusznák et al., 2008) enabling fast action potential repolarization and high frequency firing (Rudy and McBain, 2001). The reason for this inability of fusiform cells to follow 100 Hz stimuli could be linked to the type of stimulus used. Previous studies showed that characteristics like pulse amplitude, variability, injection of Gaussian distributed low-pass noise current versus squared pulses through the stimulating electrode will affect spike timing and frequency (Street and Manis, 2007). Another reason for the inability to fire up to 100 Hz could be due to the insufficient amount of recruited fibres, potentially because of fibres being cut during the slicing procedure.

Stimulating multisensory inputs with increasing voltages increased the fusiform cell firing frequency. Increasing the stimulating voltage is directly linked to the number of recruited fibres. As the stimulus voltage is increased, more parallel fibres got activated translating into larger fusiform cell EPSPs (spatial summation) and into an increased fusiform cell firing rate. Blocking inhibitory synaptic transmission increased the fusiform cell firing frequency. This effect was predominant at threshold voltage where not many parallel fibres are recruited and therefore the inhibitory inputs can counteract the action of the excitatory inputs. At higher stimulus voltages more fibres are recruited (i.e.

100,000 are likely to project onto a single fusiform cells) and therefore the effect of inhibition is less consistent. Altogether, my results show that the fusiform cell firing frequency is dependent on the stimulation voltage and on the stimulation frequency when stimulating multisensory inputs. Multisensory input synaptic integration is therefore displaying properties of input temporal and spatial summation. Inhibition recruited by multisensory input stimulation also modulates the firing frequency of fusiform cells up to a certain extent indicating that the firing pattern is controlled by the number of excitatory inputs and also by the inhibitory inputs.

By contrast, stimulating auditory inputs triggered failures at all stimulation frequencies and increasing stimulation voltages while stimulating auditory inputs still failed to trigger action potentials. This is unlikely to be due to the passive properties of fusiform cells as I have just shown that those cells can fire reliably up to a frequency of 50 Hz in response to multisensory input stimulation. When the inhibitory inputs were blocked while stimulating auditory inputs, fusiform cells displayed a reliable firing and even fired aberrantly at high stimulation voltages. The strong inhibition elicited by auditory nerve stimulation is in accordance with previous physiological studies reporting inhibitory synaptic inputs originating from tuberculoventral cells and D-stellate cells suppressing fusiform cell activity (Voigt and Young, 1990; Oertel and Young, 2004). Fusiform cells are excited by broadband stimuli and inhibited by narrowband stimuli (Oertel and Young, 2004). This inhibition is due to tuberculoventral cells which are activated by narrowband stimuli (Spirou et al., 1999; Rhode, 1999). Inhibition has therefore a profound impact on the way fusiform neurons encode temporal stimulus patterns (Voigt and Young, 1990; Middlebrooks, 1992; Oertel

and Young, 2004). Under physiological condition, this powerful inhibition is activated only by specific acoustic signals (narrowband stimuli). In my studies the stimulus was electrical and not acoustical. It is possible that the stimulation conditions activate all the inhibitory fibres close to the stimulating electrode explaining why auditory synaptic inputs get constantly inhibited while stimulating auditory inputs. The functional role of the inhibitory synaptic inputs carried by the multisensory system is not known so far. The specific function of the diverse somatosensory input pathways to the auditory system is not yet well understood. The experiments performed in this thesis allow us to make some suggestions regarding their role and this will be discussed in the following sections.

The ability of following a stimulus is important feature for a cell as it can guarantee the correct transmission of the signal. In the case of multisensory input stimulation this characteristic is dependent on the number of excitatory parallel fibres that are activated and partially by the activation of inhibitory inputs. By contrast, in the case of auditory fibre stimulation, this property depends entirely on the presence of the inhibitory inputs.

6.7.6. Functional role of the DCN in the auditory system

The firing rate and the spike timing are important features in the information encoding (Berry et al., 1997; Nowak et al., 1997; Shadlen and Newsome, 1998; Buonomano, 2003). I showed that both properties depend on inhibitory synaptic inputs onto fusiform cells. One issue is how fusiform cells might engage different firing activities within the auditory system. In the deep layer, excitatory inputs from the auditory nerve and inhibitory inputs from tuberculoventral cells allow fusiform cells to detect particular windows in the acoustic spectra. In the

molecular layer, fusiform cells integrate vestibular and trigeminal inputs carrying information regarding the position and movements of the head and neck (Oertel and Young, 2004). The superficial layers of the DCN therefore provide fusiform cells with multimodal inputs that are relevant to sound localization whereas the deep layer provides information regarding the sound characteristics. We can hypothesize that precise action potential timing is important when information regarding the position of the pinna or the head are transmitted.

Not every action potential conveys information by its precise timing. For example, in the deep layer, information on the spectral content of the acoustic stimulus is conveyed through the fusiform cell mean firing rate (Oertel and Young, 2004). DCN neurons also exhibit poor phase locking to high-frequency tones (Goldberg and Brownell, 1973; Rhode and Smith, 1986b). The inhibition carried by the auditory system is essential for fusiform cells to detect differences in the sound spectra but it could also play a fundamental role in shaping the responses to somatosensory stimuli, by altering the profile of the firing in fusiform cells. Additional studies on stimulating both multisensory and auditory inputs at the same time are needed to address this issue. *In vivo* experiments using bimodal stimulation showed that bimodal interaction occurs in fusiform cells and the results of this interaction allow fusiform cells to detect relevant acoustic signals (Dehmel et al., 2008). The different neuronal responses to stimulation of somatosensory and auditory inputs *in vivo* are complex and depend on the stimulation site (dorsal column, spinal trigeminal nucleus, trigeminal nucleus) and also on the temporal relationship between the inputs from both modalities and the strength of stimulation (Dehmel et al., 2008).

These results further support the hypothesis that timing of synaptic input integration is critical for fusiform cell activity.

6.7.7. The importance of studying the excitatory and inhibitory synaptic transmission

Stimulations of the multisensory or the auditory inputs elicited mixed EPSPs composed of EPSPs and IPSPs. I will first discuss the effects of acoustic over-exposure on the excitatory inputs onto fusiform cells and this will be followed by the effects on the inhibitory inputs. Ultimately I will consider how the changes observed at the level of the synaptic transmission can affect fusiform cell firing.

Normal functioning of neural networks in the central nervous system depends on a balance between excitatory and inhibitory mechanisms (Meldrum, 1990). For example, in various neurodegenerative disorders, over-activation of *N*-methyl-d-aspartate (NMDA)-type glutamate receptors may lead to neuronal cell damage and NMDA receptor blockage increases the chance of survival of neuronal cells (Lipton, 2007; Estrada Sanchez et al., 2008). Inhibitory synaptic inputs mediated by glycine and GABA receptors play important roles in neuronal survival (Banks et al., 2005) by counteracting neuronal depolarization and subsequent cascade of biochemical events that result in neuronal cell death (Green et al., 2000; Wang et al., 2007).

6.7.8. Effects of acoustic over-exposure on the excitatory synaptic transmission to DCN fusiform cells

The excitatory inputs to fusiform cells arise from the parallel fibres in the molecular layer and auditory nerve fibres in the deep layer.

Acoustic over-exposure increased the EPSP threshold of activation while stimulating multisensory inputs. This can be explained by the degeneration of a

proportion of parallel fibres projecting onto fusiform cells leading to higher stimulating voltages required to stimulate the remaining functional fibres. However if this was the case, parallel fibre degeneration should translate into a decrease of the maximal amplitude and the maximal area of the isolated EPSP. Such a decrease is hard to quantify as parallel fibres are numerous (Mugnaini et al. 1980b; Napper and Harvey, 1988; Harvey and Napper, 1991) and continued to get recruited while increasing the stimulating voltage up to 15-20 V. Passed this voltage value, action potentials were elicited in fusiform cells and this made impossible to characterize further the EPSPs. EPSP characteristics were normalized to the threshold voltages in order to compare their amplitude and peaks in the different conditions (i.e. at threshold, threshold + 5V etc.). After normalisation, I observed similar EPSP areas and peaks between the unexposed and the over-exposed condition suggesting that EPSPs had conserved characteristics and displayed similar kinetics as expected if they would be evoked by a common pool of parallel fibres. Altogether, parallel fibre degeneration is a likely explanation of the effect of acoustic over-exposure on the EPSP evoked by multi sensory input stimulation. Fibre degeneration would be however limited as a large proportion of parallel fibres is still functional, leading to summing EPSPs and action potentials after acoustic over-exposure.

Another likely explanation of the EPSPs' higher threshold of activation could be linked to the change of the granule cell passive membrane properties. I showed in section 6.2.1. that acoustic over-exposure led to granule cells exhibiting more hyperpolarized resting potentials and reduced membrane resistance. These two factors contributed to decrease granule cell excitability

and could also be responsible for the higher activation threshold of the parallel fibres and consequently for the higher threshold of activation of the fusiform cell EPSPs. Damages could occur at the level of cochlear hair cells and be transmitted all the way to DCN granule cells and to the DCN fusiform cells. A change of the granule cell membrane properties could constitute a milder alternative to parallel fibre degeneration generated by acoustic over-exposure. A shift of parallel fibre excitability could also be part of the preliminary stages of plastic adjustment triggered by an acoustic insult and as such, those mild plastic changes could be reversed by contrast to terminal fibre degeneration.

By contrast to the multisensory inputs, acoustic over-exposure did not seem to affect the activation threshold of the EPSP evoked by auditory fibre stimulation. This could be due to the variability of the stimulating voltages required to evoke EPSPs. The EPSP peaks and areas seemed to be decreased by about half after acoustic overexposure (at 5 V above threshold) but values were only close to be significantly different from the values measured in unexposed condition. When performing a power test, I found that a larger number of data ($n= 15$ instead of 6 per condition) is required to determine if there are differences between the EPSPs evoked in the unexposed and over-exposed condition at this stimulus voltage. When analyzing the first peak of the EPSP generated by stimuli trains of 10 Hz and high voltages (i.e. 50-60V) I observed that the peak of the first EPSPs was indeed fifty percent smaller after acoustic over-exposure. This finding supports the hypothesis that less auditory inputs are recruited after acoustic over-exposure leading to smaller EPSPs and this becomes clear when additional fibres get recruited with higher stimulating voltages. Smaller EPSPs translated in a decrease of the firing frequency of

fusiform cells. In the unexposed condition, 80% of the cells fired an action potential in response to auditory input stimulation. By contrast, after acoustic over-exposure, only a third of fusiform cells reached the threshold for the action potential after auditory fibre stimulation, and this even when held at the relatively depolarized potential of -60 mV. Blocking the inhibitory inputs led to the same high proportion of fusiform cells failing to fire action potentials in the over-exposed condition. Previous studies reported that acoustic over-exposure is associated with degeneration of the auditory nerve axonal endings in the cochlear nucleus and this process occurs 4-8 days after the acoustic over-exposure (Morest and Bone, 1983; Kim et al., 1997; Morest et al., 1998). It is therefore likely that acoustic over-exposure led to a significant proportion of auditory fibres having degenerated. Based on the difference in the EPSP peak amplitude, this could be as high as fifty percent of the auditory nerve fibres (or terminals) being lost after acoustic over exposure. Anatomical studies suggests that one fusiform cell could get synaptic projections from 10 auditory fibres (and 10 terminals) (Ryugo and May, 1993) and from 10000 parallel fibres (Mugnaini et. al. 1980b; Napper and Harvey, 1988; Harvey and Napper, 1991). Consequently, degeneration or reduction of the auditory excitatory synaptic inputs to the DCN could influence the DCN network excitability to a greater extent than parallel fibre degeneration.

In summary, I have shown that acoustic over-exposure decreased the excitatory synaptic transmission onto DCN fusiform cells. This decrease seems to operate via different means depending on the origin of the inputs (auditory versus multisensory). In the case of the multisensory inputs, a proportion of degenerating parallel fibres and/or a change of the DCN granule cell membrane

properties could increase the threshold of activation of DCN fusiform cells without compromising their ability to fire action potentials. By contrast the EPSPs evoked by auditory input stimulation are strongly affected by acoustic over-exposure (as the action potential firing is abolished in the majority of the cells) and this could be linked to the degeneration of a proportion of auditory nerve fibres leading to DCN fusiform cells losing their ability to fire. These two situations have been addressed with modelling studies discussed in the section 6.7.11.

6.7.9. Effects of acoustic over-exposure on the inhibitory synaptic transmission to DCN fusiform cells

The inhibitory inputs to fusiform cells arise from parallel fibres activating cartwheel and stellate cells located at the interface of the fusiform layer and the molecular layer (Mugnaini 1985, Golding and Oertel 1997; Davis and Young 2000; Oertel and Young, 2004) and from the auditory nerve fibres activating tuberculoventral in the deep layer and D-stellate in the VCN (Caspary et al. 1987; Wickesberg and Oertel 1990; Oertel and Young 2004).

Like previously described for the EPSPs triggered by multisensory input stimulation, acoustic over-exposure resulted in higher thresholds of activation for the IPSPs. When increasing the stimulation voltage, IPSPs were found to be absent in about a third of the fusiform cells after acoustic over-exposure, and this was in contrast with the unexposed conditions where IPSPs could always be triggered at similar stimulating voltages. The inhibitory inputs onto fusiform cells are indirectly activated via the parallel fibres system and the effects obtained on the IPSPs could be a consequence of the increased threshold voltage activation observed for the parallel fibres. Previous *in vivo* recordings

from cartwheel cells showed that cells originating from aged animals display higher threshold of activation compared to their cellular counterpart originating from younger animals; this could be due to a loss of the excitatory drive from granule cells (Casparly et al., 2006). However I cannot exclude that the effect observed in my studies is additionally linked to passive or active property modifications that occur at the level of the inhibitory interneurons themselves (The influence of the decrease of the synaptic inhibition onto DCN fusiform cellular excitability was addressed with modelling studies discussed in 6.7.11).

The size of IPSPs elicited upon auditory stimulation was significantly reduced after acoustic over-exposure and this could also be in response to the degeneration of the excitatory auditory nerve fibres. Indeed, tuberculoventral cells are activated by auditory nerve fibres and their degeneration 3-4 days after acoustic over-exposure (Morest and Bone, 1983; Kim et al., 1997; Morest et al., 1998) could explain the decrease of the IPSP size. Previous studies reported that three days after cochlea damage (caused by either unilateral labyrinthectomy or disruption of the middle ear ossicles) there is a decrease of the mRNA levels of GLYT-2 mainly in the DCN deep layer (Barmack et al., 1999). The decreased transcription of GLYT2 mRNA could lead to a reduction in the glycine uptake that could translate in the reduced IPSC amplitudes (Zafra and Gilmenez, 2008). Numerous circuits in the auditory system respond to a loss of excitatory inputs by down regulating the inhibitory inputs (Syka, 2002). A decreased inhibition after acoustic over-exposure was for example found in the inferior colliculus and in the auditory cortex a few days after acoustic over-exposure (Syka, 2002). In the inferior colliculus, the GABA synthetic enzyme glutamate decarboxylase was found to be below control levels from 2 to

30 days after acoustic over-exposure (Szczepaniak and Moller, 1995; Abbot et al., 1999).

6.7.10. Effect of acoustic over-exposure on spike timing in fusiform cells

Studies on spike timing-dependent plasticity have underlined the potential roles of spike timing in processing and storage of information in neural circuits (Dan and Poo, 2006). The importance of spike-timing-dependent plasticity has been shown at the level of DCN parallel fibres where action potentials evoked 5 ms after parallel-fibre excitatory postsynaptic potentials led to long-term potentiation whereas action potentials evoked 5 ms before EPSPs led to long-term depression of the synapse (Tzounopoulos et al., 2004). Changing the time window between the action potential and the EPSP failed to exhibit synaptic plasticity (Tzounopoulos et al., 2004). This underlines the importance of spike timing in the DCN and further suggests that modifying spike timing precision in fusiform cells could have profound consequences on the way auditory or multisensory signals are transmitted to higher auditory centres.

I showed that synaptic transmission from multisensory inputs is precisely timed and this is likely to be due to di-synaptic inhibitory connections from the cartwheel cells to the fusiform cells (discussed in paragraph 6.7.4) that sharpen the time window of the monosynaptic excitatory transmission from the parallel fibres. Acoustic over-exposure abolished the timing precision of the multisensory synaptic inputs and this could be due to an altered timing of the IPSP. The role of the inhibitory interneurons on cellular excitability, spike timing, synchrony and oscillatory activity is well reported (Klausberger and Somogyi, 2008; McBain and Kauer, 2009). Plastic changes involving the presynaptic release machinery of the inhibitory interneurons (Klausberger and

Somogyi, 2008; McBain and Kauer, 2009) and plastic changes related to inhibitory DCN interneurons could be responsible of the loss of temporal encoding after acoustic-overexposure.

By contrast, auditory input stimulations evoked inaccurate action potential timing, likely to be due to the IPSPs evoked in synchrony with the EPSPs. Acoustic over-exposure did not alter the timing of the action potentials evoked by auditory input stimulation. Spike timing seemed to be relatively specific to the multisensory synaptic integration and several lines of research have provided physiological (King et al., 1988; Knudsen and Brainard 1991), psychophysical (Sekuler et al., 1997; Bushara et al., 2001; Spence and Squire, 2003) and cellular (Bi and Poo, 2001) evidence that temporal cues are of major importance for perceptual binding of visual and auditory scenes.

Synchronization of action potentials evoked by multisensory inputs coupled to cellular plasticity could be intrinsic properties linked to our multimodal environment encoding. Perception would therefore not only depend on the localization of the neural activity, but also on the precise temporal pattern of activity in neural assemblies. Although the specific role of the temporal encoding the DCN is still unknown, it has been suggested that it may aid in responding to novel sounds by suppressing the response to self-generated sounds (Oertel and Young, 2004). The presence of these self-generated sounds could be additionally linked with the tinnitus perception, also triggered by acoustic over-exposure and correlated with DCN dysfunctions (Kaltenbach and Godfrey, 2008).

6.7.11. Effects of acoustic over-exposure on the synaptic integration

Effects of acoustic over-exposure previously reported on the EPSPs and the IPSPs should affect the discharge frequency of fusiform cells. Surprisingly, acoustic over-exposure left the fusiform firing rate evoked by multisensory input stimulation unaffected. A likely explanation of this apparent absence of effect could be due to a similar decrease of the excitatory and the inhibitory synaptic transmission leaving the balance of the incoming excitatory and inhibitory inputs unaffected. Indeed, a reduced firing after acoustic over-exposure was unmasked by blocking the inhibitory synaptic transmission onto fusiform cells, indicating that acoustic over-exposure *i)* decreases the excitatory synaptic transmission onto fusiform cells, *ii)* also decreases the inhibitory synaptic transmission onto fusiform cells. The effects on the synaptic excitability were specifically observed when parallel fibres were stimulated at low voltage and low stimulating frequencies i.e. at minimal spatial and temporal input recruitment respectively. Fusiform cell firing rate was unaffected by acoustic over-exposure as more parallel fibres were recruited or when performing high frequency stimulations, This suggests that acoustic over-exposure affects a small proportion of parallel fibres which are preferentially recruited at threshold voltage and that the large proportion of parallel fibres is still fully functional. I previously suggested that the increased threshold voltage activation for both EPSPs and IPSPs carried by the multisensory system is likely to be linked to changes in the passive properties of granule cells or to a small proportion of degenerated parallel fibres. The results here are consistent with this suggestion.

I used an *integrate and fire* model generated by Dr M .Ison (Engineering Department, University of Leicester) with *Matlab* to simulate the firing pattern of

DCN fusiform cells in the different experimental conditions. I explored whether acoustic over-exposure only affected a small proportion of parallel fibres that are degenerating or whether changes could be attributed to changes in the granule cell passive properties (or both). I also explored whether the decrease of the inhibitory synaptic transmission onto fusiform cells was due to a direct effect on the number of inhibitory inputs or to a change in the synaptic strength of those inputs. Modelled data perfectly fitted my experimental data as acoustic over-exposure reduced the granule cell membrane resistance (from 1.9 to 1.1 G Ω), affected only a small (0.03%) proportion of parallel fibres and massively decreased the strength of the inhibitory synaptic transmission onto fusiform cells (from 25 to 0.3 a.u.). In addition, data modelling also showed that the spontaneous activity of the interneurons is reduced after acoustic over-exposure and this could be triggered by a reduced excitatory influence from the parallel fibre system.

In summary, my results as well as their computational simulations suggest that acoustic over-exposure leads to a small proportion of parallel fibres degenerating and to changes in the granule cell passive properties. This in turn decreases the spontaneous activity and the synaptic strength of the inhibitory cartwheel cells. All those effects could be overcome when a larger proportion of parallel fibres are activated. Given the diverse sources of the multisensory inputs, parallel fibres are most effectively driven by the integration of those different inputs and it is therefore likely that the physiological function of these cells is still preserved at this stage, following acoustic over-exposure.

By contrast to the previous observations, acoustic over-exposure decreased the fusiform cell firing evoked by auditory input stimulation, even

when blocking inhibitory synaptic transmission, suggesting that the effect is mainly via a reduction of the excitatory synaptic transmission. I previously reported that fusiform cell firing rate was unaffected by acoustic over-exposure as more parallel fibres were recruited. This was not the case when stimulating auditory inputs as a decrease of fusiform cell excitability could be observed at high stimulating voltages, suggesting that a significant proportion of auditory nerve fibres have degenerated or have lost their ability to transfer information onto fusiform cells. This is also consistent with hearing loss linked to the degeneration of the auditory nerve axonal endings in the cochlear nucleus (Morest and Bone, 1983; Morest et al., 1998), within the time frame of my experiments i.e. 4-8 days after the acoustic-over-exposure (Kim et al., 1997).

My previous results showed that acoustic over-exposure decreased the IPSPs alongside the EPSPs evoked by auditory input stimulation. To understand its relative effects on the excitatory and synaptic transmission, I modelled the data and showed that they fitted my experimental data as acoustic over-exposure reduced the total number of functional auditory inputs by half (consistent with the 50% reduction in the EPSPs described above and with the literature reports on the auditory nerve fibre degeneration (Morest and Bone, 1983; Morest et al., 1998). Furthermore, data modelling are consistent with a decrease of the synaptic strength of the inhibitory and remaining excitatory inputs that could be due to either a decrease of the GLYT-2 vesicular transporter (Barmack et al., 1999) or to a decrease of the vesicular glutamate transporter V-GLUT1 (Zeng et al., 2009) after auditory damage. It is worth noticing that no action potentials could be evoked in fusiform cells when the inhibitory synapses were left unaffected in the modelling situation, suggesting a

down regulation of the inhibitory synaptic transmission is necessary to maintain a minimal firing rate in fusiform cells. Interestingly, the effects described above were all overcome when auditory or multisensory inputs were stimulated at high frequencies leading to temporal summation compensating for the decrease of excitability and the restoration of the functional firing. Synaptic temporal integration can alter the firing of neurons in lateral geniculate nucleus in order to create a more efficient representation of visual signals that comes from cells within the retina (Sincich et al., 2009). The fusiform cells neurons might be well suited to use this mechanism to preserve high frequency transmitted signals. This was also suggested from passive properties; fusiform cells have a large capacitance which confers a long time constant (around 15 ms) allowing repetitive inputs to get integrated.

6.7.12. Homeostatic plasticity in the DCN neuronal network

Homeostatic synaptic plasticity allows neural circuits to function stably despite fluctuations to their inputs. Synaptic homeostasis has been framed as a process of uniform scaling that preserves information stored as relative synaptic weights by multiplying all weights to the same degree (Turrigiano et al., 1998). Plastic adjustments have been shown to influence synaptic integration (Marder et al., 1996; Storm, 1988) the pattern and rate of firing (Turrigiano et al., 1995) and synaptic plasticity (Hoffman et al., 1997; Magee and Johnston, 1997).

Homeostatic plasticity has been intensively described in the primary somatosensory, visual, and auditory cortices (Feldman, 2009), in the hippocampus (Deeg et al., 2009) and the results in this thesis strongly suggest that homeostatic plastic adjustments occur in the DCN so that fusiform cells function stably despite fluctuations to their inputs due to acoustic over-

stimulations. The mechanisms that lead to the development of the DCN hyperactivity have been previously studied by using computational modelling studies (Schaette and Kemper, 2006) and showed that the decreased firing of the auditory nerve triggers the decrease of the firing rate of neurons in the DCN. In an effort to counteract this decreased activity and restore the normal firing DCN neurons will then become hyperactive, as a result of plastic changes that are engaged to restore the network stability.

Acoustic over-exposure weakened the excitatory and inhibitory synapses and this might preserve the overall network stability. Rearing animals in dark for days reduces the evoked IPSC amplitudes in the visual cortex and this appears to be a compensatory mechanism to restore the network excitability (Tang et al., 2007). Similarly I observed a down-regulation of the inhibitory inputs evoked by both multisensory and auditory fibre stimulation which could be a compensatory mechanism triggered by the reduced activity of parallel and auditory nerve fibres respectively. Dark rearing is related to altered presynaptic mechanisms, such as the release probability and the rate of fast recycling of transmitter vesicles (Tang et al., 2007). Both mechanisms could occur at the level of the inhibitory cartwheel and tuberculoventral cell where the rate of recycling of transmitter vesicles is likely to be affected due to down-regulation of GLYT-2 vesicular transporters (Barmack et al., 1999). Postsynaptic mechanisms could also be involved for example in the decrease of the synaptic strength of the remaining auditory fibres. In cultured cortical neurons, the strength of excitatory synaptic connections between pyramidal neurons can be scaled up or down globally as a function of firing rate and this is likely to result from changes in postsynaptic AMPA-receptor number (Rutherford et al., 1997;

Turrigiano et al., 1998). The decrease of cellular excitability due to acoustic over-exposure could also be due to a significant retrograde degeneration of auditory nerve fibres and also to decrease of the membrane resistance observed in granule cells. This could be carried by two pore K^+ leak currents important in setting the resting membrane potential and cell excitability and thought to underlie the time dependence of synaptic plasticity (Chechik, 2003).

Acoustic over-exposure triggered bursts in fusiform cells indicating that the firing rate of fusiform cells can be modified from a regular to an irregular firing pattern. It has been suggested in the hippocampus that the competition between the single spikes versus the burst presents a homeostatic regulatory mechanism to maintain synaptic strength and consequently the firing rate in pyramidal cells (Buzsáki et al., 2002). A similar switch between tonic and bursting firing has also been shown in invertebrate preparations (Turrigiano et al., 1995). Similar mechanisms could also occur in the DCN where the regular pattern of activity competes with bursts neurons to maintain the physiological condition, ultimately explaining why bursts affect only a proportion of fusiform cells. Alternatively, harmful bursting could trigger an imbalance within the auditory network, leading to tinnitus.

Indeed, traumatic brain injuries are often followed by abnormal hyperexcitability, leading to acute seizures and epilepsy (Salazar et al., 1985; Dinner, 1993; Topolnik et al., 2003). Similarly, one week after acoustic over-exposure the DCN became hyperactive and this hyperactivity is thought to be correlated with the tinnitus sensation (Kaltenbach and Afman, 2000; Kaltenbach and Godfrey, 2008). The developmental hyperactivity in the DCN may use synaptic changes similar to that used for learning and memory and the

continuous perception of sound experience during tinnitus might represent the memory of this sound.

The results described in this thesis suggest that homeostatic plastic adjustments that are ultimately responsible for the increased spontaneous activity might take place 3-4 days after acoustic-overexposure. It is surprising that such adjustments affect the whole DCN circuitry after such a short time but plastic adjustments can occur on a time scale of days (Turrigiano et al., 1998).

6.7.13. Conclusions: Homeostatic plasticity, a role in tinnitus?

So far the neuronal mechanisms of tinnitus are not fully understood and therefore there are no effective treatments available. Several approaches have been used to reduce the tinnitus symptoms such as local application of the local anaesthetic lidocaine (Trellakis et al., 2007), administration of benzodiazepines and GABAergic agonists (Bahmad et al., 2006; Witsell et al., 2007), Ca²⁺ channel antagonists (Theopold, 1985; Davies et al., 1994) and NMDA antagonists (Ehrenberger et al., 2005). Although some neurones display a lower excitability after noise exposure, it has been suggested that the pathophysiology of tinnitus is linked to a general upregulation of the excitability in the central auditory pathway and specifically in the DCN (Kaltenbach et al., 2000; 2004; Brozoski et al., 2002; Basta and Ernest, 2004; Kaltenbach and Chang, 2004; 2007) and therefore to a likely increase of glutamate release. Indeed, Muly *et al.* (2004) showed that unilateral acoustic trauma increased electrically evoked glutamatergic release increased in the DCN whereas it decreased its uptake. It has also been suggested that the pathophysiology of acoustic-trauma-induced tinnitus is linked to a loss of inhibition in the central auditory pathway (Eggermont and Roberts, 2004). Vigabatrin, a specific blocker of GABA transaminase, the

catabolic enzyme for GABA, eliminates the psychophysical evidence of chronic tinnitus in an animal model (Brozoski et al., 2007). The GABA analog gabapentin has been tested in controlled clinical trials and has been shown to be effective in reducing tinnitus in some individuals, with the best therapeutic response obtained in individuals with associated acoustic trauma (Bauer and Brozoski, 2006) although a later study has shown that gabapentin is no more effective than placebo for the relief of idiopathic subjective tinnitus (Piccirillo et al., 2007). Both basic science and clinical research indicate that glutamate and GABA neurotransmitters might be a reasonable focus for tinnitus research and this thesis has shown that acoustic overexposure can act on both excitatory and inhibitory neurotransmission in the DCN. Interestingly transcranial magnetic stimulation which was suggested to evoke long term depression in cortical neurones led to clinical improvements of tinnitus in patients (Langguth et al., 2007). This suggests that it might possible to reverse the effects of the plastic changes that are established during tinnitus and further support the hypothesis that tinnitus is a form of long lasting synaptic plasticity. An alternative cure to tinnitus might consider the necessity of acting downstream before the hyperactivity gets installed. The data provided here suggest that other targets might be explored, like for example the Kv3 potassium channels or calcium channels likely to be responsible for the bursting activity of fusiform cells or two pore domain potassium channels likely to trigger the reduced firing gain in granule cells. Other targets that enhance synaptic transmission might also be considered. Multiple hypotheses have been raised concerning the mechanisms that induced tinnitus after an acoustic insult including peripheral and central auditory modifications (Chung et al., 1984; Nicolas-Puel et al., 2002 Eggermont

and Roberts, 2004, Kaltenbach and Godfrey 2008). It is likely that tinnitus starts at the peripheral level and evolves throughout the central auditory pathway via a process that resembles memory consolidation. If this is the case, treating the first symptoms linked to acoustic over-exposure could be proven effective in stopping developing tinnitus at a later stage.

Action potentials of granule cells

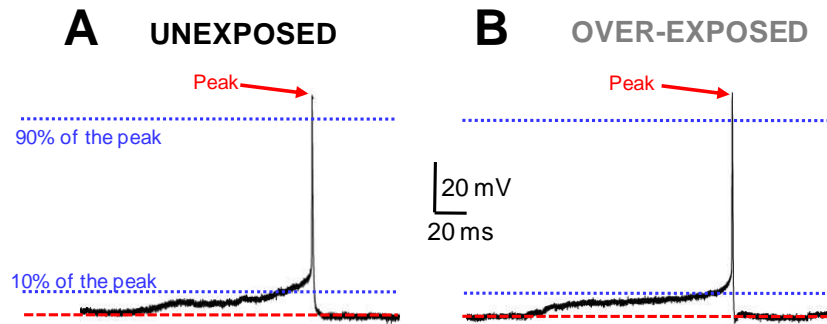


Figure 6.1: Action potentials recorded in granule cells. Example of a granule cell action potential coming from a Wistar rat unexposed to loud single tone (**A**) and from a Wistar rat previously exposed to loud single tone (**B**). Action potentials were recorded at their minimal firing frequency (threshold) at a membrane potential of -70 mV. The dashed line represents the baseline whereas the two dotted lines represent the 10-90% values relative to the action potential peak (arrows). Note that the two action potentials are similar (see also table 6.2).

Action potential firing in granule cells

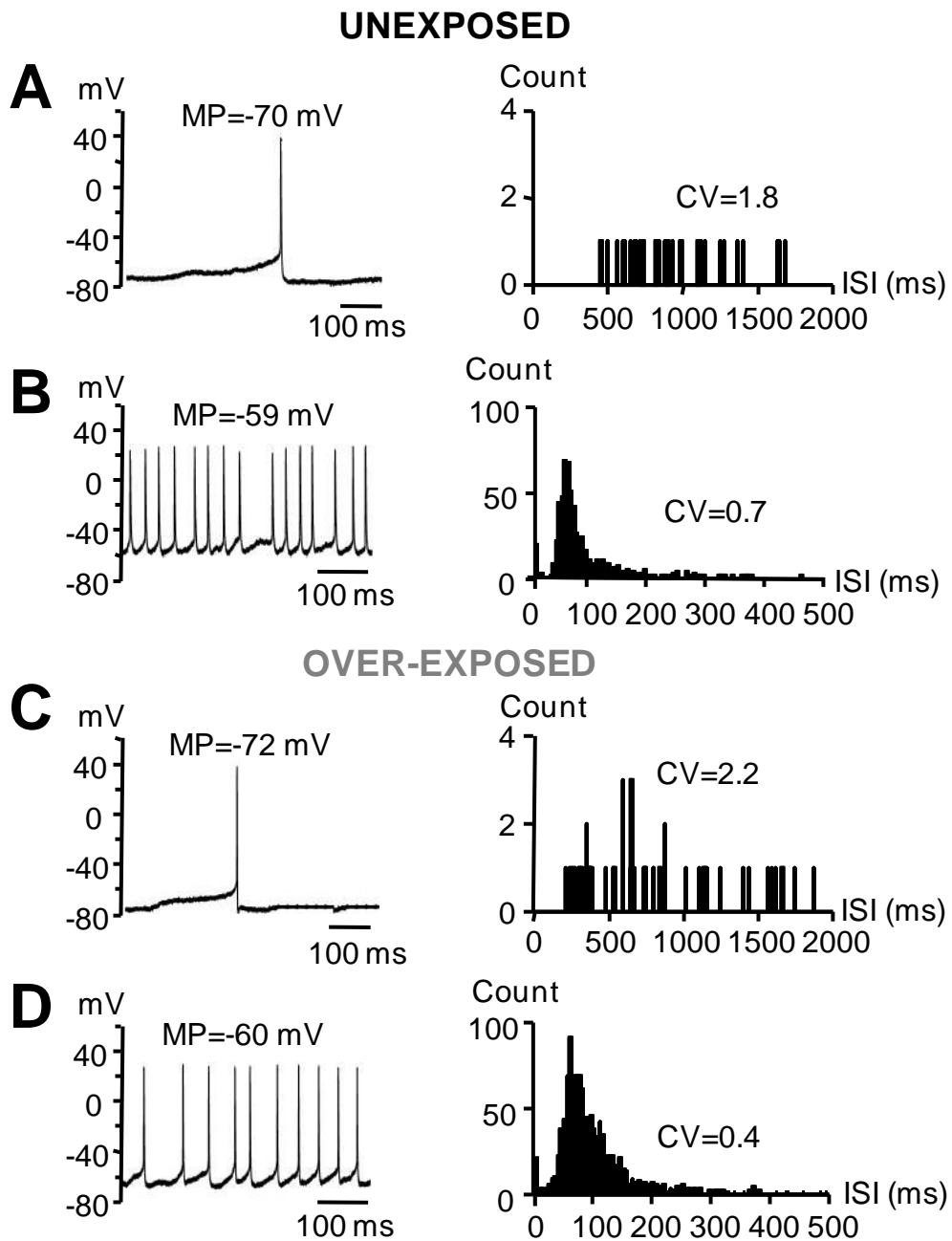


Figure 6.2: Firing properties of two granule cells originating from Wistar rats unexposed (A,B) or previously exposed to loud single tone (C,D). Action potentials were taken at threshold (A,C) and at maximal frequency (B,D). Examples of granule cell firing are shown at the left with cells firing at 0.7 Hz, 11 Hz, 0.4 Hz, 10 Hz for A, B C and D respectively. Membrane potentials are mentioned above the traces. Histograms showing the distribution of the interspike intervals (ISI) for those cells and the coefficient of variation (CV) are shown at the right. Note the absence of effect of acoustic over-exposure on the firing of granule cells (see also tables 6.3 and 6.4).

Acoustic over-exposure decreases the firing frequency of granule cells

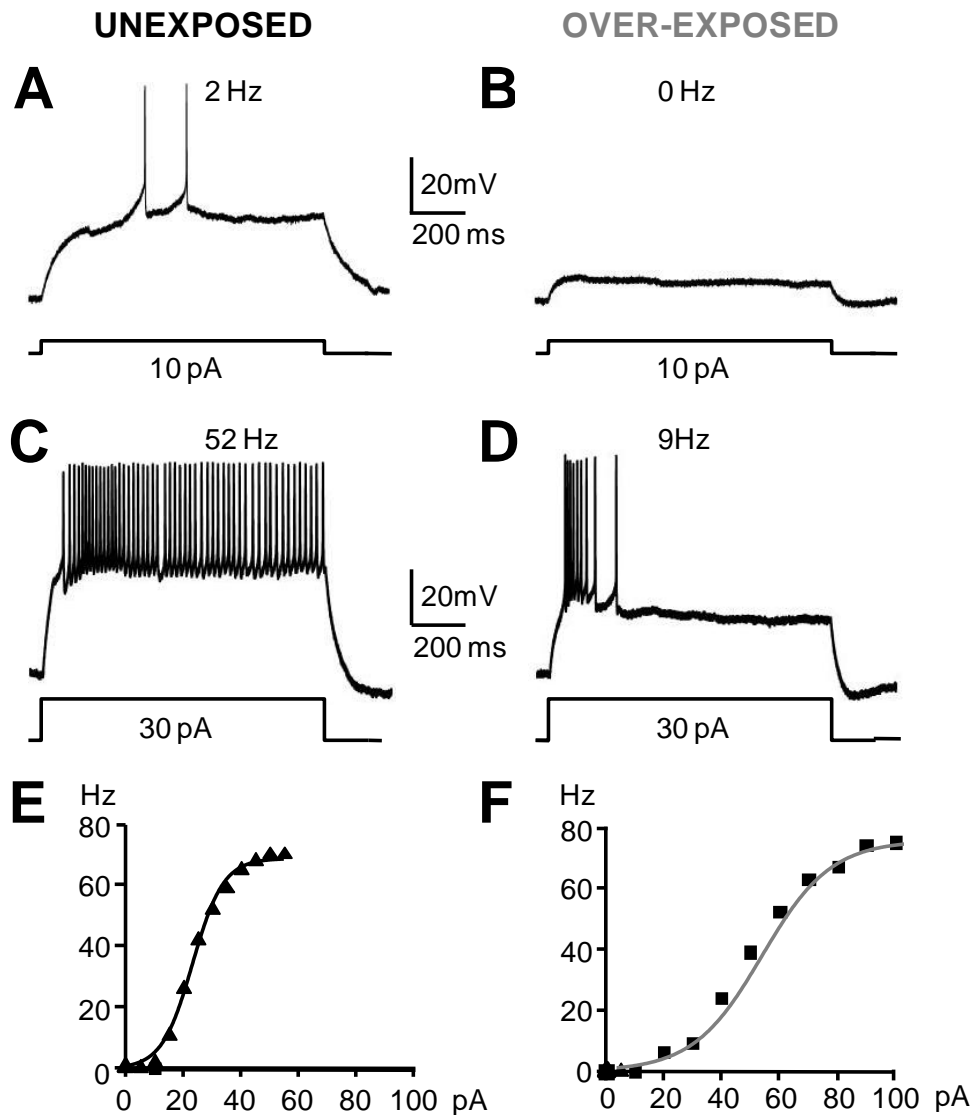


Figure 6.3: Effects of acoustic over-exposure on the action potential firing of granule cells. Voltage responses followed 1 s step current injection of 10 pA (A,B) or 30 pA (C,D). Responses originate from two littermate Wistar rats that have been unexposed (A,C) or previously exposed to loud single tone (B,D). Firing frequencies are mentioned above the traces. Note the lower firing frequency in B and D compared to A and C respectively. Granule cells membrane potential was -80 mV (E,F) Current-frequency curve fitted with a sigmoidal function for the two cells recorded above. Note that acoustic over-exposure decreases the slope (gain) of the curve without affecting the maximal firing frequency.

Effect of acoustic over-exposure on the firing frequency of granule cells

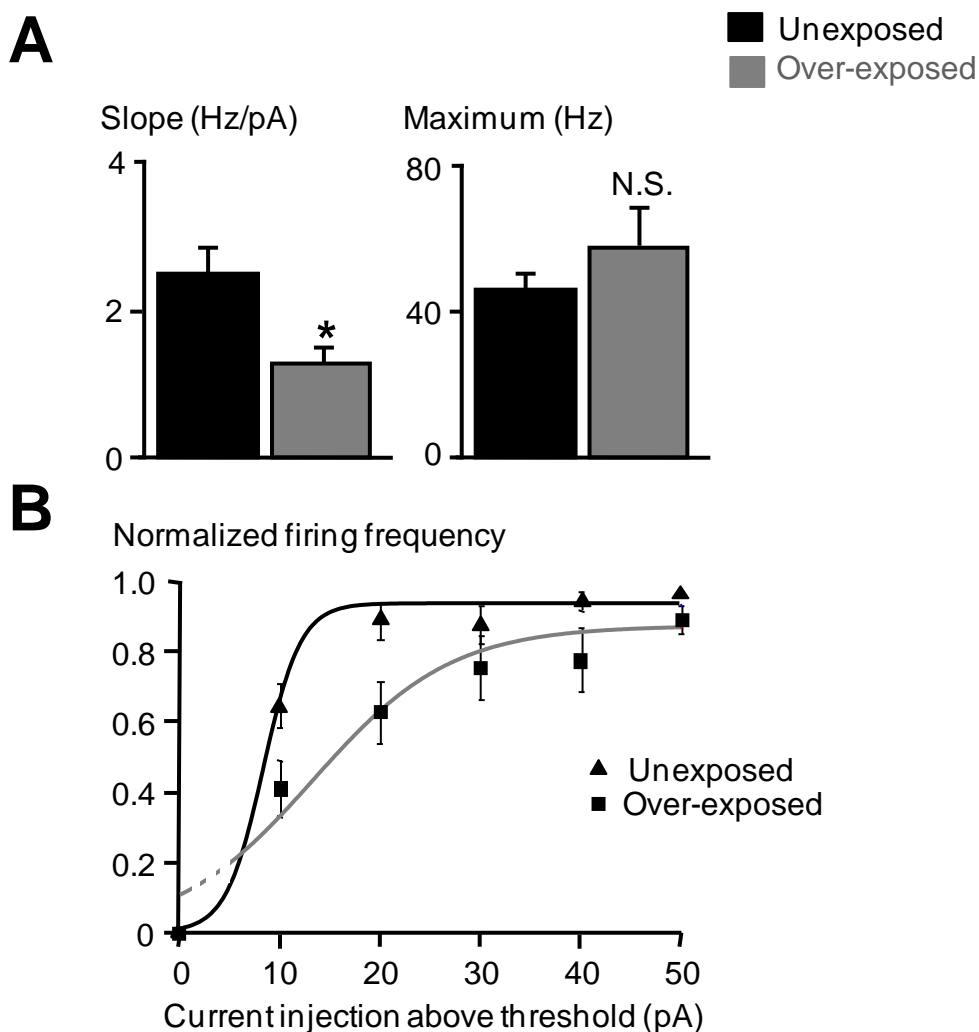


Figure 6.4: Summary of the effects of acoustic over-exposure on the granule cell firing frequency using the same protocol as in figure 6.3. (A) Histograms represents means \pm s.e.m of the slope (Hz/pA) and the maximal firing frequency (Hz) of the current-frequency curve calculated for each cell (10 cells from 3 unexposed rats, and 9 cells from 5 rats previously exposed to loud tone). **(B)** The firing frequency is normalized to the maximal firing frequency. normalized mean \pm s.e.m. values are plotted in function of the current above the threshold current. The dotted line in B represents the part of the curve that crosses the y axis instead of starting at the origin. The fit does not reach the value of 1 on the y axis as maximal firing frequencies were reached for currents exceeding 50 pA. Note that acoustic over-exposure significantly decreases the gain of the granule cell firing frequency whereas the maximum firing frequency is unaffected (see also tables 6.5 and 6.6).

Action potential accommodation of granule cells

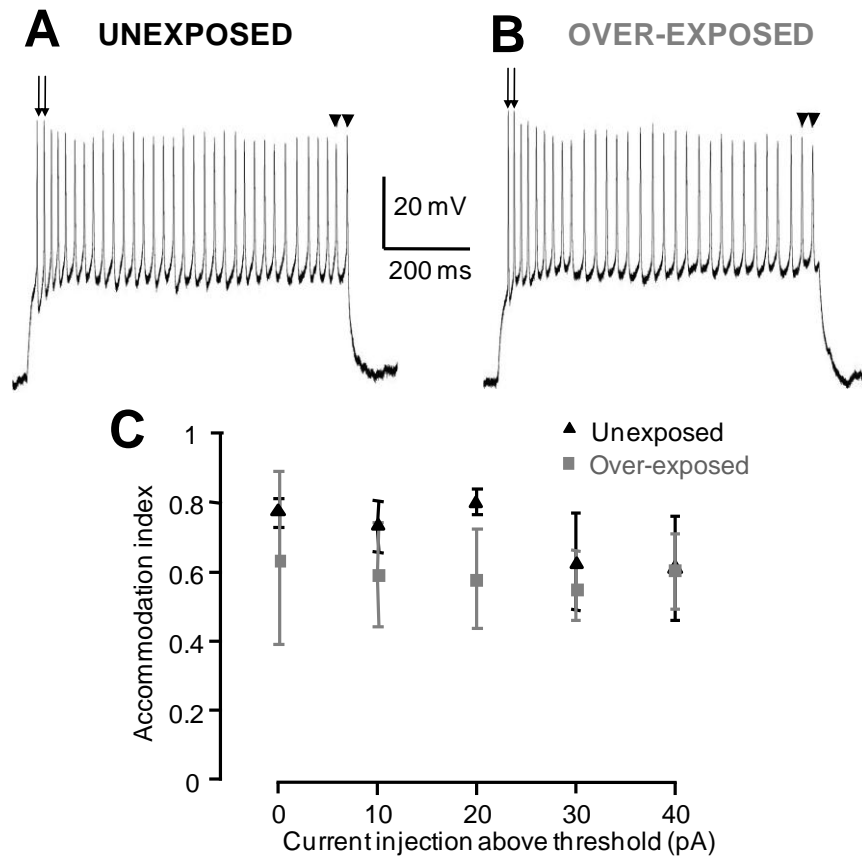


Figure 6.5: Accommodation of granule cell firing when Wistar rats were either unexposed (A) or exposed to loud single tone (B). Action potentials in A and B were recorded upon injection of a 1 sec step current of 20 pA above current at threshold. Same membrane potential of -80mV and scale bars for A and B. **(C)** Mean \pm s.e.m. ($n= 4-10$) of the accommodation index calculated as the ratio of the interspike interval (ISI) between the first and second action potential (arrows in A and B) and the ratio of the ISI between the penultimate and the last action potential (arrowheads in A and B). Accommodation indexes are represented in function of the currents exceeding the value of the currents at threshold. Accommodation indexes for A and B are 0.79 and 0.55, respectively. Note that acoustic over-exposure does not affect the accommodation in granule cells (see also table 6.7).

Action potentials of fusiform cells

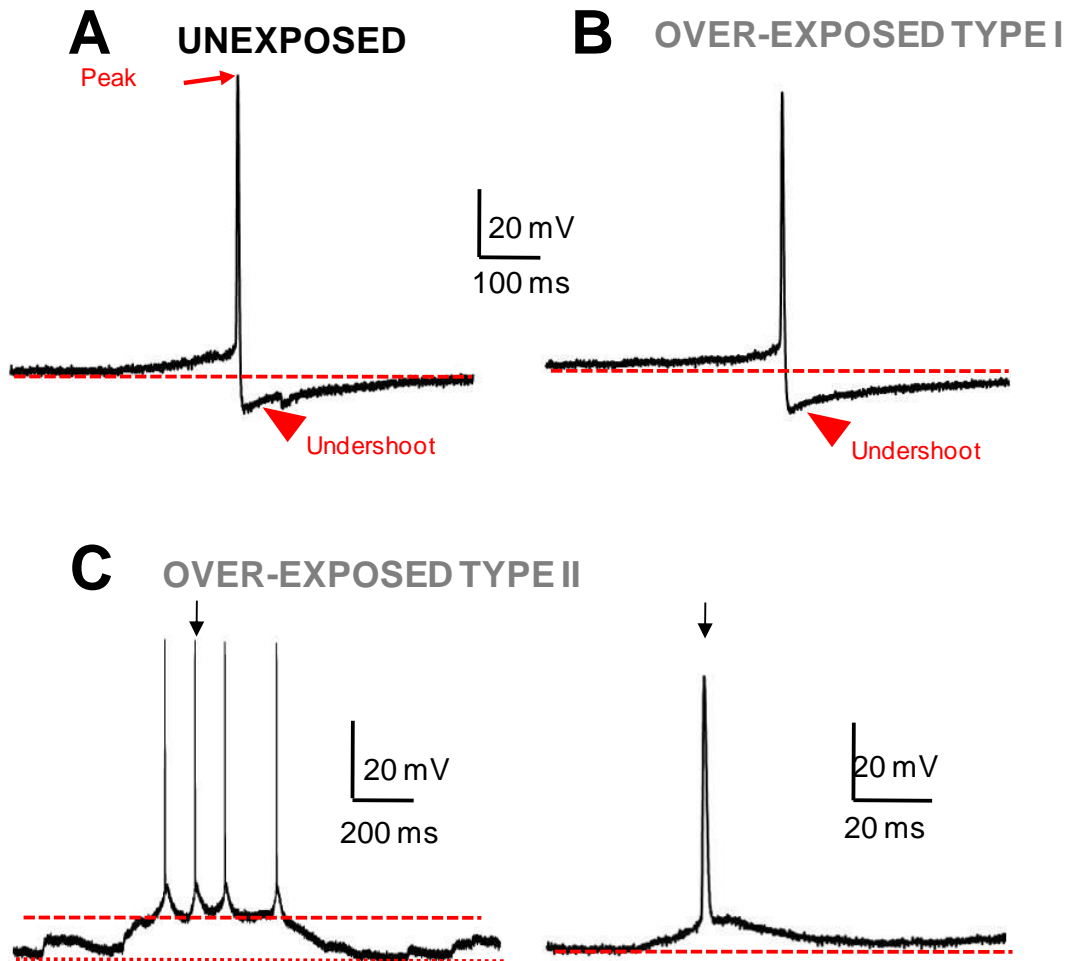


Figure 6.6: Action potentials recorded in fusiform cells. Example of a fusiform cell action potential coming from a Wistar rat unexposed to loud single tone (**A**) and two Wistar rats previously exposed to loud single tone (**B,C**). The action potential is characterized by an undershoot (arrowhead) in the unexposed (**A**) and in the over-exposed type I population (**B**) whereas there is no undershoot for the cell belonging to the over-exposed type II population (**C**). The cell in **C** is firing a burst of action potentials (represented **C** left) and a single action potential within the burst is shown by the arrow and is represented **C** right. Action potentials were all recorded at their minimal firing frequency (action potential threshold) at a membrane potential between -75 and -60 mV. The dashed line represents the baseline from which measurements for the action potential were taken whereas the dotted line represents the baseline of the burst in **C**. (See also table 6.9).

The action potential decay time is affected by acoustic over-exposure

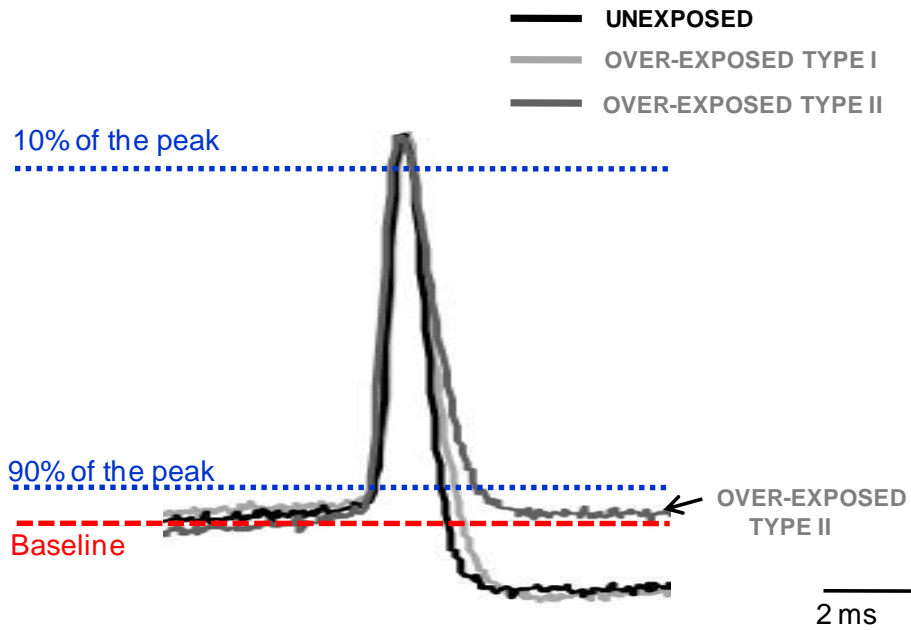


Figure 6.7: Action potential decay time of fusiform cells is prolonged after acoustic over-exposure. Superimposed and scaled to the peak traces of three action potentials represented in Figure 6.6. Action potentials were recorded at their minimal firing frequency (action potential threshold) at a membrane potential between -75 and -60 mV. The baseline is indicated by the dashed line and the 90-10% decay time is estimated between the two dotted lines. Note the longer decay time in the fusiform cell of the over-exposed type II population compared to the unexposed and over-exposed type I populations whereas the 10-90% rise time is the same in the three populations (see also table 6.9).

Bursts are unaffected by specific pharmacological blockers

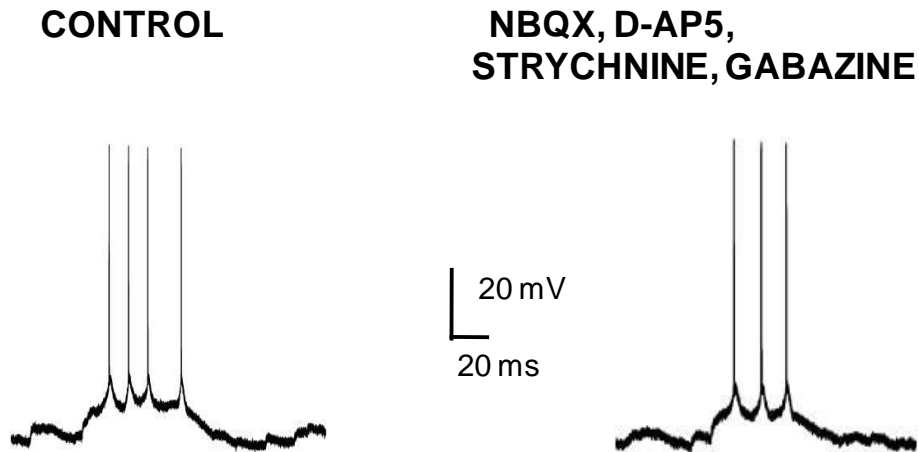


Figure 6.8: A burst of action potentials in a fusiform cell from the over-exposed type II population in control medium (left) and in presence of specific pharmacological blockers (right). Blockers are 10 μM NBQX, 50 μM D-AP5, 10 μM strychnine and 20 μM gabazine. Note that bursts alongside the depolarizing phase that leads to spike initiation persist when AMPA NMDA, glycine and GABA-A receptors are blocked. Action potentials were recorded at their minimal firing frequency (action potential threshold) at a membrane potential of -75 mV.

Acoustic over-exposure triggers bursts in a sub-population of fusiform cells

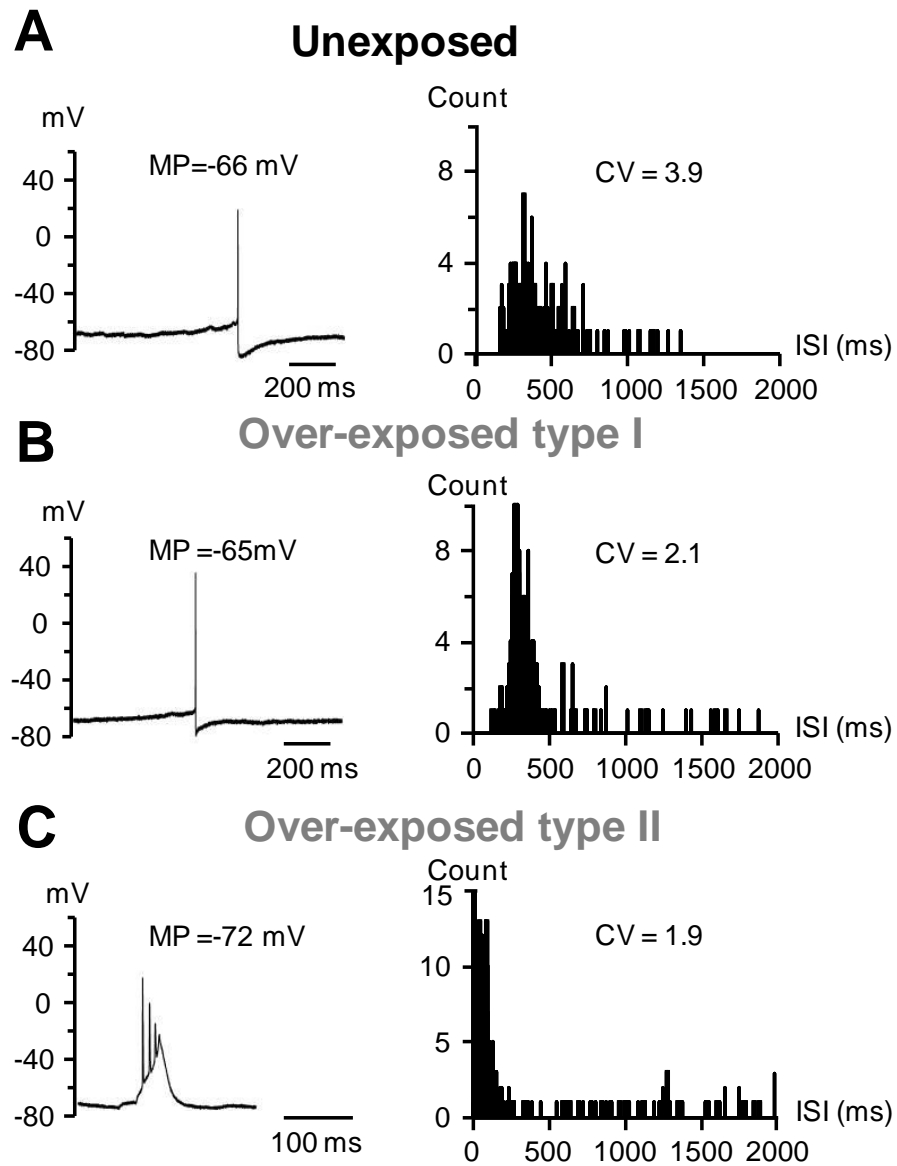


Figure 6.9: Firing properties of DCN fusiform cells held at action potential threshold. Left: Examples of three fusiform cells from rats unexposed (**A**) or previously exposed to loud single tone (**B,C**). Values of membrane potentials are above the traces and injected currents for A, B, C was -240 pA, -67 pA and -78 pA respectively. Right: Histograms showing the distribution of the interspike intervals (ISI) for those cells. Events with ISI larger than 2000 ms are not represented in the graphs in B and C. Cells are firing at 1.0 Hz, 1.3 Hz and 1.6 Hz for A, B and C respectively. Note the presence of a burst of action potentials in C. This bursting pattern was present in 30% of the fusiform cells recorded after acoustic over-exposure (see also table 6.11).

Acoustic over-exposure triggers bursts (firing at half maximal frequency)

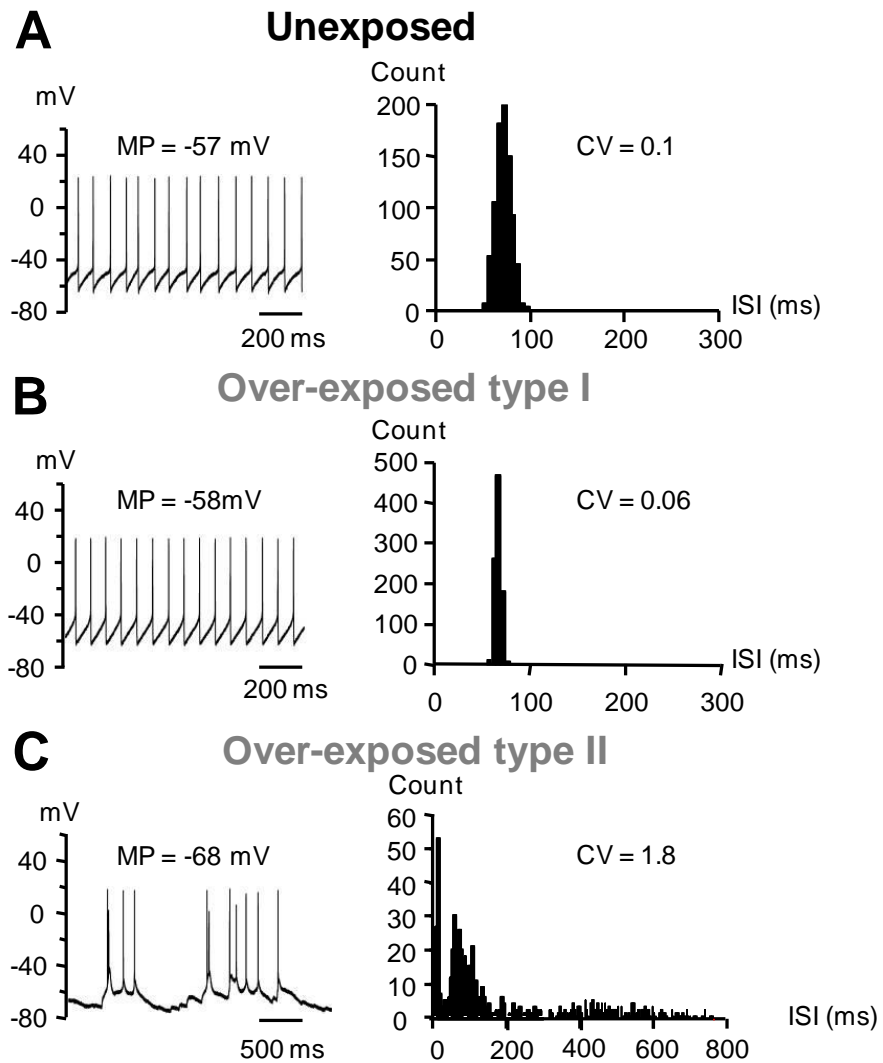


Figure 6.10: Firing properties of DCN fusiform cells at membrane potentials above action potential threshold. Same cell as in fig 6.9. Left: Examples of three fusiform cells from rats unexposed (**A**) or previously exposed to loud single tone (**B,C**). Membrane potential is mentioned above the trace and the injected current for A, B, C was +62 pA, +35 pA and -66 pA respectively. Right: Histograms showing the distribution of the interspike intervals (ISI) for those cells. Cells are firing at 14 Hz, 15 Hz and 3.4 Hz for A,B and C respectively. Note the presence of bursts of action potentials in C generating a broadening of the total ISI distribution and a larger value of coefficient of variation (CV). The two peaks of the ISI distribution represent the ISI within the burst (at around 20 ms) and the ISI between the bursts (at around 70 ms), (see also table 6.12).

Acoustic over-exposure triggers bursts (firing at maximal frequency)

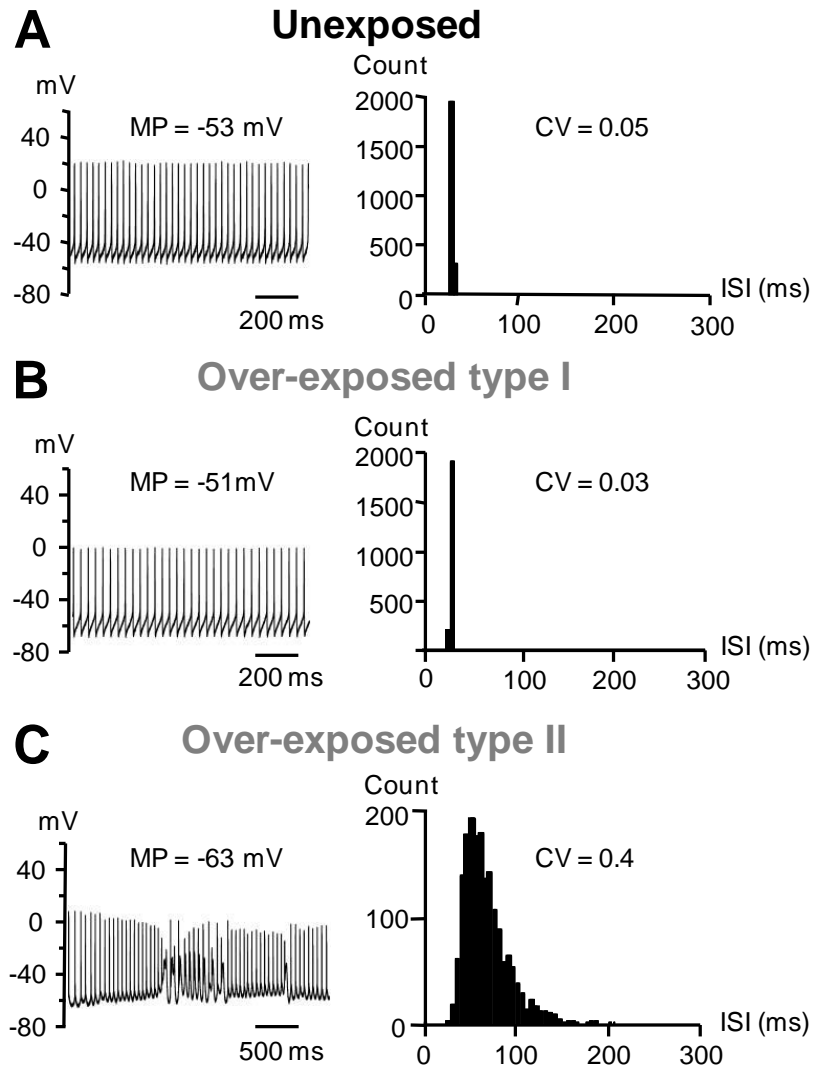


Figure 6.11: Firing properties of DCN fusiform cells at their maximal firing frequency. Same cells as in figs 6.9 and 6.10 originating from rats unexposed (**A**) and previously exposed to a loud single tone (**B,C**). Left, cells are held at depolarized membrane potentials (MP) and reach the maximal firing frequency. membrane potential is mentioned above the trace and the injected current for A, B, C was +251 pA, +244 pA and -27 pA respectively. Right: Histograms showing the distribution of the interspike interval (ISI) for those cells. Cells are firing at 35 Hz, 32 Hz and 14 Hz for A,B and C respectively. The cell is C is firing with a mixture of regular and irregular (bursts) action potentials which is responsible for the broad distribution of the ISI and the larger value of the coefficient of variation (CV) (see also table 6.13).

Acoustic over-exposure decreases the firing frequency of fusiform cells

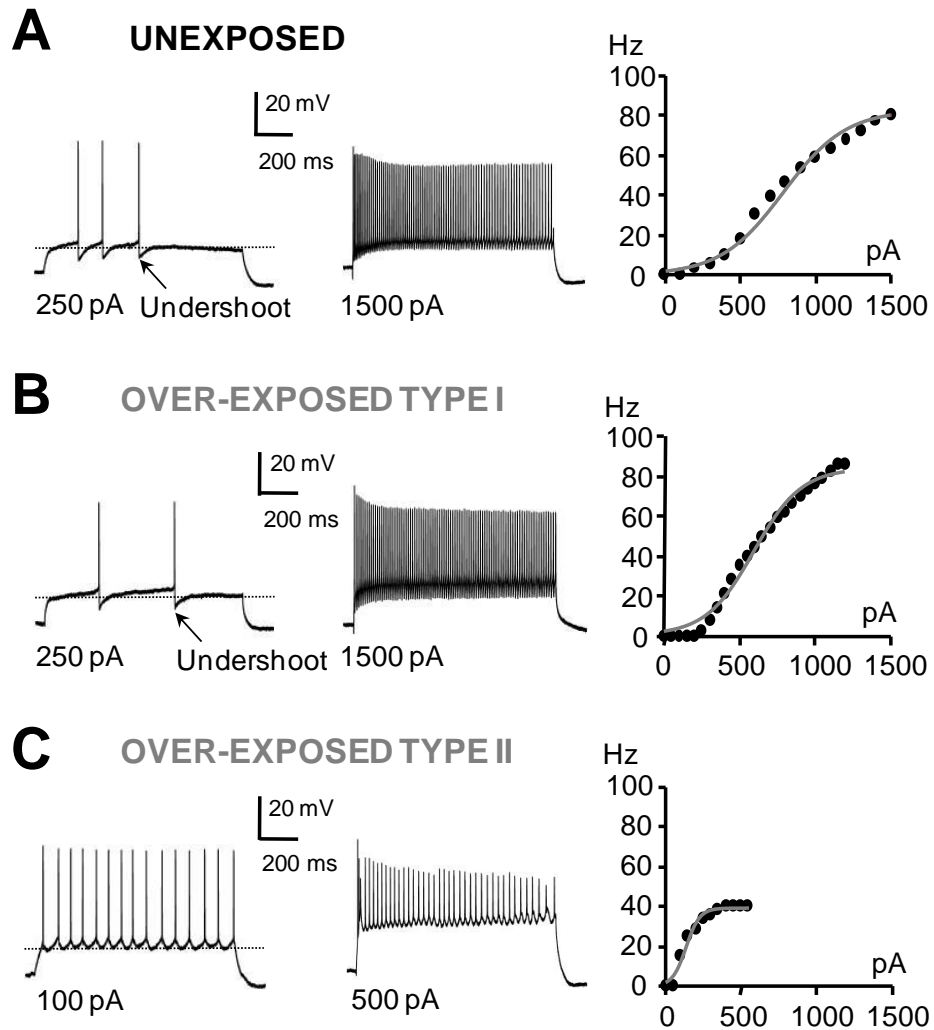


Figure 6.12: Action potential firing of fusiform cells in response to 1 s step current injection. Responses originate from rats that have been unexposed (**A**) or previously exposed to loud single tone (**B,C**). Traces represent the firing at threshold (left) and at maximal frequency (middle). The injected step current is detailed below each trace and the dashed lines show the baseline. Note that the action potential is characterized by an undershoot in (A) and (B) whereas there is no undershoot in (C). Right: current-frequency curves fitted with a sigmoidal function for the three cells at the left. Note the larger slope (gain) of the curve and the lower maximal firing frequency of the cell in C compared to the cells in A and B. (see also table 6.14). All cells start from a membrane potential of -80 mV.

Fusiform cell bursts in response to step current injections

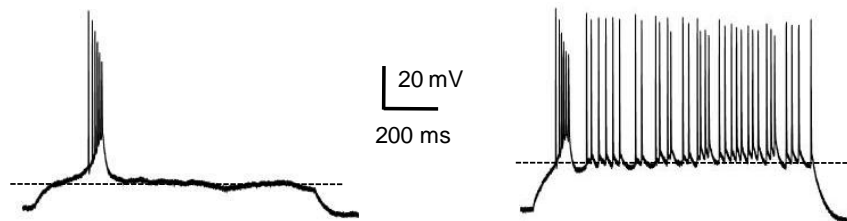


Figure 6.13: Action potential of an over-exposed type II fusiform cell in response to 1 s step current injection. Responses originate from a rat previously exposed to a loud single tone and represent the firing at threshold (left) and at maximal firing frequency (right). The cell membrane potential was -80 mV and the injected currents were 50 pA (left) and 75 pA (right). The dashed lines show the baseline. Note that the cell is firing with clusters of action potentials (bursts).

Location of the auditory and multisensory inputs to the DCN fusiform cells

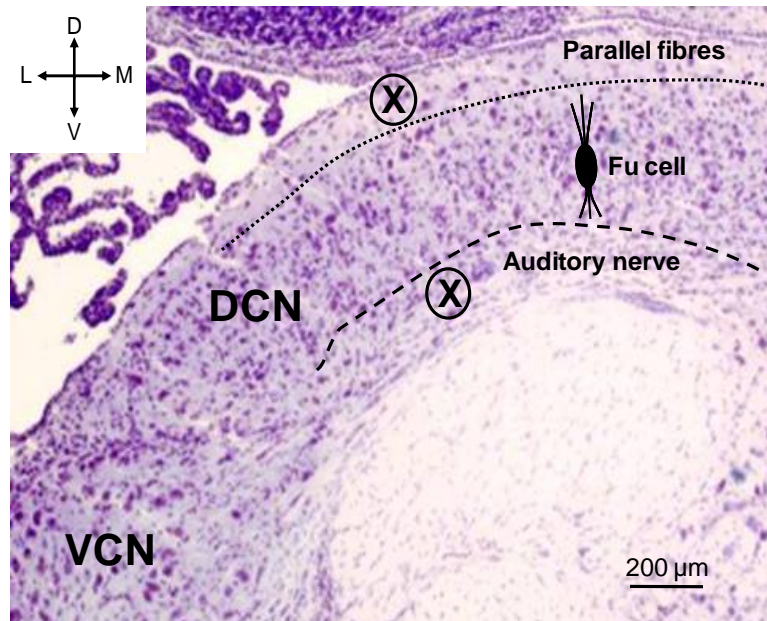


Figure 6.14 : Coronal slice of the cochlear nucleus labelled with cresyl violet. (x) shows the location of the stimulation electrode positioned either on the parallel fibres (multisensory inputs) in the molecular layer or on the auditory nerve fibres in the deep layer. The dotted and dashed lines are approximate boundaries between the molecular layer and the fusiform cell layer and between the deep layer and the fusiform layer respectively. Abbreviations: (DCN) dorsal cochlear nucleus, (VCN) ventral cochlear nucleus, (Fu cell) fusiform cell, (L) lateral, (M) medial, (V) ventral, (D) dorsal.

Synaptic responses of a fusiform cell to the stimulation of the multisensory inputs

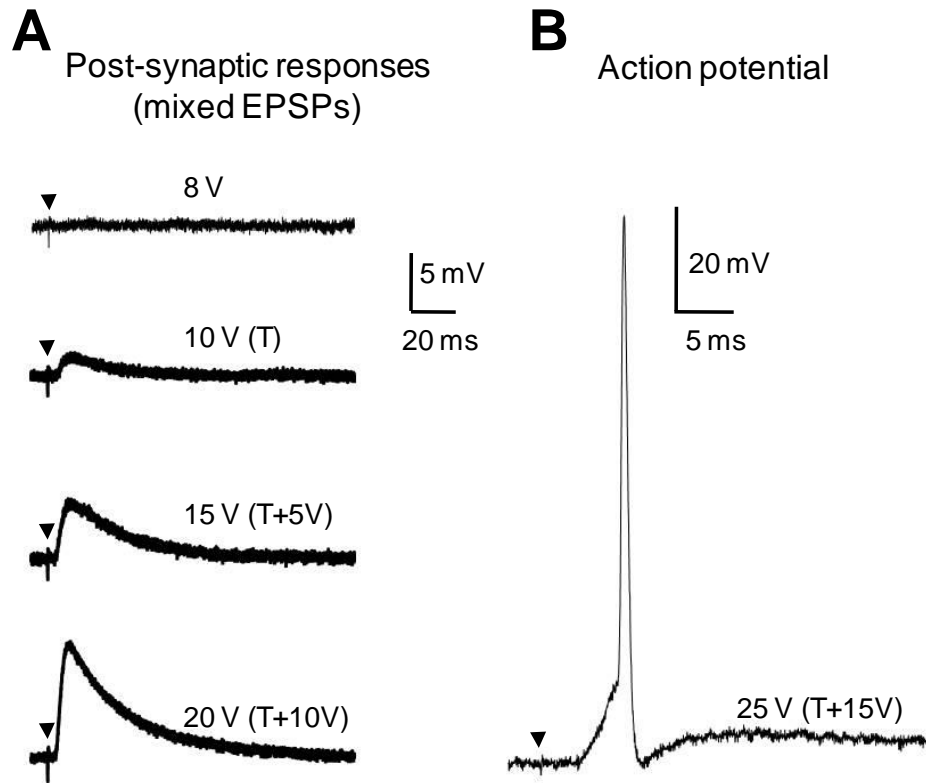


Figure 6.15: Examples of depolarisations elicited in a fusiform cell by stimulation of the parallel fibres (multisensory inputs). (A) Postsynaptic responses were elicited at different stimulation voltages indicated above the baseline. Whereas 8 V elicited no response, the post synaptic response (mixed EPSP) gradually increased as the stimulation voltage increased. The mixed EPSP is recorded in absence of synaptic blockers and therefore represents a combination of EPSPs and IPSPs. The minimal voltage applied in order to elicit a mixed EPSP in this cell was 10 V (threshold voltage for the mixed EPSP). The traces in A represent averages from 15-25 traces. (B) When the stimulation was increased to 25V the cell fired an action potential. The fusiform cell membrane potential was -70mV and the parallel fibres were stimulated at 0.3 Hz. The arrowhead marks the stimulus artefact for both A and B. Abbreviations: (EPSP) excitatory post synaptic potential, (T) threshold.

Excitatory and inhibitory postsynaptic potentials (multisensory input stimulation)

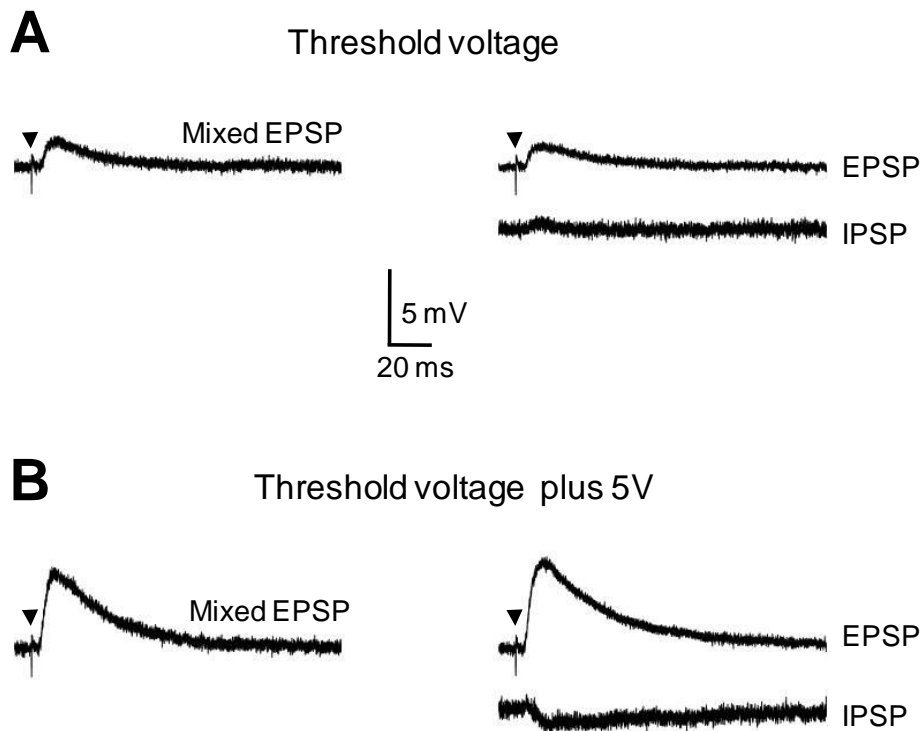


Figure 6.16: Post synaptic responses recorded in a fusiform cell at threshold voltage stimulation for the mixed EPSP (A) or 5V above this threshold voltage (B). Left traces represent a combination of EPSPs and IPSPs (mixed EPSP recorded in absence of blockers). EPSPs on the right were recorded in presence of 20 μ M gabazine and 10 μ M strychnine while IPSPs were obtained after subtracting the EPSPs from the mixed EPSP. Note the absence of IPSP at threshold in A and the smaller amplitude of the IPSP compared to the EPSP in both A and B. Multisensory inputs were stimulated at 0.3 Hz and fusiform cell membrane potentials were -70 mV. Traces represent averages from 15-25 traces. Same calibration bars for A and B. The arrowhead marks the stimulus artefact. Abbreviations: (EPSP) excitatory post synaptic potential, (IPSP) inhibitory post synaptic potential.

Characteristics of the EPSP and of the IPSP elicited by stimulation of the multisensory inputs

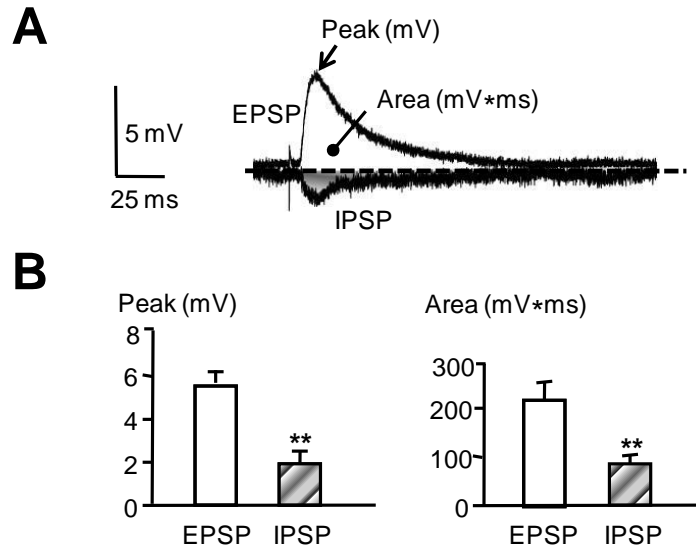


Figure 6.17: Analysis of the EPSPs and of the IPSPs elicited by the stimulation of the multisensory inputs to fusiform cells. (A) Example of an EPSP and of an IPSP recorded in a fusiform cell after stimulating the multisensory inputs at 0.3Hz and 20V (5V above the threshold voltage for the mixed EPSP). Peak and area are indicated in the case of the EPSP. The EPSP was recorded in presence of 20 μ M gabazine and 10 μ M strychnine while the IPSP was obtained after subtracting the EPSP from the mixed EPSP. A dashed line separates the EPSP from the IPSP. **(B)** Summary histograms representing the mean \pm s.e.m. values of the peak (mV) and the area (mV*ms) of the EPSP and IPSP measured in 8 cells and elicited at 5V above the threshold for the mixed EPSP (table 6.15). The IPSP amplitude and area of 2 ± 0.4 mV ($n=8$) and 83 ± 17 mV*ms ($n=8$) respectively were smaller compared to the EPSP amplitude and the EPSP area of 5.5 ± 0.6 mV ($n=8$, $P=0.0002$ paired T test) and 216 ± 35 mV*ms ($n=8$, $P= 0.002$ paired T test) respectively. Abbreviations: (EPSP) excitatory postsynaptic potentials, (IPSP) inhibitory postsynaptic potentials, (**) P values <0.01.

Fusiform cell after-potential phases following stimulation of multisensory inputs

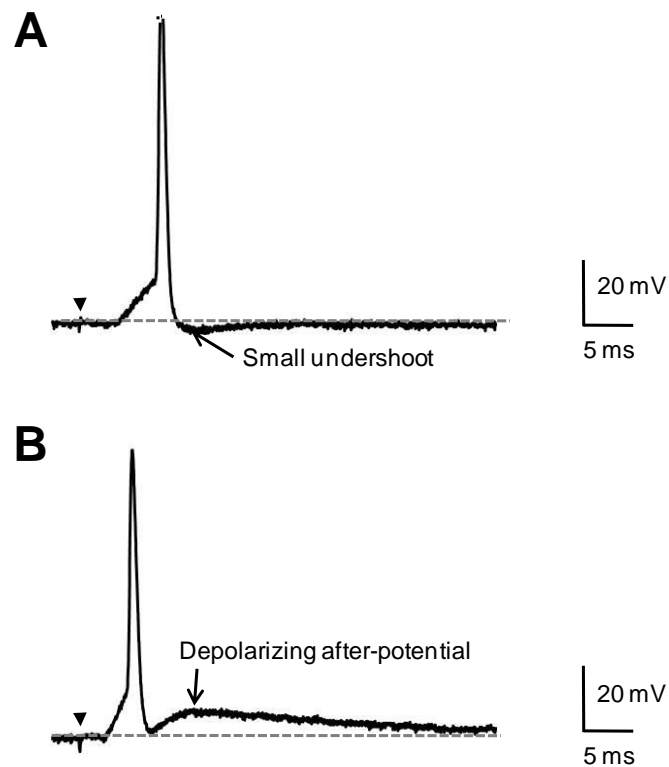


Figure 6.18: Fusiform cells after-potential phases following stimulation of multisensory inputs. Two typical examples of after-potential phases following the fusiform action potential show either a small (hyperpolarizing) undershoot (**A**) or a depolarizing after-potential (**B**). Action potentials were evoked by stimulating the multisensory inputs at 0.3 Hz at 25 V while fusiform cell membrane potential was -70 mV. The dashed line represents the baseline and the arrowhead points to the stimulating artefact. Each action potential represent 50% of the cases.

Accurate spike timing of fusiform cells following stimulation of the multisensory inputs

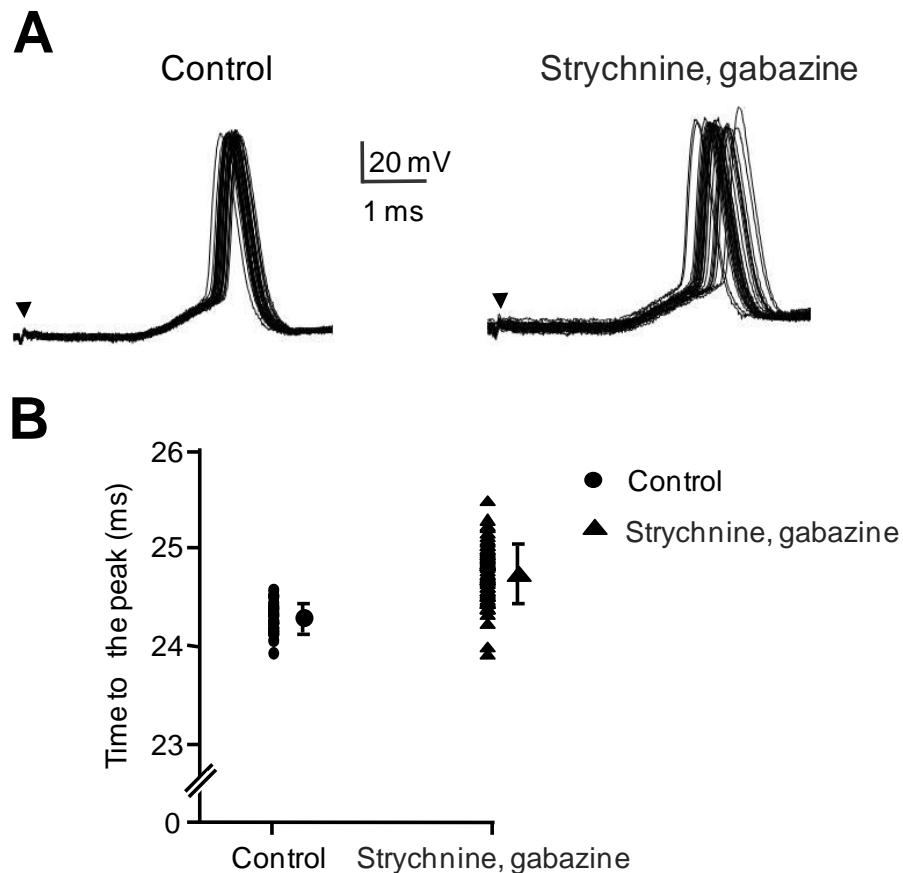


Figure 6.19: Action potential timing in fusiform cells is related to inhibitory inputs. (A) Forty action potentials recorded in control medium (left) and in presence of 10 μ M strychnine and 20 μ M gabazine (right) were superimposed on the stimulus artefact (arrowhead). Action potentials were evoked by stimulating the multisensory inputs at 0.3 Hz at 26 V and the fusiform cell membrane potential was -70 mV. **(B)** The time to the peak of each action potential was calculated for the traces in control (circle) and in strychnine and gabazine (triangle). The mean and S.D. are also shown for the 40 traces. Note that the latency (time to the action potential peak) shows little variation in control (accurate spike timing) whereas action potentials are jittering in presence of strychnine and gabazine. This pattern was present in 7 out of 10 cells. Same cell in A and B is also cell 8 in table 6.17. The time of peak was 24.3 ± 0.14 ms in control and 24.6 ± 0.28 ms in strychnine and gabazine (P value for the F test is $6 \cdot 10^{-5}$).

Synaptic responses of a fusiform cell to the stimulation of the auditory inputs

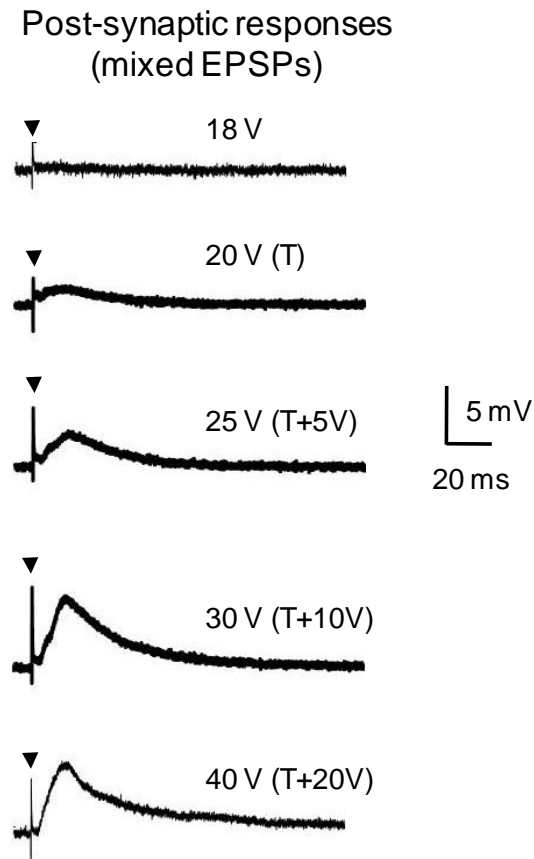


Figure 6.20: Examples of depolarisations (mixed EPSPs) elicited in a fusiform cell by stimulation of the auditory fibres. Postsynaptic responses were elicited at different stimulation voltages indicated above the baseline. The mixed EPSP was recorded in absence of any synaptic blocker. Whereas 18V elicited no response, 20V started to elicit a mixed EPSP in this cell (threshold of the mixed EPSP). Mixed EPSPs then gradually increased as the applied voltage increased until a maximal amplitude was reached at 30V (amplitude of the EPSP similar when elicited at 30V and 40V). Note the absence of action potentials. The fusiform cell membrane potential was -70mV and the auditory nerve fibres were stimulated at 0.3 Hz. The arrowhead marks the stimulus artefact and the traces represent averages from 15-25 traces. Abbreviations: (EPSP) excitatory post synaptic potential, (T) threshold.

Comparison between the mixed EPSPs elicited upon auditory and multisensory stimulation

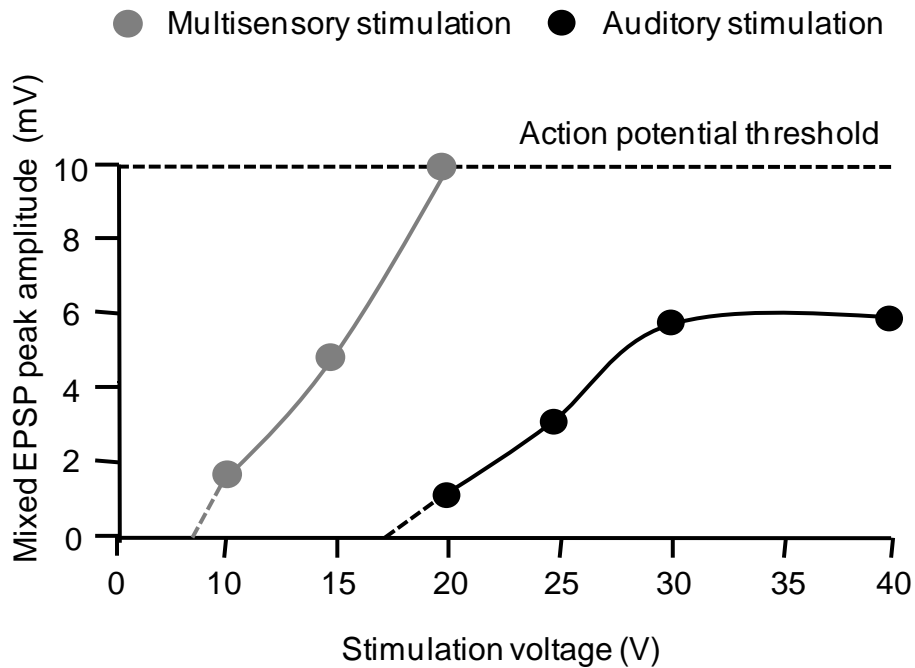


Figure 6.21: Graph representing the mixed EPSP peak amplitude in relation the stimulus voltage when auditory (black) or multi sensory (grey) inputs were stimulated. Note the higher threshold voltage to elicit an EPSP when stimulating the auditory fibres compared to multisensory inputs. Note also that stimulating multisensory inputs elicit an action potential (represented by the dashed line) by contrast to stimulating the auditory nerve fibres that triggered EPSPs solely. The two cells are typical examples represented in figure in 6.15 and 6.20 and membrane potential were -70 mV.

Excitatory and inhibitory postsynaptic potentials (auditory input stimulation)

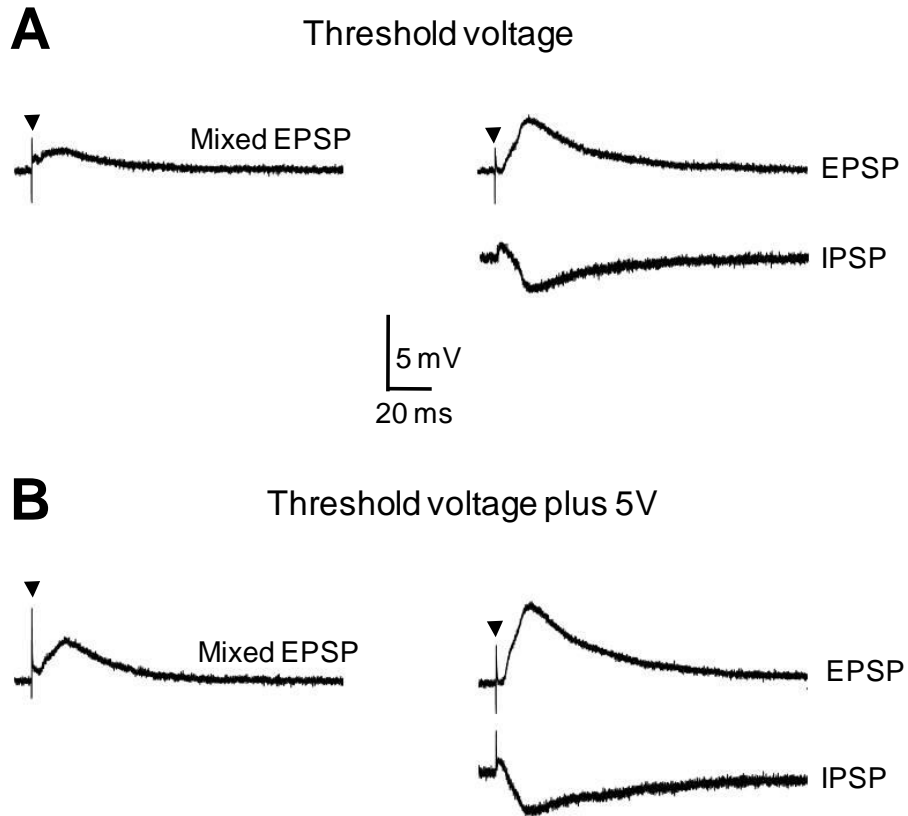


Figure 6.22: Post synaptic responses recorded in a fusiform cell after stimulating the auditory inputs at threshold voltages for the mixed EPSP (A) or 5V above this threshold voltage (B). Left traces represent a combination of EPSPs and IPSPs (mixed EPSP recorded in absence of blockers). EPSPs on the right were recorded in presence of 20 μ M gabazine and 10 μ M strychnine while IPSPs are obtained after subtracting the EPSPs from the mixed EPSP. Note the large IPSPs at threshold voltages for the mixed EPSP and above those threshold voltages. Auditory inputs were stimulated at 0.3 Hz and fusiform cells membrane potential was -70 mV. Traces represent averages from 15-25 traces. Same calibration bars for A and B. The arrow headmarks the stimulus artefact. Abbreviations: (EPSP) excitatory post synaptic potential, (IPSP) inhibitory post synaptic potential.

Characteristics of the EPSP and of the IPSP elicited by stimulation of auditory and multisensory inputs

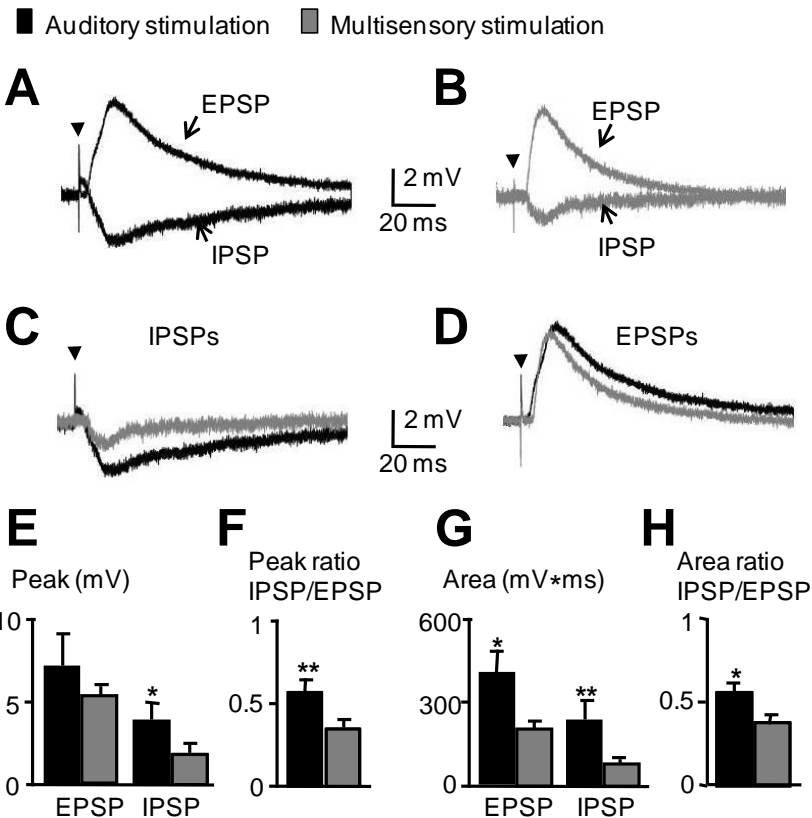


Figure 6.23: Comparison between EPSPs and IPSPs evoked in fusiform cells after stimulating the multisensory and auditory inputs. Typical examples of EPSPs and IPSPs after stimulating the auditory inputs (**A**, same cell as in figure 6.22) or the multisensory inputs (**B**, same cell as in figure 6.17). Stimulations were performed at 0.3Hz for a membrane potential of -70 mV. (**C**) Overlay of the IPSPs from A and B. (**D**) overlay of the EPSP from A and B. **E-H**. Summary histograms representing the mean \pm s.e.m. ($n=4-8$, table 6.19 and 6.20) values of the EPSP and the IPSP peaks (**E**), the peak ratio of the IPSP relative to the EPSP (**F**), the EPSP and the IPSP area (**G**), the area ratio of the IPSP relative to the EPSP (**H**). Measurements were performed after stimulating auditory (black) or multisensory (grey) inputs, at 5 V above threshold voltage for the mixed EPSP. Note that the stimulation of the auditory fibres are characterised by larger IPSPs and EPSPs compared to the stimulation of multisensory inputs (with * P values < 0.05, ** P values < 0.01). The arrowhead marks the stimulus artefact. Abbreviations: (EPSP) excitatory post synaptic potential, (IPSP) inhibitory post synaptic potential.

Action potentials elicited in fusiform cells following stimulation of the auditory inputs

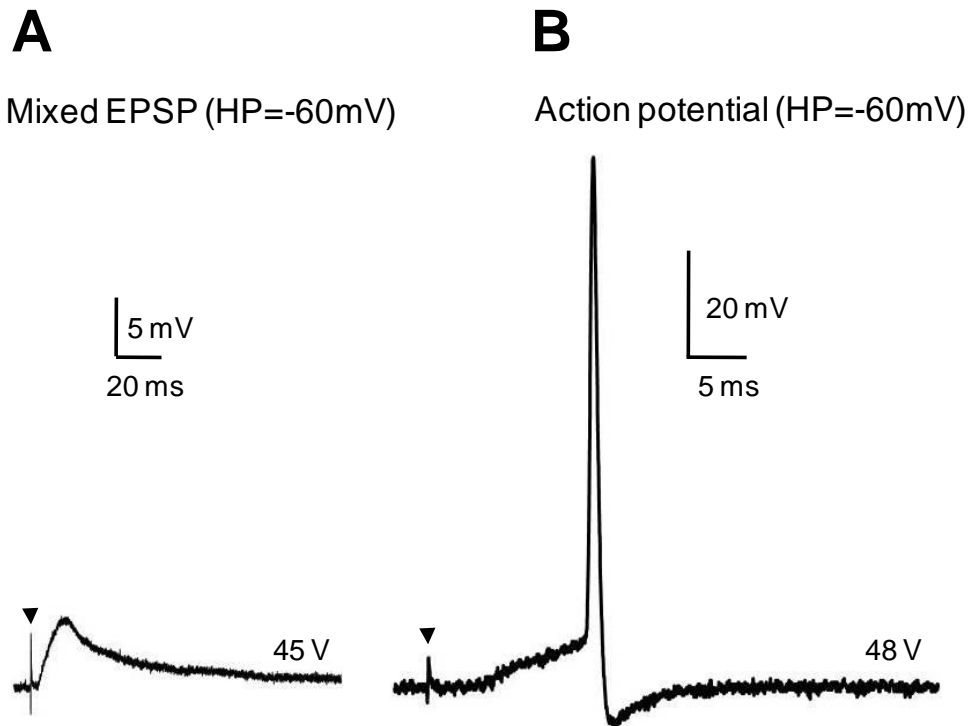


Figure 6.24: Examples of an EPSP and an action potential that could be elicited by stimulation of the auditory inputs and from a fusiform cell membrane potential of -60 mV. Auditory fibres were stimulated at 0.3 Hz with the voltage value mentioned above the baseline. Whereas 45 V stimulus voltage triggered a mixed EPSP (**A**) an action potential got triggered at 48 V (**B**). The arrowhead points to the stimulus artefact. The traces in A represent averages from 15-25 traces and the trace in B is a single action potential.

Example of spike timing in a fusiform cell following stimulation of the auditory inputs

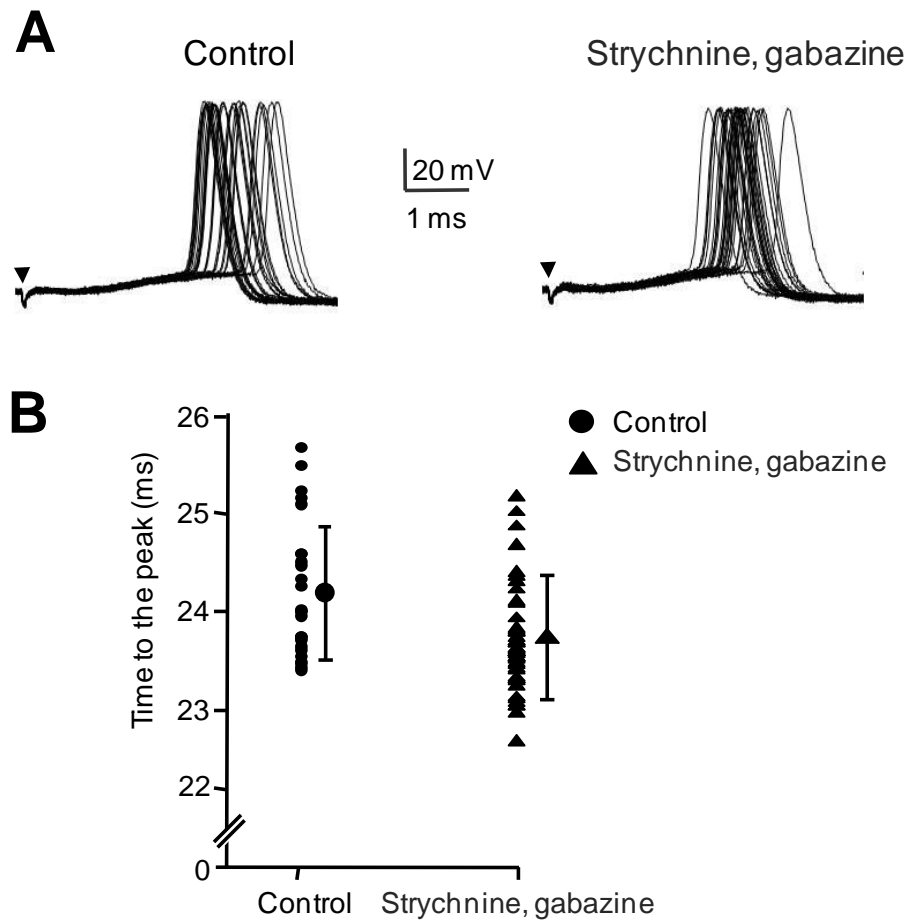


Figure 6.25: Action potentials are jittering when stimulating the auditory inputs. (A) Thirty action potentials were elicited in a fusiform cell and superimposed on the stimulation artefact in control (A left) and in presence of 10 μM strychnine and 20 μM gabazine (A right). Action potentials were evoked by stimulating the auditory inputs at 0.3 Hz and the fusiform cell membrane potential was -60 mV. (B) The time to the peak of each action potential was calculated for the traces recorded in control medium (circle) and in strychnine and gabazine (triangle). The mean and S.D. are also shown for the 30 traces. Note that the latency (time to the action potential peak) shows a large variation in both control and in strychnine and gabazine (action potentials jittering). This pattern was present in half of the cells ($n=6$). The cell in the figure is cell 5 in table 6.23. The time of peak was 24.1 ± 0.67 ms in control and 23.6 ± 0.51 ms in strychnine and gabazine (P value for the F test is 0.15).

Example of spike timing in a fusiform cell following stimulation of the auditory inputs

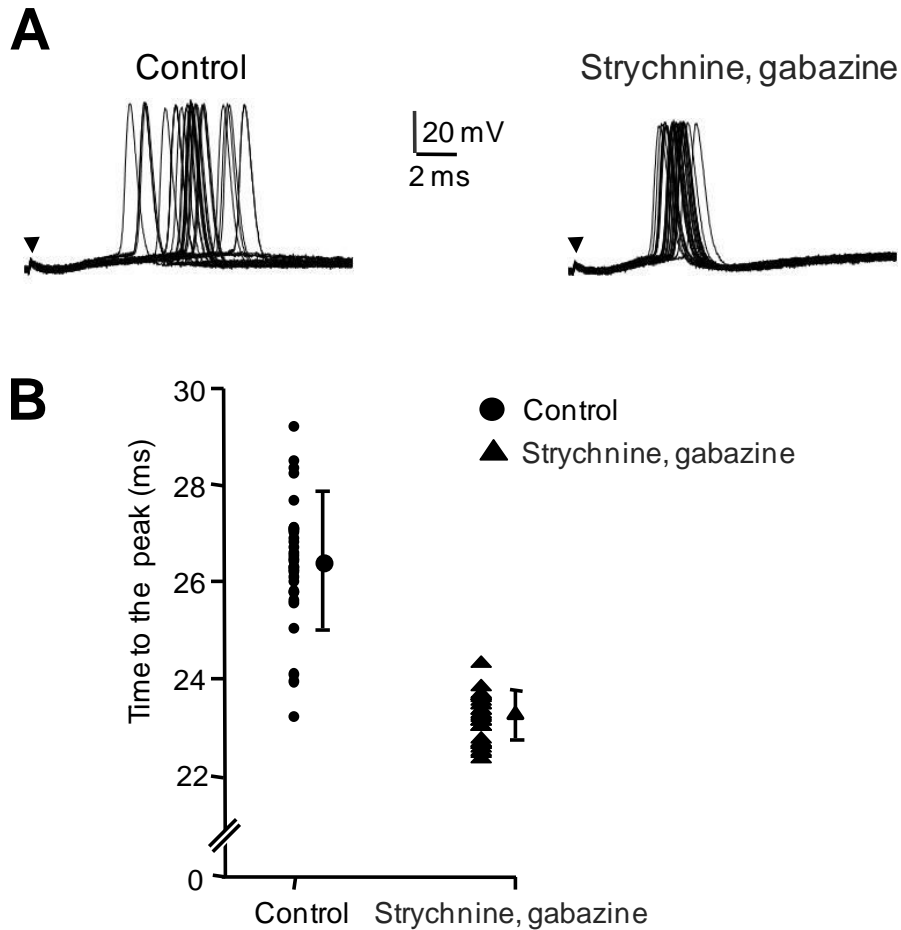


Figure 6.26: Abolishing inhibitory synaptic transmission when stimulating the auditory inputs elicit accurate spike timing in half of the fusiform cells. (A) Thirty action potentials were elicited in a fusiform cell and superimposed on the stimulation artefact in control (A left) and in presence of 10 μ M strychnine and 20 μ M gabazine (A right). Action potentials were evoked by stimulating the auditory inputs at 0.3 Hz and the fusiform cell membrane potential was -60 mV. **(B)** The time to the peak of each action potential was calculated for the traces recorded in control medium (circle) and in strychnine and gabazine (triangle). The mean and S.D. are shown for the 30 traces. Note that the strychnine and gabazine abolish the variation of the time from the stimulation artifact to the action potential peak. This pattern was present in half of the cells ($n=6$). The cell in the figure is cell 4 in table 6.23. The time of peak was 26.4 ± 1.37 ms in control and 23.2 ± 0.49 ms in strychnine and gabazine (P value for the F test is $2 \cdot 10^{-7}$).

Characteristics of the EPSC and of the IPSC elicited by stimulation of multisensory and auditory inputs

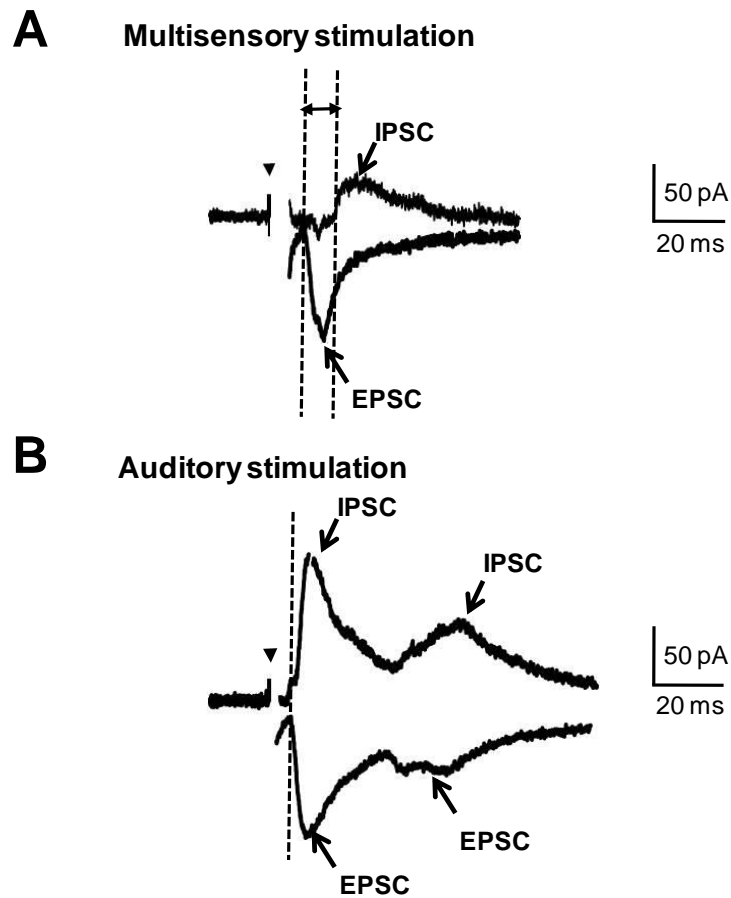


Figure 6.27: IPSCs and EPSCs elicited by stimulating multisensory fibres (A) or auditory inputs (B) to fusiform cells. Voltage clamp recordings were performed while holding the fusiform cells at -75 mV and stimulating at 0.3Hz and at 10 V above the threshold for the mixed EPSC (recorded in current clamp). EPSCs were recorded in presence of strychnine and gabazine while IPSCs are obtained after subtracting the EPSCs from the mixed EPSC. Note the long latency of the IPSC while stimulating the multi sensory inputs (shown by the dashed line) and the presence of multiple EPSC and IPSC peaks in (B) The artefact of stimulation has been removed for clarity and pointed out with an arrowhead. All traces represent averages from 15-25 traces. Abbreviations: (EPSC) excitatory postsynaptic current, (IPSC) inhibitory postsynaptic current.

Effects of acoustic over-exposure

Post- synaptic responses of a fusiform cell after stimulation of the multisensory inputs

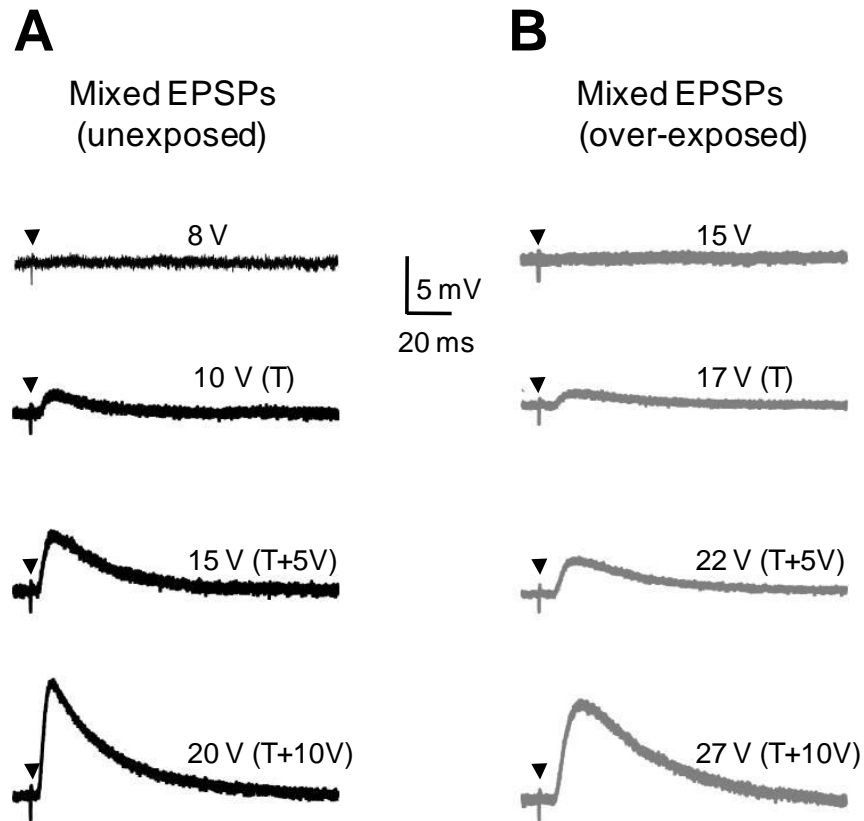


Figure 6.28: Examples of mixed EPSPs elicited in two fusiform cells after stimulation of the multisensory inputs in unexposed (A) and over-exposed conditions (B). The fusiform cell membrane potentials were -70mV and inputs stimulated at 0.3 Hz using stimulation voltages indicated above the trace. The mixed EPSPs were recorded in absence of synaptic blockers and represent a combination of IPSPs and EPSPs. Note that the stimulation voltage required to elicit a mixed EPSP was higher in the over-exposed condition. The arrowhead marks the stimulus artefact and the traces represent averages from 15-25 individual traces. Abbreviations: (EPSP) excitatory post synaptic potential, (IPSP) inhibitory post synaptic potential, (T) threshold.

Excitatory and inhibitory postsynaptic potentials after multisensory input stimulation

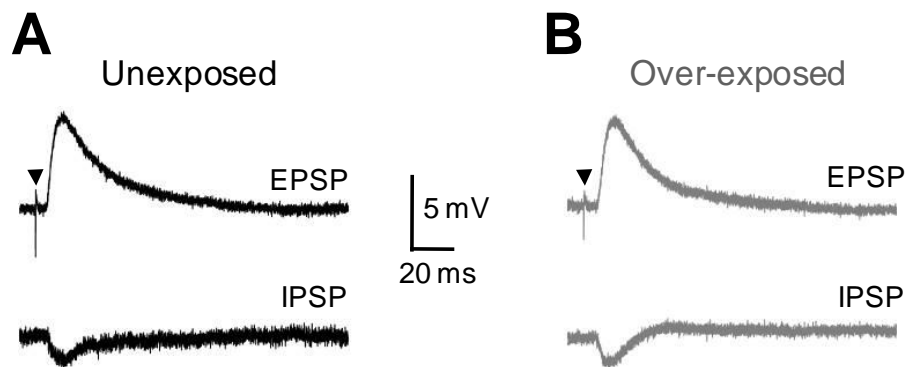


Figure 6.29: EPSPs and IPSPs recorded in fusiform cells unexposed (A) and over-exposed condition (B). Mixed EPSPs (not shown here) were recorded at 5V above the threshold voltage and EPSPs were recorded in presence of 20 μ M gabazine and 10 μ M strychnine. IPSPs were obtained after subtracting the EPSPs from the mixed EPSP. Note that EPSPs as well as IPSPs are similar between the unexposed and the over-exposed conditions. All traces represent averages from 15-25 traces recorded at a membrane potential of -70 mV and elicited at a stimulation of 0.3 Hz. The arrowhead marks the stimulus artefact. Abbreviations: (EPSP) excitatory post synaptic potential, (IPSP) inhibitory post synaptic potential.

Summary of the EPSP and IPSP characteristics after stimulation of the multisensory inputs

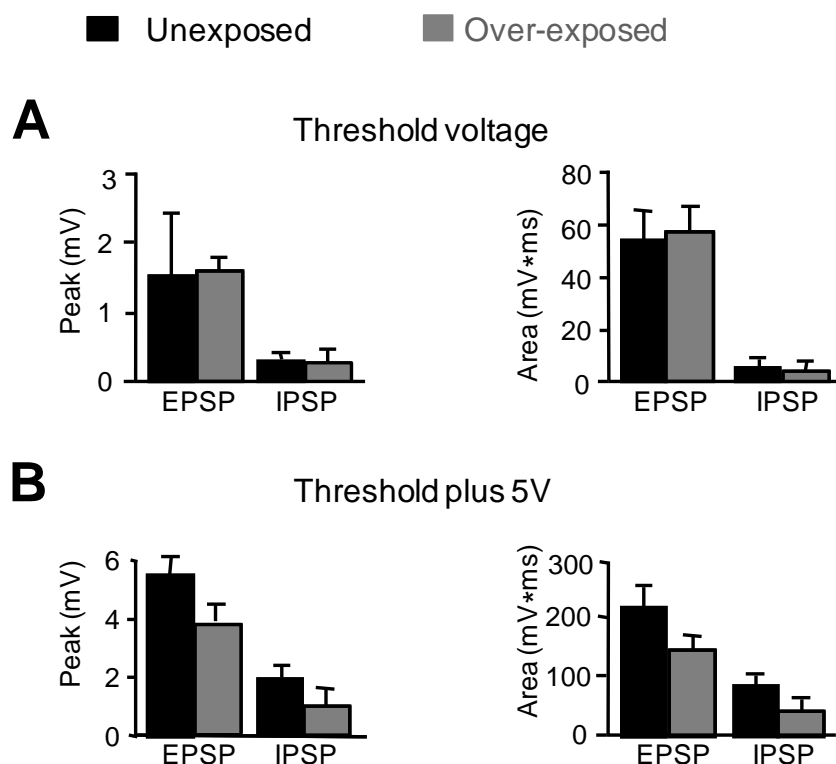


Figure 6.30: Analysis of the EPSPs and the IPSPs elicited in fusiform cells by stimulation of the multisensory inputs. Summary histograms represent the synaptic input characteristics in unexposed (black) and after acoustic over-exposure (in grey). **(A)** Mean \pm s.e.m. values obtained at threshold voltage for the mixed EPSP. P values comparing the unexposed and the over-exposed conditions (6-8 cells per condition) were 0.57 and 0.90 for the IPSP amplitude and area respectively, 0.26 and 0.83 for the EPSP amplitude and area respectively. **(B)** represents the mean \pm s.e.m. values obtained at threshold + 5V (table 6.24). P values comparing the unexposed and the over-exposed conditions (6-8 cells per condition) were 0.33 and 0.13 for the IPSP amplitude and area respectively, 0.22 and 0.11 for the EPSP amplitude and area respectively. Note that acoustic over-exposure does not affect the characteristics of the EPSPs and IPSPs. Abbreviations: (EPSP) excitatory postsynaptic potentials, (IPSP) inhibitory postsynaptic potentials.

The accurate action potential timing evoked by multisensory stimulation is lost after acoustic over-exposure

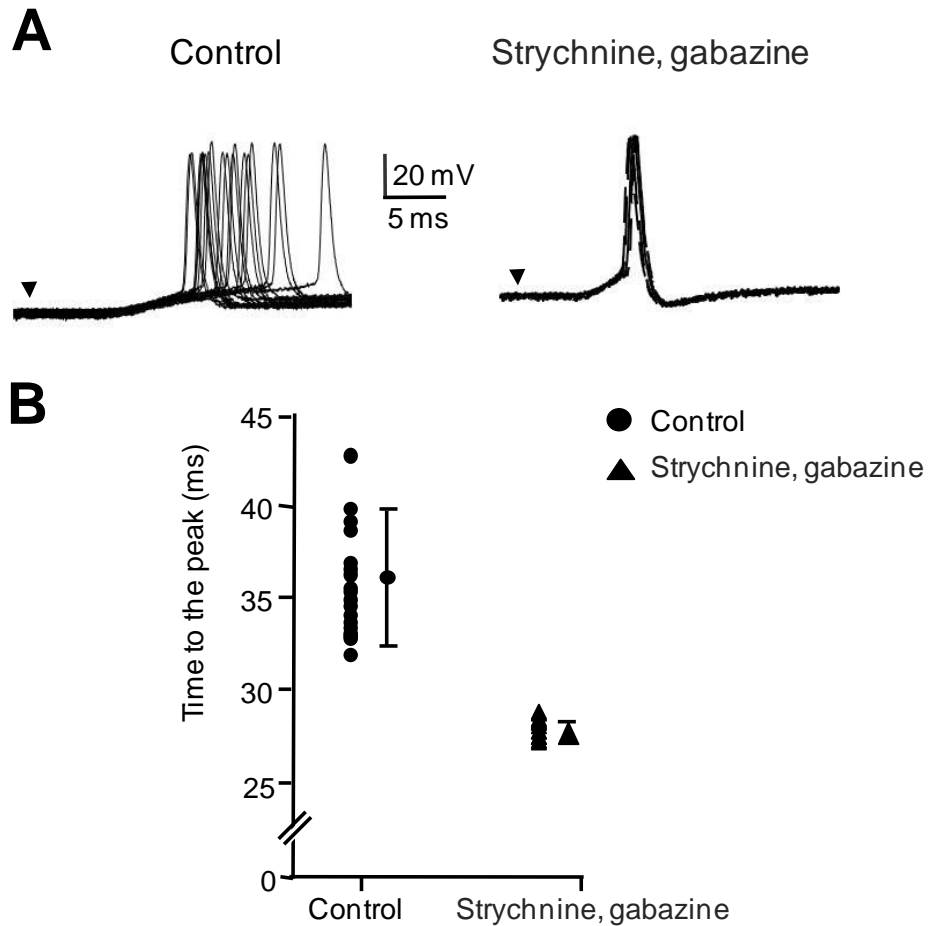


Figure 6.31: Action potentials elicited by stimulating multisensory inputs to a fusiform cell after acoustic over-exposure. (A) left shows thirty traces superimposed on the stimulation artefact and obtained in control medium whereas A right shows the same traces after perfusion of 10 μM strychnine and 20 μM gabazine. Note that the latency (time to the action potential peak) shows a large variation in control medium whereas action potentials become more timed in presence of strychnine and gabazine. This pattern was present in 3 out of 5 cells. Stimulations were at 0.3 Hz and fusiform cell membrane potential was -70 mV. **(B)** is a graph representing the time to the peak of each action potential measured in A for the control medium (circle) and in strychnine and gabazine (triangle). The mean and S.D. are also shown at the right of the individual points. The cell in the figure is cell 1 in table 6.26. The time of peak was 36.1 ± 3.72 ms in control and 28.3 ± 0.28 ms in strychnine and gabazine (P value for the F test is $6 \cdot 10^{-17}$).

Post-synaptic responses of a fusiform cell to the stimulation of the auditory inputs

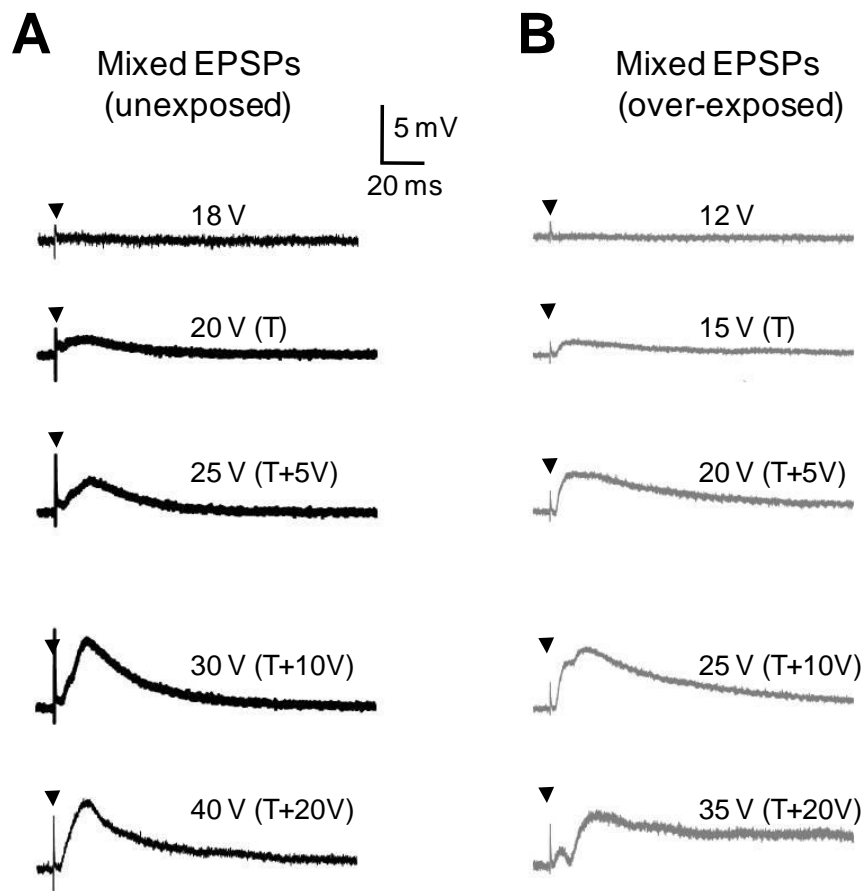


Figure 6.32: Examples of depolarisations (mixed EPSPs) elicited in two fusiform cells after stimulation of the auditory fibres in unexposed (A) and over-exposed condition (B). The fusiform cell membrane potentials were -70 mV and inputs stimulated at 0.3 Hz. Postsynaptic responses were elicited at different stimulation voltages indicated above the trace. Note that the amplitude of the mixed EPSPs increased with the stimulus voltage until reaching a maximum at 30 V and 25 V for the unexposed and over-exposed condition respectively. The arrowhead marks the stimulus artefact and the traces represent averages from 15-25 individual traces .

Excitatory and inhibitory postsynaptic potentials after auditory input stimulation

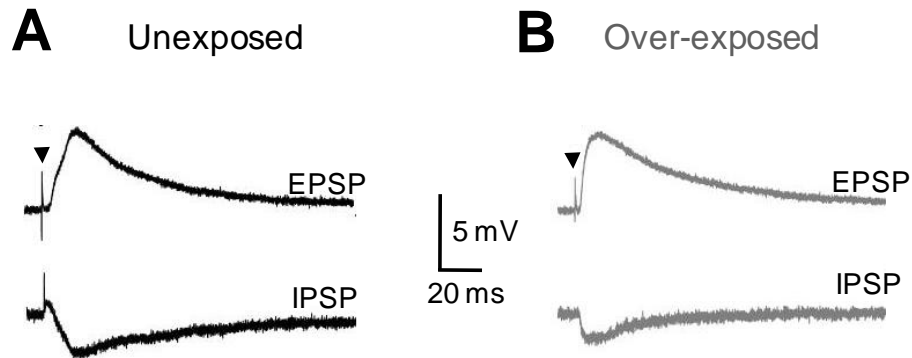


Figure 6.33: EPSPs and IPSPs recorded in two fusiform cells recorded in unexposed (A) and over-exposed condition (B). All traces represent averages from 15-25 individual traces recorded at a membrane potential of -70 mV and elicited at a stimulation of 0.3 Hz. The arrowhead marks the stimulus artefact. Mixed EPSPs (not shown here) were recorded at 5V above the voltage threshold and EPSPs were recorded in presence of 20 μ M gabazine and 10 μ M strychnine. IPSP traces result from subtracting the EPSPs from the mixed EPSPs. Note a similar EPSP between the unexposed and the over-exposed conditions whereas the IPSP is smaller after acoustic over-exposure.

Summary of the EPSP and IPSP characteristics after stimulation of the auditory inputs

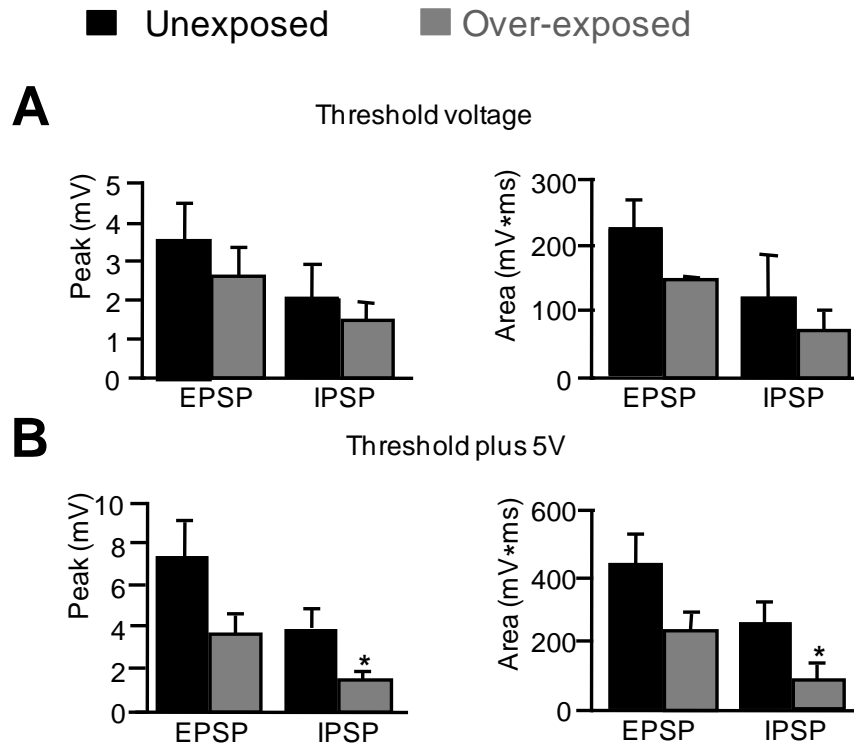


Figure 6.34: Analysis of the EPSPs and the IPSPs elicited in fusiform cells by stimulation of the multisensory inputs after acoustic over-exposure. Summary histograms represent the synaptic input characteristics in unexposed (black) and after acoustic over-exposure (in grey). **(A)** represents the values obtained at threshold voltage. P values comparing the unexposed and the over-exposed conditions (4-6 cells per condition) were 0.40 and 0.57 for the IPSP amplitude and area respectively, 0.48 and 0.28 for the EPSP amplitude and area respectively. **(B)** represents the values obtained at threshold+5V (table 6.27). P values comparing the unexposed and the over-exposed conditions (4-6 cells per condition) were 0.03 for both the IPSP amplitude and the IPSP area, 0.11 and 0.09 for the EPSP amplitude and area respectively. Note that acoustic overexposure decreases the IPSP peak amplitude and area at threshold + 5V stimulus voltage and does not affect the EPSP. Abbreviations: (EPSP) excitatory postsynaptic potentials, (IPSP) inhibitory postsynaptic potentials, (*P \leq 0.05, unpaired T test).

Action potential timing evoked by auditory stimulation after acoustic over-exposure

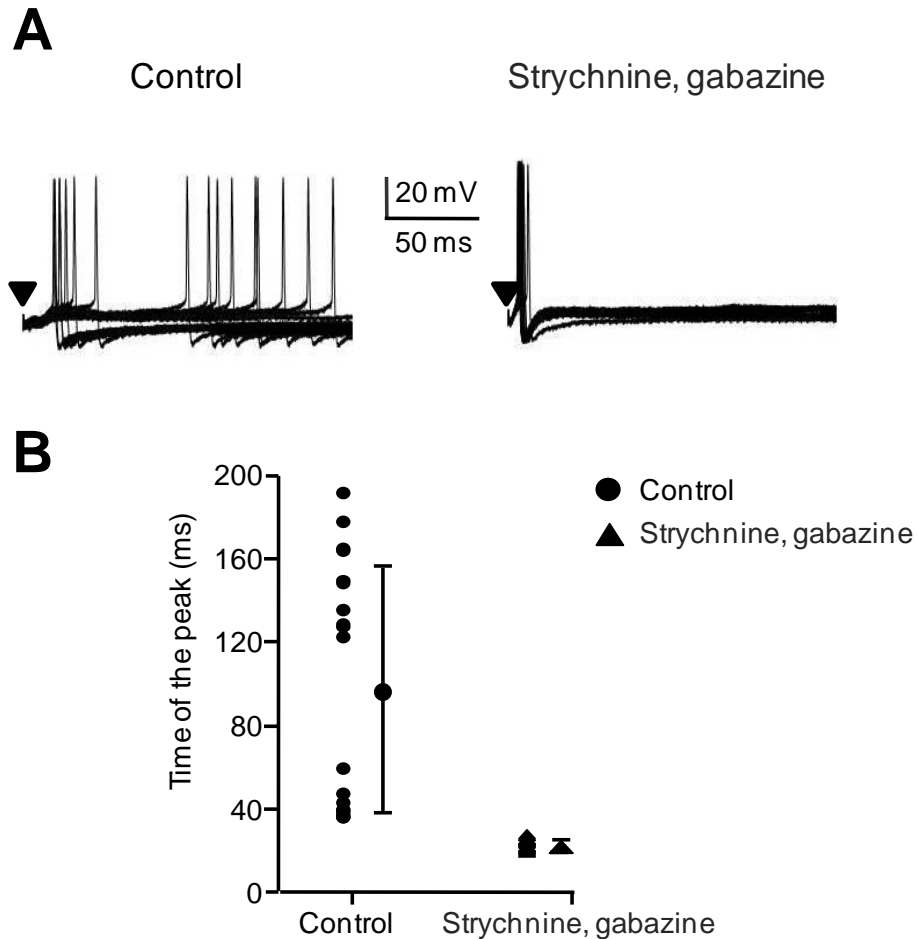


Figure 6.35: Action potentials elicited by stimulating the auditory inputs to a fusiform cell after acoustic over-exposure. (A) left shows twenty traces superimposed on the stimulation artefact and obtained in control medium whereas A right shows the same traces after perfusion of 10 μ M strychnine and 20 μ M gabazine. Note that the latency (time to the action potential peak) shows a large variation in control medium whereas action potentials become more timed in presence of strychnine and gabazine. This pattern was present in 2 out of 3 cells. Stimulation was at 0.3 Hz and fusiform cell membrane potential was -60 mV. **(B)** is a graph representing the time to the peak of each action potential measured in A for the control medium (circle) and in strychnine and gabazine (triangle). The mean and S.D. are also shown at the right of the individual points. The cell in the figure is cell 2 in table 6.29. The time of peak was 97 ± 58 ms in control and 24.1 ± 1.38 ms in strychnine and gabazine (P value for the F test is $3 \cdot 10^{-36}$).

Multisensory input stimulation triggers reliable and unreliable firing in fusiform cells

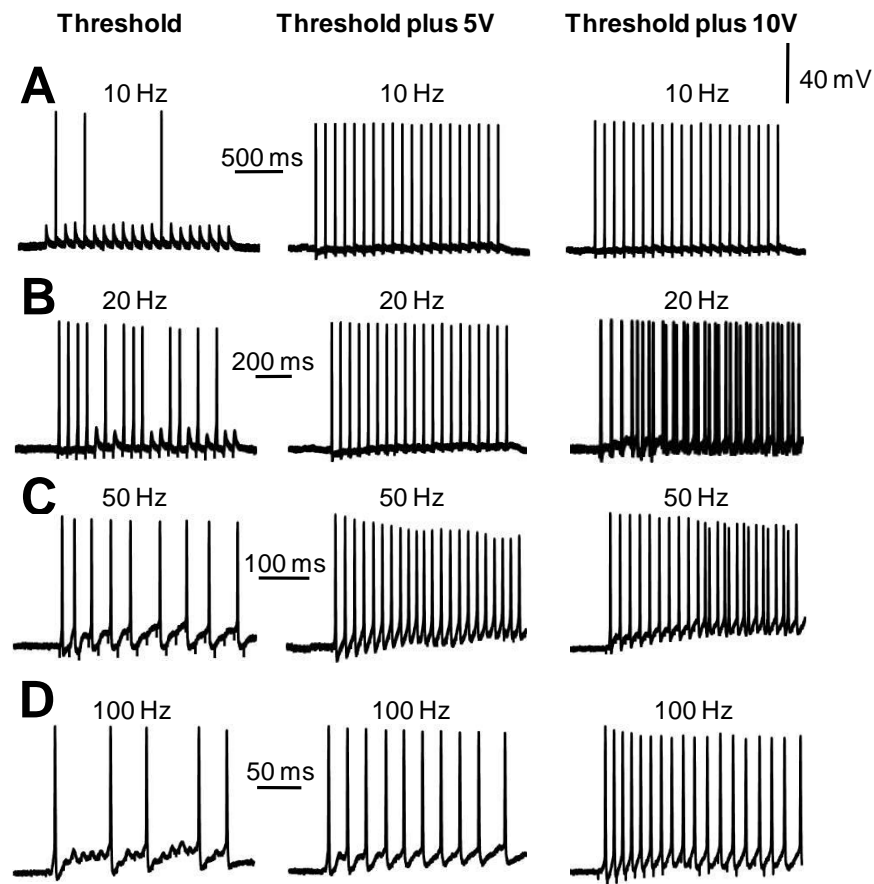


Figure 6.36: Fusiform cell firing in response to stimulating the multisensory inputs at different stimulating voltages and frequencies (A-D). The fusiform cell membrane potential was -70 mV and the multisensory inputs were stimulated with threshold voltages to elicit action potentials (21V, left), suprathreshold voltages (26V, middle and 31V, right) and with stimulating frequencies (indicated above each trace) varying from 10 to 100 Hz. Note the unreliable firing pattern with failures at threshold voltages (for the action potentials), the reliable firing pattern mainly at threshold voltages plus 5V, and the mixed firing pattern (aberrant and with failures) at threshold voltage plus 10V. Action potentials sometimes exceeded the duration of the pulses explaining why they fail reaching the baseline after the pulse.

Effects of multisensory input stimulation on fusiform cell firing frequencies

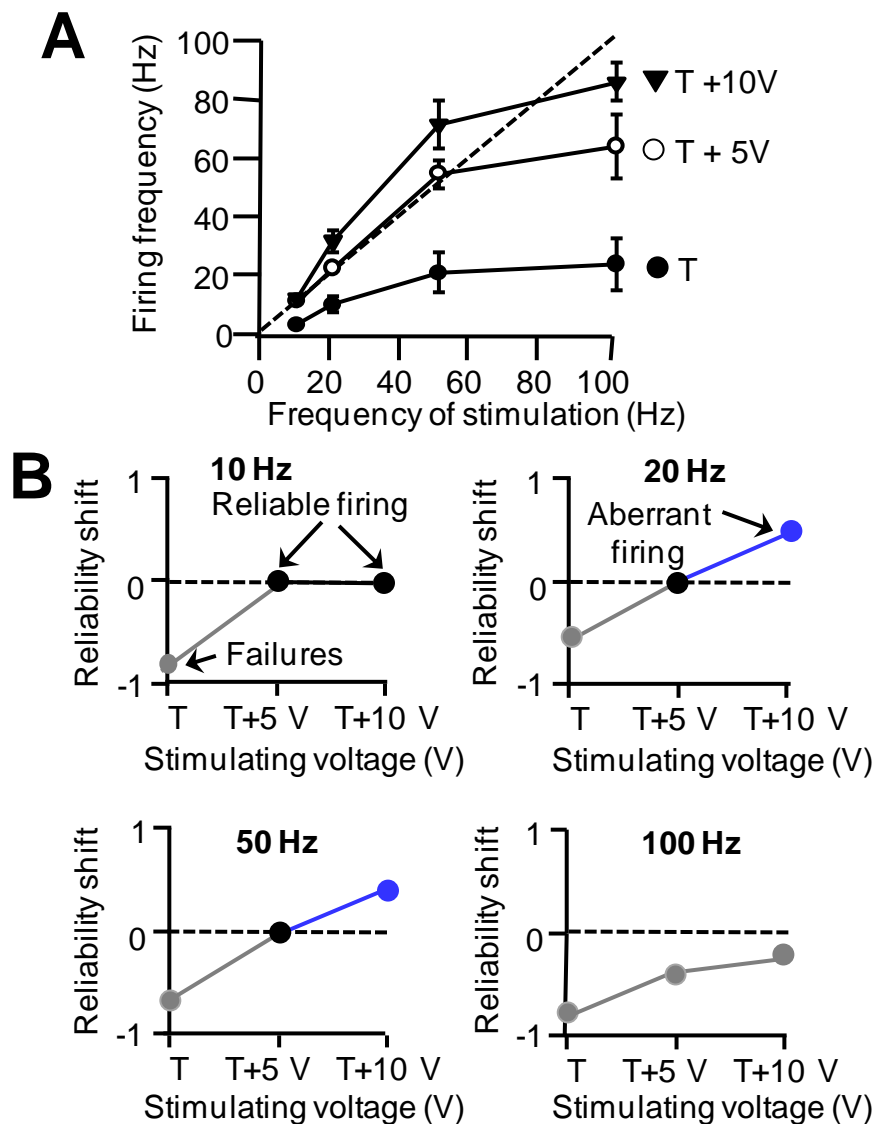


Figure 6.37: Summary of the effects of multisensory input stimulation on fusiform cell firing frequencies. (A) Mean \pm s.e.m. ($n=6$) firing frequencies are plotted in relationship to the stimulation frequency at different voltages of stimulation. Note the presence of failures at threshold voltages for the action potential (T). At 5V above threshold the firing is nearly reliable (for 10, 20, 50 Hz stimulus) and unreliable firing with failures (100 Hz stimulus). At 10V above threshold cells fired reliably (for 10 Hz stimulation), with aberrant firing (for 20 and 50 Hz stimulus) and with failures (for 100 Hz stimulus). All cells had a membrane potential of -70 mV. See also table 6.30. (B) Mean reliability shift is explained in the methods and is calculated based on the data shown in graph A. Black circles indicate reliable firing, blue and grey circles indicate a predominant aberrant firing or firing with failures respectively.

Inhibitory synaptic transmission affects the firing reliability when stimulating multisensory inputs

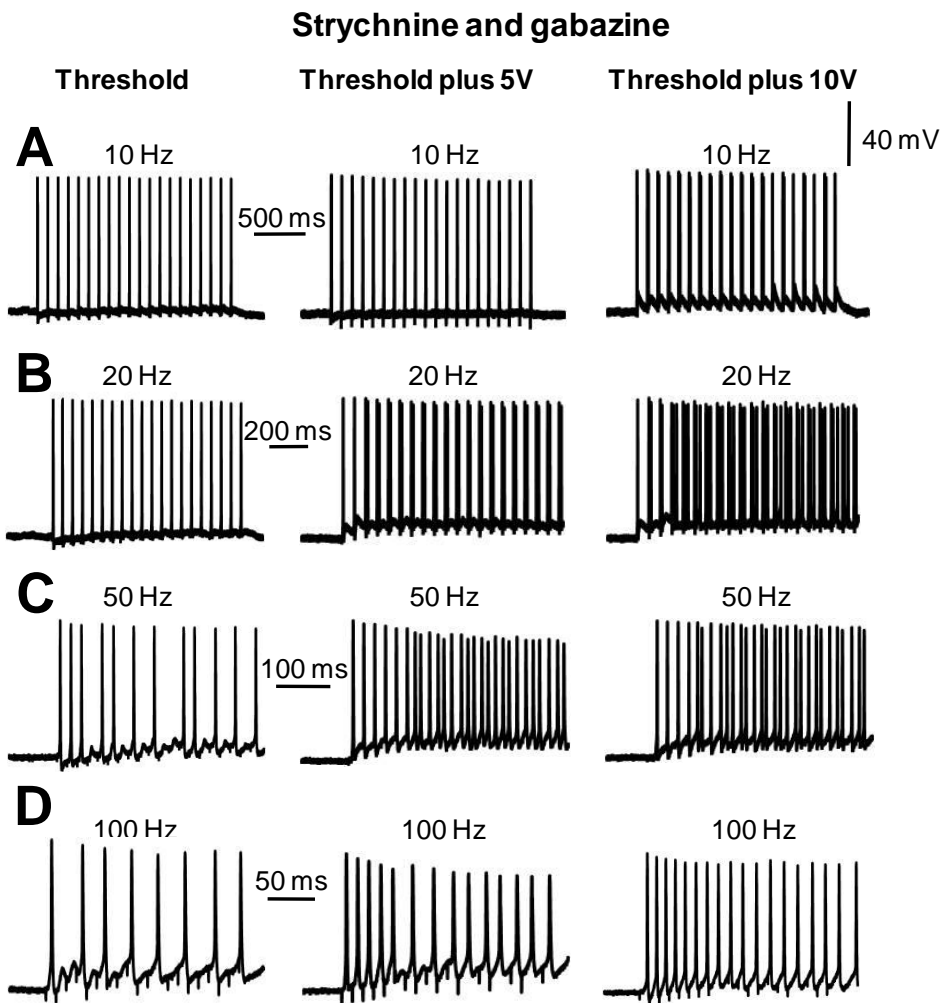


Figure 6.38: Fusiform cell firing in response to stimulating the multisensory inputs at different stimulating voltages and frequencies and in presence of strychnine and gabazine (A-D). The fusiform cell membrane potential was -70 mV and the multisensory inputs were stimulated with threshold voltages to elicit action potentials (21V, left), suprathreshold voltages (26V, middle and 31V, right) and with frequencies (indicated above each trace) varying from 10 to 100 Hz. Note the firing is reliable (10,20Hz) or with failures (50-100Hz) at threshold voltages and predominantly aberrant at higher voltages (threshold voltages plus 5V and 10V). Action potentials sometimes exceeded the duration of the pulses explaining why they fail reaching the baseline after the pulse. Same cell as in figure 6.36.

Effect of strychnine and gabazine on fusiform cell firing frequencies

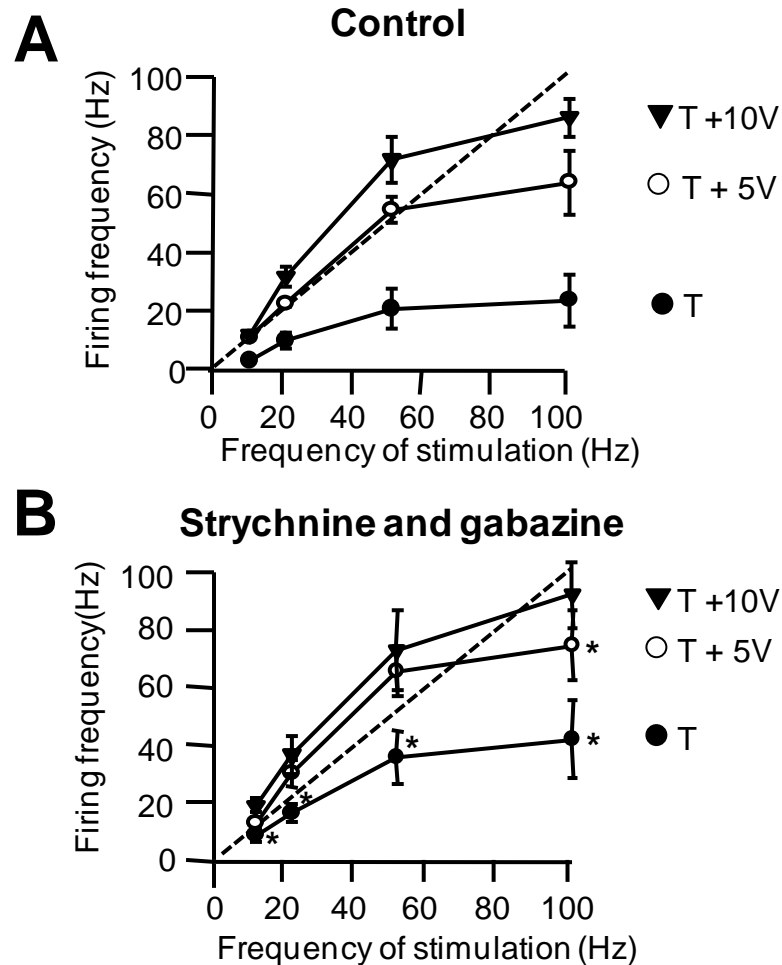


Figure 6.39: Summary of the effects of multisensory input stimulation on fusiform cell firing frequencies in control (A) and in presence of strychnine and gabazine (B). Mean \pm s.e.m. ($n=6$) of the firing frequency is plotted in relationship to the frequency of stimulation at different stimulation voltages. (A) is the same graph as in fig. 6.37. All cells were held at -70mV . (B) At threshold voltages for the action potential (T) the firing is nearly reliable (for 10, 20, 50 Hz stimulus) and unreliable firing with failures (100 Hz stimulus). At 5V above threshold the firing is reliable (for 10stimulus), aberrant (for 20 and 50 Hz stimulus) and with failures (100 Hz stimulus). At 10V above threshold cells fired with aberrant firing (for 10, 20 and 50 Hz stimulus) and with failures (for 100Hz stimulus). See also table 6.30. All cells had membrane potential of -70mV . Note that the presence of strychnine and gabazine significantly increases the firing frequency at threshold voltage and at 5V above threshold voltage (*). (*) $P \leq 0.05$ for unpaired T test comparing the firing frequency in control medium (A) and in strychnine and gabazine (B).

Blocking inhibitory synaptic transmission alters the firing pattern in fusiform cells

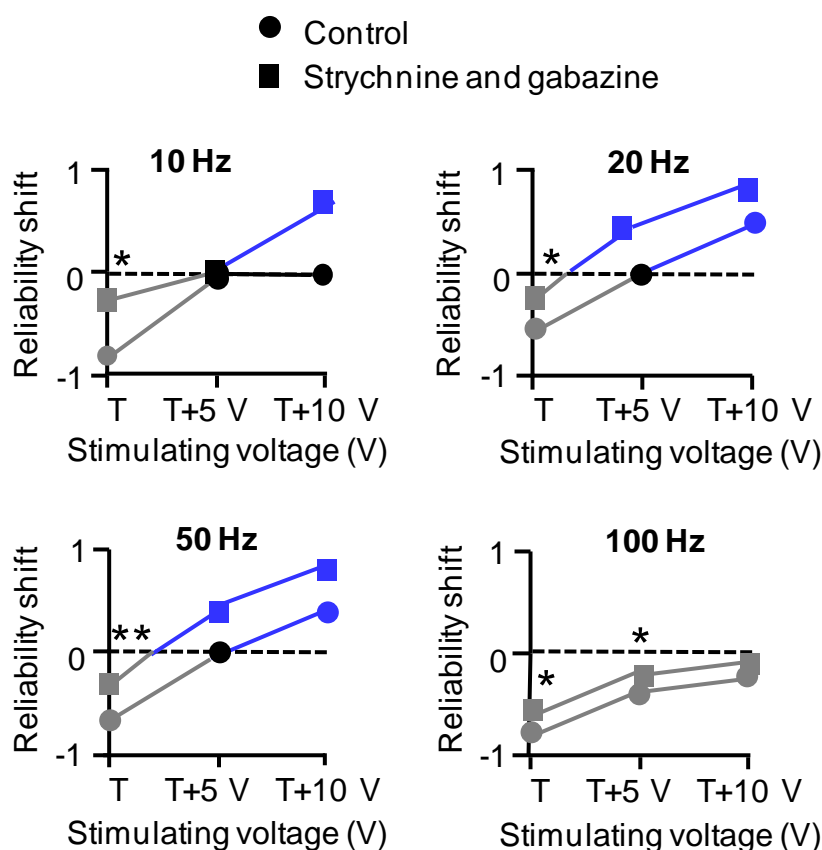


Figure 6.40: Effects of blocking inhibitory synaptic transmission on the firing pattern of fusiform cells following stimulation of the multisensory fibres. Graphs showing the shift of the firing reliability for different firing frequencies and stimulus voltages in control condition (circles, same as figure 6.36B) and following removal of the inhibitory inputs with gabazine and strychnine (squares). Mean reliability shift is explained in the methods and is calculated based on the data shown in figure 6.39A and B. Black symbols indicate reliable firing, blue and grey symbols indicate a predominant aberrant firing or firing with failures respectively. Note that the presence of gabazine and strychnine shifts the reliability pattern of the response towards the left. (*) $P \leq 0.05$ and (**) $P \leq 0.01$ for unpaired T test comparing the reliability shift in control medium and in strychnine and gabazine..

Auditory input stimulation results in a mixture of action potentials and failures in fusiform cells

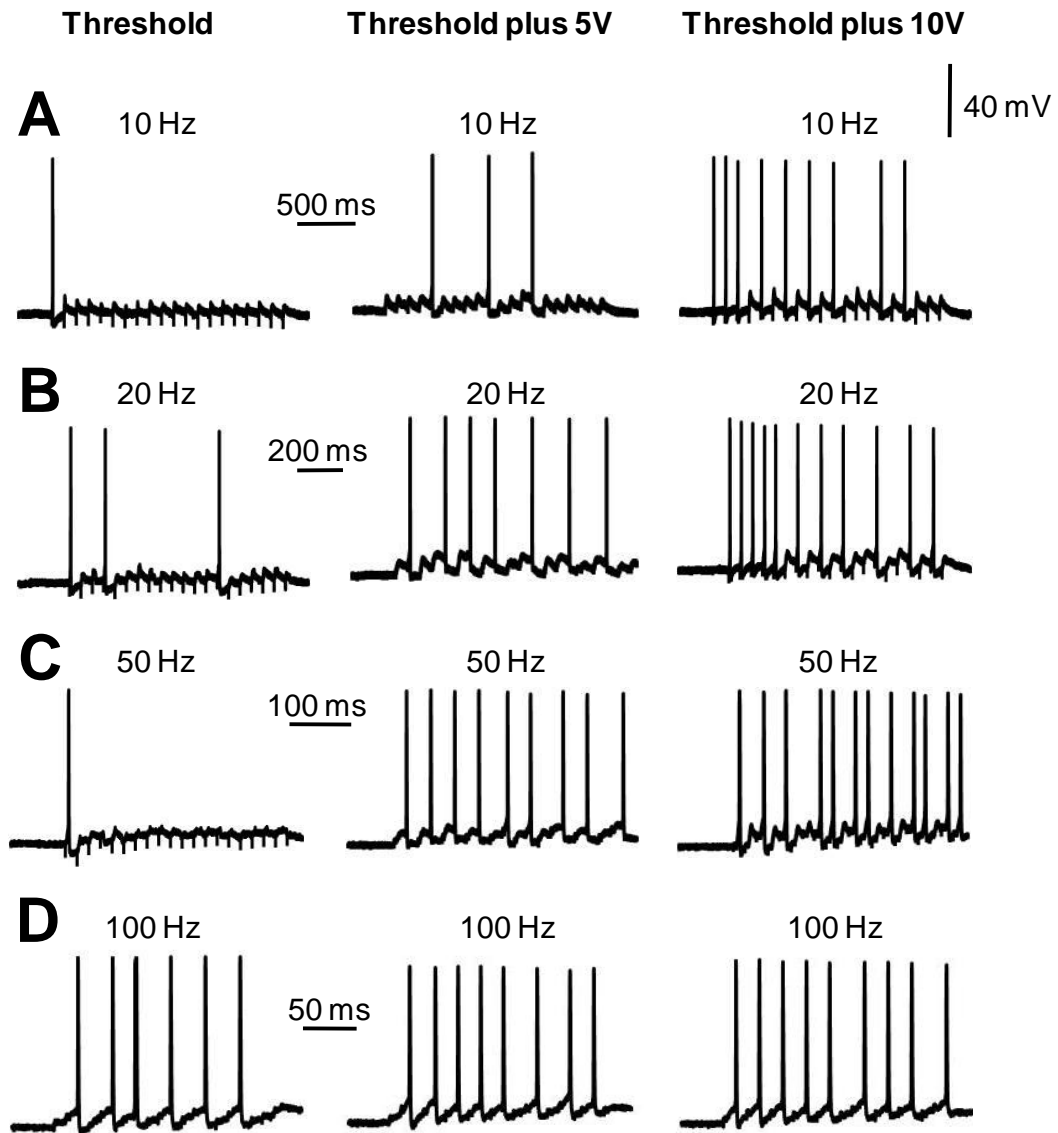


Figure 6.41: Fusiform cell firing in response to stimulating the auditory inputs at different stimulating voltages and frequencies. A-D. The fusiform cell membrane potential was -60 mV and the auditory inputs were stimulated with threshold voltages for eliciting action potentials (35V, left) suprathreshold voltages (40V, middle and 45V, right) and with frequencies (indicated above each trace) varying from 10 to 100 Hz. Note the unreliable firing pattern with failures for all parameters of stimulation.

Effects of auditory input stimulation on fusiform cell firing frequencies

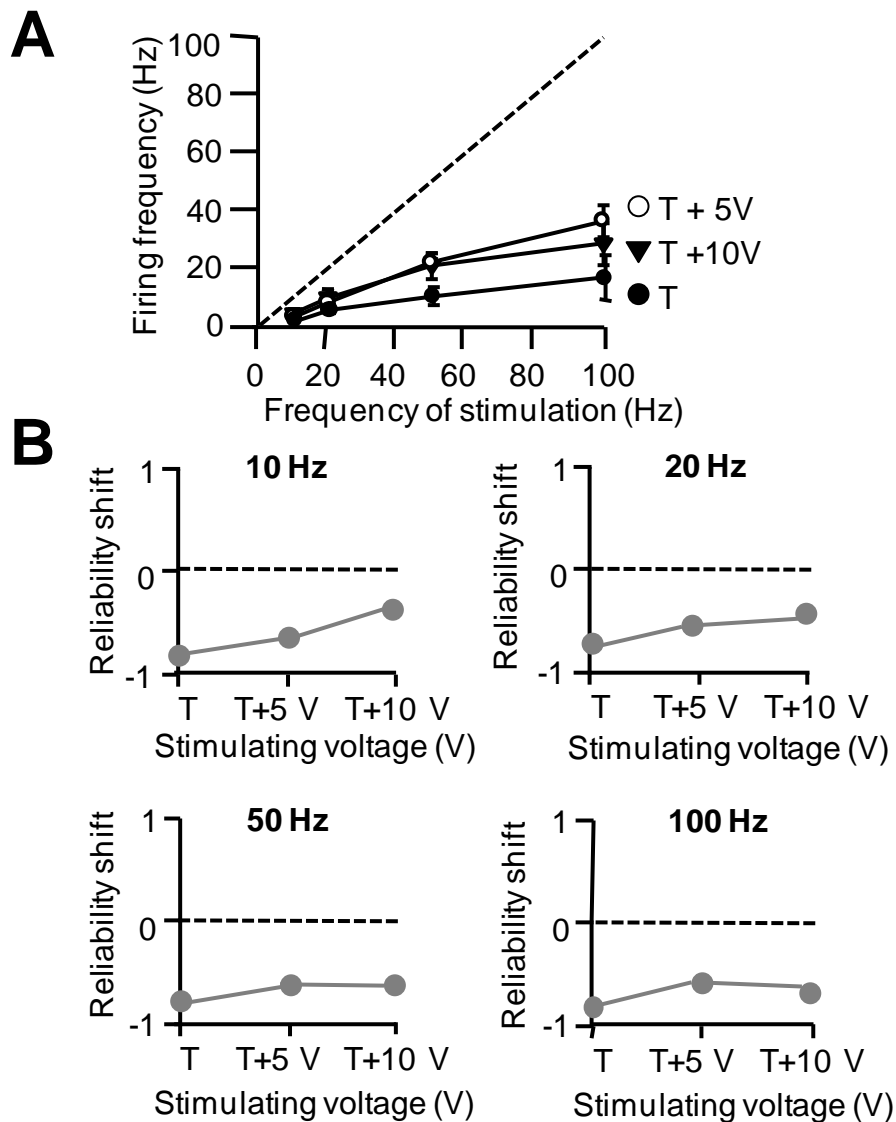


Figure 6.42: Summary of the effects of auditory input stimulation on fusiform cell firing frequencies. (A) Mean \pm s.e.m. ($n=4-5$) firing frequencies are plotted in relationship to the frequency of stimulation at different voltages of stimulation. See also table 6.31. Note the firing with failures for all stimulus voltages and frequencies. All cells had a membrane potential of -60mV . (B) Mean reliability shift is explained in the methods and is calculated based on the data shown in graph A. Grey circles indicate an overall firing with failures (also shown by values being below 0).

Blocking inhibitory synaptic transmission allows firing reliability in fusiform cells

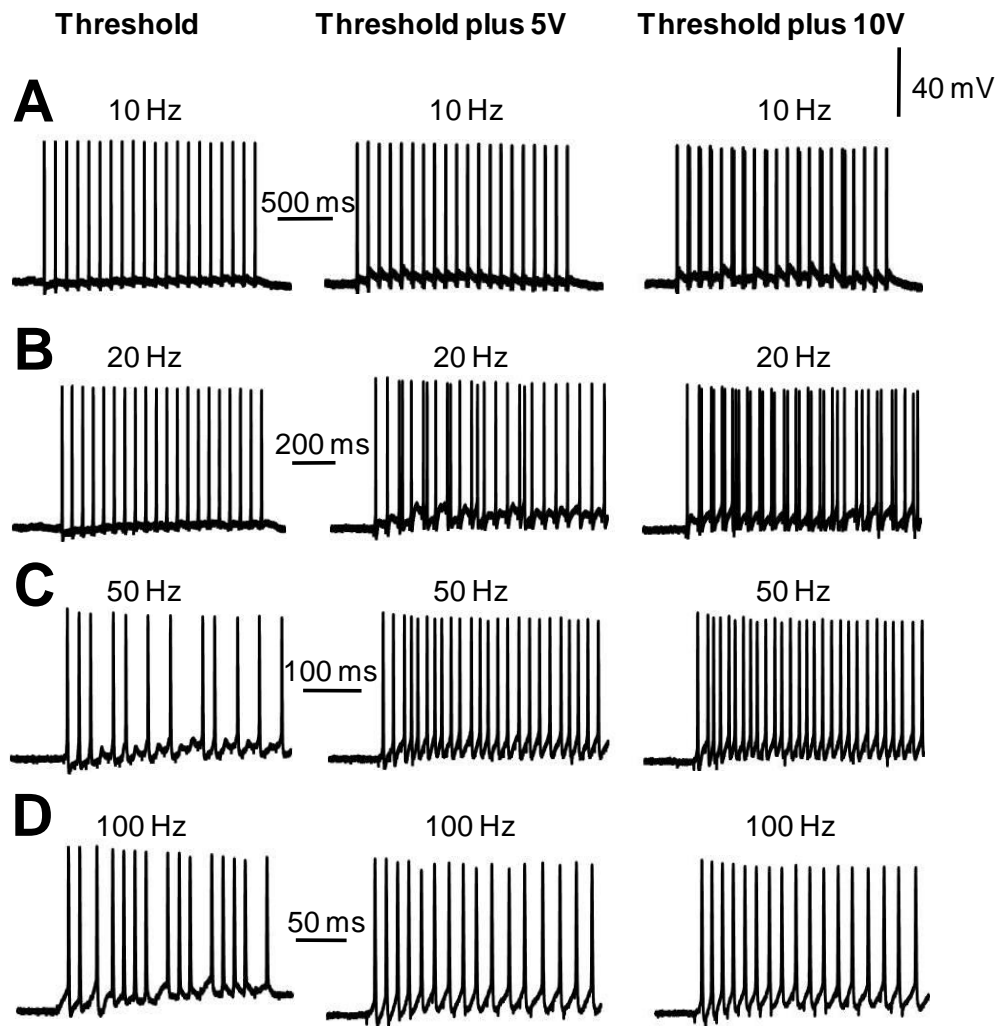


Figure 6.43: Fusiform cell firing in response to stimulating the auditory inputs at different stimulating voltages and frequencies in presence of strychnine and gabazine (A-D). The fusiform cell membrane potential was -60 mV and the auditory inputs were stimulated with threshold voltages for the action potential (35V, left), suprathreshold voltages (40V, middle and 45 V, right) and with frequencies (indicated above each trace) varying from 10 to 100 Hz. Note the firing pattern is reliable or with failures at threshold voltages and predominantly aberrant at higher voltages (threshold voltages plus 5V and 10V). Same cell as in figure 6.41. Action potentials sometimes exceeded the duration of the pulses explaining why they fail reaching the baseline after the pulse.

Effect of strychnine and gabazine on fusiform cell firing frequencies

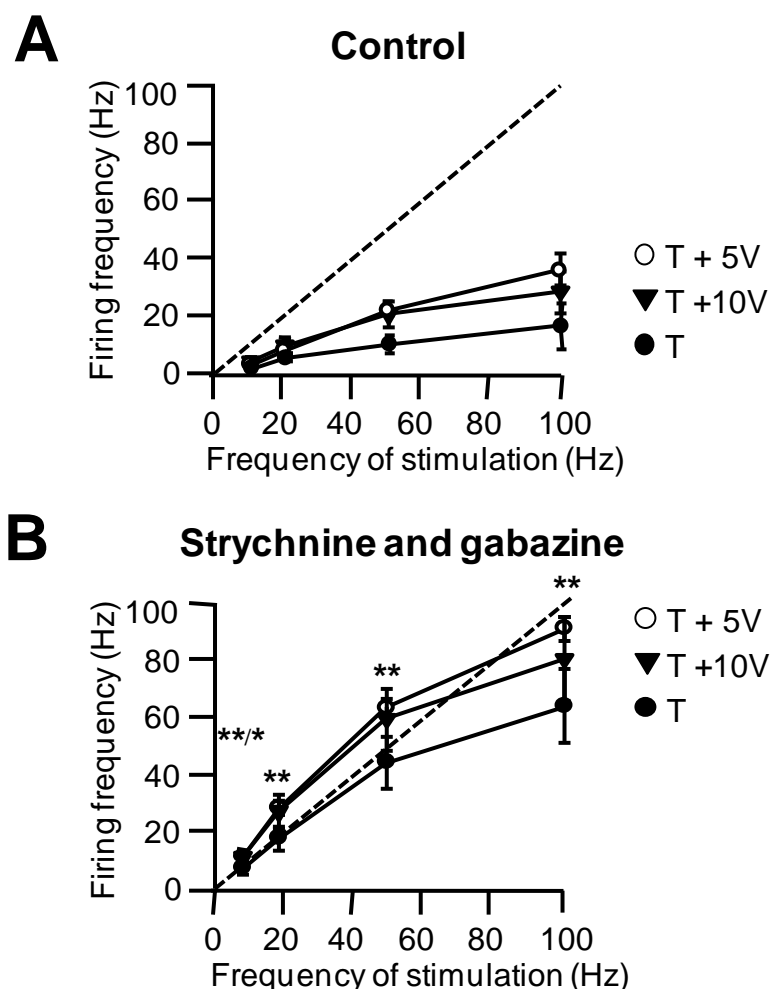


Figure 6.44: Summary of the effects of auditory input stimulation on fusiform cell firing frequencies in control (A) and in presence of strychnine and gabazine (B). Mean \pm s.e.m. (n=5) of the firing frequency is plotted in relationship to the frequency of stimulation at different voltages of stimulation (A) is the same graph as in fig 6.42.A (B) Note that the presence of strychnine and gabazine significantly increases (*) the overall firing frequencies with a nearly reliable firing pattern at threshold stimulus voltages (for 10 and 20 Hz stimulus) and with failures (following 50 and 100 Hz stimulus respectively). At 5V above threshold, the firing is reliable (10 Hz stimulus), aberrant (for 20 and 50 Hz stimulus) or with failures (for 100 Hz stimulus). At 10V above the threshold, the firing is reliable (for 10 Hz stimulus) aberrant (for 20 and 50 Hz stimuli respectively) or with failures (for 100 Hz stimulus). See also table 6.31. All cells had a membrane potential of -60mV. Results were significantly different ($P \leq 0.01$) between A and B except at 10 Hz threshold voltage where $P \leq 0.05$. (**/*) are represented above 3 data points for clarity.

Blocking inhibitory synaptic transmission alters the firing pattern in fusiform cells

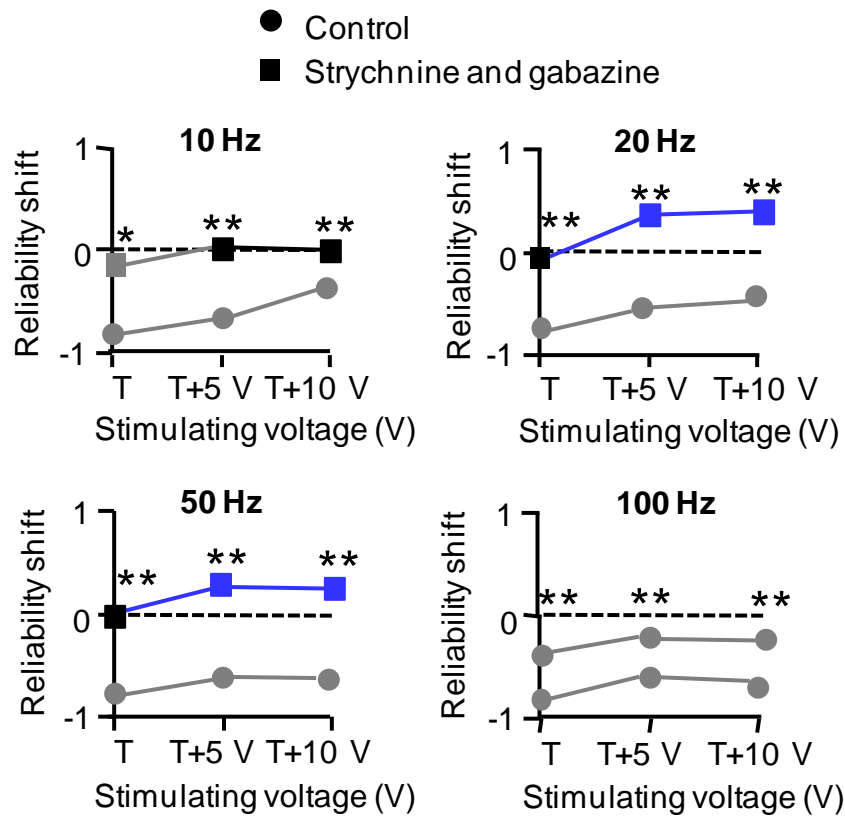


Figure 6.45: Effects of blocking inhibitory synaptic transmission on the firing pattern of fusiform cells following stimulation of the auditory fibres. Graphs showing the shift of the firing reliability for different firing frequencies and stimulus voltages in control condition (circles, same as figure 6.42B) and following the removal of the inhibitory inputs with gabazine and strychnine (squares). Note that when the inhibitory inputs are removed, cells fire reliably at 10-50 Hz stimuli. Mean reliability shift is explained in the methods and is calculated based on the data shown in figure 6.44A and B. Black symbols indicate a reliable firing, blue and grey symbols indicate a predominant aberrant firing or firing with failures respectively. (*) $P \leq 0.05$ and (**) $P \leq 0.01$ for unpaired T test comparing the reliability shift in control medium and in strychnine and gabazine.

Effects on fusiform cell firing evoked upon multisensory input stimulation

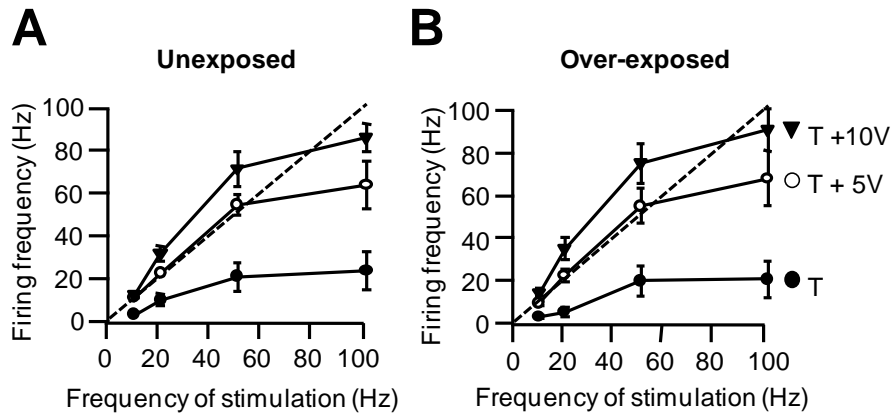


Figure 6.46: Effect of acoustic over-exposure on fusiform cell firing evoked upon multisensory stimulation. The mean \pm s.e.m. ($n=6$ cells each) firing frequencies in control medium are plotted for different stimulating voltages, in relationship to the frequency of stimulation in the unexposed condition (**A**) and in the over-exposed condition (**B**). (A) is the same graph as in figure 6.37A. Values for (A) are in table 6.30 and values for (B) are in table 6.32. Note that the firing frequency is unaffected by acoustic over-exposure for all stimulating voltages and frequencies. All the cells had a membrane potential of -70mV .

Effects on fusiform cell firing evoked upon multisensory input stimulation in the presence of strychnine and gabazine

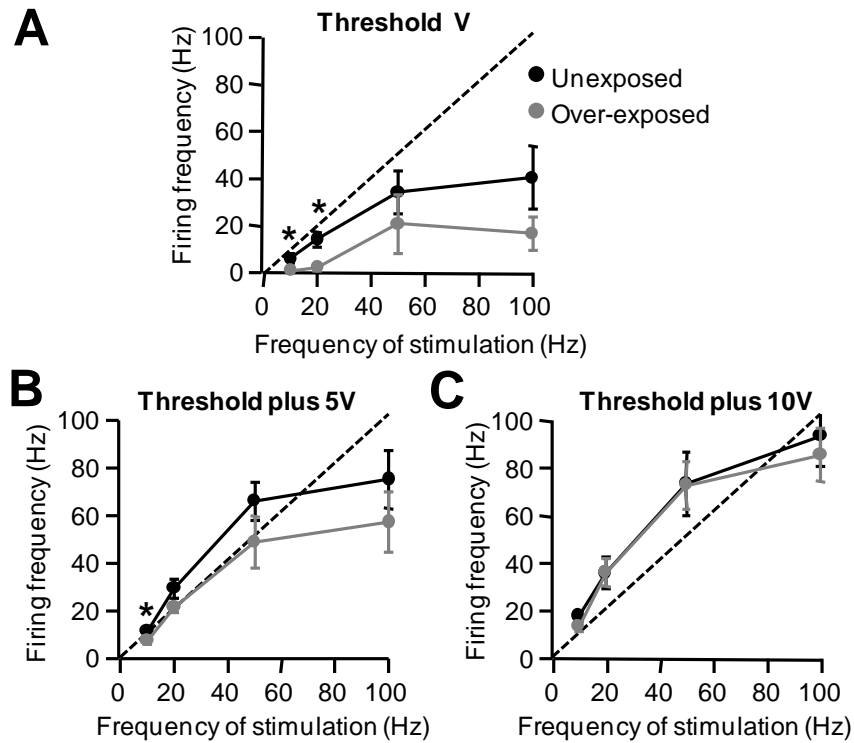


Figure 6.47: Effect of acoustic over-exposure on fusiform cell firing evoked upon multisensory stimulation in presence of strychnine and gabazine. The mean \pm s.e.m. firing frequency is plotted in relationship to the frequency of stimulation for different stimulating voltages (A-C) mentioned above the graphs. The black symbols represent the unexposed conditions (same values as in figure 6.39B also detailed in table 6.33) and the grey symbols represent the over-exposed conditions (detailed in table 6.33). Note that acoustic over-exposure decreases the firing frequency for specific low stimulus voltages and frequencies. (*) $P \leq 0.05$ for unpaired T test comparing the firing frequencies in unexposed and over-exposed condition.

Effects on the firing reliability following stimulation of the multisensory inputs

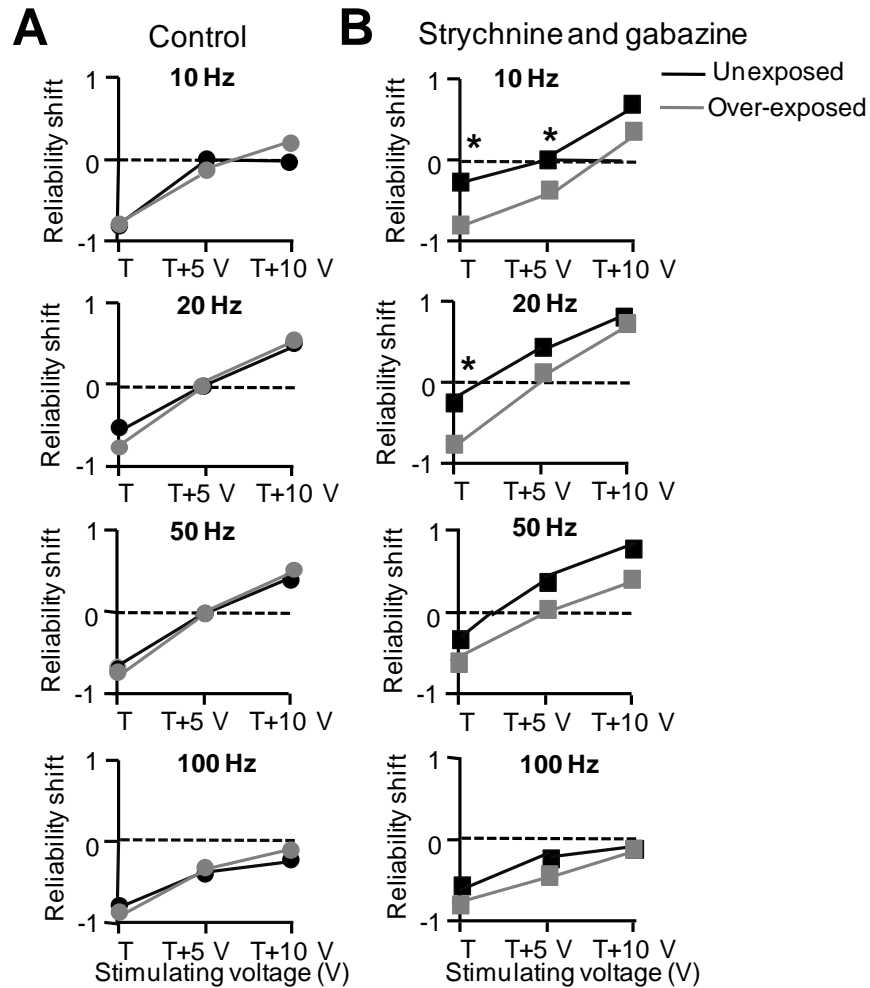


Figure 6.48: Effect of acoustic over-exposure on the firing reliability following stimulation of the multisensory inputs in control medium (A) and in presence of strychnine and gabazine (B). Mean reliability shift is explained in the methods and is calculated based on the data shown in figures 6.46 and 6.47. The values for the unexposed condition are the same as in figure 6.40. Note that in control medium (A) the firing pattern is similar between the unexposed and the over-exposed condition whereas in presence of strychnine and gabazine (B) more failures are observed after acoustic over-exposure for threshold voltages and 10 Hz stimuli. (*) $P \leq 0.05$ values for unpaired T test comparing the unexposed condition and over-exposed condition in control and in strychnine and gabazine.

Effects on fusiform cell firing evoked upon auditory input stimulation

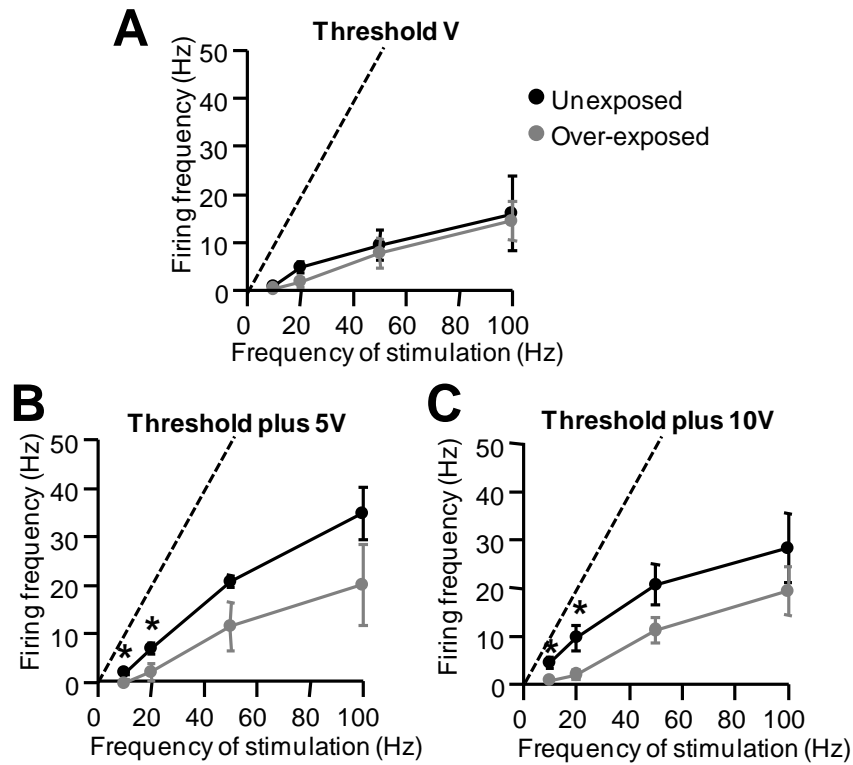
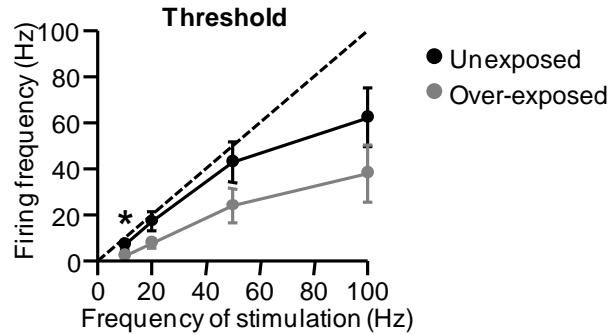


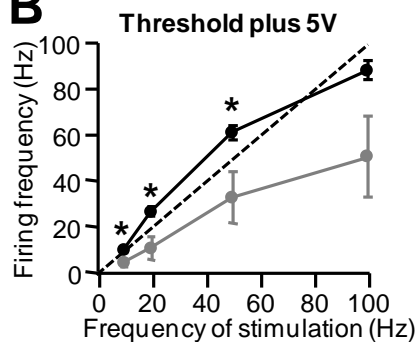
Figure 6.49: Effect of acoustic over-exposure on fusiform cell firing evoked upon auditory stimulation in control medium. The mean \pm s.e.m. firing frequency is plotted in relationship to the frequency of stimulation for different stimulating voltages (A-C) mentioned above the graphs. The black symbols represent the unexposed conditions (same values as in figure 6.42A also detailed in table 6.34) and the grey symbols represent the over-exposed conditions (detailed in table 6.34). Note that the acoustic over-exposure decreases the firing frequency at low stimulating frequencies in B and C. All the cells had a membrane potential of -60mV. (*) P values \leq 0.05 for unpaired T test comparing the firing frequencies in unexposed and over-exposed condition

Effects on fusiform cell firing evoked upon auditory input stimulation in the presence of strychnine and gabazine

A



B



C

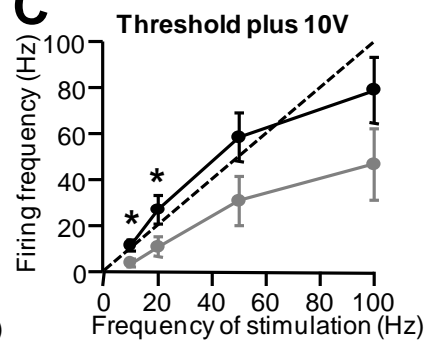


Figure 6.50: Effect of acoustic over-exposure on fusiform cell firing evoked upon auditory stimulation in strychnine and gabazine. The mean \pm s.e.m. firing frequency is plotted in relationship to the frequency of stimulation for different stimulating voltages (**A-C**) mentioned above the graphs. The black symbols represent the unexposed conditions (same values as in figure 6.44B also detailed in table 6.35) and the grey symbols represent the over-exposed conditions (detailed in table 6.35). Note that the acoustic over-exposure decreases the firing frequency at low stimulating frequencies in A, B and C. All the cells had a membrane potential of -60mV . (*) P values ≤ 0.05 for unpaired T test comparing the firing frequencies in unexposed and over-exposed condition

Effects on the firing reliability following stimulation of the auditory inputs

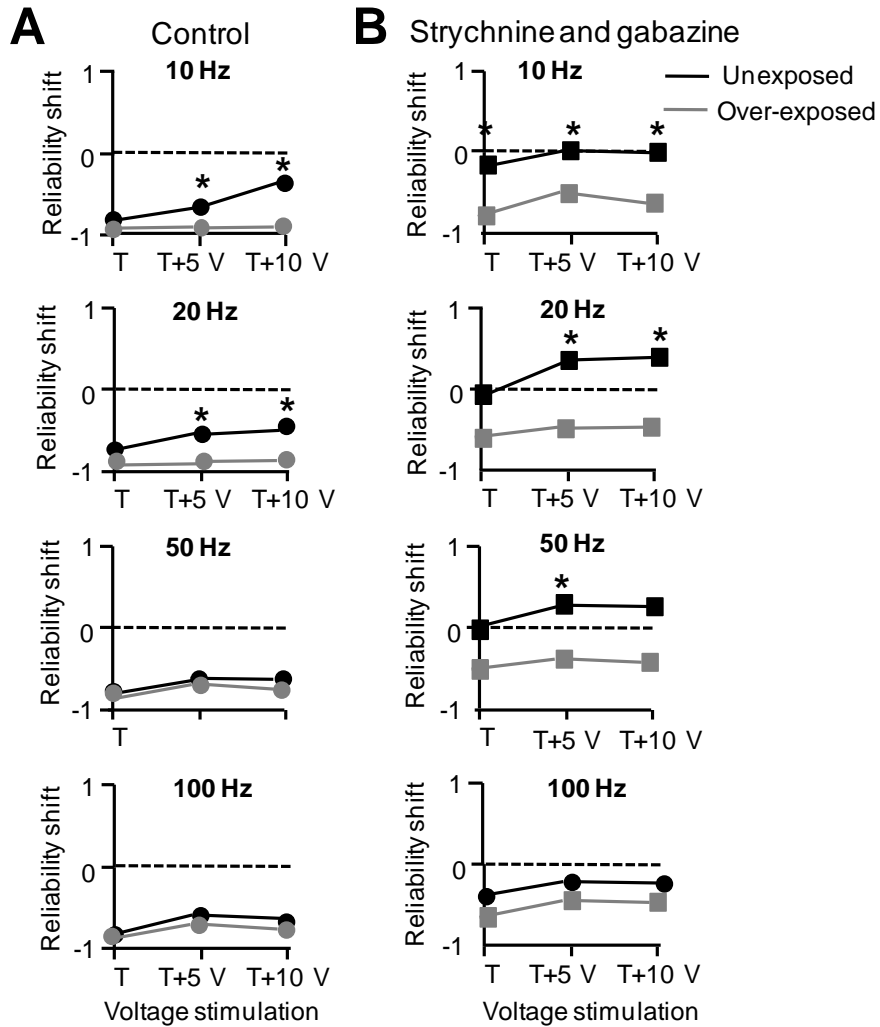


Figure 6.51: Effect of acoustic over-exposure on the firing reliability following stimulation of the auditory inputs in control (A) and in presence of strychnine and gabazine (B). Mean reliability shift is explained in the methods and is calculated based on the data shown in figures 6.49 and 6.50. The values for the unexposed condition are the same as in figure 6.45. Note that acoustic over-exposure increases the firing reliability for specific stimulus frequencies and voltages in both A and B. (*) $P \leq 0.05$ P values for unpaired T test comparing the unexposed condition and over-exposed condition in control and in strychnine and gabazine.

Simulations of fusiform cell firing in response to parallel fibre stimulation: Effect of acoustic over-exposure

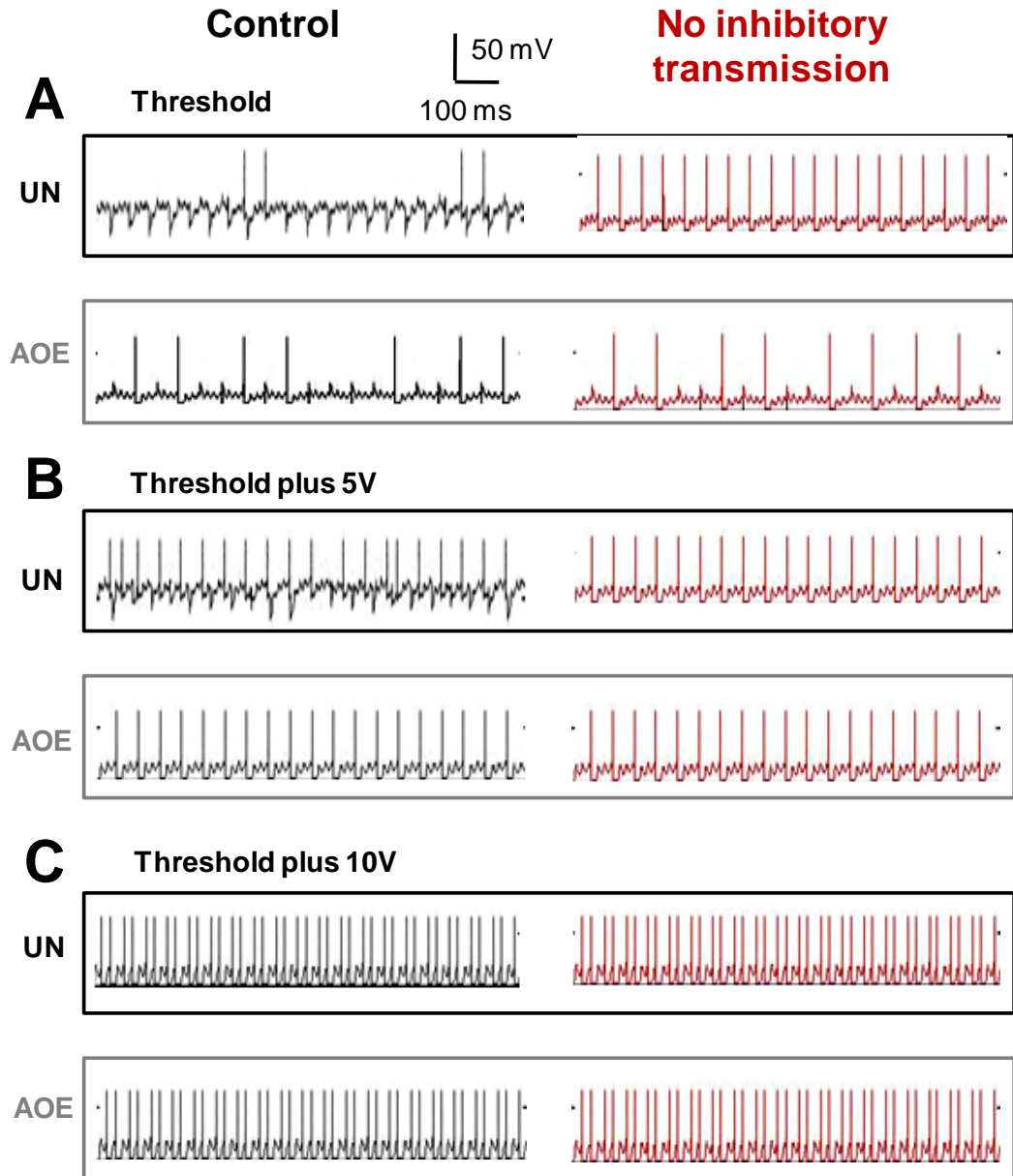


Figure 6.52: Fusiform cell model neuron firing in unexposed and over-exposed condition following parallel fibre stimulations at 20 Hz. Firing was reported for different stimulation voltages (A-C) in the unexposed condition (UN) and after acoustic over-exposure (AOE) in the presence (black) and in the absence of the inhibitory synaptic transmission (red).

Simulations of fusiform cell firing in response to auditory fibre stimulation: Effect of acoustic over-exposure

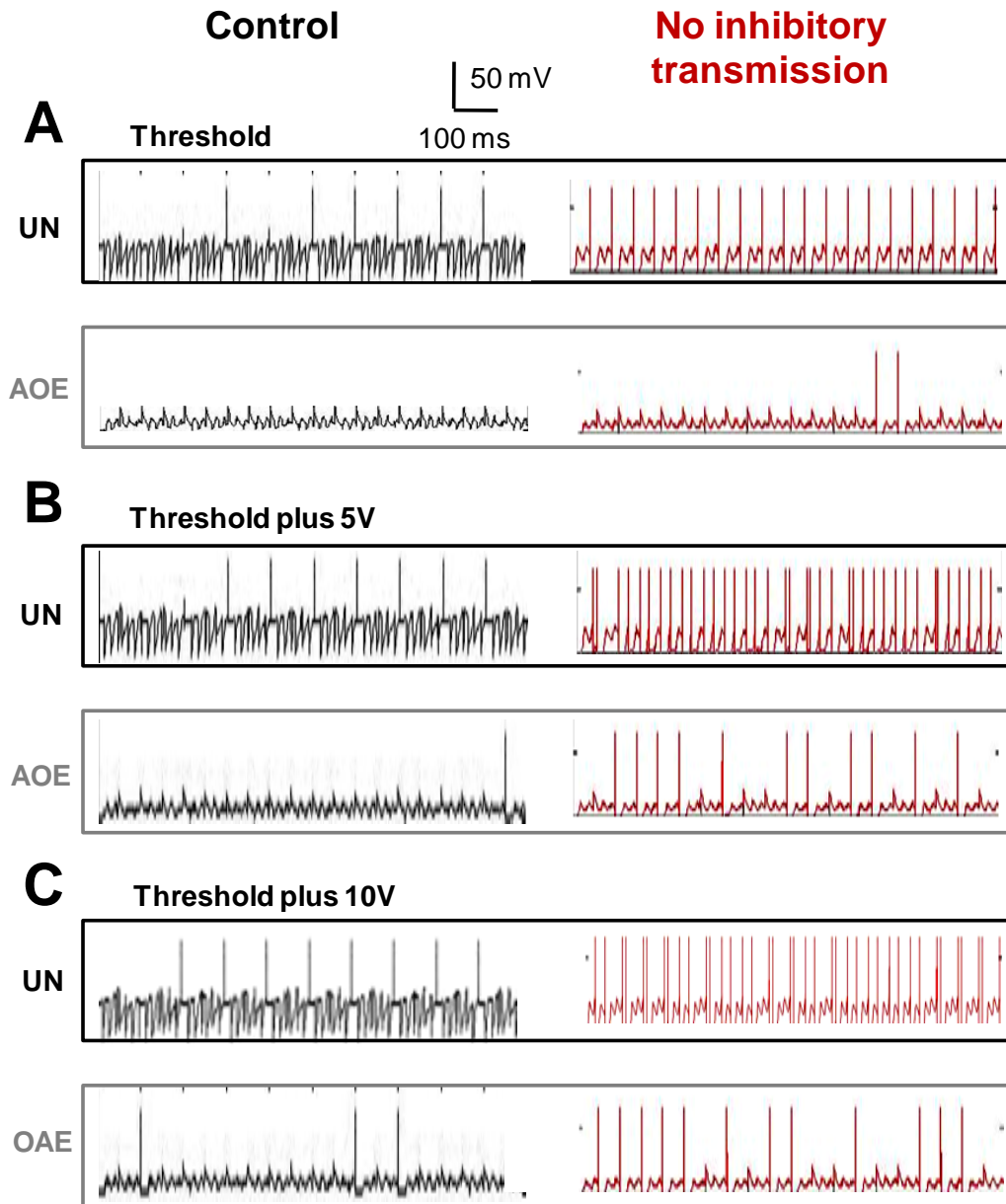


Figure 6.53: Fusiform cell model neuron firing in unexposed and over-exposed condition following auditory nerve fibre stimulations at 20 Hz. Firing was reported for different stimulation voltages (A-C) in the unexposed condition (UN) and after acoustic over-exposure (AOE) in the presence (black) and in the absence of the inhibitory synaptic transmission (red).

APPENDIX I: ABBREVIATIONS

ABR	auditory brainstem response
AC	auditory cortex
A.I.	accommodation index
AN	auditory nerve
AOE	acoustic-overexposure
AU	auditory thalamus
aVCN	antero ventral cochlear nucleus
BK	big conductance
C	capacitance
CH	chloral hydrate
CV	coefficient of variation
CW	cartwheel cell
D	coefficient of diffusion
DCN	dorsal cochlear nucleus
DL	deep layer
dN	dorsal nucleus (of the lateral lemniscus)
E	equilibrium potential
EPSP	excitatory post synaptic potential
F	fusiform cell
FL	fusiform layer
Fmax	maximal frequency
Gi	giant cell
G	conductance
gr	granule cell
grD	granule cell domain
GT	glutaraldehyde
MP	membrane potential
I	current
IC	inferior colliculus
ILD	Inter aural level difference
iN	intermediate nucleus (of the lateral lemniscus)
IPSP	inhibitory post synaptic potential
ISI	inter spike interval
ITD	Inter aural time difference
LH	Lister Hooded
L	lamina
LL	lateral lemniscus
LSO	lateral superior olivary nucleus

LTD	long term depression
LTP	long term potentiation
ML	molecular layer
MNG	medial geniculate nucleus
MNTB	medial nucleus of the trapezoid body
MSO	medial superior olive
PBS	phosphate buffer
PF	paraformaldehyde
R_s	series resistance
R_m	membrane resistance
SD	standard deviation
s.e.m.	standard error of the mean
S	stellate cell
Sc	Strial corner
SC	superior colliculus
SK	small conductance
τ	time constant
T	Threshold
TV	tuberculoventral cell
Ub	unipolar brush cell
UN	unexposed
V	membrane potential
VC	vestibular complex
VCN	ventral cochlear nucleus
vN	ventral nucleus (of the lateral lemniscus)
Vs	versus

APPENDIX II: SOURCE OF CHEMICALS

AgNO₃ (Sigma-Alderich)

Ascorbic acid (Sigma-Alderich)

CaCl₂ (Fluka)

Cresyl Violet (Raymond A. Lamb)

D-AP5 (Ascent)

D-Glucose (Fisher)

DPX (Agar)

Gabazine (Tocris)

NBQX disodium salt (Ascent)

Lucifer Yellow CH dilithium salt (Fluka)

MgCl₂ (Fluka)

Myo-inositol (Sigma)

NaHCO₃ (Fluka)

Na₂HPO₄ (Fluka)

NaH₂PO₄ (Fluka)

Paraformaldehyde (Sigma)

KCl (Sigma)

K₂CrO₇ (Sigma)

NaCl (Fisher)

Na-Pyruvate (Sigma)

Strychnine (Sigma)

QX314 (Sigma)

Xylene (Fisher)

ARTICLE

A Rapid Method Combining Golgi and Nissl Staining to Study Neuronal Morphology and Cytoarchitecture

Nadia Pilati, Matthew Barker, Sofoklis Panteleimonitis, Revers Donga, and Martine Hamann

Department of Cell Physiology and Pharmacology (NP,MB,SP,MH) and Departments of Infection, Immunity, and Inflammation and Medical and Social Care Education (SP,RD), Leicester University, Leicester, United Kingdom

SUMMARY The Golgi silver impregnation technique gives detailed information on neuronal morphology of the few neurons it labels, whereas the majority remain unstained. In contrast, the Nissl staining technique allows for consistent labeling of the whole neuronal population but gives very limited information on neuronal morphology. Most studies characterizing neuronal cell types in the context of their distribution within the tissue slice tend to use the Golgi silver impregnation technique for neuronal morphology followed by deimpregnation as a prerequisite for showing that neuron's histological location by subsequent Nissl staining. Here, we describe a rapid method combining Golgi silver impregnation with cresyl violet staining that provides a useful and simple approach to combining cellular morphology with cytoarchitecture without the need for deimpregnating the tissue. Our method allowed us to identify neurons of the facial nucleus and the supratrigeminal nucleus, as well as assessing cellular distribution within layers of the dorsal cochlear nucleus. With this method, we also have been able to directly compare morphological characteristics of neuronal somata at the dorsal cochlear nucleus when labeled with cresyl violet with those obtained with the Golgi method, and we found that cresyl violet-labeled cell bodies appear smaller at high cellular densities. Our observation suggests that cresyl violet staining is inadequate to quantify differences in soma sizes. (*J Histochem Cytochem* 56:539–550, 2008)

KEY WORDS

Lucifer yellow
neuron
dendrite
soma

THE GOLGI SILVER impregnation method is a powerful method still routinely used for studying neuronal morphology (Hani et al. 2007; Mendizabal-Zubiaga et al. 2007). Its usefulness for quantitative analysis of labeled neurons is limited by its capricious nature. In contrast, the Nissl staining approach allows for the visualization of all somata in appropriately prepared tissue sections while being poor in labeling neuronal processes. Thus, a combined approach using the Golgi silver impregnation technique and the Nissl staining method would allow for the establishment of the detailed morphological profiles of neurons within a nucleus or a laminar structure. Although it is possible to counterstain cells previously treated with the Golgi silver impregnation

technique with the Nissl stain (Werner and Brauer 1984; Werner et al. 1986,1989), a drawback with this approach is that the Golgi-stained neurons must be deimpregnated before counterstaining with Nissl stains. Under these conditions, most Golgi-labeled neurons lose their morphological characteristics before they take up the Nissl stain. Recently, Friedland et al. (2006) described staining for cresyl violet around neurons labeled with the Golgi method that was rather faint and suggested that pH changes during the Golgi staining might reduce affinity for cresyl violet. We report here the first successful combination of Golgi and cresyl violet staining methods that allowed us to simultaneously characterize the morphology of individual neurons together with the cytoarchitecture of the rat dorsal cochlear nucleus (DCN). Our method also allowed us to identify neuronal somata within the brainstem or cerebellum and to directly compare the morphological characteristics of the somata when labeled with cresyl violet and with the Golgi silver impregnation method.

Correspondence to: Martine Hamann, Department of Cell Physiology and Pharmacology, Medical Sciences Building, PO Box 138, University Road, Leicester LE1 9HN, UK. E-mail: mh86@le.ac.uk

Received for publication November 15, 2007; accepted February 7, 2008 [DOI: 10.1369/jhc.2008.950246].

Materials and Methods

Twenty-nine Lister Hooded rats, 17 to 18 days old, were used, and all procedures were performed in accordance with the United Kingdom Home Office regulations.

Fixation

Brains were dissected out of the skull and immediately fixed in 5% paraformaldehyde for at least 2 days at a temperature of 21°C. The paraformaldehyde fixative solution was buffered at various pH levels (pH 5.8, 7.4, or 7.6) according to the chromation process. When the chromation process was performed in distilled water (i.e., no buffer) the initial fixative medium was buffered at pH 7.4.

Rapid Golgi Staining

After initial fixation, brains were transferred into freshly prepared chromating solution containing 3% potassium dichromate and 4% or 5% paraformaldehyde in either distilled water (i.e., not buffered) or in PBS solutions of pH 5.8, 7.4, or 7.6 (i.e., in concert with the initial fixation mentioned above). Additionally, the chromating solutions also contained either 2% glutaraldehyde or 2% chloral hydrate. All chromating solutions were changed daily with freshly prepared solutions. After 48 hr of chromation, the brains were washed several times with a 2% silver nitrate solution in distilled water before incubation in silver nitrate for another 48 hr for heavy metal precipitation to occur. During the whole staining process, brains were covered with aluminum foil to avoid light exposure. Tissue blocks labeled with the Golgi method were sectioned as detailed below.

Cresyl Violet Staining

Tissue slices (50 μm thick) were mounted on targeting molecule polysine-coated slides (VWR International; Braunschweig, Germany) and stained with 0.1% fast cresyl violet (Lamb; London, UK) dissolved in distilled water and filtered. Slices were stained in cresyl violet for 4 min and maintained under agitation. When the brains were previously labeled with the Golgi method, the staining time in cresyl violet was extended to 6–7 min. Slices were dehydrated for 2 min using 100% ethanol, cleared in xylene for another 2 min, and covered with DPX and a coverslip. In some cases, slices were stained with cresyl violet using a progressive dehydration protocol procedure. Here, brain slices were first hydrated in MilliQ water for 30 min and then placed under agitation in cresyl violet staining solution for 3–5 min before being rinsed in MilliQ water. Brain slices were progressively dehydrated in 70% alcohol (for 10 min), 95% alcohol (with a few drops of 10% acetic acid; for 2–3 min), and finally 100% alcohol (for 10 min). Slices were cleared in xylene for 5 min before being covered with DPX and a coverslip.

Lucifer Yellow Labeling

In some separate experiments, fresh slices were used, and cells were filled with Lucifer yellow (Fluka; Buchs, Switzerland), and the size of the cell body was measured and compared with the soma size of Golgi-stained cells. Lucifer yellow cell filling was performed on freshly dissected tissue and freshly cut slices. Whole cell recordings of DCN neurons were performed under microscopic control with glass borosilicate electrodes (3–5 M Ω) containing 0.1% Lucifer yellow and (in mM) 97.5 Kgluconate, 32.5 KCl, 5.4 EGTA, 10 HEPES, and 1 MgCl₂ (pH 7.1 with KOH). Lucifer yellow was allowed to fill up the cell for at least 30 min. Slices containing the labeled cells were transferred into 4% paraformaldehyde dissolved in phosphate buffer (pH 7.4) and fixed for ~12 hr before being rinsed with the phosphate buffer (pH 7.4), mounted on a polysine slide, and covered with 1% agarose and a coverslip.

Tissue Slicing

For slicing of fresh tissue (used for Lucifer yellow staining), 150- μm -thick coronal slices containing the DCN were cut under binocular guidance using a Leica Vibroslicer VT1000S (Nussloch, Germany), in an ice cold low sodium artificial cerebrospinal fluid containing (in mM): 2.5 KCl, 1.2 NaH₂PO₄, 10 D-glucose, 0.5 ascorbic acid, 25 sucrose, 26 NaHCO₃, 0.1 CaCl₂, and 4 MgCl₂, bubbled with 95% O₂ and 5% CO₂ (pH 7.4). Slices were transferred to a recording chamber on a Zeiss Axiovert microscope (Göttingen, Germany) and perfused with oxygenated artificial cerebrospinal fluid containing (in mM) 125 NaCl, 2.5 KCl, 1.2 NaH₂PO₄, 10 D-glucose, 0.5 ascorbic acid, 2 Na pyruvate, 3.0 myo-inositol, 26 NaHCO₃, 2 CaCl₂, and 1 MgCl₂ bubbled with 95% O₂ and 5% CO₂ (pH 7.4). When using fixed tissue (used for Golgi and/or cresyl violet staining), slices were cut at 50 μm thickness in distilled water, collected and mounted on polysine-coated slides, and left to dry overnight at room temperature in a dust-free enclosure before they were counterstained with cresyl violet.

Image Acquisition

Slices were visualized using a Nikon Eclipse TE2000-U inverted microscope, and images were acquired with a Nikon DXM1200F digital camera and Nikon NIS Elements 2.20 software (Kanagano, Japan). Images of Golgi-labeled cells were obtained using a z-stack of two to four microphotographs taken at 1- to 2- μm intervals throughout the slice and put into a single focused image with the software Image-J 1.36. Lucifer yellow-filled cells were examined on an Olympus confocal microscope (IX70) with a $\times 60$ objective (Nagano-Ken, Japan). Images of Lucifer yellow-stained cells were obtained using a z-stack of 20–90 microphotographs

taken at a 0.5- μm interval throughout the slice and put into a single-focused image with the Olympus Fluoview software.

Analysis

Nissl-stained Cells. Analysis of cell density and cell soma surface areas was performed on two to three slices per rat, and three rats were used per staining condition. The whole DCN was cut from its caudal to its rostral end, and DCN slices were analyzed at three depths throughout the nucleus (i.e., 100, 250, and 400 μm deep). Analysis of cell numbers and cell soma surface areas was performed using rectangular areas ($89 \times 55 \mu\text{m}$) placed as a fixed matrix (as in King et al. 2002) of three rows and three columns, and the three rows represented the three layers: the external (molecular), intermediate (fusiform), and internal (deep) layers. In the vertical plane, each rectangle was separated by a 60- μm gap between the molecular and the fusiform layer and by a 100- μm gap between the fusiform and the deep layer. In the horizontal plane, rectangles were separated from each other by a 90- μm gap. Analysis of cell density and cell soma surface area was performed on all cells that were in the optical focal plane lying within or were crossing the inclusion boundaries, using a method similar to that of King et al. (2002). Cell density was measured per area and not volume. Cell soma surface was analyzed for all cell profiles contained

within the six rectangles (two rectangles per layer). Cell soma surface analysis was done by outlining the soma border but excluding the emerging dendrites and axon using the method and the terms described by McDonagh et al. (2002) and Zwaagstra and Kernell (1981). Only cell soma surface areas $\geq 39 \mu\text{m}^2$ corresponding to a diameter $\geq 7 \mu\text{m}$ were included in the analysis. This lower limit was set to include granule cells known to have diameters of $\sim 7\text{--}9 \mu\text{m}$ (Mugnaini et al. 1980b; Alibardi 2003). A diameter lower limit of 7 μm also excluded glial cells from the counting (Skoglund et al. 1996). Area localization was based on the rat stereotaxic atlas of Paxinos and Watson (1998).

Golgi- and Lucifer Yellow-stained Cells. The number of Golgi-labeled cells was estimated throughout the total DCN, and both left and right sides of three brains were used for every staining condition reported in Figure 1, giving a total of 61–74 slices analyzed per condition. The surface of the non-neuronal (a-specific) Golgi staining (defined as all the black to orange precipitates) was estimated in 8 DCN slices per rat from both left and right sides, giving a total number of 24 slices analyzed per condition (three rats per condition). Surface (or profile) areas were measured using the Image-J 1.36 freehand selection tool (National Institutes of Health; Bethesda, MD), allowing selection of the contour of the DCN, the nonspecific staining, and the cell soma surface area together, with the Image-J 1.36

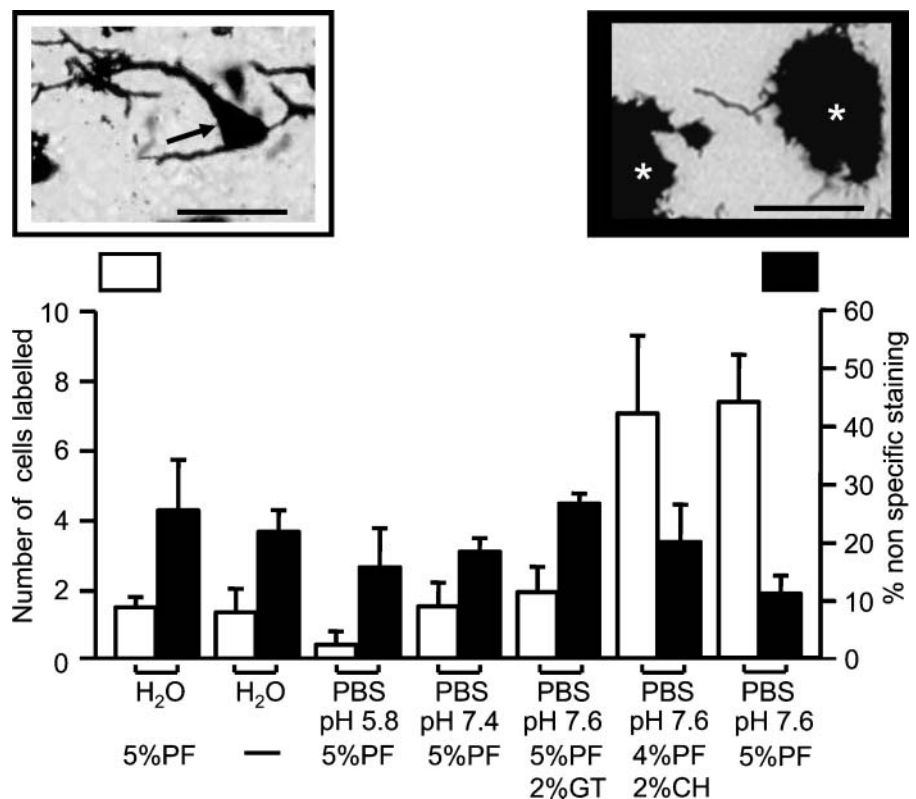


Figure 1 Golgi staining of dorsal cochlear nucleus (DCN) neurons is dependent on the chromating solution. Summary histograms representing the following: white, mean \pm SD number of labeled cells per DCN slice ($n=6$); black, mean \pm SD percentage of area not specifically stained relative to the total DCN area ($n=6$). CH, chloral hydrate; GT, glutaraldehyde; PF, paraformaldehyde. Inset at left is an example of a neuron-specific labeling highlighted by arrow (potassium dichromate solution was dissolved in PBS, pH 7.6, and 4% paraformaldehyde plus 2% chloral hydrate). Inset at right is an example of nonspecific staining highlighted by white asterisks (potassium dichromate dissolved in H₂O and 5% paraformaldehyde). Bar = 50 μm .

area calculator plug-ins, allowing estimating the surface areas.

Statistics

Data are expressed as mean \pm SD. Unless specified otherwise, data were analyzed by one- or two-factor ANOVA (general linear model) tests followed by Tukey's test using the statistical software ezANOVA (<http://www.sph.sc.edu/comd/rorden/ezanova/home.html>) or Mini Tab 14. Post hoc power analysis was performed using Gpower 2.0 software (<http://www.psych.uni-duesseldorf.de/aap/projects/gpower/>).

Results

We started by setting up optimal staining conditions for labeling individual neurons of the rat DCN using the rapid Golgi silver impregnation method before combining it with cresyl violet staining so that we could characterize the morphology of individual neurons within the context of layers of the DCN.

Cell Labeling Using the Rapid Golgi Method

We used the rapid variant of the Golgi silver impregnation method to label neurons of the DCN over 4 days. This labeling method can be divided into two steps. First, cells were impregnated with both trivalent and hexavalent chromium ions over 2 days, and this is known as the chromation step. This process requires the presence of aldehydes and is known to be influenced by time, temperature, and pH (Kopsch 1896; Colonnier 1964). The chromation step was followed by a precipitation step also lasting 2 days, in which the chromium ions react with heavy metal ions, silver in this case, to give a chromogenic reaction product that serves as the visual marker of the labeled cells. We optimized our protocols by experimenting with various aldehyde donors during the chromation step, namely paraformaldehyde, glutaraldehyde, or chloral hydrate, and also using phosphate buffer to give us a pH range of 5.8–7.6. In another set, the chromation step was carried out in the absence of buffer with or without paraformaldehyde (5%). The quality of the Golgi staining was assessed by determining whether the staining was confined to neurons (pointed with the arrow in Figure 1, left inset) or to nonspecific staining (shown as asterisks in Figure 1, right inset). The stained neuron in Figure 1 showed a clearly visible cell body with a pyramidal shape and dendrites, whereas nonspecific labeling in Figure 1 had an undefined patchy presentation instead of a neuronal shape. Figure 1 also shows a histogram plot illustrating the effects of pH and aldehyde on neuronal and non-neuronal staining by plotting the average number of labeled neurons per DCN slice (white bars) and the surface area of the non-neuronal staining relative to the total DCN area (black bars). We quan-

Table 1 One-factor ANOVA–Tukey tests comparing the labeling obtained in various chromating solutions

PBS (pH 7.6) and 5% PF vs condition below	Number of labeled cells	Percentage of aspecific staining
H ₂ O, 5% PF	$p < 0.0001$	$p = 0.18$
H ₂ O	$p < 0.0001$	$p = 0.09$
PBS (pH 5.8), 5% PF	$p < 0.0001$	$p = 0.29$
PBS (pH 7.4), 5% PF	$p < 0.0001$	$p < 0.05$
PBS (pH 7.6), 5% PF, 2% GT	$p < 0.0001$	$p < 0.01$
PBS (pH 7.6), 4% PF, 2% CH	$p = 0.74$	$p < 0.05$

p values refer to comparing the chromating condition in PBS, pH 7.6, and 5% paraformaldehyde vs the other conditions. *p* values are reported for the number of labeled cells per DCN slice and the nonspecifically stained area relative to the total DCN area. PF, paraformaldehyde; GT, glutaraldehyde; CH, chloral hydrate; DCN, dorsal cochlear nucleus.

tified the number of labeled cells and the extent of the non-neuronal staining and compared the different conditions using one-factor ANOVA and Tukey tests. We found that the highest number of labeled cells were obtained when we used either PBS, pH 7.6, with 5% paraformaldehyde or PBS, pH 7.6, with 4% paraformaldehyde and 2% chloral hydrate (Figure 1, white bars; Tables 1 and 2, left columns). Using a PBS solution, pH 7.6, with 5% paraformaldehyde also led to reduced non-neuronal labeling (Figure 1, black bars; Tables 1 and 2, right columns). Using a PBS solution, pH 7.6, with glutaraldehyde instead of paraformaldehyde reduced the number of labeled cells (Figure 1), suggesting that glutaraldehyde is not ideal for neuronal staining with the Golgi silver impregnation method. Similarly, more acidic pH conditions or aqueous solutions produced only few labeled neurons (Figure 1; Table 1, left column).

Cell Labeling Using the Combined Cresyl Violet–Rapid Golgi Method

Brains were previously labeled with the Golgi method using the optimal chromating conditions in a PBS solution, pH 7.6, with 5% paraformaldehyde, and slices containing the DCN were subsequently counterstained with cresyl violet. In addition to acting as a control stain of the neuronal tissue, cresyl violet allowed us to study

Table 2 One factor ANOVA–Tukey tests comparing the labeling obtained in various chromating solutions

PBS (pH 7.6), 4% PF and 2% CH vs condition below	Number of labeled cells	Percentage of aspecific staining
H ₂ O, 5% PF	$p < 0.001$	$p = 0.60$
H ₂ O	$p < 0.0001$	$p = 0.78$
PBS (pH 5.8), 5% PF	$p < 0.0001$	$p = 0.32$
PBS (pH 7.4), 5% PF	$p < 0.001$	$p = 0.55$
PBS (pH 7.6), 5% PF, 2% GT	$p < 0.001$	$p = 0.08$
PBS (pH 7.6), 5% PF	$p = 0.74$	$p < 0.05$

p values refer to comparing the chromating condition in PBS, pH 7.6, 4% paraformaldehyde, and 2% chloral hydrate vs the other conditions. *p* values are reported for the number of labeled cells per DCN slice and the nonspecifically stained area relative to the total DCN area. See Table 1 for abbreviations.

the silver-impregnated neurons in the context of the DCN laminated structure. While staining the tissue with cresyl violet, studies report first hydrating the slices with distilled water, then staining them with cresyl violet, and finally dehydrating them by using progressively graded solutions of ethanol, namely 50–70% and 100% (Gittins and Harrison 2004; Friedland et al. 2006). In our experience, we found that this commonly used approach produced cracking within Golgi-labeled tissue, leading us to modify our protocol such that sections were transferred directly to the cresyl violet solution without prior hydration and from the cresyl violet solution directly to 100% ethanol for 2 min.

Figure 2 shows the morphologies of silver-impregnated neurons before (Figure 2A) and after (Figure 2B) counterstaining the tissue with cresyl violet. The cresyl violet stain shows laminated areas of higher density of labeling suggestive of cell layering within the DCN, whereas Golgi-stained cells showed typical neuronal morphologies. We also used the combined Golgi–cresyl violet staining in slices containing the cerebellum and other brainstem nuclei easily recognizable by the cresyl violet staining. Figure 3A shows cerebellar Purkinje cells aligned in the Purkinje cell layer, with their typical spiny dendritic tree oriented toward the molecular layer (Palay and Chan-Palay 1974; Friedland et al. 2006).

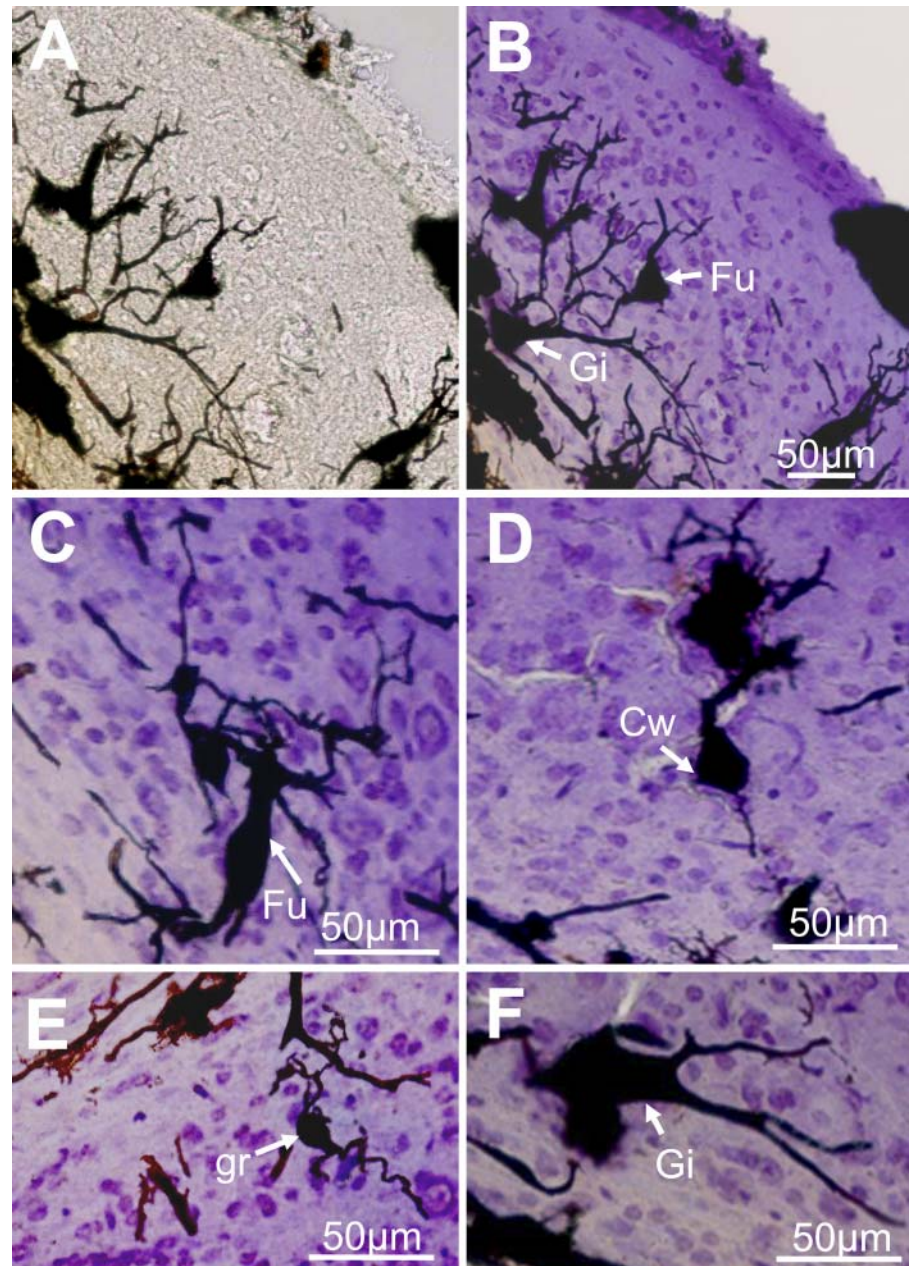


Figure 2 Combined cresyl violet and Golgi labeling of DCN neurons and cytoarchitecture. (A) Photomicrograph showing two DCN fusiform neurons and a giant cell stained with the Golgi method. In B, the same fusiform cells (Fu) and giant cell (Gi) are shown after counterstaining the slice with cresyl violet. The chromating solution contained potassium dichromate dissolved in PBS, pH 7.6, and 5% paraformaldehyde. (C–F) Photomicrographs of DCN cell types obtained after labeling slices with the combined Golgi–cresyl violet method (same conditions as for B). (C) Arrow points to another fusiform cell (Fu) in the fusiform cell layer with its large elongate cell body and its basal dendrites lying in the deep layer, whereas the apical dendrites are oriented toward the molecular layer. (D) Arrow indicates a cartwheel cell (Cw) with its small oval cell body between the fusiform and the molecular layer, an axon extending into the fusiform layer, and a large spiny dendritic tree in the molecular layer. (E) Arrow points to a granule cell (gr) in the deep layer with two main dendrites ending in claw-like protuberances. (F) Arrow indicates a giant cell (Gi) with its large soma exceeding 30 μm diameter and many thick dendrites, both located in the deep layer.

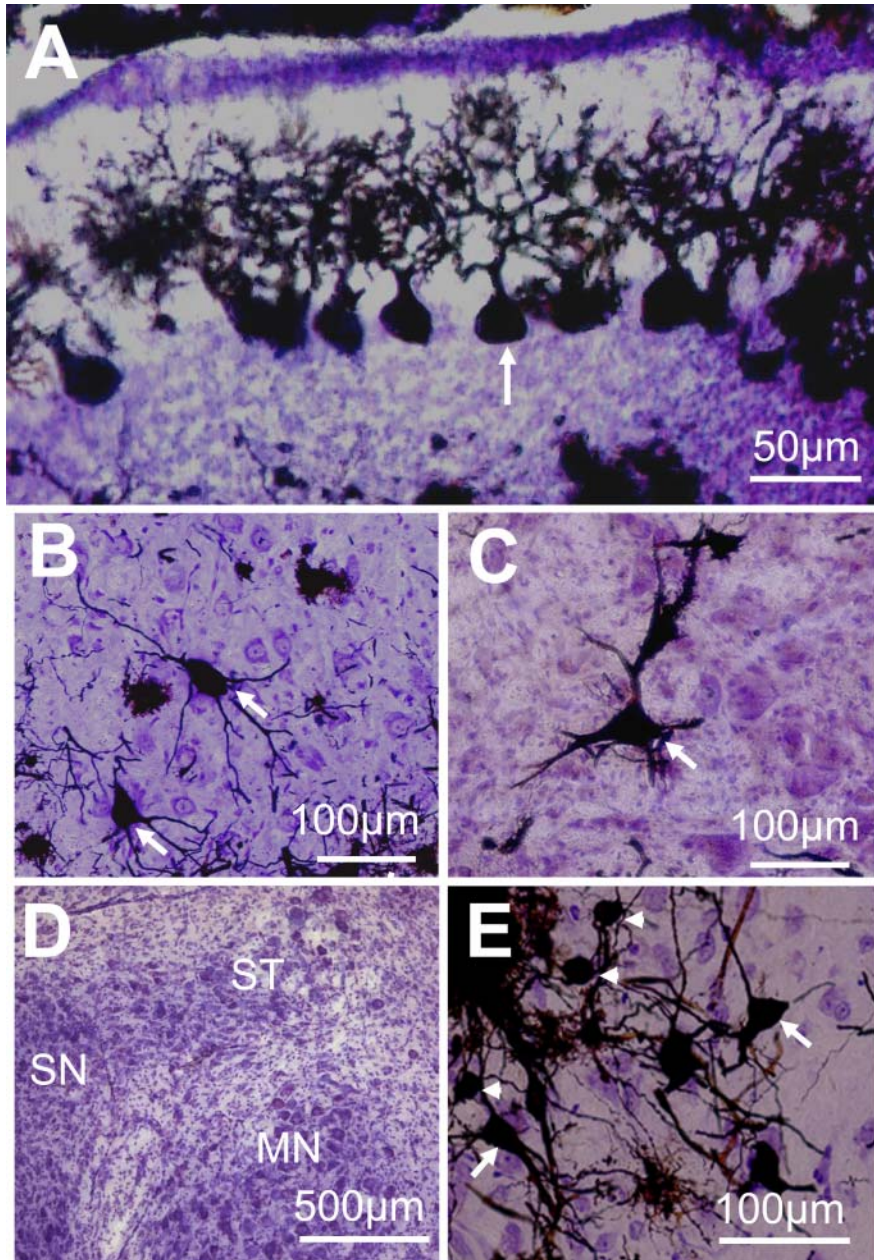


Figure 3 Combined labeling of neurons and cytoarchitecture in the cerebellum and brainstem nuclei. (A) Arrow points to one Purkinje cell. Purkinje cells lie all aligned in the Purkinje cell layer with their typical spiny dendritic trees oriented toward the molecular layer. (B) Arrows indicate large motoneurons in the facial nucleus. (C) Arrow points to a large multipolar cell from the lateral vestibular nucleus. (D) Cresyl violet staining of a slice containing the supratrigeminal nucleus (ST) showing its position relative to the trigeminal motor nucleus (MN) and the trigeminal main sensory nucleus (SN). (E) Combined Cresyl violet and Golgi labeling of neurons in the supratrigeminal nucleus. Arrows point to pyramidal neurons, whereas arrowheads point to small ovoid neurons.

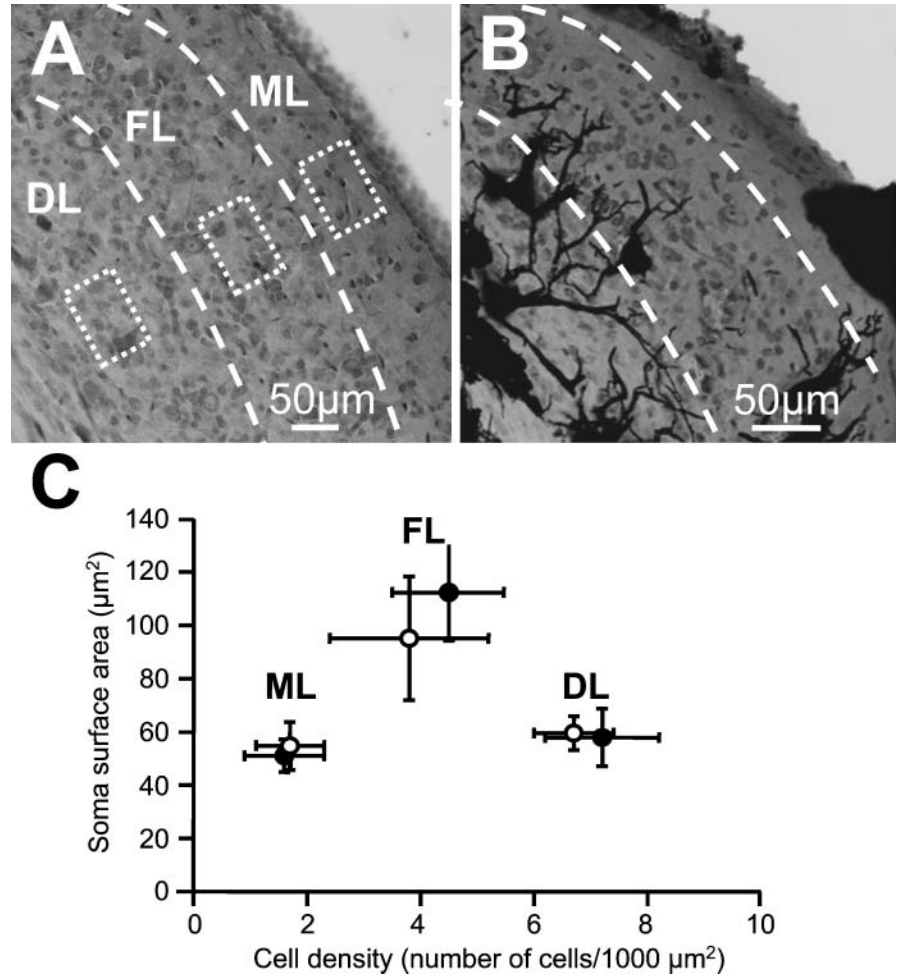
Figures 3B and 3C show two labeled motoneurons in the facial nucleus (Grinevich et al. 2005) and a giant neuron in the lateral vestibular nucleus (Uno et al. 2003), respectively. The supratrigeminal nucleus is easily recognizable by its capping of the trigeminal motor nucleus (Figure 3D), and it contains pyramidal and small ovoid neurons as shown in Figure 3E.

Characterization of the DCN Cytoarchitecture and Cellular Localization Within the Layers

We tested whether the DCN is made from a homogeneous cell population or whether it can be subdivided

into layers. We validated the layers by labeling slices with Cresyl violet and by establishing a matrix of nine rectangles distributed as three rows, an external, intermediate, and inner layer (see Materials and Methods), and we quantified the cellular density and the cell soma surface area within those rectangles (three rectangles are shown in Figure 4A). Figure 4C shows a plot of the soma surface area as a function of the cell density within those three layers. The external layer was characterized by the lowest cell density of 1.6 ± 0.7 cells/1000 μm^2 ($n=27$ rectangles) compared with the cell density of 4.5 ± 1.0 cells/1000 μm^2 ($n=27$) in the me-

Figure 4 Analysis of the DCN architecture labeled with cresyl violet before and after Golgi staining. (A,B) Photomicrographs of the DCN stained with cresyl violet (A) and with cresyl violet and Golgi labeling (B). In A and B, dashed lines define the boundaries between the external or molecular layer (ML), the intermediate or fusiform cell layer (FL), and the inner or deep layer (DL). For each layer, areas within the rectangles are analyzed (three rectangles shown in A). (C) Summary plot representing the mean \pm SD values of the cell soma surface area ($n=16-18$ rectangles) and of the cell density ($n=24-27$ rectangles) for the different layers. Slices were labeled with cresyl violet (black circles) or with the combined Golgi and cresyl violet labeling method (white circles). The cell density and soma surface areas were analyzed from cresyl violet-stained cells in both conditions.



dial layer and the cell density of 7.2 ± 1.0 cells/1000 μm^2 ($n=27$) in the inner layer ($p < 0.0001$, two-factor ANOVA test). Cells in the intermediate layer were also characterized by a larger soma surface area ($112 \pm 18 \mu\text{m}^2$, $n=18$) compared with cells within the external layer ($51 \pm 6 \mu\text{m}^2$, $n=18$) and with cells within the inner layer ($58 \pm 11 \mu\text{m}^2$, $n=18$, $p = 0.002$, two-factor ANOVA test). Cell soma surface areas were similar for the same layer when the slices were chosen at three different depths within the DCN ($n=6$ rectangles and 3 rats, two-factor ANOVA test, $p = 0.167$). Our DCN cell layer organization is similar to the DCN laminar organization reported in previous studies (see Discussion), and we refer to the external layer as the molecular layer, the intermediate layer as the fusiform cell layer, and the inner layer as the deep layer. The combined Golgi-cresyl violet staining method therefore made it possible to localize the different cells within the three layers with a high degree of certainty. Figure 2 gives an overview of some morphological cell types observed in this study. Within the fusiform cell layer, fusiform cells are characterized by an elongated cell body of $34 \pm 4 \mu\text{m}$

diameter ($n=5$) across their major axis and a diameter of $19 \pm 3 \mu\text{m}$ ($n=5$) across their minor axis (Figures 2B and 2C) (Maruyama and Ohmori 2006). Fusiform cells are also characterized by basal dendrites directed toward the deep layer and apical dendrites directed toward the molecular layer. Usually, the apical dendrite divides into several branches (Figure 2C). Cartwheel cells are found at the boundary between the molecular layer and the fusiform cell layer and have a diameter of 14 and 22 μm ($n=2$), as well as a thick primary dendrite that gives rise to arborizations in the form of a tree that extends into the molecular layer (Figure 2D; Wouterlood and Mugnaini 1984). Giant cells with a cell body exceeding 30- μm diameter (diameter of $38 \pm 7 \mu\text{m}$, $n=6$) (Zhang and Oertel 1993) are characterized by multiple thick dendrites projecting along the deep layer and toward the fusiform cell layer (Figures 2B and 2F). Small-diameter cells likely to be granule cells (Mugnaini et al. 1980b) with an oval cell body and two to three primary dendrites were mainly found in the deep layer (diameter of $11 \pm 2 \mu\text{m}$, $n=3$) and also in the molecular layer (diameter of $9 \pm 2 \mu\text{m}$, $n=3$). Figure 2E

shows a granule cell with its classically described dendritic claws (Mugnaini et al. 1980b).

DCN Cytoarchitecture After Golgi Staining

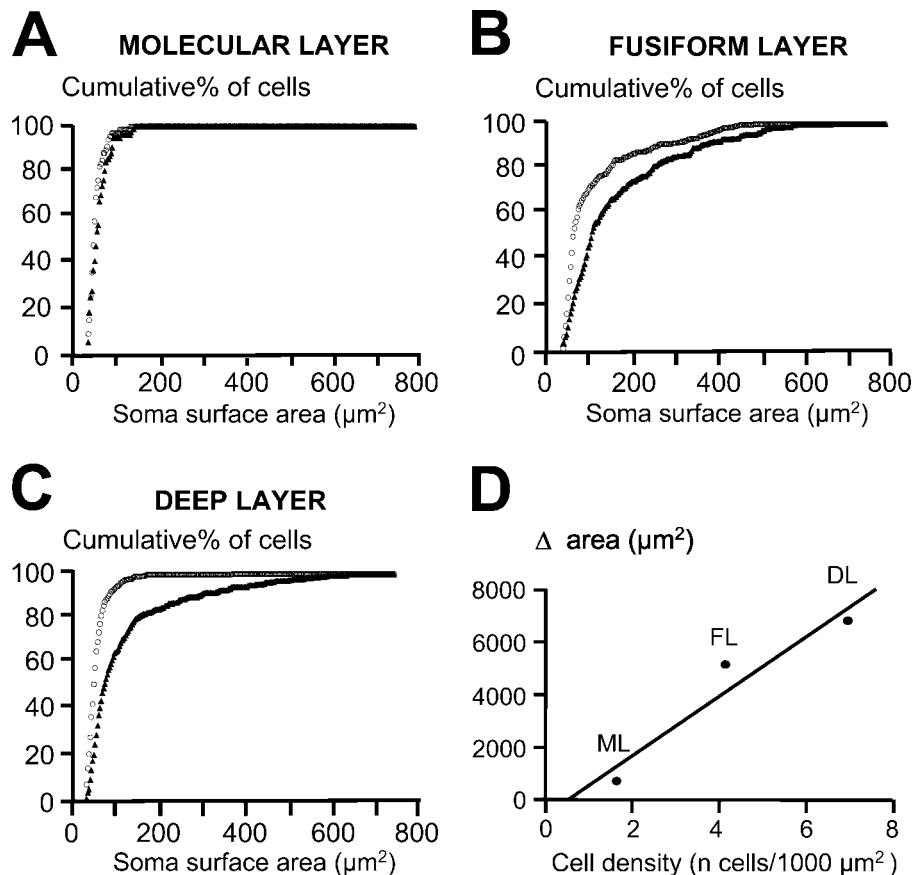
We checked whether the Golgi staining procedures did not interfere fundamentally with the native cytoarchitecture of the DCN and quantified the cell density and the soma surface area of cresyl violet-stained sections previously stained with the Golgi method. Figure 4C represents an analysis of the DCN architecture on cresyl violet-stained cells without any previous Golgi staining (black circles) and after having previously labeled the tissue with the Golgi method (white circles). After Golgi and cresyl violet staining, DCN layers could still be distinguished by differences in their cell density and cell soma surface area. The external or molecular layer was still characterized by the lowest cell density of 1.7 ± 0.6 cells/1000 μm^2 ($n=24$ rectangles) compared with the cell density of 3.8 ± 1.4 cells/1000 μm^2 in the intermediate or fusiform layer ($n=24$) and to the cell density of 6.7 ± 0.7 cells/1000 μm^2 ($n=24$) in the inner or deep layer ($p < 0.00001$, two-factor ANOVA test). After Golgi and cresyl violet staining, cells in the fusiform layer were also characterized by a larger soma surface area ($95 \pm 23 \mu\text{m}^2$, $n=16$ rectangles) compared with cells within the molecular layer ($55 \pm 9 \mu\text{m}^2$, $n=16$) and with cells within the inner or deep layer ($59 \pm 6 \mu\text{m}^2$, $n=16$, $p < 0.00001$, two-factor ANOVA test). Within each layer, Nissl-stained cell bodies had a similar soma surface area with or without previously labeling the tissue with the Golgi method (two-factor ANOVA test, $p = 0.58$, $n=5$ and 6 rectangles, respectively, containing between 100 and 400 cells per layer). Power analysis with values of 80% and 100% for 100 and 400 cells, respectively, indicates that our sample size is sufficient to detect a 10% variation of cell soma surface areas between the two staining conditions, further suggesting similar Nissl staining conditions in the presence or absence of Golgi staining. Cell densities were also similar for the same layer when the slices were chosen at three different depths within the DCN ($n=9$ rectangles and 3 rats, two-factor ANOVA test, $p = 0.602$), supporting the idea that the layer distribution is uniform throughout the DCN. Cell density was also similar within each particular layer, with or without previously labeling tissue with the Golgi method (two-factor ANOVA test, $p = 0.73$, $n=9$ and 6, respectively), showing that Nissl-stained layer characteristics stayed unchanged despite Golgi labeling.

Estimation of the Soma Surface Areas After Golgi or Cresyl Violet Staining

Although we found no difference in the Nissl-stained cytoarchitecture when we analyzed the cell bodies labeled with cresyl violet, we noticed that some cells

labeled with the Golgi method had a bigger cell soma surface area compared with the average cell soma surface area obtained with cresyl violet staining. For example, giant cells are characterized by a soma surface area of $426 \pm 181 \mu\text{m}^2$ ($n=16$) while stained with the Golgi method. This value exceeds by 2.5 times the highest values of the cell soma area measured in cresyl violet staining condition ($172 \pm 63 \mu\text{m}^2$, Student *t*-test, $p = 1 \times 10^{-5}$, $n=16$). We represented the ability of the two staining methods to differently label the cell soma surface area by their cumulative distributions of the soma surface areas (Figure 5). Cumulative distributions were represented for each cell layer (Figures 5A–5C) and seem to be different for the fusiform cell layer (Figure 5B) and the deep layer (Figure 5C), whereas no major difference was observed for the molecular layer (Figure 5A). This suggests that Golgi-labeled cells are bigger than cresyl violet-stained cells within the fusiform and the deep layers. This difference in the cell soma surface area between Golgi- and Nissl-stained cells can be represented as the area difference between the two curves represented in Figures 5A–5C. In the molecular layer (Figure 5A), 50% of cells have a soma surface area $953 \mu\text{m}^2$ when labeled with cresyl violet ($n=67$), and 50% of cells have a soma surface area $960 \mu\text{m}^2$ when labeled with the Golgi method ($n=76$). Maximal values (representing the total number of cells) are similar for both staining conditions (reaching $\sim 100 \mu\text{m}^2$). In the fusiform cell layer (Figure 5B), 50% of cells have a soma surface area $964 \mu\text{m}^2$ when labeled with cresyl violet ($n=284$), and 50% of cells have a soma surface area $9107 \mu\text{m}^2$ ($n=291$) when labeled with the Golgi method. Cell soma surface areas do not exceed $490 \mu\text{m}^2$ when stained with cresyl violet, whereas cell soma surface areas of Golgi-stained cells reach $674 \mu\text{m}^2$ when stained with the Golgi method. In the deep layer (Figure 5D), 50% of cells have a soma surface area $958 \mu\text{m}^2$ when labeled with cresyl violet ($n=488$), and 50% of cells have a soma surface area $981 \mu\text{m}^2$ when labeled with the Golgi method ($n=377$ cells). Cell soma surface area does not exceed $398 \mu\text{m}^2$ when staining with cresyl violet, whereas cell soma surface area of Golgi stained cells reach values of $883 \mu\text{m}^2$. We further tested whether there was any correlation between this area difference and the cell density reported for the different layers. Figure 5D shows a correlation ($r^2 = 0.83$) between the difference in the cell surface soma area obtained between the two staining methods and the cell density, indicating that bigger cells within a dense layer are more likely to be underestimated when quantified with the cresyl violet staining method. We estimated the soma surface area of cresyl violet stained cells using a standard cresyl violet staining method that used progressive dehydration and found similar soma surface area values using the standard cresyl violet staining procedure or the abbreviated

Figure 5 Comparative analysis of the cell soma surface area between cresyl violet-stained cells and Golgi-stained cells. A cumulative frequency plot represents the cumulative percentage of cells in function of the soma surface area of cells labeled with cresyl violet (white circle) and with the Golgi method (black triangle) for the molecular layer (A), the fusiform layer (B), and the deep layer (C). (D) The area between the two curves represented as white circles and black triangles was calculated for the three layers and plotted against the cell density values of those layers. The correlation factor obtained after linear regression (r^2) is 0.83. ML, molecular layer; FL, fusiform layer; DL, deep layer.



cresyl violet staining of 55 ± 17 (61 cells) and $53 \pm 19 \mu\text{m}^2$ (87 cells), respectively, in the molecular layer ($p = 0.39$, unpaired Student t -test), 123 ± 54 (88 cells) and $106 \pm 98 \mu\text{m}^2$ (286 cells), respectively, in the fusiform layer ($p = 0.12$, unpaired Student t -test), and 56 ± 17 (124 cells) and $58 \pm 24 \mu\text{m}^2$ (390 cells), respectively, in the deep layer ($p = 0.48$, unpaired Student t -test). We finally filled cartwheel, fusiform, and giant cells with Lucifer yellow to compare their cell soma surface area with those obtained with the Golgi method and found similar values of soma surface areas when cells were filled with Lucifer yellow or when labeled with the Golgi method (Figure 6).

Discussion

The aim of this work was to set up a rapid method combining Golgi and Nissl staining so that we could study detailed neuronal morphology together with cytoarchitecture without using any form of intracellular labeling such as horseradish peroxidase (Oertel et al. 1990). We were able to characterize neuronal morphology directly from single tissue sections without having to reconstruct the neurons of interest (Blackstad et al. 1984). Using cresyl violet allowed us to characterize the cell layers within the DCN similar to those reported in

previous studies from different species or different rat strains (Osen 1969; Brawer et al. 1974; Mugnaini et al. 1980a,b; Browner and Baruch 1982; Hackney et al. 1990). We used the Nissl stain alongside the Golgi silver staining method to place labeled neurons within those layers, and we were able to counterstain our tissue sections without the need to deimpregnate the silver stain as has been the case in previously published literature (Pasternak and Woolsey 1975; Werner and Brauer 1984; Werner et al. 1986,1989). We also used this rapid method combining Golgi and Nissl staining in other brain areas. We had to overcome two major obstacles that attend the Golgi silver impregnation technique, first on its own and second, in combination with cresyl violet.

Cell Labeling Using the Rapid Golgi Method

The Golgi silver impregnation method is unreliable because potassium dichromate and silver nitrate can react unselectively, forming bulk crystals on the surface of the specimen in question (Pasternak and Woolsey 1975); therefore, the Golgi silver impregnation method has been modified by adding either formaldehyde to the potassium dichromate solution (Kopsch 1896) or glutaraldehyde (Colonnier 1964) to the potassium dichro-

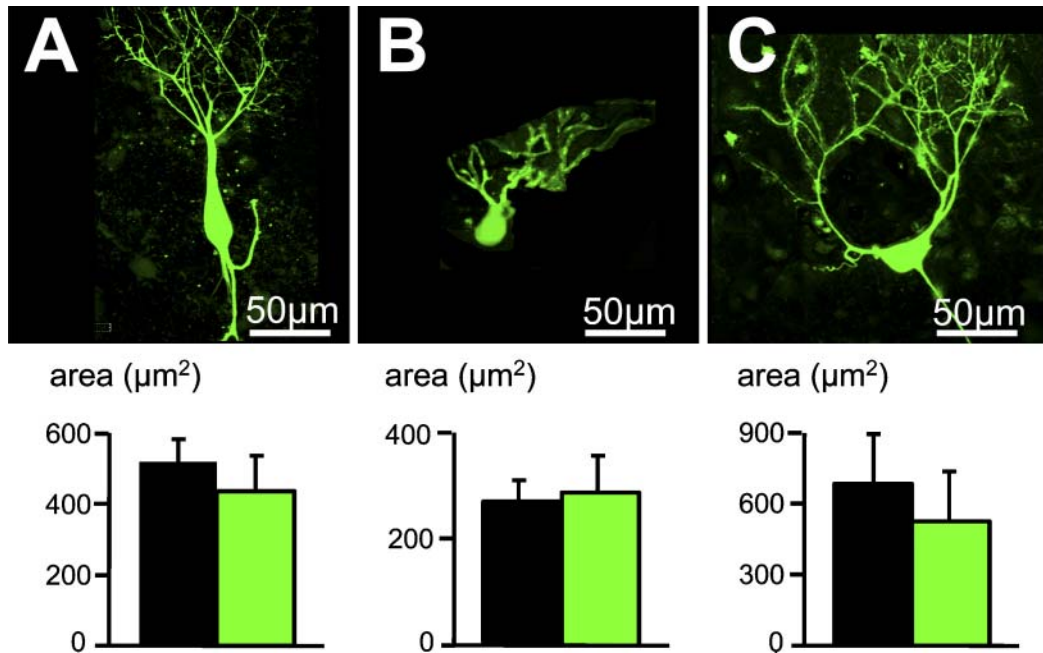


Figure 6 Comparative analysis of the cell soma surface area between Lucifer yellow-filled cells and Golgi-stained cells. (A–C) Photomicrographs of various DCN cells filled with the fluorescent dye Lucifer yellow. (A) Example of a fusiform cell. (B) Example of a cartwheel cell. (C) Example of a giant cell. Below each micrograph, histograms show a summary of the soma surface areas calculated for the cell type represented above, when cells were labeled with the Golgi method (black bars) and when cells were labeled with Lucifer yellow (green bars). Data are represented as mean \pm SD from 3–6 neurons. *p* values of 0.67, 0.15, and 0.32 (Student *t*-test) for cartwheel cells, fusiform cells, and giant cells, respectively.

mate solution. Those methods have been shown to improve the quality and the reaction time of the Golgi staining. Other modifications such as using microwaves (Marani et al. 1987; Zhang et al. 2003), altering the composition of the chromation solution and its pH (Van der Loos 1956; Morest and Morest 1966; Adams 1979; Grandin et al. 1988; Angulo et al. 1994,1996), or using a vacuum (Friedland et al. 2006) improved the labeling of neurons. We compared the quality of the Golgi staining by altering the aldehyde types (paraformaldehyde, glutaraldehyde, or chloral hydrate) and the pH of the phosphate buffer used in the chromating solution. We showed that potassium dichromate added into a phosphate-buffered medium at a weak basic pH (pH 7.6) with 5% paraformaldehyde favored the labeling of neurons over nonspecific labeling within the tissue. The nonspecific staining is likely caused by the uncontrolled chemical reaction between potassium dichromate, which acts as the primary impregnation compound, and the chromogen, silver nitrate. This chemical reaction is governed by the ratio of Cr^{3+} and $\text{Cr}_2\text{O}_7^{2-}$ ions, which is dependent on the concentration of protons and the presence of aldehydes (Angulo et al. 1996). Chromium (III) cross-links the carboxyl terminal of intracellular proteins and binds to $\text{Cr}_2\text{O}_7^{2-}$ (Angulo et al. 1996). Nevertheless, Cr^{3+} does not react with the silver nitrate in contrast to $\text{Cr}_2\text{O}_7^{2-}$, which produces the black silver

chromate, thereby defining the morphological profile of neurons. The low-quality staining obtained at more acidic pH could be related to an excess of Cr^{3+} relative to $\text{Cr}_2\text{O}_7^{2-}$. Good labeling conditions are therefore dependent on an adequate ratio of Cr^{3+} and $\text{Cr}_2\text{O}_7^{2-}$ (Angulo et al. 1996).

Cytoarchitecture Labeling and Distribution of the Cell Types

Our analysis of the cell density and soma surface areas allowed us to characterize three layers within the Lister Hooded rat DCN similar to previous studies performed in other species or rat strains (Osen 1969; Brawer et al. 1974; Mugnaini et al. 1980a,b; Browner and Baruch 1982; Webster and Trune 1982; Oertel and Wu 1989; Hackney et al. 1990; Alibardi 2006). The peripheral (molecular) layer is characterized by a low density of cells in Nissl staining, and this is probably because of the fact that it contains mainly parallel fibers and processes of fusiform cells and cartwheel cells. In contrast to the molecular layer, the fusiform and the deep layers had higher densities of cells. Another difference was that cells within the fusiform cell layer had larger soma surface areas in Nissl stain compared with cells of the molecular and deep layers. Our results further showed that the laminar organization of the DCN seems to be

unaffected by the Golgi staining histological procedures. Consequently, our combined Nissl–Golgi staining method can be used to characterize different cell types and assign them to specific DCN layers. From the observations made in this study, the predominant DCN cell types have been characterized and mapped within the three cell layers. Cartwheel cells are localized between the molecular and the fusiform cell layer, whereas fusiform cells are localized in the fusiform cell layer (Mugnaini 1985; Hackney et al. 1990; Maruyama and Ohmori 2006). Giant cells were localized in the deep layer (Hackney et al. 1990; Zhang and Oertel 1993), and granule cells are present mainly in the deep layer (Mugnaini et al. 1980b). The cellular composition and localization within the Lister Hooded rat DCN is similar to previous studies and therefore validates our rapid method combining the Golgi silver impregnation technique with Nissl staining, without the need for deimpregnation as an intervening step. Using the Golgi silver staining method, we were also able to label morphologically identified cells within the supratrigeminal nucleus that could only be located by its position relative to the trigeminal motor nucleus. The presence of pyramidal and small ovoid neurons within this structure suggests the coexistence of neuronal subgroups that could be involved in modulating the process of mastication (Donga and Lund, 1991).

Estimation of the Cell Soma Surface Area

Previous reports are based on quantifying differences in sizes and shapes of neuron somata within the cochlear nucleus using cresyl violet staining (Seldon and Clark 1991; Saada et al. 1996). Our study showed that Golgi-labeled cells had larger cell soma compared with their equivalents labeled with Nissl stain. This could be explained by Golgi precipitates bursting out of the cell body, making the cell body appear larger, but this is unlikely to be the case because cells filled with Lucifer yellow had similar soma surface areas as those measured in Golgi-stained cells. It is likely that cresyl violet staining tends to underestimate the cell soma surface area because of the Nissl stain being directed primarily at the Nissl substance of the cytoplasm and not at the boundaries of the cell (cell membrane). This might therefore explain why the general cell outline is underestimated by Nissl stain, hence the discrepancies in cell sizes between the Nissl and Golgi staining.

Given our use of an abbreviated Nissl staining procedure, it is theoretically possible that cell bodies may not have taken the stain satisfactorily, thereby explaining this discrepancy. To control for this possibility, we also measured neuronal cell bodies using the standard cresyl violet staining method that used progressive tissue dehydration (using graded ethanol solutions). When comparing neuronal staining obtained with the

full and abbreviated dehydration methods, we found that cell body sizes were very similar, suggesting that we were unlikely to have underestimated neuronal cell body sizes as a result of the abbreviated dehydration procedure. Interestingly, Geisler et al. (2002) reported an increased staining intensity of the cell bodies when cresyl violet at a pH of 4.5–5 was used in combination with Luxol fast blue, and it is possible that the pH of the cresyl violet solution may have affected staining intensity, and possibly, neuronal cell body size. Our study showed that bigger cells within a dense layer are more likely to be underestimated when quantified with the cresyl violet staining method. This can be explained by the cellular overlap at high density making the estimation of the cell size unreliable. In contrast, Golgi-stained cells are easily distinguished from their background (unstained neighboring cells).

Acknowledgments

This work was supported by GlaxoSmithkline, Medisearch, and the Wellcome Trust.

The authors thank Ian Forsythe and Margaret Barnes Davies for comments on the manuscript, Tim Ecclestone from Nikon Instruments for technical advice, and Mike Mulheran for advice on power analysis.

Literature Cited

- Adams JC (1979) A fast, reliable silver-chromate Golgi method for perfusion-fixed tissue. *Stain Technol* 54:225–226
- Alibardi L (2003) Ultrastructural distribution of glycinergic and GABAergic neurons and axon terminals in the rat dorsal cochlear nucleus, with emphasis on granule cell areas. *J Anat* 203:31–56
- Alibardi L (2006) Review: cytological characteristics of commissural and tuberculo-ventral neurons in the rat dorsal cochlear nucleus. *Hear Res* 216–217:73–80
- Angulo A, Fernandez E, Merchan JA, Molina M (1996) A reliable method for Golgi staining of retina and brain slices. *J Neurosci Methods* 66:55–59
- Angulo A, Merchan JA, Molina M (1994) Golgi-Colonnier method: correlation of the degree of chromium reduction and pH change with quality of staining. *J Histochem Cytochem* 42:393–403
- Blackstad TW, Osen KK, Mugnaini E (1984) Pyramidal neurones of the dorsal cochlear nucleus: a Golgi and computer reconstruction study in cat. *Neuroscience* 13:827–854
- Brawer JR, Morest DK, Kane EC (1974) The neuronal architecture of the cochlear nucleus of the cat. *J Comp Neurol* 155:251–300
- Browner RH, Baruch A (1982) The cytoarchitecture of the dorsal cochlear nucleus in the 3-month- and 26-month-old C57BL/6 mouse: a Golgi impregnation study. *J Comp Neurol* 211:115–138
- Colonnier M (1964) The tangential organization of the visual cortex. *J Anat* 98:327–344
- Donga R, Lund JP (1991) Discharge patterns of trigeminal commissural last-order interneurons during fictive mastication in the rabbit. *J Neurophysiol* 66:1564–1578
- Friedland DR, Los JG, Ryugo DK (2006) A modified Golgi staining protocol for use in the human brain stem and cerebellum. *J Neurosci Methods* 150:90–95
- Geisler S, Heilmann H, Veh RW (2002) An optimized method for simultaneous demonstration of neurons and myelinated fiber tracts for delineation of individual trunco- and palliothalamic nuclei in the mammalian brain. *Histochem Cell Biol* 117:69–79
- Gittins R, Harrison PJ (2004) Neuronal density, size and shape in the human anterior cingulate cortex: a comparison of Nissl and NeuN staining. *Brain Res Bull* 63:155–160

- Grandin T, Demotte OD, Greenough WT, Curtis SE (1988) Perfusion method for preparing pig brain cortex for Golgi-Cox impregnation. *Stain Technol* 63:177-181
- Grinevich V, Brecht M, Osten P (2005) Monosynaptic pathway from rat vibrissa motor cortex to facial motor neurons revealed by lentivirus-based axonal tracing. *J Neurosci* 25:8250-8258
- Hackney CM, Osen KK, Kolston J (1990) Anatomy of the cochlear nuclear complex of guinea pig. *Anat Embryol (Berl)* 182:123-149
- Hani SA, Al-Haidari MH, Saboba MM (2007) Neuronal types in the human anterior ventral thalamic nucleus: a Golgi study. *Cell Mol Neurobiol* 27:745-755
- King MA, Scotty N, Klein RL, Meyer EM (2002) Particle detection, number estimation, and feature measurement in gene transfer studies: optical fractionator stereology integrated with digital image processing and analysis. *Methods* 28:293-299
- Kopsch F (1896) Erfahrungen über die Verwendung des Formaldehyds bei der Chromsilber-Imprägnation. *Anat Anz* 11:727-729
- Marani E, Guldemond JM, Adriolo PJ, Boon ME, Kok LP (1987) The microwave Rio-Hortega technique: a 24 hour method. *Histochem J* 19:658-664
- Maruyama A, Ohmori H (2006) Fluorescent labeling of rat auditory brainstem circuits for synaptic and electrophysiological studies. *J Neurosci Methods* 152:163-172
- McDonagh JC, Hornby TG, Reinking RM, Stuart DG (2002) Associations between the morphology and physiology of ventral-horn neurons in the adult turtle. *J Comp Neurol* 454:177-191
- Mendizabal-Zubiaga JL, Reblet C, Bueno-Lopez JL (2007) The underside of the cerebral cortex: layer V/VI spiny inverted neurons. *J Anat* 211:223-236
- Morest DK, Morest RR (1966) Perfusion-fixation of the brain with *chromium-osmium* solutions for the rapid Golgi method. *Am J Anat* 1118:811-831
- Mugnaini E (1985) GABA neurons in the superficial layers of the rat dorsal cochlear nucleus: light and electron microscopic immunocytochemistry. *J Comp Neurol* 235:61-81
- Mugnaini E, Osen KK, Dahl AL, Friedrich VL Jr, Korte G (1980a) Fine structure of granule cells and related interneurons (termed Golgi cells) in the cochlear nuclear complex of cat, rat and mouse. *J Neurocytol* 9:537-570
- Mugnaini E, Warr WB, Osen KK (1980b) Distribution and light microscopic features of granule cells in the cochlear nuclei of cat, rat, and mouse. *J Comp Neurol* 191:581-606
- Oertel D, Wu SH (1989) Morphology and physiology of cells in slice preparations of the dorsal cochlear nucleus of mice. *J Comp Neurol* 283:228-247
- Oertel D, Wu SH, Garb MW, Dizack C (1990) Morphology and physiology of cells in slice preparations of the posteroventral cochlear nucleus of mice. *J Comp Neurol* 295:136-154
- Osen KK (1969) Cytoarchitecture of the cochlear nuclei in the cat. *J Comp Neurol* 136:453-484
- Palay SL, Chan-Palay V (1974) *Cerebellar Cortex. Cytology and Organization*. New York, Springer
- Pasternak JF, Woolsey TA (1975) On the "selectivity" of the Golgi-Cox method. *J Comp Neurol* 160:307-312
- Paxinos G, Watson C (1998) *The Rat Brain in Stereotaxic Coordinates*. 2nd ed. San Diego, Academic Press
- Saada AA, Niparko JK, Ryugo DK (1996) Morphological changes in the cochlear nucleus of congenitally deaf white cats. *Brain Res* 736:315-328
- Seldon HL, Clark GM (1991) Human cochlear nucleus: comparison of Nissl-stained neurons from deaf and hearing patients. *Brain Res* 551:185-194
- Skoglund TS, Pascher R, Berthold CH (1996) Aspects of quantitative analysis of neurons in the cerebral cortex. *J Neurosci Methods* 70:201-210
- Uno A, Idoux E, Beranek M, Vidal PP, Moore LE, Wilson VJ, Vibert N (2003) Static and dynamic membrane properties of lateral vestibular nucleus neurons in guinea pig brain stem slices. *J Neurophysiol* 90:1689-1703
- Van der Loos H (1956) Une combinaison de deux vieilles méthodes histologiques pour le système nerveux central. *Monatsschr Psychiatr Neurol* 132:330-334
- Webster DB, Trune DR (1982) Cochlear nuclear complex of mice. *Am J Anat* 163:103-130
- Werner L, Brauer K (1984) Neuron types in the rat dorsal lateral geniculate nucleus identified in Nissl and deimpregnated Golgi preparations. *J Hirnforsch* 25:121-127
- Werner L, Hedlich A, Koglin A (1986) Classification of neurons in the visual cortex of the guinea pig (*Cavia porcellus*). A combined Golgi-Nissl study using deimpregnation technics. *J Hirnforsch* 27:213-236
- Werner L, Winkelmann E, Koglin A, Nesper J, Rodewohl H (1989) A Golgi deimpregnation study of neurons in the rhesus monkey visual cortex (areas 17 and 18). *Anat Embryol (Berl)* 180:583-597
- Wouterlood FG, Mugnaini E (1984) Cartwheel neurons of the dorsal cochlear nucleus: a Golgi-electron microscopic study in rat. *J Comp Neurol* 227:136-157
- Zhang H, Weng SJ, Hutsler JJ (2003) Does microwaving enhance the Golgi methods? A quantitative analysis of disparate staining patterns in the cerebral cortex. *J Neurosci Methods* 124:145-155
- Zhang S, Oertel D (1993) Giant cells of the dorsal cochlear nucleus of mice: intracellular recording in slices. *J Neurophysiol* 69:1398-1408
- Zwaagstra B, Kernell D (1981) Sizes of soma and stem dendrites in intracellularly labelled α -motoneurons of the cat. *Brain Res* 204:295-309

REFERENCES

- Abeles M., Bergman H., Margalit E., Vaadia E. (1993). Spatiotemporal firing patterns in the frontal cortex of behaving monkeys. *J Neurophysiol.*, 70: 1629-1638
- Abbott S.D., Hughes L.F., Bauer C.A., Salvi R., Caspary D.M. (1999). Detection of glutamate decarboxylase isoforms in rat inferior colliculus following acoustic exposure. *Neurosci.*; 93: 1375-1381
- Abrahams V.C., Richmond F.J., Keane J. (1984). Projections from C2 and C3 nerves supplying muscles and skin of the cat neck: a study using transganglionic transport of horseradish peroxidase. *J Comp Neurol.*; 230: 142-154
- Adams J.C. (1979a). Ascending projections to the inferior colliculus. *J Comp Neurol.*; 183: 519-538
- Adams J.C. (1979b). A fast, reliable silver-chromate Golgi method for perfusionfixed tissue. *Stain Technol.*; 54: 225-226
- Adams J.C. (1983). Multipolar cells in the ventral cochlear nucleus project to the dorsal cochlear nucleus and the inferior colliculus. *Neurosci Let.*; 37: 205-208
- Adams J.C., Mugnaini E. (1990). Immunocytochemical evidence for inhibitory and disinhibitory circuits in the superior olive. *Hear. Res.*; 49: 281-298
- Adams J.C., Warr W.B. (1976). Origins of axons in the cat's acoustic striae determined by injection of horseradish peroxidase into severed tracts. *Comp. Neurol.*; 170: 107-112
- Aghajanian G.K., Rasmussen K. (1989). Intracellular studies in the facial nucleus illustrating a simple new method for obtaining viable motoneurons in adult rat brain slices. *Synapse*; 3: 331-338
- Aitkin L.M., Boyd J. (1975). Responses of single units in cerebellar vermis of the cat to monaural and binaural stimuli. *J Neurophysiol.*; 38: 418-429
- Aizenman C.D., Akerman C.J., Jensen K.R., Cline H.T. (2003). Visually driven regulation of intrinsic neuronal excitability improves stimulus detection in vivo. *Neuron*; 39: 831-842

- Akaishi T., Nakazawa K., Sato K., Saito H., Ohno Y., Ito Y. (2004). Hydrogen peroxide modulates whole cell currents through L-type channels in cultured rat dentate granule cells. *Neurosci Lett.*; 356: 25-28
- Akhoun I., Gallego S., Moulin A., Menard M., Veuillet E., Berger-Vachon C., Collet L., Thai-Van H. (2008). The temporal relationship between speech auditory brainstem responses and the acoustic pattern of the phoneme /ba/ in normal-hearing adults. *Clin. Neurophysiol.*; 119: 922-933
- Akhtar, N.D., Land, P.W. (1991). Activity-dependent regulation of glutamic acid decarboxylase in the rat barrel cortex: effects of neonatal versus adult sensory deprivation. *J. Comp. Neurol.*; 307: 200-213
- Alagramam K.N., Murcia C.L., Kwon H.Y., Pawlowski K.S., Wright C.G., Woychik R.P. (2001). The mouse Ames waltzer hearing-loss mutant is caused by mutation of *Pcdh15*, a novel protocadherin gene. *Nat. Genet.*; 27: 99-102
- Alibardi L. (2004). Mossy fibers in granule cell areas of the rat dorsal cochlear nucleus from intrinsic and extrinsic origin innervate unipolar brush cell glomeruli. *J. Submicrosc. Cytol. Pathol.*; 36: 193-210
- Alibardi L. (2006). Review: cytological characteristics of commissural and tuberculo-ventral neurons in the rat dorsal cochlear nucleus. *Hear. Res.*; 216-217: 73-80
- Allen G.I., Tsukahara N. (1974). Cerebrocerebellar communication systems. *Physiol. Rev.*; 54: 957-1006
- Aller M.I., Veale E.L., Linden A.M., Sandu C., Schwaninger M., Evans L.J., Korpi E.R., Mathie A., Wisden W., Brickley S.G. (2005). Modifying the subunit composition of TASK channels alters the modulation of a leak conductance in cerebellar granule neurons. *J Neurosci.*; 25: 11455-11467
- Anderson L.A., Malmierca M.S., Wallace M.N., Palmer A.R. (2006). Evidence for a direct, short latency projection from the dorsal cochlear nucleus to the auditory thalamus in the guinea pig. *Eur J Neurosci.*; 24: 491-498
- Andersen R. A., Roth G. L., Aitkin L. M., Merzenich M. M. (1980). The efferent projections of the central nucleus and the pericentral nucleus of the inferior colliculus in the cat. *J. Comp. Neurol.*; 194: 649-662

Angulo A., Fernandez E., Merchan J.A., Molina M. (1996). A reliable method for Golgi staining of retina and brain slices. *J. Neurosci. Methods*; 66: 55-59

Arda H.N., Tuncel U., Akdogan U. and Ozluoglu L.N. (2003). The role of zinc in the treatment of tinnitus. *Otol Neurotol.*; 24: 86-89

Arnold T., Oestreicher E., Ehrenberger K., Felix D. (1998). GABA (A) receptor modulates the activity of inner hair cell afferents in guinea pig cochlea. *Hear. Res.*; 125: 147-153

Arras M., Autenried P., Rettich A., Spaeni D., Rulicke T. (2001). Optimization of intraperitoneal injection anesthesia in mice: drugs, dosages, adverse effects and anesthesia depth. *Comp. Med.*; 51: 443-456

Ashmore J. F. (1987). A fast motile response in guinea-pig outer hair cells: the cellular basis of the cochlear amplifier. *J. Physiol. (Lond.)*; 388: 323-347

Augustine G.J. (2001). How does calcium trigger neurotransmitter release? *Curr. Opin. Neurobiol.*; 11: 320-326

Augustine G.J., Neher E. (1992). Neuronal $[Ca^{2+}]$ signaling takes the local route. *Curr Opin Neurobiol.*; 2: 302-307

Augustine G. Santamaria F. Tanaka K. (2003). Local Calcium Signaling in Neurons. *Neuron*; 40: 331-346

Awatramani G.B., Turecek R., Trussell L.O. (2005). Staggered development of GABAergic and glycinergic transmission in the MNTB. *J Neurophysiol.*; 93: 819-828

Axelsson A., Sandh A. (1985). Tinnitus in noise-induced hearing loss. *Br. J. Audiol.*; 19: 271-276

Azizi S.A., Burne R.A., Woodward D.J. (1985). The auditory corticopontocerebellar projection in the rat: inputs to the paraflocculus and midvermis. An anatomical and physiological study. *Exp. Brain Res.*; 59: 36-49

Azouz R., Gray C.M. (2000). Dynamic spike threshold reveals a mechanism for synaptic coincidence detection in cortical neurons in vivo. *Proc. Natl. Acad. Sci. USA*; 97: 8110-8115

- Babalian A.L. (2005). Synaptic influences of Pontine nuclei on cochlear nucleus cells. *Exp. Brain Res.*; 167: 451-457
- Baguley D.M., Humphriss R.L., Axon P.R., Moffat D.A. (2006). The clinical characteristics of tinnitus in patients with vestibular schwannoma. *Skull Base*; 16: 49-58
- Bahmad F.M. Jr, Venosa A.R., Oliveira C.A. (2006). Benzodiazepines and GABAergic in treating severe disabling tinnitus of predominantly cochlear origin. *Int Tinnitus J.*; 12: 140-144
- Bailey G.P., Sewell W.F. (2000). Calcitonin gene-related peptide suppresses hair cell responses to mechanical stimulation in the *Xenopus* lateral line organ. *J. Neurosci.*; 20: 5163-5169
- Balakrishnan V., Trussell L.O. (2008). Synaptic inputs to granule cells of the dorsal cochlear nucleus. *J. Neurophysiol.*; 99: 208-219
- Banks G.B., Kanjhan R., Wiese S., Kneussel M., Wong L.M., O'Sullivan G., Sendtner M., Bellingham M.C., Betz H., Noakes P.G. (2005). Glycinergic and GABAergic synaptic activity differentially regulate motoneuron survival and skeletal muscle innervation, *J. Neurosci.*; 25: 1249-1259
- Barmack N.H., Guo H., Kim H.J., Qian H., Qian Z. (1999). Neuronally modulated transcription of a glycine transporter in rat dorsal cochlear nucleus and nucleus of the medial trapezoid body. *J. Comp. Neurol.*; 415: 175-188
- Barnes-Davies M., Forsythe I.D. (1995). Pre- and postsynaptic glutamate receptors at a giant excitatory synapse in the rat auditory brain stem. *J. Physiol. (Lond.)*; 488: 387-406
- Barry P.H. (1994). JPCalc, a software package for calculating liquid junction potential corrections in patch-clamp, intracellular, epithelial and bilayer measurements and for correcting junction potential measurements. *J. Neurosci. Methods.*; 51: 107-116
- Barry P.H., Lynch J.W. (1991). Liquid junction potentials and small cell effects in patch-clamp analysis. *J. Membr. Biol.*; 121: 101-117. Review
- Basta D., Ernest A. (2004). Noise-induced changes of neuronal spontaneous activity in mice inferior colliculus brain slices. *Neurosci. Lett.*; 368: 297-302

- Bauer C.A., Brozoski T.J. (2006). Effect of gabapentin on the sensation and impact of tinnitus. *Laryngoscope*; 116: 675-681
- Bauer C.A., Turner J.G., Caspary D.M., Myers K.S., Brozoski T.J. (2008). Tinnitus and inferior colliculus activity in chinchillas related to three distinct patterns of cochlear trauma. *J Neurosci. Res.*; 86: 2564-2578
- Beckius G.E., Batra R., Oliver D.L. (1999). Axons from anteroventral cochlear nucleus that terminate in medial superior olive of cat: observations related to delay lines. *J Neurosci.*; 19: 3146 -3161
- Belin P., Zatorre R.J., Lafaille P., Ahad P., Pike B. (2000). Voice-selective areas in human auditory cortex. *Nature*; 403: 309-312
- Bell C., Bodznick D., Montgomery J., Bastian J. (1997). The generation and subtraction of sensory expectations within cerebellum-like structures. *Brain Behav. Evol.*; 50 Suppl.; 1: 17- 31
- Bender K.J., Trussell L.O. (2009). Axon initial segment Ca^{2+} channels influence action potential generation and timing. *Neuron*; 61: 259-271
- Benson T.E., Brown M.C. (2004). Postsynaptic targets of type II auditory nerve fibers in the cochlear nucleus. *J. Assoc. Res. Otolaryngol.*; 5: 111-125
- Bergles D.E., Diamond J.S., Jahr, C.E. (1999). Clearance of glutamate inside the synapse and beyond. *Curr. Opin. Neurobiol.*; 9: 293-298
- Berglund A.M., Benson T.E., Brown M.C. (1996). Synapses from labelled type II axons in the mouse cochlear nucleus. *Hear. Res.*; 94: 31-46
- Berglund A.M., Brown M.C. (1994). Central trajectories of type II spiral ganglion cells from various cochlear regions in mice. *Hear. Res.*; 75: 121-130
- Berglund A.M., Ryugo D.K. (1987). Hair cell innervation by spiral ganglion neurons in the mouse. *J. Comp. Neurol.*; 255: 560-570
- Berkley K.J., Blomqvist A, Pelt A, Flink R. (1980). Differences in the collateralization of neuronal projections from the dorsal column nuclei and lateral cervical nucleus to the thalamus and tectum in the cat: an anatomical study using two different double-labeling techniques. *Brain Res.*; 202: 273-290

- Berntson A.K., Walmsley B. (2008). Characterization of a potassium-based leak conductance in the medial nucleus of the trapezoid body. *Hear. Res.*; 244: 98-106
- Berrebi A.S., Mugnaini E. (1988). Effects of the murine mutation 'nervous' on neurons in cerebellum and dorsal cochlear nucleus *J. Neurocytol.*; 17: 465-484
- Berrebi A.S., Mugnaini E. (1991). Distribution and targets of the cartwheel cell axon in the dorsal cochlear nucleus of the guinea pig. *Anat. Embryol. (Berl)*; 183: 427-454
- Berry M.J., Warland D.K., Meister M. (1997). The structure and precision of retinal spike trains. *Proc. Natl. Acad. Sci. USA*; 94: 5411-5416
- Berthie B, Axelrad H. (1994). Granular layer collaterals of the unipolar brush cell axon display rosette-like excrescences. A Golgi study in the rat cerebellar cortex. *Neurosci. Lett.*; 167: 161-165
- Bi G., Poo M. (2001). Synaptic modification by correlated activity: Hebb's postulate revisited. *Annu. Rev. Neurosci.*; 24: 139-166
- Bitner-Glindzicz, M. Lindley K.J., Rutland P., Blaydon D., Smith V.V., Milla P.J., Hussain K., Furth-Lavi J., Cosgrove K.E., Shepherd R.M., Barnes P.D., O'Brien R.E., Farndon P.A., Sowden J., Liu X.Z., Scanlan M.J., Malcolm S., Dunne M.J., Aynsley-Green A., Glaser B. (2000). A recessive contiguous gene deletion causing infantile hyperinsulinism, enteropathy and deafness identifies the Usher type 1C gene. *Nat. Genet.*; 26: 56-60
- Blackstad T. W., Osen K. K., Mugnaini E. (1984). Pyramidal neurones of the dorsal cochlear nucleus: a Golgi and computer reconstruction study in cat. *Neurosci.*; 13: 827-854
- Błaszczak J.W., Tajchert K. (1997). Effect of acoustic stimulus characteristics on the startle response in hooded rats. *Acta. Neurobiol. Exp. (Wars)*; 57: 315-321
- Blatchley B.J., Cooper W.A., Coleman J.R. (1987). Development of auditory brainstem response to tone pip stimuli in the rat. *Brain Res.*; 429: 75-84
- Boeda B., El-Amraoui A., Bahloul A., Goodyear R., Daviet L., Blanchard S., Perfettini I., Fath K.R., Shorte S., Reiners J., Houdusse A., Legrain P., Wolfrum

- U., Richardson G., Petit C. (2002). Myosin VIIa, harmonin and cadherin 23, three Usher I gene products that cooperate to shape the sensory hair bundle. *EMBO J.*; 21: 6689-6699
- Bolz. von Brederlow B., Ramírez A., Bryda E.C., Kutsche K., Nothwang H.G., Seeliger M., del C-Salcedó Cabrera M., Vila M.C., Molina O.P., Gal A., Kubisch C. (2001). Mutation of CDH23, encoding a new member of the cadherin gene family, causes Usher syndrome type 1D. *Nat. Genet.*; 27: 108-112
- Bork, J.M. Peters L.M., Riazuddin S., Bernstein S.L., Ahmed Z.M., Ness S.L., Polomeno R., Ramesh A., Schloss M., Srisailpathy CR, Wayne S., Bellman S., Desmukh D., Ahmed Z., Khan S.N., Kaloustian V.M., Li X.C., Lalwani A., Riazuddin S., Bitner-Glindzicz M., Nance WE, Liu XZ, Wistow G., Smith R.J., Griffith A.J., Wilcox E.R., Friedman TB, Morell RJ. (2001). Usher syndrome 1D and nonsyndromic autosomal recessive deafness DFNB12 are caused by allelic mutations of the novel cadherin-like gene CDH23. *Am. J. Hum. Genet.*; 68: 26-37
- Bostock H., Sears, T.A. Sherratt, R.M. (1983). The spatial distribution of excitability and membrane current in normal and demyelinated mammalian nerve fibres. *J. Physiol. (Lond.)*; 341: 41-58
- Boudreau J.C., Tsuchitani C. (1970). Cat superior olive S-segment cell discharge to tonal stimulation. In: *Contributions to Sensory Physiology*, edited by W. D. Neff. New York: Academic, 1970, vol. IV; 143-213
- Boudreau J.C., Tsuchitani C. (1973). *Sensory Neurophysiology with special reference to the cat*. Van Nostrand Reinhold, New York
- Brand A., Behrend O., Marquardt T., McAlpine D., Grothe B. (2002). Precise inhibition is essential for microsecond interaural time difference coding. *Nature*; 417: 543–547
- Brawer J.R., Morest D.K., Kane E.C. (1974). The neuronal architecture of the cochlear nucleus of the cat. *J. Comp. Neurol.*; 155: 251-300
- Brickley S.G. (2005). Modifying the subunit composition of TASK channels alters the modulation of a leak conductance in cerebellar granule neurons and is associated with impaired motor performance. *J Neurosci.*; 25: 11455–11467

- Brickley S. G., Cull-Candy S. G., Farrant M. (1996). Development of a tonic form of synaptic inhibition in rat cerebellar granule cells resulting from persistent activation of GABA_A receptors. *J. Physiol. (Lond.)*; 497: 753-759
- Brickley, S.G., Revilla, V., Cull-Candy, S.G., Wisden, W., Farrant, M. (2001). Adaptive regulation of neuronal excitability by a voltage-independent potassium conductance. *Nature* 409: 88-92
- Brodal P., Bjaalie J.G. (1992). Organization of the pontine nuclei. *Neurosci Res.*; 13: 83–118
- Brown M.C. (1987). Morphology of labeled afferent fibers in the guinea pig cochlea. *J. Comp. Neurol.*; 260: 591-604
- Brown M.C., Berglund A.M., Kiang N.Y., Ryugo D.K. (1988). Central trajectories of type II spiral ganglion neurons. *J. Comp. Neurol.*; 278: 581–590
- Brown M.C., Ledwith J.V. 3rd. (1990). Projections of thin (type-II) and thick (type-I) auditory-nerve fibers into the cochlear nucleus of the mouse. *Hear. Res.*; 49: 105–118
- Brownell W. E., Bader C. R., Bertrand D. de Ribaupierre Y. (1985). Evoked mechanical responses of isolated cochlear outer hair cells. *Science*; 227: 194-196
- Browner R.H., Baruch A. (1982). The cytoarchitecture of the dorsal cochlear nucleus in the 3-month- and 26-month-old C57BL/6 mouse: a Golgi impregnation study. *J. Comp. Neurol.*; 211:115-138
- Brozoski, T.J., Bauer, C.A., Caspary, D.M. (2002). Elevated fusiform cell activity in the dorsal cochlear nucleus of chinchillas with psychophysical evidence of tinnitus. *J. Neurosci.*; 22: 2383-2390
- Brozoski T.J., Spires T.J., Bauer C.A. (2007). Vigabatrin, a GABA transaminase inhibitor, reversibly eliminates tinnitus in an animal model. *J. Assoc. Res. Otolaryngol.*; 8: 105-118
- Brugge J.F., Anderson D.J., Aitkin L.M. (1970). Responses of neurons in the dorsal nucleus of the lateral lemniscus of cat to binaural tonal stimulation. *J Neurophysiol.*; 33: 441–458

- Bucurenciu I., Kulik A., Schwaller B., Frotscher M., Jonas P. (2008). Nanodomain coupling between Ca^{2+} channels and Ca^{2+} sensors promotes fast and efficient transmitter release at a cortical GABAergic synapse. *Neuron*; 57: 536-545
- Bukowska D. (2002). Morphological evidence for secondary vestibular afferent connections to the dorsal cochlear nucleus in the rabbit. *Cells Tissues Organs*; 170: 61–68
- Buonomano D.V. (2003). Timing of neural responses in cortical organotypic slices. *Proc. Natl. Acad. Sci. USA*; 100: 4897-4902
- Burian M., Gstoettner W. (1988). Projection of primary vestibular afferent fibres to the cochlear nucleus in the guinea pig. *Neurosci. Lett.*; 84: 13-17
- Bushara K.O., Grafman J., Hallett M. (2001) Neural correlates of auditory-visual stimulus onset asynchrony detection. *J. Neurosci.*; 21: 300-304
- Buzsáki G., Csicsvari J., Dragoi G., Harris K., Henze D., Hirase H. (2002) Homeostatic maintenance of neuronal excitability by burst discharges in vivo. *Cereb. Cortex*; 12: 893-839
- Cacace A.T. (2003). Expanding the biological basis of tinnitus: crossmodal origins and the role of neuroplasticity. *Hear. Res.*; 175: 112-132
- Cadetti L., Tranchina D., Thoreson W.B. (2005). A comparison of release kinetics and glutamate receptor properties in shaping rod-cone differences in EPSC kinetics in the salamander retina. *J. Physiol. (Lond.)*; 569: 773-788
- Caicedo A., d'Aldin C., Puel J.L., Eybalin M. (1996). Distribution of calcium-binding protein immunoreactivities in the guinea pig auditory brainstem. *Anat. Embryol. (Berl.)*; 194: 465-487
- Caicedo A., Herbert H. (1993). Topography of descending projections from the inferior colliculus to auditory brainstem nuclei in the rat. *J. Comp. Neurol.*; 328: 377-392
- Cajal R.S. (1888). Estructura de los centros nerviosos de las aves. *Rev. Trimestr. Histol.*; 1: 1-10

Cajal R.S. (1909). *Histologie du Systeme Nerveux de l'homme et des Verte'bre's*. Madrid: Instituto Ramo'n y Cajal.

Cajal R.S., De Castro O F. (1933). *Elementos de tecnica micrografika del sistema nervioso*. Madrid, Tipografia Artistica. 2nd ed. Barcelona, Salvat Editores SA, 1972

Calford M.B. (1983). The parcellation of the medial geniculate body of the cat defined by the auditory response properties of single units. *J. Neurosci.* 3: 2350-2364

Campos M.L., de Cabo C., Wisden W., Juiz J.M., Merlo D. (2001). Expression of GABA(A) receptor subunits in rat brainstem auditory pathways: cochlear nuclei, superior olivary complex and nucleus of the lateral lemniscus. *Neuroscience*; 102: 625-638

Cant N.B., Benson C.G. (2003). Parallel auditory pathways: projection patterns of the different neuronal populations in the dorsal and ventral cochlear nuclei. *Brain Res. Bull.*; 60: 457-474

Cant N.B., Gaston K.C. (1982). Pathways connecting the right and left cochlear nuclei. *J. Comp. Neurol.*; 212: 313-326

Cardin J.A., Palmer L.A., Contreras D. (2008) Cellular mechanisms underlying stimulus-dependent gain modulation in primary visual cortex neurons in vivo. *Neuron*; 59: 150-160

Caspary D.M., Hughes L.F., Schatteman T.A., Turner J.G. (2006). Age-related changes in the response properties of cartwheel cells in rat dorsal cochlear nucleus. *Hear. Res.*; 216: 207-217

Caspary D.M., Ling L., Turner J.G., Hughes L.F. (2008). Inhibitory neurotransmission, plasticity and aging in the mammalian central auditory system. *J. Exp. Biol.*; 211: 1781-1791

Caspary D.M., Pazara K.E., Kossel M., Faingold C.L. (1987). Strychnine alters the fusiform cell output from the dorsal cochlear nucleus. *Brain. Res.*; 417: 273-282

- Cazals Y., Aran J.M., Erre J.P., Guilhaume A., Aurousseau C. (1983). Vestibular acoustic reception in the guinea pig: a saccular function? *Acta Otolaryngol.*; 95: 211-217
- Chan S.W., Reade, P.C. (1994). Tinnitus and temporomandibular pain-dysfunction disorder. *Clin. Otolaryngol.*; 19: 370-380
- Chan-Palay V., Palay S.L. (1972). The stellate cells of the rat's cerebellar cortex. *Z. Anat. Entwicklungsgesch.*; 136: 224-248
- Chance F.S., Abbott L.F., Reyes A.D. (2002). Gain modulation from background synaptic input. *Neuron*; 35: 773-782
- Chang H., Chen K., Kaltenbach J.A., Zhang J., Godfrey D.A. (2002). Effects of acoustic trauma on dorsal cochlear nucleus neuron activity in slices. *Hear. Res.*; 164: 59-68
- Chapman, E.R. (2002). Synaptotagmin: a Ca^{2+} sensor that triggers exocytosis? *Nat. Rev. Mol. Cell Biol.*; 3: 498-508
- Chechik G. (2003). Spike-timing-dependent plasticity and relevant mutual information maximization. *Neural Comput.*; 15: 1481-1510
- Chen G., Jastreboff P.J. (1995). Salicylate-induced abnormal activity in the inferior colliculus of rats. *Hear. Res.*; 82: 158-78
- Chen L., Kelly J.B., Wu S.H. (1999). The commissure of Probst as a source of GABAergic inhibition. *Hear. Res.*; 138: 106-114
- Chen K., Waller H.J., Godfrey D.A. (1998) Effects of endogenous acetylcholine on spontaneous activity in rat dorsal cochlear nucleus slices. *Brain Res.* (2):219-226
- Chiu C.S., Brickley S., Jensen K., Southwell A., McKinney S., Cull-Candy S., Mody I., Lester H.A. (2005). GABA transporter deficiency causes tremor, ataxia, nervousness, and increased GABA-induced tonic conductance in cerebellum. *J. Neurosci.*; 25: 3234 -3245
- Church M.W., Kaltenbach J.A. (1993). The hamster's auditory brain stem response as a function of stimulus intensity, tone burst frequency, and hearing loss. *Ear Hear.*; 14: 249-257

- Church M.W., Jen K.L., Stafferton T., Hotra J.W., Adams B.R. (2007). Reduced auditory acuity in rat pups from excess and deficient omega-3 fatty acid consumption by the mother. *Neurotoxicol. Teratol.*; 29: 203-210
- Church M.W., Williams H.L., Holloway J.A. (1984). Postnatal development of the brainstem auditory evoked potential and far-field cochlear microphonic in non-sedated rat pups, *Brain Res.*; 316: 23-31
- Clem R.L., Celikel T., Barth A.L. (2008). Ongoing in vivo experience triggers synaptic metaplasticity in the neocortex. *Science*; 319: 101-104
- Conquet F., Bashir Z.I., Davies C.H., Daniel H., Ferraguti F., Bordi F., Franz-Bacon K., Reggiani A., Matarese V., Conde F., et al. (1994). Motor deficit and impairment of synaptic plasticity in mice lacking mGluR1. *Nature*; 372: 237-243
- Cohen E. S., Brawer J. R., Morest D. K. (1972). Projections of the cochlea to the dorsal cochlear nucleus of the cat. *Exp. Neurol.*; 35: 470-479
- Colonnier M. (1964). The tangential organization of the visual cortex. *J. Anat.*; 98: 327-344
- Commissaris R.L., Palmer A., Neophytou S., Graham M., Beckett S., Marsden C.A. (2000). Acoustically elicited behaviours in Lister hooded and Wistar rats. *Physiol. Behav.*; 68: 521-531
- Conlee J.W., Parks T.N., Romero C., Creel D.J. (1984). Auditory brainstem anomalies in albino cats: II: Neuronal atrophy in the superior olive. *J. Comp. Neurol.*; 225: 141-148
- Corey D.P., Hudspeth A.J., (1979). Response latency of vertebrate hair cells, *Biophys. J.*; 26: 499–506
- Corey D.P., Hudspeth A.J. (1983). Kinetics of the receptor current in bullfrog saccular hair cells, *J. Neurosci.*; 3: 962-976
- Couve E., Cabello J.F., Krsulovic J., Roncagliolo M. (1997). Binding of microtubules to transitional elements in oligodendrocytes of the myelin mutant taiep rat. *J. Neurosci. Res.*; 47: 573-581

- Cransac H., Cottet-Emard J.M., Hellstroëm S., Peyrin L. (1998). Specific sound-induced noradrenergic and serotonergic activation in central auditory structures. *Hear. Res.*; 118: 151-156
- Creel, D., Garber S.R., King R.A., Witkop C.J. (1980). Auditory brainstem anomalies in human albinos. *Science*; 209: 1253-1255
- Cunningham J., Nicol T., Zecker S.G., Bradlow A., Kraus N. (2001). Neurobiologic responses to speech in noise in children with learning problems: deficits and strategies for improvement. *Clin. Neurophysiol.*; 112: 758–767
- Dallos P. (1973). *The auditory periphery*. New York: Academic Press
- Dallos P., Evans B.N., Hallworth R. (1991). Nature of the motor element in electrokinetic shape changes of cochlear outer hair cells. *Nature*; 350: 155-157
- Dallos P., Harris D. (1978). Properties of auditory nerve responses in absence of outer hair cells. *J. Neurophysiol.*; 41: 365-383
- Dan Y., Poo M.M. (2006). Spike timing-dependent plasticity: from synapse to perception. *Physiol. Rev.*; 86: 1033-1048
- D'Angelo E., De Filippi G., Rossi P., Taglietti V. (1998). Ionic mechanism of electroresponsiveness in cerebellar granule cells implicates the action of a persistent sodium current. *J. Neurophysiol.*; 80: 493-503
- D'Angelo E., De Filippi G., Rossi P., Taglietti V. (1995) Synaptic excitation of individual rat cerebellar granule cells in situ: evidence for the role of NMDA receptors. *J. Physiol. (Lond.)*; 482: 397-413
- Darrat I., Ahmad N., Seidman K., Seidman M.D. (2007). Auditory research involving antioxidants. *Curr. Opin. Otolaryngol. Head Neck Surg.*; 15: 358-363
- Darrow K.N., Maison S.F., Liberman MC. (2007). Selective removal of lateral olivocochlear efferents increases vulnerability to acute acoustic injury. *J. Neurophysiol.*; 97: 1775-1785
- Duan M., Chen Z., Qiu J., Ulfendahl M., Laurell G., Borg E., Ruan R. (2006). Low-dose, long-term caroverine administration attenuates impulse noise-induced hearing loss in the rat. *Acta Otolaryngol.* , 126: 1140-1147

- Davies E., Knox E., Donaldson I. (1994). The usefulness of nimodipine, an L-calcium channel antagonist, in the treatment of tinnitus. *Br. J. Audiol.*; 28: 125-129
- Davis, H. (1983). An active process in cochlear mechanics. *Hear. Res.*; 9: 79-90
- Davis K.A. (1999). Effects of somatosensory stimulation on neurons in the inferior colliculus. *Assoc. Res. Otolaryngol. Abstr.*; 22: 215-216
- Davis G.W., Bezprozvanny I. (2001). Maintaining the stability of neural function: a homeostatic hypothesis. *Annu. Rev. Physiol.*; 63: 847-69. Review.
- Davis K.A., Ding J., Benson T.E., Voigt H.F. (1996b). Response properties of units in the dorsal cochlear nucleus of unanesthetized decerebrate gerbils. *J. Neurophysiol.*; 75: 1411-1431
- Davis K.A., Miller R.L., Young E.D. (1996a). Effects of somatosensory and parallel-fiber stimulation on neurons in dorsal cochlear nucleus. *J. Neurophysiol.*; 76: 3012-3024
- Davis K.A., Young E.D. (2000). Pharmacological evidence of inhibitory and disinhibitory neuronal circuits in the dorsal cochlear nucleus. *J. Neurophysiol.*; 8: 926–940
- Dean B, Scarr E, McLeod M. Changes in hippocampal GABA_A receptor subunit composition in bipolar 1 disorder. (2005). *Brain Res. Mol. Brain Res.*; 138: 145-155
- DeBello W.M., Feldman D.E., Knudsen E.I. (2001). Adaptive axonal remodeling in the midbrain auditory space map. *J. Neurosci.*; 21: 3161-3174
- Deeg KE. (2009). Synapse-specific homeostatic mechanisms in the hippocampus. *J. Neurophysiol.*; 101: 503-506. Review.
- Dehmel S., Cui Y.L., Shore S.E. (2008). Cross-modal interactions of auditory and somatic inputs in the brainstem and midbrain and their imbalance in tinnitus and deafness. *Am. J. Audiol.*; 17: S193-S209
- De Ribaupierre F. (1997). Acoustical information processing in the auditory thalamus and cerebral cortex. In: *The Central Auditory System*, edited by Ehret G. and Romand R. New York: Oxford, chapt. 5: 317-397

- Desai N.S., Rutherford L.C., Turrigiano G.G. (1999). Plasticity in the intrinsic excitability of cortical pyramidal neurons. *Nat. Neurosci.*; 2: 515-520
- Destexhe A., Paré D. (1999) Impact of network activity on the integrative properties of neocortical pyramidal neurons in vivo. *J. Neurophysiol.*; 81: 1531-1547
- DiGregorio D.A., Nusser Z., Silver R.A. (2002). Spillover of glutamate onto synaptic AMPA receptors enhances fast transmission at a cerebellar synapse. *Neuron*; 35: 521-533
- Dinner D.S. (1993). Posttraumatic epilepsy. In: *The treatment of epilepsy: principles* (Wyllie E, ed): 654-658. Philadelphia: Lea and Fibinger
- Ding J., Benson T.E., Voigt H.F. (1999). Acoustic and current-pulse responses of identified neurons in the dorsal cochlear nucleus of unanesthetized, decerebrate gerbils. *J. Neurophysiol.*; 82: 3434-3457
- Ding J, Voigt H.F. (1997). Intracellular Response Properties of Units in the Dorsal Cochlear Nucleus of Unanesthetized Decerebrate Gerbil. *J. Neurophysiol.*; 77: 2549-2572
- Dobie R.A. (2003). Depression and tinnitus. *Otolaryngol. Clin. North Am.*; 36: 383-388
- Dobie R.A., Sullivan M.D. (1998). Antidepressant drugs and tinnitus. In: Vernon, J.A. (Ed.), *Tinnitus, Treatment and Relief*. Allyn and Bacon, Boston, MA: 43-51
- Donatien P., Jeffery G. (2002). Correlation between rod photoreceptor numbers and levels of ocular pigmentation. *Invest. Ophthalmol. Vis. Sci.*; 43: 1198-1203
- Doucet J.R., Ross A.T., Gillespie M.B., Ryugo D.K. (1999). Glycine immunoreactivity of multipolar neurons in the ventral cochlear nucleus which project to the dorsal cochlear nucleus. *J. Comp. Neurol.*; 408: 515–531
- Doucet J.R., Ryugo D.K. (1997). Projections from the ventral cochlear nucleus to the dorsal cochlear nucleus in rats. *J. Comp. Neurol.*; 385: 245-264
- Dringen R., Pawlowski P., Hirrlinger J. (2005). Peroxide detoxification by brain cells. *J. Neurosci Res.* 79:157-165

- Duncan I., Lunn K.F., Moller J.R. (1992). The taiep rat: a myelin mutant with a putative oligodendrocyte microtubular abnormality. *J. Neurocytol.*; 21: 870-884.
- Ebert U., Ostwald J. (1992). Serotonin modulates auditory information processing in the cochlear nucleus of the rat. *Neurosci. Lett.*, 145: 51-54
- Echteler S.M. (1992). Developmental segregation in the afferent projections to mammalian auditory hair cells. *Proc. Natl. Acad. Sci. USA*; 89: 6324-6327
- Edeline J.M., Manunta Y., Nodal F.R., Bajo V.M.(1999). Do auditory responses recorded from awake animals reflect the anatomical parcellation of the auditory thalamus? *Hear. Res* 131: 135-152
- Eggermont J.J. (1998). Representation of spectral and temporal sound features in three cortical fields of the cat. Similarities outweigh differences. *J Neurophys.* 80: 2743-2764
- Eggermont J.J. (2003). Central tinnitus. *Auris. Nasus. Larynx*; 30: S7-S12
- Eggermont J.J., Kenmochi M. (1998). Salicylate and quinine selectively increase spontaneous firing rates in secondary auditory cortex. *Hear. Res.*; 117: 149-160
- Eggermont J.J., Komiya H. (2000). Moderate noise trauma in juvenile cats results in profound cortical topographic map changes in adulthood. *Hear. Res.*; 142: 89-101
- Eggermont J.J., Roberts, L.E. (2004). The neuroscience of tinnitus. Review. *Trends Neurosci.*; 27: 676-682
- Eggers E.D., Lukasiewicz P.D. (2006). Receptor and Transmitter Release Properties Set the Time Course of Retinal Inhibition. *J. Neurosci.*; 26: 9413-9425
- Ehrenberger K. (2005). Topical administration of Caroverine in somatic tinnitus treatment: proof-of-concept study. *Int. Tinnitus J.*; 11: 34-37
- Eisenman L.N., Kress G., Zorumski C.F., Mennerick S. (2006). A spontaneous tonic chloride conductance in solitary glutamatergic hippocampal neurons. *Brain Res.*; 1118: 66-74

- El-Badry M.M., Ding D.L., McFadden S.L., Eddins A.C. (2007). Physiological effects of auditory nerve myelinopathy in chinchillas. *Eur. J. Neurosci.*; 25: 1437-1446
- Elgoyhen A.B., Vetter D.E., Katz E., Rothlin C.V., Heinemann S.F., Boulter J. (2001). $\alpha 10$: a determinant of nicotinic cholinergic receptor function in mammalian vestibular and cochlear mechanosensory cells. *Proc. Natl. Acad. Sci. USA*; 98: 3501-3506
- Elverland H.H (1978). Ascending and intrinsic projections of the superior olivary complex in the cat. *Exp. Brain. Res.* 32: 117-134
- Ermilov S.A., Murdock D.R., El-Daye D., Brownell W.E., Anvari B. (2005). Effects of salicylate on plasma membrane mechanics. *J. Neurophysiol.*; 94: 2105-2110
- Estrada Sanchez A.M., Mejia-Toiber J., Massieu L. (2008). Excitotoxic neuronal death and the pathogenesis of Huntington's disease. *Arch. Med. Res.*; 39: 265-276
- Evans E.F., Borerwe T.A. (1982). Ototoxic effects of salicylates on the responses of single cochlear nerve fibres and on cochlear potentials. *Br. J. Audiol.*;16: 101-108
- Evans E.F., Nelson P.G. (1973). The responses of single neurones in the cochlear nucleus of the cat as a function of their location and the anaesthetic state. *Exp. Brain Res.*; 17: 402-427
- Farago A.F., Awatramani R.B., Dymecki S.M. (2006). Assembly of the brainstem cochlear nuclear complex is revealed by intersectional and subtractive genetic fate maps. *Neuron*; 50: 205-218
- Farrant M., Nusser Z. (2005). Variations on an inhibitory theme: phasic and tonic activation of GABA(A) receptors. *Nat. Rev. Neurosci.*; 6: 215-229
- Farris H.E., LeBlanc C.L., Goswami J., Ricci A.J. (2004). Probing the pore of the auditory hair cell mechanotransducer channel in turtle. *J. Physiol. (Lond.)*; 558: 769-792

- Feliciano, M. Saldaña E., Mugnaini E. (1995). Direct projections from the rat primary auditory neocortex to nucleus sagulum, paralemniscal regions, superior olivary complex and cochlear nuclei. *Aud. Neurosci.* 1: 287-308
- Felix D., Ehrenberger K. (1992). The efferent modulation of mammalian inner hair cell afferents. *Hear. Res.*; 64: 1-5
- Fekete D.M. Roullier E.M., Liberman M.C., Ryugo D.K. (1984). The central projections of intracellularly labelled auditory nerve fibers in cats. *Journal of Comparative Neurology* 229: 432-450.
- Feldman D.E. (2009). Synaptic mechanisms for plasticity in neocortex. *Annu. Rev. Neurosci.*; 32: 33-55.
- Fettiplace R., Fuchs P.A. (1999). Mechanisms of hair cell tuning. *Annu. Rev. Physiol.*; 61: 809-834
- Flecknell P.A., Mitchell M. (1984). Midazolam and fentanyl-fluanisone: assessment of anaesthetic effects in laboratory rodents and rabbits. *Lab. Anim.* 18: 143-146
- Forge A., Schacht J. (2000). Aminoglycoside antibiotics. *Audiol. Neuro-Otol.*; 5: 3-22
- Forsythe, I.D. Barnes-Davies M., Brew H.M. (1995). The calyx of Held: a model for transmission at mammalian glutamatergic synapses. In *Excitatory Amino Acids and Synaptic Transmission* (Wheal, H. And Thomson, A., eds.), Academic Press 133-144
- Forsythe I.D., Barnes-Davies M. (1993). The binaural auditory pathway: excitatory amino acid receptors mediate dual time course excitatory postsynaptic currents in the rat medial nucleus of the trapezoid body. *Proc. R. Soc. London Ser. B*; 251: 151-157
- Forsythe I.D., Westbrook G.L. (1988). Slow excitatory postsynaptic currents mediated by N-methyl-D-aspartate receptors on cultured mouse central neurones. *J. Physiol. (Lond.)*; 396: 515-533
- Francis H.W., Manis P.B. (2000). Effects of deafferentation on the electrophysiology of ventral cochlear nucleus neurons. *Hear. Res.*; 149: 91-105

- Fricker D., Miles R. (2000). EPSP amplification and the precision of spike timing in hippocampal neurons. *Neuron*; 28: 559-569
- Fridberger A., Flock A., Ulfendahl M., Flock B. (1998). Acoustic overstimulation increases outer hair cell Ca^{2+} concentrations and causes dynamic concentrations of the hearing organ. *Proc. Natl. Acad. Sci. USA*; 95: 7127-7132
- Friedland D.R., Eernisse R., Popper P. (2007). Potassium channel gene expression in the rat cochlear nucleus. *Hear. Res.*; 228: 31-43
- Friedland D.R., Los J.G., Ryugo D.K. (2006). A modified Golgi staining protocol for use in the human brain stem and cerebellum. *J. Neurosci. Methods*; 150: 90-95
- Friedland D.R., Popper P., Eernisse R., Cioffi J.A., (2006). Differentially expressed genes in the rat cochlear nucleus. *Neuroscience*; 142: 753-768
- Frisina R.D., Walton J.P., Karcich K.J. (1994). Dorsal cochlear nucleus single neurons can enhance temporal processing capabilities in background noise. *Exp. Brain Res.*; 102: 160-164
- Fuchs, P. A., Evans, M. G., Murrow, B. W. (1990). Calcium currents in hair cells isolated from the cochlea of the chick. *J. Physiol. (Lond.)*; 429: 553-568
- Fuchs J.L., Salazar E. (1998). Effects of whisker trimming on GABA (A) receptor binding in the barrel cortex of developing and adult rats. *J. Comp. Neurol.*; 395: 209-216
- Fujino K., Oertel D. (2003). Bidirectional synaptic plasticity in the cerebellum-like mammalian dorsal cochlear nucleus. *Proc. Natl. Acad. Sci. U S A*; 100: 265-270
- Funabiki K., Koyano K., Ohmori H. (1998). The role of GABAergic inputs for coincidence detection in the neurons of nucleus laminaris of the chick. *J. Physiol (Lond.)*; 508: 851-869
- Funfschilling U., Reichardt L.F. (2002). Cre-mediated recombination in rhombic lip derivatives. *Genesis*; 33: 160-169

- Galbraith, G.C., Bhuta, S.M., Choate, A.K., Kitahara, J.M., and Mullen, T.A., Jr. (1998). Brain stem frequency-following response to dichotic vowels during attention. *Neuroreport*; 9: 1889-1893
- Gale J.E., Ashmore J.F. (1997). An intrinsic frequency limit to the cochlear amplifier. *Nature*; 389: 63-66
- Gardner S.M., Trussell L.O., Oertel D. (1999). Time course and permeation of synaptic AMPA receptors in cochlear nuclear neurons correlate with input. *J. Neurosci.*; 19: 8721-8729
- Gardner S.M., Trussell L.O., Oertel D. (2001). Correlation of AMPA receptor subunit composition with synaptic input in the mammalian cochlear nuclei. *J. Neurosci.*; 21: 7428-7437
- Gates T.S., Weedman D.L., Pongstaporn T., Ryugo D.K. (1996). Immunocytochemical localization of glycine in a subset of cartwheel cells of the dorsal cochlear nucleus in rats. *Hear. Res.*; 96: 157-166
- Gauck V., Jaeger D. (2000). The control of rate and timing of spikes in the deep cerebellar nuclei by inhibition. *J. Neurosci.*; 20: 3006-3016
- Gauck V., Jaeger D. (2003). The contribution of NMDA and AMPA conductances to the control of spiking in neurons of the deep cerebellar nuclei. *J. Neurosci.*; 23: 8109-8118
- Geiger J.R.P., Melcher T., Koh D.S. (1995). Relative abundance of subunit mRNAs determines gating and Ca²⁺ permeability of AMPA receptors in principal neurons and interneurons in rat CNS. *Neuron*; 15: 193-204
- Geisler S., Heilmann H., Veh R.W. (2002). An optimized method for simultaneous demonstration of neurons and myelinated fiber tracts for delineation of individual trunco- and palliothalamic nuclei in the mammalian brain. *Histochem. Cell Biol.*; 117: 69-79
- Gerken G.M. (1996). Central tinnitus and lateral inhibition: an auditory brainstem model. *Hear. Res.*; 97: 75-83
- Gillessen T., Alzheimer C. (1997). Amplification of EPSPs by low Ni²⁺- and amiloride-sensitive Ca²⁺ channels in apical dendrites of rat CA1 pyramidal neurons. *J. Neurophysiol.*; 77: 1639-1643

- Gittins R., Harrison P.J. (2004). Neuronal density, size and shape in the human anterior cingulate cortex: a comparison of Nissl and NeuN staining. *Brain. Res. Bull.*; 63: 155-160
- Glendenning K.K., Hutson K.A., Nudo R.J., Masterton R.B. (1985). Acoustic chiasm II: Anatomical basis of binaurality in lateral superior olive of cat. *Comp. Neurol.*, 232: 261-285
- Goldberg J., Brown P. (1969). Response of binaural neurons of dog superior olivary complex to dichotic tonal stimuli: some physiological mechanisms of sound localization. *J. Neurophysiol.*; 32: 613- 636
- Goldberg J.M., Brownell W.E. (1973). Discharge characteristics of neurons in anteroventral and dorsal cochlear nuclei of cat. *Brain Res.*; 64: 35-54
- Golding, N.L. Jung H.Y., Mickus T., Spruston N. (1999). Dendritic calcium spike initiation and repolarization are controlled by distinct potassium channel subtypes in CA1 pyramidal neurons. *J. Neurosci.*; 19: 8789-8798
- Golding N.L., Oertel D. (1997). Physiological identification of the targets of cartwheel cells in the dorsal cochlear nucleus. *J. Neurophysiol.*; 78: 248-260
- Golding N.L. Robertson D. Oertel D. (1995). Recordings from slices indicate that octopus cells of the cochlear nucleus detect coincident firing of auditory nerve fibers with temporal precision. *J. Neurosci.*; 15, 3138-3153
- Goldstein S.A., Bockenhauer D., O'Kelly I., Zilberberg N. (2001). Potassium leak channels and the KCNK family of two-P-domain subunits. *Nat. Rev. Neurosci.*; 2: 175-184
- Goldstein B., Shulman A. (1996). Tinnitus stress test. In: Reich, G.E.,Vernon, J.A. (Eds.), *Proc. 5th Int. Tinnitus Sem., 1995*. Am. Tinnitus Assoc., Portland, OR; : 142-147
- Grandin T., Demotte O.D., Greenough W.T., Curtis S.E. (1988). Perfusion method forpreparing pig brain cortex for Golgi–Cox impregnation. *Stain. Technol.*; 63: 177-181.
- Green C.J. (1975). Neuroleptanalgesic drug combinations in the anaesthetic management of small laboratory animals. *Lab. Anim.*; 9: 161-178

- Green A.R., Hainsworth A.H., Jackson D.M. (2000). GABA potentiation: a logical pharmacological approach for the treatment of acute ischaemic stroke, *Neuropharmacol.*; 39: 1483-1494.
- Grothe B., Sanes D.H. (1994). Synaptic inhibition influences the temporal coding properties of medial superior olivary neurons: an in vitro study. *J. Neurosci.*; 14: 1701-1709,
- Guitton M.J., Caston J., Ruel J., Johnson R.M., Pujol R., Puel J.L. (2003). Salicylate induces tinnitus through activation of cochlear NMDA receptors. *J. Neurosci.*; 23: 3944-3952
- Gulledge A.T., Kampa B.M., Stuart G.J. (2005). Synaptic integration in dendritic trees. *J. Neurobiol.*; 64: 75-90. Review
- Gustavson K.H. (1956). The chemistry of tanning processes. New York, Academic Press
- Gutierrez A., Khan Z.U., De Blas A.L. (1996). Immunocytochemical localization of the alpha 6 subunit of the gamma-aminobutyric acidA receptor in the rat nervous system. *J. Comp. Neurol.*; 365: 504-510
- Haberham Z.L., van den Brom W.E., Venker-van Haagen A.J., de Groot H.N., Baumans V., Hellebrekers L.J. (2000). The rat vertex-middle latency auditory-evoked potential as indicator of anaesthetic depth: a comparison with evoked-reflex testing. *Brain. Res.*; 873: 287-290
- Hackney C.M., Osen K.K., Kolston J. (1990). Anatomy of the cochlear nuclear complex of guinea pig. *Anat. Embryol. (Berl.)* 182: 123-149
- Haenggeli C.A., Pongstaporn T., Doucet J.R., Ryugo D.K. (2005). Projections from the spinal trigeminal nucleus to the cochlear nucleus in the rat. *J. Comp. Neurol.*; 484: 191-205
- Hamann M., Rossi D.J., Attwell D. (2002). Tonic and spillover inhibition of granule cells control information flow through the cerebellar cortex. *Neuron*; 33: 625-633
- Hancock K.E., Voigt H.F. (2002). Intracellularly labeled fusiform cells in dorsal cochlear nucleus of the gerbil. I. Physiological response properties. *J. Neurophysiol.*; 87: 2505-2519

- Harvey R.J., Napper R.M.A. (1991). Quantitative studies on the mammalian cerebellum. *Prog. Neurobiol.*; 36: 437-463
- Hasan S.M., Joe M., Alshuaib W.B. (2007). Oxidative stress alters physiological and morphological neuronal properties. *Neurochem. Res.*; 32: 1169-1178
- Häusser M., Clark B.A. (1997). Tonic synaptic inhibition modulates neuronal output pattern and spatiotemporal synaptic integration. *Neuron*; 19: 665–678
- Hawkes R., Mascher C. (1995). The development of molecular compartmentation in the cerebellar cortex. *Acta. Anat.*; 151: 139-149
- Heck D., Borst A., Antkowiak B. (2003). Passive spatial and temporal integration of excitatory synaptic inputs in cerebellar Purkinje cells of young rats. *Neurosci. Lett.*; 341: 79-83
- Heffner H.E., Harrington I.A. (2002). Tinnitus in hamsters following exposure to intense sound. *Hear. Res.*; 170: 83-95
- Heffner H.E., Koay G., Heffner R.S. (2008). Comparison of behavioral and auditory brainstem response measures of threshold shift in rats exposed to loud sound. *J. Acoust. Soc. Am.*; 124: 1093-1104
- Hefft S., Jonas P. (2005). Asynchronous GABA release generates long-lasting inhibition at a hippocampal interneuron-principal neuron synapse. *Nat. Neurosci.*; 8: 1319-1328.
- Heiduschka P., Schraermeyer U. (2008). Comparison of visual function in pigmented and albino rats by electroretinography and visual evoked potentials. *Graefes Arch. Clin. Exp. Ophthalmol.*; 246: 1559-1573
- Heneghan C.P.H., Thornton C., Navaratnarajah M., Jones J.G. (1987). Effect of isoflurane on the auditory evoked response in man. *Br. J. Anaesth.*; 59: 277-282
- Held H. (1893). Die zentrale Gehörleitung. *Arch. Anat. Physiol. Anat. Abtheil.*; 17: 201-248
- Helfert R.H. , Schwartz I.R. (1986). Morphological evidence for the existence of multiple neuronal classes in the cat lateral superior olivary nucleus. *J. Comp. Neurol.*; 244: 533-549

- Herring B.E., Xie Z., Marks J.D., Fox A.P. (2009). Isoflurane inhibits the neurotransmitter release machinery. *J Neurophysiol.*;102: 1265-1273
- Hiel H., Erre J.P., Arousseau C., Bouali R., Dulon D., Aran J.M. (1993). Gentamicin uptake by cochlear hair cells precedes hearing impairment during chronic treatment. *Audiology*; 32: 78-87
- Higgs M.H., Slee S.J., Spain W.J. (2006). Diversity of gain modulation by noise in neocortical neurons: regulation by the slow afterhyperpolarization conductance. *J. Neurosci.*; 26: 8787-8799
- Hille B. (1992). *Ionic channels of excitable membranes*. Sinauer Associates, Sunderland, Mass., 2nd edition
- Hirota K., Lambert D.J. (1996). Ketamine: its mechanism(s) of action and unusual clinical uses. *Br. J. Anaesth.* 77: 441-444
- Hirsh, J. A., Oertel, D. (1988). Intrinsic properties of neurones in the dorsal cochlear nucleus of mice, in vitro *J. Physiol. (Lond.)*; 396: 535-548
- Hodgkin A., Huxley A. (1952). A quantitative description of membrane current and its application to conduction and excitation in nerve. *J. Physiol. (Lond.)*; 117: 500-544
- Hoffman D.A., Magee J.C., Colbert C. M., Johnston D. (1997). K⁺ channel regulation of signal propagation in dendrites of hippocampal pyramidal neurons. *Nature*; 387: 869-875
- Hollander H., Tietze J., Distel H. (1979). An autoradiographic study of the subcortical projections of the rabbit striate cortex in the adult and during postnatal development. *J. Comp. Neurol.*; 184: 783-794
- Hollmann M., Hartley M., Heinemann S. (1991). Ca²⁺ permeability of KA-AMPA-gated glutamate receptor channels depends on subunit composition. *Science*; 252: 851-853
- Holt A.G., Asako M., Duncan R.K., Lomax CA, Juiz JM, Altschuler RA. (2006). Deafness associated changes in expression of two-pore domain potassium channels in the rat cochlear nucleus. *Hear. Res.*; 216-217:146-153

- Huang C.M., Burkard R. (1986). Frequency sensitivities of auditory neurons in the cerebellum of the cat. *Brain Res.*; 371: 101-108
- House J.W., Brackmann D.E. (1981). Tinnitus: surgical treatment. *Ciba Found Symp.*; 85: 204-216
- Housley G.D., Ashmore J.F. (1991). Direct measurement of the action of acetylcholine on isolated outer hair cells of the guinea pig cochlea. *Proc. R. Soc. Lond. B. Biol. Sci.*; 244: 161-167
- Howard J., Hudspeth A.J. (1988). Compliance of the hair bundle associated with gating of mechano-electrical transduction channels in the bullfrog's saccular hair cell. *Neuron*; 1: 189-199
- Hsu W.H. (1981). Xylazine-induced depression and its antagonism by alpha adrenergic blocking agents. *J. Pharm. Exp. Ther.* 218: 188-192
- Hudspeth A.J. (1989). How the ear's works work. *Nature*; 341:397- 404
- Hudspeth A.J. (2005). How the ear's works work: mechano-electrical transduction and amplification by hair cells. *C. R. Biol.*; 328: 155-162. Review.
- Inoue M., Ates N., Vossen J.M., Coenen A.M. (1994). Effects of the neuroleptanalgesic fentanyl-fluanisone (Hypnorm) on spike-wave discharges in epileptic rats. *Pharmacol. Biochem. Behav.*; 48: 547-551
- Irie T., Fukui I., Ohmori H. (2006). Activation of GIRK channels by muscarinic receptors and group II metabotropic glutamate receptors suppresses Golgi cell activity in the cochlear nucleus of mice. *J Neurophysiol.* 96:2633-2644
- Isaacson J.S., Walmsley B. (1996). Amplitude and time course of spontaneous and evoked excitatory postsynaptic currents in bushy cells of the anteroventral cochlear nucleus. *J. Neurophysiol.*; 76: 1566-1571
- Ito M. (1984). *The Cerebellum and Neural Control*. Raven Press, New York
- Ito M. (2001). Cerebellar long-term depression: characterization, signal transduction, and functional roles. *Physiol. Rev.*; 81: 1143-1195
- Itoh K., Kamiya H., Mitani A., Yasui Y., Takada M., Mizuno N. (1987). Direct projections from the dorsal column nuclei and the spinal trigeminal nuclei to the cochlear nuclei in the cat. *Brain Res.*; 400: 145–150

- Iwasa H., Potsic W.P. (1982). Maturation change of early, middle, and late components of the auditory evoked responses in rats. *Otolaryngol. Head Neck Surg.*; 90: 95-102
- Jack J.J.B., Noble D., Tsien R.W. (1975) *Electric Current Flow in Excitable Cells*, Oxford University Press, Oxford; 218-223
- Jacquin M.F., Renehan W.E., Mooney R.D., Rhoades R.W. (1986). Structure-function relationships in rat medullary and cervical dorsal horns. I. Trigeminal primary afferents. *J. Neurophysiol.*; 55: 1153-1186
- Jacquin M.F., Stennett R.A., Renehan W.E., Rhoades R.W. (1988). Structure-function relationships in the rat brainstem subnucleus interpolaris: II. Low and high threshold trigeminal primary afferents *J. Comp. Neurol.*; 267: 107-130
- Jacquin M.F., Zahm D.S., Henderson T.A., Golden J.P., Johnson E.M., Renehan W.E., Klein B.G. (1993). Structure-function relationships in rat brainstem subnucleus interpolaris. X. Mechanisms underlying enlarged spared whisker projections after infraorbital nerve injury at birth. *J. Neurosci.*; 13: 2946-2964
- Jaeger D., Bower J.M. (1999). Synaptic control of spiking in cerebellar Purkinje cells: dynamic current clamp based on model conductances. *J. Neurosci.*; 19: 6090-6101
- Jagger D.J., Housley G.D. (2003). Membrane properties of type II spiral ganglion neurones identified in a neonatal rat cochlear slice. *J. Physiol. (Lond.)*; 552: 525-533
- Jain R., Shore S. (2006). External inferior colliculus integrates trigeminal and acoustic information: unit responses to trigeminal nucleus and acoustic stimulation in the guinea pig. *Neurosci. Lett.*; 395: 71-75
- Jannetta P.J., Moller M.B., Moller A.R., Sekhar L.N. (1986). Neurosurgical treatment of vertigo by microvascular decompression of the eighth cranial nerve. *Clin. Neurosurg.*; 33: 645-665
- Jeffress L. A. (1948). A place theory of sound localisation. *J. Comp. Physiol. and Psychol.*; 4: 35-39

- Johnstone B.M., Patuzzi R., Syka J., Sykova' E. (1989). Stimulus-related potassium changes in the organ of Corti of guinea-pig. *J. Physiol. (Lond.)*; 408: 77-92
- Jones E.G., Burton H. (1974). Cytoarchitecture and somatic sensory connectivity of thalamic nuclei other than the ventrobasal complex in the cat. *J. Comp. Neurol.*; 154: 395-432
- Jones D.R., Casseday J.H. (1979). Projections to laminae in dorsal cochlear nucleus in the tree shrew, *Tupaia glis*. *Brain Res.*; 160: 131-133
- Joris P.X., Carney L.H., Smith P.H., Yin T.C. (1994). Enhancement of neural synchronization in the anteroventral cochlear nucleus. I. Responses to tones at the characteristic frequency. *J. Neurophysiol.*; 71: 1022-1036
- Joris P.X., Smith P.H., Yin T.C.T. (1998). Coincidence detection in the auditory system: 50 years after Jeffress. *Neuron*; 21: 1235-1238
- Joris P.X., Smith P.H. (1998). Temporal and binaural properties in dorsal cochlear nucleus and its output tract. *J Neurosci.*; 18: 10157-10170
- Joris P., Yin T.C. (2007). A matter of time: internal delays in binaural processing. *Trends Neurosci.*; 30: 70-78
- Joseph A.W., Hyson R.L. (1993). Coincidence detection by binaural neurons in the chick brain stem. *J. Neurophysiol.*; 69: 1197-1211
- Kaczmarek L.K., Levitan I.B. (1987). *Neuromodulation: the biochemical control of neuronal excitability*. New York: Oxford UP
- Kadner A., Pressimone V.J., Lally B.E., Salm A.K., Berrebi A.S. (2006). Low-frequency hearing loss in prenatally stressed rats. *Neuroreport*; 17: 635-638
- Takehata S., Santos-Sacchi J. (1996). Effects of salicylate and lanthanides on outer hair cell motility and associated gating charge. *J. Neurosci.*; 16: 4881-4889
- Kalinec F., Holley M.C., Iwasa K.H., Lim D.J., Kachar A. (1992). A membrane-based force generation mechanism in auditory sensory cells. *Proc. Natl. Acad. Sci. U S A*; 89: 8671-8675

Kaltenbach J.A. (2007). The dorsal cochlear nucleus as a contributor to tinnitus: mechanisms underlying the induction of hyperactivity. *Prog. Brain. Res.*; 166: 89-106. Review.

Kaltenbach J.A., Afman C.E. (2000). Hyperactivity in the dorsal cochlear nucleus after intense sound exposure and its resemblance to tone-evoked activity: a physiological model for tinnitus *Hear. Res.*; 140: 165-72

Kaltenbach J.A., Godfrey D.A. (2008). Dorsal cochlear nucleus hyperactivity and tinnitus: are they related? *Am. J. Audiol.*; 17: S148-161. Review.

Kaltenbach J.A., Godfrey, D.A., Neumann J.B., McCaslin D.L., Afman C.E., Zhang J. (1998). Changes in spontaneous neural activity in the dorsal cochlear nucleus following exposure to intense sound: relation to threshold shift. *Hear. Res.*; 124: 78-84

Kaltenbach J.A., McCaslin D.L. (1996). Increases in spontaneous activity in the dorsal cochlear nucleus following exposure to high intensity sound: a possible neural correlate of tinnitus. *Audit. Neurosci.*; 3: 57-78

Kaltenbach J.A., Rachel J.D., Mathog T.A., Zhang J., Falzarano P.R., Lewandowski M. (2002). Cisplatin-induced hyperactivity in the dorsal cochlear nucleus and its relation to outer hair cell loss: relevance to tinnitus. *J. Neurophysiol.*; 88: 699-714

Kaltenbach J.A., Zacharek M.A., Zhang J., Frederick S. (2004). Activity in the dorsal cochlear nucleus of hamsters previously tested for tinnitus following intense tone exposure. *Neurosci. Lett.*; 355: 121-125

Kaltenbach J.A., Zhang J.S. (1998). Increases in spontaneous activity in the dorsal cochlear nucleus of the rat following exposure to high-intensity sound. *Neurosci. Lett.*; 250: 197-200

Kaltenbach J.A., Zhang J.S. (2004). *In vivo* optical imaging of tone-evoked activity in the dorsal cochlear nucleus with a voltage sensitive dye. *J. Neurosci. Res.*; 78: 908-917

Kaltenbach J.A., Zhang J.S. (2007). Intense sound-induced plasticity in the dorsal cochlear nucleus of rats: evidence for cholinergic receptor upregulation. *Hear. Res.*; 226: 232-243

- Kaltenbach J.A., Zhang J., Afman C.E. (2000). Plasticity of spontaneous neural activity in the dorsal cochlear nucleus after intense sound exposure. *Hear. Res.*; 147: 282-292
- Kane E.C. (1974). Synaptic organization in the dorsal cochlear nucleus of the cat: A light and electron microscopic study. *J. Comp. Neurol.*; 155: 301-330
- Kane E.S. (1977). Descending inputs to the cat dorsal cochlear nucleus: an electron microscopic study. *J. Neurocytol.*; 6: 583-605
- Kanjhan R., Balke C.L., Housley G.D., Bellingham M.C., Noakes P.G. (2004). Developmental expression of two-pore domain K⁺ channels, TASK-1 and TREK-1, in the rat cochlea. *Neuroreport*; 15: 437-441
- Kanold P.O., Manis P.B. (1999). Transient potassium currents regulate the discharge patterns of dorsal cochlear nucleus pyramidal cells. *J. Neurosci.*; 19: 2195-2208
- Kanold P.O., Manis P.B. (2005). Encoding the timing of inhibitory inputs. *J. Neurophysiol.*; 93: 2887-2897
- Kanold P.O., Young E.D. (2001a). Proprioceptive information from the pinna provides somatosensory input to cat dorsal cochlear nucleus. *J. Neurosci.*, 21: 7848-7858
- Kanold P.O., Young E.D., and Manis P.B. (2001b). Auditory-Somatosensory Interactions in the Dorsal Cochlear Nucleus. *Psychophysical and Physiological Advances in Hearing. Proceedings of the 12th International Symposium on Hearing.*
- Karschin, C., Dissmann, E., Stuhmer, W., Karschin, A. (1996). IRK(1–3) and GIRK(1–4) inwardly rectifying K⁺ channel mRNAs are differentially expressed in the adult rat brain. *J. Neurosci.*; 16: 3559-3570
- Karschin C., Wischmeyer E., Preisig-Muller R., Rajan S., Derst C., Grzeschik K.H., Daut, J., Karschin, A. (2001). Expression pattern in brain of TASK-1, TASK-3, and a tandem pore domain K(+) channel subunit, TASK-5, associated with the central auditory nervous system. *Mol. Cell Neurosci.*, 18: 632-648

- Kataoka Y., Ohmori H. (1994). Activation of glutamate receptors in response to membrane depolarization of hair cells isolated from chick cochlea. *J. Physiol.*; 477: 403-414
- Katz B. (1969). *The Release of Neural Transmitter Substances*, Liverpool University Press 5 Johnson.
- Kawahara Y., Tanonaka K., Daicho T., Nawa M., Oikawa R., Nasa Y., Takeo S. (2005). Preferable anesthetic conditions for echocardiographic determination of murine cardiac function. *J. Pharmacol. Sci.*; 99: 95-104
- Kelly J.B., Buckthrought A.D., Kidd S.A. (1998). Monaural and binaural response properties of single neurons in the rat's dorsal nucleus of the lateral lemniscus. *Hear. Res.*; 122: 25-40
- Keros S., Hablitz J.J. (2005). Subtype-specific GABA transporter antagonists synergistically modulate phasic and tonic GABA_A conductances in rat neocortex. *J. Neurophysiol.*; 94: 2073-2085
- Kevetter G.A., Perachio A.A. (1989). Projections from the sacculus to the cochlear nuclei in the Mongolian gerbil. *Brain. Behav. Evol.*; 34: 193-200
- Khaliq Z.M., Raman I.M. (2005). Axonal propagation of simple and complex spikes in cerebellar Purkinje neurons. *J. Neurosci.* 25: 454-463
- Kiang N.Y.S., Moxon E.C., Levine R.A. (1970). Auditory-nerve activity in cats with normal and abnormal cochleas. In: Wolstenholme, G.E.W., Knight, J. (Eds.), *Sensorineural hearing loss*, J and A Churchill, 241-273
- Kim J., Morest D.K., Bohne B.A. (1997). Degeneration of axons in the brainstem of the chinchilla after auditory overstimulation. *Hear. Res.*; 103: 169-191
- Kim Y., Trussell L.O. (2007). Ion channels generating complex spikes in cartwheel cells of the dorsal cochlear nucleus. *J. Neurophysiol.*; 97: 1705-17025
- Kim J., Tsien R.W. (2008). Synapse-specific adaptations to inactivity in hippocampal circuits achieve homeostatic gain control while dampening network reverberation. *Neuron*; 58: 925-937

- Kimitsuki T., Ohmori H, (1993). Dihydrostreptomycin modifies adaptation and blocks the mechano-electric transducer in chick cochlear hair cells. *Brain Res.*; 624: 143-150
- Kimura A., Donishi T., Okamoto K., Tamai Y. (2004). Efferent connections of “posterodorsal” auditory area in the rat cortex: implications for auditory spatial processing. *Neuroscience*; 128: 399-419
- King A.J., Hutchings M.E., Moore D.R., Blakemore C. (1988). Developmental plasticity in the visual and auditory representations in the mammalian superior colliculus. *Nature*; 332: 73-76
- Kiss A., Majorossy K., (1983). Neuron morphology and synaptic architecture in the medial superior olivary nucleus. Light- and electron microscope studies in the cat. *Exp. Brain. Res.*; 52: 315-327
- Klausberger T., Somogyi P. (2008). Neuronal diversity and temporal dynamics: the unity of hippocampal circuit operations. *Science*; 321: 53-57
- Klepper A., Herbert H. (1991). Distribution and origin of noradrenergic and serotonergic fibers in the cochlear nucleus and inferior colliculus of the rat. *Brain Res.*; 557: 190-201
- Knöpfel T., Grandes P. (2002). Metabotropic glutamate receptors in the cerebellum with a focus on their function in Purkinje cells. *Cerebellum*; 1: 19-26
- Knowlton B.J., Thompson J.K., Thompson R.F. (1993). Projections from the auditory cortex to the pontine nuclei in the rabbit. *Behav. Brain. Res.*; 56: 23-30
- Knudsen E.I., Brainard M.S. (1991). Visual instruction of the neural map of auditory space in the developing optic tectum. *Science*; 253: 85-87
- Kolston J., Osen K.K., Hackney C.M., Ottersen O.P., Storm-Mathisen J. (1992). An atlas of glycine- and GABA-like immunoreactivity and colocalization in the cochlear nuclear complex of the guinea pig. *Anat. Embryol. (Berl)*; 186: 443-465
- Komiya H., Eggermont J.J. (2000). Spontaneous firing activity of cortical neurons in adult cats with reorganized tonotopic map following pure-tone trauma. *Acta. Otolaryngol.*; 120: 750-756

- Konist T., Salt A.N., Hamrick P.E. (1982). Effects of exposure to noise on permeability to potassium of the endolymph-perilymph barrier in guinea pigs. *Acta. Otolaryngol.*; 94: 395-401
- Kopsch F. (1986). Erfahrungen über die Verwendung des Formaldehyds bei der Chromsilber-Imprägnation. *Anat Anz.*; 11: 727-729
- Kotak, V.C., Fujisawa, S., Lee, F.A., Karthikeyan, O., Aoki, C., Sanes, D.H. (2005). Hearing loss raises excitability in the auditory cortex. *J. Neurosci.*; 25: 3908-3918
- Kotak V.C., Korada S., Schwartz I.R., and Sanes D.H. (1998). A developmental shift from GABAergic to glycinergic transmission in the central auditory system. *J. Neurosci.*; 18: 4646-4655
- Kraus N., Bradlow A.R., Cheatham M.A., Cunningham J., King C.D., Koch D.B., Nicol T.G., McGee T.J., Stein L.K., Wright B.A. (2000). Consequences of neural asynchrony: a case of auditory neuropathy. *J. Assoc. Res. Otolaryngol.*; 1: 33-45
- Kraushaar U., Jonas P. (2000). Efficacy and stability of quantal GABA release at a hippocampal interneuron-principal neuron synapse. *J. Neurosci.*; 20: 5594-5607
- Krishnan A., Xu, Y., Gandour J., Cariani P. (2005). Encoding of pitch in the human brainstem is sensitive to language experience. *Brain Res. Cogn. Brain Res.*; 25: 161-168
- Kroese A.B.A., Das A., Hudspeth A.J. (1989). Blockage of the transduction channels of hair cells in the bullfrog's sacculus by aminoglycoside antibiotics. *Hear. Res.*; 37: 203-218
- Kros C.J., Ruppersberg J.P., Rüscher A. (1998). Expression of a potassium current in inner hair cells during development of hearing in mice. *Nature*; 394: 281-284
- Kudo M., Niimi K. (1980). Ascending projections of the inferior colliculus in the cat: an autoradiographic study. *J. Comp. Neurol.*; 191: 545-556

- Kuhse J., Betz H., Kirsch. J. (1995). The inhibitory glycine receptor: architecture, synaptic localization and molecular pathology of a postsynaptic ion-channel complex. *Curr. Opin. Neurobiol.*; 5: 318-323
- Kurata K., Nishida N., Tsukuda R., Suzuki T., Sato S., Tokuriki M. (1997). Frequency selectivity on aspirin-induced hearing loss in rats with auditory stimulus-induced conditioned suppression. *J Vet. Med. Sci.*; 59: 879-884
- Kuriyama H., Albin R. L., Altschuler R. A. (1993). Expression of NMDA-receptor messenger RNA in the rat cochlea. *Hear. Res.*; 69: 215-220
- Kushmerick C., Renden R., Gersdorff H. Von (2006). Physiological temperatures reduce the rate of vesicle pool depletion and short-term depression via an acceleration of vesicle recruitment. *J. Neurosci.*; 26: 1366-1377
- Kuwabara N., Zook J. M. (1992). Projection to the medial superior olive from the medial and lateral nuclei of the trapezoid body on rodents and bats. *J. Comp. Neurol.*; 324: 522-538
- Kuwada S., Fitzpatrick D.C., Batra R., Ostapoff E.M. (2006). Sensitivity to interaural time differences in the dorsal nucleus of the lateral lemniscus of the unanesthetized rabbit: comparison with other structures. *J. Neurophysiol.*; 95: 1309-1322
- Langguth B., Kleinjung T., Marienhagen J., Binder H., Sand P.G., Hajak G, Eichhammer P. (2007). Transcranial magnetic stimulation for the treatment of tinnitus: effects on cortical excitability. *B.M.C. Neurosci.*; 2: 8-45
- Layton M.G., Robertson D., Everett A.W., Mulders W.H., Yates G.K. (2005). Cellular localization of voltage-gated calcium channels and synaptic vesicle-associated proteins in the guinea pig cochlea. *J. Mol. Neurosci.*; 27: 225-244
- Leão R.N., Berntson A., Forsythe I.D., Walmsley B. (2004). Reduced low-voltage activated K^+ conductances and enhanced central excitability in a congenitally deaf (dn/dn) mouse. *J. Physiol. (Lond.)*; 559: 25-33
- Leão R.N., Naves M.M., Leão K.E., Walmsley B. (2006). Altered sodium currents in auditory neurons of congenitally deaf mice. *Eur. J. Neurosci.*; 24: 1137-1146

- Legg C.R., Mercier B., Glickstein M. (1989). Corticopontine projection in the rat: the distribution of labelled cortical cells after large injections of horseradish peroxidase in the pontine nuclei. *J. Comp. Neurol.*; 286: 427-441
- Lenn N.J., Reese T.S. (1966). The fine structure of nerve endings in the nucleus of the trapezoid body and the ventral cochlear nucleus. *Am. J. Anat.*; 118: 375-389
- Lesage F. (2003). Pharmacology of neuronal background potassium channels. *Neuropharmacology*; 44: 1-7
- Levine R.A. (1999). Somatic (craniocervical) tinnitus and the dorsal cochlear nucleus hypothesis. *Am. J. Otolaryngol.*; 20: 351-362
- Levine R. A., Abel M., Cheng H. (2003). Cross somatosensory-auditory interactions elicit or modulate tinnitus. *Exp. Brain Res.*; 153: 643-648
- Levine, R.A., Nam, E.C., Oron, Y., Melcher, J.R. (2007) Evidence for a tinnitus subgroup responsive to somatosensory based treatment modalities. *Prog. Brain. Res.*; 166: 195-207
- Liberman, M.C., Dodds, L.W., (1984a). Single neuron labeling and chronic cochlear pathology. II. Stereocilia damage and alterations of spontaneous discharge rates. *Hear. Res.*; 16: 43-53
- Liberman M.C., Dodds L.W. (1984b). Single-neuron labeling and chronic cochlear pathology. III. Stereocilia damage and alterations of threshold tuning curves. *Hear. Res.*; 16: 55-74
- Liberman, M. C. Gao J., He D.Z., Wu X., Jia S., Zuo J. (2002). Prestin is required for electromotility of the outer hair cell and for the cochlear amplifier. *Nature*; 419: 300-304
- Lin X., Chen S. (2000). Endogenously generated spontaneous spiking activities recorded from postnatal spiral ganglion neurons in vitro. *Brain. Res. Dev. Brain. Res.*; 119: 297-305
- Linden D.J., Connor J.A. (1991). Participation of postsynaptic PKC in cerebellar long-term depression in culture. *Science*; 254: 1656-1659

- Linke R. (1999). Differential projection patterns of superior and inferior collicular neurones onto posterior paralamina nuclei of the thalamus surrounding the medial geniculate body in the rat. *Eur. J. Neurosci.*; 11: 187-203
- Lipowsky, R. Gillessen T., Alzheimer C. (1996). Dendritic Na⁺ channels amplify EPSPs in hippocampal CA1 pyramidal cells. *J. Neurophysiol.*; 76: 2181-2191
- Lipski J., Park T.I., Li D., Lee S.C., Trevarton A.J., Chung K.K., Freestone P.S., Bai J.Z. (2006). Involvement of TRP-like channels in the acute ischemic response of hippocampal CA1 neurons in brain slices. *Brain Res.*; 1077: 187-199
- Lipton S.A. (2007). Pathologically-activated therapeutics for neuroprotection: mechanism of NMDA receptor block by memantine and S-nitrosylation, *Curr. Drug Targets*; 8: 621-632
- Liu S.Q.J., Cull-Candy S.G. (2000). Synaptic activity at calcium-permeable AMPA receptors induces a switch in receptor subtype. *Nature*; 405: 454-458
- Liu L.F., Palmer A.R., Wallace M.N. (2006). Phase-locked responses to pure tones in the inferior colliculus. *J. Neurophysiol.*; 95: 1926-1935
- Loeb M., Smith R.P. (1967). Relation of induced tinnitus to physical characteristics of the inducing stimuli. *J. Acoust. Soc. Am.*; 42: 453-455
- Loup F., Wieser H.G., Yonekawa Y., Aguzzi A., Fritschy J.M. (2000). Selective alterations in GABA_A receptor subtypes in human temporal lobe epilepsy. *J. Neurosci.*; 15: 20-24
- Lorente de No', R. (1933). Anatomy of the eighth nerve. The central projection of nerve endings of the internal ear. *Laryngoscope (St. Louis)*; 43: 1-38
- Lorente de No', R. (1981). *The Primary Acoustic Nuclei*, Raven Press, New York.
- Ma W.L., Hidaka H., May B.J. (2006). Spontaneous activity in the inferior colliculus of CBA/J mice after manipulations that induce tinnitus. *Hear. Res.*; 212: 9-2

- Magee J.C., Carruth M. (1999). Dendritic voltage-gated ion channels regulate the action potential firing mode of hippocampal CA1 pyramidal neurons. *J. Neurophysiol.*; 82: 1895-1901
- Magee J.C., Johnston D.A. (1997). Synaptically controlled, associative signal for Hebbian plasticity in hippocampal neurons. *Science*; 275: 209-213
- Magistretti J., Castellil., Forti L., D'Angelo E. (2006). Kinetic and functional analysis of transient, persistent and resurgent sodium currents in rat cerebellar granule cells *in situ*: an electrophysiological and modelling study *J. Physiol. (Lond.)*; 1: 83-106
- Magnusson A.K., Kapfer C., Grothe B., Koch U. (2005). Maturation of glycinergic inhibition in the gerbil medial superior olive after hearing onset. *J. Physiol. (Lond.)*; 568: 497-512
- Malmierca M.S., Merchan M.A., Henkel C.K., Oliver D.L. (2002). Direct projections from cochlear nuclear complex to auditory thalamus in the rat. *J. Neurosci.*; 22: 10891-10897
- Malosio M.L., Marqueze-Pouey B., Kuhse J., Betz H. (1991). Widespread expression of glycine receptor subunit mRNAs in the adult and developing rat brain. *EMBO J.*; 10: 2401-2409
- Manabe Y., Yoshida S., Saito H., Oka H. (1997). Effects of lidocaine on salicylate-induced discharge of neurons in the inferior colliculus of the guinea pig. *Hear. Res.*; 103: 192-198
- Manis, P.B. (1990). Membrane properties and discharge characteristics of guinea pig dorsal cochlear nucleus neurons studied in vitro. *J. Neurosci.*; 10: 2338-2351
- Manis P.B., Marx S.D. (1991). Outward currents in isolated ventral cochlear nucleus neurons. *J. Neurosci.*; 11: 2865-2880
- Manis P.B., Molitor S.C. (1996). N-methyl-D-aspartate receptors at parallel fiber synapses in the dorsal cochlear nucleus. *J. Neurophysiol.*; 76: 1639-1656
- Manis P.B., Spirou G.A., Wright D.D., Paydar S., Ryugo D.K. (1994). Physiology and morphology of complex spiking neurons in the guinea pig dorsal cochlear nucleus. *J. Comp. Neurol.*; 348: 261-276

- Marani E., Guldemond J.M., Adriolo P.J., Boon M.E., Kok L.P. (1987). The microwave Rio-Hortega technique: a 24 h method. *Histochem. J.*; 19: 658-664
- Marcaggi P., Billups D., Attwell D. (2003). The role of glial glutamate transporters in maintaining the independent operation of juvenile mouse cerebellar parallel fibre synapses. *J. Physiol.*; 552: 89-107
- Marcotti W., Van Netten S.M., Kros C.J. (2005). The aminoglycoside antibiotic dihydrostreptomycin rapidly enters mouse outer hair cells through the mechano-electrical transducer channels. *J. Physiol.*; 567: 505-521
- Marder E., Abbott L.F., Turrigiano G.G., Liu Z., Golowasch, J. (1996). Memory from the dynamics of intrinsic membrane currents. *Proc. Natl. Acad. Sci. USA*; 93: 13481-13486
- Markand O.N. (1994). Brainstem auditory evoked potentials. *J. Clin. Neurophysiol.*; 11: 319-342
- Markram H. and Sakmann B. (1994). Calcium transients in dendrites of neocortical neurons evoked by single subthreshold excitatory postsynaptic potentials via low-voltage- activated calcium channels. *Proc. Natl. Acad. Sci. USA*; 91: 5207-5211
- Marriage J., Barnes N.M. (1995). Is central hyperacusis a symptom of 5-hydroxytryptamine (5-HT) dysfunction? *J. Laryngol. Otol.*; 109: 915-921
- Maruyama A., Ohmori H. (2006). Fluorescent labeling of rat auditory brainstem circuits for synaptic and electrophysiological studies. *J. Neurosci. Methods*; 152: 163-172
- Maslany S., Crockett D.P.; Egger M.D. (1991). Somatotopic organization of the dorsal column nuclei in the rat: Transganglionic labeling with B-HRP and WGA-HRP. *Brain Res.*; 564: 56-65
- Matsubara A., Laake J.H., Davanger S., Usami S., Ottersen O.P. (1996). Organization of AMPA receptor subunits at a glutamate synapse: a quantitative immunogold analysis of hair cell synapses in the rat organ of Corti. *J. Neurosci.*; 16: 4457-4467

- Matthies C., Samii M. (1997). Management of vestibular schwannomas (acoustic neuromas): the value of neurophysiology for evaluation and prediction of auditory function in 420 cases. *Neurosurgery*; 40: 919-929
- May B.J. (2000). Role of the dorsal cochlear nucleus in the sound localization behavior of cats. *Hear. Res.*; 48: 74-87
- May P.J. (2005). The mammalian superior colliculus: laminar structure and connections. *Prog. Brain Res.*; 151: 321-378
- Mayer M., Westbrook G. L. Guthrie P. B. (1984). Voltage-dependent block by Mg^{2+} of NMDA responses in spinal cord neurones. *Nature*; 309: 261-263.
- Mathews G.C., Bolos-Sy A.M., Holland K.D., Isenberg K.E., Covey D.F., Ferrendelli J.A., Rothman S.M. (1994). Developmental alteration in GABAA receptor structure and physiological properties in cultured cerebellar granule neurons. *Neuron*; 13: 149-158
- Matzenbach B., Maulet Y., Sefton L., Courtier B., Avner P., Guenet J.L., Betz H. (1994). Structural analysis of mouse glycine receptor alpha subunit genes. Identification of a chromosomal localization of a novel variant. *J. Biol Chem.*; 269: 2607-2612
- Mburu P., Liu X.Z., Walsh J., Saw D., Jr, Cope M.J., Gibson F., Kendrick- Jones J., Steel K.P., Brown S.D. (1997). Mutation analysis of the mouse myosin VIIA deafness gene. *Genes Funct.*; 1: 191-203
- McAlpine D, Grothe B. (2003). Sound localization and delay lines--do mammals fit the model? *Trends Neurosci.*; 26: 347-350
- McAlpine D., Jiang D., Palmer A.R. (2001). A neural code for low-frequency sound localization in mammals. *Nat. Neurosci.*; 4: 396-401
- McBain C.J., Kauer J.A. (2009). Presynaptic plasticity: targeted control of inhibitory networks. *Curr Opin Neurobiol.* 4. (Epub ahead of print)
- McCue M.P., Guinan J.J. Jr. (1994). Acoustically responsive fibers in the vestibular nerve of the cat. *J. Neurosci.*; 14: 6058-6070
- McCue M.P., Guinan J.J. Jr. (1997). Sound-evoked activity in primary afferent neurons of a mammalian vestibular system. *Am. J. Otol.*; 18: 355-360

- Meinrenken C.J., Borst, J.G.G., Sakmann B. (2002). Calcium secretion coupling at calyx of Held governed by nonuniform channel-vesicle topography. *J. Neurosci.*; 22: 1648-1667
- Meldrum B. (1990). Protection against ischaemic neuronal damage by drugs acting on excitatory neurotransmission. *Cerebrovasc. Brain Metab. Rev.*; 2: 27-57
- Meng Z., Nie A. (2004). Effects of hydrogen peroxide on sodium current in acutely isolated rat hippocampal CA1 neurons. *Toxicol. Lett.*; 147: 45-52
- Middlebrooks J.C. (1992). Narrow-band sound localization related to external ear acoustics. *J. Acoust. Soc. Am.*; 92: 2607-2624
- Millar J.A., Barratt L., Southan A.P., Page K.M., Fyffe R.E, Robertson B., Mathie A. (2000). A functional role for the two-pore domain potassium channel TASK-1 in cerebellar granule neurons. *Proc. Natl. Acad. Sci. USA*; 97: 3614-3618
- Miller, J., Basbaum A.I. (1975). Topography of the projection of the body surface of the cat to cuneate and gracile nuclei. *Exp. Neurol.*; 49: 281-290
- Mitchell C.R., Creedon T.A. (1995). Psychophysical tuning curves in subjects with tinnitus suggest outer hair cell lesions. *Otolaryngol. Head Neck Surg.*; 113: 223-233
- Mitchell C.R., Ellingson R.M., Henry J.A., Fausti S.A. (2004). Use of auditory brainstem responses for the early detection of ototoxicity from aminoglycosides or chemotherapeutic drugs. *J. Rehabil. Res. Dev.*; 41: 373-382
- Moller A.R. (2001). Symptoms and signs caused by neural plasticity. *Neurol. Res.*; 23: 565-572
- Moller A.R. (2003). Pathophysiology of tinnitus. *Otolaryngol. Clin. North Am.*; 36: 249-266
- Moller M.B., Moller A.R., Jannetta P.J., Jho H.D. (1993). Vascular decompression surgery for severe tinnitus: selection criteria and results. *Laryngoscope*; 103: 421-427

- Molitor S.C., Manis P.B. (2003). Dendritic Ca²⁺ transients evoked by action potentials in rat dorsal cochlear nucleus pyramidal and cartwheel neurons. *J. Neurophysiol.*; 89: 2225-2237
- Monsivais P., Clark B.A., Roth A., Häusser M. (2005). Determinants of action potential propagation in cerebellar Purkinje cell axons. *J. Neurosci.*; 25: 464-472
- Moore K.A., Kohno T., Karchewski L.A., Scholz, J., Baba H., Woolf C.J., (2002). Partial peripheral nerve injury promotes a selective loss of GABAergic inhibition in the superficial dorsal horn of the spinal cord. *J. Neurosci.*; 22: 6724-6731
- Morest D.K. (1965). The lateral tegmental system of the midbrain and the medial geniculate body: study with Golgi and Nauta methods in cat. *J. Anat.*; 99: 611-634
- Morest D.K., Bohne B.A. (1983). Noise-induced degeneration in the brain and representation of inner and outer hair cells. *Hear. Res.*; 9: 145-151
- Morest D.K., Kim J., Potashner S.J., Bohne B.A. (1998). Long-term degeneration in the cochlear nerve and cochlear nucleus of the adult chinchilla following acoustic overstimulation. *Microsc. Res. Tech.*; 41: 205-216
- Morest D.K., Morest R.R. (1966). Perfusion-fixation of the brain with chromeosmium solutions for the rapid Golgi method. *Am. J. Anat.*; 118: 811-831
- Mugnaini E. (1985). GABA neurons in the superficial layers of the rat dorsal cochlear nucleus: light and electron microscopic immunocytochemistry. *J. Comp Neurol.*; 235: 61-81
- Mugnaini E., Dino M.R., Jaarsma D. (1997). The unipolar brush cells of the mammalian cerebellum and cochlear nucleus: cytology and microcircuitry. *Prog. Brain. Res.*; 114: 131-150
- Mugnaini E., Morgan J.I. (1987). The neuropeptide cerebellin is a marker for two similar neuronal circuits in rat brain. *Proc. Natl. Acad. Sci. USA.*; 84: 8692-8696
- Mugnaini E., Osen K.K., Dahl A.L., Friedrich V.L., Korte G. (1980a). Fine structure of granule cells and related interneurons (termed Golgi cells) in the cochlear nuclear complex of cat, rat and mouse. *J. Neurocytol.*; 9: 537-570

- Mugnaini E., Warr W.B., Osen K.K. (1980b). Distribution and light microscopic features of granule cells in the cochlear nuclei of cat, rat, and mouse. *J. Comp. Neurol.*; 191: 581-606
- Mühlickel W., Elbert T., Taub E., Flor H. (1998). Reorganization of auditory cortex in tinnitus. *Proc. Natl. Acad. Sci. USA*; 95: 10340-10343
- Muly S.M., Gross J.S. Potashner S.J. (2004). Noise trauma alters d-[3H]aspartate release and AMPA binding in chinchilla cochlear nucleus. *J. Neurosci. Res.*; 75: 585-596.
- Musacchia G., Sams M., Skoe E., Kraus N. (2007). Musicians have enhanced subcortical auditory and audiovisual processing of speech and music. *Proc. Natl. Acad. Sci. USA*; 104: 15894-15898.
- Musicant A.D., Chan J.C., Hind J.E. (1990). Direction-dependent spectral properties of cat external ear: new data and cross-species comparisons. *J. Acoust Soc. Am.*; 87: 757-781
- Nabekura J., Katsurabayashi S., Kakazu Y., Shibata S., Matsubara A., Jinno S., Mizoguchi Y., Sasaki A., Ishibashi H. (2004). Developmental switch from GABA to glycine release in single central synaptic terminals. *Nat. Neurosci.*; 7: 7-8
- Nakamura T., Barbara J.G., Nakamura K., Ross W.N. (1999). Synergistic release of Ca^{2+} from IP3-sensitive stores evoked by synaptic activation of mGluRs paired with backpropagating action potentials. *Neuron*; 24: 727-737
- Nakashima T., Teranishi M., Hibi T., Kobayashi M., Umemura M. (2000). Vestibular and cochlear toxicity of aminoglycosides – a review. *Acta. Otolaryngol.*; 120: 904-911
- Napper R.M., Harvey R.J. (1988). Number of parallel fiber synapses on an individual Purkinje cell in the cerebellum of the rat. *J. Comp. Neurol.*; 274: 168-177
- Neher E. (1992). Correction for liquid junction potentials in patch clamp experiments. *Methods Enzymol.*; 207: 123-131
- Neher E. (2006). A comparison between exocytic control mechanisms in adrenal chromaffin cells and a glutamatergic synapse. *Pflügers Arch.*; 453: 261-268

- Neher E., Sakaba T. (2008). Multiple roles of calcium ions in the regulation of neurotransmitter release. *Neuron*; 59: 861-872. Review
- Nelken I., Young E.D. (1994). Two separate inhibitory mechanisms shape the responses of the dorsal cochlear nucleus type VI units to narrowband and wideband stimuli. *J. Neurophysiol.*; 71: 2446-2462
- Neophytou S.I., Graham M., Williams J., Aspley S., Marsden C.A., Beckett S.R. (2000). Strain differences to the effects of aversive frequency ultrasound on behaviour and brain topography of c-fos expression in the rat. *Brain Res.*; 854: 158-164
- Neuert V., Verhey J.L., Winter I.M. (2005). Temporal representation of the delay of iterated rippled noise in the dorsal cochlear nucleus. *J. Neurophysiol.*; 93: 2766-2776
- Nicolas-Puel C., Faulconbridge R. L., Guitton M., Puel J.-L., Mondain M., Uzie A. (2002). Characteristics of tinnitus and etiology of associated hearing loss: a study of 123 patients. *Int. Tinnitus J.* 8: 37-44
- Nichols C.G., Lopatin A.N. (1997). Inward rectifier potassium channels. *Annu. Rev. Physiol.*; 59: 171-191
- Niedzielski A.S., Wenthold R.J. (1995). Expression of AMPA, kainate and NMDA receptors subunits in cochlear and vestibular ganglia. *J. Neurosci.*; 15: 2338-2353
- Nixon P.D. (2003). The role of the cerebellum in preparing responses to predictable sensory events. *Cerebellum*; 2: 114-122. Review.
- Nixon P.D., Passingham R.E. (2001). Predicting sensory events. The role of the cerebellum in motor learning. *Exp. Brain. Res.*; 138: 251-257
- Nodar R.H. (1996). C.A.P.P.E' a strategy for counseling tinnitus patients. *Int. Tinnitus J.*; 2: 111-113
- Norena A.J., Eggermont J.J. (2003). Changes in spontaneous neural activity immediately after an acoustic trauma: implications for neural correlates of tinnitus. *Hear. Res.*; 183: 137-153

- Nowak L., Bregestovski P., Ascher P., Herbet A., Prochiantz A. (1984). Magnesium gates glutamate-activated channels in mouse central neurones. *Nature*; 307: 462-465
- Nowak L.G., Sanchez-Vives M.V., McCormick D.A. (1997). Influence of low and high frequency inputs on spike timing in visual cortical neurons. *Cereb. Cortex*; 7: 487-501
- Nuwer M.R. (1986). Brainstem auditory monitoring and related techniques. In: Nuwer MR, ed. *Evoked potential monitoring in the operating room*. New York: Raven Press; 158-161
- Ochi K., Kinoshita H., Kenmochi M., Nishino H. and Ohashi T. (2003). Zinc deficiency and tinnitus. *Auris Nasus Larynx*; 30: 25-28
- Oertel D. (1983). Synaptic responses and electrical properties of cells in brain slices of the mouse anteroventral cochlear nucleus. *J. Neurosci.*; 3: 2043-2053
- Oertel D., Wickesberg R.E.(1993). Glycinergic inhibition in the cochlear nuclei: evidence for tuberculoventral neurons being glycinergic. In: *The Mammalian Cochlear Nuclei: Organization and Function*. edited by M. A. Merchan, J. M. Juiz, D. A. Godfrey, and E. Mugnaini, New York: Plenum: 225-237
- Oertel D.,Wickesberg R.E. (2002). Ascending pathways through ventral nuclei of the lateral lemniscus and their possible role in pattern recognition in natural sounds. In: *Integrative Functions in the Mammalian Auditory Pathway*, edited by Oertel D, Popper AN, and Fay RR. New York: Springer: 207-237
- Oertel D., Wu S.H. (1989). Morphology and physiology of cells in slice preparations of the dorsal cochlear nucleus of mice. *J. Comp. Neurol.*; 283: 228-247
- Oertel D., Wu S.H., Garb M. W., Dizack C. (1990). Morphology and physiology of cells in slice preparations of the posteroventral cochlear nucleus of mice. *J. Comp. Neurol.*; 295: 136-154
- Oertel D., Young E.D. (2004). What's a cerebellar circuit doing in the auditory system? *Trends Neurosci.*; 27: 104-110
- Ohlrogge M., Doucet J.R., Ryugo D.K. (2001). Projections of the pontine nuclei to the cochlear nucleus in rats. *J. Comp. Neurol.*; 436: 290-303

- Ohmori, H. (1984). Studies of ionic currents in the isolated vestibular hair cell of the chick. *J. Physiol. (Lond.)*; 350: 561-581
- Ohmori H. (1985). Mechano-electrical transduction currents in isolated vestibular hair cells of the chick. *J. Physiol. (Lond.)*; 359: 189-217
- Okada M., Onodera K., Van Renterghem C., Sieghart W., Takahashi T. (2000). Functional correlation of GABA_A receptor subunits expression with the properties of IPSCs in the developing thalamus. *J. Neurosci.*; 20: 2202–2208
- Oliver D.L. (1984). Dorsal cochlear nucleus projections to the inferior colliculus in the cat: a light electron microscopic study. *J. Comp. Neurol.*; 224: 155-172
- Oliver D.L., Hall W.C. (1978). The medial geniculate body of the tree shrew, *Tupaia glis*. II. Connections with the neocortex. *J. Comp. Neurol.*; 182: 459-493
- Oliver D., He D.Z.Z., Klocker N., Ludwig J., Schulte U., Waldegger S., Ruppertsberg J.P., Dallos P., Fakler B. (2001). Intracellular anions as the voltage sensor of prestin, the outer hair cell motor protein. *Science*; 292: 2340-2343
- Osen K.K. (1969). Cytoarchitecture of the cochlear nuclei in the cat. *J. Comp. Neurol.*; 136: 453-484
- Osen K.K. (1970). Course and termination of the primary afferents in the cochlear nuclei of the cat. An experimental anatomical study. *Arch. Ital. Biol.*; 108: 21-51
- Osen K.K., Ottersen O.P., Storm-Mathisen J. (1990). Colocalization of glycinelike and GABA-like immunoreactivities: a semiquantitative study of individual neurons in the dorsal cochlear nucleus. In: Ottersen OP, Storm-Mathisen J, editors. *Glycine neurotransmission*. Chichester, UK: John Wiley & Sons; 417-451
- Otis T.S., Kavanaugh M.P., Jahr C.E. (1997). Postsynaptic glutamate transport at the climbing fiber-Purkinje cell synapse. *Science*; 277: 1515-1518
- Oviedo H., Reyes A.D. (2002). Boosting of neuronal firing evoked with asynchronous and synchronous inputs to the dendrite. *Nat. Neurosci.*; 5: 261-266

- Pál B., Pór A., Szucs G., Kovács I., Rusznák Z. (2003). HCN channels contribute to the intrinsic activity of cochlear pyramidal cells. *Cell. Mol. Life. Sci.*; 60: 2189-2199
- Palay S.L., Chan-Palay V. (1974). *Cerebellar Cortex, Cytology, and Organization*. New York: Springer-Verlag.
- Palmer A.R., King A.J. (1982). The representation of auditory space in the mammalian superior colliculus. *Nature*; 299: 248-249
- Parham K., Sun X.M., Kim D.O. (2001). Noninvasive assessment of auditory function in mice: auditory brainstem response and distortion product otoacoustic emissions. In: Willot JP (ed) *Handbook of Mouse Auditory Research: From Behavior to Molecular Biology*. CRC Press, New York, 37–58
- Paolini A.G., FitzGerald J.V., Burkitt A.N., Clark G.M. (2001). Temporal processing from the auditory nerve to the medial nucleus of the trapezoid body in the rat. *Hear. Res.*; 159: 101-116
- Parham K., Kim D.O. (1992). Analysis of temporal discharge characteristics of dorsal cochlear nucleus neurons of unanesthetized decerebrate cats. *J. Neurophysiol.*; 67: 1247-1263
- Pasternak J.F., Woolsey T.A. (1975). On the “selectivity” of the Golgi–Cox method. *J. Comp. Neurol.*; 160: 307-312
- Patel A.J., Honore´ E. (2001). Properties and modulation of mammalian 2P domain K channels. *Trends Neurosci.*; 24: 339-346
- Patuzzi R, Rajan R. (1992). Additivity of threshold elevations produced by disruption of outer hair cell function. *Hear. Res.*; 60: 165-177
- Patuzzi R.B., Yates G.K., Johnstone B.M. (1989) The origin of low frequency microphonic in the first cochlear turn of guinea pig. *Hear. Res.*; 39: 177-188
- Pecka M., Brand A., Behrend O., Grothe B. (2008). Interaural time difference processing in the mammalian medial superior olive: the role of glycinergic inhibition. *J. Neurosci.*; 28: 6914-6925

- Perez R., Freeman S., Sohmer H. (2004). Effect of an initial noise induced hearing loss on subsequent noise induced hearing loss. *Hear. Res.*; 192: 101-106
- Petralia R.S., Rubio M.E., Wang Y.X., Wenthold R.J. (2000). Differential distribution of glutamate receptors in the cochlear nuclei. *Hear. Res.*; 147: 59-69
- Petralia R.S., Wang Y.X., Zhao H.M., Wenthold R.J. (1996). Ionotropic and metabotropic glutamate receptors show unique postsynaptic, presynaptic, and glial localizations in the dorsal cochlear nucleus. *J. Comp. Neurol.*; 372: 356-383
- Pfeiffer R. R. (1996). Classification of response patterns of spike discharges for units in the cochlear nucleus: tone-burst stimulation. *Exp. Brain Res.*; 1: 220-235
- Piccirillo J.F., Finnell J., Vlahiotis A., Chole R.A., Spitznagel E. Jr. (2007) Relief of idiopathic subjective tinnitus: is gabapentin effective? *Arch. Otolaryngol. Head Neck Surg.*; 133: 390-397
- Piechotta K., Weth F., Harvery R.J., Friauf E. (2001). Localization of rat glycine receptor $\alpha 1$ and $\alpha 2$ subunit transcripts in the developing auditory brainstem. *J. Comp. Neurol.*; 438: 336-352
- Pilati N., Barker M., Panteleimonitis S., Donga R., Hamann M. (2008). A rapid method combining Golgi and Nissl staining to study neuronal morphology and cytoarchitecture. *J. Histochem. Cytochem.*; 56: 539-550
- Plourde G., Villemure C. (1996). Comparison of the effects of enflurane/N₂O on the 40-Hz auditory steady-state response versus the auditory middle-latency response. *Anesth. Analg.*; 82: 75-83
- Potashner S.J., Suneja S.K., Benson C.G. (1997). Regulation of D-aspartate release and uptake in adult brain stem auditory nuclei after unilateral middle ear ossicle removal and cochlear ablation. *Exp. Neurol.*; 148: 222-235
- Pouille F., Scanziani M. (2001). Enforcement of temporal fidelity in pyramidal cells by somatic feed-forward inhibition. *Science*; 293: 1159-1163

Prescott S.A., De Koninck Y. (2003). Gain control of firing rate by shunting inhibition: roles of synaptic noise and dendritic saturation. *Proc. Natl. Acad. Sci. U S A*; 100: 2076-2081

Pritchard T.C., Alloway K.D. (1999). *Medical neuroscience*. First edition.

Puel J.L. (1995). Chemical synaptic transmission in the cochlea. *Prog. Neurobiol.* 47: 449-476

Puel J.L., Bobbin R.P., Fallon M. (1988). The active process is affected first by intense sound exposure. *Hear. Res.*; 37: 53-63

Pujol R., Rebillard, G., Puel J. -L., Lenoir M., Eybalin M., Recasens, M. (1991). Glutamate neurotoxicity in the cochlea: A possible consequence of ischaemic or anoxic conditions occurring in aging. *Acta Otolaringol. (Stockh.)*, suppl.; 476: 32-36.

Punke M.A., Licher T., Pongs O., Friederich P. (2003). Inhibition of human TREK-1 channels by bupivacaine. *Anesth. Analg.* 96: 1665-1673

Purves (1981). *Microelectrode, Methods for Intracellular Recording and Ionophoresis*. Academic Press 146

Redies H, Brandner S. (1991). Functional organization of the auditory thalamus in the guinea pig. *Exp. Brain Res.*; 86: 384-392

Reyes A.D., Rubel E.W., Spain W.J. (1996). *In vitro* analysis of optimal stimuli for phase-locking and time-delayed modulation of firing in avian nucleus laminaris neurons. *J. Neurosci.*; 16: 993-1007

Rhode W.S. (1999). Vertical cell responses to sound in cat dorsal cochlear nucleus. *J. Neurophysiol.*; 82: 1019-1032

Rhode W.S., Smith P.H. (1986a). Encoding timing and intensity in the ventral cochlear nucleus of the cat. *J. Neurophysiol.*; 56: 261-286

Rhode W.S., Smith P.H. (1986b). Physiological studies on neurons in the dorsal cochlear nucleus of cat. *J. Neurophysiol.*; 56: 287-307

Rhode W.S., Smith P.H., Oertel D. (1983). Physiological response properties of cells labelled intracellularly with horseradish peroxidase in cat dorsal cochlear nucleus. *J. Comp. Neurol.*; 213: 426-447

- Rice J.J., May B.J., Spirou G.A., Young E.D. (1992). Pinna-based spectral cues for sound localization in cat. *Hear. Res.*; 58: 132-152
- Roberts M.T., Bender K.J., Trussell L.O. (2008). Fidelity of complex spike-mediated synaptic transmission between inhibitory interneurons. *J. Neurosci.*; 28: 9440-9450
- Robertson D. (1983). Functional significance of dendritic swelling after loud sounds in the guinea pig cochlea. *Hear. Res.*; 9: 263-278
- Robertson D., Paki B. (2002). Role of L-type Ca^{2+} channels in transmitter release from mammalian inner hair cells. II. Single-neuron activity. *J. Neurophysiol.*; 87: 2734-2740
- Rose J.E., Galambos R., Hughes J. R. (1960). Organization of frequency sensitive neurons in the cochlear nuclear complex of the cat. In: *Neural Mechanisms of the Auditory and Vestibular Systems*, edited by G. L. Rasmussen and W. F. Windle. Springfield, IL: Thomas: 116-136
- Rossi P., De Filippi G., Armano S., Taglietti V., D'Angelo E. (1998). The weaver mutation causes a loss of inward rectifier current regulation in premigratory granule cells of the mouse cerebellum. *J. Neurosci.*; 18: 3537-3547
- Rossi D.J., Hamann M., (1998). Spillover-mediated transmission at inhibitory synapses promoted by high affinity $\alpha 6$ subunit GABA(A) receptors and glomerular geometry. *Neuron* ; 20: 783-795
- Rossi P., Mapelli L., Roggeri L., Gall D., de Kerchove d'Exaerde A., Schiffmann S.N., Taglietti V., D'Angelo E. (2006). Inhibition of constitutive inward rectifier currents in cerebellar granule cells by pharmacological and synaptic activation of GABA receptors. *Eur. J. Neurosci.*; 24: 419-432
- Rubinstein B. (1993). Tinnitus and craniomandibular disorders--is there a link? *Swed. Dent. J. Suppl.*; 95: 1-46
- Rubio M. (2004). Differential Distribution of Synaptic Endings Containing Glutamate, Glycine, and GABA in the Rat Dorsal Cochlear Nucleus. *J. Comp. Neurol.*; 477: 253-272
- Rubio M.E., Wenthold R.J. (1997). Glutamate receptors are selectively targeted to postsynaptic sites in neurons. *Neuron*; 18: 939-950

- Rudy B., McBain C.J. (2001). Kv3 channels: voltage-gated K⁺ channels designed for high-frequency repetitive firing. *Trends Neurosci.*; 24: 517-526
- Russell I.J., Schauf C. (1995). Salicylate ototoxicity: effects on the stiffness and electromotility of outer hair cells isolated from the guinea pig cochlea. *Audit. Neurosci.*; 1: 309-319
- Russo, N.M., Skoe, E., Trommer, B., Nicol, T., Zecker, S., Bradlow, A., and Kraus, N. (2008). Deficient brainstem encoding of pitch in children with Autism Spectrum Disorders. *Clin. Neurophysiol.*; 119: 1720-1731.
- Rusznák Z., Bakondi G., Pocsai K., Pór A., Kosztka L., Pál B., Nagy D., Szucs G. (2008). Voltage-gated potassium channel (Kv) subunits expressed in the rat cochlear nucleus. *J. Histochem. Cytochem.*; 56: 443-465
- Rusznák Z., Forsythe I.D., Brew H.M., Stanfield P.R. (1997). Membrane currents influencing action potential latency in granule neurons of the rat cochlear nucleus. *Eur. J. Neurosci.*; 9: 2348-2358
- Rutherford L.C., DeWan A., Lauer H.M., Turrigiano G.G. (1997). Brain-derived neurotrophic factor mediates the activity-dependent regulation of inhibition in neocortical cultures. *J. Neurosci.*; 17: 4527-4535
- Ryan A. F., Woolf N. K., Sharp F. R. (1982). Tonotopic organization in the central auditory pathway of the mongolian gerbil: a 2-deoxyglucose study. *J. Comp. Neurol.*; 207: 369-380
- Rybalko N., Syka J. (2001). Susceptibility to noise exposure during postnatal development in rats. *Hear. Res.*; 155: 32-40
- Ryugo D.K., Haenggeli C.A., Doucet J.R. (2003). Multimodal inputs to the granule cell domain of the cochlear nucleus. *Exp. Brain Res.*; 153: 477-485.
- Ryugo D.K., May S.K. (1993). The projections of intracellularly labeled auditory nerve fibers to the dorsal cochlear nucleus of cats. *J. Comp. Neurol.*; 329: 20-35
- Safieddine S., Eybalin M. I. (1992). Co-expression of NMDA and AMPA/kainate receptors mRNAs in cochlear neurons. *NeuroReport*; 3: 1145-1148

- Sahley T.L., Kalish R.B., Musiek F.E., Hoffman D.W. (1991). Effects of opioid drugs on auditory evoked potentials suggest a role of lateral olivocochlear dynorphins in auditory function. *Hear. Res.*; 55: 133-142
- Sahley T.L., Nodar R.H. (2001). A biochemical model of peripheral tinnitus. *Hear. Res.*; 152: 43-54
- Sahley T.L., Nodar R.H., Musiek F.E. (1999). Endogenous dynorphins: possible role in peripheral tinnitus. *Int. Tinnitus J.* 5: 76-91
- Saint-Marie R.L., Benson C.G., Ostapoff E.M., Morest D.K. (1991). Glycine immunoreactive projections from the dorsal to the anteroventral cochlear nucleus. *Hear. Res.*; 51: 11-28
- Sakaba T., Stein A., Jahn R., Neher, E. (2005). Distinct kinetic changes in neurotransmitter release after SNARE protein cleavage. *Science*; 309: 491-494
- Salazar A.M., Jabbari B., Vance S.C., Grafman J., Amin D., Dillon J.D. (1985) Epilepsy after penetrating head injury. I. Clinical correlates: a report of the Vietnam Head Injury Study. *Neurology*; 35: 1406-1414
- Salinas E., Thier P. (2000). Gain modulation: a major computational principle of the central nervous system. *Neuron*; 27: 15-21
- Salvi R.J., Ahroon W.A. (1983). Tinnitus and neural activity. *J. Speech Hear. Res.* 26: 629-632
- Salvi R.J., Hamernik R.P., Henderson D. (1979). Auditory nerve activity and cochlear morphology after noise exposure. *Arch. Otorhinolaryngol.*; 224: 111-116
- Salvi R.J., Henderson D., Hamernik R., Ahroon W.A. (1983). Neural correlates of sensorineural hearing loss. *Ear Hear.*; 4: 115-129
- Salvi R.J., Saunders S.S., Gratton M.A., Arehole S., Powers N. (1990). Enhanced evoked response amplitudes in the inferior colliculus of the chinchilla following acoustic trauma. *Hear. Res.* 50: 245-257
- Salvi R.J., Wang J., Ding D. (2000). Auditory plasticity and hyperactivity following cochlear damage. *Hear. Res.*; 147: 261-274

- Samson Y., Belin P., Thivard L., Boddaert N., Crozier S., Zilbovicius M. (2001). Auditory perception and language: functional imaging of speech sensitive auditory cortex. *Rev. Neurol. (Paris)*; 157: 837-846
- Samson J., Wiktorek-Smagur A., Politanski P., Rajkowska E., Pawlaczyk-Luszczynska M., Dudarewicz A., Sha S.H., Schacht J., Sliwinska-Kowalska M. (2008). Noise-induced time-dependent changes in oxidative stress in the mouse cochlea and attenuation by D- methionine. *Neuroscience*; 152: 146-150
- Sanes D.H. (1990). An in vitro analysis of sound localization mechanisms in the gerbil lateral superior olive. *J. Neurosci.*; 10: 3494-3506
- Sanes D.H., Rubel E.W. (1988). The ontogeny of inhibition and excitation in the gerbil lateral superior olive. *J. Neurosci.*; 8: 682-700
- Santarelli R., Arslan E., Carraro L., Conti G., Capello M., Plourde G. (2003). Effects of isoflurane on the auditory brainstem responses and middle latency responses of rats. *Acta Otolaryngol.*; 123: 176-181
- Saunders J. C. Dear S.P., Flock Å. (1986). Changes in stereocilia micromechanics following overstimulation in metabolically blocked hair cells. *Hear. Res.*; 24: 217-225
- Saunders J.C. Dear S.P., Schneider M. E. (1985). The anatomical consequences of acoustic injury: A review and tutorial. *J. Acoust. Sac. Am.*; 78: 833-860
- Schaette, R., Kempster, R. (2006). Development of tinnitus-related neuronal hyperactivity through homeostatic plasticity after hearing loss: a computational model. *Eur. J. Neurosci.*; 23: 3124-3138
- Schiller J. Schiller Y., Stuart G., Sakmann B. (1997). Calcium action potentials restricted to distal apical dendrites of rat neocortical pyramidal neurons. *J. Physiol. (Lond)*; 505: 605-616
- Schmahmann J.D., Pandya D.N. (1997). The cerebrocerebellar system. *Int. Rev. Neurobiol.*; 41: 31-60
- Schmiedt R.A., Zwislocki J.J., Hamernik R.P. (1980). Effects of hair cell lesions on responses of cochlear nerve fibers. I. Lesions, tuning curves, two-tone

inhibition and responses to trapezoidal-wavepatterns. *J. Neurophysiol.*; 43: 1367-1389

Schneggenburger R., Forsythe I.D. (2006). The calyx of Held. *Cell Tissue Res.*; 326: 311-337

Schneggenburger R., Sakaba T., Neher E. (2002). Vesicle pools and short-term synaptic depression: lessons from a large synapse, *Trends Neurosci.*; 25: 206-212

Schofield B.R., Cant N.B. (1996). Origins and targets of commissural connections between the cochlear nuclei in guinea pigs. *J. Comp. Neurol.*, 375: 128-146

Schreiber S., Fellous J.M., Tiesinga P., Sejnowski T.J. (2004). Influence of ionic conductances on spike timing reliability of cortical neurons for suprathreshold rhythmic inputs. *J. Neurophysiol.* 91: 194-205

Schuerger R.J., Dino M.R., Liu Y.-B., Slater N.T., Mugnaini E. (1997). Light and electron microscopic identification of the axon terminals and postsynaptic targets of cerebellar unipolar brush cells. *Neurosci. Abstr.*; 23: 1830-1832

Schwarz C., Thier P. (1999). Binding of signals relevant for action: towards a hypothesis of the functional role of the pontine nuclei. *Trends Neurosci.*; 22: 443-451

Schwindt P.C., Crill W.E. (1995). Amplification of synaptic current by persistent sodium conductance in apical dendrite of neocortical neurons. *J. Neurophysiol.*; 74: 2220-2224

Seki S., Eggermont J.J. (2003). Changes in spontaneous Wring rate and neural synchrony in cat primary auditory cortex after localized tone induced hearing loss. *Hear. Res.*; 180: 28-38

Sekuler R., Sekuler A.B., Lau R. (1997). Sound alters visual motion perception. *Nature*; 385: 308

Semyanov A., Walker, M.C., Kullmann D.M., Silver R.A. (2004). Tonicly active GABA A receptors: modulating gain and maintaining the tone. *Trends Neurosci.*; 27: 262-269

- Shadlen M., and Newsome W. (1994). Noise, neural codes and cortical organization. *Curr. Opin. Neurobiol.* 4: 569–579
- Shadlen M.N., Newsome W.T. (1998). The variable discharge of cortical neurons: implications for connectivity, computation, and information coding. *J. Neurosci.*; 18: 3870-3896
- Shehata W.E., Brownell W.E., Dieler. (1991). Effects of salicylate on shape, electromotility and membrane characteristics of isolated outer hair cells from guinea pig cochlea. *Acta Otolaryngol.*; 111: 707-718
- Shigemoto R., Abe T., Nomura S., Nakanishi S., Hirano H. (1994). Antibodies inactivating mGluR1 metabotropic glutamate receptor block long-term depression in cultured Purkinje cells. *Neuron*; 12: 1245-1255
- Shinoda Y, Sugihara I, Wu HS, Sugiuchi Y. (2000). The entire trajectory of single climbing and mossy fibers in the cerebellar nuclei and cortex. *Prog. Brain. Res.*; 124: 173-186
- Shinoda Y., Sugiuchi Y., Futami T., Izawa R. (1992). Axon collaterals of mossy fibers from the pontine nucleus in the cerebellar dentate nucleus. *J. Neurophysiol.*; 67: 547-560
- Shneiderman A. Oliver D.L. (1989). EM autoradiographic study of the projections from the dorsal nucleus of the lateral lemniscus: a possible source of inhibitory inputs to the inferior colliculus. *J. Comp. Neurol.*; 286: 28-47
- Shneiderman A., Oliver D.L., Henkel C.K. (1988). Connections of the dorsal nucleus of the lateral lemniscus: an inhibitory parallel pathway in the ascending auditory system? *J. Comp. Neurol.*; 276:188-208
- Shore S.E. (2005). Multisensory integration in the dorsal cochlear nucleus: unit responses to acoustic and trigeminal ganglion stimulation. *Eur. J. Neurosci.*; 21: 3334-3348
- Shore S.E., El Kashlan H., Lu J. (2003). Effects of trigeminal ganglion stimulation on unit activity of ventral cochlear nucleus neurons. *Neuroscience*; 119: 1085-1101

- Shore S.E., Koehler S., Oldakowski M., Hughes L.F., Syed S. (2008). Dorsal cochlear nucleus responses to somatosensory stimulation are enhanced after noise-induced hearing loss. *Eur. J. Neurosci.*; 27: 155-168
- Shore S.E., Vass Z., Wys N.L., Altschuler R.A. (2000). Trigeminal ganglion innervates the auditory brainstem. *J. Comp. Neurol.*; 419: 271-285
- Shore S.E., Zhou J. (2006). Somatosensory influence on the cochlear nucleus and beyond. *Hear. Res.*; 216-217: 90-99. Review
- Siegel M., Marder E., Abbott L.F. (1994). Activity-dependent current distributions in model neurons. *Proc. Natl. Acad. Sci. USA*; 91: 11308-11312
- Silverstein, H. (1976). Transmeatal labyrinthectomy with and without cochleovestibular neuroectomy. *Laryngoscope* 86: 1777-1791
- Simpson J.J. and Davies W.E. (1999). Recent advances in the pharmacological treatment of tinnitus. *Trends Pharmacol. Sci.*; 20: 12-18
- Sincich L.C., Horton J.C., Sharpee T.O. (2009). Preserving information in neural transmission. *J. Neurosci.*; 29: 6207-6216
- Smith P.H., Joris P.X., Yin T.C. (1993). Projections of physiologically characterized spherical bushy cell axons from the cochlear nucleus of the cat: evidence for delay lines to the medial superior olive. *J. Comp. Neurol.*; 331: 245-260
- Smith A.J., Owens S., Forsythe I.D. (2000). Characterisation of inhibitory and excitatory postsynaptic currents of the rat medial superior olive. *J Physiol (Lond.)*; 529: 681-698
- Smith, P.H., Rhode, W.S. (1985). Electron microscopic features of physiologically characterized, HRP-labeled fusiform cells in the cat dorsal cochlear nucleus. *J. Comp. Neurol.*; 237: 127-143
- Smith P.H., Rhode W.S. (1989). Structural and functional properties distinguish two types of multipolar cells in the ventral cochlear nucleus. *J. Comp. Neurol.*; 282: 595-616
- Snyder K.V., Kriegstein A.M., Sachs F. (1999). A convenient electrode holder for glass pipettes to stabilize electrode potentials. *Pflügers Arch.* 438: 405-411

- Snyder R.L., Leake P.A. (1998). Intrinsic connections within and between cochlear nucleus subdivisions in cat. *J. Comp. Neurol.*; 278: 209-225
- Spangler K. M., Warr W. B. , Henkel C. K. (1985). The projections of the principal cells of the medial nucleus of the trapezoid body in the cat. *J. Comp. Neurol.*; 238: 249–262
- Spence C., Squire S. (2003). Multisensory integration: maintaining the perception of synchrony. *Curr. Biol.*; 13: R519- R 521
- Spirou G.A, Davis K.A., Nelken I, Young E.D. (1999). Spectral integration by type II interneurons in the dorsal cochlear nucleus. *J. Neurophysiol.*; 82: 1019-1032
- Spitzer M.W., Semple M.N. (1995). Neurons sensitive to interaural phase disparity in gerbil superior olive: diverse monaural and temporal response properties. *J. Neurophysiol.*; 73: 1668 -1690
- Spoendlin H. (1969). Innervation patterns in the organ of corti of the cat. *Acta Otolaryngol.*; 67: 239-254
- Spoendlin H. (1976). Anatomical changes following various noise exposure. In: Henderson D, Hamernik R, Dosaujk D, Mills J (eds) *The effect of noise on hearing - Critical issue*. Raven Press, New York.
- Stabler S.E., Palmer A.R., Winter I.M. (1996). Temporal and mean rate discharge patterns of single units in the dorsal cochlear nucleus of the anesthetized guinea pig. *J. Neurophysiol.*; 76: 1667-1688
- Starr A., Achor J.L. (1975). Auditory brain stem responses in neurological disease. *Arch. Neurol.*; 32: 761-768
- Stein J.F., Glickstein M. (1992). Role of the cerebellum in visual guidance of movement. *Physiol. Rev.*; 72: 967-1017
- Stern P., Edwards F.A., Sakmann B. (1992). Fast and slow components of unitary EPSCs on stellate cells elicited by focal stimulation in slices of rat visual cortex. *J. Physiol. (Lond.)*; 449: 247-278
- Storm J.F. (1988). Temporal integration by a slowly inactivating K⁺ current in hippocampal neurons. *Nature.*; 336: 379-381

- Stotler W.A. (1953). An experimental study of the cells and connections of the superior olivary complex of the cat. *J. Comp. Neurol.*; 98: 401-431
- Street S.E., Manis P.B. (2007). Action Potential Timing Precision in Dorsal Cochlear Nucleus Pyramidal Cells. *J. Neurophysiol.*; 97: 4162-4172
- Stypulkowski P.H. (1990). Mechanisms of salicylate ototoxicity. *Hear. Res.*; 46: 113-146
- Sun W., Zhang L., Lu J., Yang G., Landrie E., Salvi R. (2008). Noise exposure-induced enhancement of auditory cortex response and changes in gene expression. *Neuroscience*; 156: 374-380
- Suneja S.K., Potashner S.J., Benson C.G. (1998). Plastic changes in glycine and GABA release and uptake in adult brain stem auditory nuclei after unilateral middle ear ossicle removal and cochlear ablation. *Exp. Neurol.*; 151: 273-288
- Sutherland D.P., Masterton R.B., Glendenning K.K. (1998). Role of acoustic striae in hearing: reflexive responses to elevated sound-sources. *Behav. Brain. Res.*; 97: 1-12
- Swensen A.M., Bean B.P. (2003). Ionic mechanisms of burst firing in dissociated Purkinje neurons. *J. Neurosci.*; 23: 9650-9663
- Syka J. (2002). Plastic changes in the central auditory system after hearing loss, restoration of function, and during learning. *Physiol. Rev.*; 82: 601-636
- Syka J., Rybalko N., Popelár J. (1994). Enhancement of the auditory cortex evoked responses in awake guinea pigs after noise exposure. *Hear. Res.*; 78:158-168
- Szczepaniak W.S., Moller A.R. (1995). Evidence of decreased GABAergic influence on temporal integration in the inferior colliculus following acute noise exposure: a study of evoked potentials in the rat. *Neurosci. Lett.*; 196: 77-80
- Szczepaniak W.S., Moller A.R. (1996). Evidence of neuronal plasticity within the inferior colliculus after noise exposure: a study of evoked potentials in the rat. *Electroencephalogr. Clin. Neurophysiol.*; 100: 158-164

- Takahashi M., Kovalchuk Y., Attwell D. (1995). Pre and postsynaptic determinants of EPSC waveform at cerebellar climbing fibre and parallel fibre to Purkinje cell synapses. *J. Neurosci.*; 15: 5693-5702
- Takahashi T., Momiyama A., Hirai K., Hishinuma F., Akagi H. (1992). Functional correlation of fetal and adult forms of glycine receptors with developmental changes in inhibitory synaptic receptor channels. *Neuron*; 9: 1155-1161
- Takahashi M., Sarantis M., Attwell D. (1996). Postsynaptic glutamate uptake in rat cerebellar Purkinje cells. *J. Physiol. (Lond.)*; 497: 523-530
- Talley E.M., Lei Q., Sirois J.E., Bayliss D.A. (2000). TASK-1, a two-pore domain K channel, is modulated by multiple neurotransmitters in motoneurons. *Neuron*; 25: 399-410
- Talley E.M., Solorzano G., Lei Q., Kim D., Bayliss D.A. (2001). CNS distribution of members of the two-pore-domain (KCNK) potassium channel family. *J. Neurosci.*; 21: 7491-7505
- Tang A.H, Chai Z., Wang S.Q. (2007). Dark rearing alters the short-term synaptic plasticity in visual cortex. *Neurosci Lett.*; 422: 49-53
- Temmel AF, Kierner AC, Steurer M, Riedl S, Innitzer J. (1999). Hearing loss and tinnitus in acute acoustic trauma. *Wien Klin Wochenschr.*; 111: 891-893
- Thach W.T. (1967). Somatosensory receptive fields of single units in cat cerebellar cortex. *J. Neurophysiol.*; 30: 675-696
- Theopold H.M.(1985). Nimodipine (Bay e 9736) a new therapy concept in diseases of the inner ear? *Laryngol. Rhinol. Otol. (Stuttg)*; 64: 609-613
- Thomson A.M. (2000). Facilitation, augmentation and potentiation at central synapses. *Trends Neurosci.*; 23: 305-312. Review
- Thompson A.M., Moore K.R., Thompson G.C. (1994a). Distribution and origin of serotonergic afferents to guinea pig cochlear nucleus. *J. Comp. Neurol.*; 351: 104-116
- Thompson A.M., Moore K.R., Thompson G.C. (1995). Distribution and origin of serotonergic afferents to guinea pig cochlear nucleus. *J. Comp. Neurol.*, 351: 104-116

- Thompson G.C., Thompson A.M., Garrett K.M., Britton B.H. (1994b). Serotonin and serotonin receptors in the central auditory system. *Otolaryngol. Head Neck Surg.*; 110: 93-102
- Thompson A.M., Thompson G.C. (1987). Efferent projections from posteroventral cochlear nucleus to lateral superior olive in guinea pig. *Brain Res.*; 421: 382-386
- Thompson A.M., Thompson G.C. (1991). Projections from the posteroventral cochlear nucleus to the superior olivary complex in guinea pig: light and EM observations with the PHA-L method. *J Comp. Neurol.*; 311: 495-508
- Thompson A.M., Thompson G.C. (2001). Serotonin projection patterns to the cochlear nucleus. *Brain Res.*; 907: 195-207
- Tollin D.J., Yin T.C. (2003). Spectral cues explain illusory elevation effects with stereo sounds in cats. *J. Neurophysiol.*; 90: 525-530
- Topolnik L., Steriade M., Timofeev I. (2003). Partial cortical deafferentation promotes development of paroxysmal activity. *Cereb. Cortex* ;13: 883-893
- Trellakis S., Lautermann J., Lehnerdt G. (2007). Lidocaine: neurobiological targets and effects on the auditory system. *Prog. Brain Res.*; 166: 303-22
- Trotter Y., Celebrini S. (1999). Gaze direction controls response gain in primary visual-cortex neurons, *Nature*; 398: 239-242
- Trussell L.O. (1999). Synaptic mechanisms for coding timing in auditory neurons. *Annu. Rev. Physiol.*; 61: 477-496
- Tsuchitani C. (1997). Input from the medial nucleus of trapezoid body to an interaural level detector. *Hear. Res.*; 105: 211-224
- Tucker T., Fettiplace R. (1995). Confocal imaging of calcium microdomains and calcium extrusion in turtle hair cells. *Neuron*; 15: 1323-335
- Turner J.G., Brozoski T.J., Bauer C.A., Parrish J.L., Myers K., Hughes L.F., Caspary D.M. (2006). Gap detection deficits in rats with tinnitus: a potential novel screening tool. *Behav. Neurosci.*; 120: 188-195
- Turrigiano G.G. (1999). Homeostatic plasticity in neuronal networks: the more things change, the more they stay the same. *Trends Neurosci.*; 22: 221-227

- Turrigiano G., Abbott LF, Marder E. (1994). Activity-dependent changes in the intrinsic properties of cultured neurons. *Science*; 264: 974-977
- Turrigiano G.G., LeMasson G., Marder E. (1995). Selective regulation of current densities underlies spontaneous changes in the activity of cultured neurons. *J. Neurosci.*; 15: 3640-3652
- Turrigiano G.G., Leslie K.R., Desai N.S., Rutherford L.C., Nelson S.B. (1998). Activity-dependent scaling of quantal amplitude in neocortical neurons. *Nature*; 391: 892-896
- Tsuprun V., Santi P. (2002). Structure of outer hair cell stereocilia side and attachment links in the chinchilla cochlea. *J. Histochem. Cytochem.*; 50: 493-502
- Tzounopoulos T., Kim Y., Oertel D., Trussell L.O. (2004). Cell-specific, spike timing dependent plasticities in the dorsal cochlear nucleus. *Nat. Neurosci.*; 7: 719-725
- Tzounopoulos T., Kraus N. (2009). Learning to encode timing: mechanisms of plasticity in the auditory brainstem. *Neuron*; 62: 463-469. Review.
- Usunoff K.G., Marani E., Schoen J.H. (1997). The trigeminal system in man. *Adv. Anat. Embryol. Cell Biol.*; 136: 1-126. Review
- Vale C., Sanes D.H. (2002). The effect of bilateral deafness on excitatory and inhibitory synaptic strength in the inferior colliculus. *Eur. J. Neurosci.*, 16: 2394-2404
- Van der Loos H. (1956). combinaison de deux vieilles méthodes histologiques pour le système nerveux central. *M Schr. Psychiat. Neurol.*; 132: 330-334
- Voigt H.F., Young E.D. (1990). Cross-correlation analysis of inhibitory interactions in the dorsal cochlear nucleus. *J. Neurophysiol.*; 64: 1590-1610
- Von Gersdorff H., Borst J.G.G. (2002). Short-term plasticity at the calyx of Held. *Nat. Rev. Neurosci.*; 3: 53-64
- Voogd J., Jaarsma D., Marani E. (1996). The cerebellum: chemoarchitecture and anatomy. In: Swanson, LW, Bjorklund A, Hokfelt T, editors. *Handbook of chemical neuroanatomy*. New York: Elsevier Science B.V. 1-575

- Wallace M.N., Anderson L.A., Palmer A.R. (2007). Phase-locked responses to pure tones in the auditory thalamus. *J. Neurophysiol.*; 98: 1941-1952
- Waller H.J., Godfrey D.A. (1994). Functional characteristics of spontaneously active neurons in rat dorsal cochlear nucleus in vitro. *J. Neurophysiol.*; 71: 467-478
- Wang J., Ding D., Salvi R.J. (2002). Functional reorganization in chinchilla inferior colliculus associated with chronic and acute cochlear damage. *Hear. Res.*; 168: 238-249
- Wang G.H., Jiang Z.L., Fan X.J., Zhang L., Li X., Ke K.F. (2007). Neuroprotective effect of taurine against focal cerebral ischemia in rats possibly mediated by activation of both GABAA and glycine receptors. *Neuropharmacology*; 52: 1199-1209
- Warr W.B., Guinan J.J. Jr, White J.S. (1986). Organization of the efferent fibers: The lateral medial olivocochlear system. In: *Neurobiology of Hearing: The Cochlea*; 33-348
- Webster D.B., Trune D.R. (1982). Cochlear nuclear complex of mice. *Am. J. Anat.*, 163: 103-130
- Weedman D.L., Pongstaporn T., Ryugo D.K. (1996). Ultrastructural study of the granule cell domain of the cochlear nucleus in rats: Mossy fiber endings and their targets. *J. Comp. Neurol.* 369: 345-360
- Weedman D.L., Ryugo D.K. (1996). Projections from auditory cortex to the cochlear nucleus in rats: synapses on granule cell dendrites. *J. Comp. Neurol.*; 371: 311-324
- Weil D., Blanchard S., Kaplan J., Guilford P., Gibson F., Walsh J., Mburu P., Varela A., Levilliers J., Weston MD et al. (1995). Defective myosin VIIA gene responsible for Usher syndrome type 1B. *Nature*; 374: 60-61
- Weinberg R.J., Rustioni A. (1987). A cuneocochlear pathway in the rat. *Neuroscience*; 20: 209-219
- Weiss I.C., Di Iorio L., Feldon J., Domeney A.M. (2002). Strain differences in the isolation-induced effects on prepulse inhibition of the acoustic startle response and on locomotor activity. *Behav. Neurosci.*; 114: 364-373

- Wentholt R.J., Gulley R.L. (1977). Aspartic acid and glutamic acid levels in the cochlear nucleus after auditory nerve lesion. *Brain Res.*; 138: 111-123
- Wentholt R.J., Huie D., Altschuler R.A., Reeks K.A. (1987). Glycine immunoreactivity localized in the cochlear nucleus and superior olivary complex. *Neuroscience*; 22: 897-912
- Werner L, Brauer K. (1984). Neuron types in the rat dorsal lateral geniculate nucleus identified in Nissl and deimpregnated Golgi preparations. *J. Hirnforsch.*; 25: 121-127
- Werner L., Hedlich A., Koglin A. (1986). Classification of neurons in the visual cortex of the guinea pig (*Cavia porcellus*). A combined Golgi-Nissl study using deimpregnation technics. *J. Hirnforsch.* 27: 213-236
- Werner L., Winkelmann E., Koglin A., Naser J., Rodewohl H. (1989). A Golgi deimpregnation study of neurons in the rhesus monkey visual cortex (areas 17 and 18). *Anat. Embryol. (Berl)*; 180: 583-597
- Wersäll J., Bjorkroth B., Flock A., Lundquist P.G. (1973). Experiments on ototoxic effects of antibiotics. *Adv. Otorhinolaryngol.*; 20: 14-41
- Weyand T., G., Malpeli J.G. (1993). Responses of neurons in primary visual cortex are modulated by eye position. *J. Neurophysiol.*; 69: 2258-2260
- Wickesberg R.E., Oertel, D. (1988). Tonotopic projection from the dorsal to the anteroventral cochlear nucleus of mice. *J. Comp. Neurol.*; 268: 389-399
- Wickesberg R.E., Oertel D. (1990). Delayed, frequency-specific inhibition in the cochlear nuclei of mice: a mechanism for monaural echo suppression. *J. Neurosci.*; 10: 1762-1768
- Wiederhold ML. (1986). Physiology of the olivocochlear system. In: *Neurobiology of Hearing: The Cochlea*. Eds R. A. Altschuler, R. P. Bobbin and D. W. Hoffman. Raven Press: New York. 349-370
- Wiesendanger R., Wiesendanger M. (1982a). The corticopontine system in the rat. I. Mapping of corticopontine neurons. *J. Comp. Neurol.*; 208: 215-226
- Wiesendanger R., Wiesendanger M. (1982b). The corticopontine system in the rat. II. The projection pattern. *J. Comp. Neurol.*; 208: 227-238

- Wightman F.L., (1982). Psychoacoustic correlates of hearing loss. In:Hamernik, R.P., Henderson, D., Salvi, R.J. (Eds.), *New Perspectives on Noise-Induced Hearing Loss*, Raven Press, New York, 375-394.
- Willard F.H., Ryugo D.K. (1983). Anatomy of the central auditory system. In: *The Auditory Psychobiology of the Mouse* (1st ed.), edited by Willott JF. Springfield, IL: Charles C. Thomas.; 201-304
- Williams S.R., Christensen S.R., Stuart G.J., Häusser M. (2002). Membrane potential bistability is controlled by the hyperpolarization-activated current I(H) in rat cerebellar Purkinje neurons in vitro. *J. Physiol. (Lond.)*; 539: 469-483
- Williams S.R., Stuart, G.J. (2002). Dependence of EPSP efficacy on synapse location in neocortical pyramidal neurons. *Science* 295: 1907-1910
- Williams S.R., Stuart, G.J. (2003). Role of dendritic synapse location in the control of action potential output. *Trends in Neurosci.* 3: 147:154
- Willott J.F., Aitkin L.M., McFadden S.L. (1993). Plasticity of auditory cortex associated with sensorineural hearing loss in adult C57BL/6J mice. *J. Comp. Neurol.*; 329: 402-411
- Winkowski D.E., Knudsen E.I. (2006). Top-down gain control of the auditory space map by gaze control circuitry in the barn owl. *Nature*; 439: 336-339
- Winter I.M., Palmer A.R. (1995). Level dependence of cochlear nucleus onset unit response and facilitation by second tones or broadband noise. *J. Neurophysiol.*; 73: 141-159
- Witsell D.L., Hannley M.T., Stinnet S., Tucci D.L. (2007). Treatment of tinnitus with gabapentin: a pilot study. *Otol. Neurotol.*; 28: 11-15
- Wölfel, M., Lou, X.L., Schneggenburger, R. (2007). A mechanism intrinsic to the vesicle fusion machinery determines fast and slow transmitter release at a large CNS synapse. *J. Neurosci.*; 27: 3198–3210.
- Wölfel M., Schneggenburger R. (2003). Presynaptic capacitance measurements and Ca²⁺ uncaging reveal submillisecond exocytosis kinetics and characterize the Ca²⁺ sensitivity of vesicle pool depletion at a fast CNS synapse. *J. Neurosci.*; 23: 7059-7068

- Wolff A., Kunzle H. (1997). Cortical and medullary somatosensory projections to the cochlear nuclear complex in the hedgehog tenrec. *Neurosci. Lett.*; 221: 125-128
- Womack M., Khodakhah K. (2002). Active contribution of dendrites to the tonic and trimodal patterns of activity in cerebellar Purkinje neurons. *J. Neurosci.*; 22: 10603-10612
- Womack M.D., Khodakhah K. (2004). Dendritic control of spontaneous bursting in cerebellar Purkinje cells. *J. Neurosci.*; 24: 3511-3521
- Wong, P.C., Skoe, E., Russo, N.M., Dees, T., Kraus, N. (2007). Musical experience shapes human brainstem encoding of linguistic pitch patterns. *Nat. Neurosci.*; 10: 420-422
- Wouterlood, F.G., Mugnaini, E. (1984). Cartwheel neurons of the dorsal cochlear nucleus: a Golgi-electron microscopic study in rat. *J. Comp. Neurol.*; 227: 136-157
- Wouterlood, F.G., Mugnaini, E., Osen K.K., Dahl, A.L. (1984). Stellate neurons in rat dorsal cochlear nucleus studies with combined Golgi impregnation and electron microscopy: synaptic connections and mutual coupling by gap junctions. *J. Neurocytol.*; 13: 639-664
- Wright, D.D., Ryugo, D.K., (1996). Mossy fiber projections from the cuneate nucleus to the cochlear nucleus in the rat. *J. Comp. Neurol.*; 365:159-172
- Wu S.H., Kelly J.B. (1992). Binaural interaction in the lateral superior olive: time difference sensitivity studied in mouse brain slice. *J. Neurophysiol.*; 68: 1151-1159
- Yajima Y., Hayashi Y. (1989). Response properties and tonotopical organization in the dorsal cochlear nucleus in rat. *Exp. Brain Res.*; 75: 381-389
- Yang Y., Saint Marie R.L., Oliver D.L. (2005). Granule cells in the cochlear nucleus sensitive to sound activation detected by Fos protein expression. *Neuroscience*; 136: 865-882
- Yin T., Chan J. (1990). Interaural time sensitivity in medial superior olive of cat. *J. Neurophysiol.*; 64: 465-488

- Yin T.C., Carney L.H., Joris P.X. (1990). Interaural time sensitivity in the inferior colliculus of the albino cat. *J. Comp. Neurol.*; 295: 438-448
- Young, E.D. (1980). Identification of response properties of ascending axons from dorsal cochlear nucleus. *Brain Res.*; 200: 23-37
- Young E.D., Brownell W.E. (1976). Responses to tones and noise of single cells in dorsal cochlear nucleus of unanesthetized cats. *J. Neurophysiol.*; 39: 282-300
- Young E.D., Davis K.A. (2002). Circuitry and function of the dorsal cochlear nucleus. In *Integrative Functions in the Mammalian Auditory Pathway* (Oertel, D. et al., eds), Springer.160-206
- Young E.D., Fernandez C., Goldberg J.M. (1977). Responses of squirrel monkey vestibular neurons to audio-frequency sound and head vibration. *Acta Otolaryngol.*, 84: 352-360
- Young E.D., Nelken I., Conley R.A. (1995). Somatosensory effects on neurons in dorsal cochlear nucleus. *J. Neurophysiol.*; 73: 743-765
- Young E.D., Rice, J.J., Tong S.C. (1996). Effects of pinna position on head-related transfer functions in the cat. *J. Acoust. Soc. Am.*; 99: 3064-3076
- Yu J.J, Young E.D. (2000) Linear and nonlinear pathways of spectral information transmission in the cochlear nucleus. *Proc. Natl. Acad.Sci.USA*; 97: 11780-11876
- Zafra F., Giménez C. (2008). Glycine transporters and synaptic function. *IUBMB Life*; 60: 810-817. Review
- Zeng C., Nannapaneni N., Zhou J., Hughes L.F., Shore S. (2009). Cochlear damage changes the distribution of vesicular glutamate transporters associated with auditory and nonauditory inputs to the cochlear nucleus. *J. Neurosci.*; 29: 4210-4217
- Zeng F.G., Oba, S., Garde S., Sininger Y., Starr, A. (1999). Temporal and speech processing deficits in auditory neuropathy. *Neuroreport*; 10: 3429-3435

- Zenner H.P., Ernst A. (1993). Cochlear-motor, transduction and signal-transfer tinnitus: models for three types of cochlear tinnitus. *Eur. Arch. Otorhinolaryngol.*; 249: 447-454
- Zhao M., Wu S.H. (2001). Morphology and physiology of neurons in the ventral nucleus of the lateral lemniscus in rat brain slices. *J. Comp. Neurol.*; 433: 255-271
- Zhang J.S., Kaltenbach J.A. (1998). Increases in spontaneous activity in the dorsal cochlear nucleus of the rat following exposure to high-intensity sound. *Neurosci. Lett.*; 250: 197-200
- Zhang H., Kelly J.B. (2006). Responses of neurons in the rat's ventral nucleus of the lateral lemniscus to amplitude-modulated tones. *J. Neurophysiol.*, 96: 2905-2914
- Zhang S., Oertel D. (1993a). Giant cells of the dorsal cochlear nucleus of mice: intracellular recording in slices. *J. Neurophysiol.*; 69: 1308-1408
- Zhang S., Oertel D. (1993b). Tuberculoventral cells of the dorsal cochlear nucleus of mice: intracellular recordings in slices. *J. Neurophys.*; 69: 1409-1421
- Zhang S., Oertel D. (1993c). Cartwheel and superficial stellate cells of the dorsal cochlear nucleus of mice: intracellular recordings in slices. *J. Neurophysiol.*; 69: 1384-1397
- Zhang S., Oertel D. (1994). Neuronal circuits associated with the output of the dorsal cochlear nucleus through fusiform cells. *J. Neurophysiol.*; 71: 914-930
- Zhang S.Y., Robertson D., Yates G., Everett A. (1999). Role of L-type Ca^{2+} channels in transmitter release from mammalian inner hair cells. I. Gross sound-evoked potentials. *J. Neurophysiol.* 82: 3307-3315
- Zhang H., Weng S.J., Hutsler J.J. (2003). Does microwaving enhance the Golgi methods? A quantitative analysis of disparate staining patterns in the cerebral cortex. *J. Neurosci. Methods*; 124: 145-155
- Zheng J., Madison L.D., Oliver D., Fakler B., Dallos P. (2002). Prestin, the motor protein of outer hair cells. *Audiol. Neurootol.*; 7: 9-12

Zheng J., Shen W., He D.Z., Long K.B., Madison L.D., Dallos P. (2002). Prestin is the motor protein of cochlear outer hair cells. *Nature*; 405: 149-155

Zhou J., Nannapaneni N., Shore S. (2007). Vesicular glutamate transporters 1 and 2 are differentially associated with auditory nerve and spinal trigeminal inputs to the cochlear nucleus. *J. Comp. Neurol.*; 500: 777-787

Zhou J., Shore S.E. (2004). Projections from the trigeminal nuclear complex to the cochlear nuclei: A retrograde and anterograde tracing study in the guinea pig. *J. Neurosci. Res.*; 78: 901-907

Zhou J., Shore S. (2006) Convergence of spinal trigeminal and cochlear nucleus projections in the inferior colliculus of the guinea pig. *J. Comp. Neurol.*; 495: 100-112